

General Disclaimer

One or more of the Following Statements may affect this Document

- This document has been reproduced from the best copy furnished by the organizational source. It is being released in the interest of making available as much information as possible.
- This document may contain data, which exceeds the sheet parameters. It was furnished in this condition by the organizational source and is the best copy available.
- This document may contain tone-on-tone or color graphs, charts and/or pictures, which have been reproduced in black and white.
- This document is paginated as submitted by the original source.
- Portions of this document are not fully legible due to the historical nature of some of the material. However, it is the best reproduction available from the original submission.

**STATIC AND WIND TUNNEL NEAR FIELD/FAR FIELD
JET NOISE MEASUREMENTS FROM MODEL
SCALE SINGLE FLOW BASELINE AND
SUPPRESSOR NOZZLES**

VOLUME 2 - FORWARD SPEED EFFECTS

C. L. JAECK

Contract Report November 1976

(NASA-CR-137914) STATIC AND WIND TUNNEL
NEAR-FIELD/FAR FIELD JET NOISE MEASUREMENTS
FROM MODEL SCALE SINGLE-FLOW BASELINE AND
SUPPRESSOR NOZZLES. VOLUME 2: FORWARD
SPEED EFFECTS (Boeing Commercial Airplane

N77-17071

HC A16
MF A01

Unclas

G3/07 16253

Prepared Under Contract NAS2-8213

Boeing Commercial Airplane Company

P. O. Box 3707

Seattle, Washington 98124



National Aeronautics and
Space Administration

Ames Research Center

1. Report No. CR-137914	2. Government Accession No.	3. Recipient's Catalog No.	
4. Title and Subtitle Static and Wind Tunnel Near-Field/Far Field Jet Noise Measurements from Model Scale Single-Flow Baseline and Suppressor Nozzles. Volume 2: Forward Speed Effects		5. Report Date November 1976	6. Performing Organization Code D6-44121-2
		8. Performing Organization Report No.	
7. Author(s) Carl L. Jaeck		10. Work Unit No.	
9. Performing Organization Name and Address Boeing Commercial Airplane Company P.O. Box 3707 Seattle, Washington 98124		11. Contract or Grant No. NAS 2-8213	
		13. Type of Report and Period Covered Contract Report	
12. Sponsoring Agency Name and Address National Aeronautics and Space Administration Ames Research Center Moffett Field, California 94035		14. Sponsoring Agency Code	
15. Supplementary Notes NASA Project Manager, Adolph Atencio, Jr.			
16. Abstract <p>A model-scale flight effects test was conducted in the NASA-Ames 40 by 80 Foot Wind Tunnel to investigate the effect of aircraft forward speed on single-flow jet noise characteristics. The objectives of the test and subsequent analysis were to (1) determine apparent jet noise source location including effects of ambient velocity, (2) verify a technique for extrapolating near-field jet noise measurements into the far field, (3) determine flight effects in the near and far field for baseline and suppressor nozzles and (4) establish the wind tunnel as a means of accurately defining flight effects for model nozzles and full-scale engines.</p> <p>The models tested included a 15.24 cm baseline round convergent nozzle, a 20-lobe and annular nozzle with and without lined ejector shroud, and a 57-tube nozzle with a lined ejector shroud. Nozzle operating conditions covered jet velocities from 412 to 640 m/s at a total temperature of 844 K. Wind tunnel speeds were varied from near zero to 91.5 m/s.</p>			
17. Key Words (Suggested by Author(s)) Jet Noise Model Scale Suppressor Nozzles Flight Effects Wind Tunnel		18. Distribution Statement Unclassified--Unlimited	
19. Security Classif. (of this report) Unclassified	20. Security Classif. (of this page) Unclassified	21. No. of Pages 352	22. Price*

CONTENTS

SUMMARY.....	Page 1
INTRODUCTION.....	2
ABBREVIATIONS AND SYMBOLS.....	3
DESCRIPTION OF TEST PROGRAM.....	5
40-by 80-Foot Wind Tunnel and Test Installation.....	5
Burner Installation.....	5
Nozzle Descriptions.....	6
Flow Instrumentation.....	6
Acoustic Instrumentation.....	7
Test Procedure.....	8
Test Conditions.....	9
Data Reduction.....	9
Tunnel Acoustic Characteristics.....	10
Flow/Burner System Acoustic Characteristics.....	11
DATA ANALYSIS.....	12
Effect of Ambient Velocity on the Jet.....	12
Noise Source Locations and Extrapolation Procedure.....	12
15.24 cm RC Nozzle.....	14
Annular Nozzle.....	18
20-Lobe Nozzle.....	18
Annular and 20-Lobe Nozzles with Lined Ejector.....	19
57-Tube Nozzle with Lined Ejector.....	20
EFFECT OF FORWARD SPEED ON THE JET NOISE SUPPRESSION.....	
CHARACTERISTICS.....	22
CONCLUSIONS.....	24
REFERENCES.....	26

TABLES

No.		Page
1.	Annular Nozzle Dimensions	29
2.	Dimensions for 20-Lobe Nozzle	30
3.	Dimensions for 57-Tube Nozzle	31
4.	Model and Wind Tunnel Test Conditions	32

FIGURES

No.	Page
1. Test Installation	37
2. Nozzle Nacelle, Hot Flow "S" Duct and Burner Installation	38
3. Fixed Microphones and 15.2 m Traverse	39
4. 15.2 m Traverse with 1.5 and 3.0 m Sideline Arms	40
5. 3.6 and 15.2 m Traverse Systems	41
6. Lining, Flow and Microphone Installations	42
7. Absorption Coefficients for Acoustic Linings	43
8. Burner, "S" Duct and Flow System Schematic	44
9. Compressor/Flow System Characteristics	45
10. Flow System Characteristics	46
11. Viper/J-85 Compressor	47
12. Photographs of Baseline and Suppressor Nozzles	48
13. 57-Tube Nozzle Base and Ejector Lip Static Pressure Instrumentation	51
14. Comparison of Measured Hygrometer Relative Humidity with Calculated Values Based on Constant Specific Humidity	53
15. Microphone Installations	54
16. Comparison of Static Jet Noise Spectra Measured in the 40-by 80-Ft Wind Tunnel and the Boeing Large Anechoic (LTC) Chamber, 15.24 cm RC Nozzle, NPR = 1.44	55
17. 40-by 80-Ft Wind Tunnel Noise Floors	58
18. Narrow Band Jet Noise Spectra	62
19. Comparison of the Noise Spike Frequency with Calculated Jet Screech Frequency	67
20. Comparison of Measured 4 kHz 1/3-OBSPL Directivities from the 40 by 80 Tunnel and LTC with Jet Noise Predictions; 15.24 cm RC Nozzle	68
21. Centerline Velocity and Turbulence Intensity Distribution	69
22. Velocity and Turbulence Intensity Profiles at the Tip of the Potential Core	70
23. Calculated Peak Noise Source Locations Using the Lu/Berman Flow/Noise Analysis, 15.24 cm RC Nozzle	71
24. Coordinate System and Nomenclature	72
25. Peak Noise Source Locations and Noise Propagation Angles for the 15.24 cm RC Nozzle	73
26. Effect of Ambient Velocity on the Distributed Noise Source Locations for a 15.24 cm RC Nozzle	76
27. OASPL and 1/3-OBSPL Directivity Data for a 15.24 cm RC Nozzle Extrap- olated to a 3.05 m Sideline, NPR = 1.75, $V_A = 3$ m/s	79
28. OASPL and 1/3-OBSPL Directivity Data for a 15.24 cm RC Nozzle Extrap- olated to a 3.05 m Sideline, NPR = 1.75, $V_A = 46$ m/s	84
29. OASPL and 1/3-OBSPL Directivity Data for a 15.24 cm RC Nozzle Extrap- olated to a 3.05 m Sideline, NPR = 1.75, $V_A = 69$ m/s	89
30. OASPL Directivity and Jet Noise Spectra for a 15.24 cm RC Nozzle Extrap- olated to a 3.05 m Sideline, NPR = 2.25, $V_A = 0$ m/s	94
31. OASPL Directivity and Jet Noise Spectra for a 15.24 cm RC Nozzle Extrap- olated to a 3.05 m Sideline, NPR = 2.25, $V_A = 91.5$ m/s	99

FIGURES (Continued)

No.	Page
32. Comparison of Flight Effects Measured for a 15.24 cm RC Nozzle on a 0.6, 1.5 and 3.0 m Sideline Extrapolated to a 3.0 m Sideline.	104
33. Effect of Ambient Velocity on Subsonic Jet Noise Spectra of an RC Nozzle Referenced to the Static Case Where $V = V_j - V_A$; $T_T = 844K$, 3.0 m Sideline ..	122
34. Static Velocity Exponent for an RC Nozzle	127
35. Effect of Ambient Velocity on Jet Noise OASPL and 1/3-OBSPL Spectra for a 15.24 cm RC Nozzle, $NPR = 2.25$	128
36. Effect of Ambient Velocity on Jet Noise OASPL and 1/3-OBSPL Spectra for a 15.24 cm RC Nozzle, $NPR = 2.60$	133
37. 0.76 m RC Nozzle Flight Effects Based on 40 by 80 Tunnel Measurements, $V_j = 457$ m/s, $V_A = 68.6$ m/s	138
38. 0.76 m RC Nozzle Flight Effects Based on 40 by 80 Tunnel Measurements, $V_j = 500$ m/s, $V_A = 68.6$ m/s	140
39. 0.76 m RC Nozzle Flight Effects Based on 40 by 80 Tunnel Measurements, $V_j = 594$ m/s, $V_A = 68.6$ m/s	142
40. 0.76 m RC Nozzle Flight Effects Based on 40 by 80 Tunnel Measurements, $V_j = 640$ m/s, $V_A = 68.6$ m/s	144
41. Effect of Ambient Velocity on Shock-Cell Noise from an RC Nozzle	146
42. Variation of OASPL and PNL with Relative Velocity for an RC Nozzle	147
43. RC Nozzle Flight Velocity Exponent Based on 40 by 80 Tunnel Data	151
44. Comparison of Flight Effects on OASPL Measured in the 40 by 80 Ft Wind Tunnel with F-86 Taxi-by Results.	152
45. Peak Noise Source Locations and Noise Propagation Angles for the Annular Nozzle.	153
46. Effect of Ambient Velocity on the Distributed Noise Source Locations for an Annular Nozzle	157
47. OASPL Directivity and Jet Noise Spectra for an Annular Nozzle Extrapolated to a 3.0 m Sideline, $NPR = 1.75$, $V_A = 0$ m/s	162
48. OASPL Directivity and Jet Noise Spectra for an Annular Nozzle Extrapolated to a 3.0 m Sideline, $NPR = 1.75$, $V_A = 68.5$ m/s.	167
49. Effect of Ambient Velocity on Jet Noise OASPL and 1/3-OBSPL Spectra for an Annular Nozzle, $NPR = 1.75$	172
50. Effect of Ambient Velocity on Jet Noise OASPL and 1/3-OBSPL Spectra for and Annular Nozzle, $NPR = 2.25$	177
51. Effect of Ambient Velocity on Subsonic Jet Noise Spectra of an Annular Nozzle Referenced to the Static Case Where $V = V_j - V_A$, $T_T = 844K$, 3.0 m Sideline	182
52. Static Velocity Exponent for an Annular Nozzle	184
53. Flight Effects on OASPL of an Annular Nozzle, $NPR = 1.75$, $V_j = 503$ m/s	185
54. Flight Effects on OASPL of an Annular Nozzle, $NPR = 2.25$, $V_j = 594$ m/s	187
55. Flight Effects on PNL of an Annular Nozzle, $NPR = 1.75$, $V_j = 503$ m/s	189
56. Flight Effects on PNL of an Annular Nozzle, $NPR = 2.25$, $V_j = 594$ m/s	191
57. Peak Noise Source Locations and Noise Propagation Angles for the Bare 20-Lobe Nozzle.	193

FIGURES (Continued)

No.	Page
58. Effect of Ambient Velocity on the Distributed Noise Source Locations for the 20-Lobe Nozzle.	198
59. OASPL Directivity and Jet Noise Spectra for the 20-Lobe Nozzle Extrapolated to a 3.0 m Sideline, $\text{NPR} = 2.25$, $V_A = 0$ m/s.	203
60. OASPL Directivity and Jet Noise Spectra for the 20-Lobe Nozzle Extrapolated to a 3.0 m Sideline, $\text{NPR} = 2.25$, $V_A = 93.9$ m/s.	208
61. Effect of Ambient Velocity on Jet Noise OASPL and 1/3-OBSPL Spectra for the 20-Lobe Nozzle, $\text{NPR} = 1.75$	213
62. Effect of Ambient Velocity on Jet Noise OASPL and 1/3-OBSPL Spectra for the 20-Lobe Nozzle, $\text{NPR} = 2.25$	218
63. Effect of Ambient Velocity on Subsonic Jet Noise Spectra for the 20-Lobe Nozzle Referenced to the Static Case Where $V = V_j - V_A$, $T_T = 844\text{K}$, 3.0 m Sideline.	223
64. Static Velocity Exponent for the 20-Lobe Nozzle.	225
65. Flight Effects on OASPL of a 20-Lobe Nozzle, $\text{NPR} = 1.75$, $V_j = 503$ m/s.	226
66. Flight Effects on OASPL of a 20-Lobe Nozzle, $\text{NPR} = 2.25$, $V_j = 594$ m/s.	228
67. Flight Effects on PNL of a 20-Lobe Nozzle, $\text{NPR} = 1.75$, $V_j = 503$ m/s.	230
68. Flight Effects on PNL of a 20-Lobe Nozzle, $\text{NPR} = 2.25$, $V_j = 594$ m/s.	232
69. Ejector Performance with the Annular and 20-Lobe Nozzles.	234
70. Peak Noise Source Locations and Noise Propagation Angles for the Annular Nozzle with Lined Ejector.	237
71. Peak Noise Source Locations and Noise Propagation Angles for the 20-Lobe Nozzle with Lined Ejector.	241
72. Effect of Ambient Velocity on the Distributed Source Locations for the Annular Nozzle with Lined Ejector.	246
73. Effect of Ambient Velocity on the Distributed Source Locations for the 20-Lobe Nozzle with Lined Ejector.	251
74. OASPL Directivity and Jet Noise Spectra for the Annular Nozzle with Lined Ejector Extrapolated to a 3.0 m Sideline, $\text{NPR} = 1.76$, $V_A = 3.3$ m/s.	256
75. OASPL Directivity and Jet Noise Spectra for the Annular Nozzle with Lined Ejector Extrapolated to a 3.0 m Sideline, $\text{NPR} = 1.76$, $V_A = 69.5$ m/s.	261
76. OASPL Directivity and Jet Noise Spectra for the 20-Lobe Nozzle with Lined Ejector Extrapolated to a 3.0 m Sideline, $\text{NPR} = 2.26$, $V_A = 5.8$ m/s.	266
77. OASPL Directivity and Jet Noise Spectra for the 20-Lobe Nozzle with Lined Ejector Extrapolated to a 3.0 m Sideline, $\text{NPR} = 2.22$, $V_A = 69.2$ m/s.	271
78. Flight Effects on OASPL of an Annular Nozzle with Lined Ejector, $\text{NPR} = 1.75$, $V_j = 503$ m/s.	276
79. Flight Effects on OASPL of an Annular Nozzle with Lined Ejector, $\text{NPR} = 2.25$, $V_j = 594$ m/s.	278
80. Flight Effects on PNL of an Annular Nozzle with Lined Ejector, $\text{NPR} = 1.75$, $V_j = 503$ m/s.	280
81. Flight Effects on PNL of an Annular Nozzle with Lined Ejector, $\text{NPR} = 2.25$, $V_j = 594$ m/s.	282
82. Flight Effects on OASPL of a 20-Lobe Nozzle with Lined Ejector, $\text{NPR} = 1.75$, $V_j = 503$ m/s.	284

FIGURES (Continued)

No.	/	Page
83.	Flights Effects on OASPL of a 20-Lobe Nozzle with Lined Ejector, NPR = 2.25, $V_j = 594$ m/s.....	286
84.	Flight Effects on PNL of a 20-Lobe Nozzle with Lined Ejector, NPR = 1.75, $V_j = 503$ m/s.....	288
85.	Flight Effects on PNL of a 20-Lobe Nozzle with Lined Ejector, NPR = 2.25, $V_j = 594$ m/s.....	290
86.	Ejector Performance with the 57-Tube Nozzle	292
87.	57-Tube Nozzle Base and Ejector Lip Pressure Distributions.	294
88.	Peak Noise Source Locations and Noise Propagation Angles for the 57-Tube Nozzle with Lined Ejector.	296
89.	Effect of Ambient Velocity on the Distributed Noise Source Locations for the 57-Tube Nozzle with Lined Ejector.	301
90.	OASPL Directivity and Jet Noise Spectra for the 57-Tube Nozzle with Lined Ejector Extrapolated to a 3.0 m Sideline, NPR = 2.61, $V_A = 3.3$ m/s....	306
91.	OASPL Directivity and Jet Noise Spectra for the 57-Tube Nozzle with Lined Ejector Extrapolated to a 3.0 m Sideline, NPR = 2.60, $V_A = 68.6$ m/s....	311
92.	10 kHz 1/3-OBSPL Directivity Comparisons for the 57-Tube Nozzle with Ejector	316
93.	Flight Effects on OASPL of a 57-Tube Nozzle with Ejector, NPR = 2.25, $V_j = 594$ m/s.....	318
94.	Flight Effects on OASPL of a 57-Tube Nozzle with Ejector, NPR = 2.60, $V_j = 640$ m/s.....	320
95.	Flight Effects on PNL of a 57-Tube Nozzle with Ejector, NPR = 2.25, $V_j = 594$ m/s.....	322
96.	Flight Effects on PNL of a 57-Tube Nozzle with Ejector, NPR = 2.60, $V_j = 640$ m/s.....	324
97.	Effect of Ambient Velocity on Peak PNL of an RC Nozzle.....	326
98.	Effect of Ambient Velocity on Peak PNL of an Annular Nozzle.....	328
99.	Effect of Ambient Velocity on Peak PNL of a 20-Lobe Nozzle.....	330
100.	Effect of Ambient Velocity on Peak PNL of an Annular Nozzle with Lined Ejector	332
101.	Effect of Ambient Velocity on Peak PNL of a 20-Lobe Nozzle with Lined Ejector	334
102.	Effect of Ambient Velocity on Peak PNL of a 57-Tube Nozzle with Lined Ejector	336
103.	Peak PNL Suppression Characteristics.....	338
104.	Comparison of Baseline and Suppressor Nozzles on Basis of PNL Directivity, NPR = 1.75, $V_j = 503$ m/s	339
105.	Comparison of Baseline and Suppressor Nozzles on Basis of PNL Directivity, NPR = 2.25, $V_j = 594$ m/s	340
106.	Comparison of Baseline Nozzle and Suppressor Ejector Configurations on Basis of PNL Directivity, NPR = 1.75, $V_j = 503$ m/s	341
107.	Comparison of Baseline Nozzle and Suppressor Ejector Configurations on Basis of PNL Directivity, NPR = 2.25, $V_j = 594$ m/s	342

FIGURES (Continued)

No.	Page
108. PNL Suppression for the Suppressor Nozzles	343
109. PNL Suppression for the Suppressor Ejector Configurations.	345
110. Comparison of Static Noy Weighted Jet Noise Spectra for the Baseline and Suppressor Ejector Nozzles, $NPR = 2.25$, $V_j = 594$ m/s, $V_A = 0$ m/s	347
111. Comparison of Flight Noy Weighted Jet Noise Spectra for the Baseline and Suppressor Ejector Nozzles, $NPR = 2.25$, $V_j = 594$ m/s, $V_A = 68.6$ m/s.	350

**CORRELATION OF NEAR-FIELD/FAR-FIELD
JET NOISE MEASUREMENTS FROM MODEL
SCALE SINGLE-FLOW BASELINE AND
SUPPRESSOR NOZZLES**

VOLUME 2 - FORWARD SPEED EFFECTS

By C. L. Jaeck

Boeing Commercial Airplane Company

SUMMARY

A model-scale flight effects test was conducted in the NASA-Ames 40-by 80-Foot Wind Tunnel (40 by 80 tunnel) to investigate the effect of aircraft forward speed on single-flow jet noise characteristics. The objectives of the test and subsequent analysis were to (1) determine apparent jet noise source locations including effects of ambient velocity, (2) verify a technique for extrapolating near-field jet noise measurements into the far field, (3) determine flight effects in the near and far field for baseline and suppressor nozzles and (4) establish the wind tunnel as a means of accurately defining flight effects on jet noise for model nozzles and full-scale engines.

The models tested included a 15.24 cm baseline round convergent (RC) nozzle, a 20-lobe and annular nozzle with and without lined ejector shroud, and a 57-tube nozzle with a lined ejector shroud. Nozzle operating conditions covered jet velocities from 412 to 640 m/s at a total temperature of 844K. Wind tunnel speeds were varied from near zero to 91.5 m/s.

Noise source locations were determined for each of the six nozzles at static and wind-on conditions. The wind-on peak noise source locations exhibited the expected shift downstream due to a stretching of the potential core, while the peak noise propagation angles indicated the effect of sound convection. The distributed sound source locations for the wind-on data were found to agree with the static (volume 1, NASA CR-137914) correlations when Strouhal number was based on relative velocity and the noise propagation angle includes sound convection.

The extrapolated static and wind-on data from the 0.6 and 1.5 m sidelines were observed to agree with the measured 3.0 m data when the proper corrections were applied. The extrapolation procedure is the same one discussed in volume 1 with the added corrections for sound convection and core stretch.

Analysis of data from this test indicates flight effects on jet noise measured in the near field are the same as those measured in the far field. Data from all six nozzles at most conditions indicates that forward speed results in jet noise reduction in the aft quadrant, and little or no reduction in the forward quadrant. At supersonic conditions some of the configurations displayed an increase in noise in the forward quadrant. Shock-cell noise was shown to increase in the forward quadrant with forward speed and causes an eventual crossover of wind-on overall sound pressure level (OASPL) and perceived noise level (PNL) directivities relative to the wind-off values.

In general, forward speed produced significantly lower peak PNL suppression relative to the RC nozzle for three of the suppressor nozzles. The annular nozzle with and without lined ejector showed little reduction in peak PNL suppression with forward velocity.

Flight effects for the RC nozzle measured in the 40 by 80 tunnel were shown to be in good agreement with flight-test results from a turbojet powered F-86 airplane. The F-86 results were obtained from a taxi-by test. This comparison adds further confirmation that wind tunnels provide an accurate means for simulation and measurement of the effect of ambient velocity on aircraft engine jet noise.

INTRODUCTION

One method of simulating flight effects on engine noise is to test the engine in a wind tunnel such as the NASA-Ames 40-by 80-Foot Wind Tunnel (40 by 80 tunnel) facility. Noise measurements are made in the near field and thus, must be extrapolated into the far field, namely flight certification altitudes and sideline distances. The far-field flight noise levels and directivity can be determined by (a) direct extrapolation of the flight wind tunnel measurements and (b) by determination of a flight effects noise increment that is corrected for near-to far-field directivity changes and added to a static far-field noise measurement. In both cases knowledge of apparent noise source locations and propagation angles are required to derive the flight noise levels.

In the first phase of this study (volume 1), noise source locations and procedures were generated for the extrapolation of static near-field jet noise measurements into the far field. This study of the near/far-field noise characteristics of six baseline and suppressor nozzles under static conditions has

1. Verified the multiple sideline technique for determination of apparent jet noise source locations, on both a peak and distributed basis.
2. Determined and correlated noise source locations for six baseline and suppressors operating at subsonic and supersonic Mach numbers.
3. Established a technique for extrapolating static near-field jet noise measurements into the far field.

The established techniques must be verified for wind tunnel conditions with ambient air velocity. The presence of ambient velocity results in a convection of sound and in a shifting of the jet noise sources downstream due to a stretching of the potential core. These effects of forward speed on jet noise were studied by means of a test in the 40 by 80-tunnel. This test provides an important link between near- and far-field flight effects, and also assists in establishing the potential of wind tunnel testing as a means of accurately simulating and defining flight effects on engine noise at minimum cost.

The model-scale program in the 40 by 80 tunnel, in addition to defining the noise characteristics of the six nozzles, also yields the change in jet noise suppression characteristics in flight. A description of the test and subsequent analysis are presented in this report.

ABBREVIATIONS AND SYMBOLS

a	speed of sound, m/s
A	area, m ²
ARC	Ames Research Center
ASME	American Society of Mechanical Engineers
C _D	nozzle discharge coefficient
D	diameter, m
f	1/3-octave band center frequency, Hz
L	length, m
LTC	Boeing Large Anechoic Test Chamber
m	meters; static velocity exponent, (see equation 6)
M	Mach number
n	flight velocity exponent
N	Noy value
NASA	National Aeronautics and Space Administration
NPR	nozzle pressure ratio (upstream total to ambient static)
OASPL	overall sound pressure level, dB
1/3-OASPL	1/3-octave band sound pressure level, dB
P	pressure, N/m ²
R	radial distance from sound source to observer, m
RC	round convergent
RH	relative humidity, percent
S	Strouhal number, $fD/(V - V_A)$
SL	sideline distance, m
SPL	sound pressure level, dB
V	fully expanded jet velocity, m/s
$\sqrt{\frac{-2}{V}}$	RMS velocity fluctuation, m/s
T	temperature, °C, K
PNL	perceived noise level, PNdB
X	axial distance from nozzle or ejector exit plane, m
Y	radial distance, m
λ	wavelength, m
ρ	density, kg/m ³
ρ_j	fully expanded jet density, kg/m ³
θ_I	Angle relative to nozzle or ejector exit plane center and inlet axis
θ_S	angle relative to source location and inlet axis without ambient velocity (noise radiation angle), degrees
ψ	angle relative to source location and inlet axis (noise propagation angle, includes convection), degrees
ω	density exponent

SUBSCRIPTS

A	ambient
cl	centerline
E	extrapolated; ejector
eq	flow equivalent
I	inlet
j	jet
M	measured; microphone
S	source
T	total
1	static noise source location
2	wind-on noise source location

SUPERSCRIPTS

—	time averaged
*	sonic conditions

DATA SYMBOLS

○	NPR = 1.44
□	NPR = 1.58
△	NPR = 1.75
◇	NPR = 1.965
◻	NPR = 2.25
◼	NPR = 2.60

Open Symbols	Tunnel Velocity = 0 m/s
Hashmarked Symbols	Tunnel Velocity = 45.7 m/s
Bar Thru Symbols	Tunnel Velocity = 68.6 m/s
Filled Symbols	Tunnel Velocity = 91.5 m /s

DESCRIPTION OF TEST PROGRAM

40- BY 80-FOOT WIND TUNNEL AND TEST INSTALLATION

The NASA-Ames 40-by 80-Foot Wind Tunnel (40 by 80 tunnel) is a closed circuit tunnel driven by six 12.2 m dia fans. The tunnel test section is 12.2 m high, 24.4 m wide and 24.4 m long. The tunnel cross section has semi-circular sides with a flat horizontal ceiling and floor. The test-section walls are constructed of steel plate and therefore, the tunnel is quite reverberant. Four hundred m² of 7.62 cm thick polyurethane foam was installed on the internal wind tunnel walls and floor in the general vicinity of the test model and microphone installations to improve the acoustic characteristics. This material provides sufficient absorption to permit free-field noise measurements over a range of 500 Hz to 40 kHz out to a 3 m sideline. The placement of the foam, acoustic instrumentation and nozzle are shown in figures 1 to 6.

Reverberation tests (ref. 1) were conducted in the 40 by 80 tunnel test section which was treated with a double layer of 2.54 cm glass fibre blanket as a bulk absorber. These tests indicated that satisfactory free-field noise measurements could be made in the test section if the tunnel floor were partially lined with an acoustic material. Figure 7 (from ref. 2) shows the normal incidence absorption of 7.62 cm thick polyurethane foam sheet which is equal to or better than the glass fibre blankets. The use of deep wedges is not practical in the 40 by 80 tunnel, however, the overall acoustic performance of the foam sheet treatment is adequate to meet the objectives of the test.

The foam sheet was treated with a fire retardant chemical that fireproofs the foam without degrading the acoustic properties. The treatment process was a water solution of Ammonium Di-Hydrogen Phosphate ($\text{NH}_4\text{H}_2\text{PO}_4$). The foam sheet is dipped, squeezed to saturate the cell structure, and drip dried to retain the chemical salt within the material. The treated foam will only burn when a direct high-temperature flame is applied but is extinguished upon removal of the ignition source. Hot metal objects (800°C) do not ignite the treated foam sheet.

As an added benefit, the acoustic absorption is actually improved by the chemical treatment, as shown in figure 7 and it appears that the life of the foam sheet may be extended by a reduction of ultraviolet aging.

The foam sheet was covered with a wire mesh and held in place with fasteners and steel studs that were spot welded to the tunnel surfaces. Fairing strips were used along the edges of the wire/foam to prevent the tunnel flow from lifting the foam sheets.

BURNER INSTALLATION

The hot gas source for the test nozzles was a kerosene burner (ref. 3), designed to match a nozzle with a 180 cm² exit area. The burner was built specifically for this test, but will handle a variety of applications requiring air at elevated temperatures. Detail descriptions of the burner and operating instructions are given in references 2 and 3. The burner was mounted on the floor as shown in figure 8 to minimize flow disturbances by immersion in the tunnel boundary layer. The floor mounting of the burner and two 135° elbows mini-

mized the nozzle nacelle boundary layer growth. The internal pipe and flow system diameters were made as large as possible to maintain low internal flow velocities.

Airflow for the burner was supplied by a J-85/Viper turbo-compressor installed beneath the wind tunnel. Air was ducted through a bypass system, up through an airflow measuring nozzle and into the kerosene fuel burner where the temperature was raised to a nominal 844K, and exhausted through the nozzle. Approximately 2 m upstream of the burner was a muffler, designed to suppress any compressor or flow-system noise. Viper and flow-system characteristics are provided in figures 9 and 10. The maximum nozzle pressure ratio available was limited by system pressure losses and the J-85 exhaust gas exit temperature. Since the compressor produced more air than required by the nozzles, the excess air was ducted through an air bypass system.

Displayed in figure 10 are the flow-system temperatures, internal temperature profiles and RC nozzle discharge coefficients (C_D). The agreement between the temperature profiles upstream of the RC nozzle as measured in the Boeing Anechoic Chamber (LTC) and 40 by 80 tunnel indicates the lack of an effect of the "S" duct. The agreement of the measured C_D from the two facilities indicates the nozzle exit velocity profiles are similar and the extensive 40 by 80 tunnel air ducting was leak proof.

The turbo-compressor (fig. 11) was enclosed to reduce the surrounding community noise and contributions to the tunnel interior noise floors. The J-85 compressor produced an excess air flow beyond nozzle requirements which was ducted outside the tunnel through a variable area nozzle and lined ejector. The ejector was used for noise control, since the bypass jet operated at pressure ratios up to three.

NOZZLE DESCRIPTIONS

The four basic nozzle configurations tested in the 40 by 80 tunnel were a baseline RC nozzle, a 57-tube suppressor ejector, a 20-lobe nozzle and an annular nozzle, which are shown in figure 12. The 20-lobe and annular nozzles were tested with and without a lined ejector shroud. Geometric descriptions and important dimensions for each of the nozzles and ejectors are given in tables 1, 2 and 3, and in volume 1 of this report.

FLOW INSTRUMENTATION

The air supply system, burner and models contained instrumentation to define and monitor the burner operation and to determine the nozzle operating conditions. Parameters recorded and/or monitored on the burner were: fuel pressure, ignitor pressure and temperature, burner pressure and temperature, compressor outlet pressure, and fuel flow.

The nozzle flow conditions were measured with two sets of pressure and temperature rakes. The first set, the facility rakes, figure 8, were installed for all test models and included 10 total temperature and 10 total pressure probes. The second set, the model rakes, were installed with all test configurations except the 57-tube nozzle. The model rakes also included 10 total temperature and pressure probes as shown in figure 8. In addition, the 20-lobe and annular nozzle each contained 2 static taps located at the external nozzle lip. The nozzle installation for the 57-tube nozzle and ejector contained an additional 14 static pressure

taps along the shroud lip and nozzle base as shown in figure 13. Each ejector shroud contained a rake with 3 total pressure taps for defining ejector inlet velocity.

Model nozzle airflow was measured with a 14.981 cm (5.898 in.) throat dia ASME, long radius flow nozzle. Upstream duct pressure, nozzle differential pressure and total temperature were measured to define the airflow rate.

The tunnel freestream conditions were determined from measurement of the test-section total pressure and temperature, and the static pressure. The measurement point was located 1.8 m above the tunnel floor and 4.6 m from the jet centerline on the 90° ray line from the nozzle exit.

The tunnel temperature and relative humidity were measured with a hygrometer mounted on the guide vanes in the tunnel settling chamber, 6 m above the floor and 15 m from the side wall. The temperature measurements from the hygrometer and tunnel probes were observed to agree within 1°C.

The hygrometer relative humidity reading from three series of runs on three nozzles is shown in figure 14. The measured relative humidity values are compared with calculations based on constant specific humidity using reference 4 and measured tunnel temperature. The measured and calculated values agree except at the high ambient temperature which corresponds to high tunnel velocities ($V_A = 100$ m/s) and high settling chamber velocities. The settling chamber velocity is thought to be the cause of the hygrometer error.

Model, burner, and wind tunnel performance data were recorded on a Boeing supplied Hewlett-Packard/Dymec 2010D data system that has the capability for recording 196 channels, plus four 48-port scanivalves. The output was in two forms: (1) printed paper tape listing, 3 digits of channel identification, polarity, and 6 digits of raw data; (2) punched paper tape in IBM 8-level, odd-parity format. The system has a resolution of 1 microvolt dc and a recording speed of 5 channels per sec. The punch paper tape was later reduced or converted on the CDC 6600 computer into the desired flow parameters and engineering units.

ACOUSTIC INSTRUMENTATION

Acoustic instrumentation consisted of 10 microphones mounted in the wind tunnel. Four were mounted on the NASA-ARC 15.2 m traversing mechanism, 2 were mounted on a Boeing supplied 3.6 m mechanism and 4 were mounted on fixed stands. Their locations relative to the nozzle exit are detailed in figure 15. The microphones are Bruel and Kjar model 4136, 0.635 cm condenser type and are mounted with preamps in a metal housing. Dimensioned sketches of the microphone installations for each of the four sidelines are shown in figure 15. The 15.2 m traverse had 2 microphones positioned on each arm to record data on 1.5 and 3 m sidelines (measured from the jet axis). The 3.6 m traversing mechanism with 2 microphones was positioned on a 0.6 m sideline. The 4 fixed microphones were positioned on a 4.6 m sideline. As shown in figure 15, the microphone height and positions were designed to prevent line of sight blockage.

Each microphone data channel consisted of the following components:

1. Bruel and Kjaer Model 4136 condenser microphone
2. Bruel and Kjaer Model UAO 385 Aerodynamic Wind Screen
3. Adapter section
4. ALTEC 165A (Boeing modified) cathode follower/preamplifier
5. ALTEC microphone power supply
6. Dynamic Model 7509 P/J Data Amplifier
7. Honeywell 5600C 14-track tape recording system.

Signal monitoring during the recording process was accomplished with 14-channel monitor scopes and a Ballantine Labs Model 323-08 True RMS Voltmeter.

A frequency response was conducted on each microphone system to determine the necessary corrections for data reduction. This response check was conducted before and after the test. At the start of each shift a microphone sensitivity check was conducted using a Bruel and Kjaer Model 4220 pistonphone acoustic calibrator. The pistonphone calibration condition is 124.4dB at 250 Hz.

Each traverse mechanism contained a potentiometer which was calibrated prior to start of testing to obtain a curve of distance versus millivolts. The millivolts reading of each potentiometer was recorded on the acoustic analog tape.

In order to obtain additional forward quadrant noise measurements, the 15.2 and 3.6 m traverse rails and struts were moved forward (upstream) after completion of tests on the six nozzles. The 15.2 m traverse could only be moved 3.3 m before entering the tunnel bell-mouth sections where associated velocity gradients are present. Repositioning the 15.2 m traverse by 3.3 m allowed measurements from 30 to 160° under static conditions on the 3 m sideline. In order to obtain the same angular coverage on the 0.6 m sideline, the 3.6 m traverse was moved by 0.7 m, as shown in figure 1.

The RC nozzle and 57-tube nozzle with lined ejector were then rerun for some of the high power, low tunnel velocity conditions. These test runs and conditions are indicated in table 4.

TEST PROCEDURE

Burner/Tunnel Operation

The burner air flow and pressure ratio were controlled with the J-85 Viper compressor throttle setting and the bypass nozzle area. The burner total temperature was controlled by the burner fuel flow.

The test sequence for a given nozzle consisted of first running the static runs. At a nozzle pressure ratio of 1.8, the tunnel motor/generator was started. The tunnel fans and flow were started after completion of the last static run, and then the wind-on cases were run.

Following completion of the wind-on runs, a set of tunnel background or noise floors was run at each tunnel velocity. During the noise floor runs the burner was off, but the nozzle was operated at tunnel pressure ratio and tunnel velocity to prevent flow separation in the nozzle base region.

Data Recording

The acoustic data was recorded in two parts: (a) fixed microphones and (b) traversing microphones. At each test condition, the traverse microphones were positioned near peak noise, gains set, and data recorded. The traversing microphones were then brought to the upstream end, and a continuous "sweep" of the two traverse systems was conducted. The 15.2 and 3.6 m traverse sweep durations were 85 and 130 sec, respectively.

Nozzle performance and tunnel data were recorded shortly after the start of a traverse or sweep.

TEST CONDITIONS

A summary of operating conditions for each nozzle is summarized in table 4. Each nozzle was operated at up to six nozzle pressure ratios and four tunnel velocities. The nominal values are:

$$\begin{aligned}\text{NPR} &= 1.44, 1.58, 1.75, 1.965, 2.25, 2.6 \\ V_j &= 412, 457, 503, 549, 594, 640 \text{ m/s} \\ V_A &= 0, 45.7, 68.6, 91.5 \text{ m/s}\end{aligned}$$

The combinations of nozzle pressure ratio and tunnel velocity were selected such that the jet noise level would be higher than the tunnel noise floors.

For each wind-on condition, static noise recordings were made at the same ideal jet velocity and a velocity corresponding to wind-on jet relative velocity ($V_j - V_A$). A few addition repeat and compressor noise check cases (RC nozzle only) were also run which are not shown in table 4.

In many of the static runs, the nozzle flow was sufficient to start tunnel airflow in motion. "Static" tunnel velocities of up to 8 m/s were measured.

DATA REDUCTION

Acoustic data was recorded on a 14 channel analog tape which were later reproduced and analyzed in 1/3-octave bands covering the frequency range of 200 Hz to 40 kHz. The data from each of the traverses were analyzed at up to 25 angles using a 1 sec integration time about the specified angle. The data as recorded covered angles from 60 to 165° on the 0.6 and 3 m sidelines, and 40 to 170° on the 1.5 m sideline.

Microphone nose cone and wind screen corrections which are a function of the noise radiation angle were based on nominal values at an angle of 80°. This approximation is valid since the microphone corrections are applied to the high frequencies that peak at angles near 100 to 120°. A more precise application of the microphone corrections requires a knowledge of noise source locations and radiation angles, and would have resulted in a long, costly data reduction procedure. The microphone corrections do not affect the increment or change in jet noise levels due to ambient velocity.

Prior to start of data analysis, all wind-on acoustic measurements were corrected for ambient noise levels by subtraction of tunnel acoustic noise floors.

TUNNEL ACOUSTIC CHARACTERISTICS

Two tunnel acoustic characteristics that are important to the evaluation of wind tunnel flight-effects measurements are (a) the tunnel reverberation characteristics and (b) wind tunnel noise floors.

Reverberation Characteristics

The reverberation test (ref. 1) was conducted in the 40 by 80 tunnel with a 5.1 cm layer of glass fibre lining. The lining material used in the tunnel during flight effects study was a 7.6 cm layer of polyurethane foam. The reverberation test was conducted using spherical noise sources. A more meaningful study of the 40 by 80 tunnel reverberation characteristics is obtained by comparing static jet noise measurements from the Boeing Anechoic Chamber (LTC) and the 40 by 80 tunnel. These comparisons for the 15.24 cm RC nozzle are displayed in figure 16, where LTC data is compared with moving and stationary traverse measurements in the 40 by 80 tunnel. The measurements are in good agreement with each other. There are some small differences at the low frequencies which are attributed to reverberation effects or reflections.

The jet noise measurements at a nozzle pressure ratio of 1.44 on the 3.0 m sideline are compared with the "clean" jet noise predictions based on reference 5. The good agreement between data and predictions indicates the jet is "clean" and free of combustion and burner can noise, compressor noise, and flow-system noise sources.

During the analysis, reverberation effects were observed to influence the static low frequency data on the 3 m sideline in the forward quadrant. No attempt was made during this study to correct for reverberation effects.

Noise Floors

Extensive noise floors were recorded during the test program to determine contributions due to the tunnel, traverse mechanisms, tunnel motor/generator (MG), J-85/Viper compressor and instrumentation. A set of the noise floors for three tunnel velocities is shown in figure 17. The contributions of the previous mentioned noise sources are displayed only at the low tunnel velocity. Only the instrumentation noise tends to come close to the tunnel noise at 1.6 kHz. This noise was obtained by replacing the B&K nose cones with solid brass nose cones, and recording the tunnel noise at the three velocities. The resulting measurement should only indicate the instrumentation noise due to the microphone, preamp, and associated electronics, and the effect of tunnel induced vibration on the microphone and preamp.

The tunnel noise floor measurements varied slightly with the nozzle configuration (run to run repeatability) and angular location in the tunnel as shown in parts four and five of figure 17. The noise floors were observed to affect the 3 m sideline data at $\theta_1 = 60$ and 90° in the low frequencies, and at angles of 160° at high frequencies.

FLOW/BURNER SYSTEM ACOUSTIC CHARACTERISTICS

During the initial analysis of the static data, a "spike" was observed in the spectral data at 4 kHz. A narrow-band (18.75 Hz) analysis was performed on the spectral data for the RC nozzle as measured by the 100⁰ microphone on the 4.6 m sideline to determine the source of the 4 kHz spike. The narrow-band spectra for five pressure ratios from 1.74 to 2.6 are displayed in figure 18. These results indicate that the spike appears at a nozzle pressure ratio (NPR) of 1.96 and a frequency of 3.6 kHz. The frequency of the spike does not change as NPR is increased, but its level is decreased. Since the spike covers many band widths, it is not related to the J-85/Viper turbocompressor blade passing frequency.

A comparison of the measured spike frequency with a calculated screech frequency, based on reference 5 is shown in figure 19, as a function of nozzle pressure ratio for the RC, annular and 20-lobe nozzles. The comparison indicates the noise spike is not related to a jet shock screech tone. A comparison of 4 kHz 1/3-octave static noise measurements from the Boeing LTC, 40 by 80 tunnel, and noise predictions (refs. 6 and 7) is displayed in figure 20. These comparisons indicate the noise spike is not present in the LTC data, nor is it related to supersonic shock-cell phenomena.

The burner used in this test is a duplicate of the one used in the static test in the Boeing LTC, which did not indicate a 4 kHz spike. This would tend to rule out the burner as a possible source of the problem.

The source of the noise spike was not resolved, but was eliminated by a linear fairing between the SPL levels in the adjacent 1/3-octave bands. This in essence removes most of the spike of the 1/3-octave band spectra and its affect on the OASPL and PNL.

DATA ANALYSIS

EFFECT OF AMBIENT VELOCITY ON THE JET

The presence of ambient velocity or forward speed produces changes in the jet flow field, noise generation, and sound propagation. Ambient velocity produces a stretching of the potential core that results in a shift of the jet noise source locations downstream.

In order to estimate the effect of ambient velocity on potential core length and peak noise source locations, an analytical study was conducted using the Lu/Berman flow/noise analysis (refs. 8 and 9). The effect of ambient velocity on the centerline velocity and turbulence intensity is shown in figure 21. The tip of the potential core, indicated by the arrows in figure 21, is observed to shift downstream by two diameters for an increase in ambient velocity of 91.5 m/s. The radial velocity and turbulence profiles at the tip of the core are shown in figure 22. The velocity profile in the region of peak shear is only slightly affected by ambient velocity. The turbulence intensity profile is substantially changed, with the peak intensity decreasing from 14.5 to 12%.

The flow/noise analysis was also used to obtain the analytical peak power source locations as displayed in figure 23. The effect of ambient velocity stretching the potential core and shifting the noise source locations downstream is indicated to be largest for the low frequencies or Strouhal numbers. The collapse of the analytical results onto a single straight line at a constant modified Strouhal number indicates a means of correlating the measured peak noise source locations, which will be discussed later.

The presence of ambient velocity also changes the noise propagation angle by convecting the sound as shown in figure 24. The noise source propagation angle (ψ) is related to the static noise source radiation angle (θ_S) by the following relationship:

$$\tan (\psi - 90^\circ) = \frac{\sin (\theta_S - 90^\circ) + M_A}{\cos (\theta_S - 90^\circ)} \quad (1)$$

NOISE SOURCE LOCATIONS AND EXTRAPOLATION PROCEDURE

Previously in volume 1, the static distributed noise source locations were correlated as a function of the noise radiation angle (θ_S) and Strouhal number (fD_j/V_j). For the wind tunnel data the correlation parameters must be modified to account for ambient velocity, core stretch and convection. The previous static noise source correlation parameters were modified as follows:

$$\begin{aligned} \frac{f D_j}{V_j} &\rightarrow \frac{f D_j}{V_j - V_A} \\ \theta_S &\rightarrow \psi \end{aligned} \quad (2)$$

These distributed noise source correlations were used to extrapolate static and wind-on near-field data into the far-field, and to correct the wind-on angular location for convection and core stretch.

The near-field jet noise data is extrapolated into the far-field by correcting both the SPL and angular location. The correction in level is given by:

$$1/3\text{-OBSPL (Far Field)} = 1/3\text{-OBSPL (Near Field)} - 20 \log_{10} \frac{R_{S,E}}{R_{S,M}} - \frac{\Delta dB}{305} \frac{R_{S,E} - R_{S,M}}{305} + \Delta \text{SPL}_1 - \Delta \text{SPL}_2 \quad (3)$$

where

$R_{S,M}$ = acoustic path length from source location to near-field microphone location which has been corrected for core stretch and convection, m

$R_{S,E}$ = acoustic path length from source (through near-field location) to far-field sideline, m

$\frac{\Delta dB}{305}$ = atmospheric attenuation (ARP 866, ref. 10), dB/305 m

ΔSPL_1 = from figure 12, volume 1, where $R = R_{S,M}$ and $SL = SL_M$

ΔSPL_2 = from figure 12, volume 1, where $R = R_{S,E}$ and $SL = SL_E$

The near-field noise increments ΔSPL_1 and ΔSPL_2 are obtained from figure 12 in volume 1 of this report. The abscissa of figure 12 in volume 1 must be redefined for the wind-on cases as follows:

$$\left(\frac{R}{\lambda}\right) \left(\frac{V_j}{a_A}\right) \longrightarrow \left(\frac{R}{\lambda}\right) \left(\frac{V_j - V_A}{a_A}\right) \quad (4)$$

The correlation in figure 12 (volume 1) corrects the near-field SPL for the deviations from spherical divergence when extrapolating jet noise data into the far field.

The equivalent static microphone angle for the extrapolated wind-on data is given by the following equation:

$$\theta_I - 90^\circ = \text{Arc Tan} \left[\frac{X_{S2} + (SL_E - Y_S) \tan(\psi - 90^\circ) - M_A R_{S,E} - (X_{S2} - X_{S1})}{SL_E} \right] \quad (5)$$

which accounts for source locations, core stretch, and convection.

The measured data has been extrapolated, analyzed, and presented in the following manner:

1. Measured spectral data extrapolated to a 3.0 m sideline at measurement day temperature and relative humidity covering frequencies of 200 Hz to 40 kHz.
2. PNL (ref. 11) and OASPL calculated from measured spectral data extrapolated to a 305 m sideline and 0 altitude including corrections for a scale factor of 5,

Doppler frequency shift (but not level) and ambient conditions of 25°C and 70% relative humidity. The extrapolation to 305 m was performed in two steps: (1) to a 15.24 m sideline using the distributed source locations and model frequencies and (2) from 76.2 (5 X 15.24) to 305 m using point source located at the nozzle exit plane and scaled frequencies of 50 Hz to 8 kHz.

15.24 cm RC NOZZLE

The baseline nozzle used in the 40 by 80 tunnel flight effects test was a 15.24 cm RC nozzle. The RC nozzle was tested at both subsonic and supersonic jet exhaust Mach numbers, and at tunnel velocities up to 92 m/s. The data from the RC nozzle was analyzed to

- Verify noise source location and propagation angle correlations presented in volume 1 and modified in earlier discussions
- Verify the near-to far-field extrapolation technique
- Establish the flight effects on jet noise in both the forward and aft quadrant for subsonic and supersonic test conditions

Noise Source Locations

Peak noise source locations (X_S/D) and noise propagation angles (ψ) were determined for the RC nozzle as shown in figure 25. The experimental peak noise radiation angles show the effect of sound convection by the ambient velocity. The measured results agree with the calculated trend given by equation 1. The static or initial value of the sound radiation angle was obtained from the correlation presented in figure 17 of volume 1.

The peak noise source locations shift downstream as the ambient velocity is increased due to the stretching of the potential core. The experimental peak noise source locations display the same linear trend observed in the analytical results presented in figure 23. The faired line drawn through the data was established by using the noise propagation angle to enter figure 18 of volume 1 to determine the noise source locations. Stated another way, the peak noise source locations agree with the previous static correlations when θ_S is changed to ψ , and Strouhal number is based on the relative velocity ($V_j - V_A$).

Distributed noise source locations and propagation angles were determined for subsonic and supersonic jet conditions, static and wind-on tunnel conditions as presented in figure 26. The 40 by 80 tunnel data are shown to agree and correlate with the LTC measurements (faired curves). Further, the 40 by 80 tunnel results confirm the observation that all forward quadrant noise is generated from a point located 1 to 3 diameters downstream from the nozzle, depending on the Strouhal number.

Model-Scale Extrapolation

These noise source correlations were used in the near-to far-field extrapolation technique, described earlier, to extrapolate measured data from 0.6 and 1.5 m sidelines to the 3.0 m location. The wind-on data was corrected for the following as appropriate

- Source location

- Near-field effects
- Spherical divergence
- Atmospheric attenuation
- Core stretch
- Convection

The static data were only corrected for the first four items. The extrapolated subsonic static data for the three sidelines are in good agreement as displayed in figure 27. The wind-on cases in figures 28 and 29 also exhibit a good data collapse. A static and wind-on supersonic case is displayed in figures 30 and 31. The extrapolated static data are compared with empirical predictions for clean, shock-free jet mixing noise (ref. 6) and shock-cell noise (ref. 7). The shock-cell noise component is shown to dominate the peak and high frequency region of the forward arc spectra.

Flight Effects on Subsonic Jet Noise

Subsonic data from the RC nozzle at a pressure ratio of 1.75 and tunnel velocities of 3, 46 and 69 m/s are compared in figure 32 on the basis of overall and 1/3-octave band SPL directivity.

The measured results were extrapolated to a 3 m sideline where the resulting data from the three locations indicate the same effect of ambient velocity on jet noise. In addition, the comparisons do not indicate any noise increase in the forward quadrant.

Previous investigations (refs. 12, 13 and 14) have developed flight effects prediction procedures based on a velocity exponent in a power law applied to the OASPL. In general, these studies have shown that the flight noise spectrum changes shape relative to the static spectrum.

An attempt was made during this study to correlate the effect of ambient velocity on the subsonic jet noise spectra. Since the normalized (1/3-OBSPL - OASPL) jet noise spectra for an RC nozzle at a given jet total temperature is a function of Strouhal number and velocity ratio (V_j/a_A), the wind-on spectra should be compared with the measured static case where the jet velocity is equal to the wind-on relative velocity ($V_j - V_A$). These 1/3-OBSPL increments are presented in figure 33 as a function of angle and Strouhal number, $fD/(V_j - V_A)$. The subsonic results presented in figure 33 also represents the deviation of the measured flight effect from the full relative velocity effect, and is a measure of the distortion of the jet flow field and noise generation mechanisms by the ambient velocity. The results presented in figure 33 can be used to predict the effect of ambient velocity on subsonic and supersonic shock-free jet noise. The prediction procedure would consist of the spectral correction and an increment in OASPL due to the relative velocity ($V_j - V_A$). The effect on the OASPL can be calculated using the velocity and density exponents given in figure 34, and equation 6.

$$m = \frac{\left[\text{OASPL} - 10 \log_{10} \left(\frac{\rho_j}{\rho_A} \right)^w \right]_{V_j} - \left[\text{OASPL} - 10 \log_{10} \left(\frac{\rho_j}{\rho_A} \right)^w \right]_{V_j - V_A}}{10 \log \left(\frac{V_j}{V_j - V_A} \right)} \quad (6)$$

The static velocity and density exponents for the RC nozzle were based on the collected and normalized clean jet noise data of reference 6, since the quantity of data was much larger than measured in this test series and covers a wider range of jet conditions.

Flight Effects on Supersonic Jet Noise

The effect of ambient velocity on supersonic jet noise from an underexpanded RC nozzle is shown in figures 35 and 36 for NPR = 2.25 and 2.6, and ambient velocities of 8, 46 and 94 m/s. The predictions for static jet mixing noise and shock-cell noise are indicated. The shock-cell noise can be seen to act as a noise floor which prevents the application of the full effect of ambient velocity on jet mixing noise. In addition, when the shock-noise is the dominant noise source, ambient velocity produces a noise increase in the forward quadrant.

Scaled RC Nozzle Flight Effects

Acoustic data from the 0.6, 1.5, and 3 m sidelines were extrapolated to a 305 m sideline and were corrected for

- Scale factor of 5
- Source location and near-field effects
- Core stretch
- Convection
- Ambient conditions, 25°C and 70% R.H.
- Doppler frequency shift (but not level)

The OASPL and PNL directivities for NPR = 1.58, 1.75, 2.25 and 2.6 at a flight (wind-on) Mach number of 0.2 are displayed in figures 37 through 40.

The absolute levels are shown in the upper part of each figure and change or increment in noise due to flight is shown in the lower part. The static and wind-on measurements from the three sidelines agree reasonably well. The increment in noise level due to flight measured in the near-field (0.6 m) and the far-field (3.0 m) are in good agreement. The subsonic cases do not show an increase in noise in the forward arc, while the supersonic cases do show an increase. The increase in noise for the supersonic case is due to shock-cell noise.

Shock-Cell Noise

The shock-cell structure in a supersonic jet from an underexpanded nozzle generates noise in the mid to high frequencies and at angles in the forward arc. The shock-cell related noise is generated by shock-shock, shock-edge, and by shock-turbulence interactions. Little is presently known about these noise generation processes nor the effect of ambient velocity on these shock associated noise sources.

In order to isolate the flight effect on shock-cell noise, the measured supersonic jet noise must be broken up into a jet mixing component and a shock-cell component. The two effects have been separated in the far field by using PNL based on scaled extrapolated data from the 40 by 80 tunnel and static predictions (refs. 6 and 7) as shown in figure 41. The variation of jet mixing noise with ambient velocity has been suggested by references 12 and 13 to be of the form

$$PNL_{Flight} = PNL_{Static} - 10n \log_{10} \left[\frac{V_j}{V_j - V_A} \right] - 10 \log_{10} (1 - M_A \cos \theta_I) \quad (7)$$

The second term represents the change in jet noise source due to flight effects, and the third term accounts for the relative motion between the airplane and the ground based observer.

The value of n at 40 and 140° was obtained from a "best" fit of the subsonic data. The effect of forward speed on shock-cell noise has been shown in reference 14 to follow:

$$PNL_{Flight} = PNL_{Static} - 40 \log_{10} (1 - M_A \cos \theta_I) \quad (8)$$

The noise of a supersonic jet is dominated by shock noise in the forward quadrant, and jet mixing noise in the aft quadrant. At $\theta_I = 40^\circ$ and $NPR = 2.25$, the data lay slightly below the shock-cell prediction, but well above the jet mixing noise. At $NPR = 2.6$ the data at $\theta_I = 40^\circ$ follow the prediction given by equation 8. From these results, it can be concluded that shock-cell noise is increased in flight and represents one cause of the increase in forward arc noise in flight.

Flight Velocity Exponents

As indicated in the previous section, one of the methods of normalizing the flight effects data is through the use of a velocity exponent as given by equation 7. The flight velocity exponent can be obtained by using the following:

$$10n \log_{10} \frac{V_j}{V_j - V_A} = OASPL_{Static} - \left[OASPL_{Flight} + 10 \log_{10} (1 - M_A \cos \theta_I) \right] \quad (9)$$

The variation of OASPL and PNL with relative jet velocity is presented in figure 42 for two nozzle pressure ratios. The variation of OASPL and PNL velocity exponents with angular position and NPR are summarized in figure 43. The data are observed to vary with nozzle pressure ratio. The results presented in the figure are similar to those presented by other investigators in references 12, 15 and 16.

Wind Tunnel – Flight Comparison

A comparison of the 40 by 80 tunnel RC nozzle data and taxi-by flight data (ref. 17) from the F-86 Sabre jet aircraft are displayed in figure 44. The Orenda 14 turbojet engine which is installed in the F-86 Sabre jet aircraft was ground static tested at Paine Field, Washington with the airplane parked near the middle of a 61 m wide runway. Ground microphones were positioned on a 29 m sideline at angles from 20 to 160°. The Orenda 14 engine exhaust system consists of a tailpipe 57.4 mm in dia and 2.4 m long, with a 48.0 cm dia conical nozzle. Prior to acoustic testing the engine exhaust conditions were determined as a function of engine power.

The F-86 static data used in figure 44 are an average of 3 runs, while the flight data are an ensemble average of 10 microphones. The flight effects increment in OASPL from the wind tunnel and flight-test are in good agreement. This comparison adds further verification of the extrapolation procedures and use of a wind tunnel to simulate flight effects on jet noise.

ANNULAR NOZZLE

The peak noise source locations, radiation angles, and distributed noise source locations for the annular nozzle are presented in figure 45 and 46. The peak noise radiation angles and source locations display the effects of sound convection, and core stretch. The wind-on distributed source locations are in good agreement with the static correlation of volume 1.

The measured noise data for the annular nozzle at $\text{NPR} = 1.75$ was extrapolated to a 3.0 m sideline as shown in figures 47 and 48. The extrapolated OASPL and 1/3-octave SPL spectra are observed to be in good agreement with the measured 3.0 m sideline data for both the static and wind-on cases. The static data has been compared to a postmerged prediction. The low frequency static data at $\theta_I = 60^\circ$ shows some stratification due to reverberation effects. The wind-on data also displays this trend, which is due to reverberation effects plus interaction of the jet noise with the tunnel noise floor.

The measured flight effects for the annular nozzle at subsonic and supersonic jet conditions are shown in figure 49 and 50 for three ambient velocities. The subsonic jet noise at $\theta_I = 60^\circ$ is reduced by the ambient velocity, while the supersonic jet is unaffected. The effect of ambient velocity on subsonic jet noise for an annular nozzle has been correlated as displayed in figure 51, where flight or wind-on data has been referenced to the case where the static velocity equals the wind-on relative velocity. The data at $\theta_I = 60$ and 90° indicates the annular nozzle sees full relative velocity reduction in jet noise. At angles closer to the jet axis, the low frequency noise shows more reduction, while the high frequency noise shows less reduction. The static velocity exponent (m) for the annular nozzle is displayed in figure 52. The exponent is slightly lower than that presented earlier for the RC nozzle at angles greater than 120° .

The scaled flight effects for the annular nozzle are presented in figures 53 through 56. The OASPL and PNL measured in the near field are the same as that measured in the far field, both on an absolute basis and a flight increment basis. The supersonic case indicates a small increase in the forward quadrant PNL as presented in figure 56.

20-LOBE NOZZLE

The peak and distributed noise source locations for the bare 20-lobe nozzle are presented in figure 57 and 58. At low frequencies or Strouhal numbers the source locations stratify with nozzle pressure ratio. The distributed noise source locations, shown in figure 58, were used to extrapolate data from the near field into the far field as displayed in figures 59 and 60. The data collapse for both the static and wind-on conditions is excellent.

The static data presented in figure 59 are compared with pre and postmerged jet mixing noise and shock-cell noise predictions. The shock-cell and premerged noise predictions are based on 20 equivalent, isolated, noninteracting round jets. The difference between the data

and premerged predictions at angles of 140 and 160° is an indication of the effect of jet interaction and ambient air entrainment on jet noise. The agreement between the predictions and data at the very high frequencies indicates presence of the elemental jets, since this noise is generated at or near the nozzle exit before any interaction or mixing occurs. Comparison of the data and shock-cell prediction indicates that the high frequency region at all angles is influenced by shock noise.

The postmerged prediction is in good agreement with the data. The postmerged jet conditions for the predictions were based on one-dimensional ejector calculations with the following assumptions:

- The air entrained by a multilobe/tube nozzle is not affected by a lossless, frictionless ejector with a diameter equal to that of the nozzle exterior.
- The flow is one-dimensional, with constant and equal gas properties.

The one-dimensional ejector calculations solve the equations of continuity, momentum, and energy to obtain the ejector entrained airflow and velocity, as well as the fully mixed conditions at the ejector exit.

The effect of ambient velocity on 20-lobe nozzle jet noise at a subsonic and supersonic condition is presented in figures 61 and 62. The subsonic data at all angles and frequencies indicates a reduction in noise levels with forward speed. At the supersonic nozzle test condition, the noise measurements in the forward arc and high frequencies are not affected by forward speed. As indicated by the predictions, the high frequencies are influenced by the shock-cell noise component. In light of the earlier premerged shock noise prediction, it would appear the shock structure of the elemental jets was not affected by entrainment of ambient air or elemental jet interaction.

The subsonic spectral data from the 20-lobe nozzle was also normalized with the static case at the jet relative velocity and with Strouhal number. In the forward quadrant the jet noise from the 20-lobe nozzle is reduced by the full relative velocity (V_R) effect, as shown in figure 63. For the aft quadrant angles, the 20-lobe nozzle jet noise is reduced by more than full V_R in the low frequency postmerged region and less than full V_R in the high frequency premerged region. The static OASPL velocity exponents for the 20-lobe nozzle are given in figure 64. The static exponent is shown to peak nearer to the jet axis than the RC and annular nozzles.

The OASPL and PNL directivity for the 20-lobe nozzle are presented in figure 65 through 68 based on the scaled and extrapolated static and wind-on spectral measurements. Only the PNL at the NPR = 2.25 condition indicates a noise increase at the forward arc angles due to shock-cell noise. The OASPL and PNL based on measurements from the three sidelines display the same effect of flight on both an absolute and incremental basis. Forward speed results in less noise reduction at the supersonic conditions due to the higher relative jet velocity.

ANNULAR AND 20-LOBE NOZZLES WITH LINED EJECTOR

The annular and 20-lobe nozzles were tested with the same lined ejector as described in an

earlier section. The results of the analyses are presented in figures 69 through 85. To determine ejector performance, total and static pressure in the entrained airstream were measured. These measurements are presented in figure 69 and compared with ideal one-dimensional ejector calculations. The measured ejector inlet Mach number for the 20-lobe nozzle approaches the predictions, while the annular nozzle inlet Mach number is significantly lower. These differences are due to deviations in the actual ejector exit velocity profile from the flat, fully mixed profile used in the predictions.

The calculated, fully mixed, ejector exit velocity, and total temperature, and the ejector entrained airflow are displayed in figure 69. The static entrained airflow for this area ratio 1.8 ejector is equal to 50% of the jetflow rate and results in a fully mixed or postmerged velocity ratio (V_{mixed}/V_j) of 0.68. As ambient velocity is increased, the fully mixed ejector exit velocity and the entrained airflow are increased.

The noise source characteristics for the 20-lobe and annular nozzles with lined ejector are shown in figures 70 through 73. The noise source locations indicated are measured relative to the ejector exit, and the normalizing parameters have been based on jet exit conditions. The annular and 20-lobe nozzle distributed source locations based on 40 by 80 tunnel results are in agreement with the static correlations from volume 1. In the case of the 20-lobe nozzle with lined ejector, the source locations at high frequencies and noise propagation angles were closer to the ejector exit than the previous static results (volume 1). This change is indicated in figure 73 by the dashed lines.

The extrapolated 1/3-octave band SPL spectra for the two ejector suppressor configurations are presented in figures 74 through 77 for both static and wind-on conditions. Comparison of the extrapolated data from the 0.6 and 1.5 m sideline are in agreement with the measured 3 m sideline results. Some stratification occurs in the case of the 20-lobe ejector suppressor at high frequencies and angles near the jet axis.

The scaled and extrapolated OASPL and PNL for the two nozzle systems are presented in figures 78 through 85. Both the OASPL and PNL are reduced at all angles and for both test conditions. In general, the effect of forward velocity on OASPL and PNL is greatest at the aft quadrant angles, with equal noise reduction for the annular and 20-lobe configurations.

57-TUBE NOZZLE WITH LINED EJECTOR

The 57-tube ejector suppressor configuration was developed during the FAA-DOT Phase II program for the SST turbojet engine. The nozzle was optimized to provide maximum suppression with minimum performance losses. The measured and predicted ejector performance are presented in figure 86. The predictions are in good agreement with the measurements. The area ratio 3.0 ejector produces an entrained airflow equal to 100 to 120% of the jetflow and results in a low postmerged velocity ratio (V_{mixed}/V_j) of 0.515. The fully mixed velocity ratio increases slightly as the ambient Mach number increases, which produces increased entrained airflow.

The 57-tube nozzle base and ejector lip were instrumented for the wind tunnel test to study the effect of ambient velocity on some of the contributors to the propulsion performance losses. The location of the static pressure taps are indicated in figure 13.

The ejector inlet area which is provided for the entrainment and acceleration of ambient air by the high-velocity jet produces a reduction in static pressure that (1) results in a thrust force on the ejector lip and (2) produces a base drag on the suppressor nozzle.

Static pressure distributions across the nozzle base and along the ejector lip are presented in figure 87 for $NPR = 2.6$ at four tunnel velocities. The nozzle base pressures are slightly affected by forward velocity. Forward velocity produces a ram drag performance penalty which is indicated by the increase in lip pressures and a reduction in lip suction.

The acoustic characteristics of the 57-tube composite nozzle with lined ejector are presented in figures 88 through 96. The apparent peak and distributed noise source locations are presented in figures 88 and 89 for pressure ratios up to 2.60. The distributed source locations presented in figure 89, plus the correlation presented in figure 12, volume 1, were used to extrapolate near-field jet noise measurements into the far-field (3 m) as shown in figures 90 and 91. The extrapolated data are in good agreement with the measured OASPL's and the 1/3-octave band SPL's.

The static measured data extrapolated to a 3.0 m sideline are compared to predictions in figure 90. The low frequency postmerged prediction is based on the ejector calculations shown in figure 86.

The extrapolated data in the high frequencies at angles near the jet axis exhibit some disagreement. The 1.5 and 3.0 m sideline are in agreement, but are higher than the 0.6 m sideline data. The 0.6 m data are in agreement with the LTC test results as shown in figure 92. The cause of the discrepancy is unknown at present.

The scaled and extrapolated data from the 57-tube ejector suppressor are displayed in figures 93 through 96 on the basis of OASPL and PNL directivity. The static and flight data indicate the same flight effect both on an absolute and incremental basis. The OASPL and PNL from the 0.6 m sideline is 2 dB lower than the 1.5 and 3.0 m sideline levels at angles greater than 120° . The OASPL's and PNL's are reduced by forward speed effects in the aft quadrant, while little reduction is observed at angles in the forward quadrant.

EFFECT OF FORWARD SPEED ON THE JET NOISE SUPPRESSION CHARACTERISTICS

The effect of forward speed on the noise generation and suppression is highly dependent on the nozzle geometry, nozzle flow conditions, and location of the noise sources. The five suppressor configurations studied used the following jet noise suppression mechanisms:

- mean velocity reduction
- frequency shifting
- alteration of the directivity
- absorption by acoustic treatment in the ejector.

One of the purposes of the test series in the 40 by 80 tunnel was to determine if static jet noise suppression levels are altered by forward speed. Since aircraft are certified on the basis of a duration weighted or effective perceived noise level (EPNL), jet noise reduction must be accomplished by a reduction of both the peak PNL and PNL on either side of the peak to be effective.

The effect of ambient velocity on peak PNL for each of the six nozzles is presented in figures 97 through 102 for each of four ambient velocities. In the case of the RC nozzle the peak PNL is reduced as ambient velocity is increased. The reduction in PNL due to flight increases as jet velocity is reduced for a specified ambient velocity.

In the case of the two bare suppressor and three ejector suppressor nozzles, their peak PNL suppression capability (relative to the RC nozzle at the same ambient velocity) is reduced as jet velocity is reduced and ambient velocity is increased. For example, the peak static PNL suppression for the 57-tube nozzle with lined ejector at NPR = 2.25 is reduced from 10 Δ PNdB to 4.0 Δ PNdB at 92 m/s as displayed in figure 103. The 20-lobe suppressor ejector static peak suppression is reduced from 10 Δ PNdB to 5.0 Δ PNdB. Only the annular nozzle with a lined ejector tends to maintain its peak PNL suppression as ambient velocity is increased.

The effect of forward speed on the PNL directivity is presented in figures 104 through 107. Displayed in these four figures are comparisons of the RC with the annular and 20-lobe nozzles, and the RC with the three ejector suppressor nozzles at NPR = 1.75 and 2.25. The two bare nozzles maintain the same PNL relative to RC nozzle at NPR = 1.75. At NPR = 2.25 the difference in levels between the suppressor and baseline nozzles is narrowed for the ambient velocity case. This decrease in jet noise suppression is shown in figure 108 as the result of the RC nozzle PNL decreasing more than that for the two suppressor nozzles.

The ejector suppressor configurations tend to lose suppression near the peak noise angles (120 to 140°) as presented in figure 109. The 20-lobe nozzle with lined ejector gains 2 to 3 PNdB at angles of 140 to 160°. A maximum PNL suppression of 20 PNdB was achieved at 150° with the 57-tube nozzle/ejector operating at NPR = 2.25 as displayed in figure 109.

A comparison of the baseline RC nozzle and the three ejector/suppressor nozzles on the basis of a Noy weighted spectra $[33.3 \log(N) + 40]$ is shown in figures 110 and 111 for a

static and flight (wind-on) condition at three angles:

- 80°
- 110°, representative of peak PNL for suppressor models
- 140°, representative of peak PNL for the baseline RC and annular nozzles

The Noy weighted spectra indicate the frequency regions that have the greatest influence on PNL. The 20-lobe and 57-tube ejector suppressor nozzles are dominated by premerged (high frequency) mixing noise at the peak PNL angle of 110°. The peak PNL for the RC and annular suppressor ejector nozzles occur at 140° where the spectra are dominated by low frequency jet mixing noise.

The 57-tube nozzle produces the lowest Noy level in the low frequency region due to the large base to nozzle area ratio (3), and low postmerged jet velocity. The 20-lobe and annular nozzles used an area ratio 1.8 ejector, and had a corresponding higher postmerged velocity. The effect of ambient velocity on jet noise is greatest in the low frequencies. This effect results in a reduction of peak PNL suppression in flight for the 20-lobe and 57-tube ejector suppressor nozzles relative to the baseline RC nozzle as presented earlier.

CONCLUSIONS

Jet noise measurements were made in the 40 by 80 tunnel for six model-scale nozzles along three sideline locations extending from the near to the far field. The objectives of the test were to

- verify a technique for extrapolation of data measured in the near field into the far field.
- establish the wind tunnel as a simulation technique for measuring flight effects on engine noise components.
- determine flight effects on jet noise for baseline and suppressor nozzles.

The following conclusions are made as a result of the model-scale tests.

NEAR/FAR JET NOISE

Noise levels and flight noise increments measured in the near field were observed to agree with those in the far field for the same acoustic angle when appropriate corrections are applied for source location, near field, spherical divergence, atmospheric attenuation, core stretch, and convection.

Flight noise levels may be defined by extrapolation of wind tunnel absolute noise levels to flight conditions or by application of measured noise increments to measured or predicted far-field static noise levels.

FLIGHT EFFECTS ON JET NOISE

Forward speed reduces jet mixing noise at all angles and all test conditions.

The reduction in jet mixing noise due to forward speed is a function of frequency, power setting and nozzle configuration.

One of the causes of the increase in forward arc engine noise with increasing forward speed is supersonic shock-cell noise. Shock-cell noises increases in the forward quadrant and decreases in the aft arc as forward speed is increased.

The largest reductions in jet noise due to forward speed tend to occur at angles near the jet axis.

FLIGHT EFFECTS ON JET NOISE SUPPRESSION

Peak jet noise suppression (relative to baseline nozzle) in flight is less than that measured statically.

The loss in suppression with forward speed is dependent on nozzle configuration and jet conditions.

Only the annular nozzle with and without ejector showed little loss in suppression with forward speed.

WIND TUNNEL/FLIGHT COMPARISON

Wind tunnel measured flight effects for the baseline nozzle were shown to be in good agreement with flight-test data from the turbojet powered F-86 aircraft which adds further confirmation that wind tunnels provide an accurate means for simulation and measurement of the effect of forward speed on aircraft engine noise.

REFERENCES

1. Jaeck, C. L., "Analysis of Data from a Reverberation Test Conducted in the NASA-Ames 40-by 80-Foot Wind Tunnel Including Acoustic Lining on the Internal Tunnel Floor", Boeing Document D6-42566, October 1975.
2. Shain, W. H., "Noise Measurements in the 40-by 80-Foot Wind Tunnel -- Model Nozzle Near/Far Field Correlation -- Plan of Test", Boeing Document D6-43010-4, September 1975.
3. Stevens, R. L., "Burner System Manual -- Ames 40-by 80-Foot Wind Tunnel", Boeing Document D6-43010-5, May 1976.
4. Obert, E. F., "Concepts of Thermodynamics", McGraw-Hill, 1960, Fig. B-5.
5. Rosfjoid, T. J. and Toms, H. L., "Recent Observations Including Temperature Dependence of Axisymmetric Jet Screech", AIAA J., Vol. 13, No. 10, p. 1384, October 1975.
6. Jaeck, C. L., "Empirical Jet Noise Predictions for Single and Dual Flow Jets with and without Suppressor Nozzles - Volume 1. Single Flow Subsonic and Supersonic Jets", Boeing Document D6-42929, April 1976.
7. Evans, T., "Prediction of Single Stream Shock-Cell Noise", SAE A-21, Jet Noise Committee, April 2, 1975.
8. Lu, H., "Multiannular Axisymmetric Jet Flow Prediction Using a Two Equation Model of Turbulence", Boeing Document D6-42606, September 1975.
9. Berman, C., Jaeck, C., and Lu, H., "Analytical Prediction of Jet Noise Generation", Boeing Document D6-40614TN, July 1974.
10. Coordination Sheet AMEP-S-461, dated November 27, 1972 by R. M. Masters and Aerospace Recommended Practice 866 by the Society of Automotive Engineers, Inc., issued August 31, 1964.
11. "Definitions and Procedures for Computing the Perceived Noise Level of Aircraft Noise", Society Automotive Engineers, Inc., Aerospace Recommended Practice 865A, Revised August 15, 1969.
12. Cocking, B. J. and Bryce, W. D., "Subsonic Jet Noise in Flight Based on Some Recent Wind Tunnel Results", AIAA Paper 75-462, March 1975.
13. Bushell, K., "Measurement and Prediction of Jet Noise in Flight", AIAA Paper 75-461, March 1975.
14. Drevet, P., Duponchel, J. P. and Jacques, J. R., "Effect of Flight on the Noise from a Convergent Nozzle as Observed on the Bertain Aerotraine", AIAA Paper No. 76-557, July 1976.

15. Belleval, J., Chen, D. and Perulli, M., "*Investigation of In-Flight Jet Noise Based on Measurements in an Anechoic Wind Tunnel*", Sixth International Congress on Instrumentation, Ottawa, September 1975.
16. Strout, F. G., "*Flight Effects on Noise Generated by the JT8D-17 Engine in a Quiet Nacelle and a Conventional Nacelle as Measured in the NASA-Ames 40-by 80-Foot Wind Tunnel*", NASA-CR-137797, (Boeing Document D6-42813), January 1976.
17. Oas, S., "*Relative Velocity Jet Noise Test Using an F-86 Airplane in Taxi and Flyover*", Unpublished Boeing Document, 1976.

Table 1.— Annular Nozzle Dimensions

Nozzle flow area	186.1 cm ²
<u>Ejector inlet area</u> Nozzle flow area	1.8
Ejector length (nozzle exit to ejector exit)	30.5 cm
Overall ejector length	37.8 cm
Plug diameter	15.3 cm
Annular nozzle diameter	21.7 cm
Ejector exit diameter	21.1 cm

Table 2.— Dimensions for 20-Lobe Nozzle

Nozzle flow area	179.9 cm ²
<u>Ejector inlet area</u> Nozzle flow area	1.8
<u>Ejector exit area</u> Nozzle flow area	1.8
Ejector length (nozzle exit to ejector exit)	30.5 cm
Overall ejector length	37.8 cm
Diameter of plug	15.2 cm
Maximum diameter of lobes	25.1 cm
Ejector exit diameter	21.1 cm
Lobe width	2.0 cm
Lobe height	4.6 cm
Lobe radius (crown)	1.0 cm

PRECEDING PAGE BLANK NOT FILMED

Table 3.— Dimensions for 57-Tube Nozzle

Nozzle flow area	163.9 cm ²
Nozzle base area (outer edge of tubes)	475.2 cm ²
Ejector area	489.0 cm ²
Ejector length (nozzle exit to ejector exit)	29.7 cm
Ejector set back (tube exit to ejector lip)	2.0 cm
Overall ejector length	27.7 cm
Nozzle base area/nozzle flow area	2.9
Ejector area/nozzle flow area	3.0

	Number
Row 5	24 (elliptical)
4	12
3	12
2	8
1	1

Table 4.— Model and Wind Tunnel Test Conditions

15.24 cm Round Convergent Nozzle													
Static and wind-on conditions							Equivalent static V_r conditions						
Run	NPR	T_T , K	V_j , m/s	V_A , m/s	T_A , °C	RH, %	Run	NPR	T_T , K	V_j , m/s	V_A , m/s	T_A , °C	RH, %
49	2.60	827	633	8.2	12.2	74.5							
50	2.60	828	634	45.7	15.5	62.0	48	2.26	832	592	7.3	12.2	74.5
59	2.60	830	634	68.9	21.1	41.0	47	2.093	847	571	5.8	11.7	74.5
60	2.60	839	638	93.5	23.9	33.0	46	1.962	846	548	6.7	11.7	74.5
48	2.26	832	592	7.6	12.2	74.5							
51	2.25	812	584	46.0	16.7	51.5	46	1.962	846	548	6.7	11.7	74.5
58	2.25	833	591	68.9	20.6	43.0	44	1.874	843	530	7.6	13.3	65.0
61	2.245	838	590	93.5	26.1	28.0	43	1.744	834	498	3.3	13.3	65.0
46	1.965	846	548	6.7	11.7	74.5							
52	1.952	828	540	48.6	17.2	55.0	43	1.744	834	498	3.3	13.3	65.0
57	1.962	836	544	68.9	19.4	47.0	42	1.655	834	476	3.3	13.3	65.0
62	1.967	858	553	93.9	27.8	22.0	41	1.582	849	459	4.6	13.3	65.0
43	1.744	834	498	3.3	13.3	65.0							
45	1.765	840	505	5.8	11.7	74.5							
53	1.744	836	499	46.0	17.8	54.0	41	1.582	849	459	4.6	13.3	65.0
56	1.752	837	500	68.9	17.7	52.0	40	1.498	846	432	5.8	13.3	65.0
41	1.582	839	456	4.7	13.3	65.0							
54	1.579	813	448	46.0	17.8	53.0	39	1.431	833	405	5.8	13.3	65.0
63	1.580	813	448	46.8	27.8	21.0	39	1.431	833	405	5.8	13.3	65.0
55	1.582	814	449	68.6	16.1	56.0	38	1.372	827	380	4.6	13.3	65.0
39	1.431	833	405	5.8	13.3	65.0							
15.24 cm RC Nozzle — Forward arc													
158	2.60	826	633	6.7	15.5	44.5							
160	2.60	829	633	46.3	17.8	40.5	157	2.244	829	589	6.7	15.5	44.5
157	2.244	829	589	6.7	15.5	44.5							
159	2.243	822	586	46.0	17.2	42.0	156	1.964	832	54.4	5.8	15.5	44.5
156	1.964	832	544	5.8	15.5	44.5							
161	1.948	829	540	46.0	18.3	39.5	155	1.75	823	496	0	15.5	44.5
155	1.75	823	496	0	15.5	44.5							
162	1.75	824	497	46.0	18.3	39.0	154	1.575	834	453	0	15.5	44.5
154	1.575	834	453	0	15.5	44.5							

Table 4.— (Continued)

Annular Nozzle													
Static and wind-on conditions							Equivalent static V_p condition						
Run	NPR	T_T , K	V_j , m/s	V_A , m/s	T_A , °C	RH, %	Run	NPR	T_T , K	V_j , m/s	V_A , m/s	T_A , °C	RH, %
106	1.44	834	409	5.8	15.5	48							
108	1.58	832	454	3.3	15.5	48							
117	1.56	818	444	46.6	20.0	42	106	1.44	834	409	5.8	15.5	48
118	1.57	815	447	69.1	20.0	40	105	1.38	772	369	4.6	15.5	48
110	1.75	820	494	5.8	15.0	50							
116	1.745	813	493	46.3	19.4	42	108	1.58	832	454	3.3	15.5	48
119	1.760	823	497	69.5	22.2	36	107	1.49	830	425	3.3	15.5	48
112	1.96	835	543	6.7	15.5	52							
115	1.96	822	539	46.3	18.9	43	110	1.75	820	494	5.8	15.0	50
120	1.97	826	543	69.8	23.3	34	109	1.66	836	476	4.6	15.5	50
123	1.94	826	538	94.5	28.9	21	108	1.58	832	454	3.3	15.5	48
113	2.25	836	592	7.6	15.5	52							
114	2.25	824	588	46.3	18.3	44	112	1.96	835	543	6.7	15.5	52
121	2.26	826	589	69.8	23.9	32	111	1.86	830	523	5.8	15.5	50
122	2.25	822	587	94.2	26.7	25	110	1.75	820	494	5.8	15.0	50

Table 4.-- (Continued)

20-Lobe Nozzle													
Static and wind-on conditions							Equivalent static V_r condition						
Run	NPR	T_T , K	V_j , m/s	V_A , m/s	T_A , °C	RH, %	Run	NPR	T_T , K	V_j , m/s	V_A , m/s	T_A , °C	RH, %
87	1.44	819	403	0	11.7	70.5							
89	1.58	843	455	6.7	11.7	70.0							
98	1.59	825	454	46.0	17.8	50.0	87	1.44	819	403	0	11.7	70.5
99	1.57	825	449	68.9	19.4	46.0	86	1.38	824	384	5.8	11.7	70.5
91	1.75	836	500	4.9	12.2	69.5							
97	1.74	805	489	46.0	17.8	51.0	89	1.58	843	455	6.7	11.7	70.0
100	1.76	822	498	69.2	20.5	42.0	88	1.50	832	430	6.7	11.7	70.0
93	1.95	839	544	5.8	12.2	69.5							
96	1.97	814	538	46.0	17.2	53.0	91	1.75	836	500	4.9	12.2	69.5
101	1.96	839	543	69.2	21.1	39.5	90	1.66	827	476	5.8	12.2	70.0
104	1.97	803	536	94.2	27.8	22.0	89	1.58	843	455	6.7	11.7	70.0
94	2.24	827	588	7.6	12.8	69.0							
95	2.24	827	587	46.0	16.1	57.0	93	1.95	839	544	5.8	12.2	69.5
102	2.24	825	588	69.2	22.8	35.0	92	1.85	834	522	6.7	12.2	69.5
103	2.24	828	589	93.9	25.6	28.0	91	1.75	836	500	4.9	12.2	69.5

Table 4.— (Continued)

Annular Nozzle with Lined Ejector													
Static and wind-on conditions							Equivalent static V_r condition						
Run	NPR	T_T , K	V_j , m/s	V_A , m/s	T_A , °C	RH, %	Run	NPR	T_T , K	V_j , m/s	V_A , m/s	T_A , °C	RH, %
125	1.432	828	404	4.6	12.8	66							
127	1.58	830	434	0	12.8	66							
136	1.578	822	451	46.0	17.8	48	125	1.432	828	404	4.6	12.8	66
137	1.569	827	449	69.5	18.3	46.5	124	1.378	829	382	5.8	12.8	66
129	1.76	822	498	3.3	12.8	66							
135	1.75	828	498	46.0	17.8	49	127	1.58	830	454	0	12.8	66
138	1.766	820	499	69.5	20.0	42.5	126	1.51	826	431	4.6	12.8	66
131	1.95	833	541	5.8	12.8	66							
134	1.973	833	546	46.3	17.8	51	129	1.76	822	498	3.3	12.8	66
139	1.974	829	544	69.2	21.1	40	128	1.66	822	475	0	12.8	66
142	1.951	832	541	94.5	26.7	24	127	1.58	830	454	0	12.8	66
132	2.26	828	590	0	12.8	66							
133	2.27	824	590	46.3	16.6	55	131	1.95	833	541	5.8	12.8	66
140	2.235	838	590	69.8	21.7	37	130	1.85	827	520	4.6	12.8	66
141	2.252	833	591	93.9	23.9	32	129	1.76	822	498	3.3	12.8	66

Table 4.— (Continued)

20-Lobe Nozzle with Lined Ejector													
Static and wind-on conditions							Equivalent static V_r condition						
Run	NPR	T_T , K	V_j , m/s	V_A , m/s	T_A , °C	RH, %	Run	NPR	T_T , K	V_j /m/s	V_A , m/s	T_A , °C	RH, %
68	1.433	824	403	3.3	13.9	54							
70	1.58	827	452	0	13.9	54							
76	1.58	815	449	45.7	16.7	50	68	1.433	824	403	3.3	13.9	54
83	1.59	815	451	69.2	23.3	33	67	1.383	819	382	0	13.9	54
73	1.75	827	497	5.79	13.9	55							
77	1.75	818	494	46.6	17.8	48	70	1.580	827	452	0	13.9	54
82	1.74	812	490	69.2	22.8	34	69	1.503	825	428	0	13.9	54
74	1.95	839	543	3.3	13.9	55							
78	1.94	833	539	46.0	17.8	46	73	1.75	827	496	5.8	13.9	55
81	1.96	819	539	68.9	22.2	36	71	1.65	817	470	0	13.9	54
84	1.95	820	537	93.9	26.7	25	70	1.58	827	452	0	13.9	54
75	2.267	829	592	5.8	13.9	55							
79	2.24	828	588	46.0	18.9	44	74	1.95	839	543	3.3	13.9	55
80	2.22	825	584	69.2	20.0	40							
85	2.25	825	589	94.5	27.8	23	73	1.75	827	497	5.8	13.9	55

Table 4.— (Concluded)

57-Tube Nozzle with Lined Ejector													
Static and wind-on conditions							Equivalent static V_r condition						
Run	NPR	T_T , K	V_j , m/s	V_A , m/s	T_A , °C	RH, %	Run	NPR	T_T , K	V_j , m/s	V_A , m/s	T_A , °C	RH, %
1	1.58	833	454	0	13.3	55							
25	1.753	826	497	0	24.4	29							
16	1.76	822	498	46.0	18.3	47	1	1.58	833	454	0	13.3	55
5	1.966	855	551	3.3	13.9	56	25	1.753	826	498	0	24.4	29
17	1.963	833	543	45.4	18.9	46							
7	2.245	854	598	0	13.9	56	5	1.966	855	551	3.3	13.8	56
18	2.255	841	594	45.4	19.4	45	4	1.863	850	529	0	13.8	56
21	2.254	827	589	68.9	22.2	38							
9	2.61	852	644	3.3	13.9	58	7	2.245	854	598	0	13.8	56
19	2.60	831	635	45.7	20.0	43	6	2.10	848	572	0	13.8	56
20	2.60	833	636	68.6	21.1	41	5	1.936	855	551	0	13.8	56
22	2.60	829	635	93.3	25.5	31							
57-Tube Nozzle with Lined Ejector Forward arc													
169	1.756	866	511	8.8	12.7	51							
170	1.972	873	558	9.4	12.7	51							
175	1.955	878	557	46.3	16.1	44.5	169	1.756	866	510	8.8	12.7	51
171	2.26	873	607	7.3	12.2	51	170	1.972	873	558	9.4	12.7	51
174	2.26	873	607	46.3	15.5	46							
172	2.60	873	652	8.2	12.7	52	171	2.26	873	607	7.3	12.2	51
173	2.60	882	654	463	15.0	47							

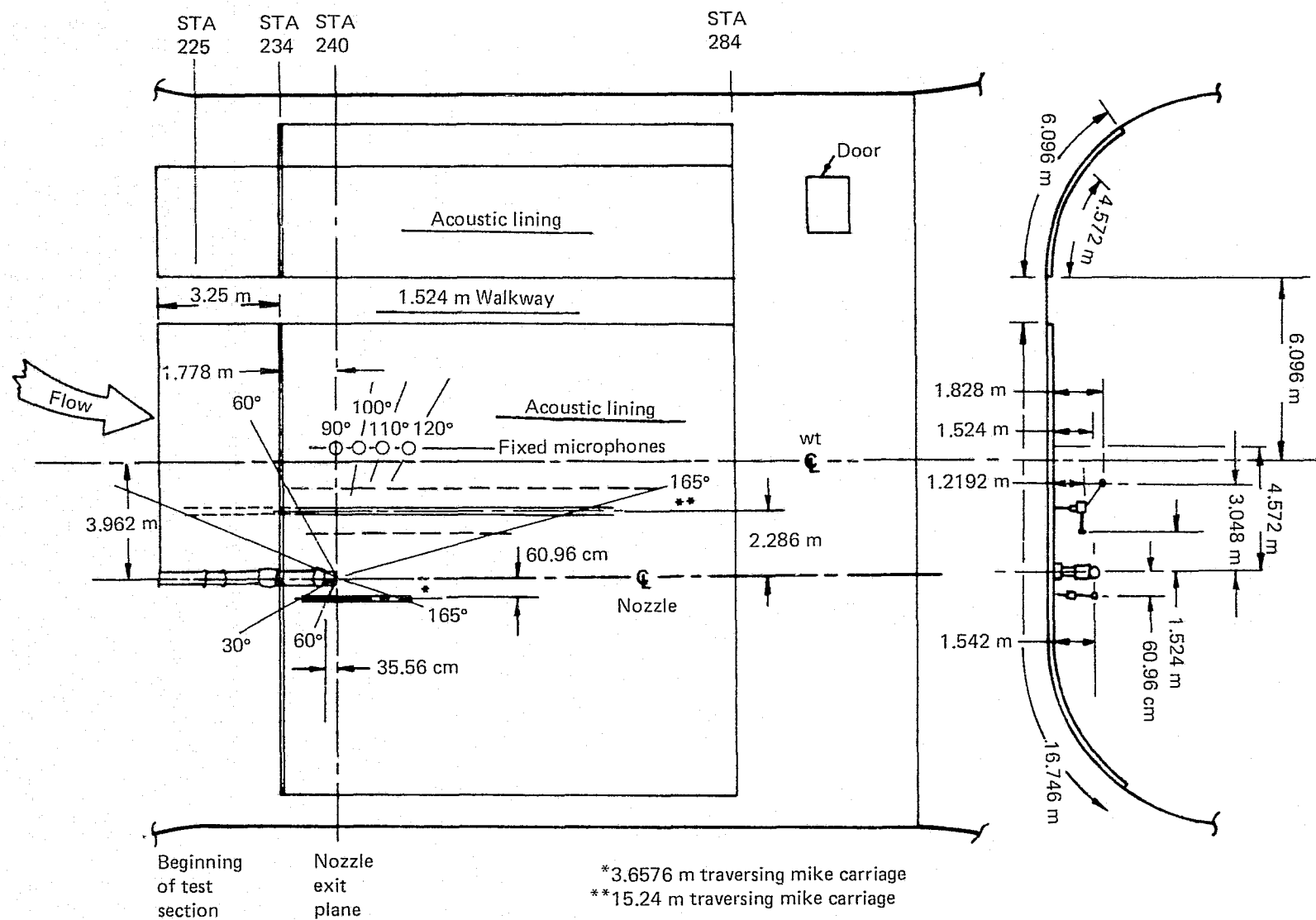


Figure 1.— Test Installation

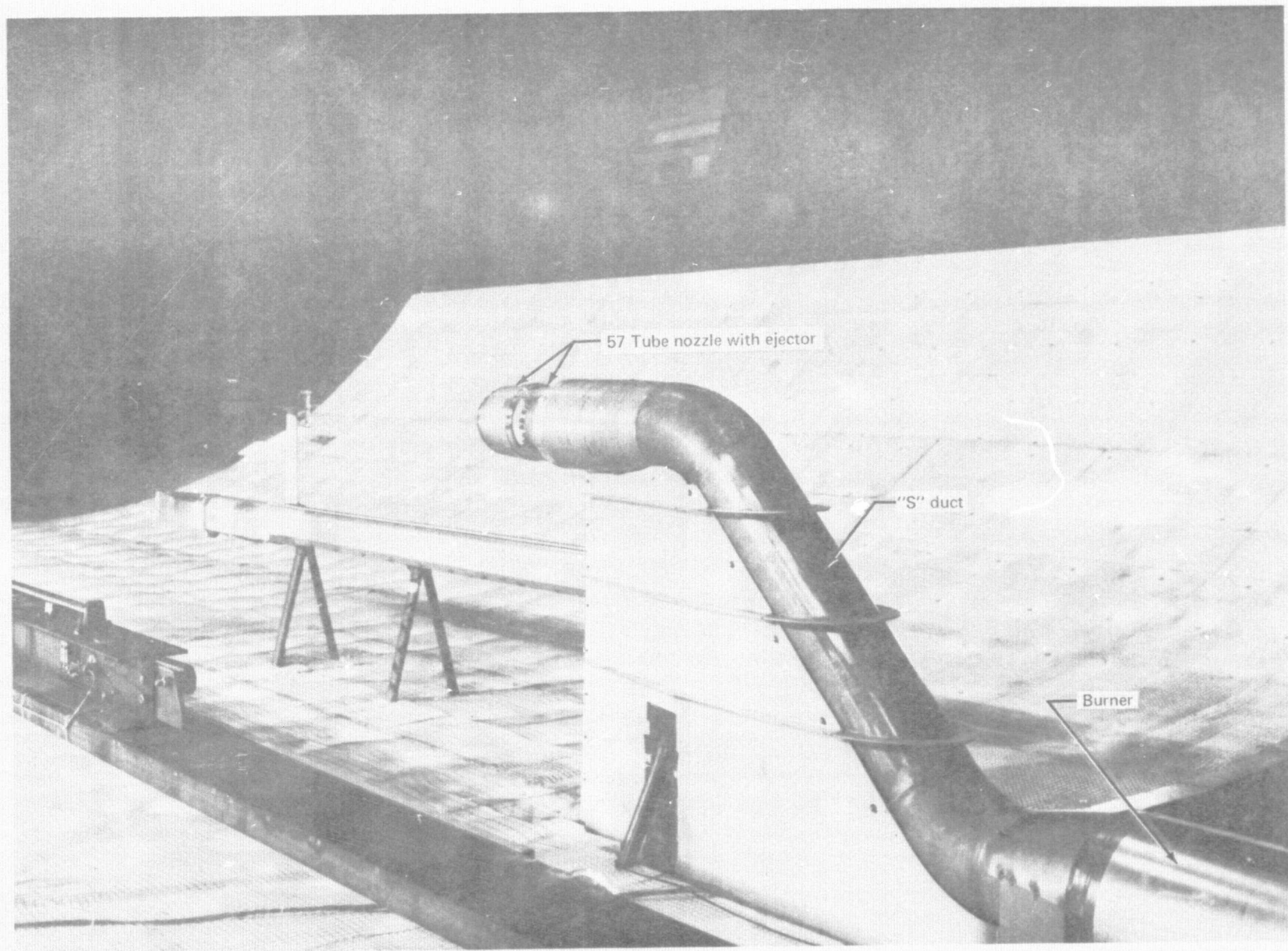


Figure 2.— Nozzle Nacelle, Hot Flow "S" Duct and Burner Installation

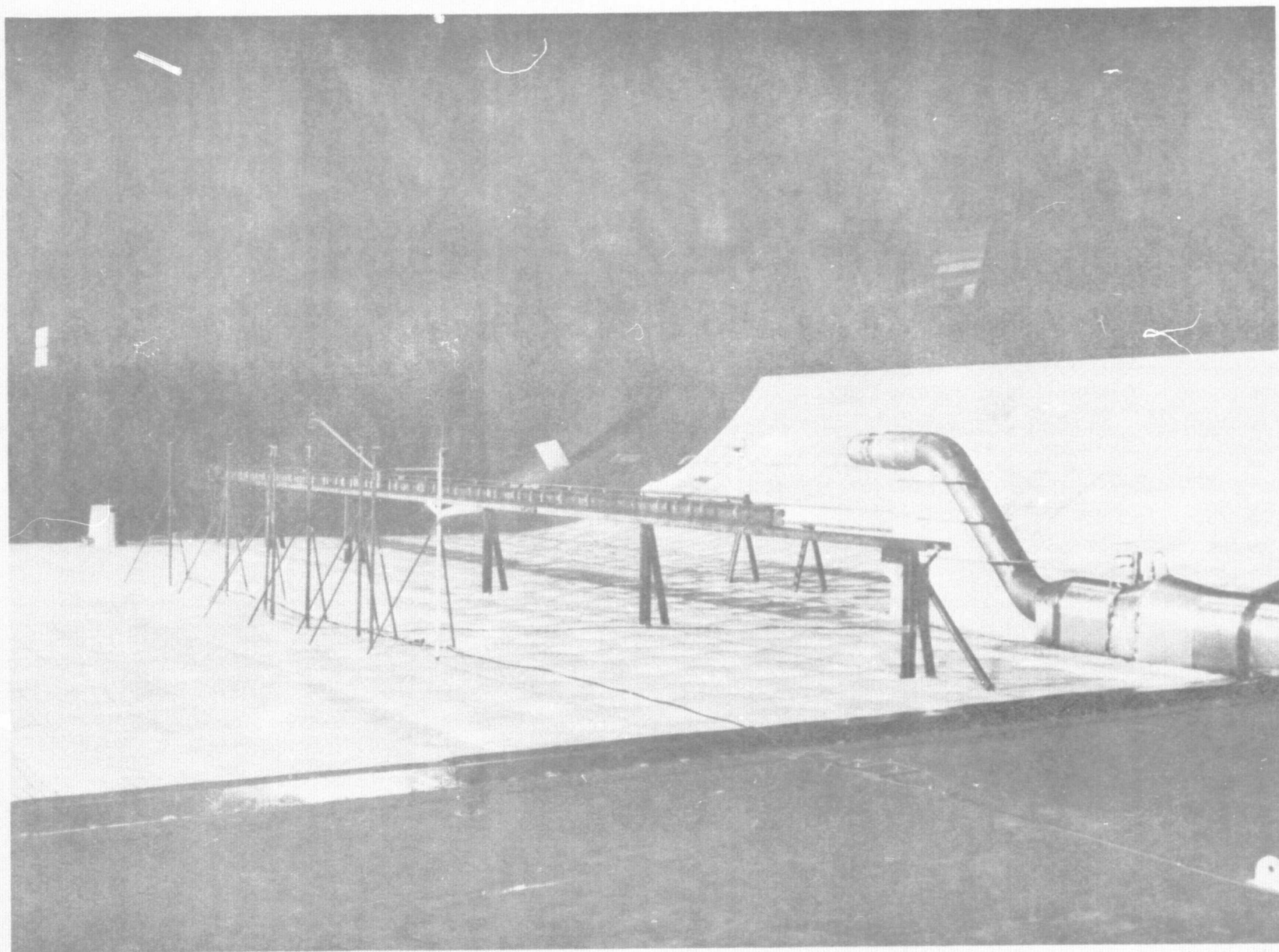


Figure 3.— Fixed microphones and 15.2 m Traverse

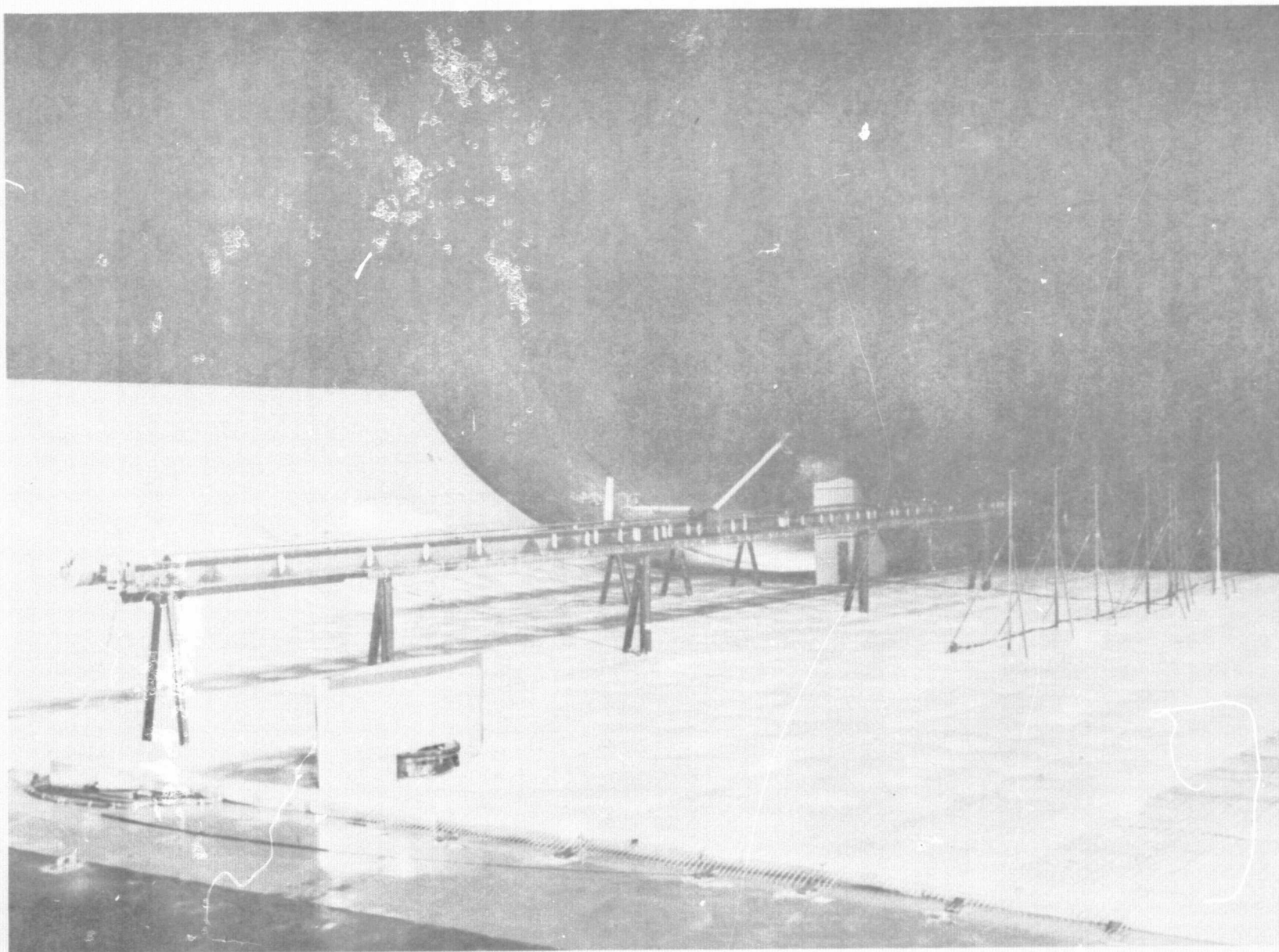


Figure 4.— 15.2 m Traverse with 1.5 and 3.0 m Sideline Arms

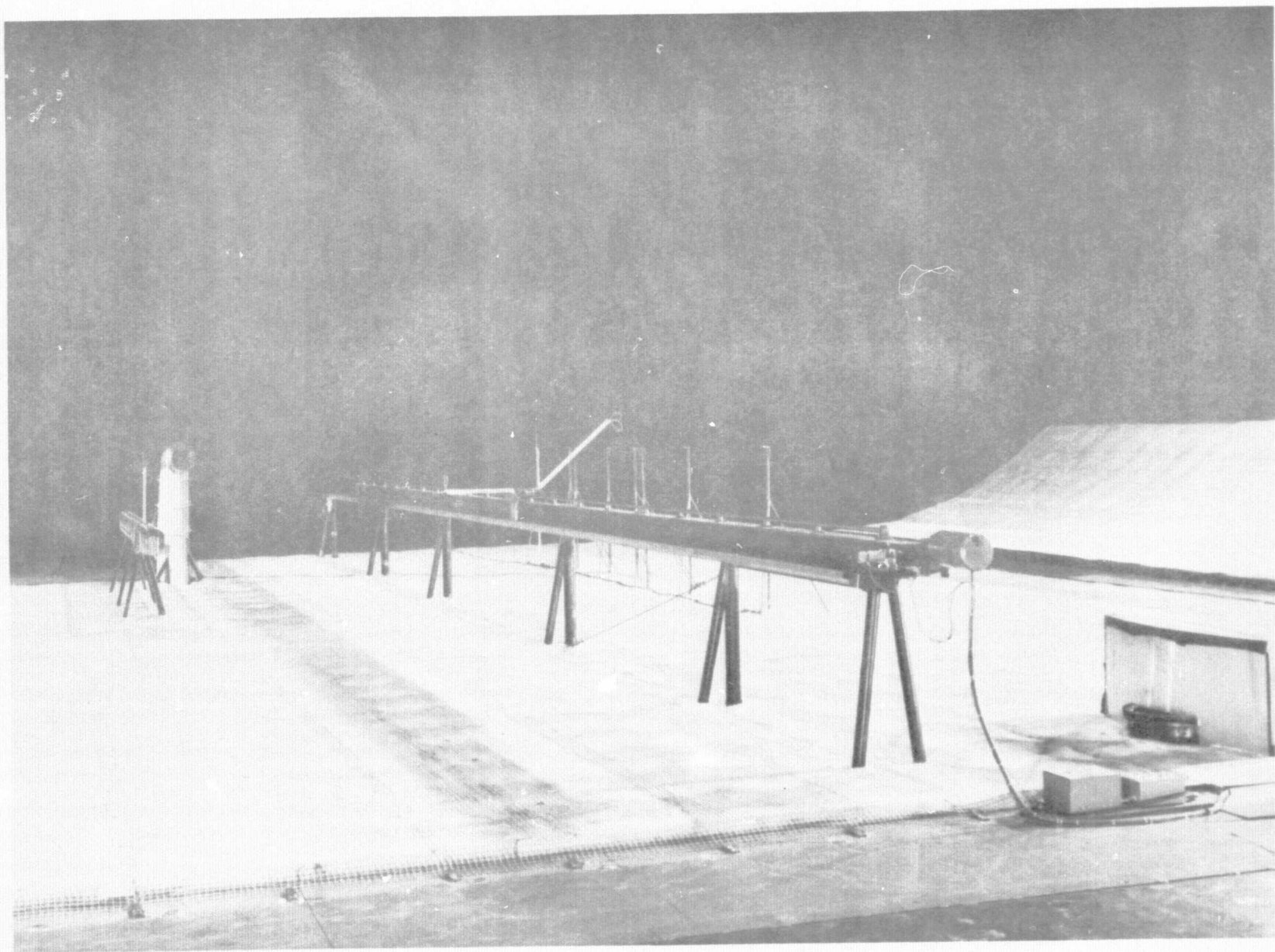


Figure 5.— 3.6 and 15.2 m Traverse Systems

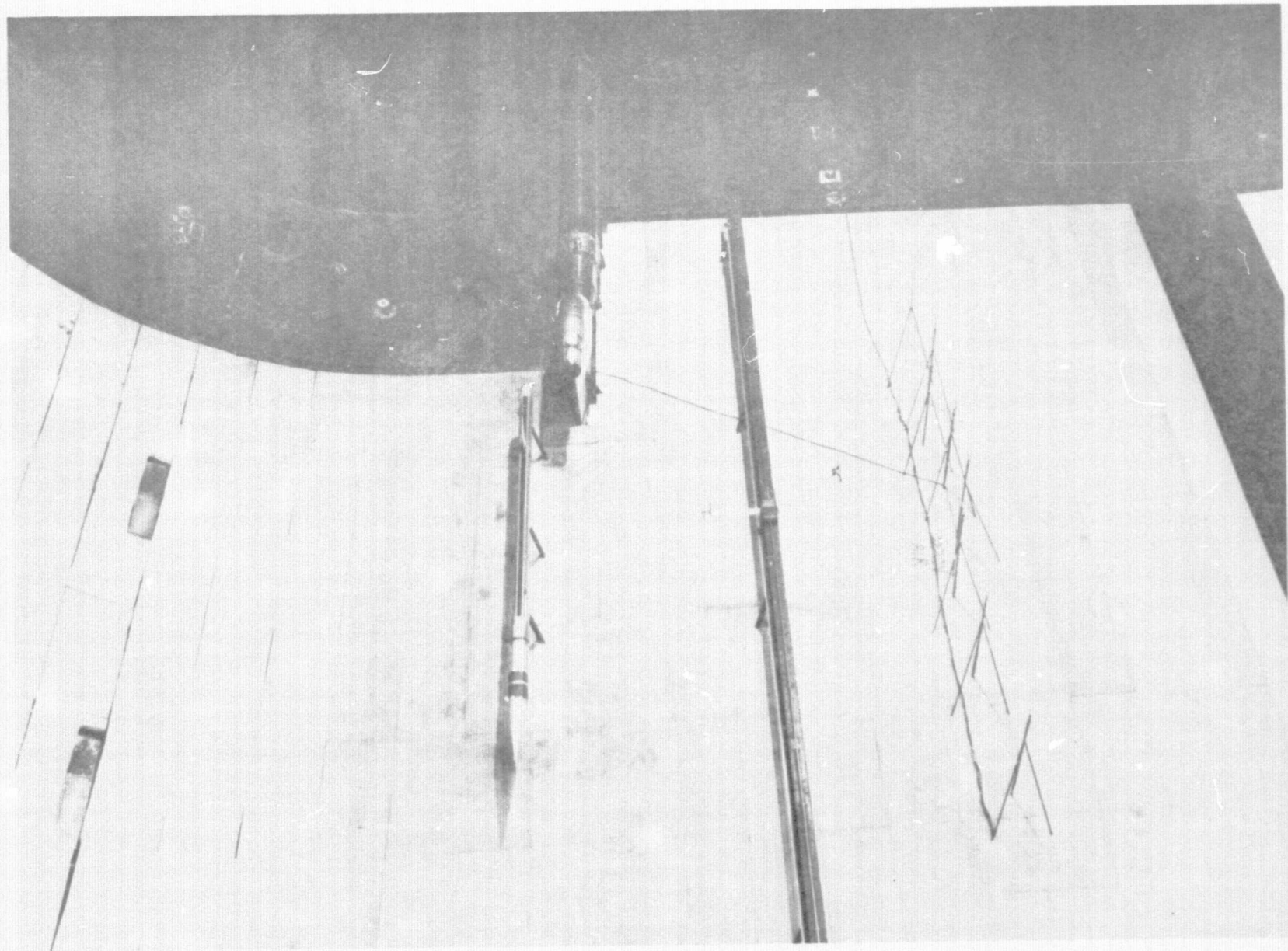


Figure 6.— Lining, Flow and Microphone Installations

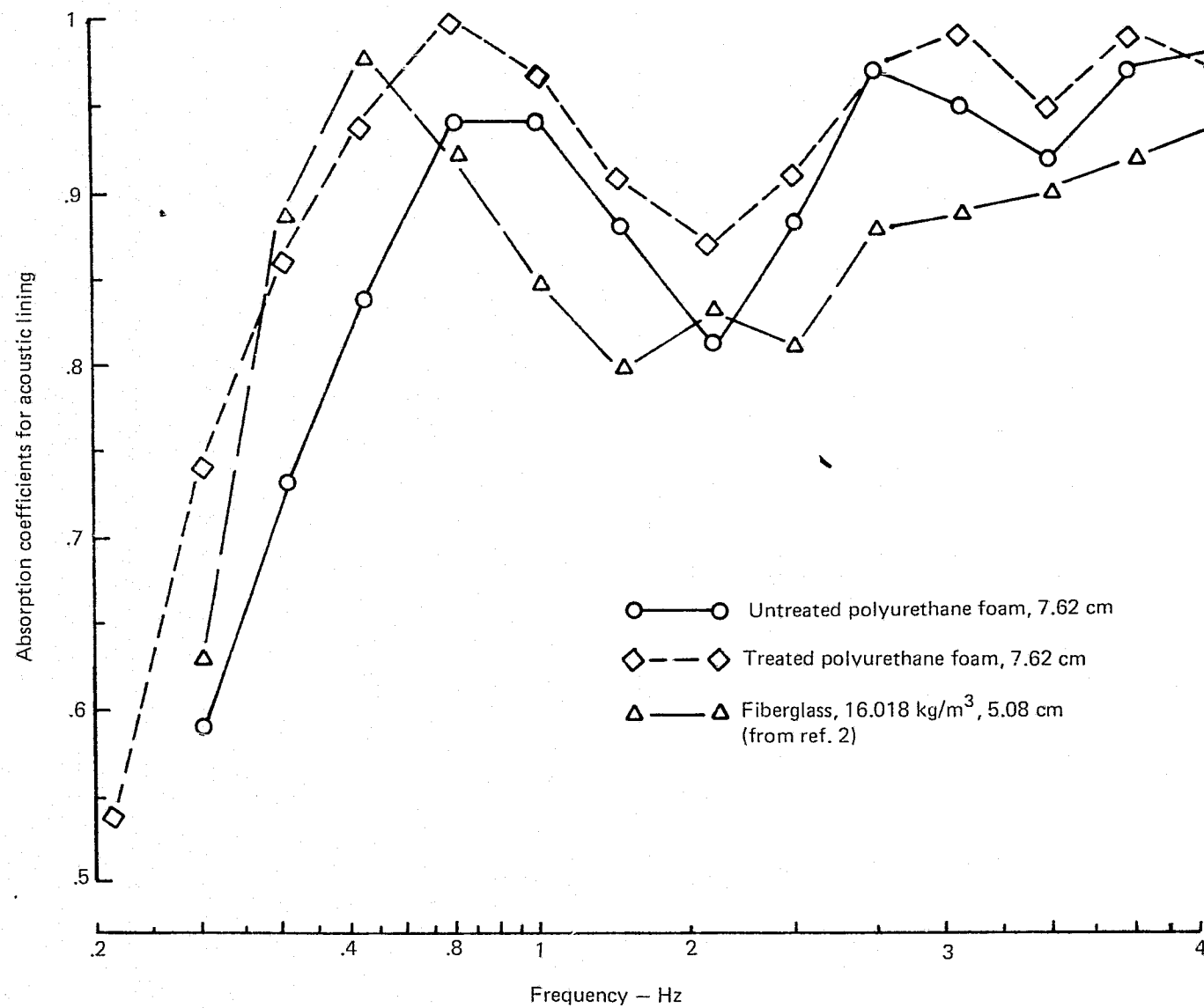


Figure 7.— Absorption Coefficients for Acoustic Linings

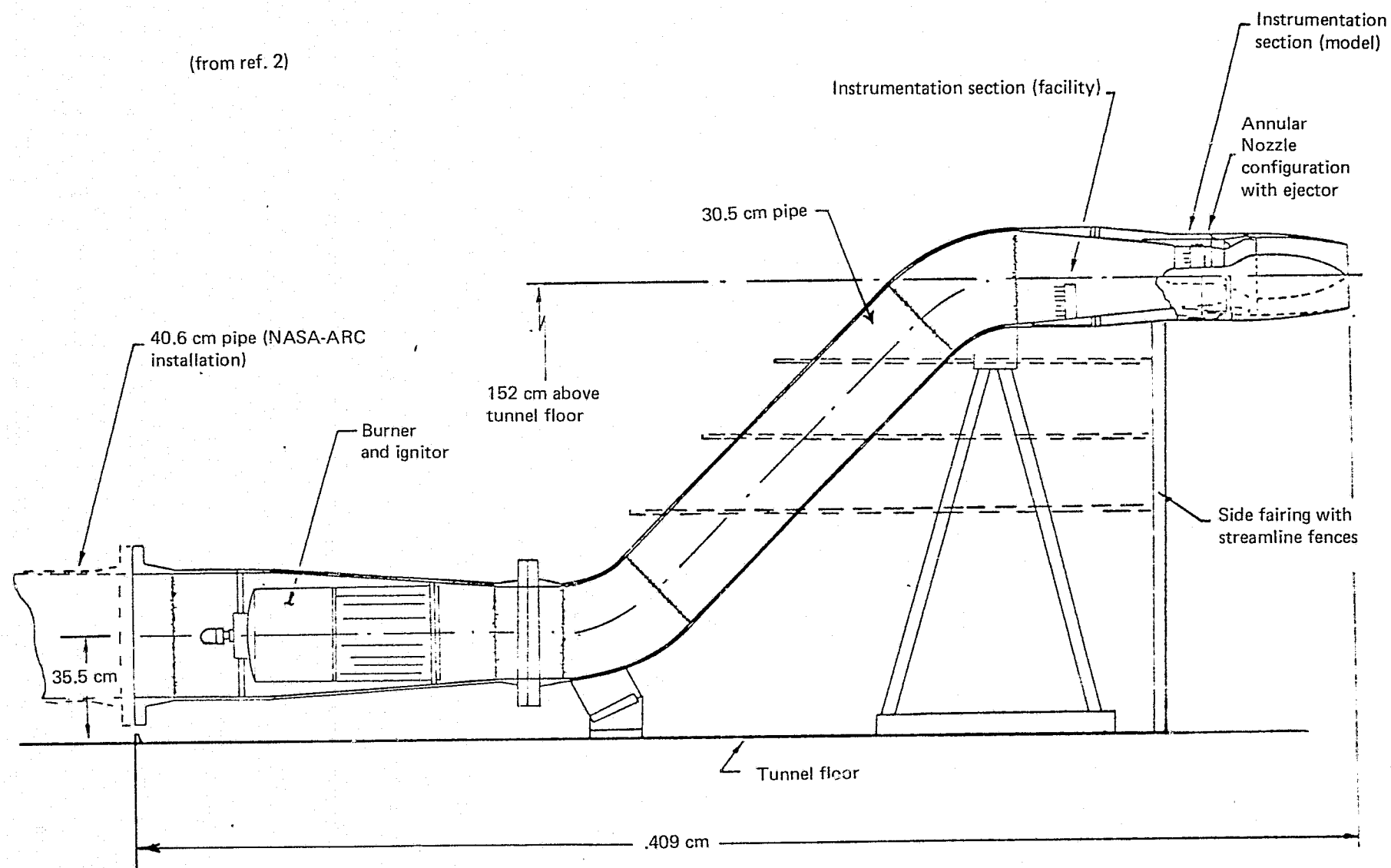


Figure 8.— Burner, S Duct and Flow System Schematic

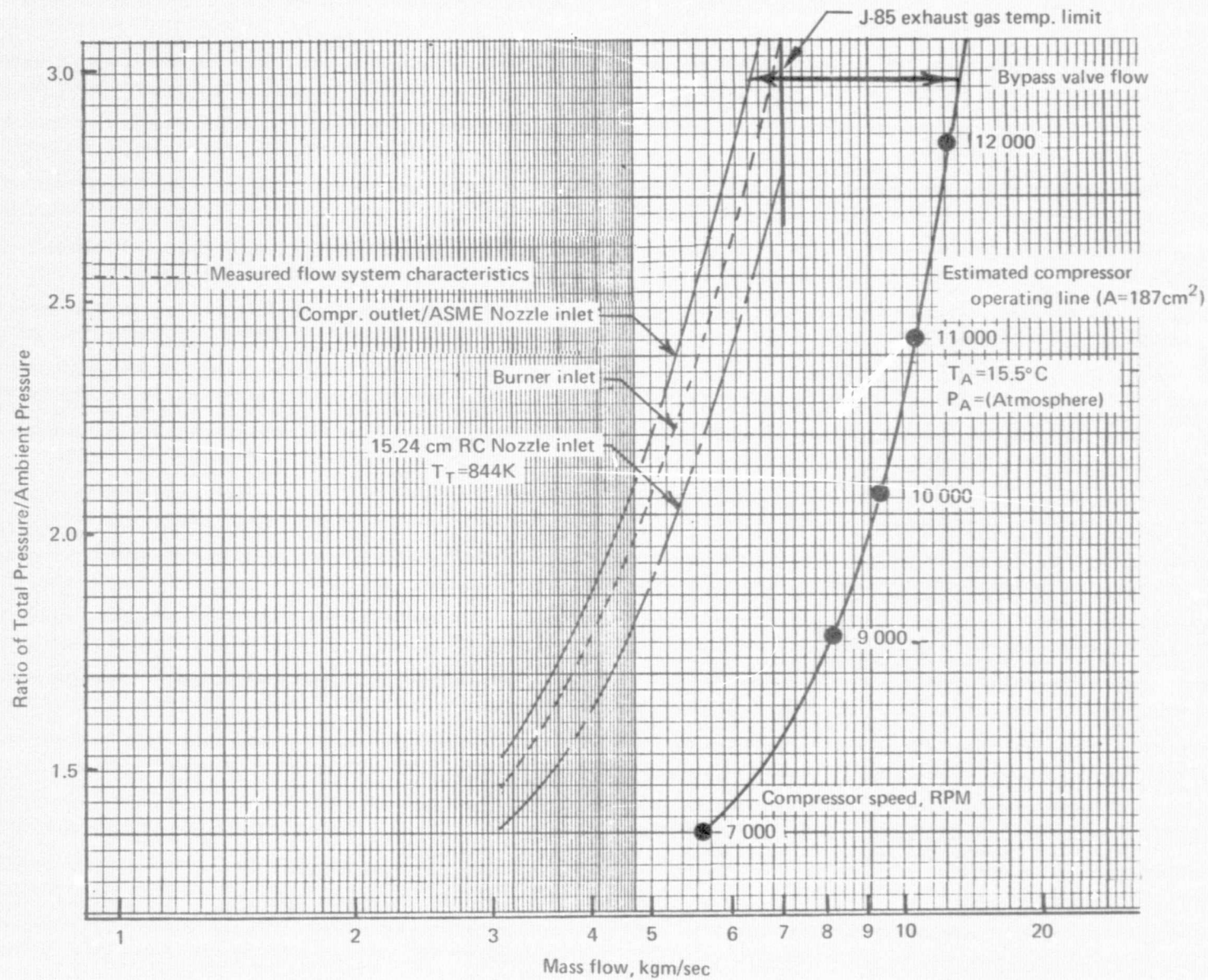


Figure 9.—Compressor/Flow System Characteristics

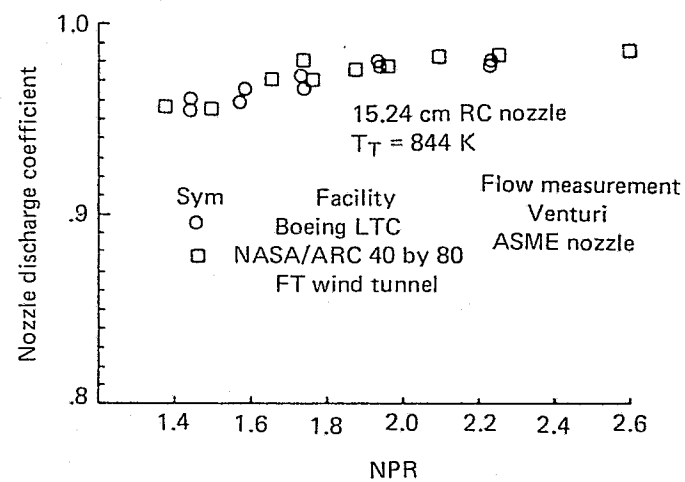
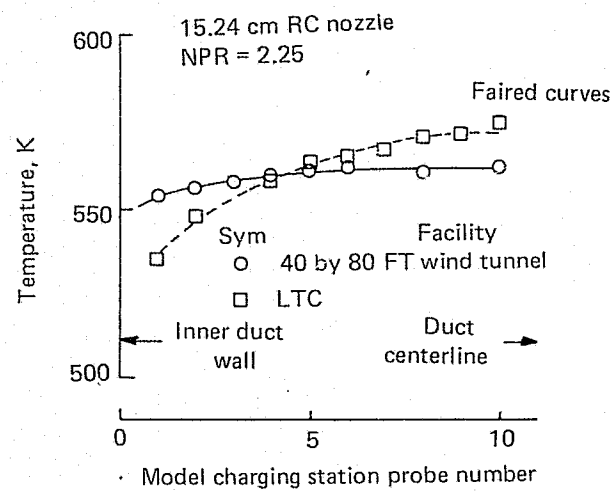
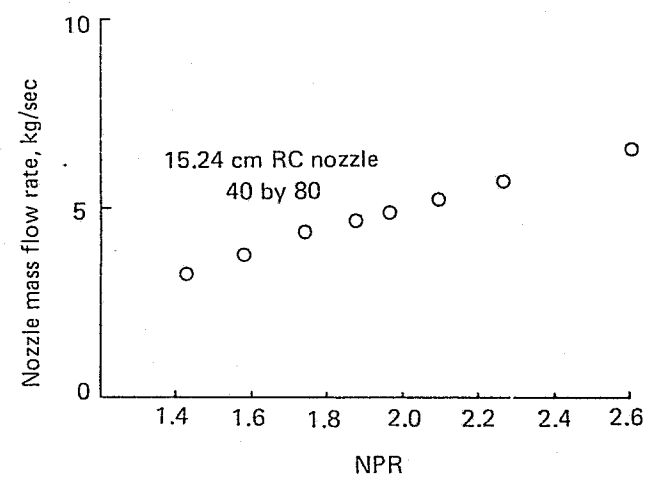
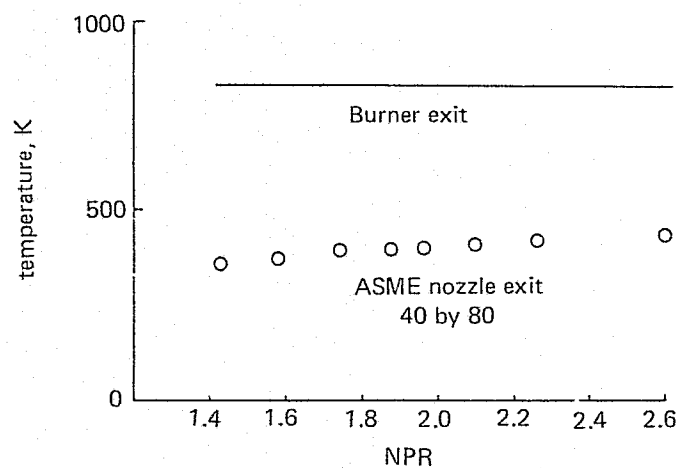


Figure 10.— Flow System Characteristics

ORIGINAL PAGE IS
OF POOR QUALITY

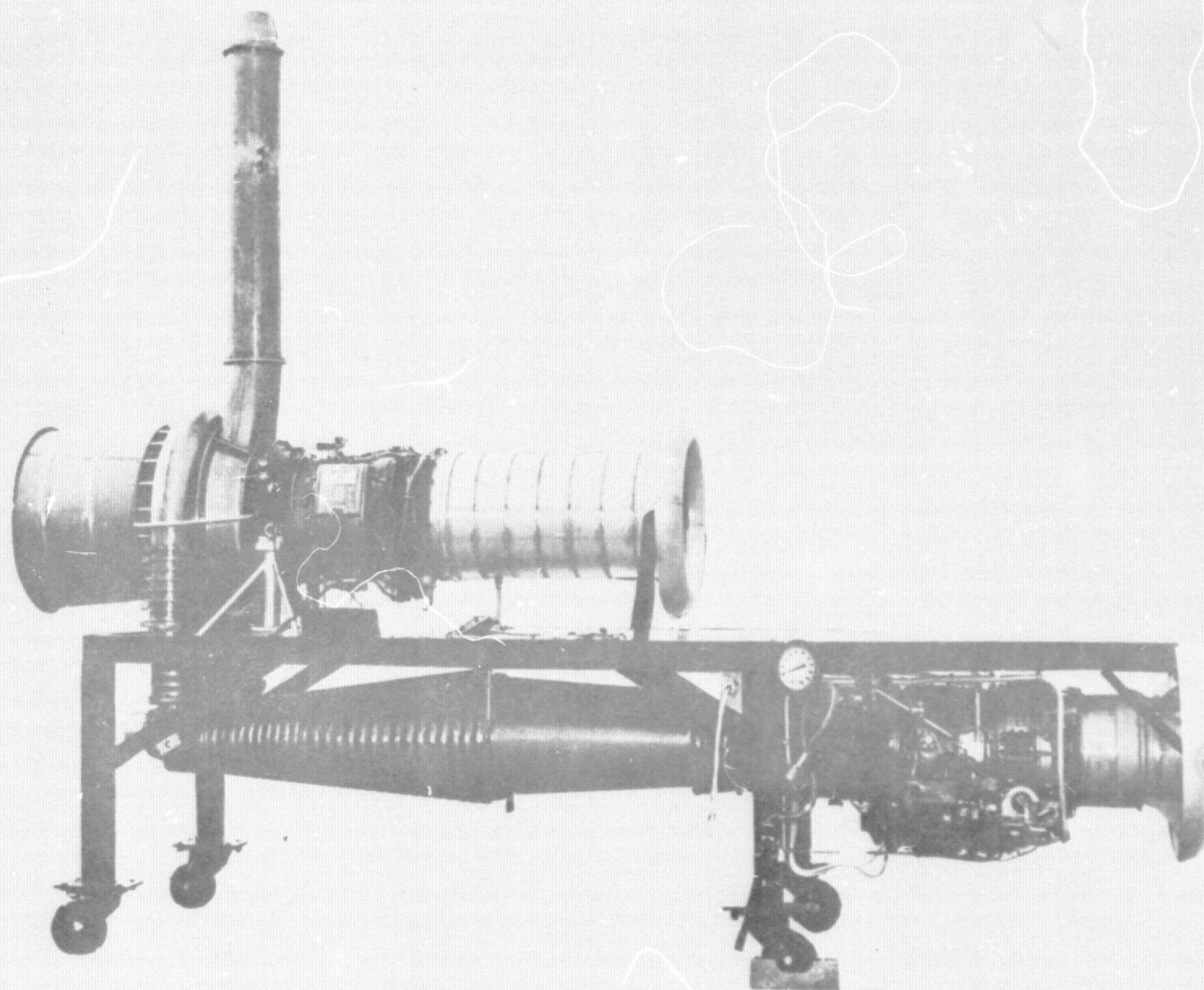


Figure 11.— Viper / J-85 Compressor

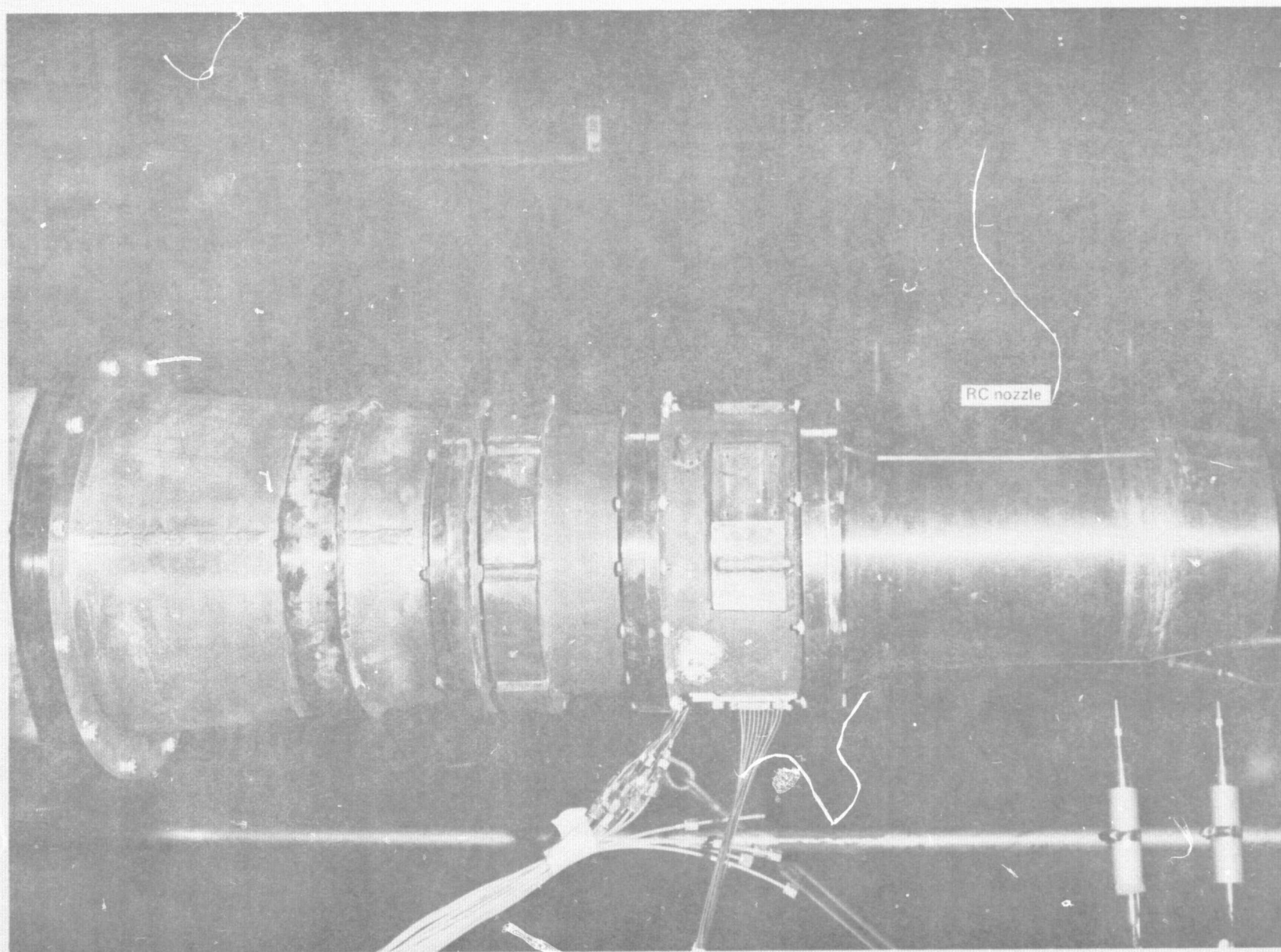


Figure 12.— Photographs of Baseline and Suppressor Nozzles

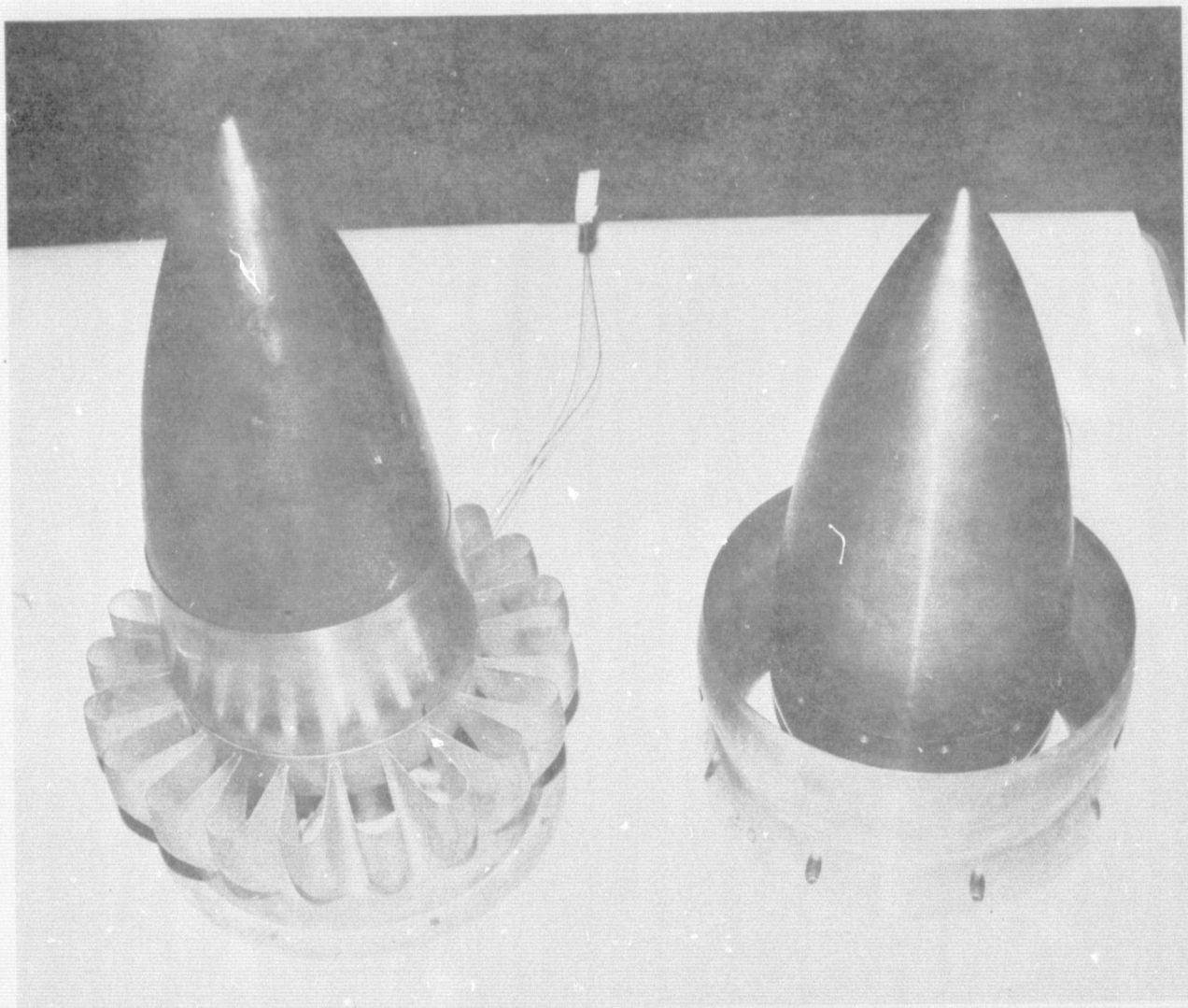


Figure 12.— (Continued)

ORIGINAL PAGE IS
OF POOR QUALITY

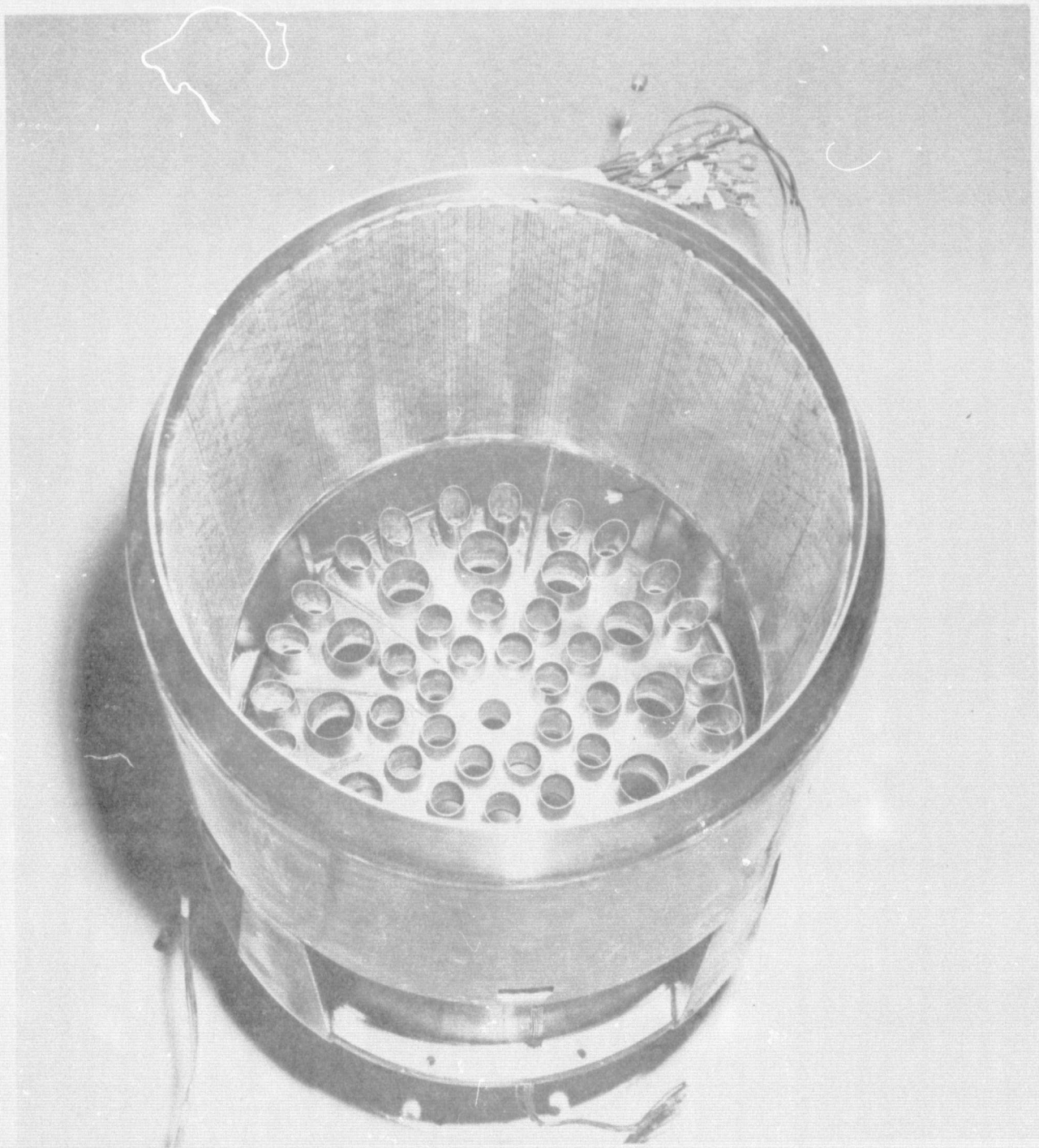
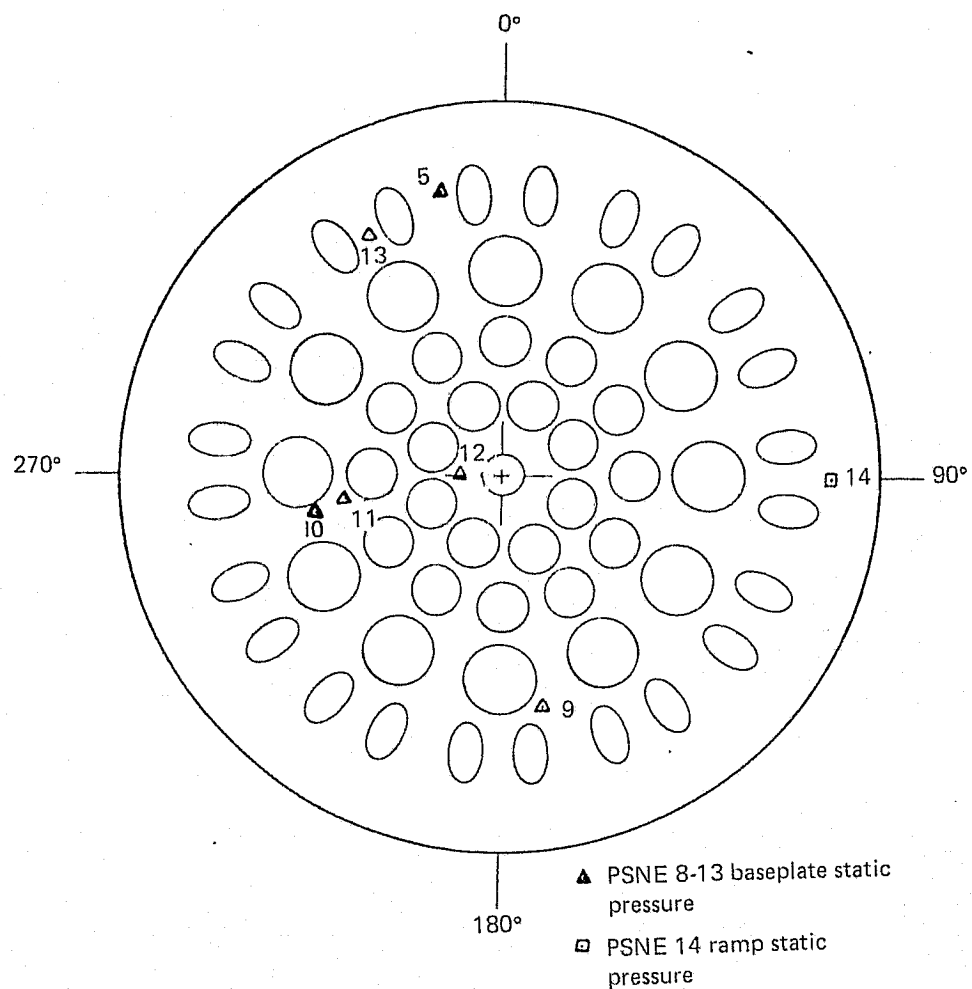
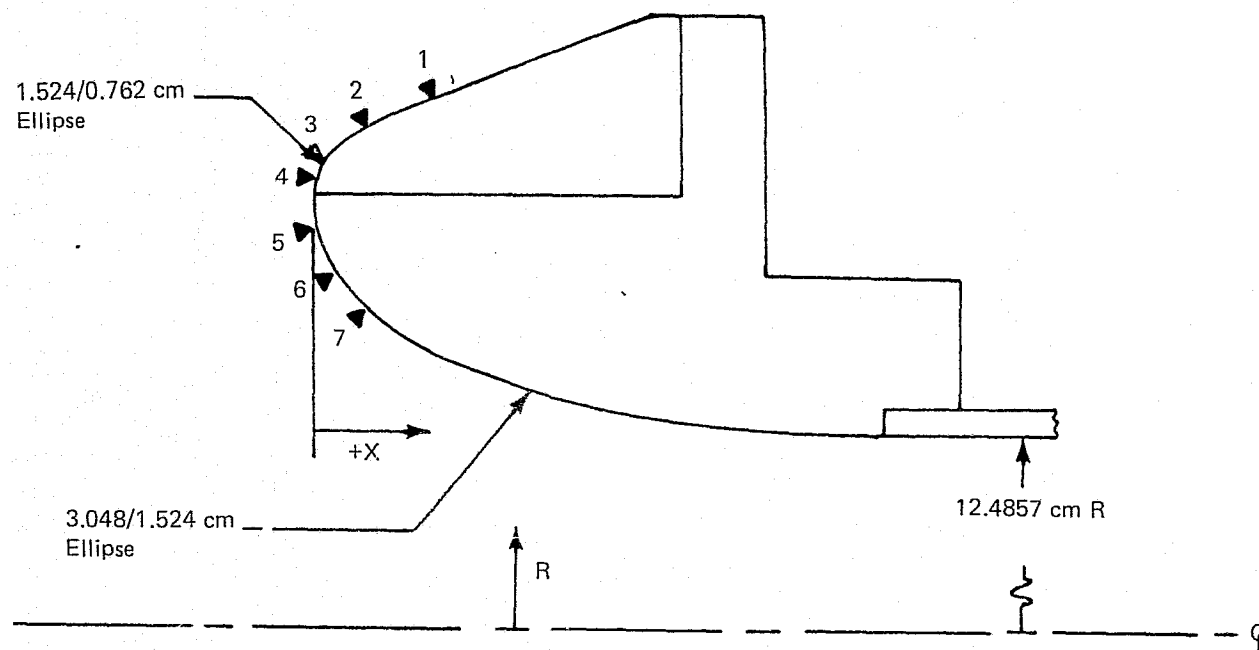


Figure 12.— (Concluded)



Tap No.	R (cm)	θ°
8	11.4554	347.6
9	9.2456	169.7
10	7.3406	258.0
11	6.2992	261.2
12	1.8288	270.0
13	10.7696	330.0
14 (static)	12.8778	90

Figure 13.— 57-Tube Nozzle Base and Ejector Lip Static Pressure Instrumentation



Tap No.	X (Cm)	R (cm)	0°
1	1.841	12.583	0
2	0.6096	13.068	↓
3	0.1397	13.525	
4	0.020	14.109	
5	0.076	14.22	
6	0.282	14.43	
7	0.762	14.64	0

Figure 13.— (Concluded)

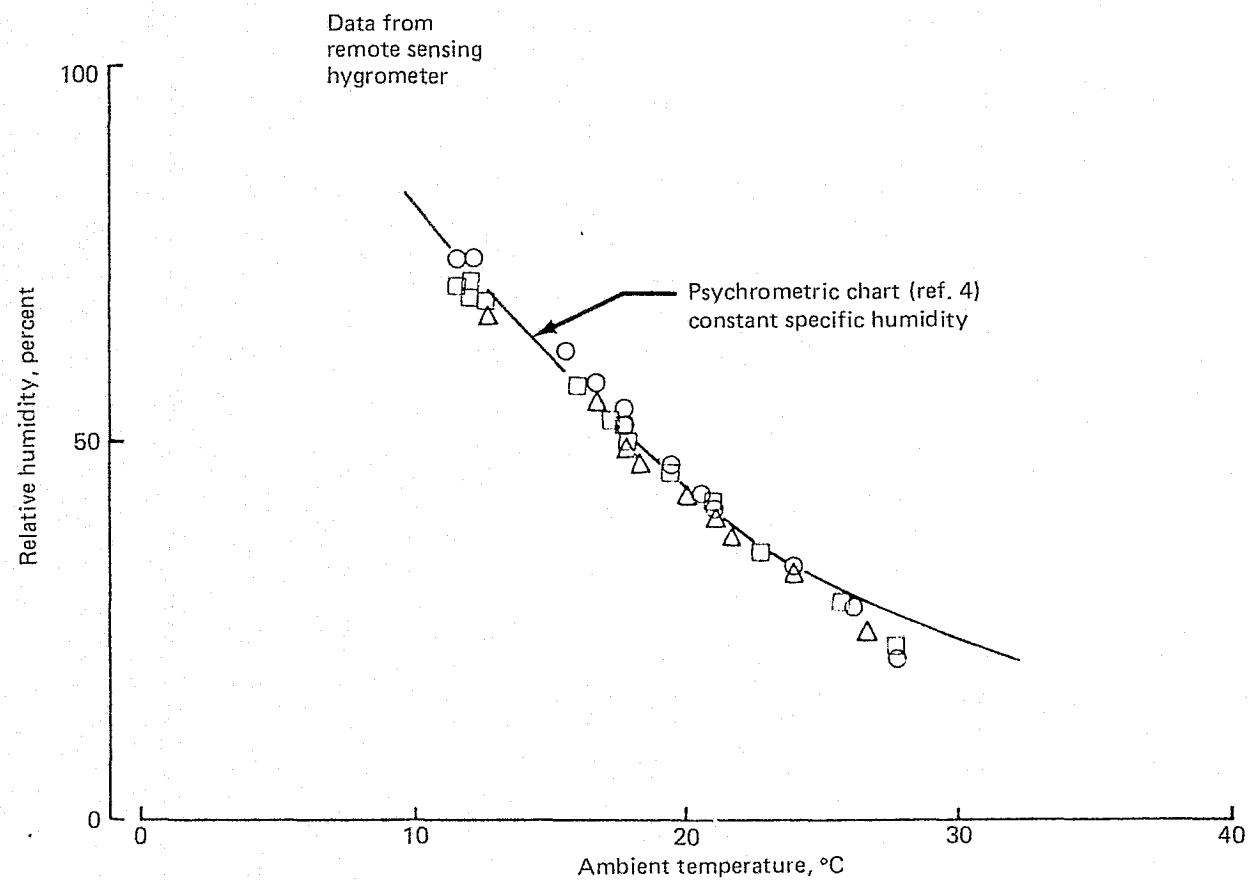
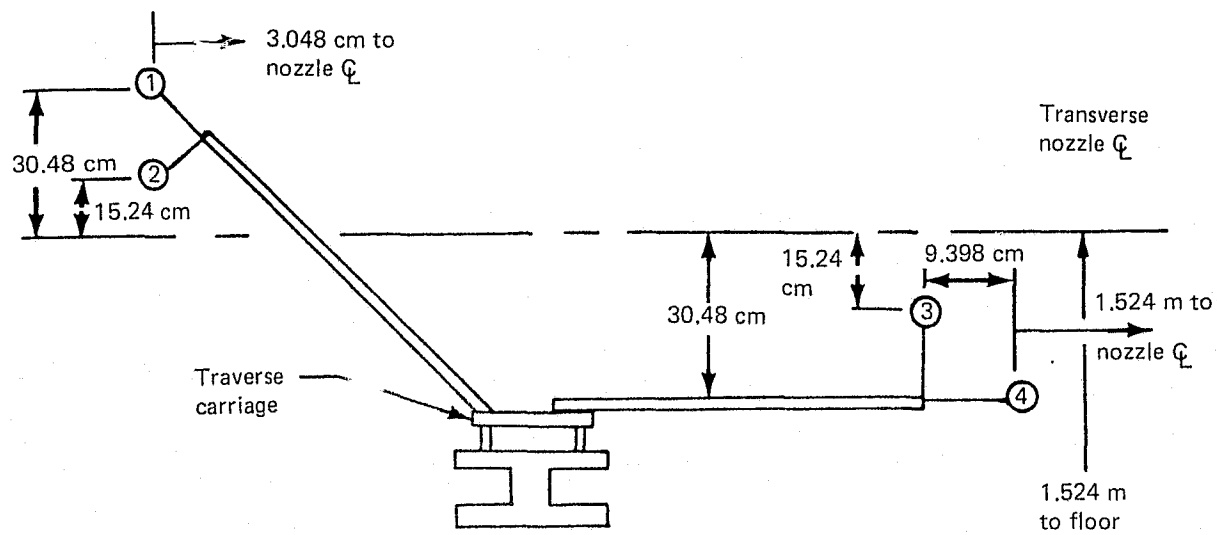
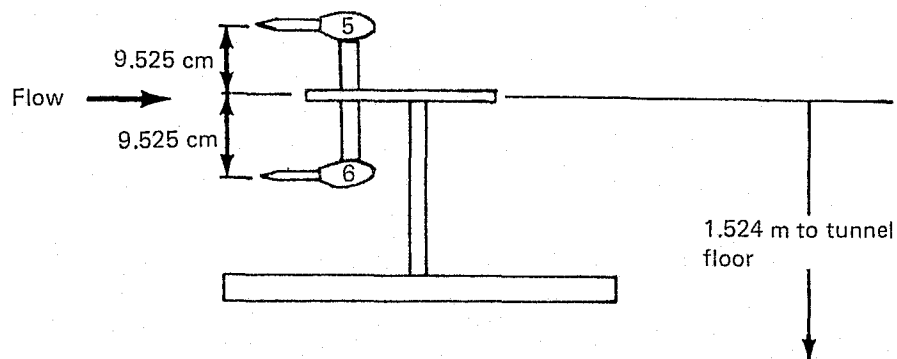


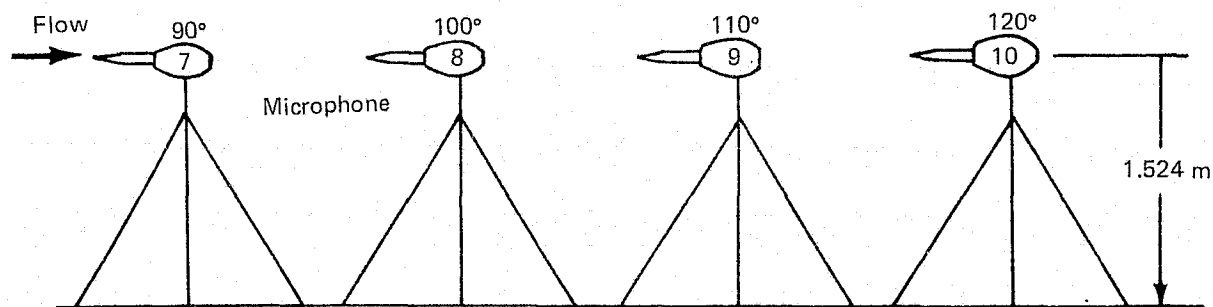
Figure 14.— Comparison of Measured Hygrometer Relative Humidity with Calculated Values Based on Constant Specific Humidity



15.24 m Traverse with 1.52 & 3.048 m sideline microphones (looking downstream)



3.657 m Traverse with 0.6096 m sideline mics (side view)



4.57 m Sideline fixed mic (sideview)

Figure 15.— Microphone Installations

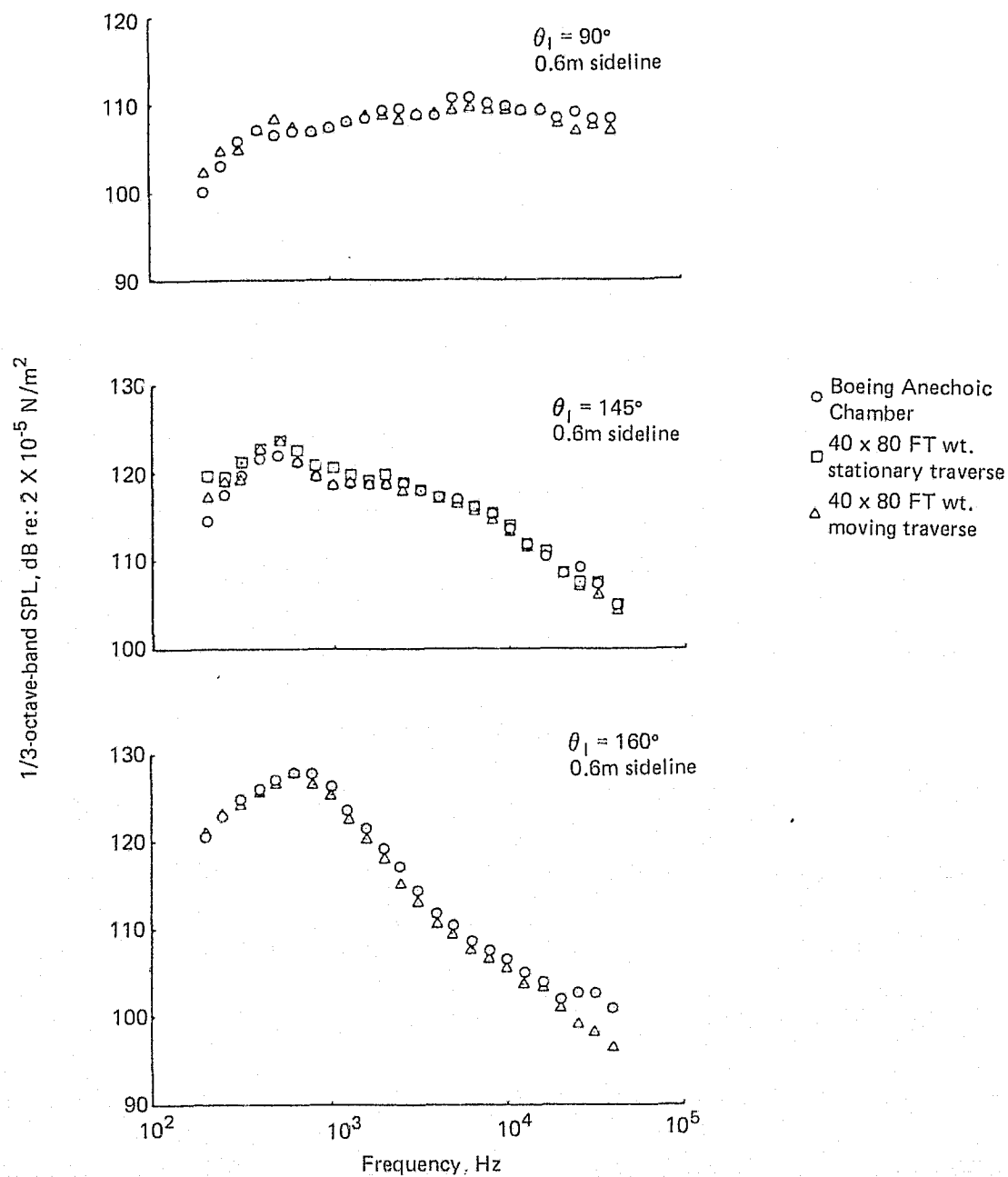


Figure 16.-- Comparison of Static Jet Noise Spectra Measured in the 40-by 80-Ft Wind Tunnel and the Boeing Anechoic Chamber, 15.24cm RC Nozzle, NPR = 1.44

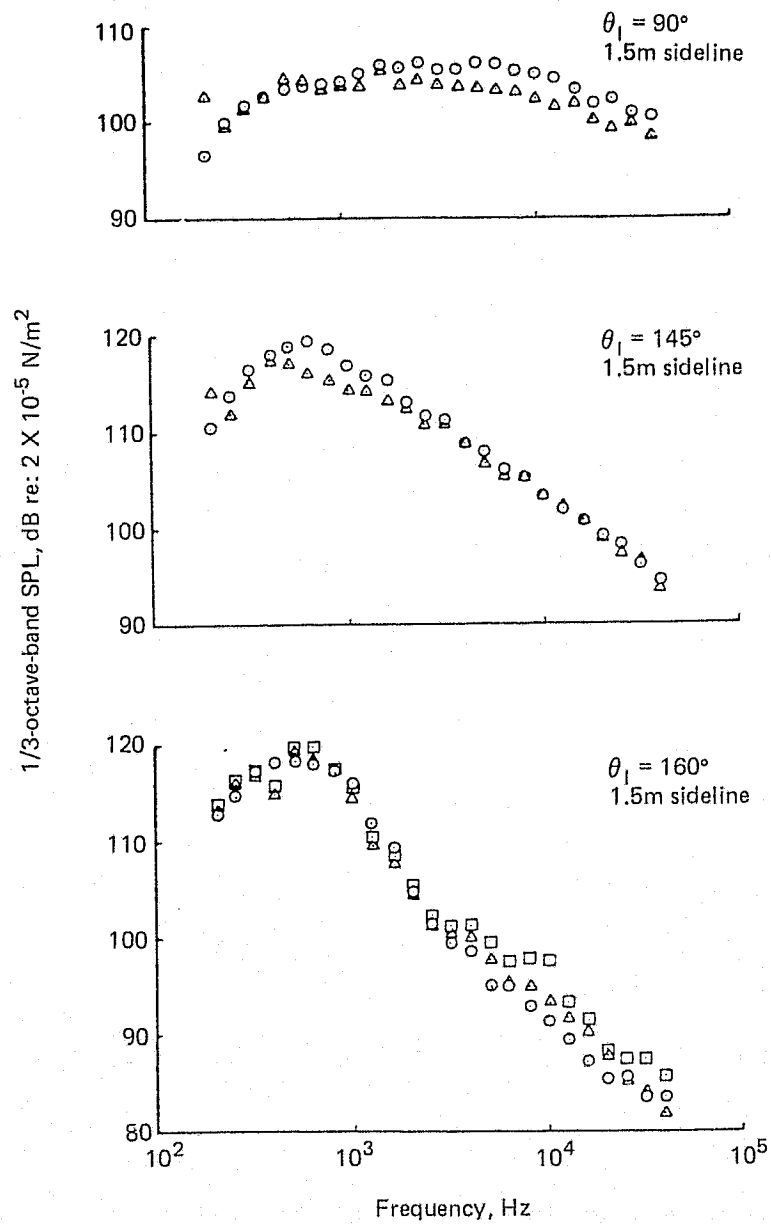


Figure 16.— (Continued)

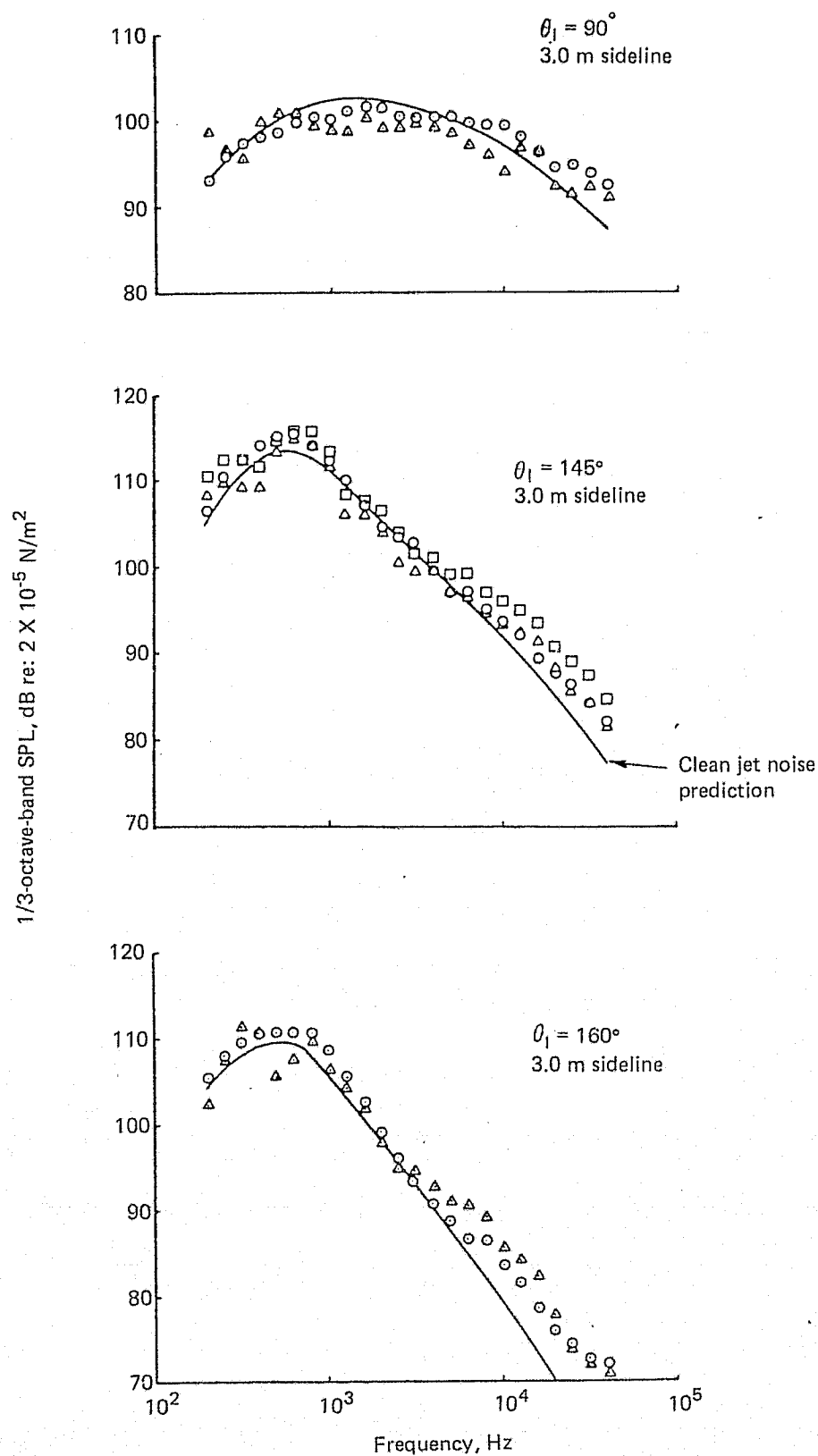


Figure 16.— (Concluded)

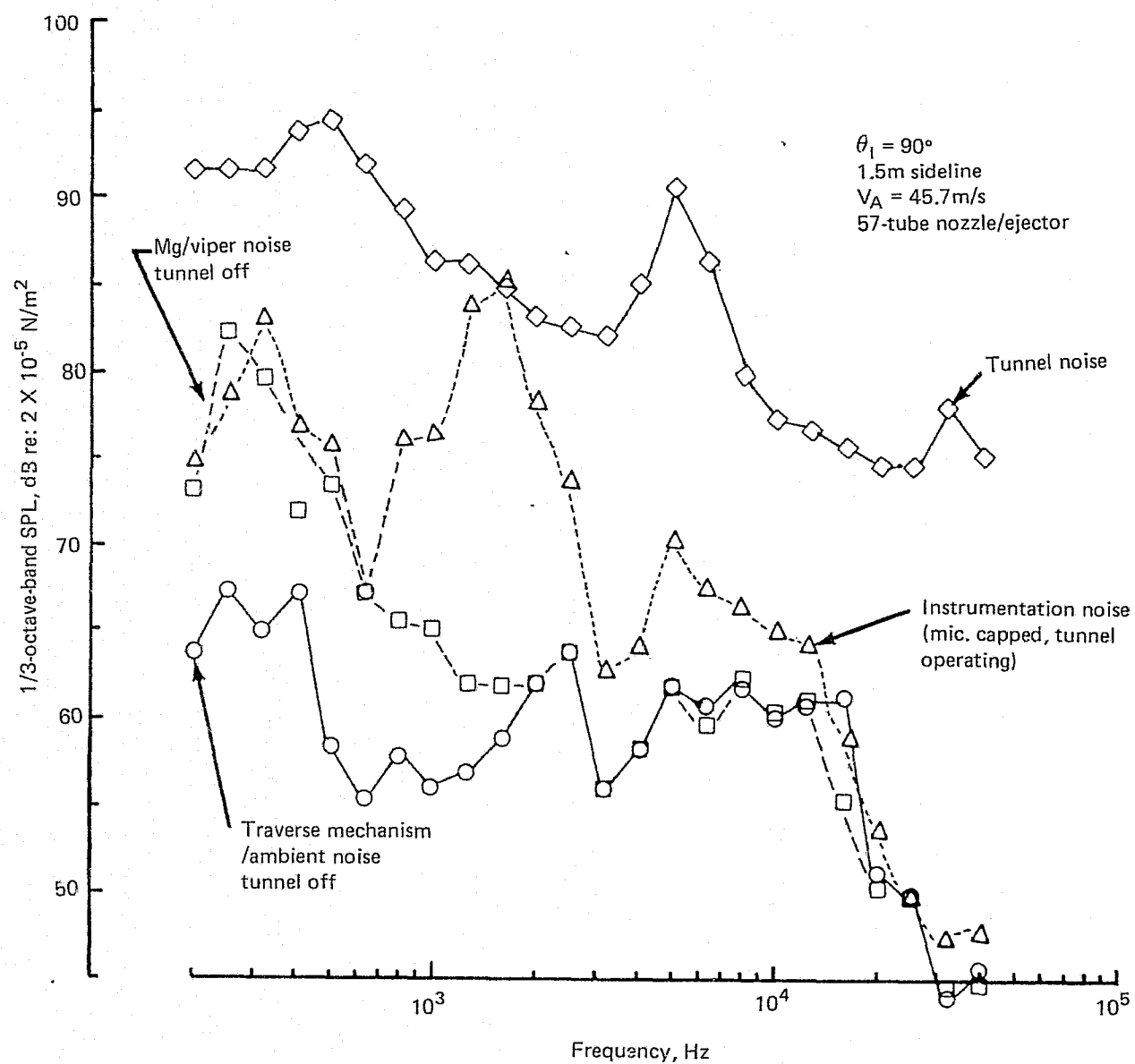


Figure 17.— 40 by 80 Ft Wind Tunnel Noise Floors

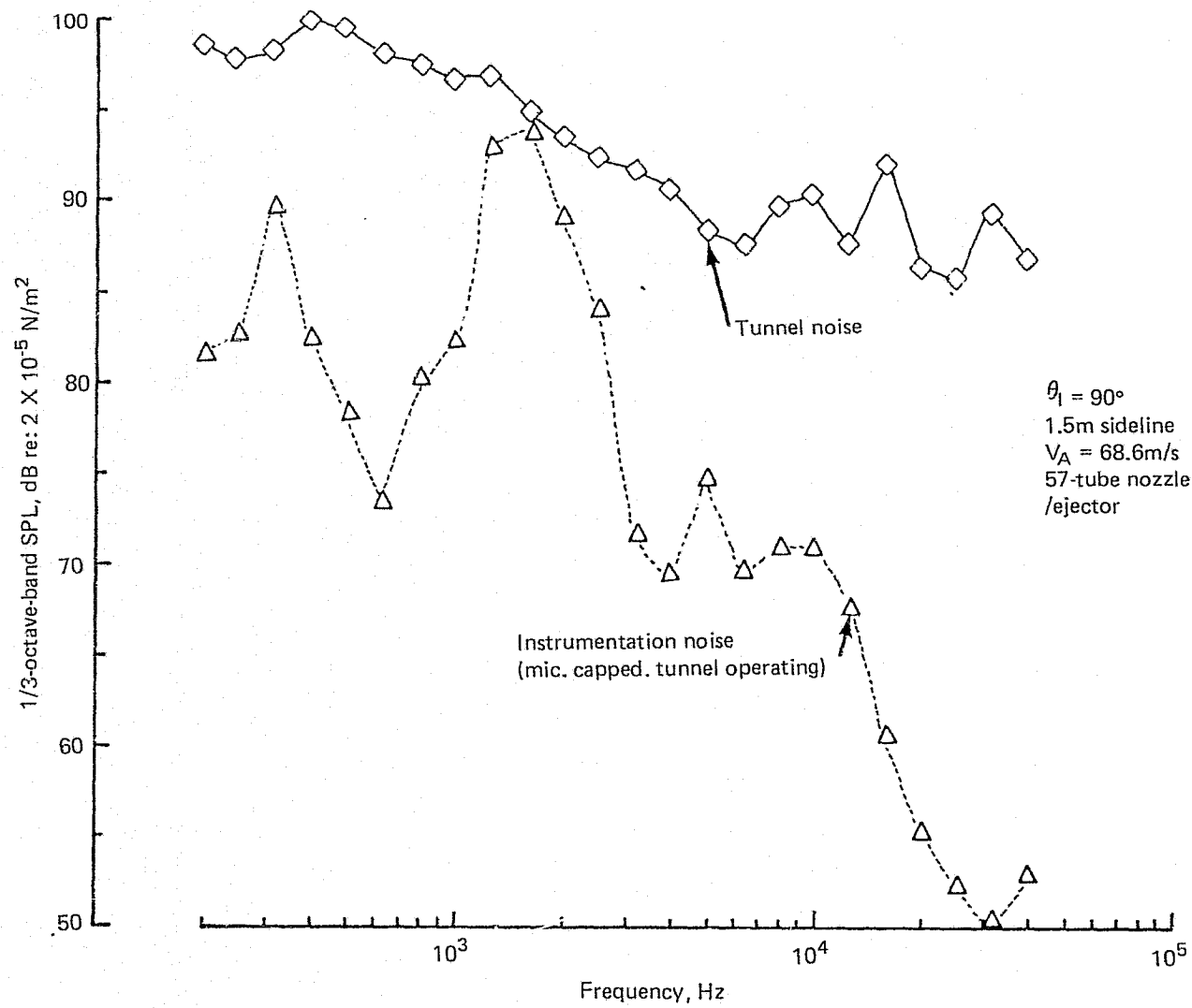


Figure 17.— (Continued)

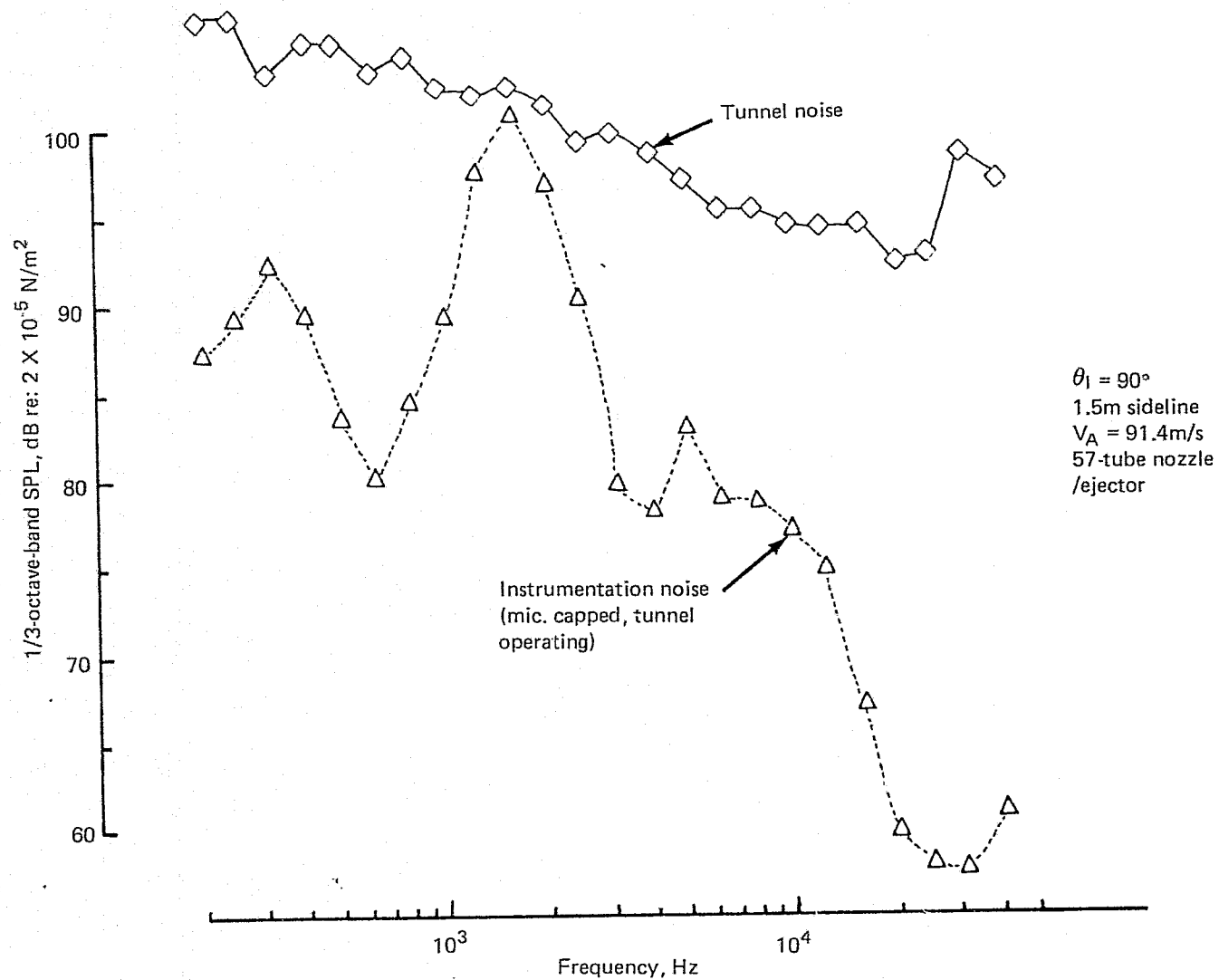


Figure 17.— (Continued)

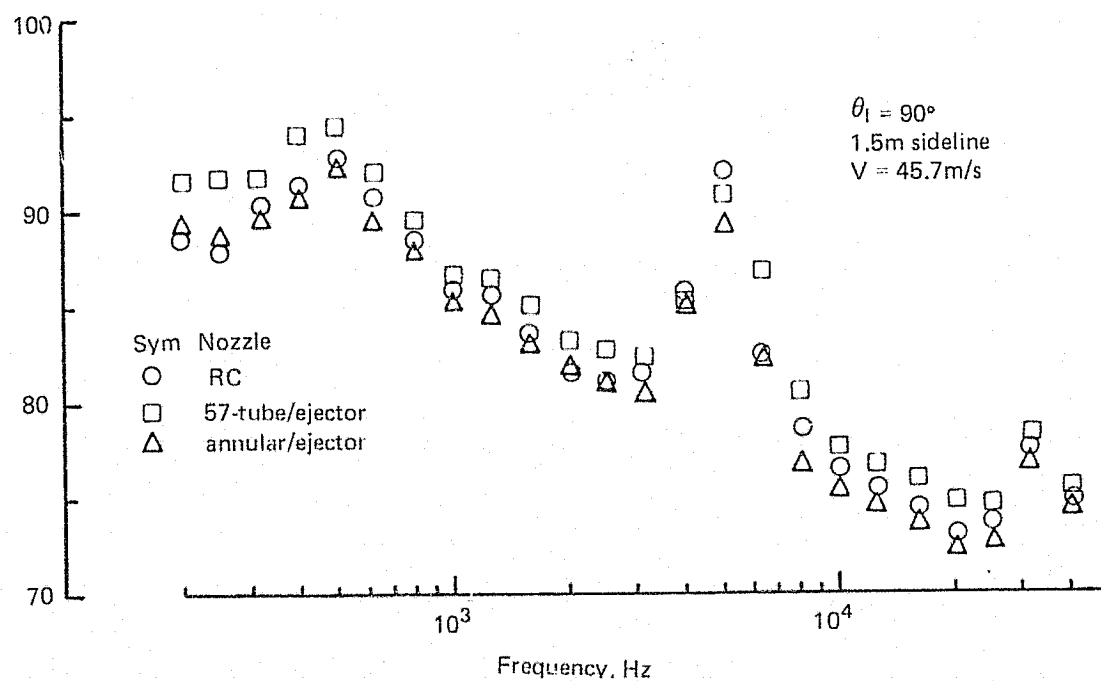
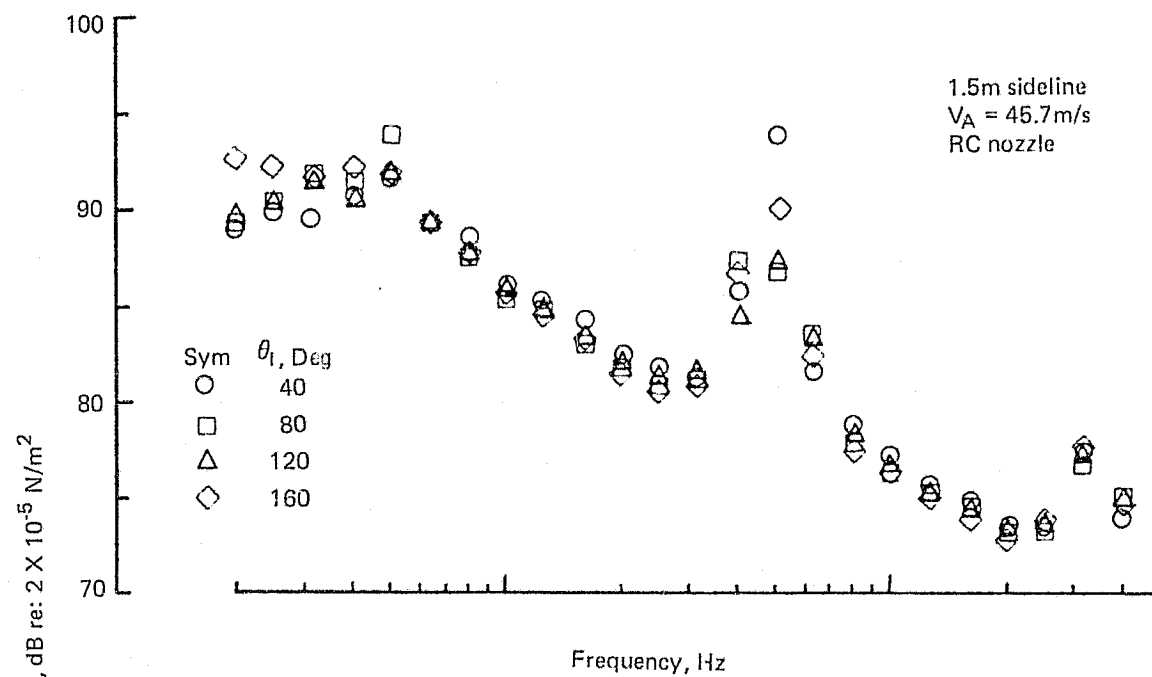


Figure 17.— (Concluded)

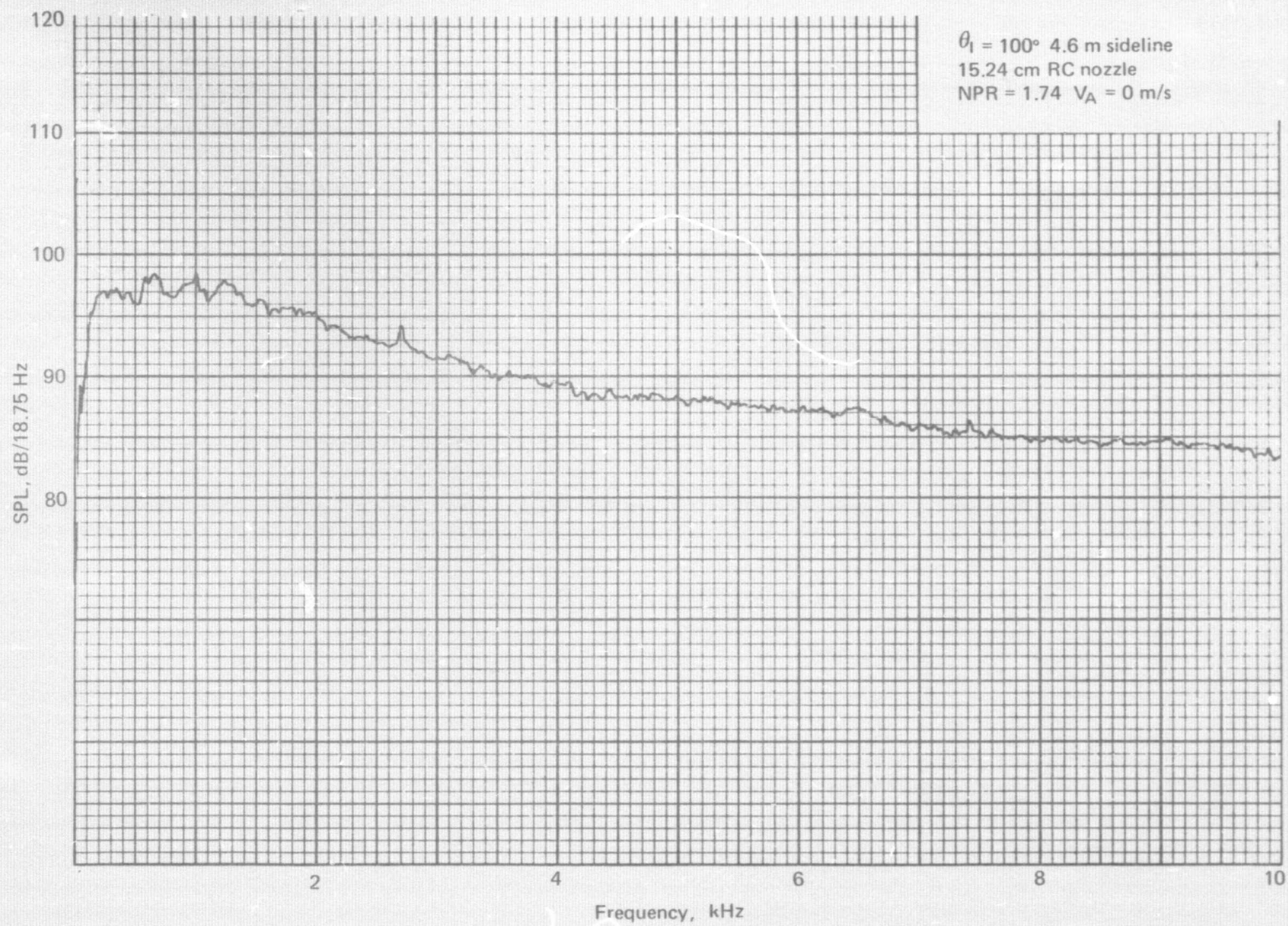


Figure 18.— Narrow Band Jet Noise Spectra

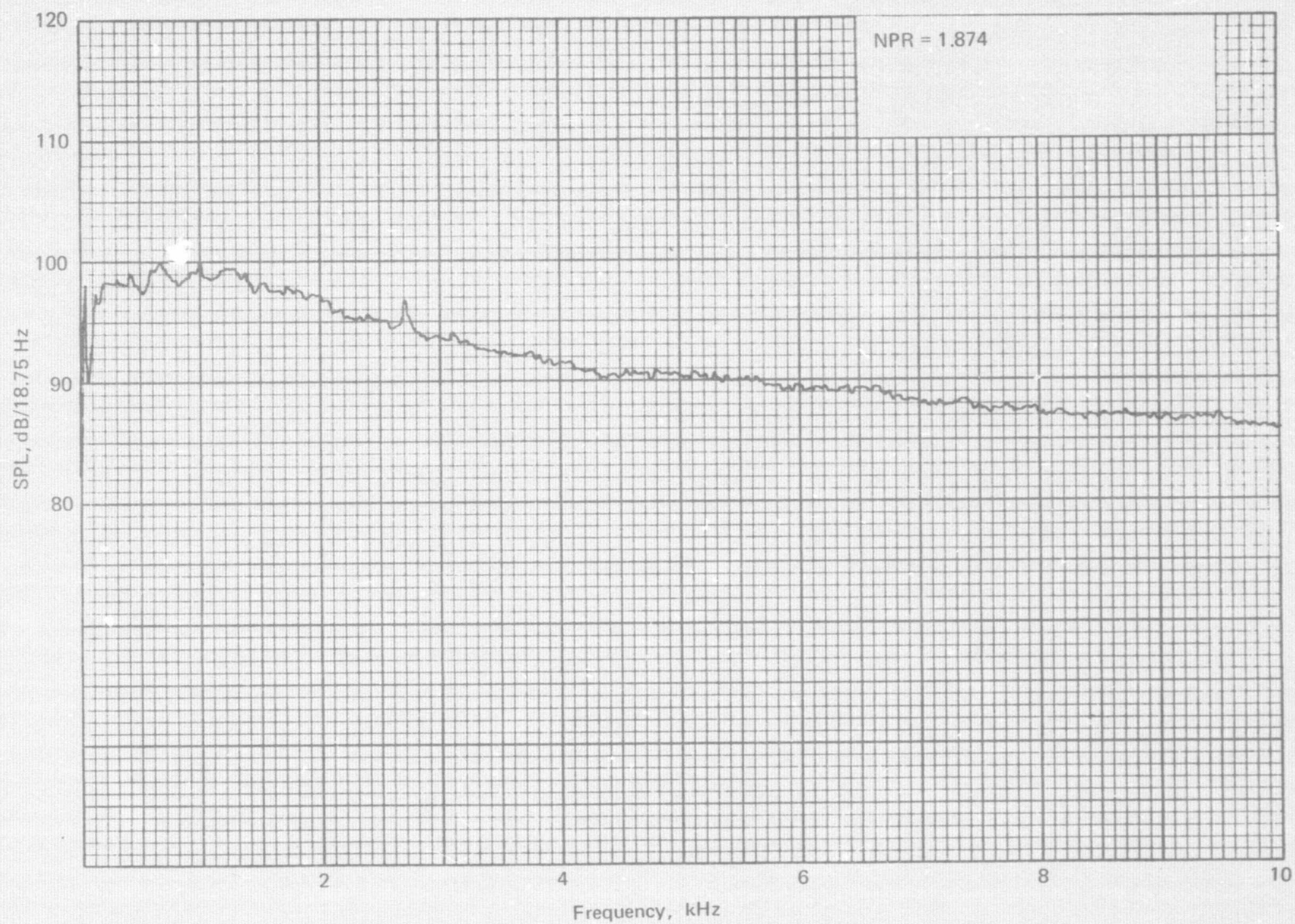


Figure 18.— (Continued)

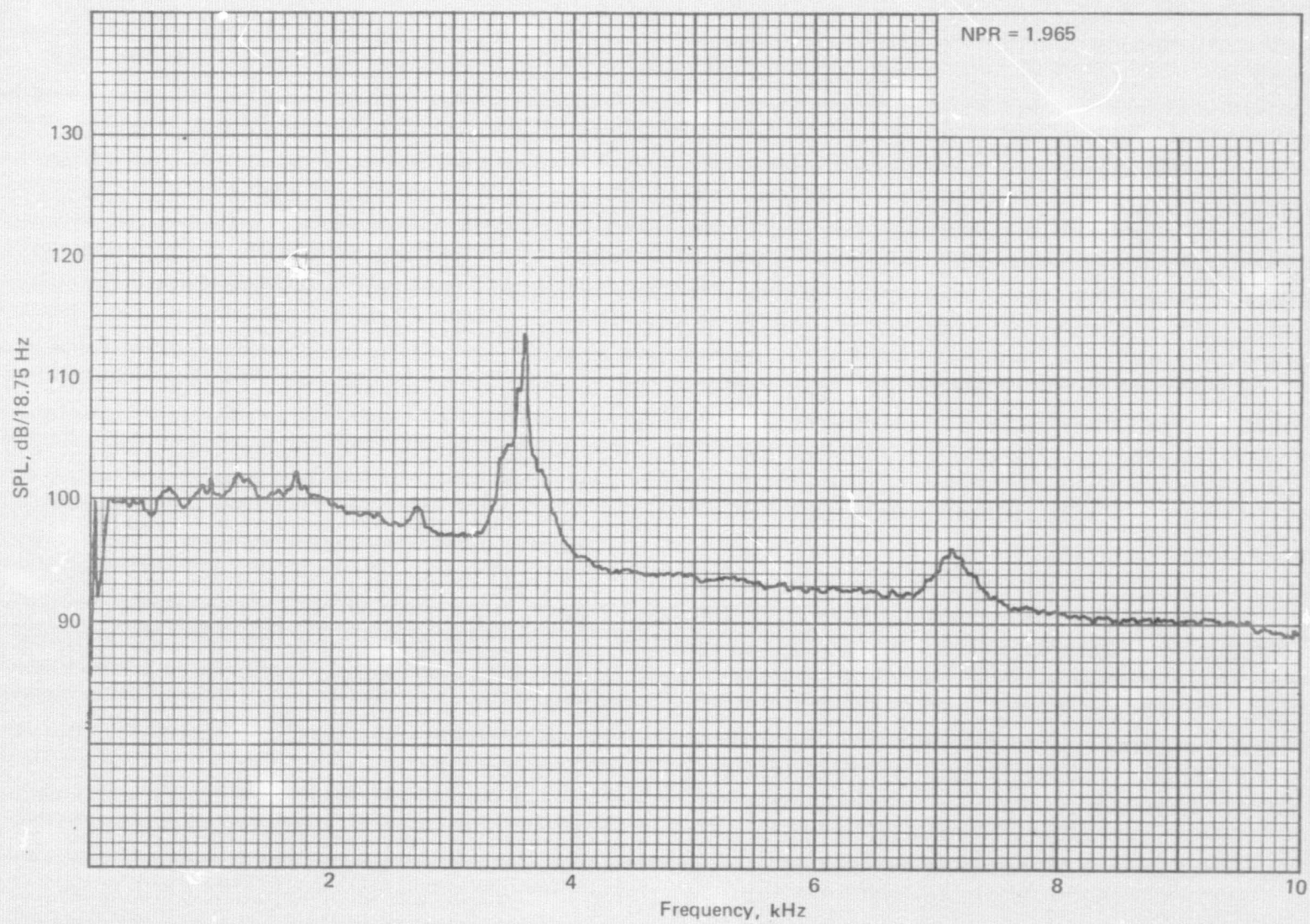


Figure 18.— (Continued)

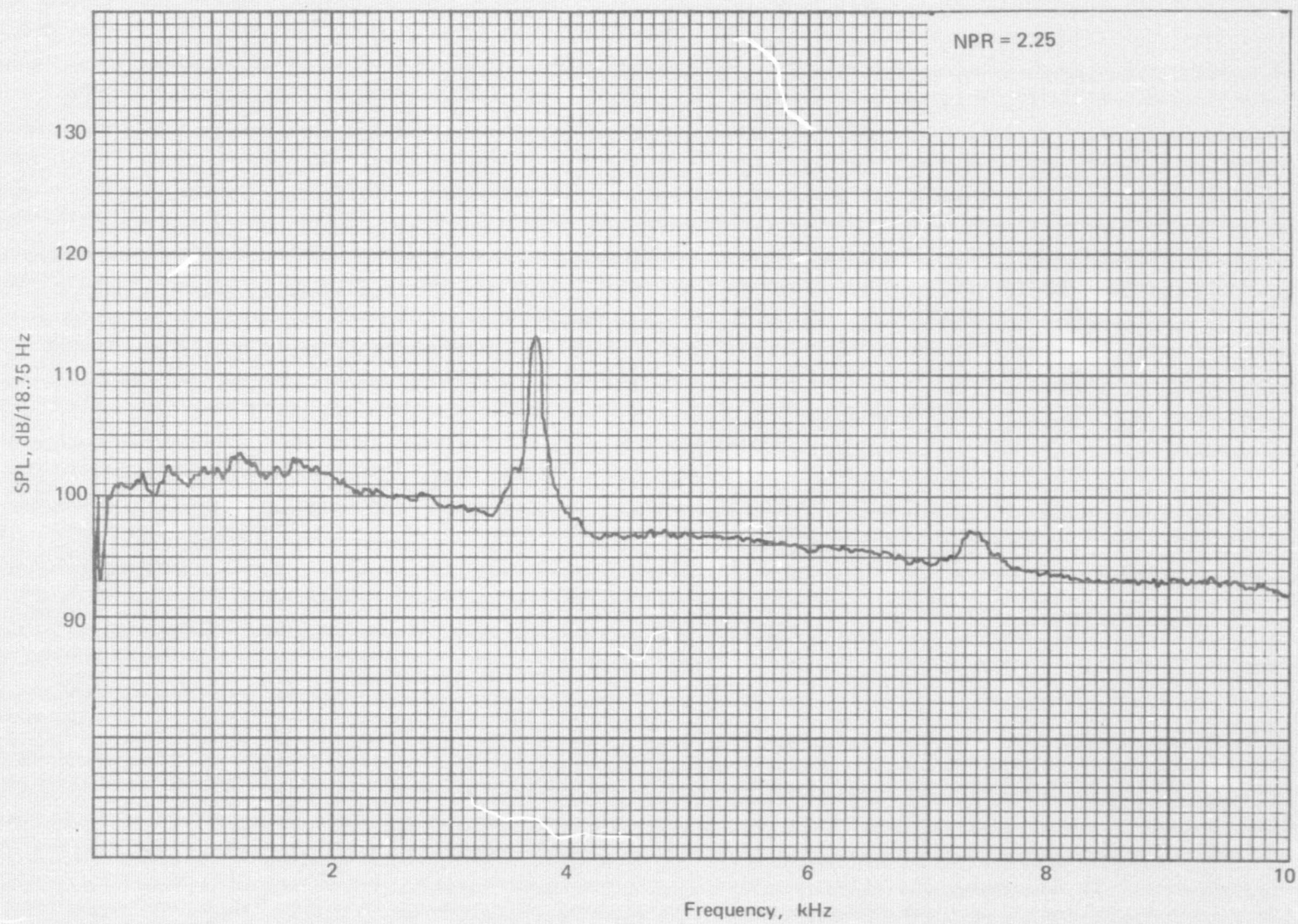


Figure 18.— (Continued)

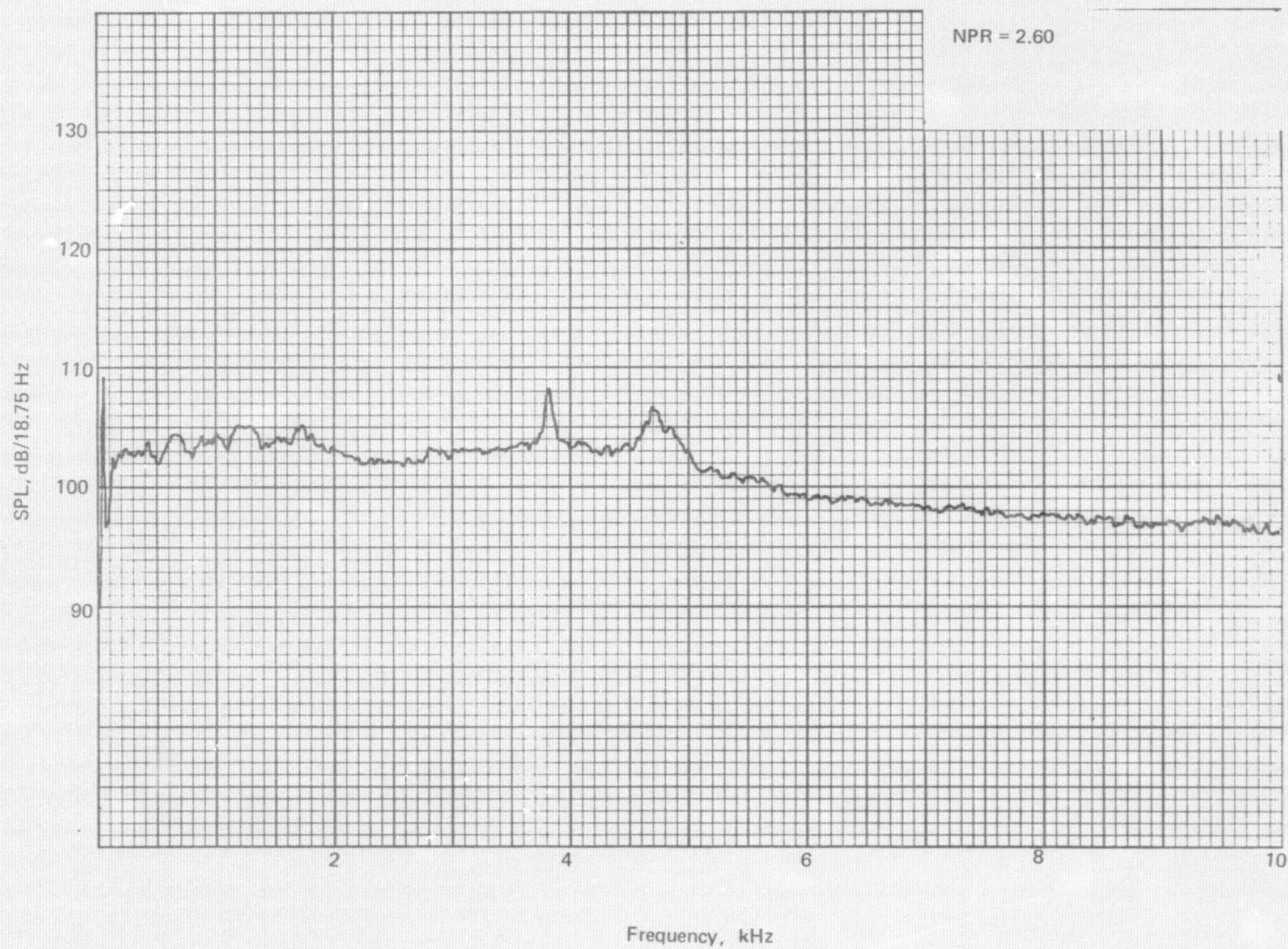


Figure 18.— (Concluded)

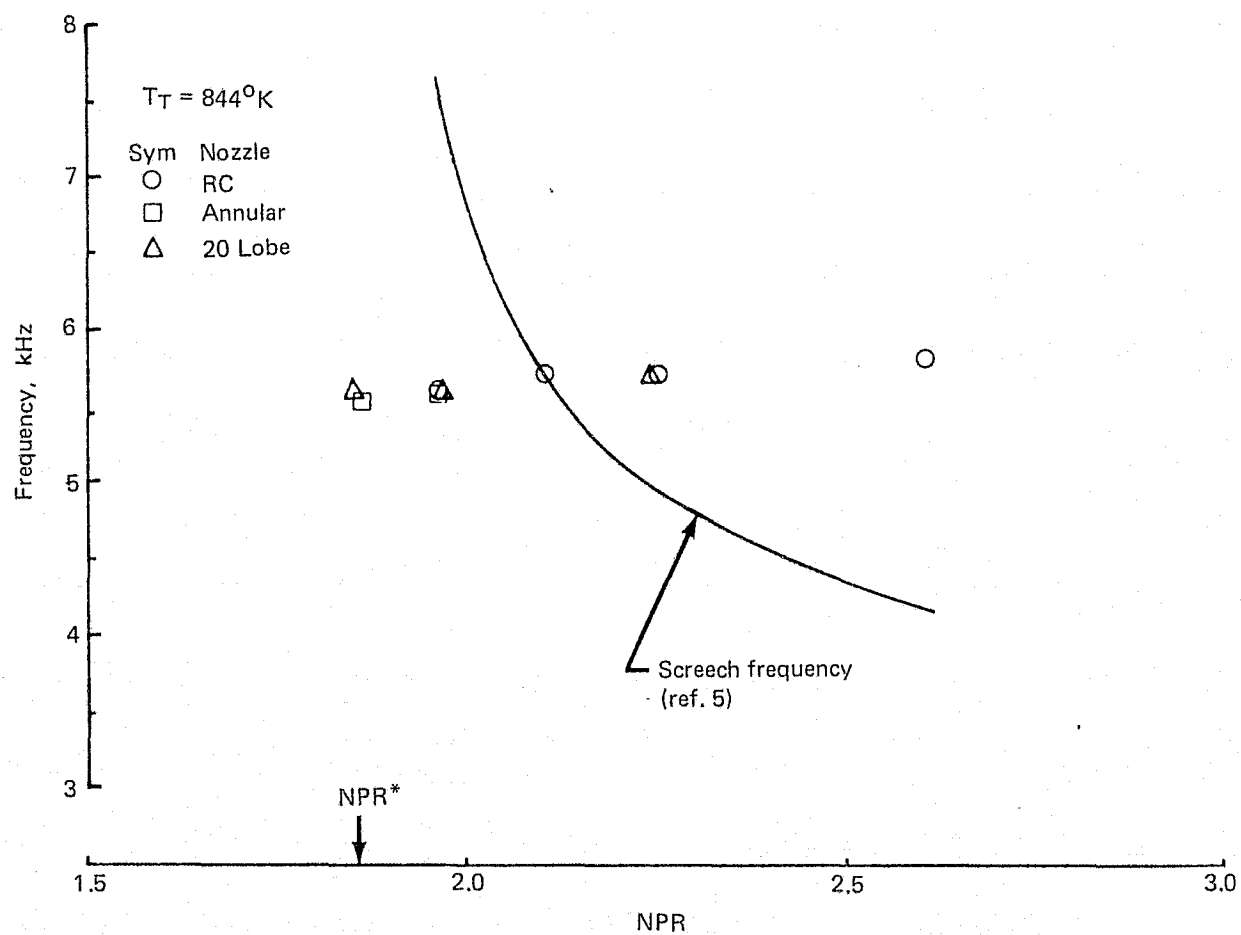


Figure 19.— Comparison of the Noise Spike Frequency with the Calculated Jet Screech Frequency

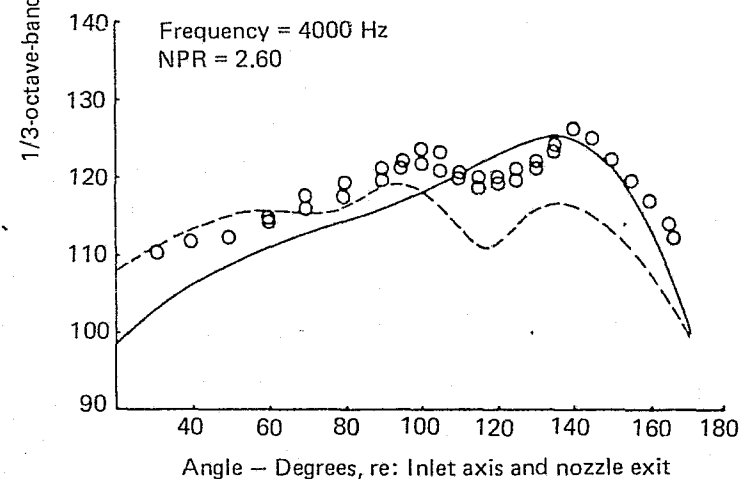
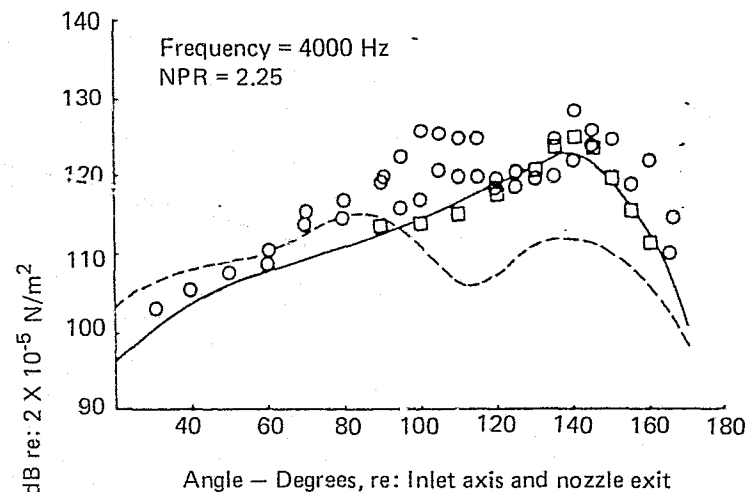
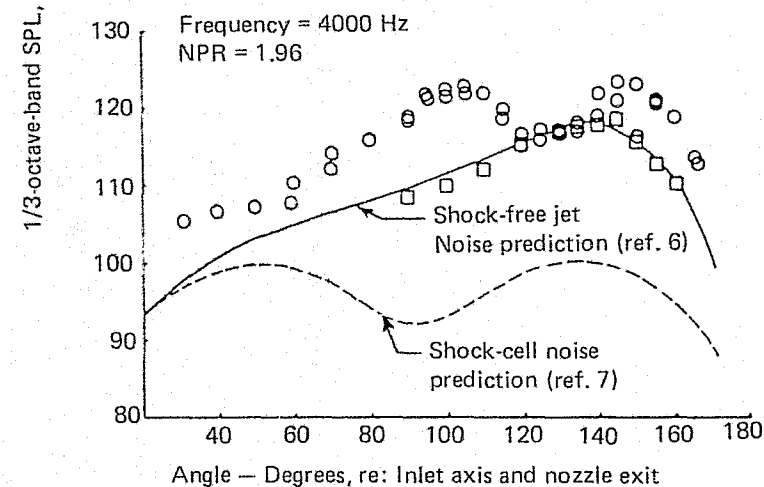
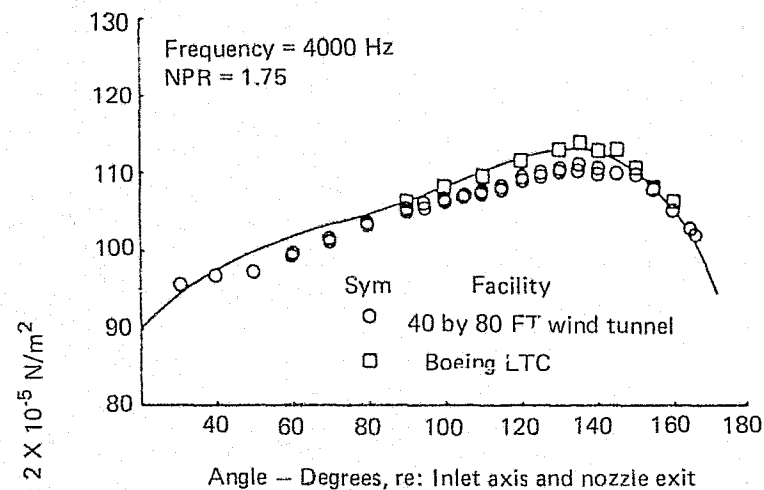


Figure 20.— Comparison of Measured 4 Hz 1/3-Octave-Band SPL Directivities from the 40x80 Tunnel and LTC with Jet Noise Predictions; 15.24cm RC Nozzle

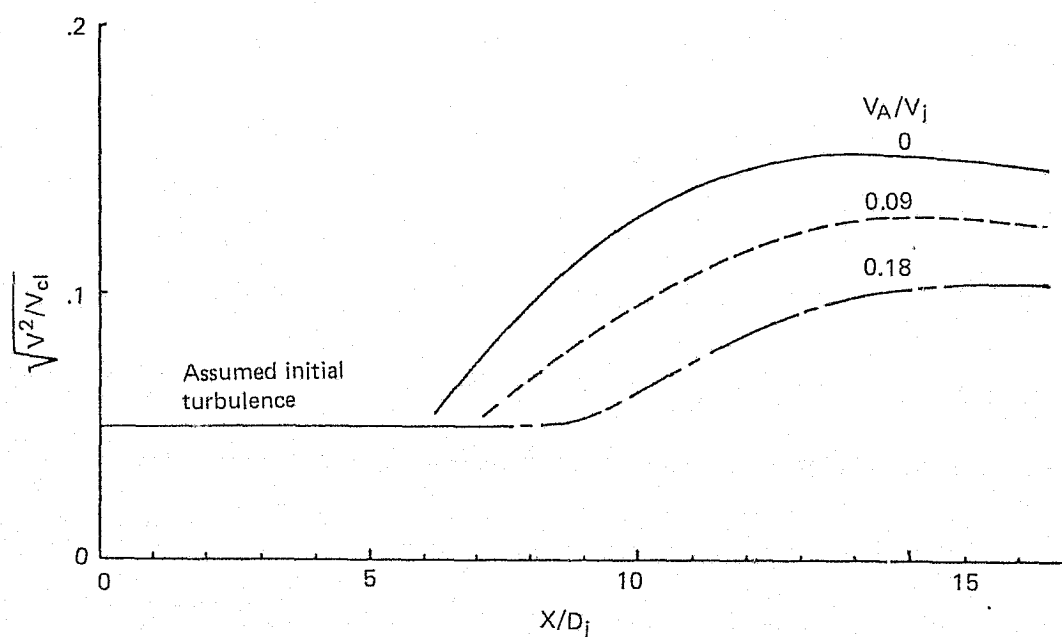
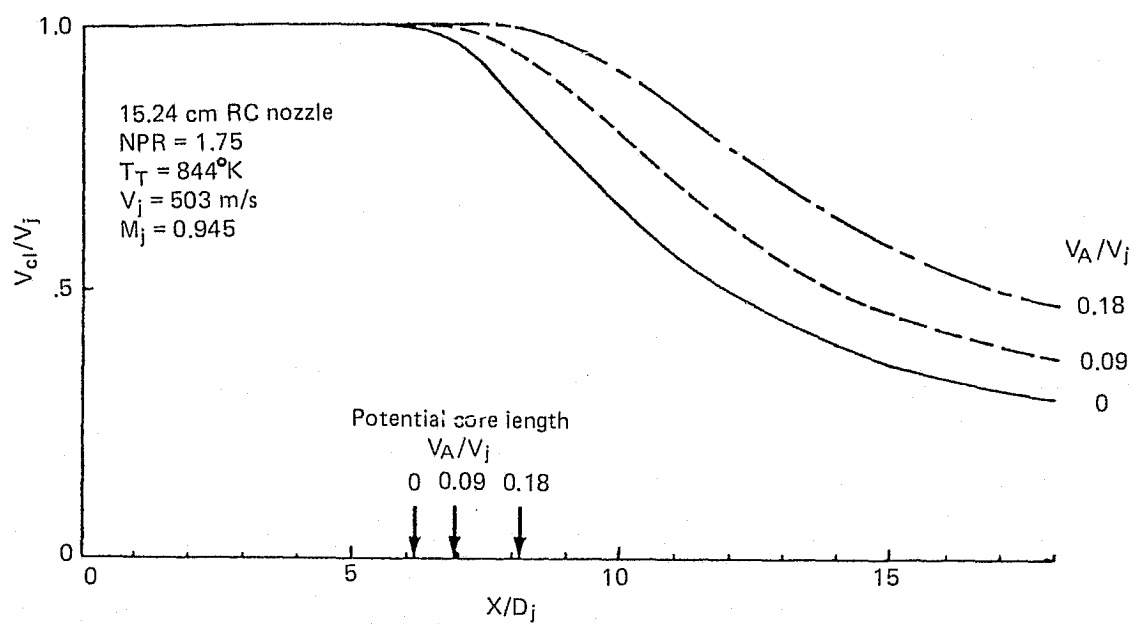


Figure 21.— Centerline Velocity and Turbulence Intensity Distribution

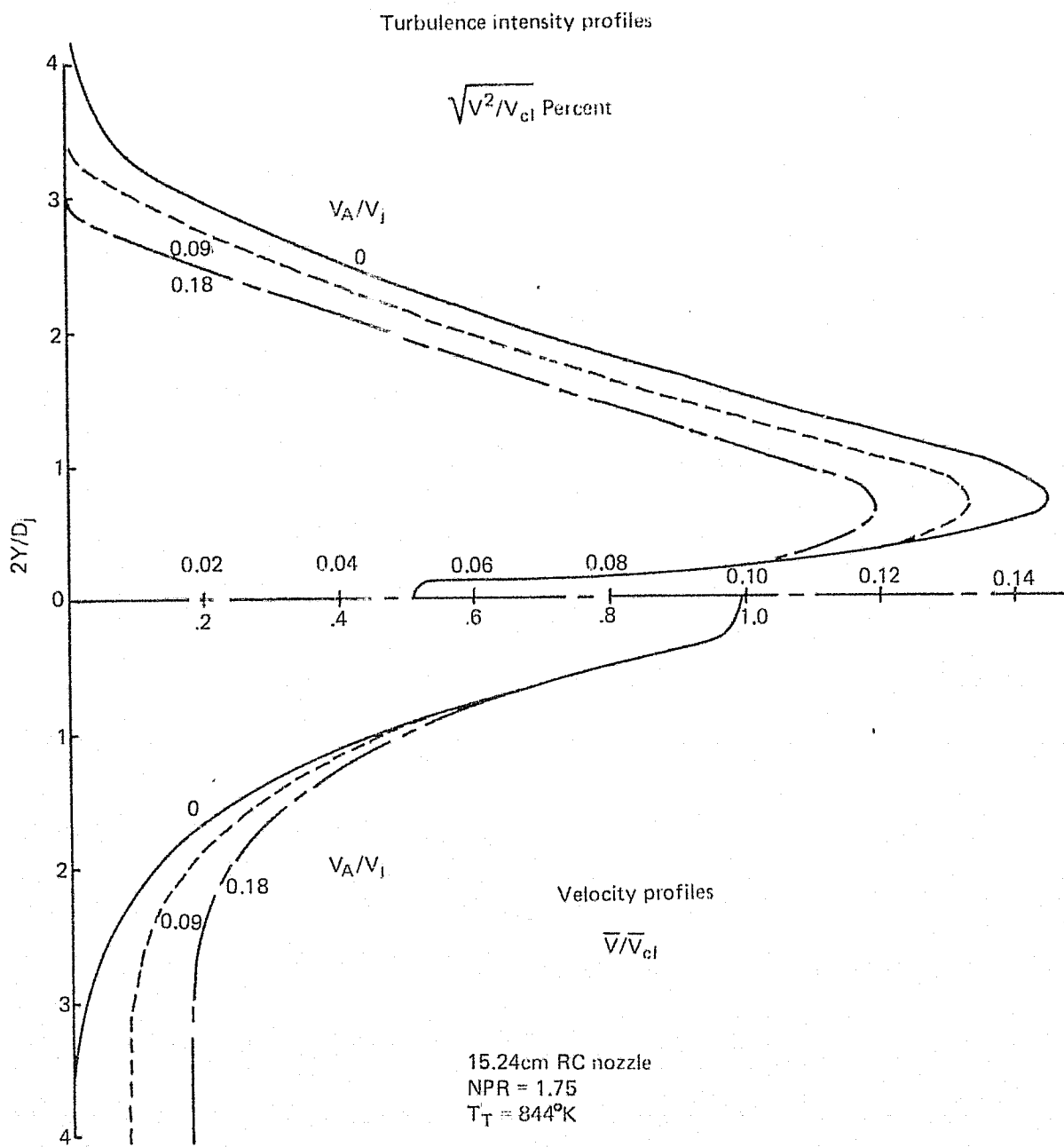


Figure 22.-- Velocity and Turbulence Profiles at the Tip of the Potential Core

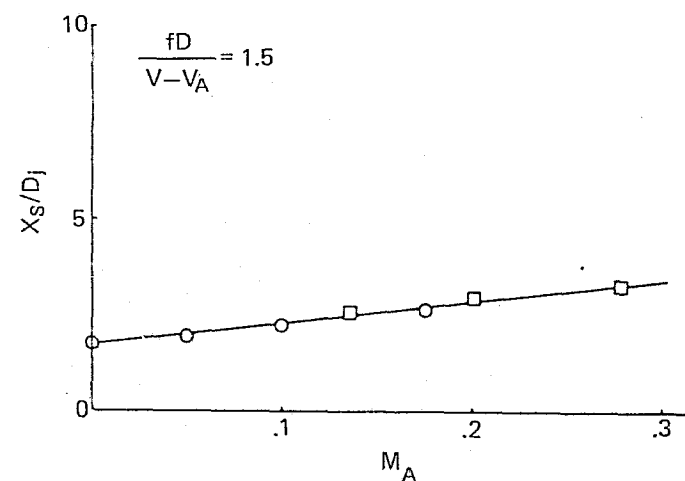
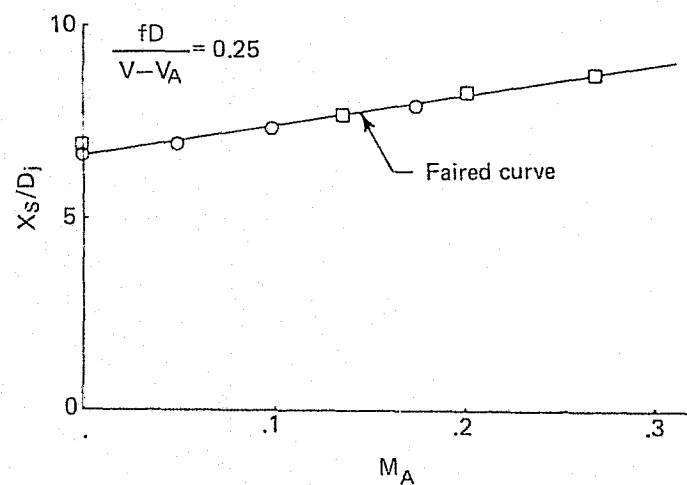
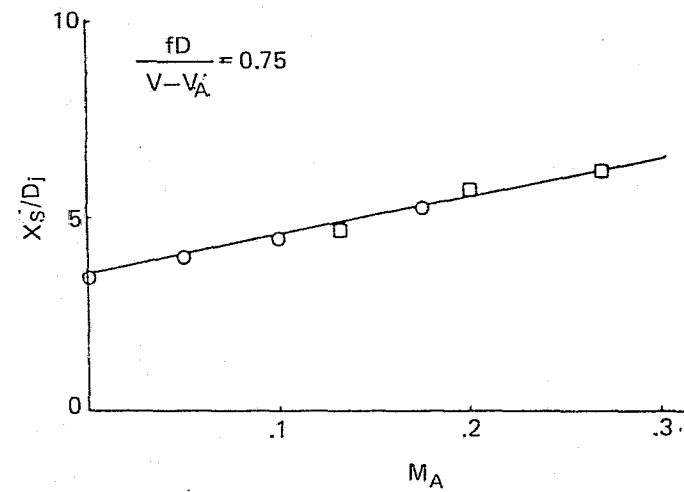
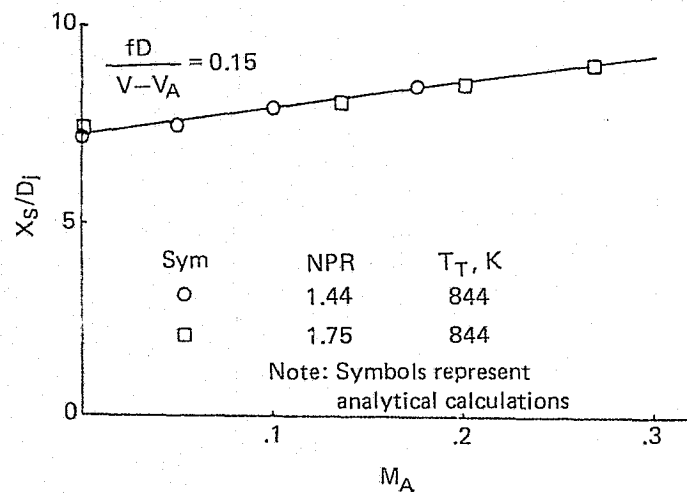


Figure 23.— Calculated Peak Noise Source Locations Using the Lu/Berman Flow/Noise Analysis, 15.24cm RC Nozzle

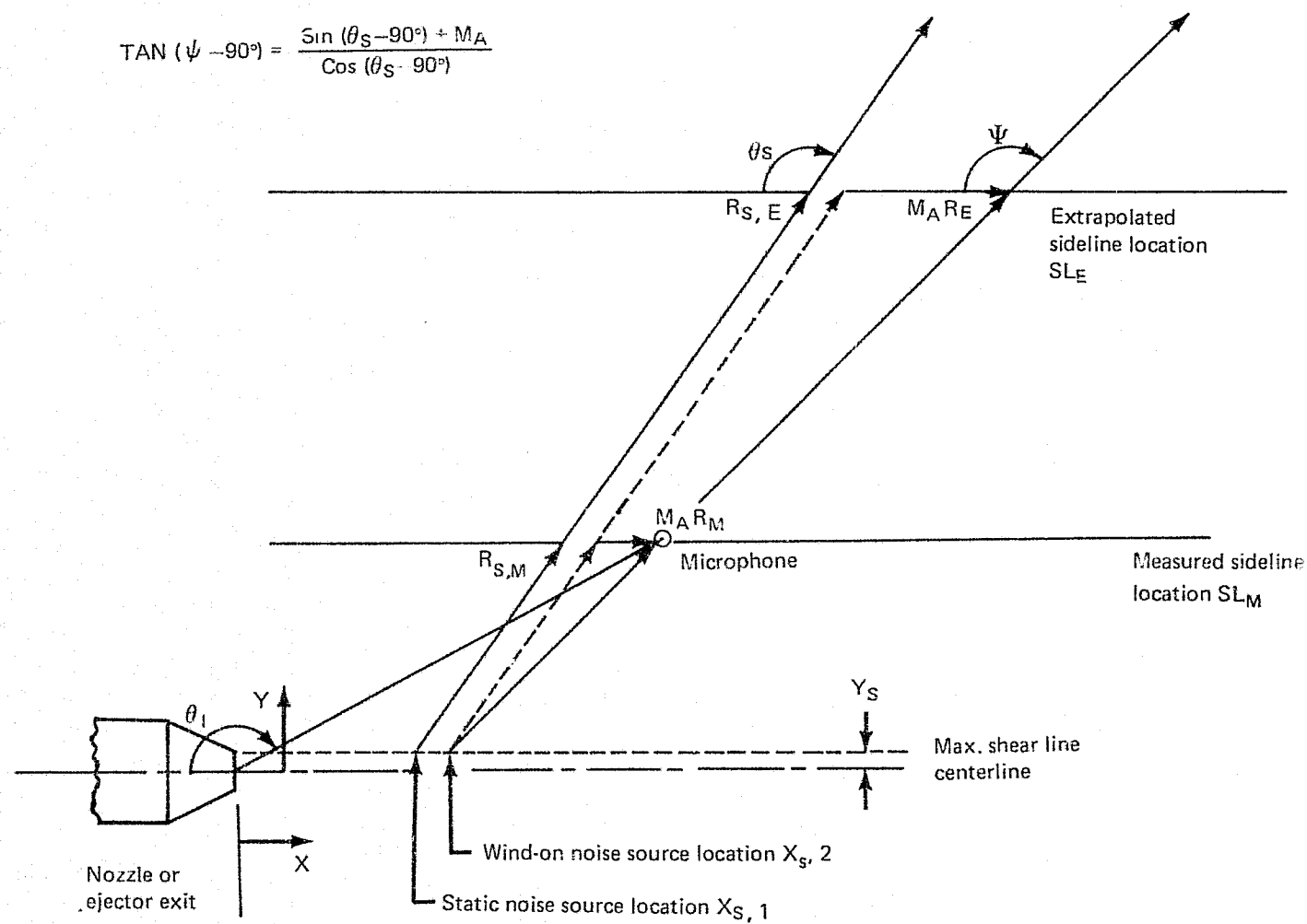


Figure 24.— Coordinate System and Nomenclature

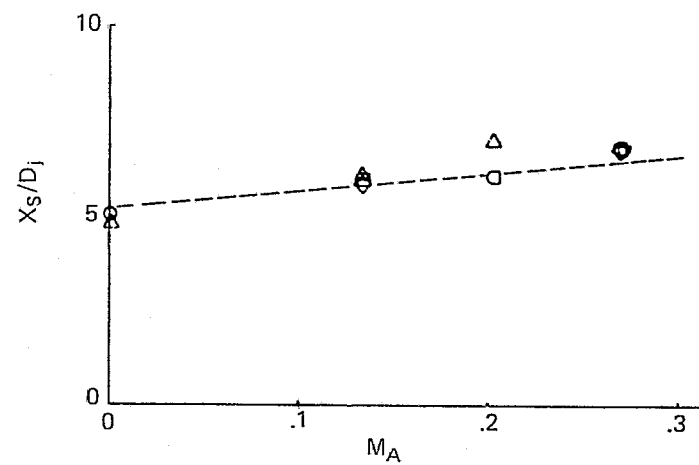
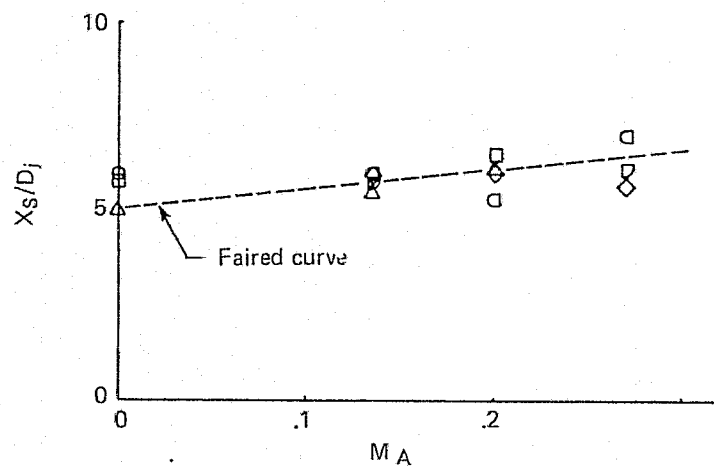
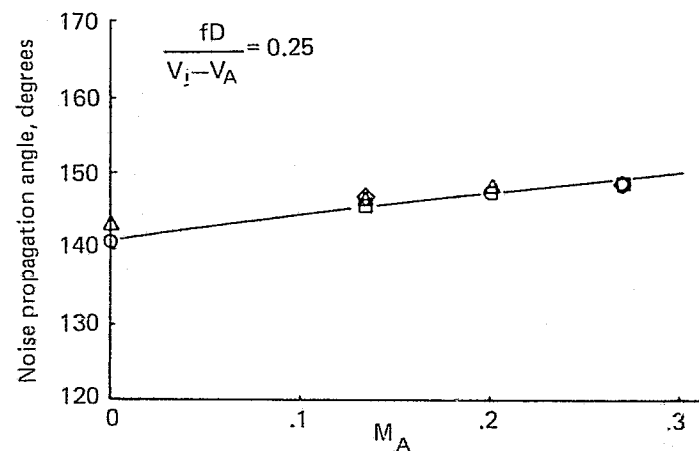
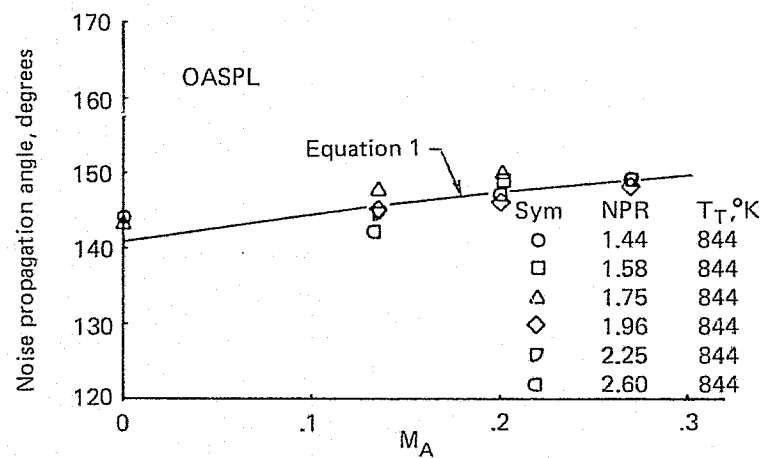


Figure 25. - Peak Noise Source Locations and Noise Propagation Angles for the 15.24 cm RC Nozzle

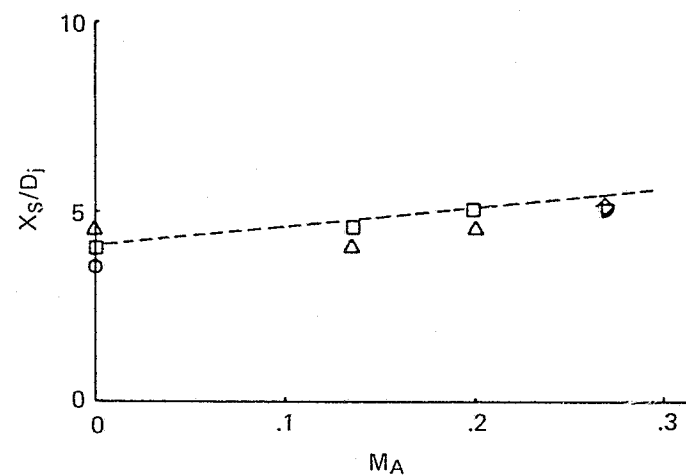
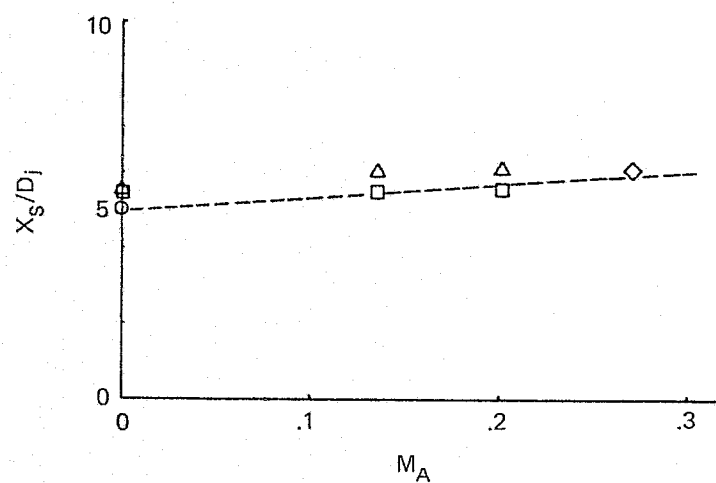
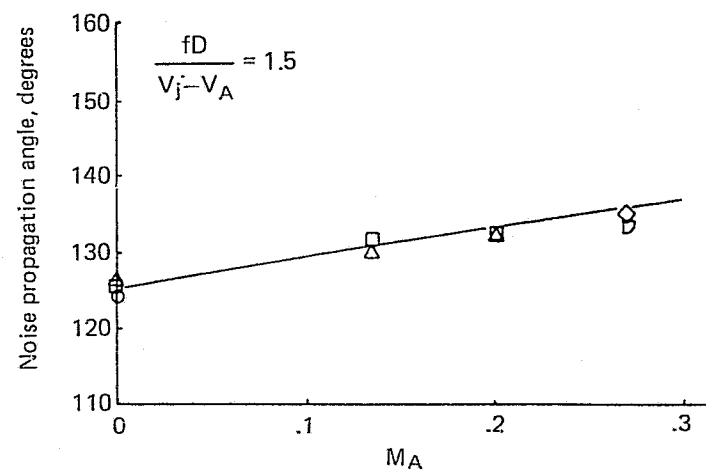
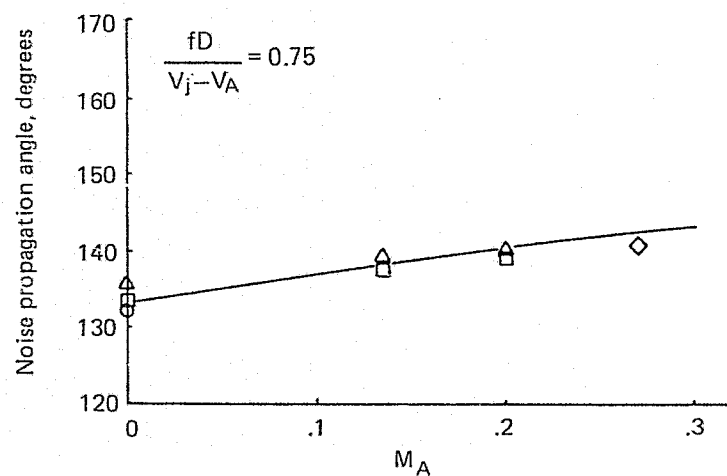


Figure 25.— (Continued)

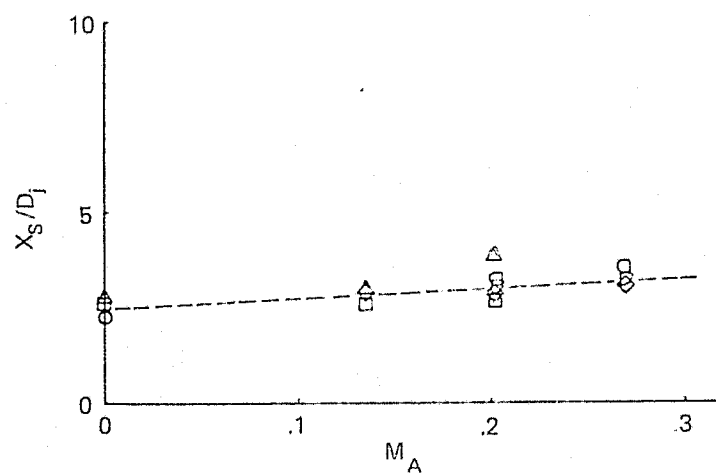
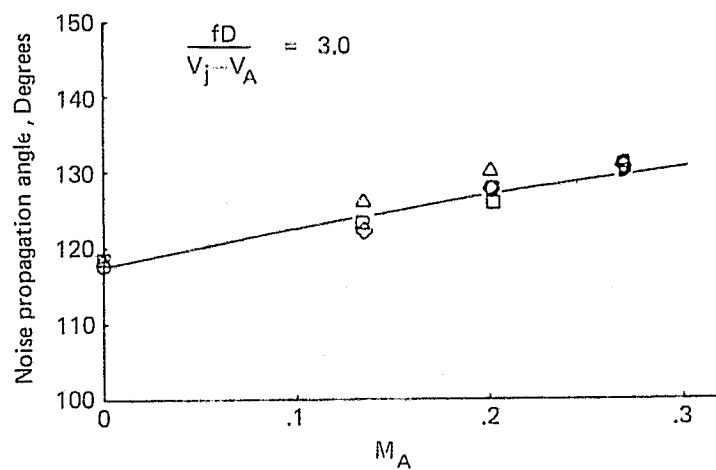


Figure 25.— (Concluded)

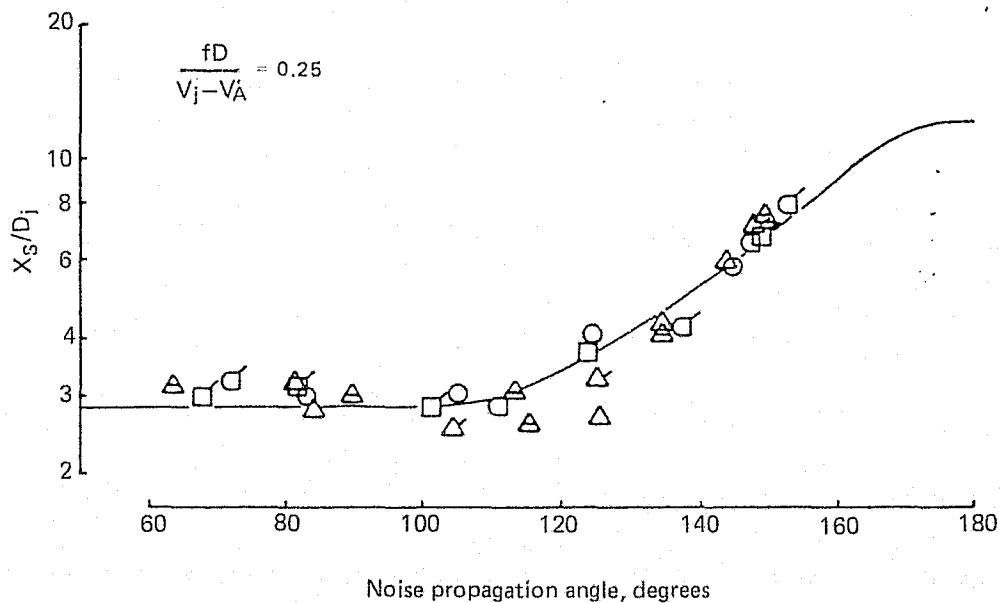
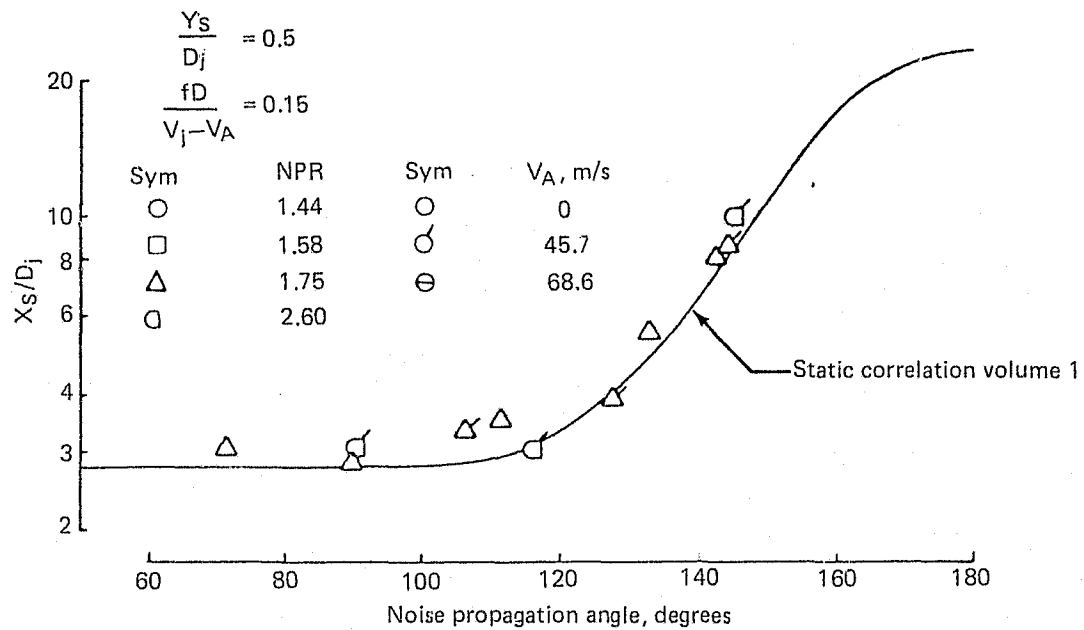


Figure 26.— Effect of Ambient Velocity on the Distributed Noise Source Locations for a 15.24cm RC Nozzle

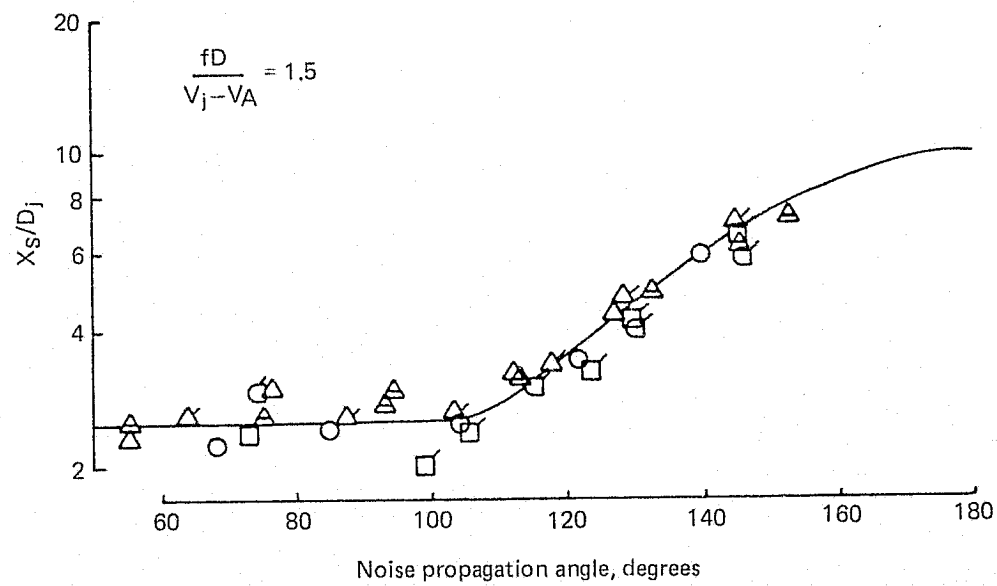
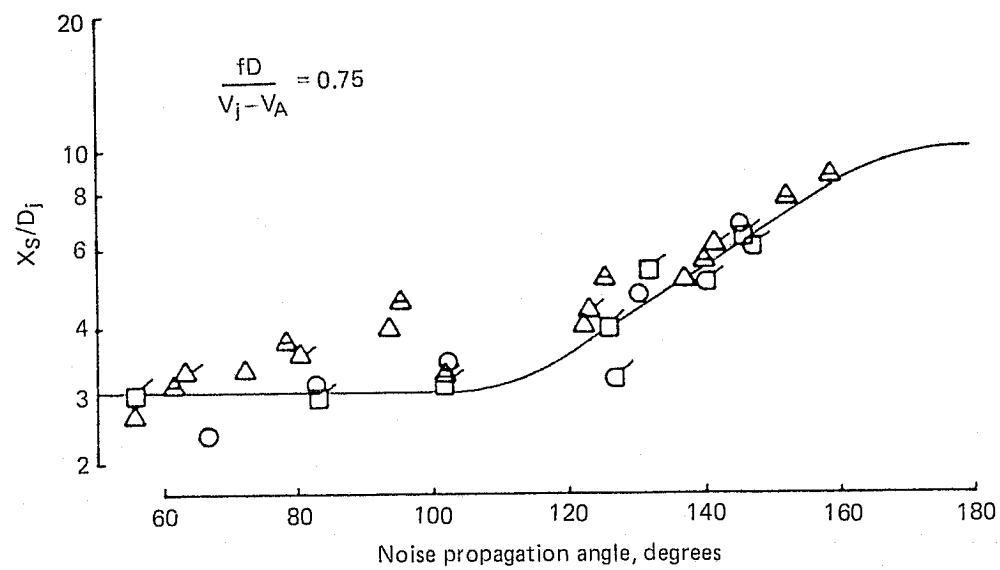


Figure 26.— (Continued)

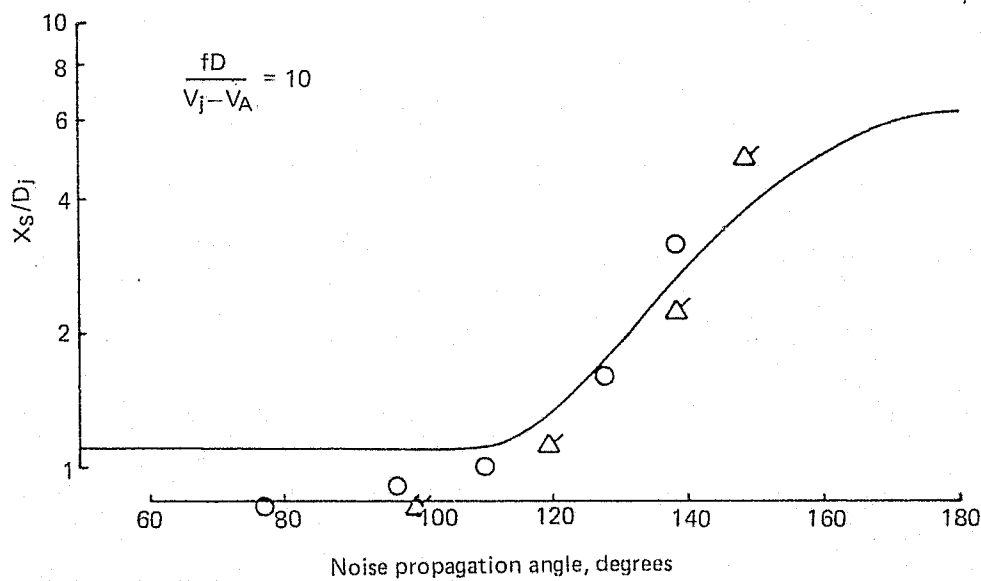
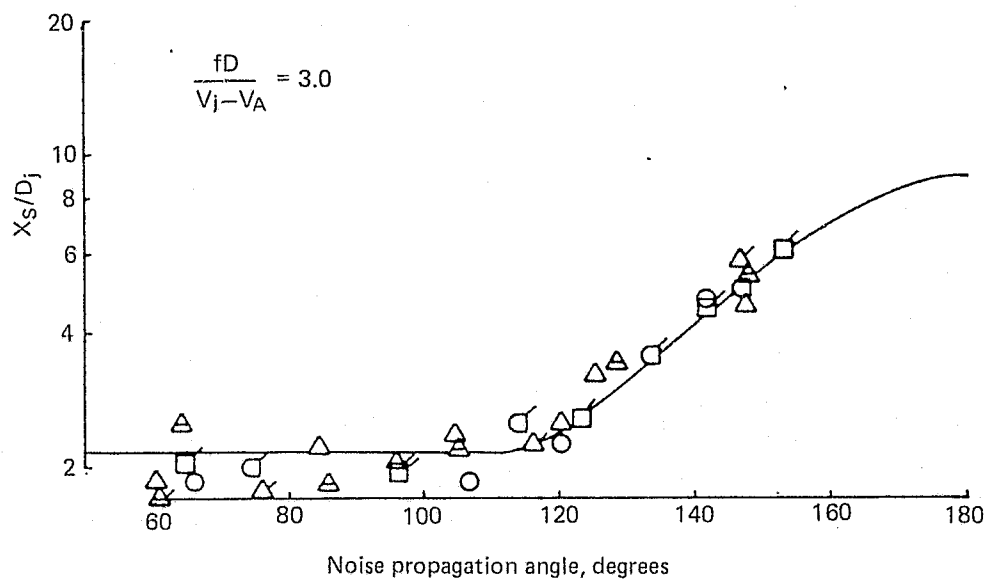


Figure 26.— (Concluded)

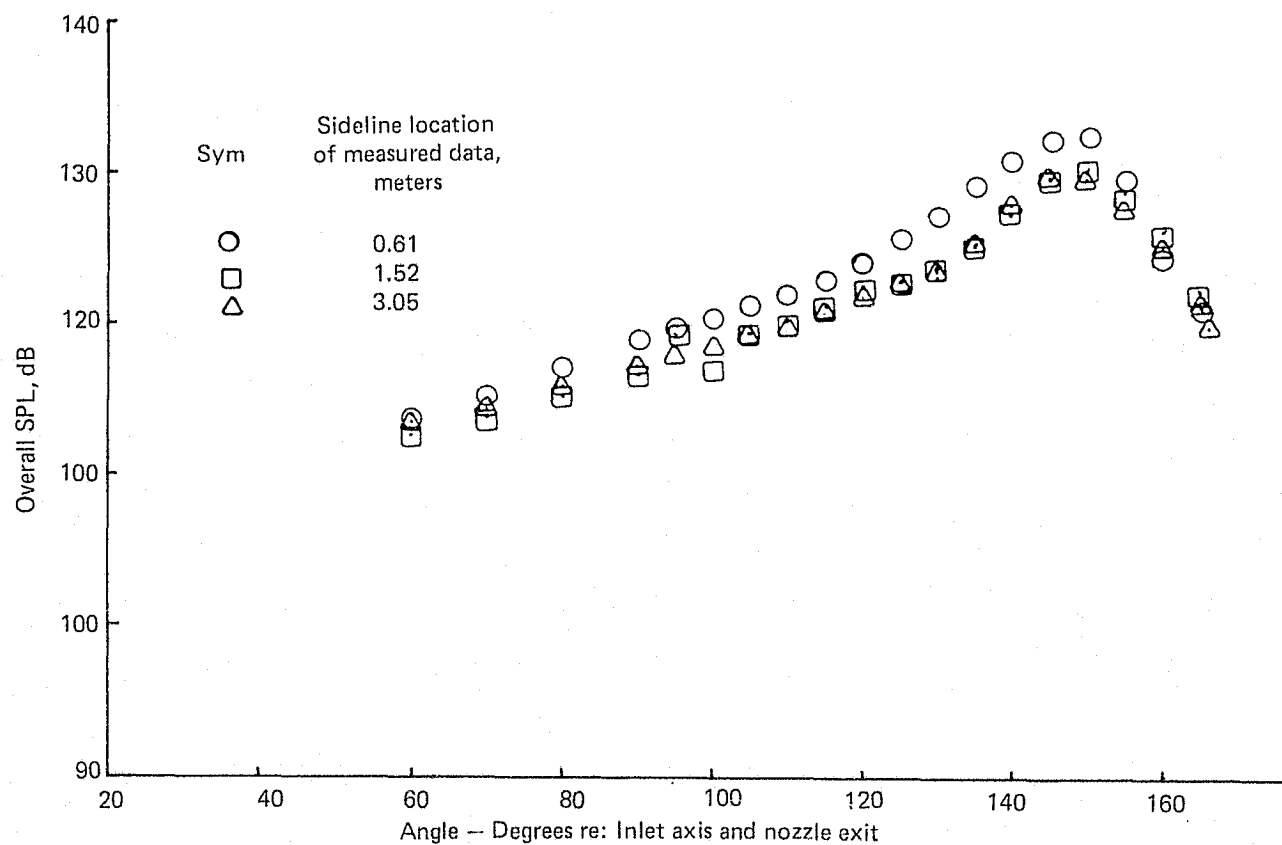


Figure 27.— OASPL and 1/3-OBSPL Directivity Data for a 15.24 cm RC Nozzle
Extrapolated to a 3.05 m Sideline. NPR = 1.75 $V_A = 3$ m/s

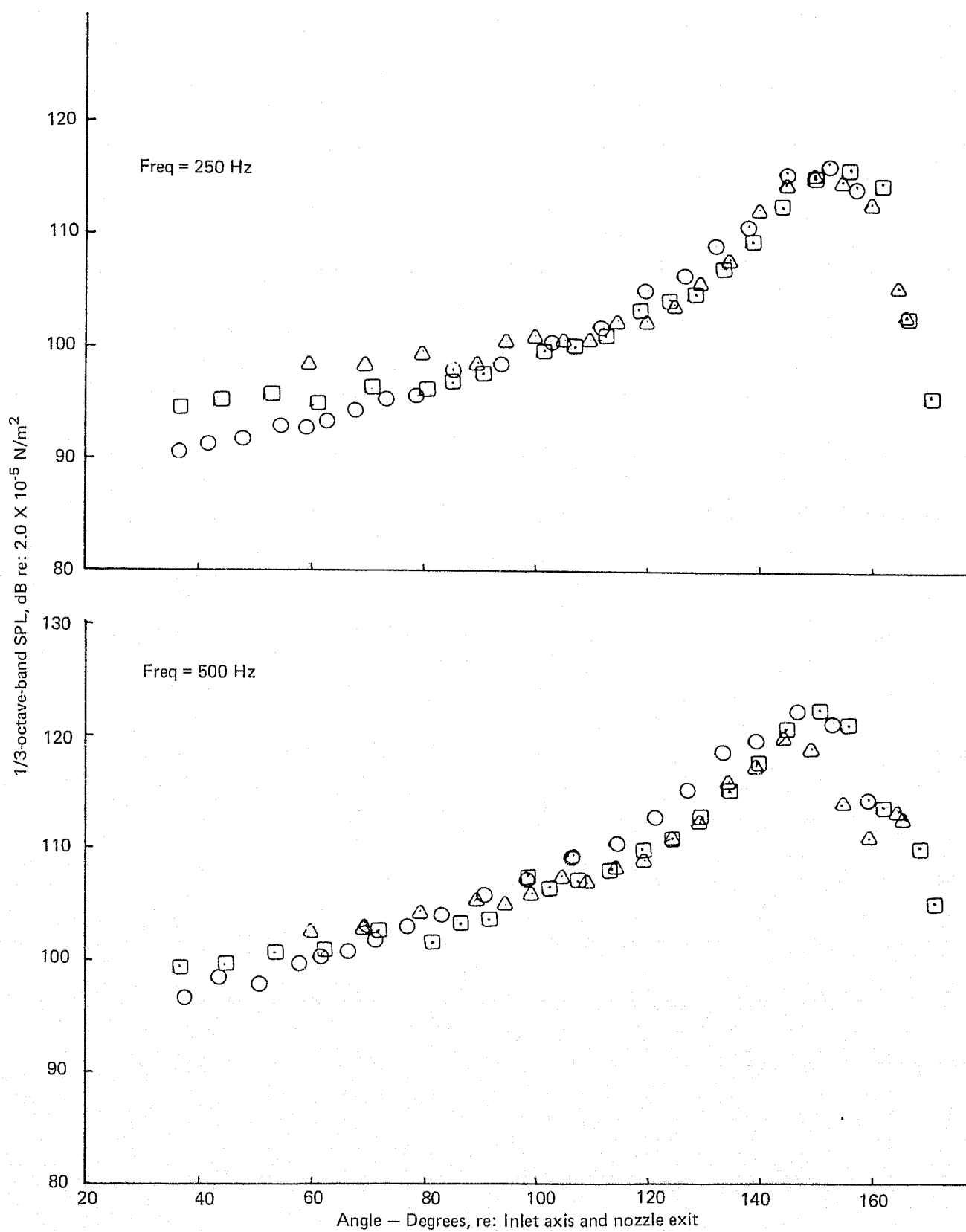


Figure 27.— (Continued)

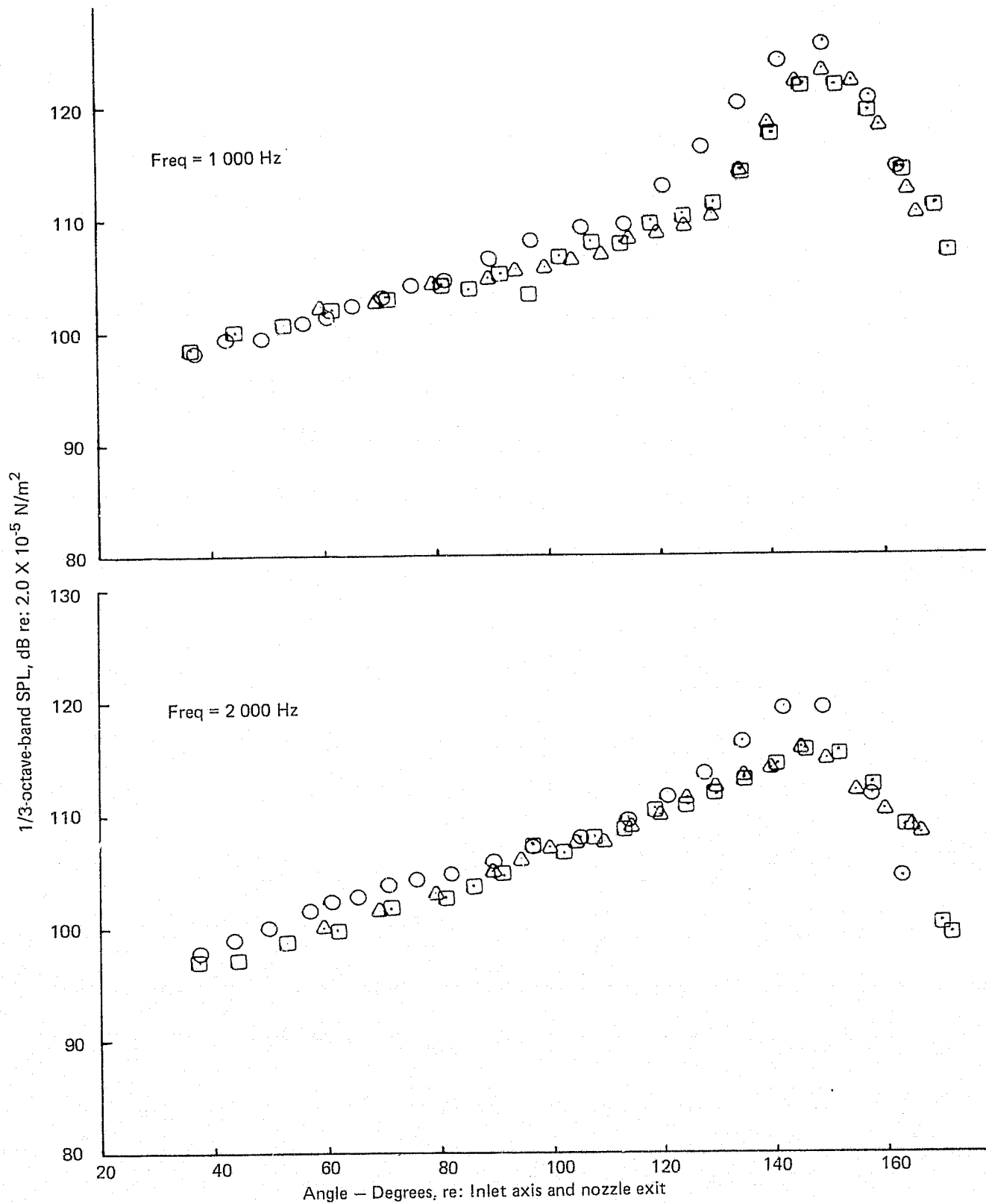


Figure 27.— (Continued)

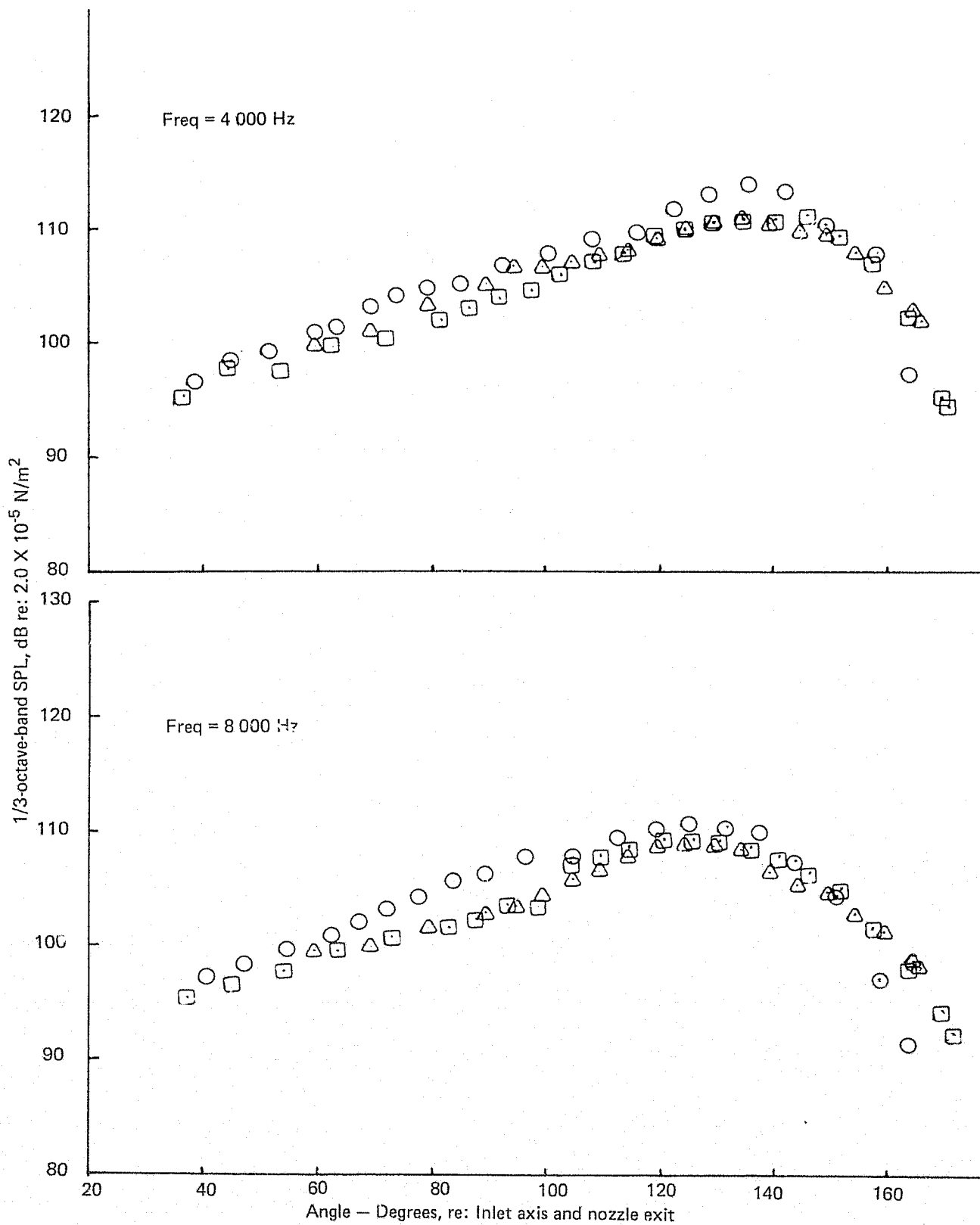


Figure 27.— (Continued)

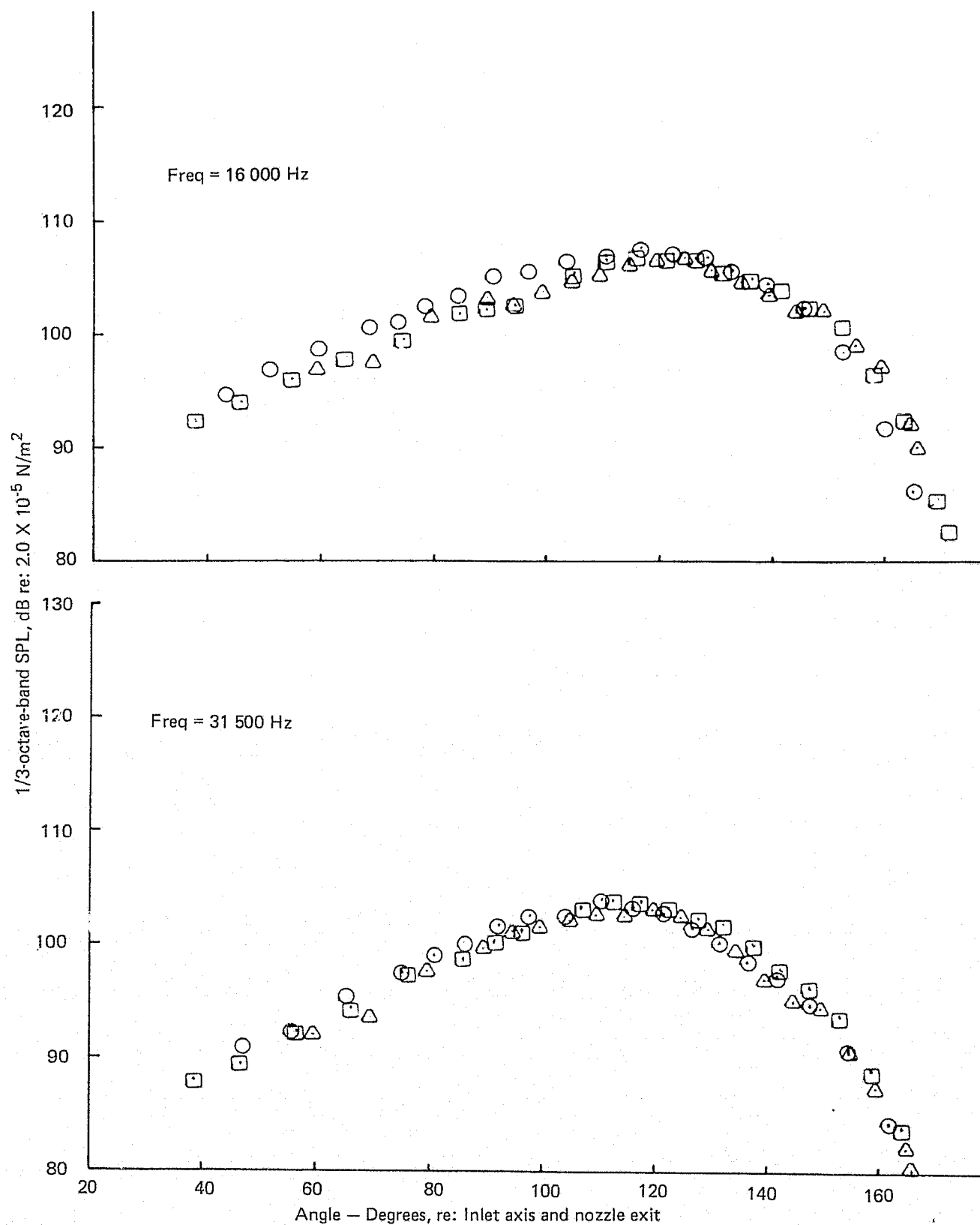


Figure 27.— (Concluded)

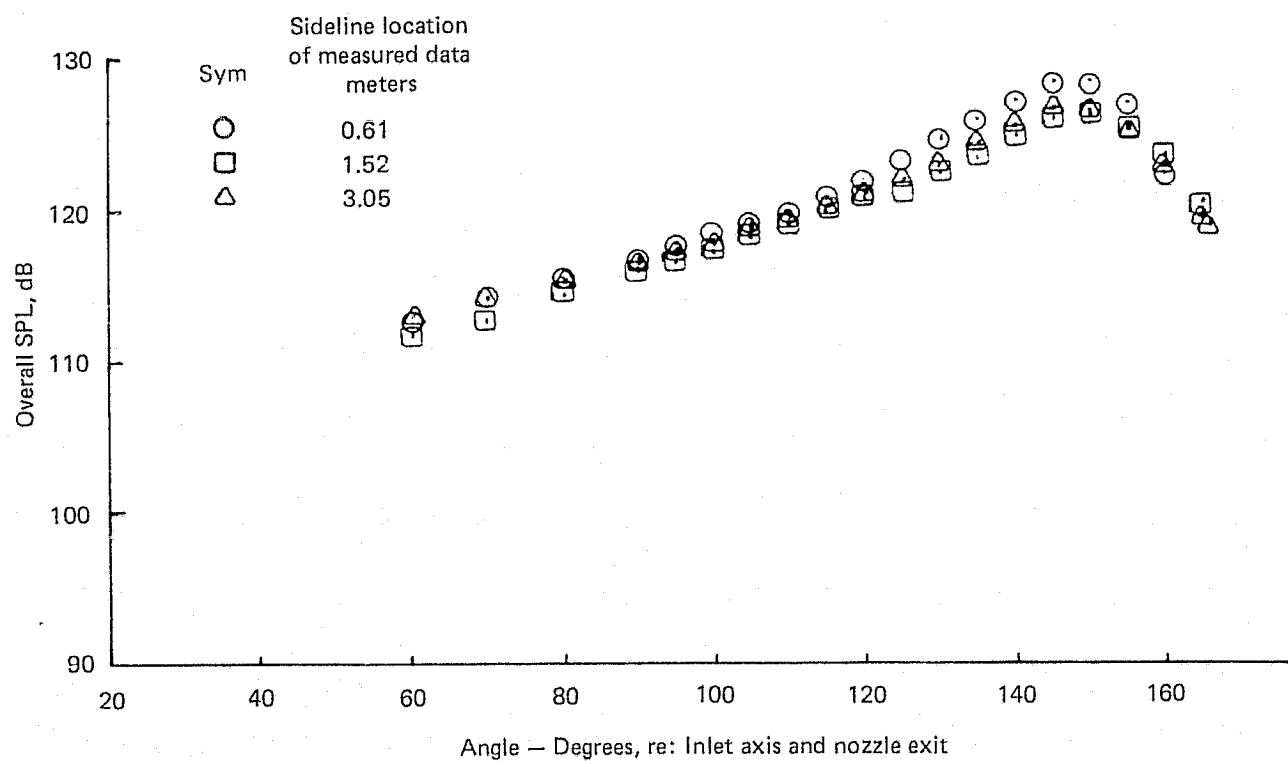


Figure 28.— OASPL and 1/3-OBSPL Directivity Data for A 15.24 cm RC Nozzle
Extrapolated to a 3.05 m Sideline. NPR = 1.75 $V_A = 46$ m/s

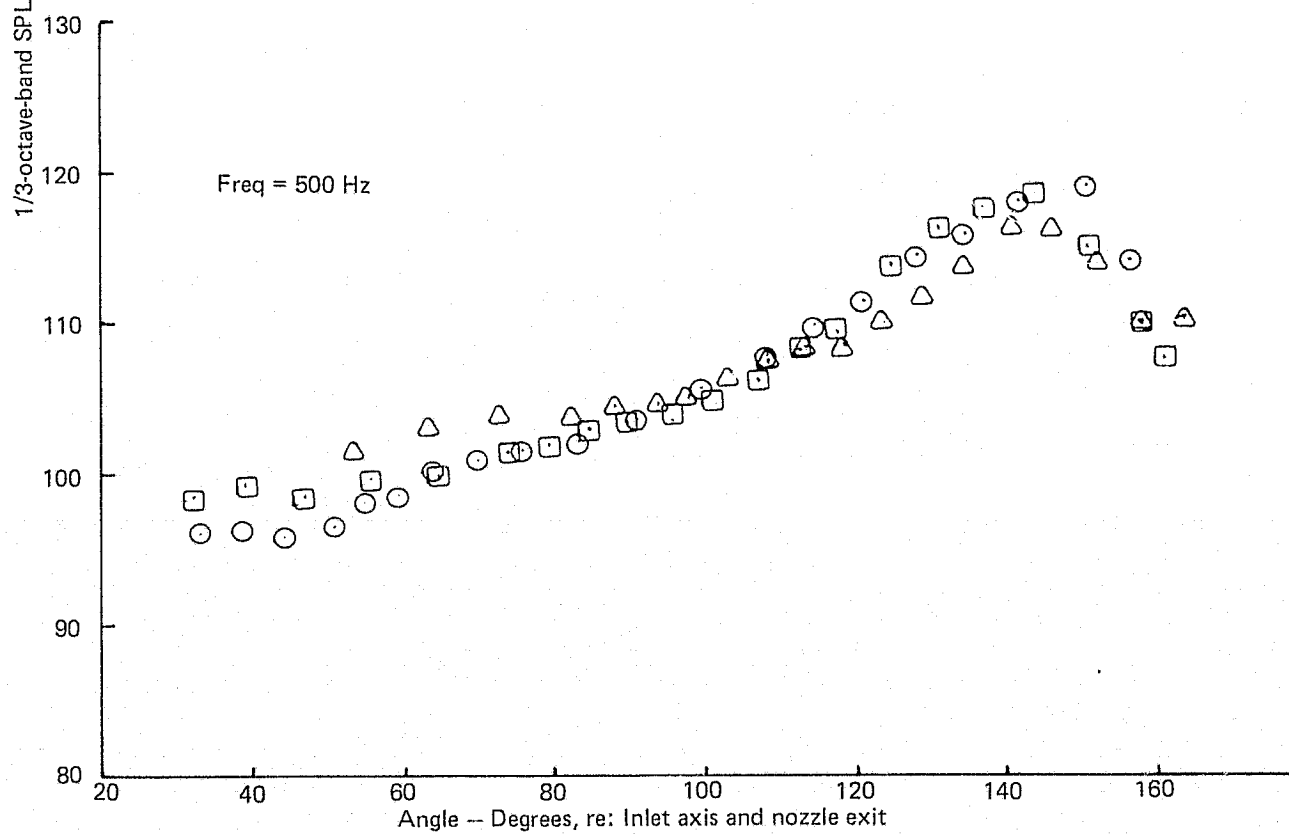
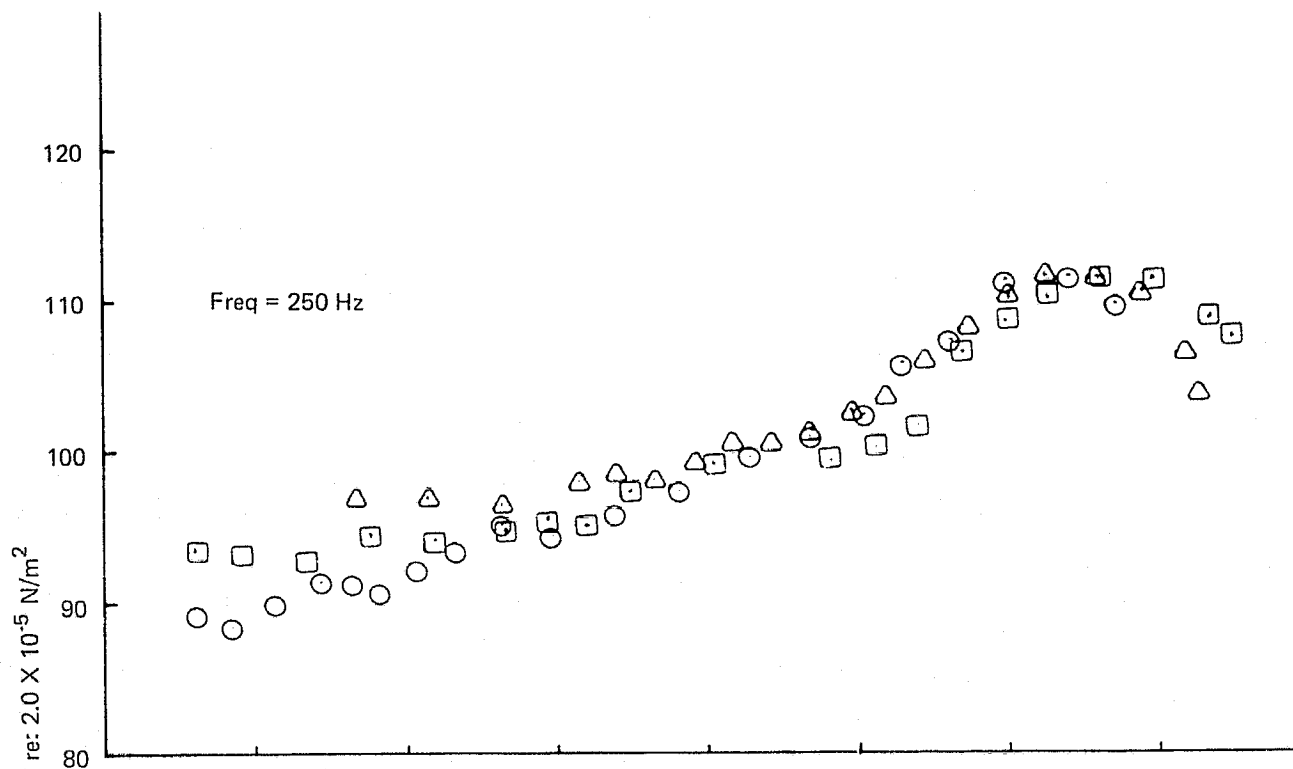


Figure 28.— (Continued)

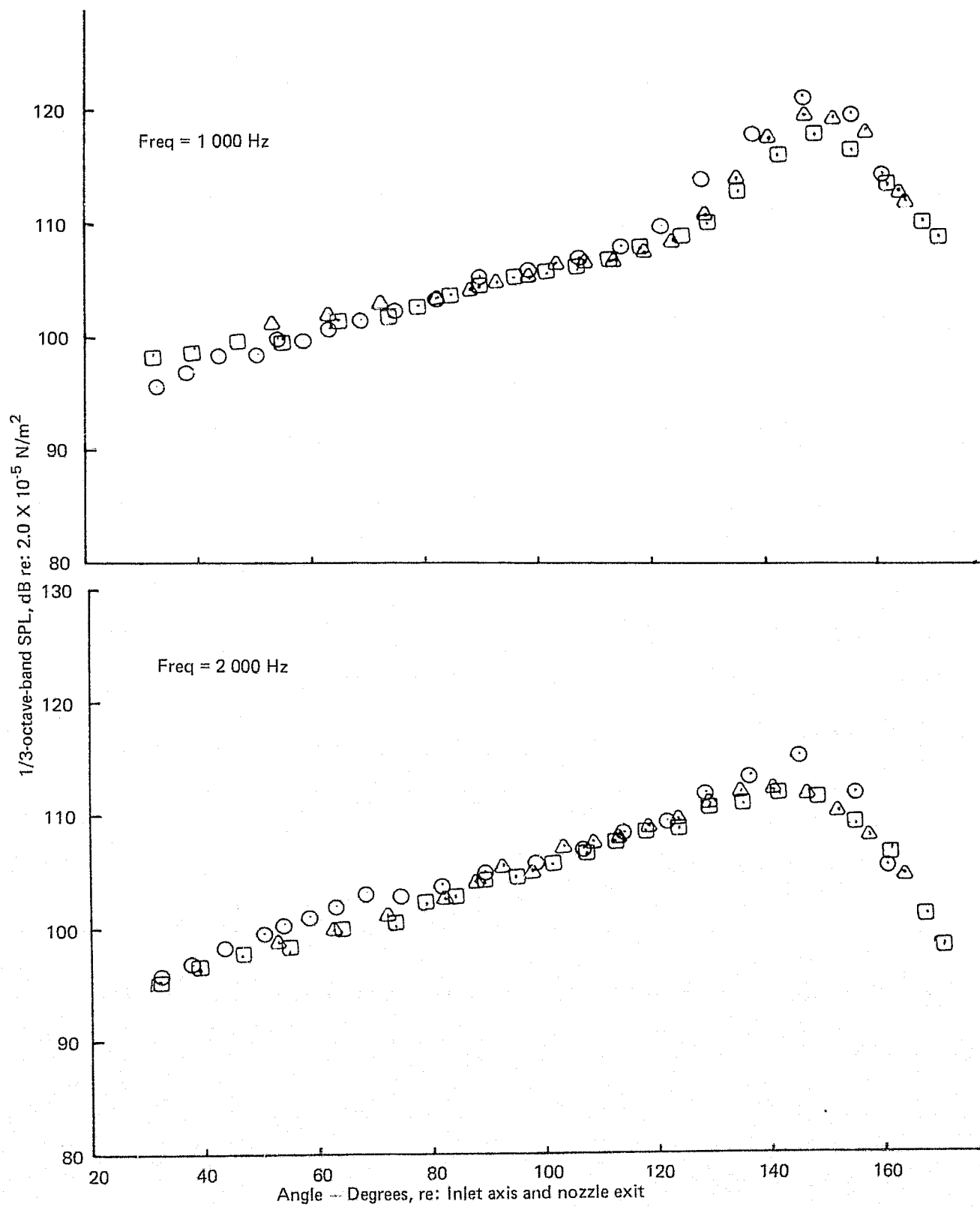


Figure 28.— (Continued)

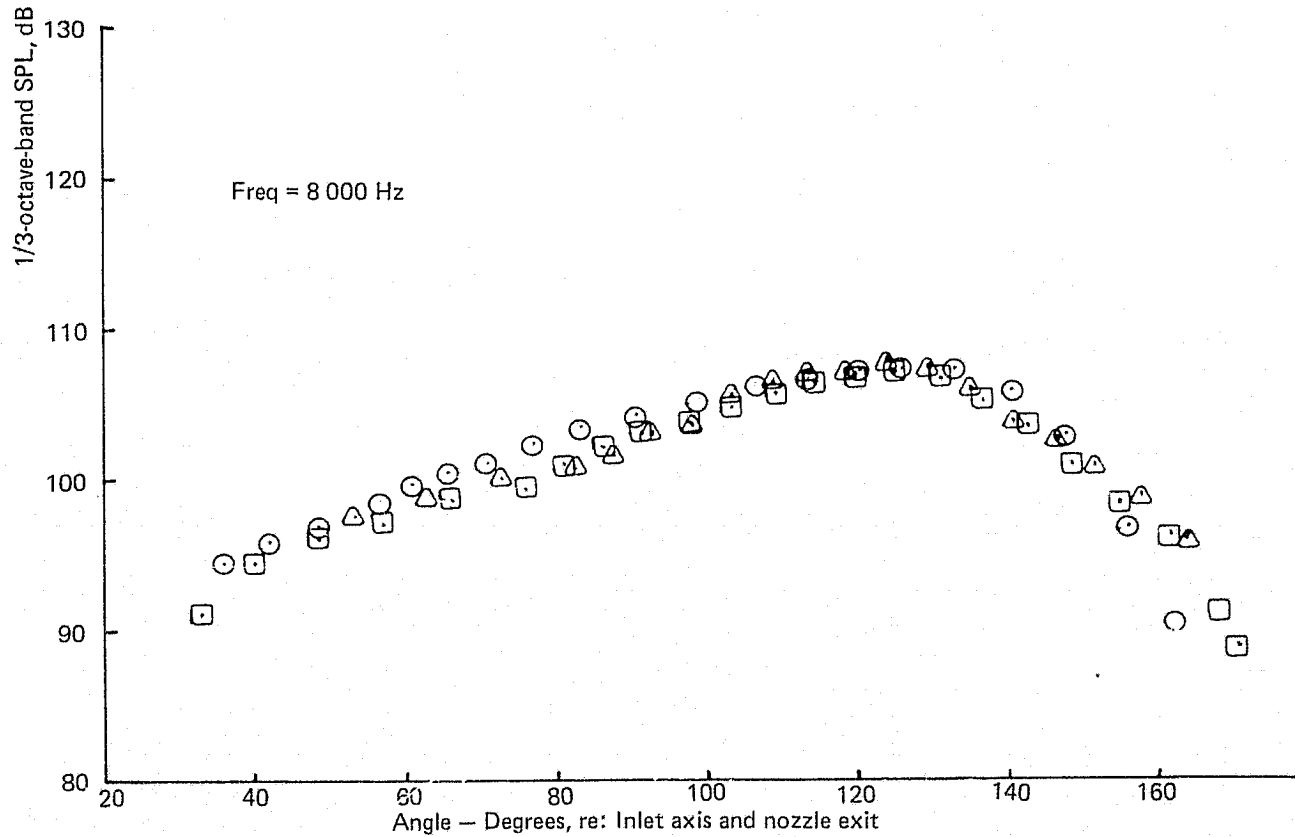
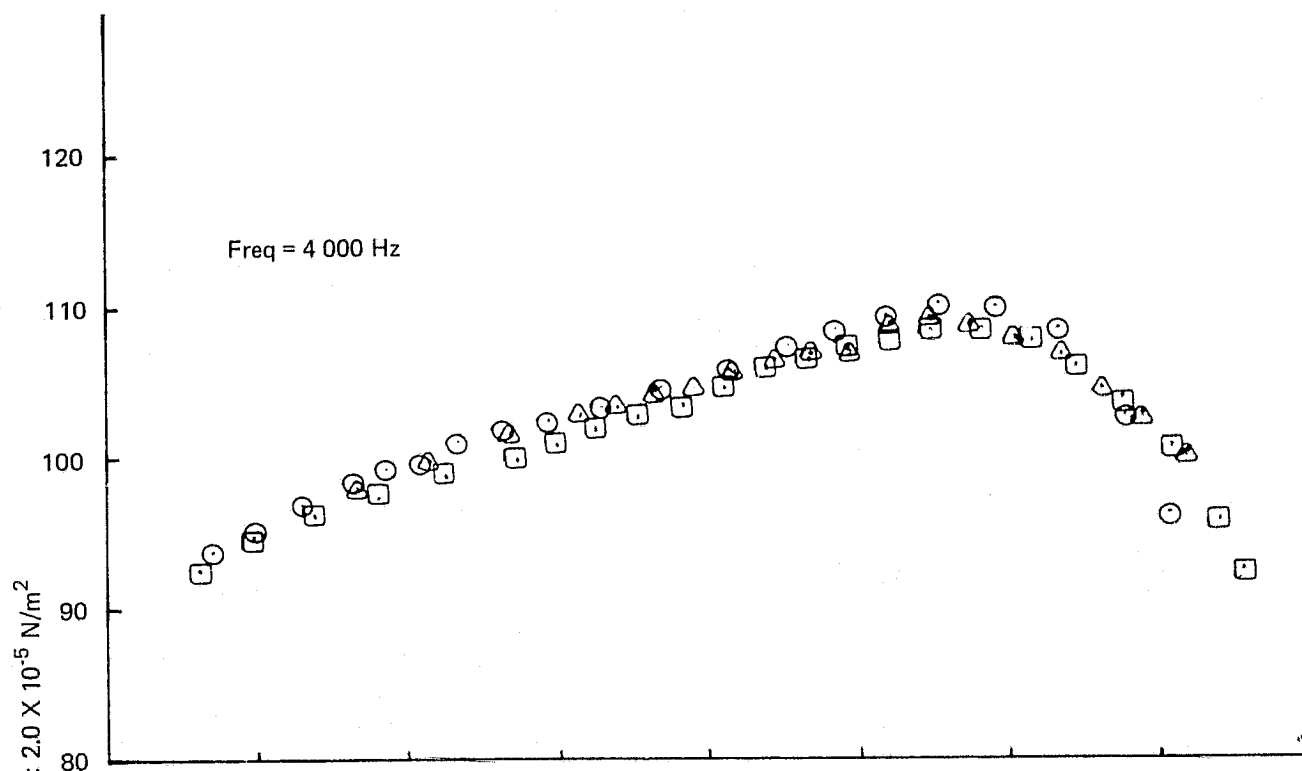


Figure 28.— (Continued)

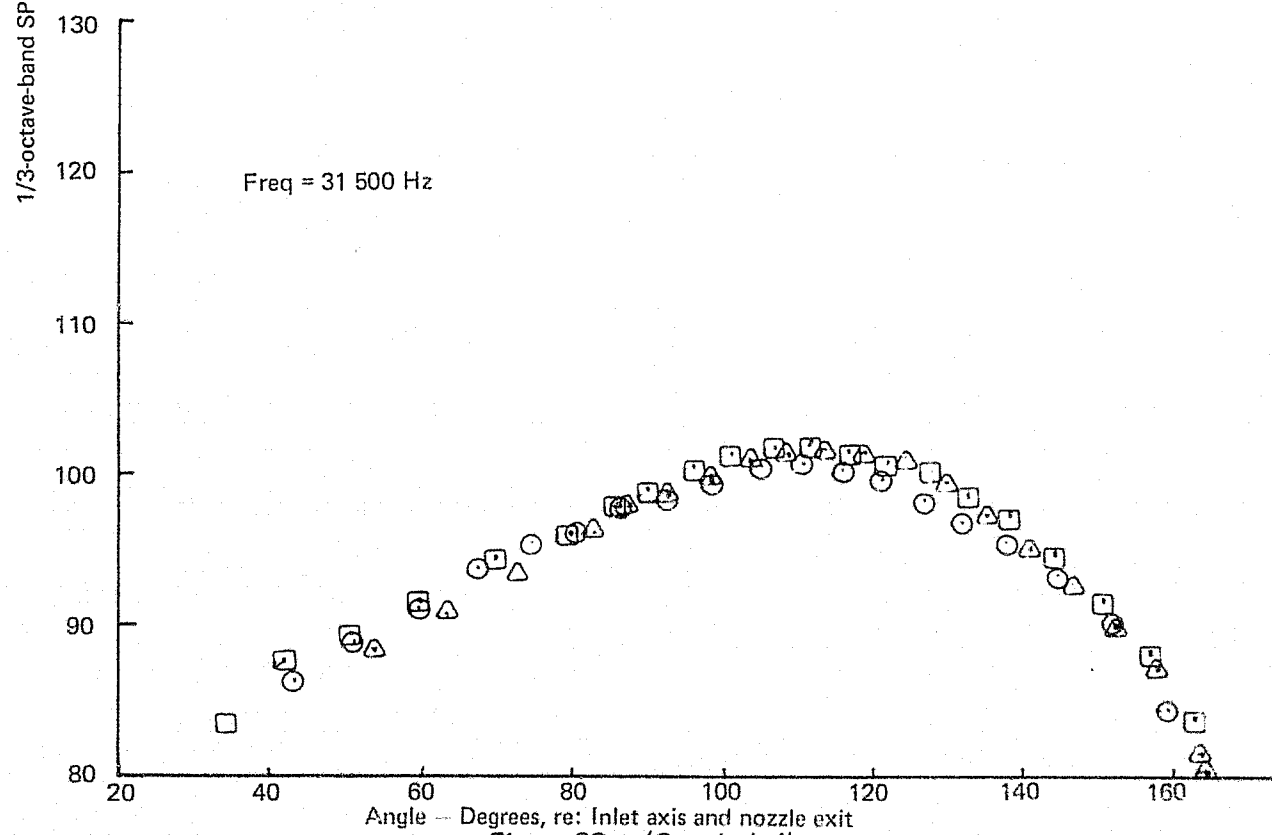
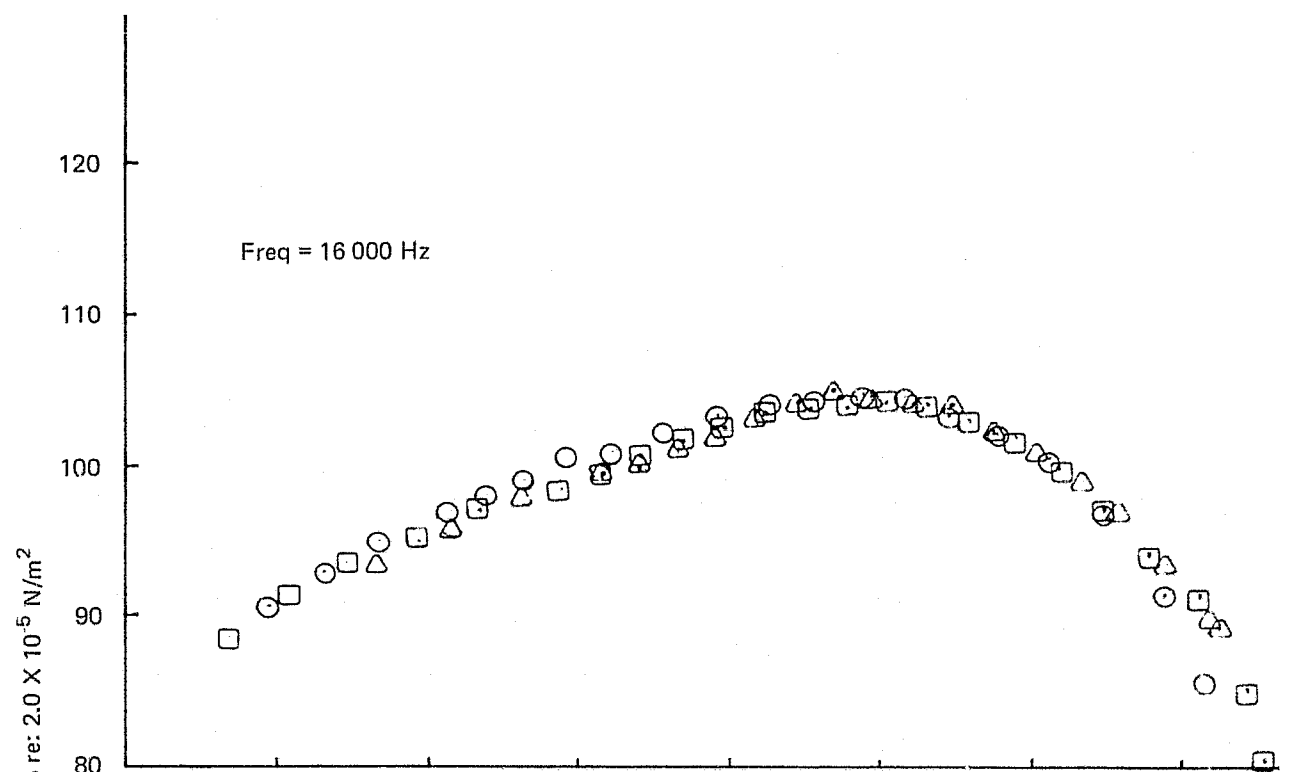


Figure 28. (Concluded)

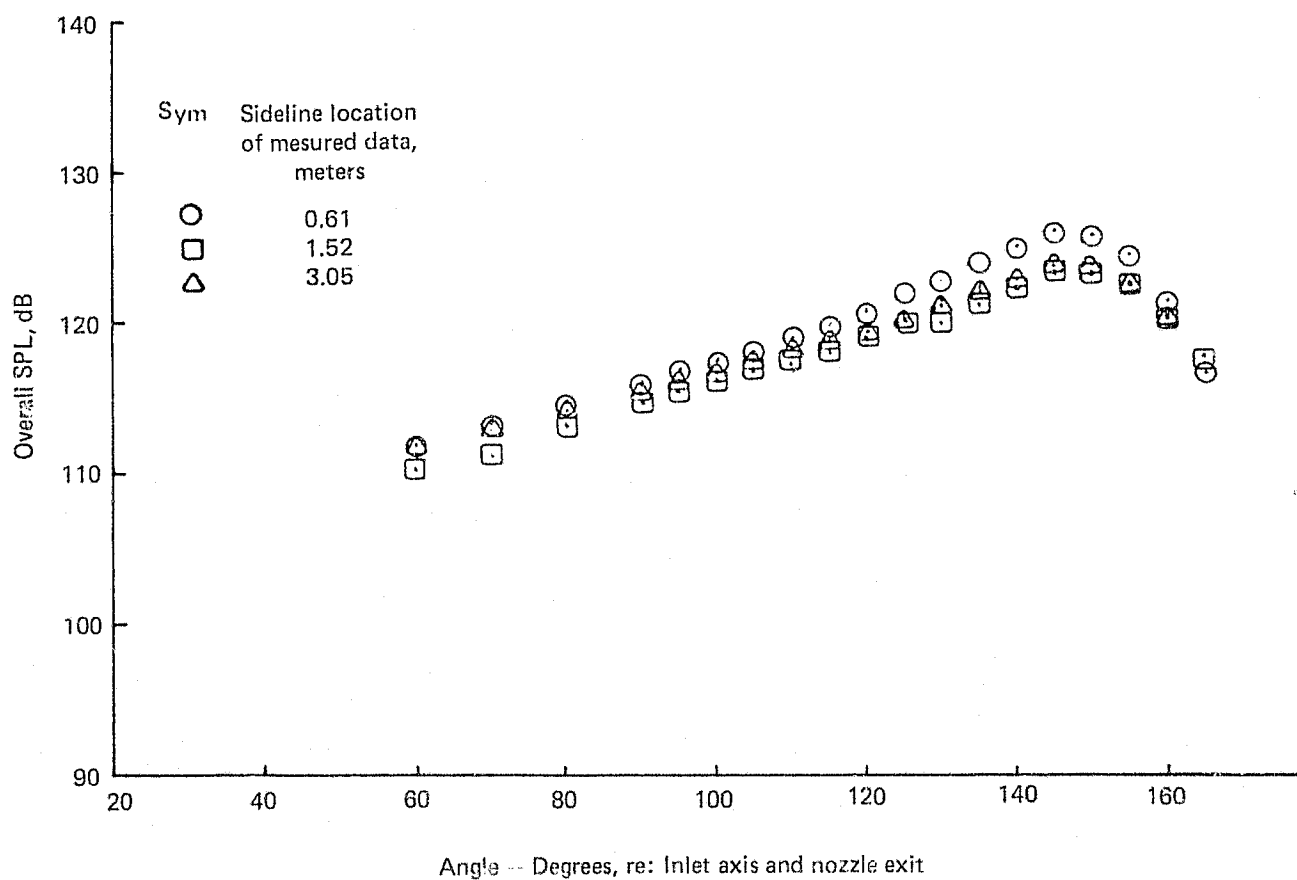


Figure 29.-- OASPL and 1/3-OB SPL Directivity Data for a 15.24 cm RC Nozzle
Extrapolated to a 3.05 m Sideline. NPR = 1.75 $V_A = 69$ m/s

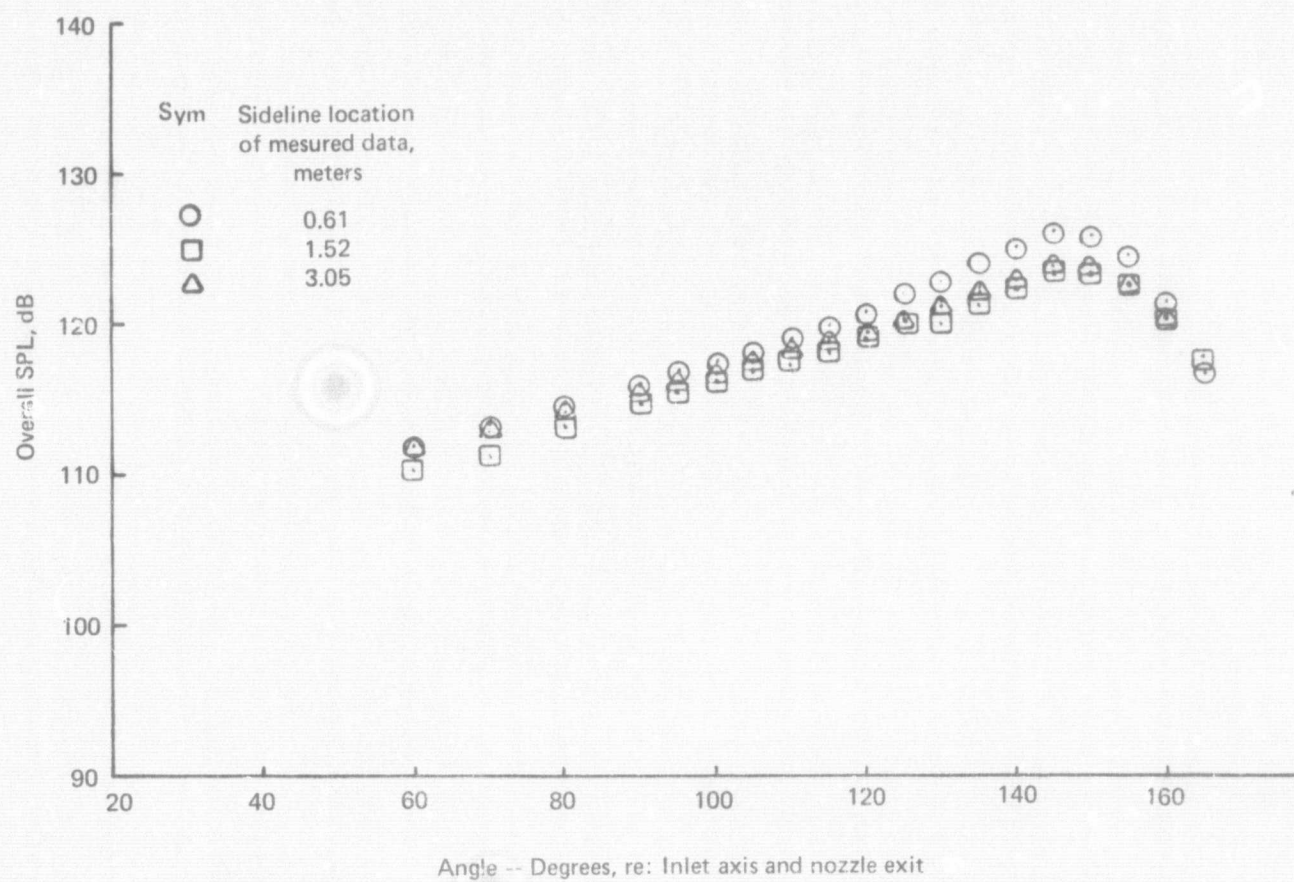


Figure 29.-- OASPL and 1/3-OB SPL Directivity Data for a 15.24 cm RC Nozzle
Extrapolated to a 3.05 m Sideline. NPR = 1.75 $V_A = 69$ m/s

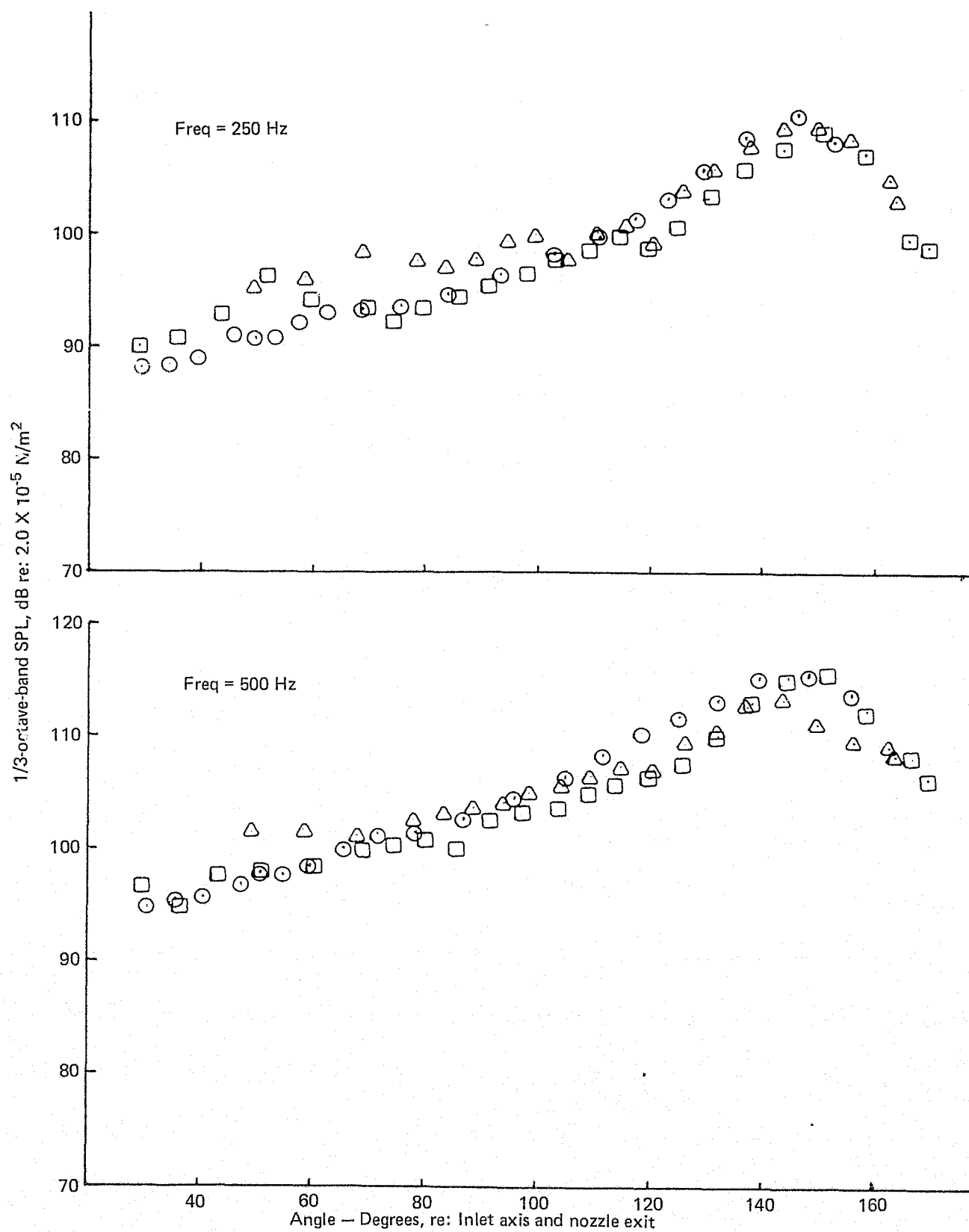


Figure 29.— (Continued)

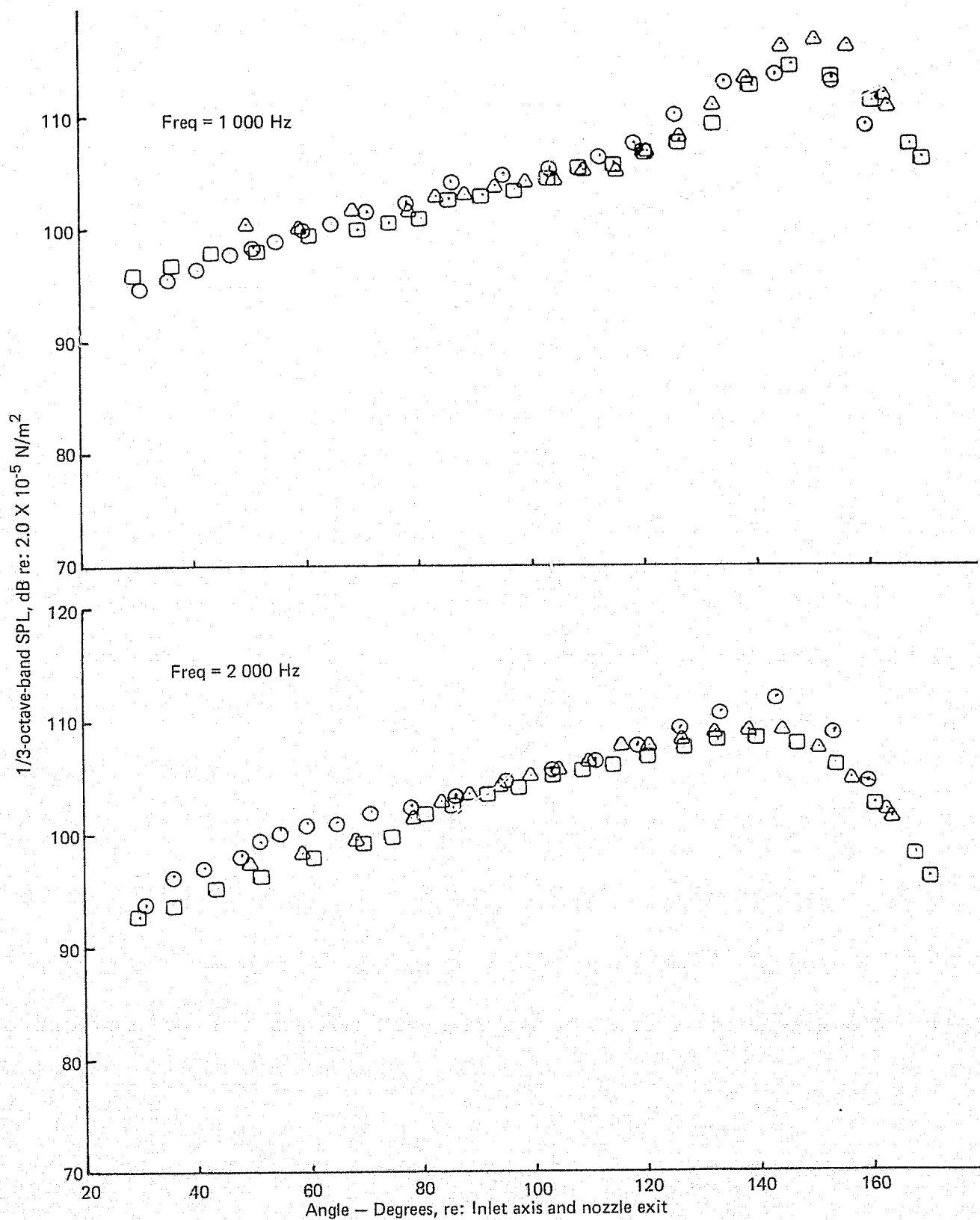


Figure 29.— (Continued)

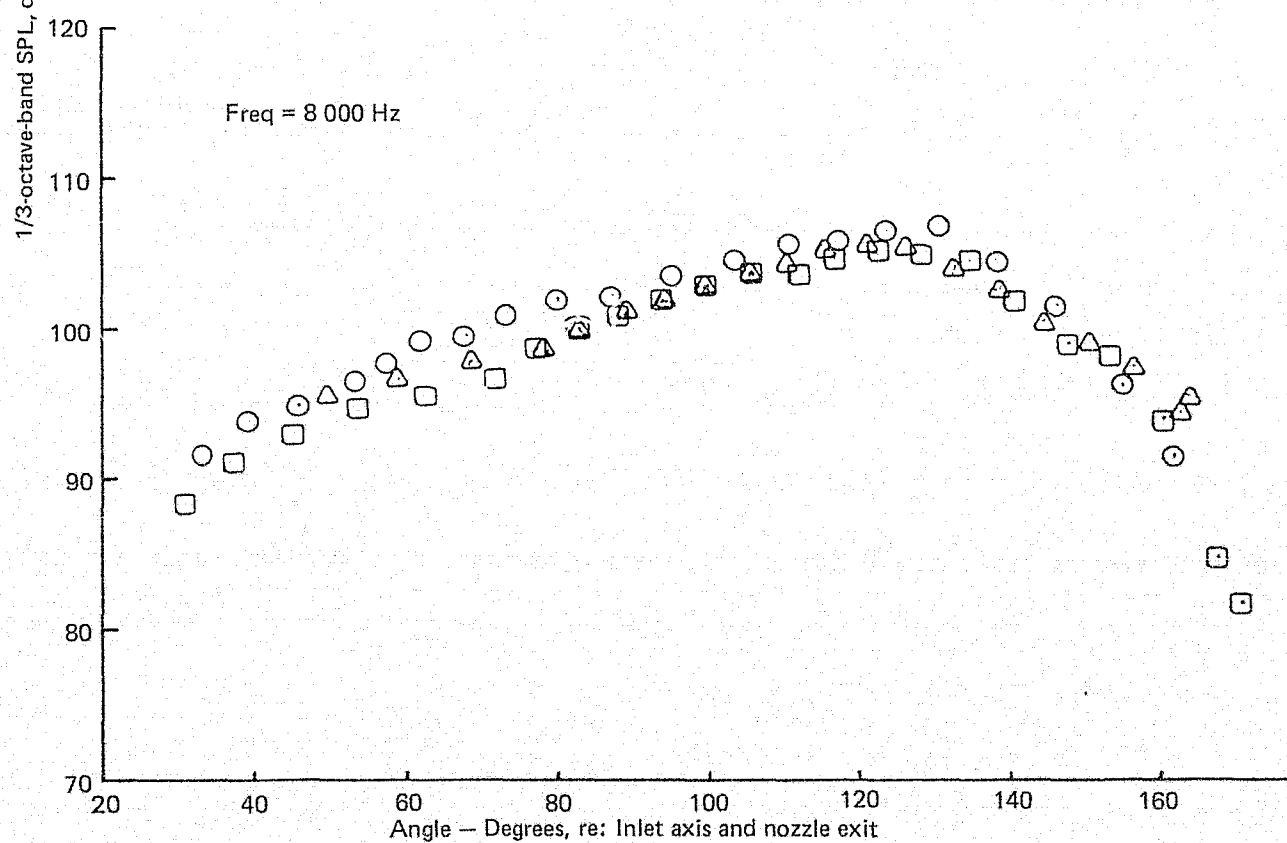
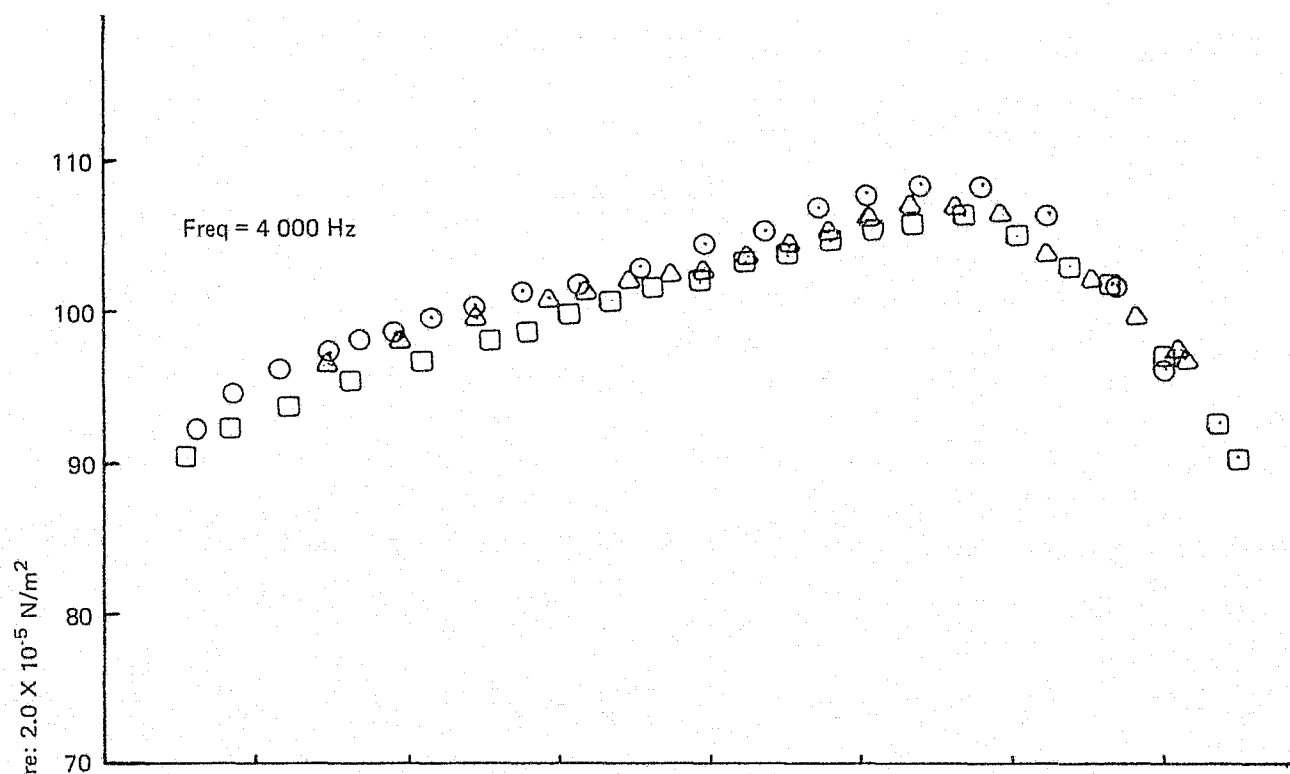


Figure 29.— (Continued)

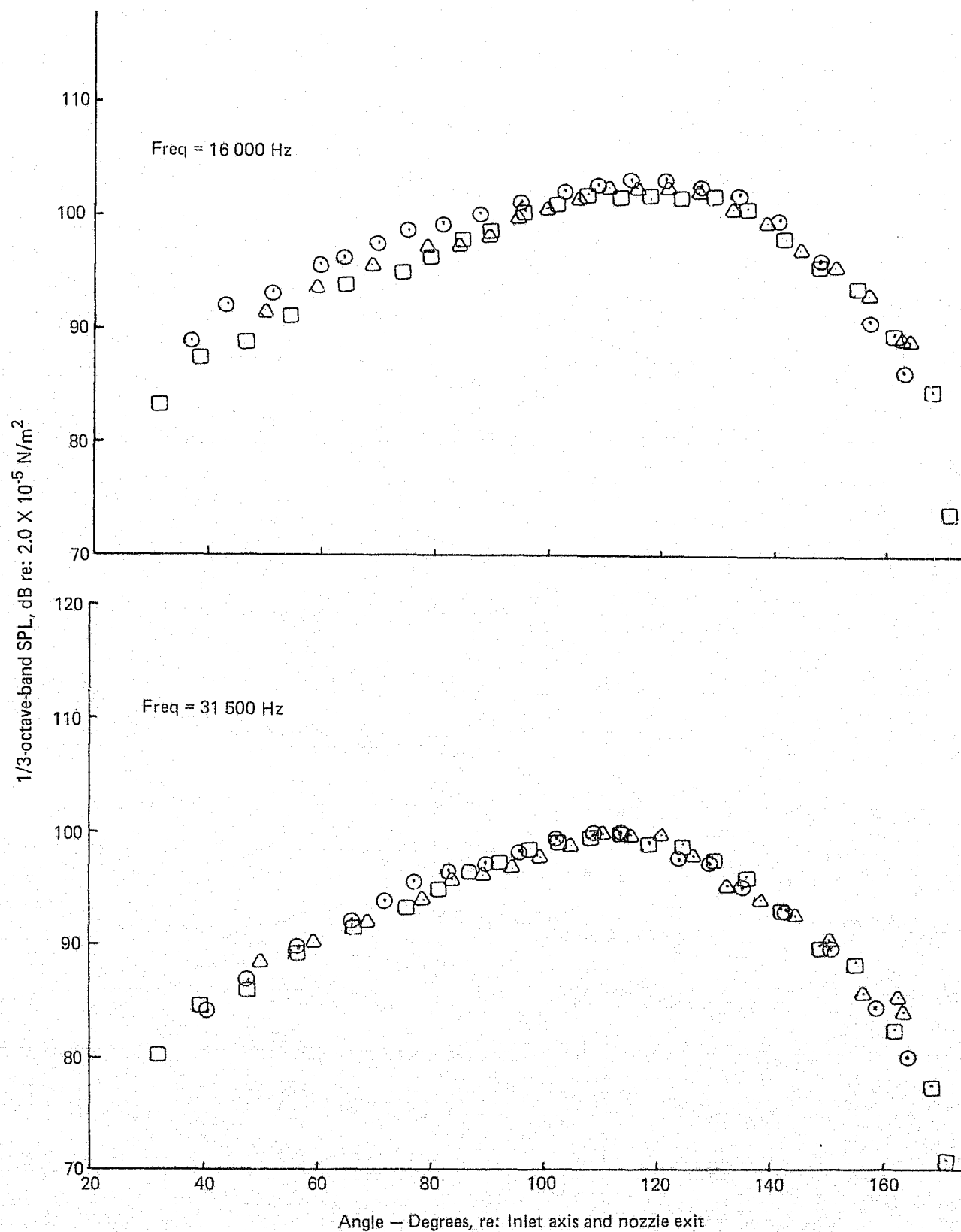


Figure 29.— (Concluded)

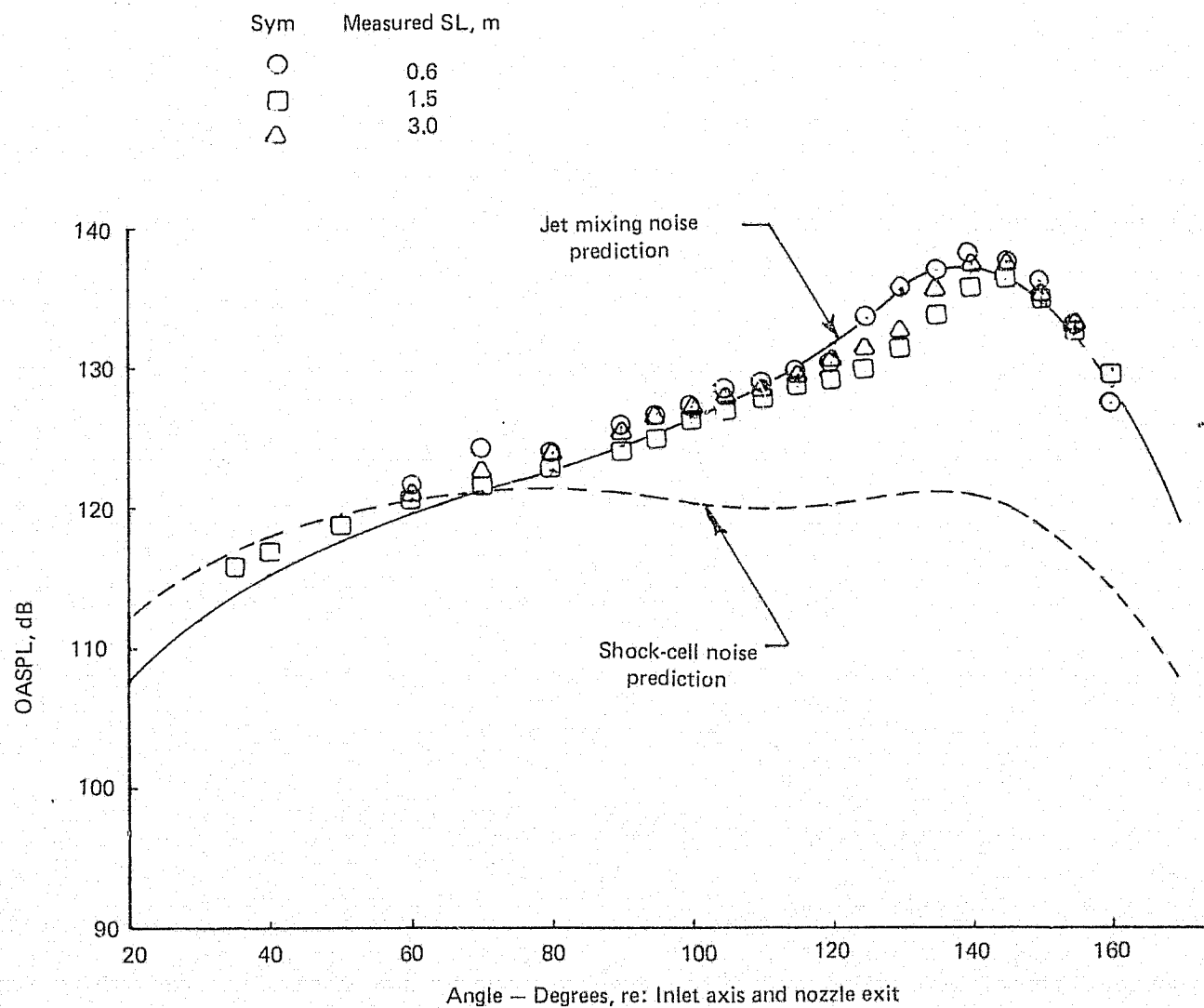


Figure 30.— OASPL Directivity and Jet Noise Spectra for a 15.24 cm RC Nozzle
Extrapolated to a 3.05 m Sideline, NPR = 2.25, $V_A = 0$ m/s

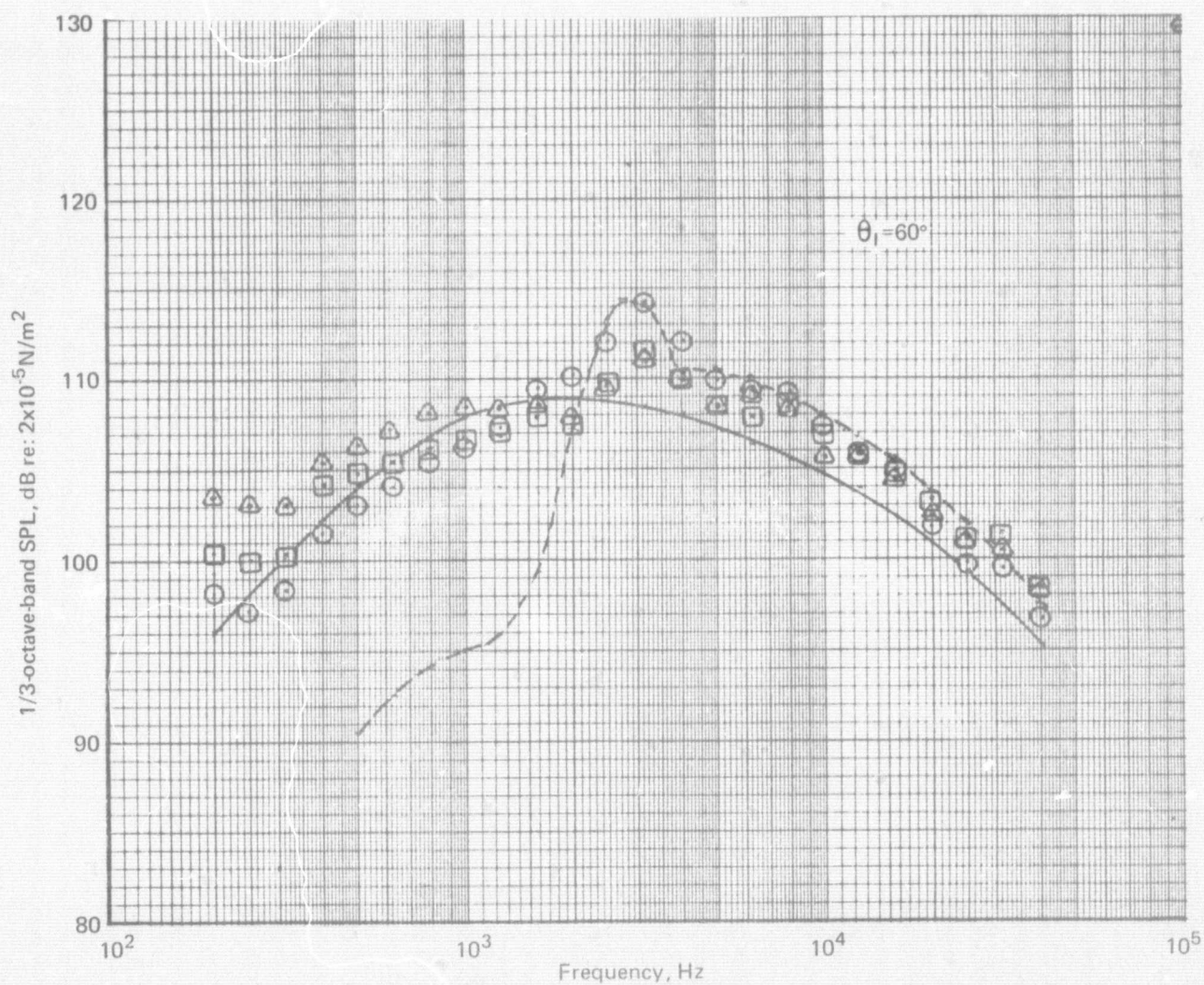


Figure 30.—(Continued)

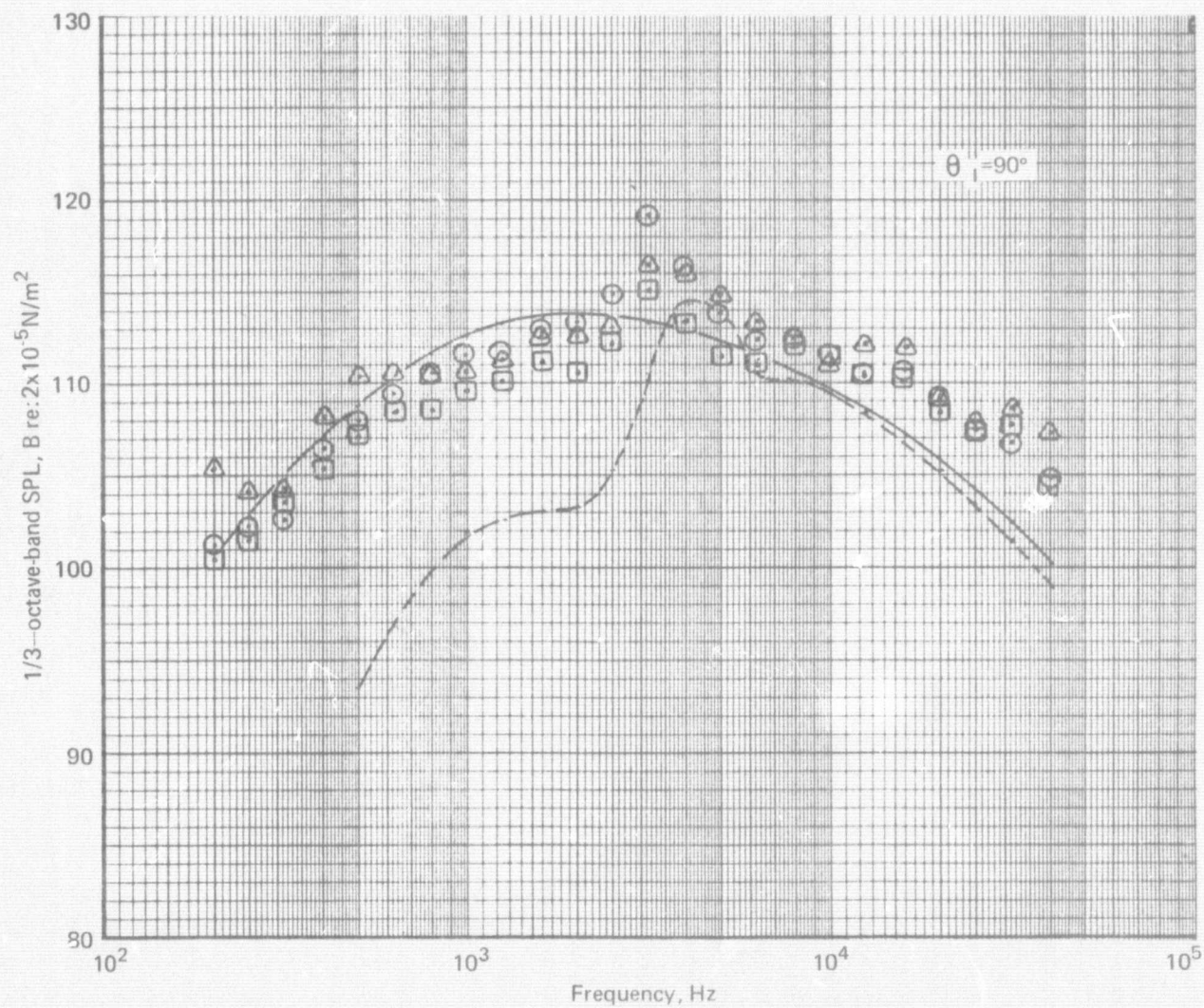


Figure 30.--(Continued)

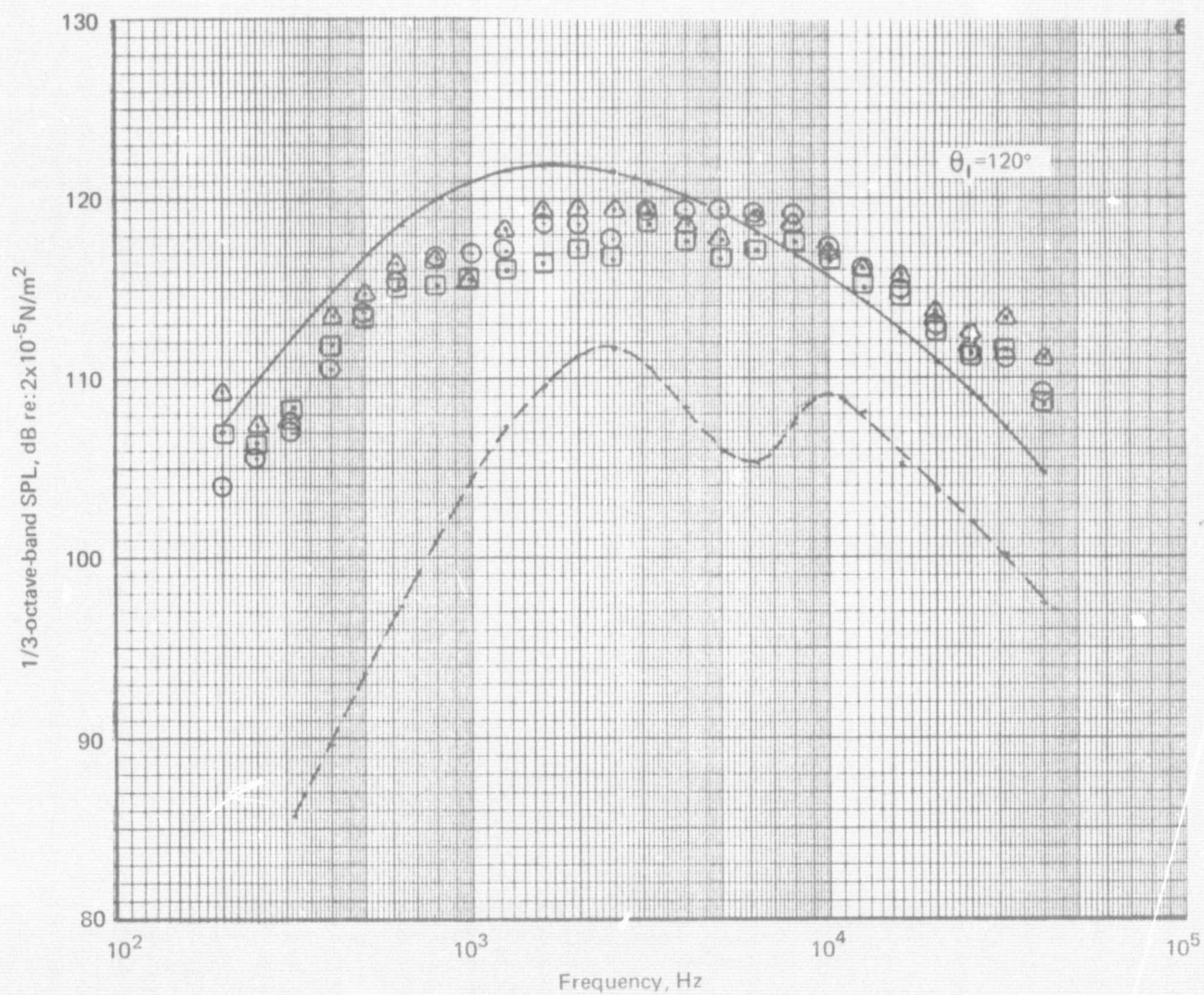


Figure 30.—(Continued)

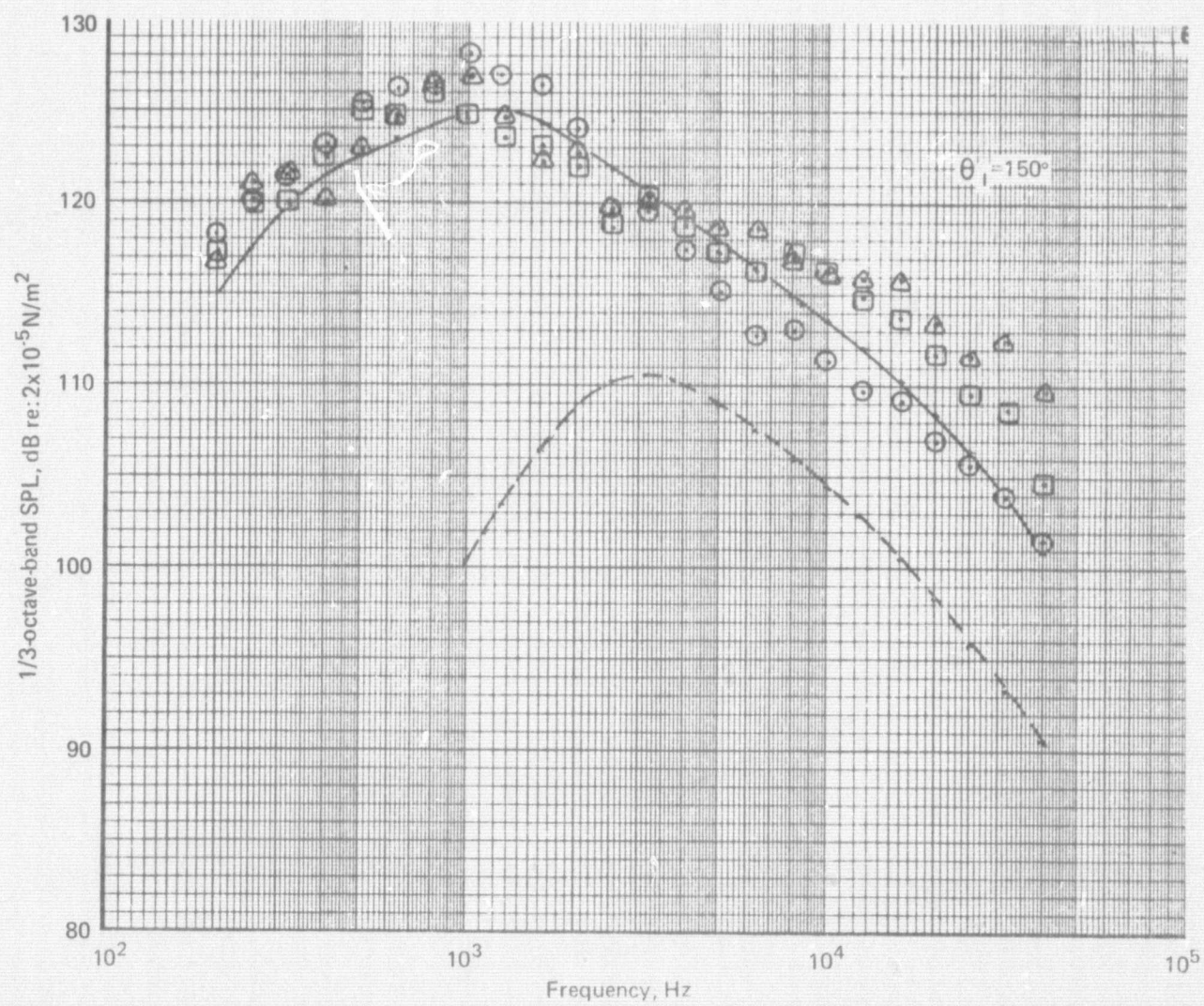


Figure 30.—(Concluded)

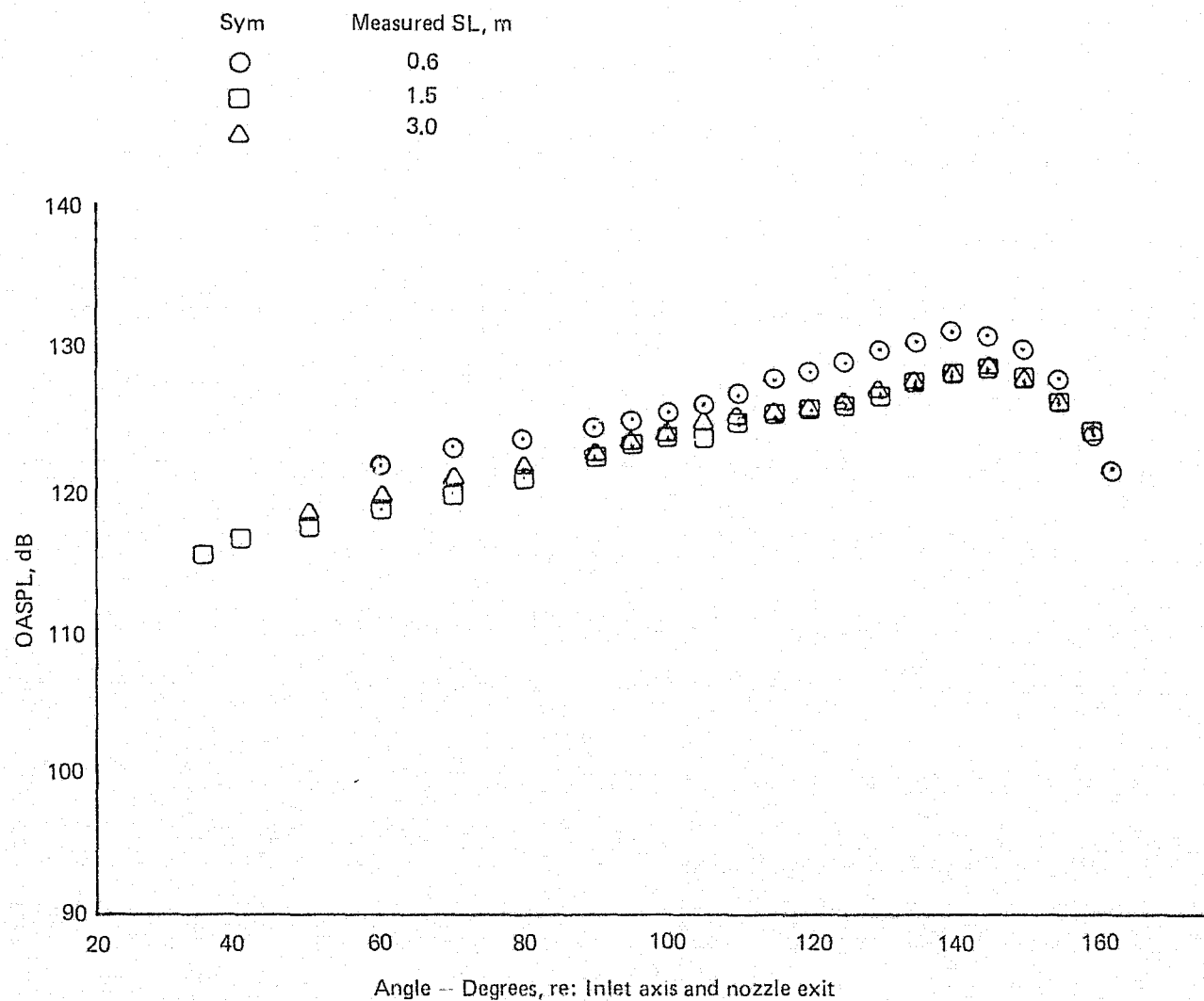


Figure 31.— OASPL Directivity and Jet Noise Spectra for a 15.24 cm RC Nozzle
Extrapolated to a 3.05 m Sideline, NPR = 2.25, $V_A = 91.5$ m/s

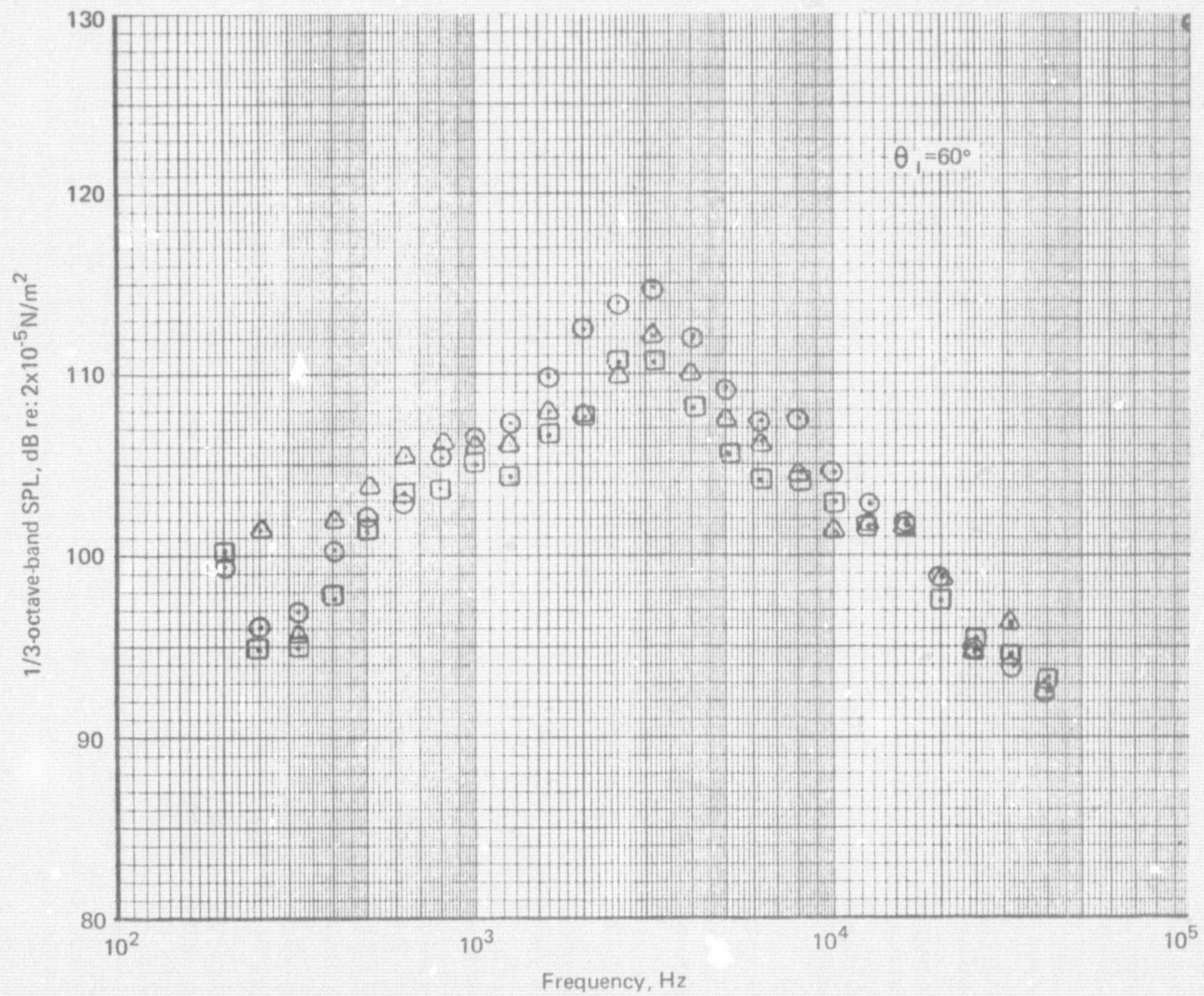


Figure 31.—(Continued)

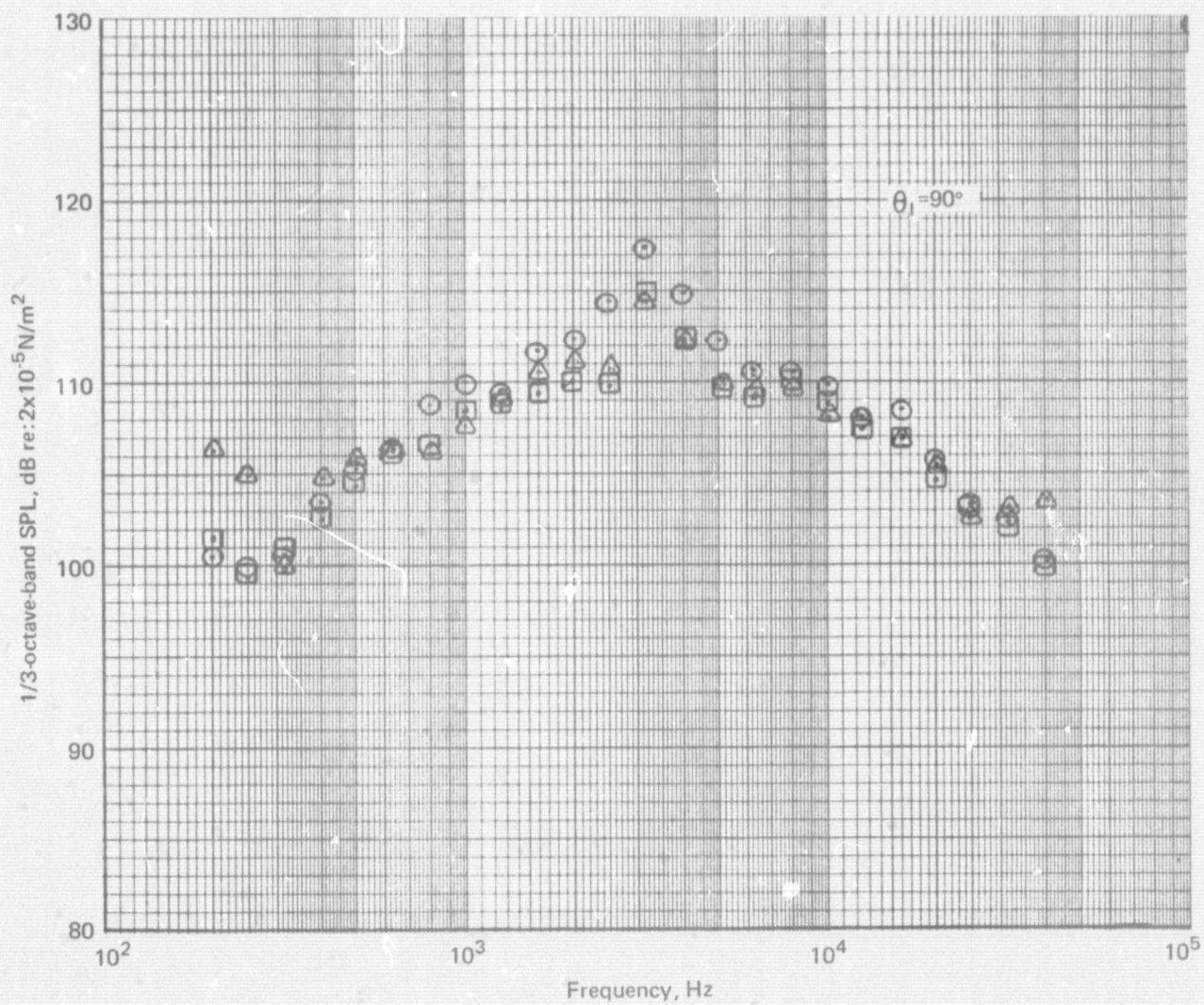


Figure 31.—(Continued)

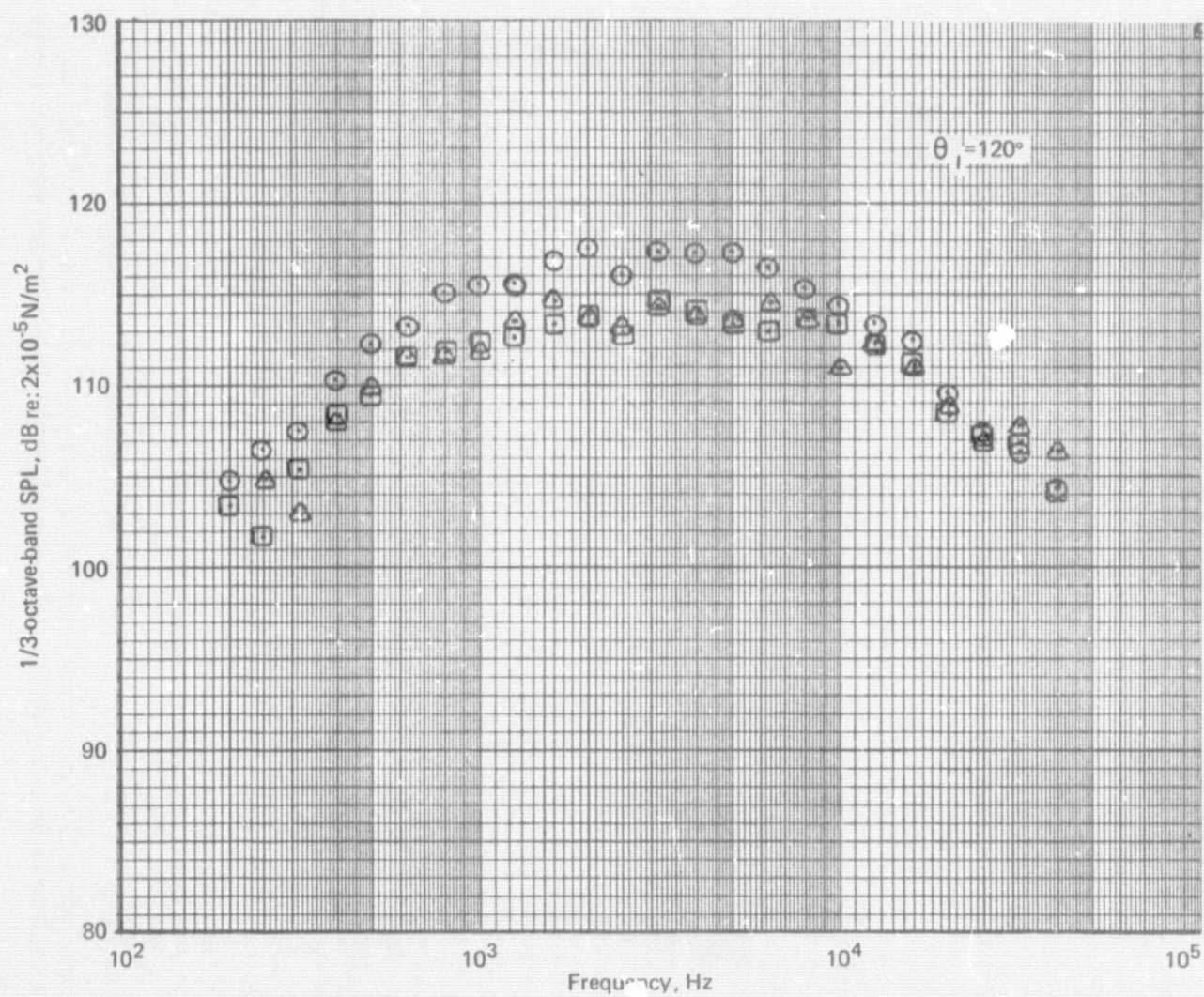


Figure 31.—(Continued)

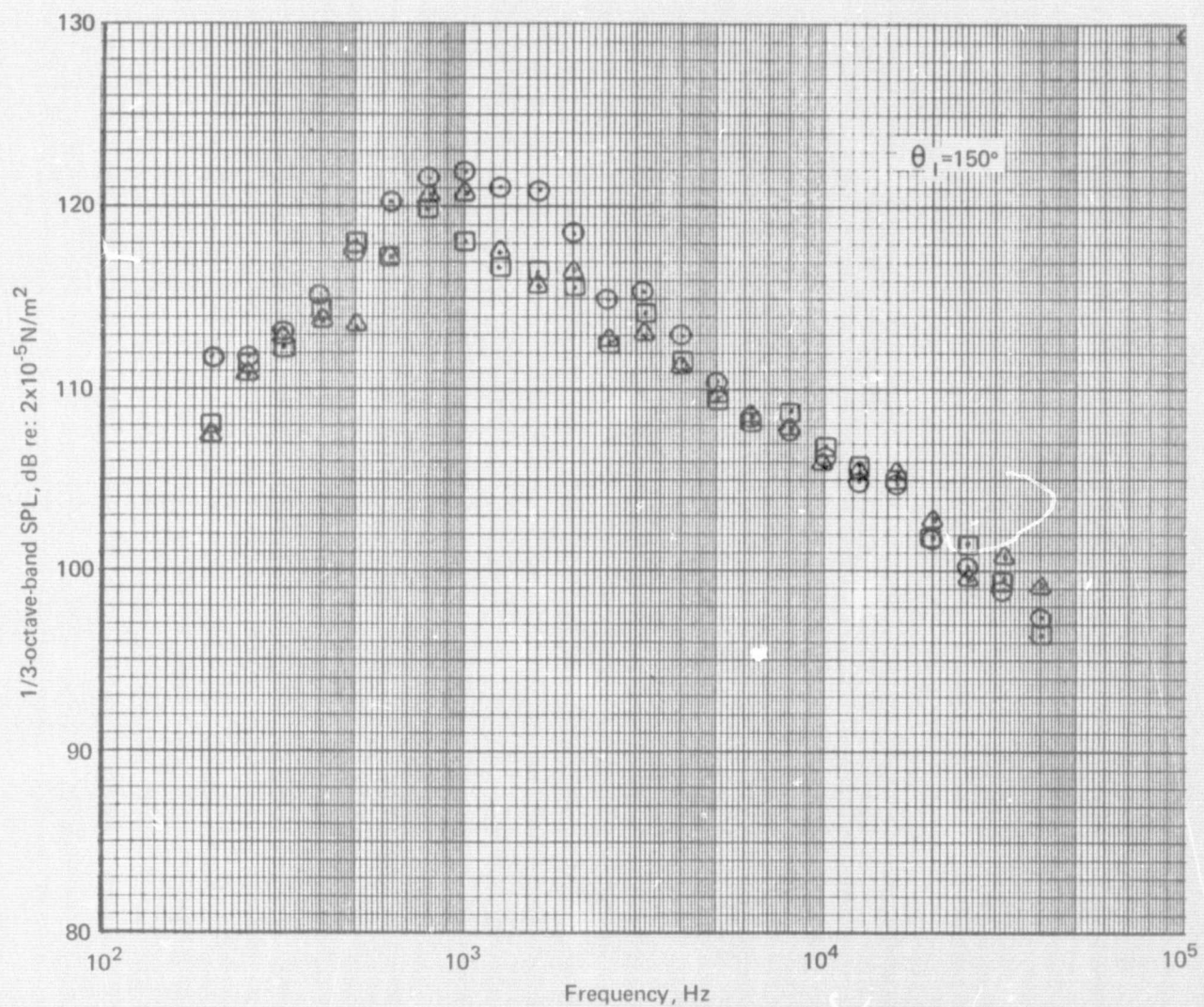


Figure 31.—(Concluded)

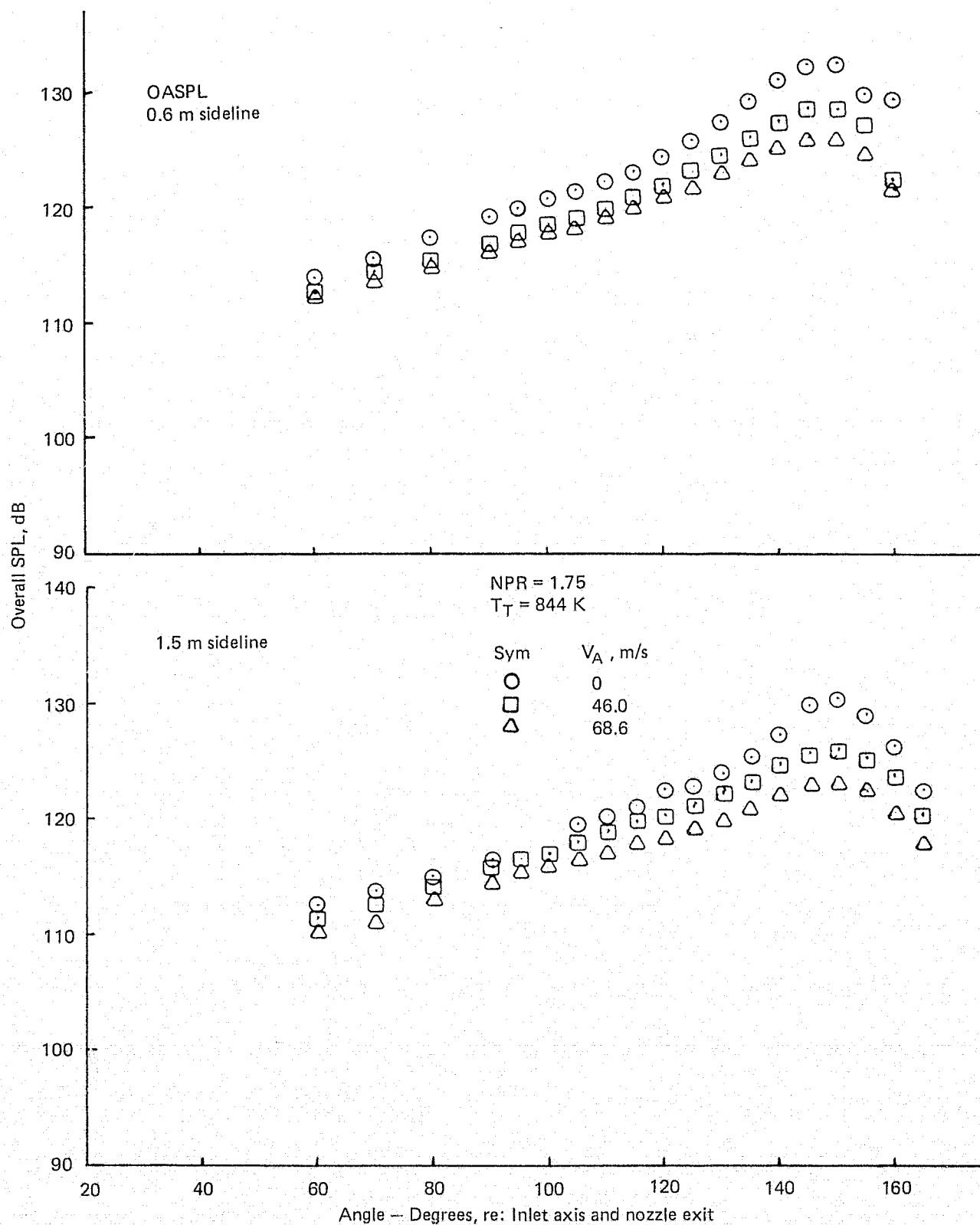


Figure 32.— Comparison of Flight Effects Measured for a 15.24 cm RC Nozzle on a 0.6, 1.5 and 3 m Sidelines Extrapolated to a 3.0 m Sideline.

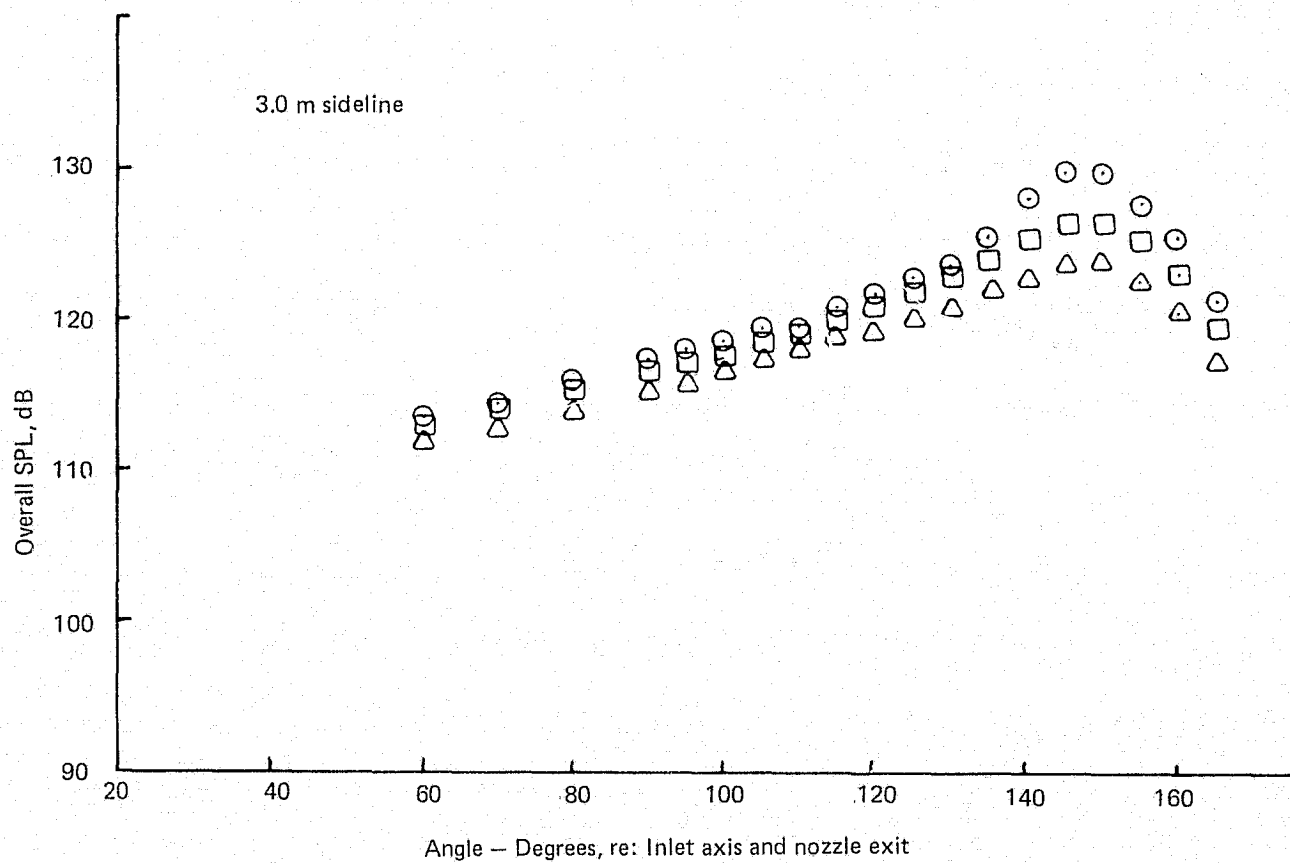


Figure 32.— (Continued)

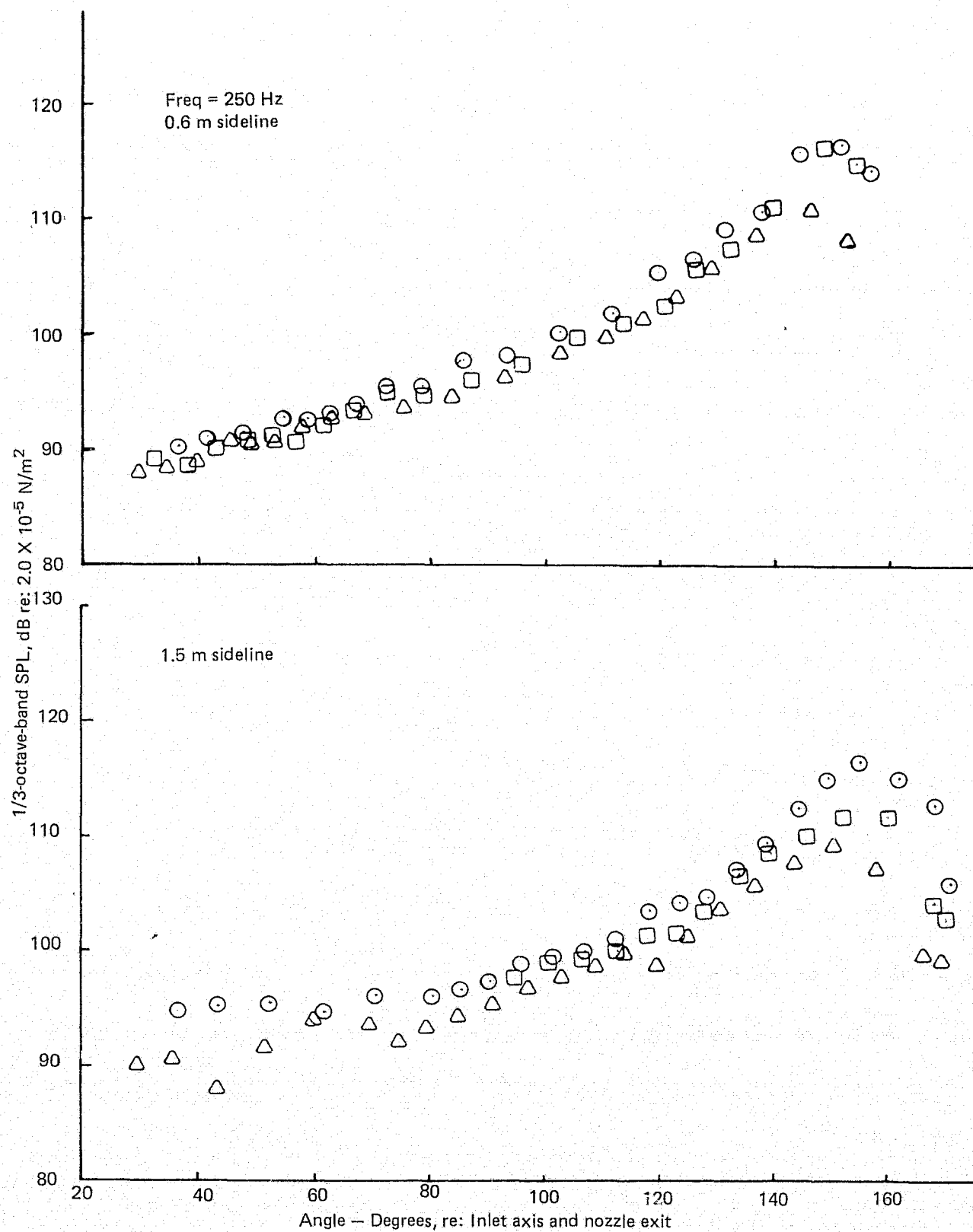


Figure 32.— (Continued)

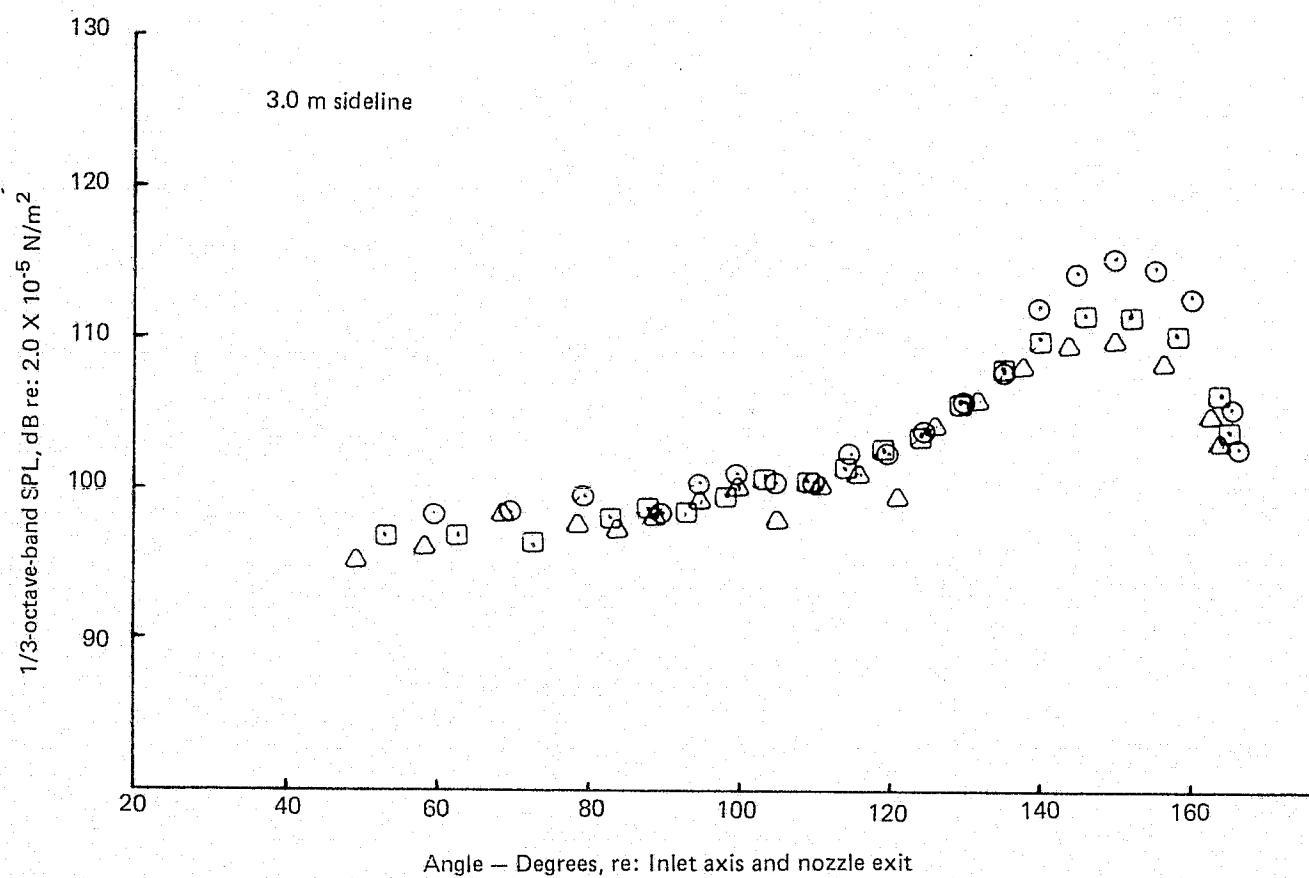


Figure 32.— (Continued)

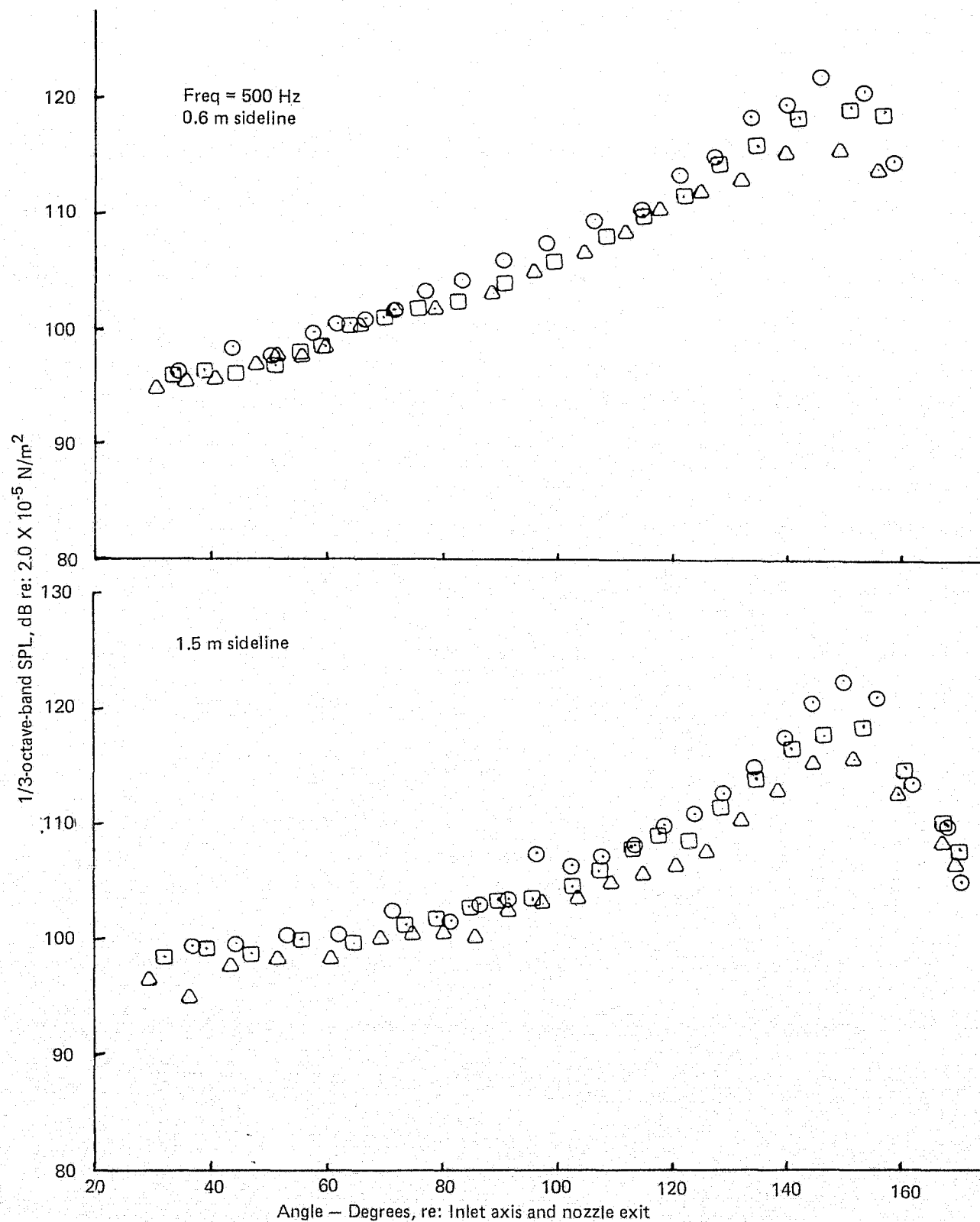


Figure 32.— (Continued)

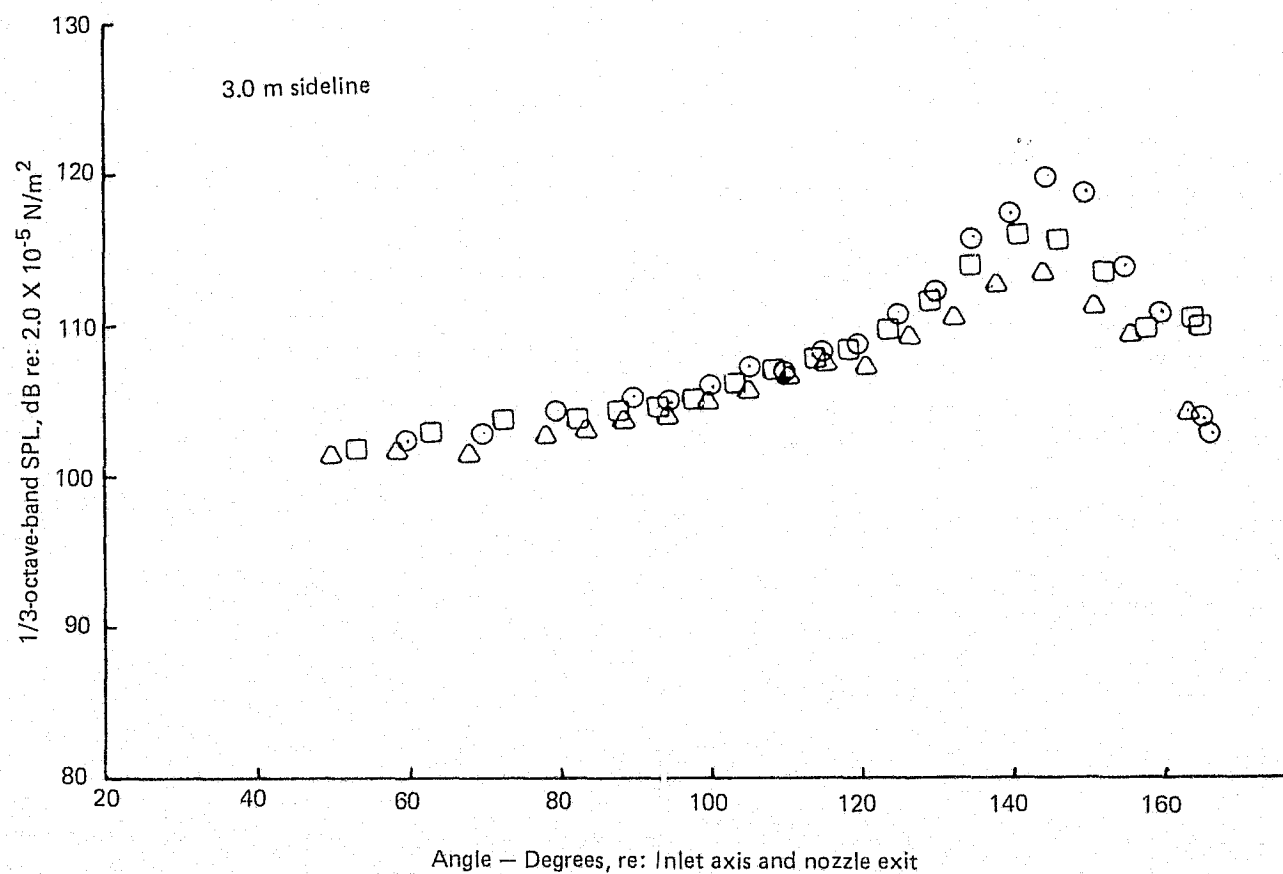


Figure 32.— (Continued)

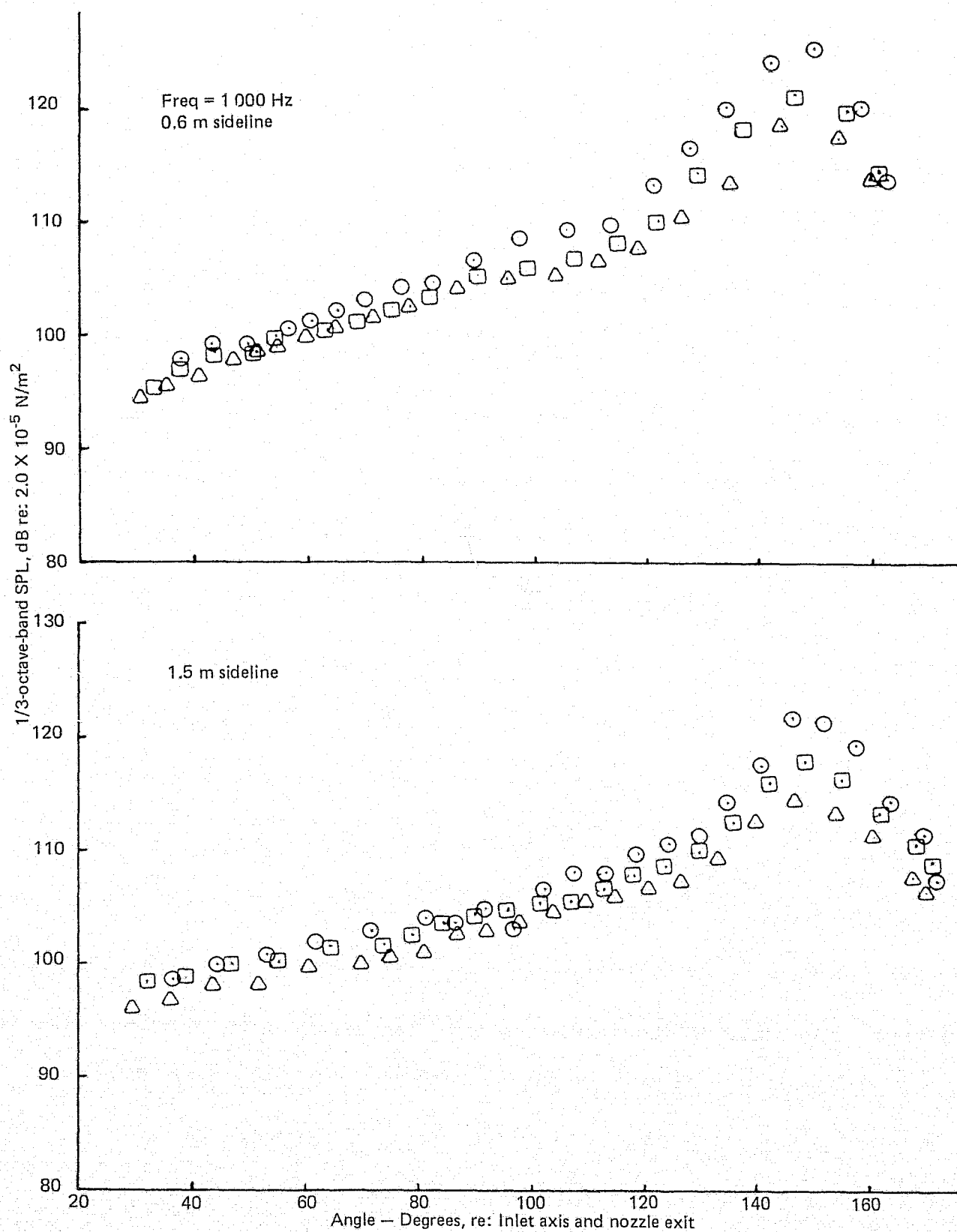


Figure 32.— (Continued)

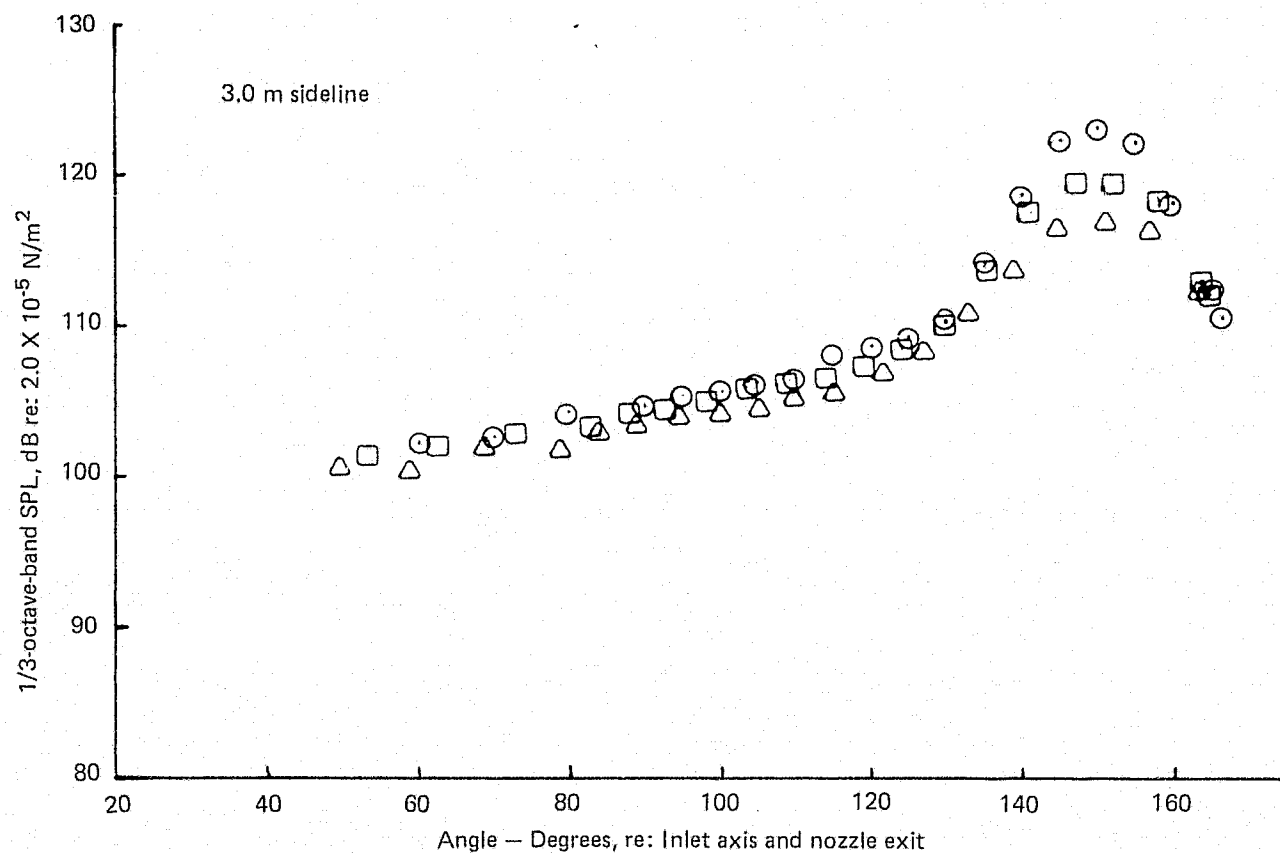


Figure 32.— (Continued)

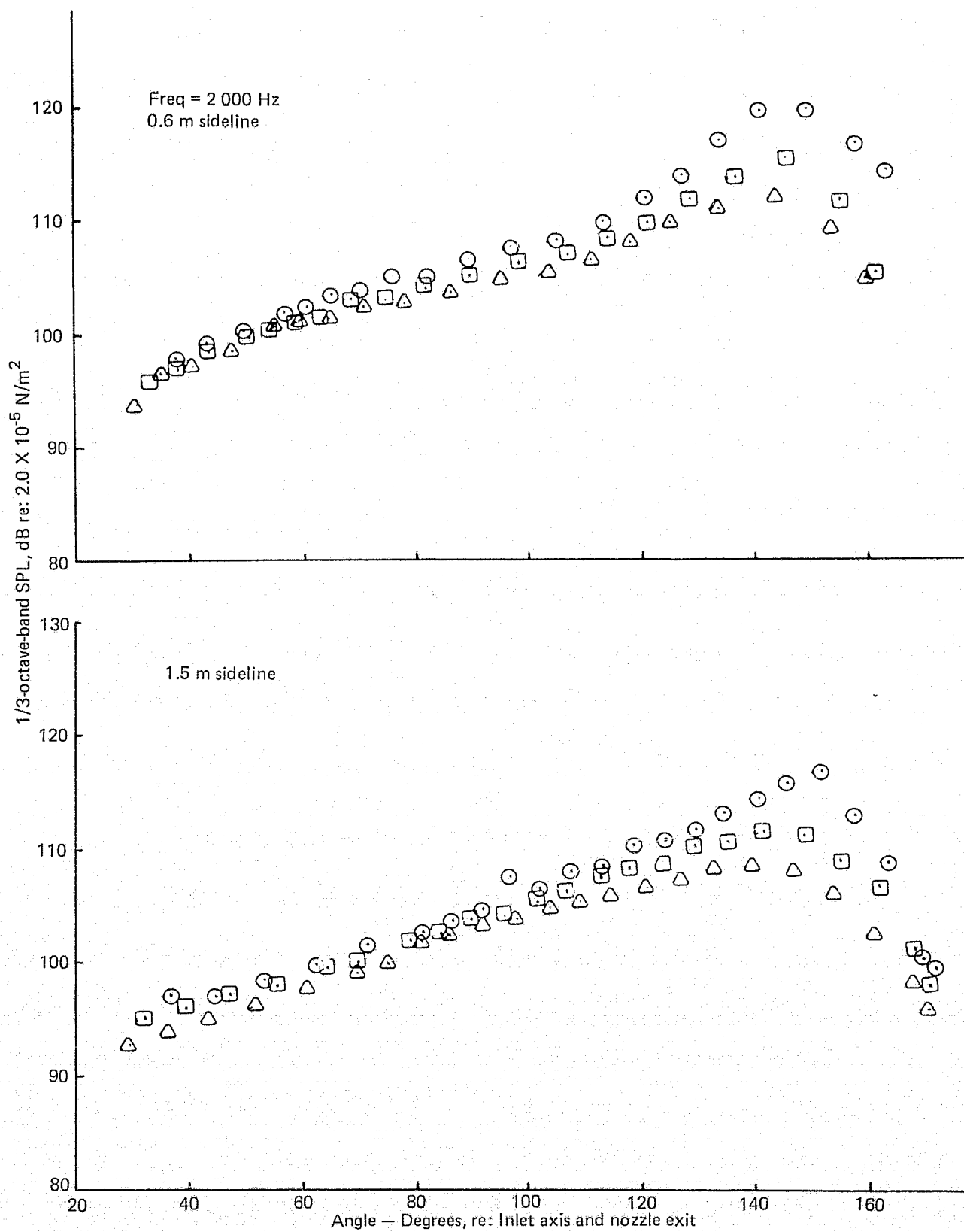


Figure 32.— (Continued)

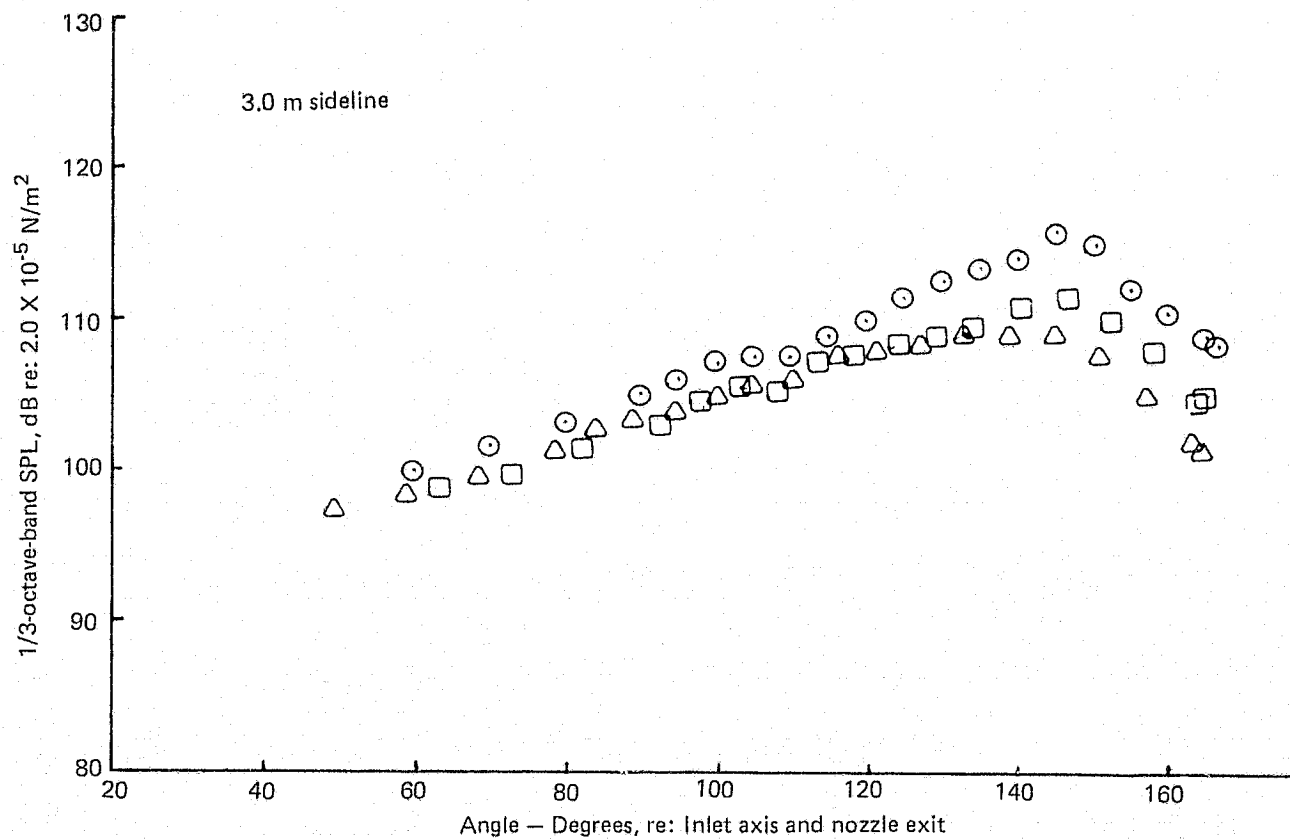


Figure 32.— (Continued)

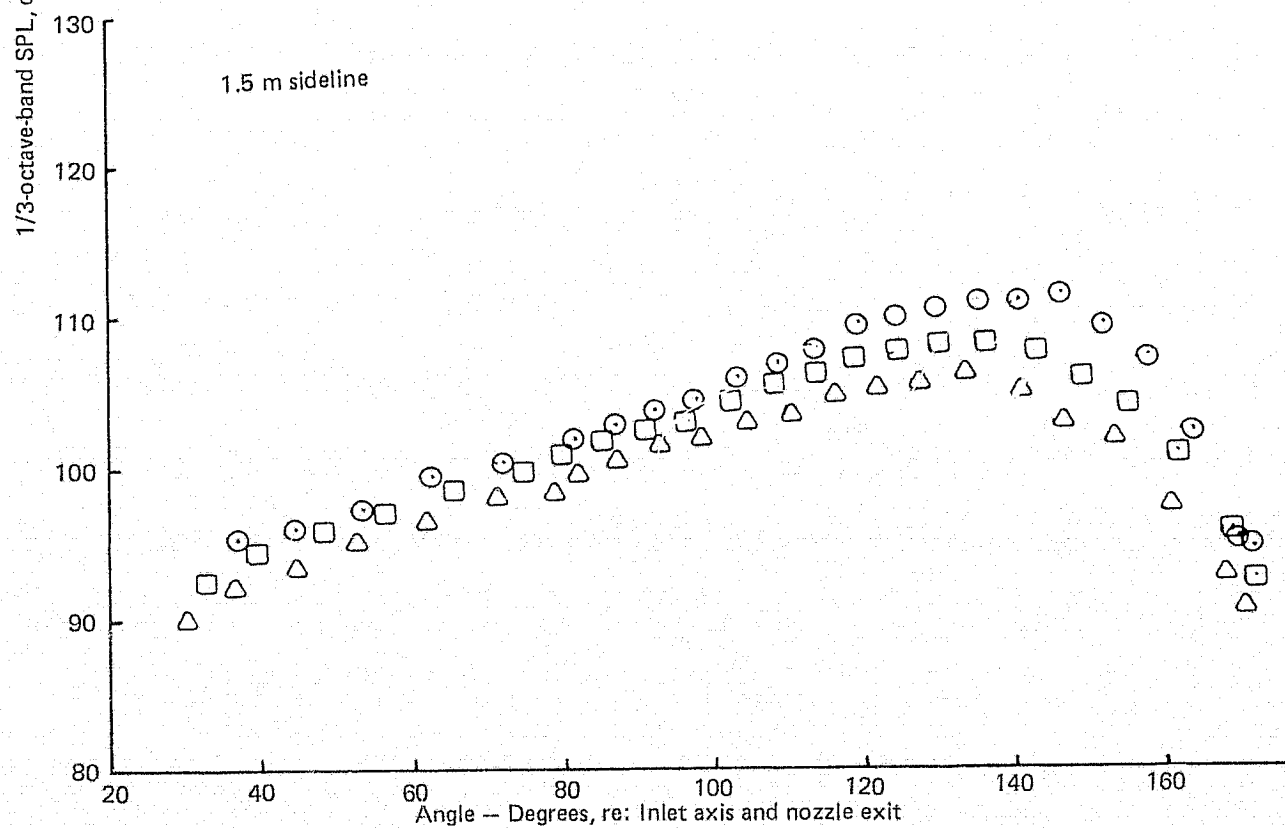
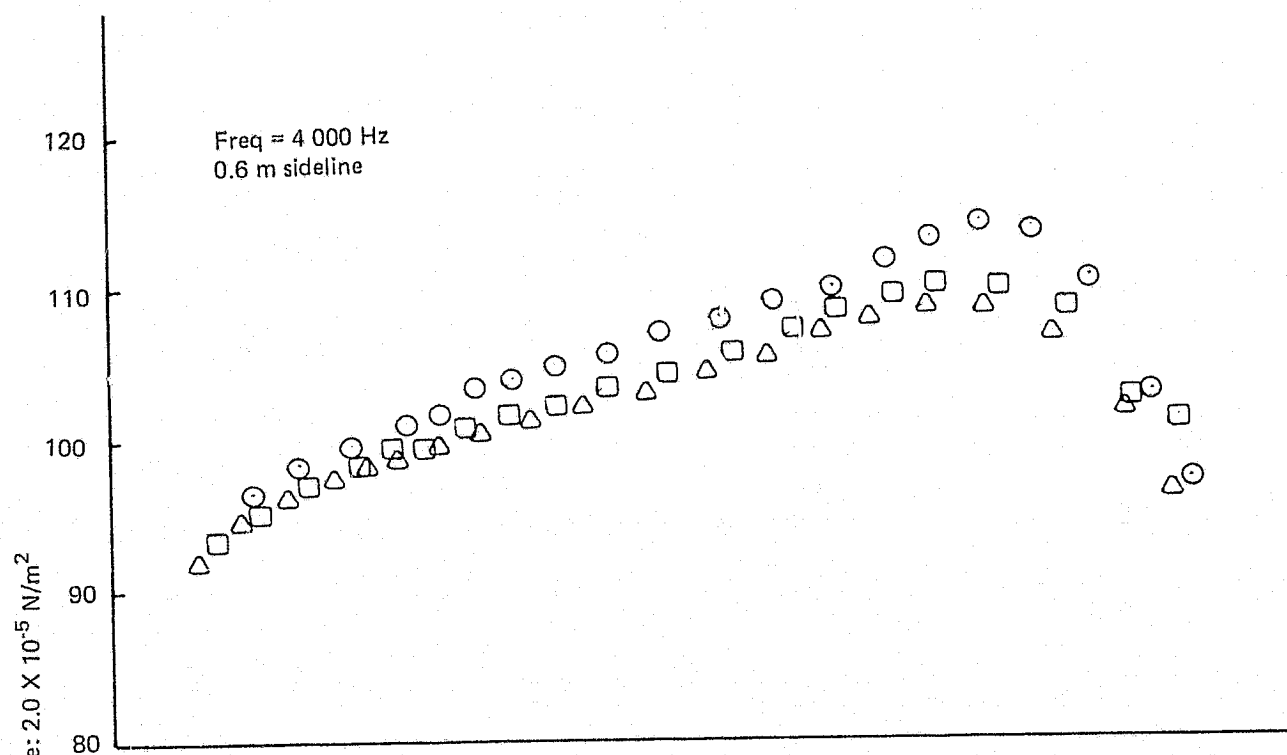


Figure 32.— (Continued)

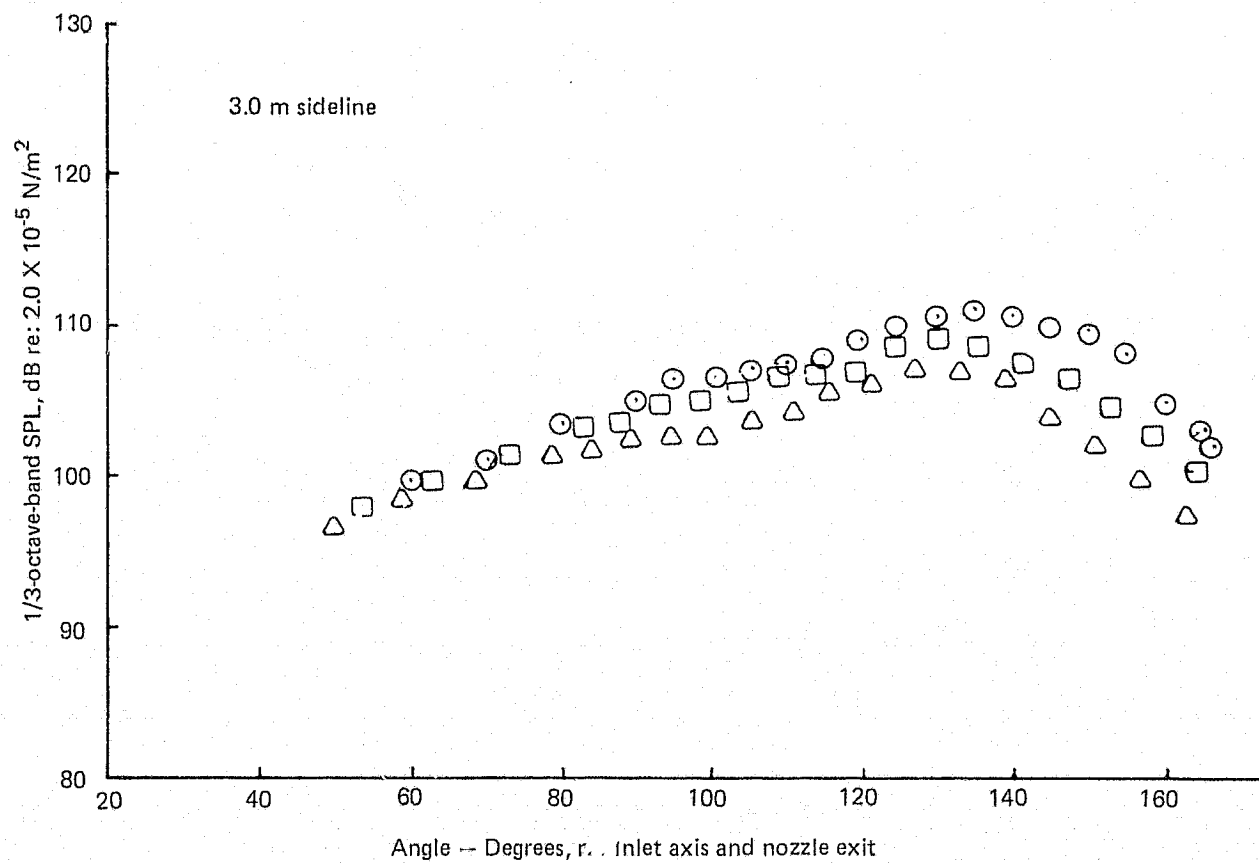


Figure 32.— (Continued)

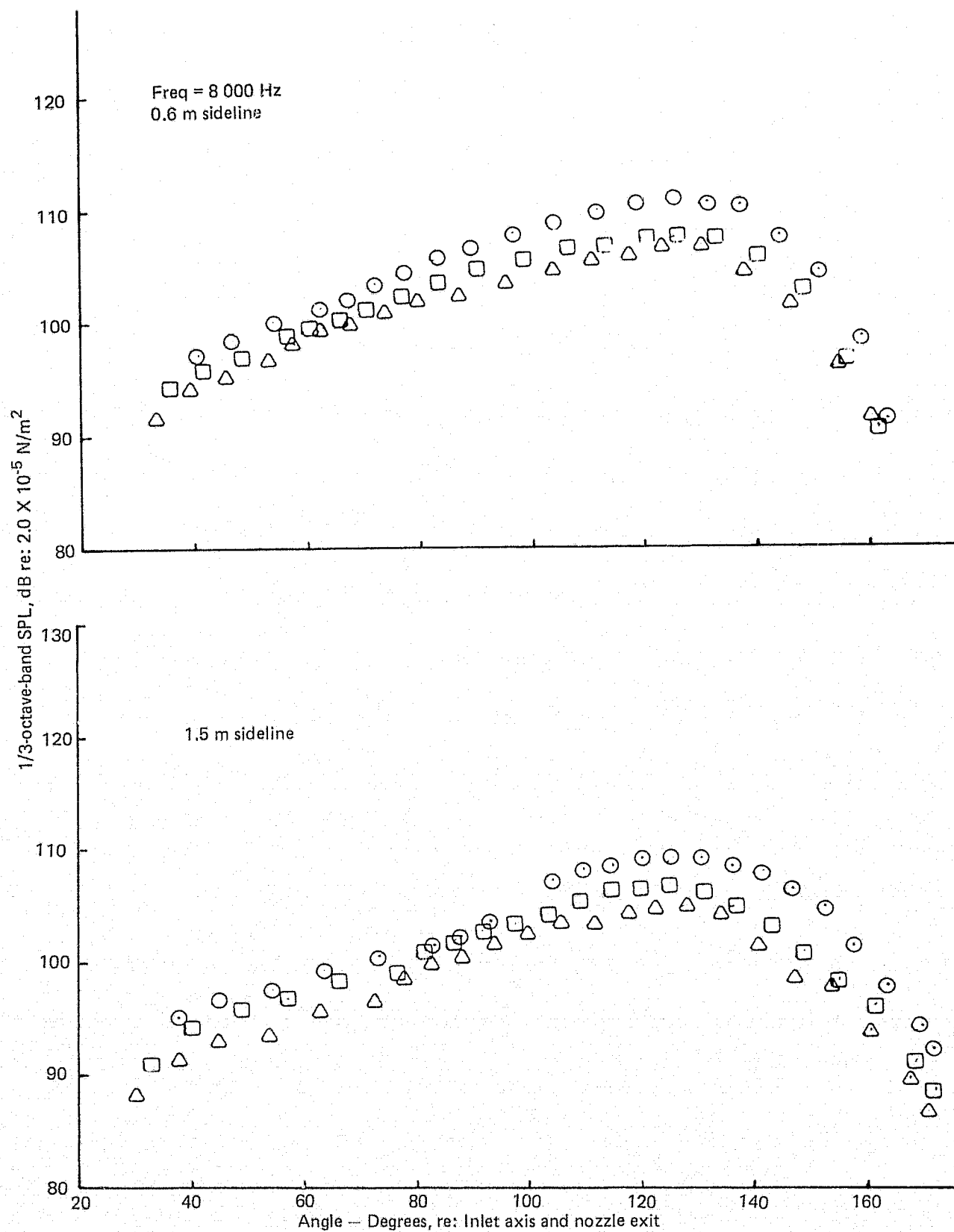


Figure 32.— (Continued)

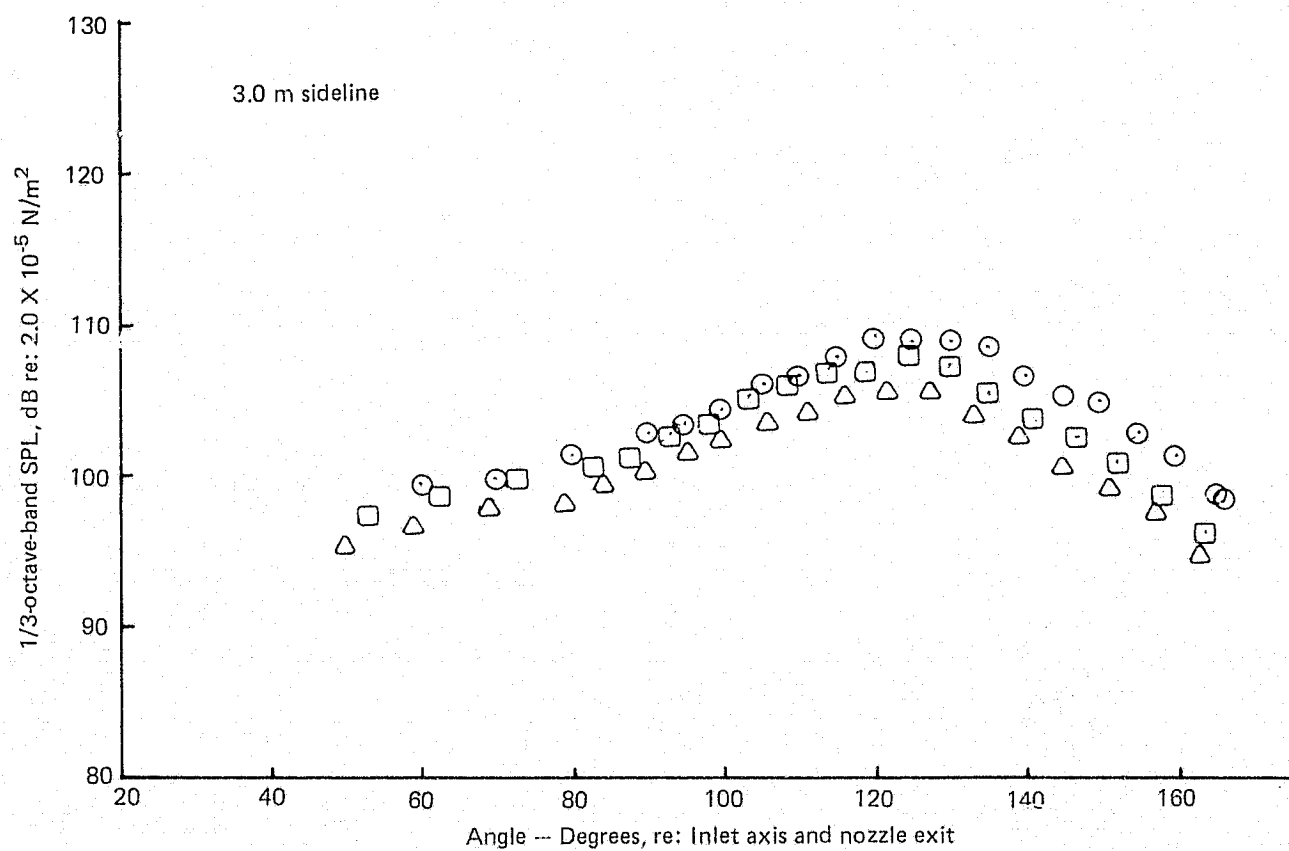


Figure 32.— (Continued)

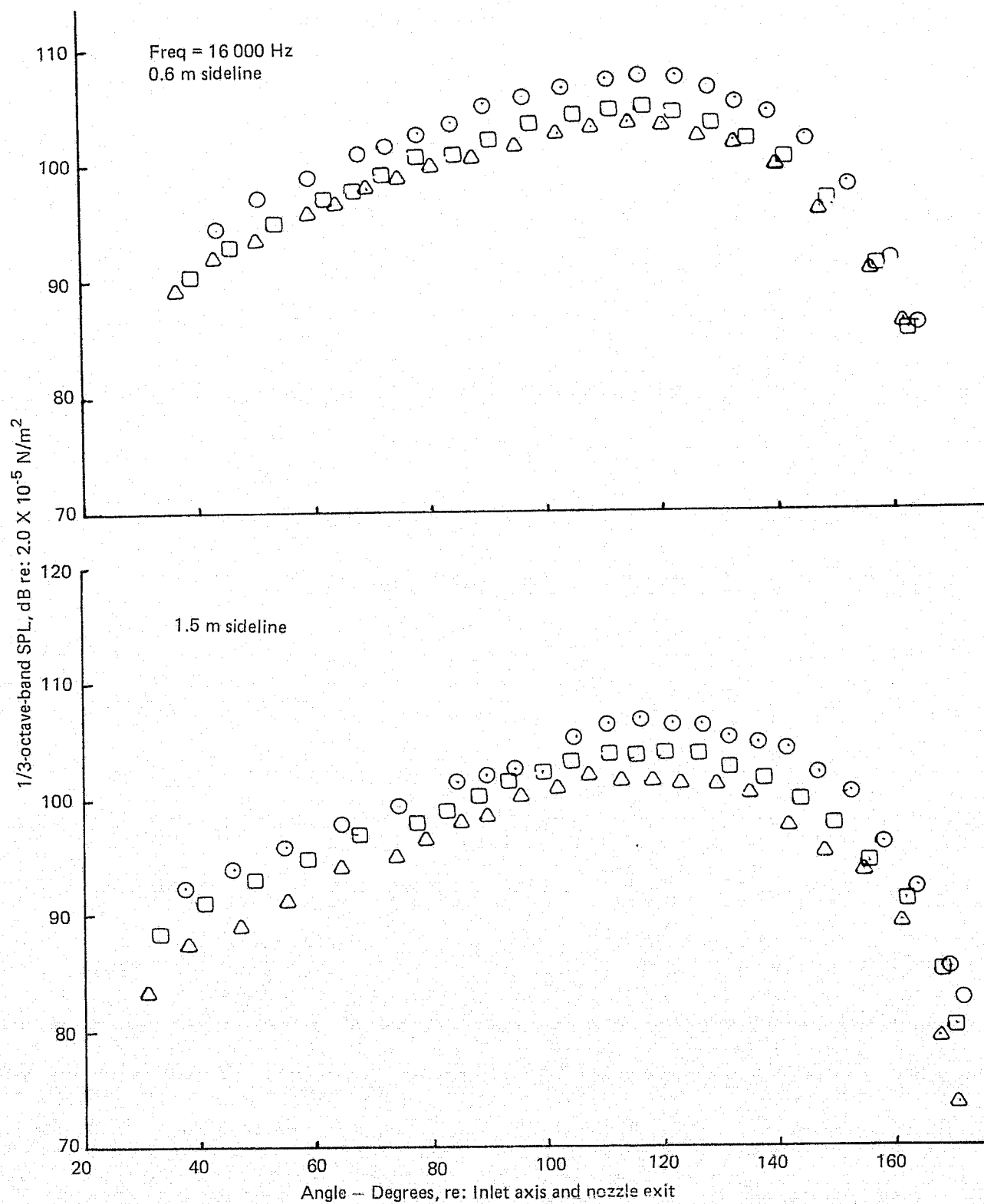


Figure 32.— (Continued)

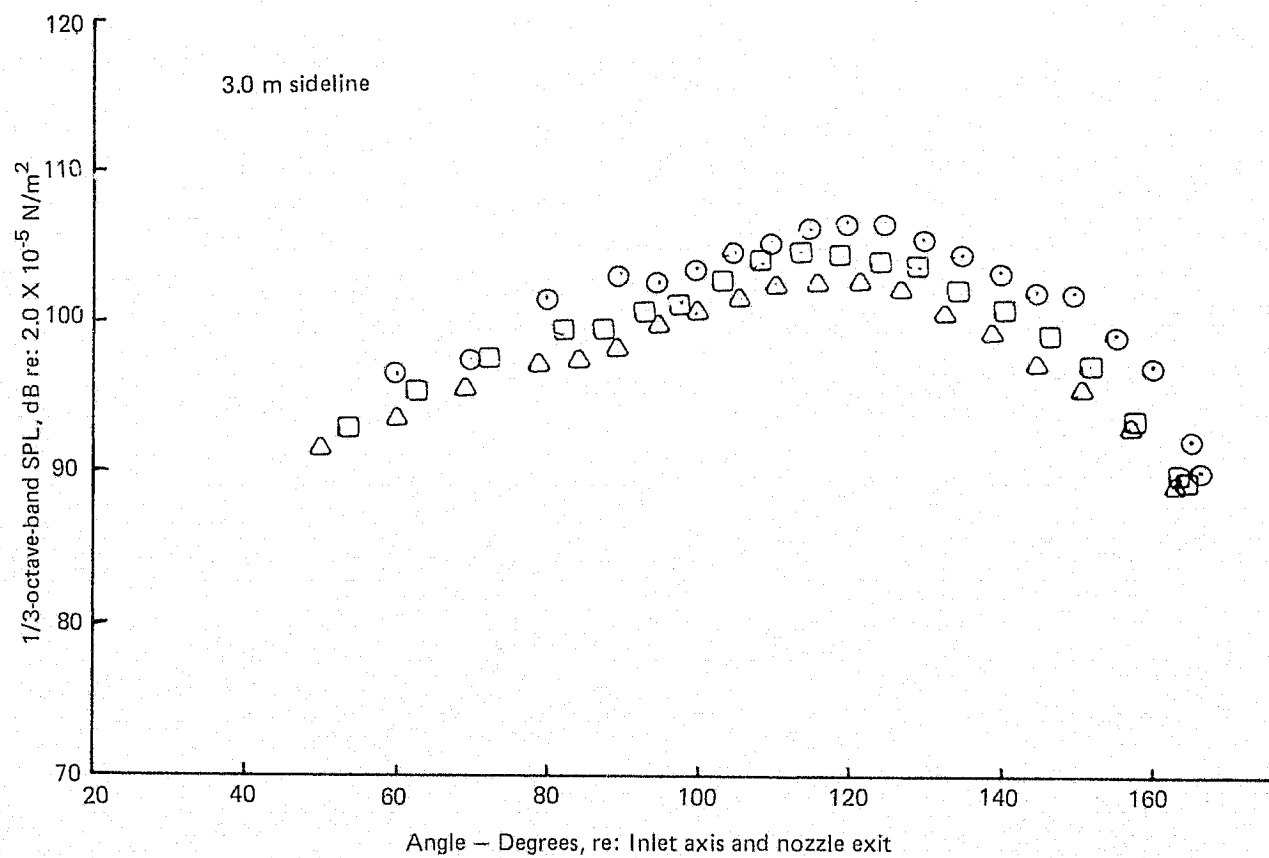


Figure 32.— (Continued)

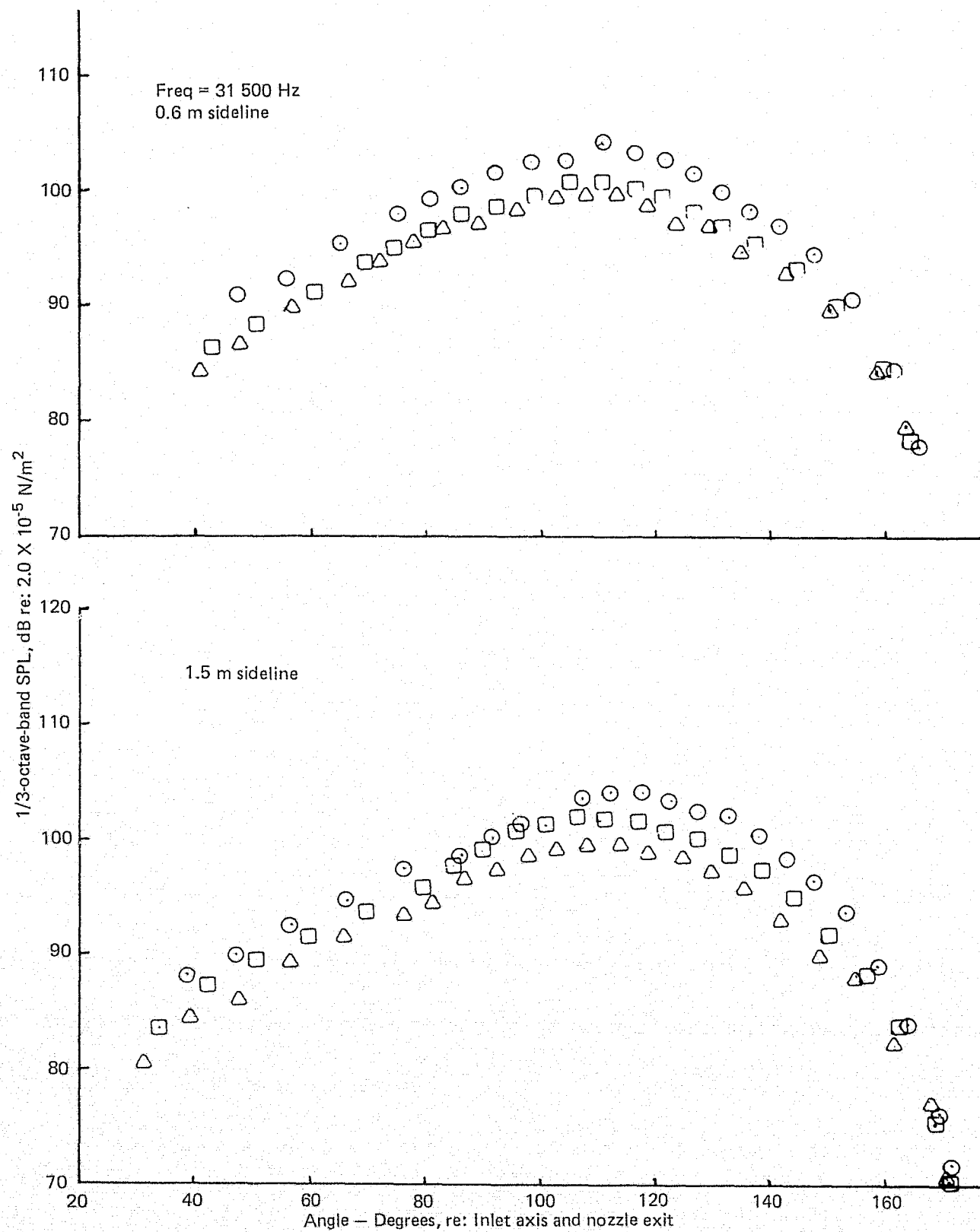


Figure 32.— (Continued)

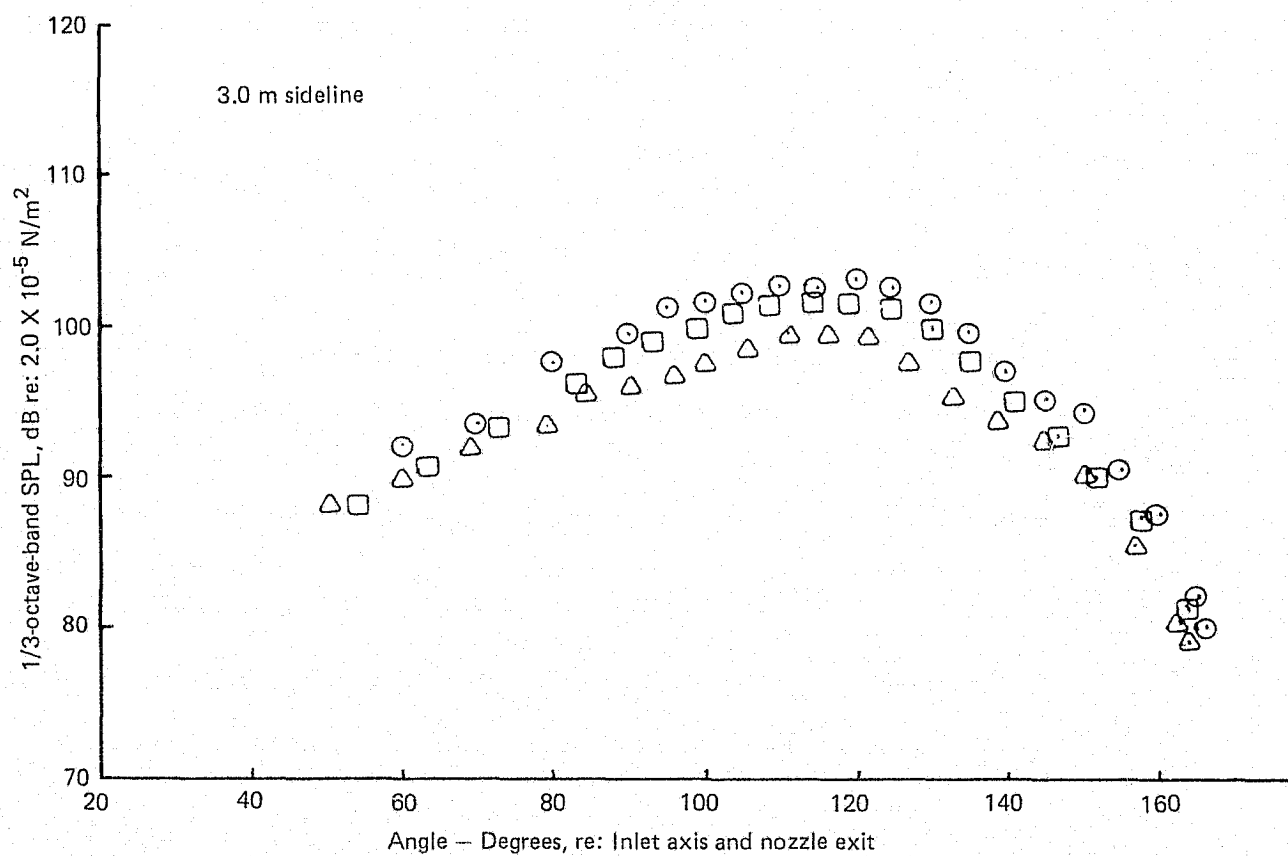


Figure 32.— (Concluded)

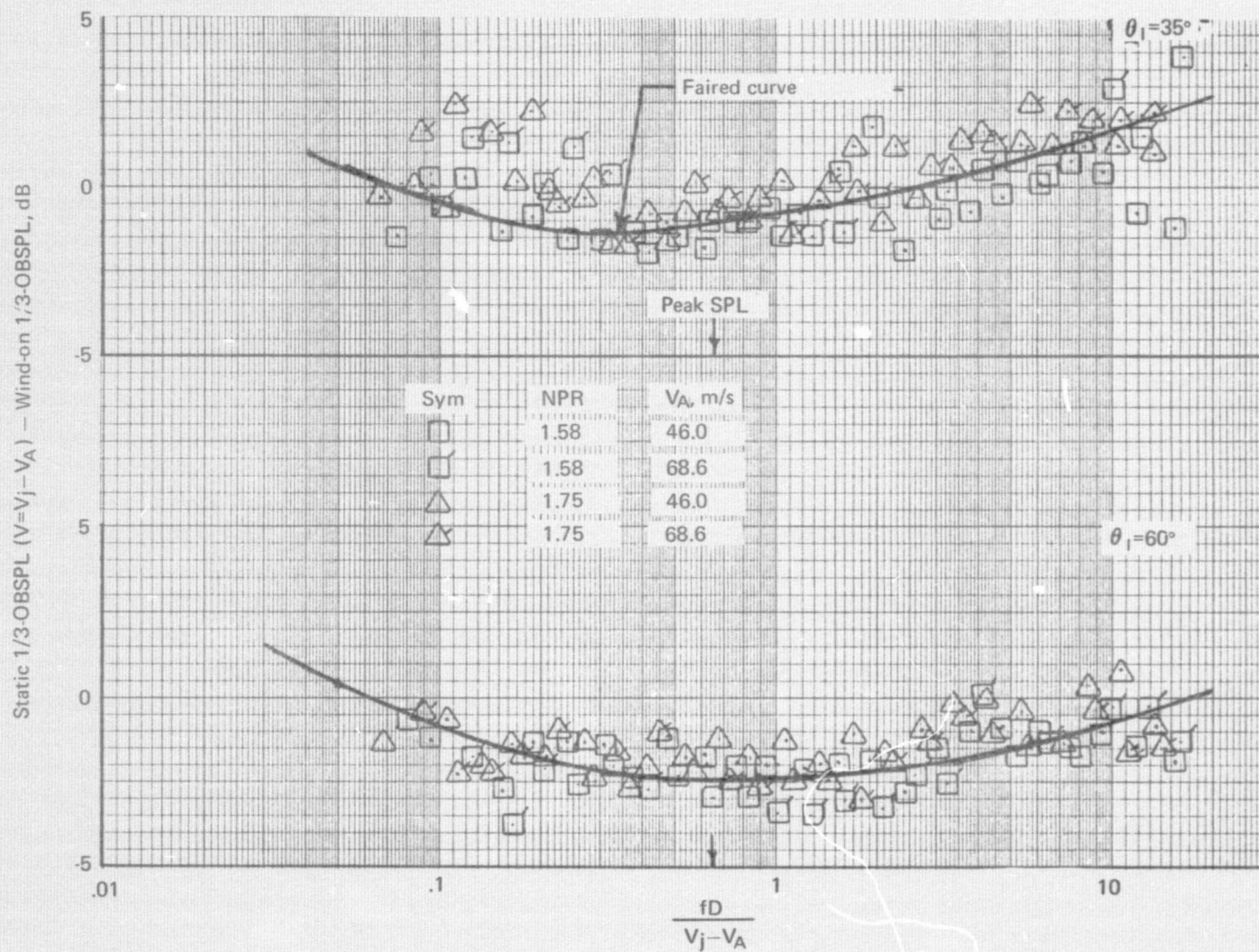


Figure 33.—Effect of Ambient Velocity on Subsonic Jet Noise Spectra or an RC Nozzle Referenced to the Static Case Where $V=V_j-V_A$, $T_T=844K$

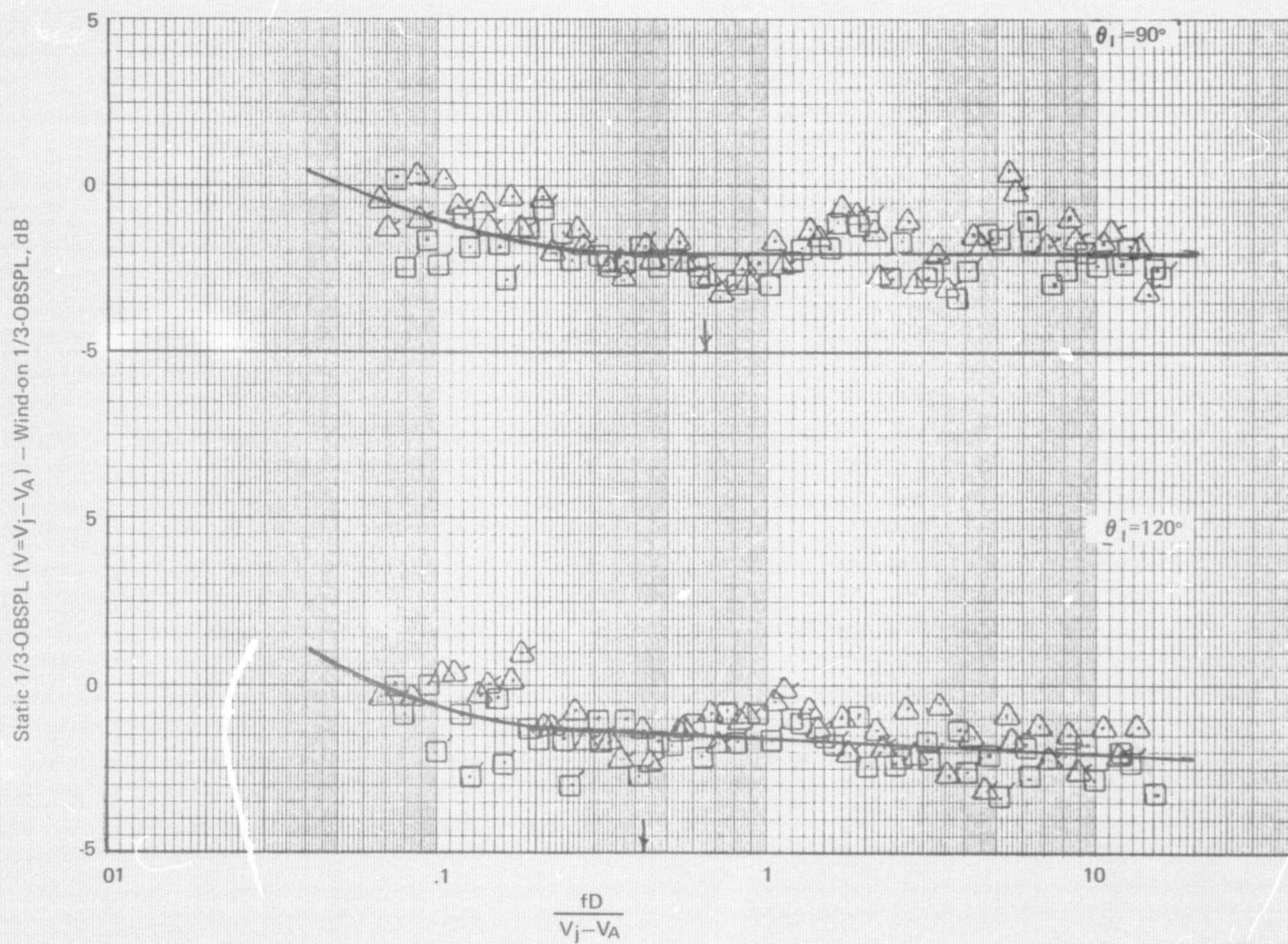


Figure 33.—(Continued)

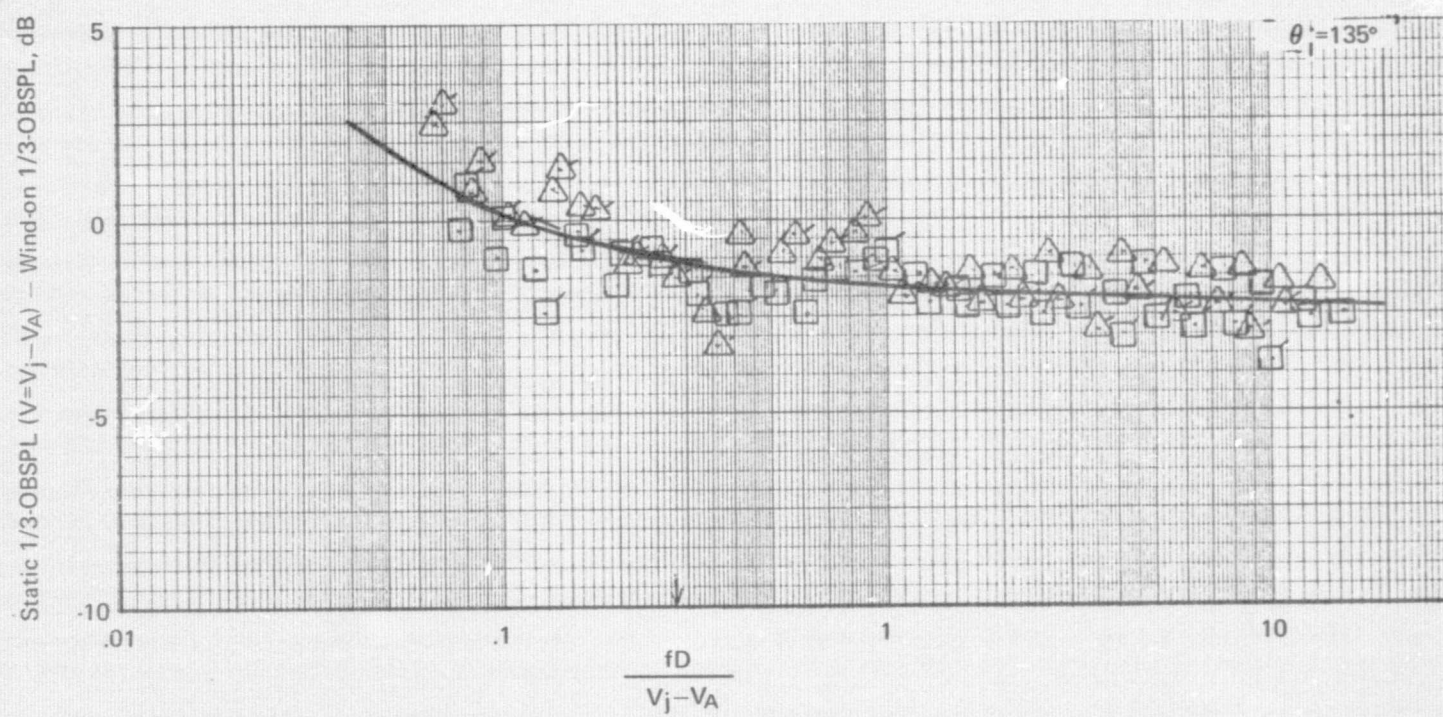


Figure 33.—(Continued)

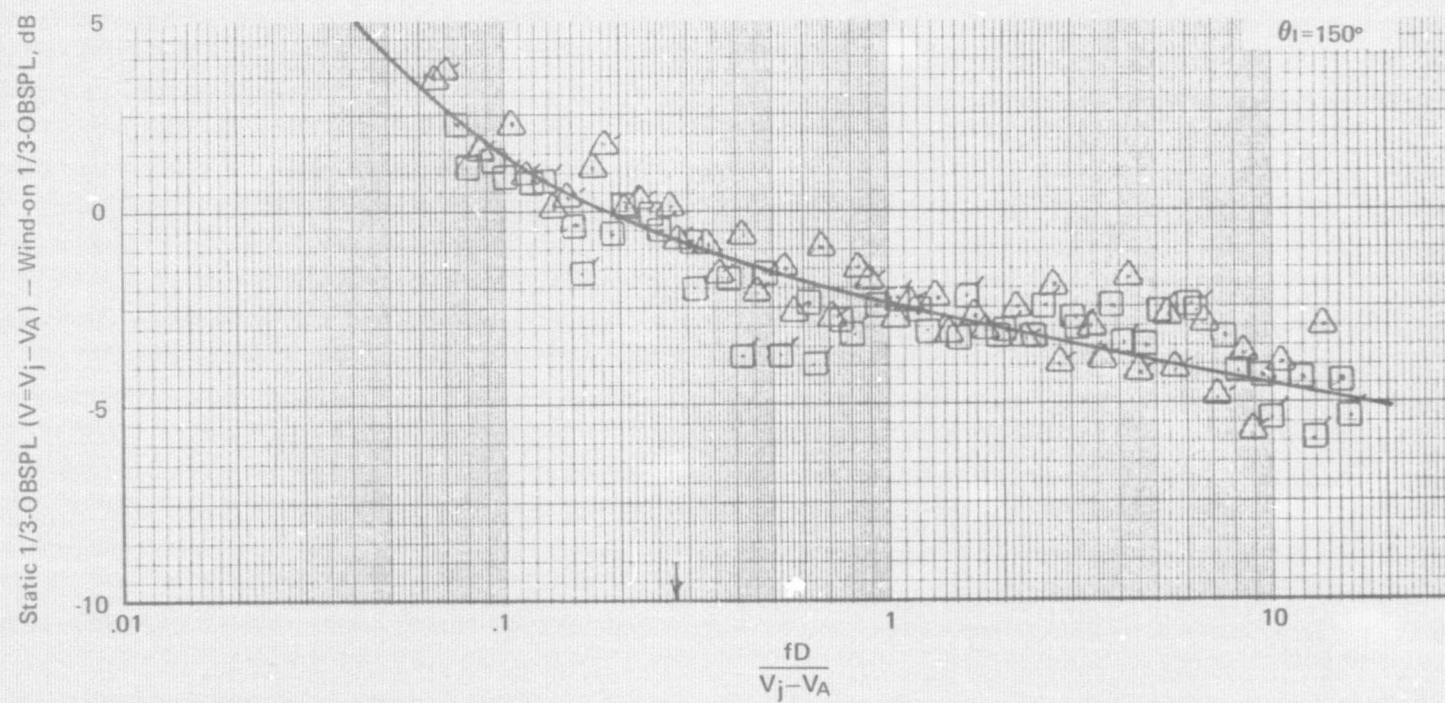


Figure 33.—(Continued)

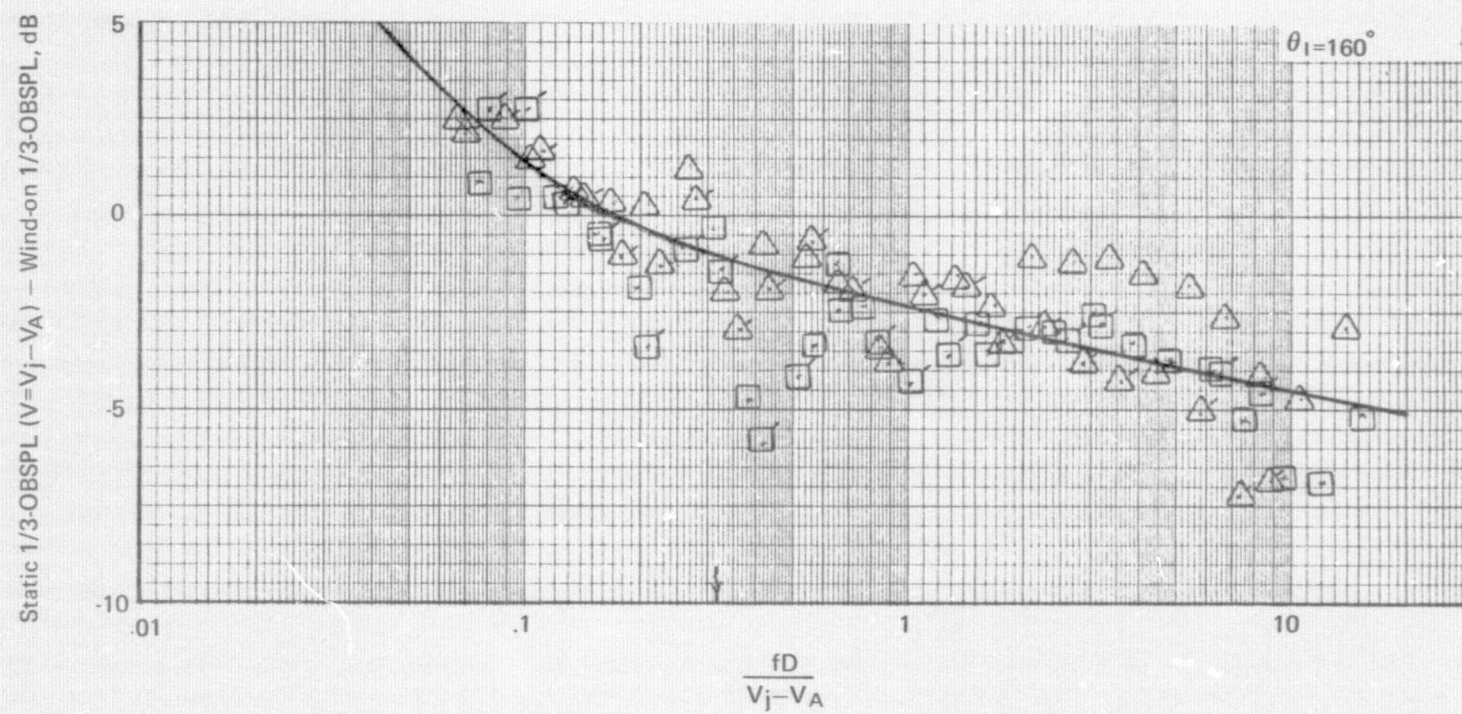


Figure 33.—(Concluded)

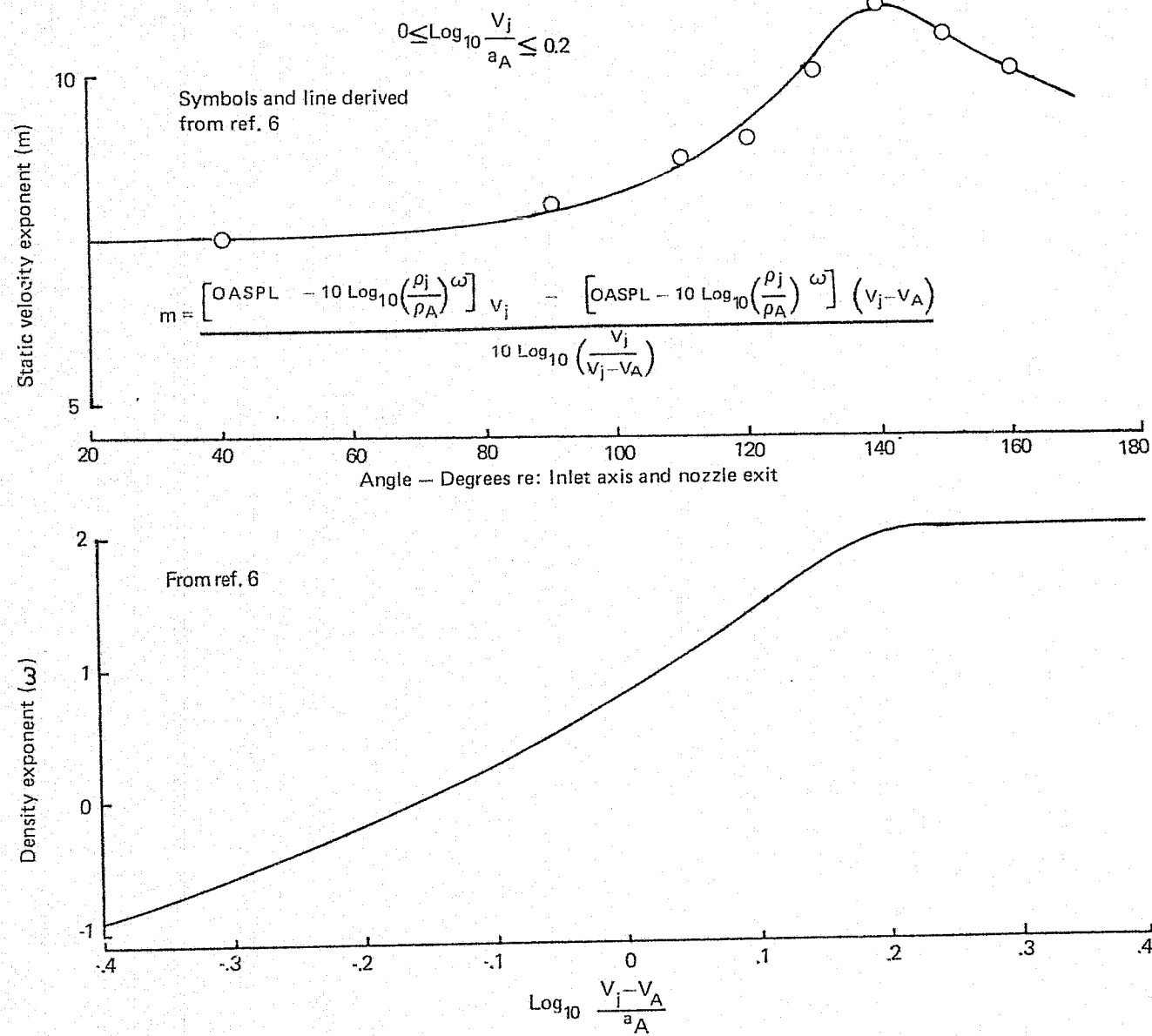


Figure 34.— Static Velocity Exponent for an RC Nozzle

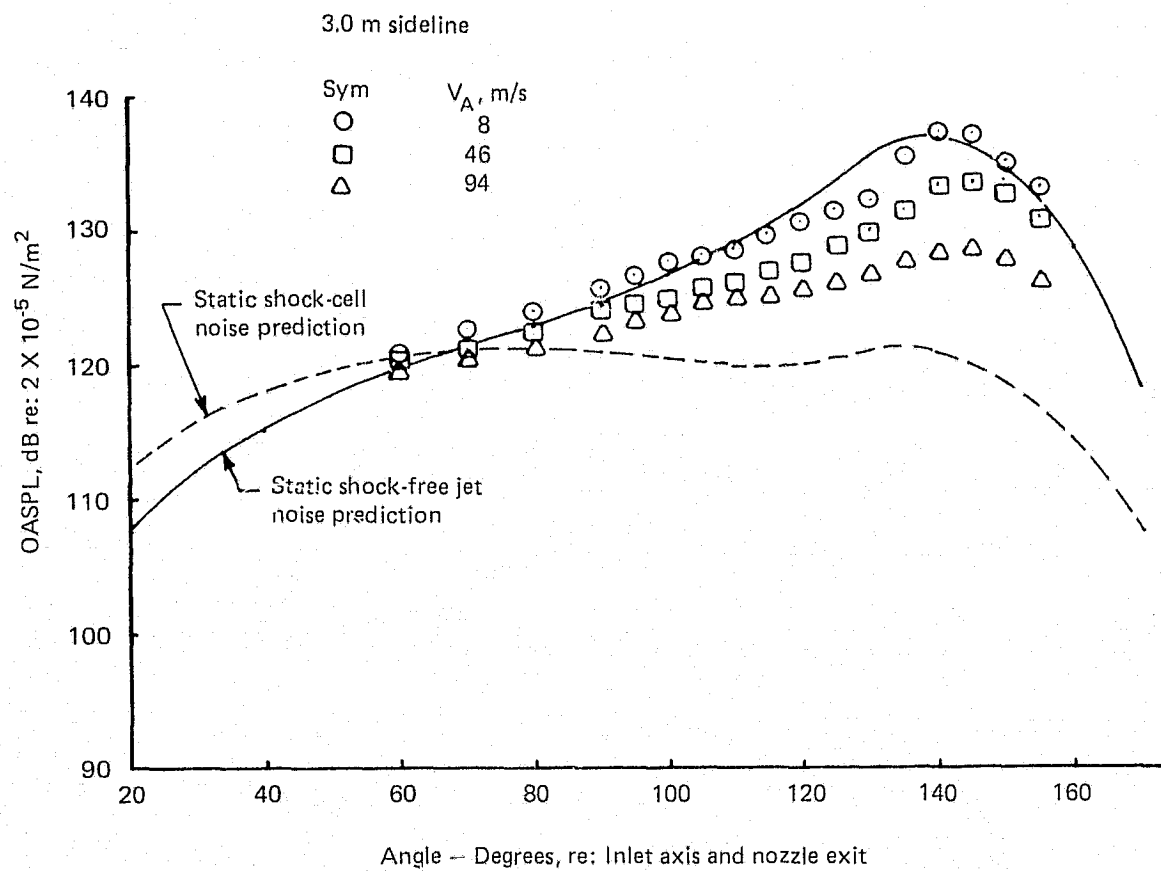


Figure 35.— Effect of Ambient Velocity on Jet Noise OASPL and 1/3-OBSPL Spectra for a 15.24 cm RC Nozzle NPR = 2.25

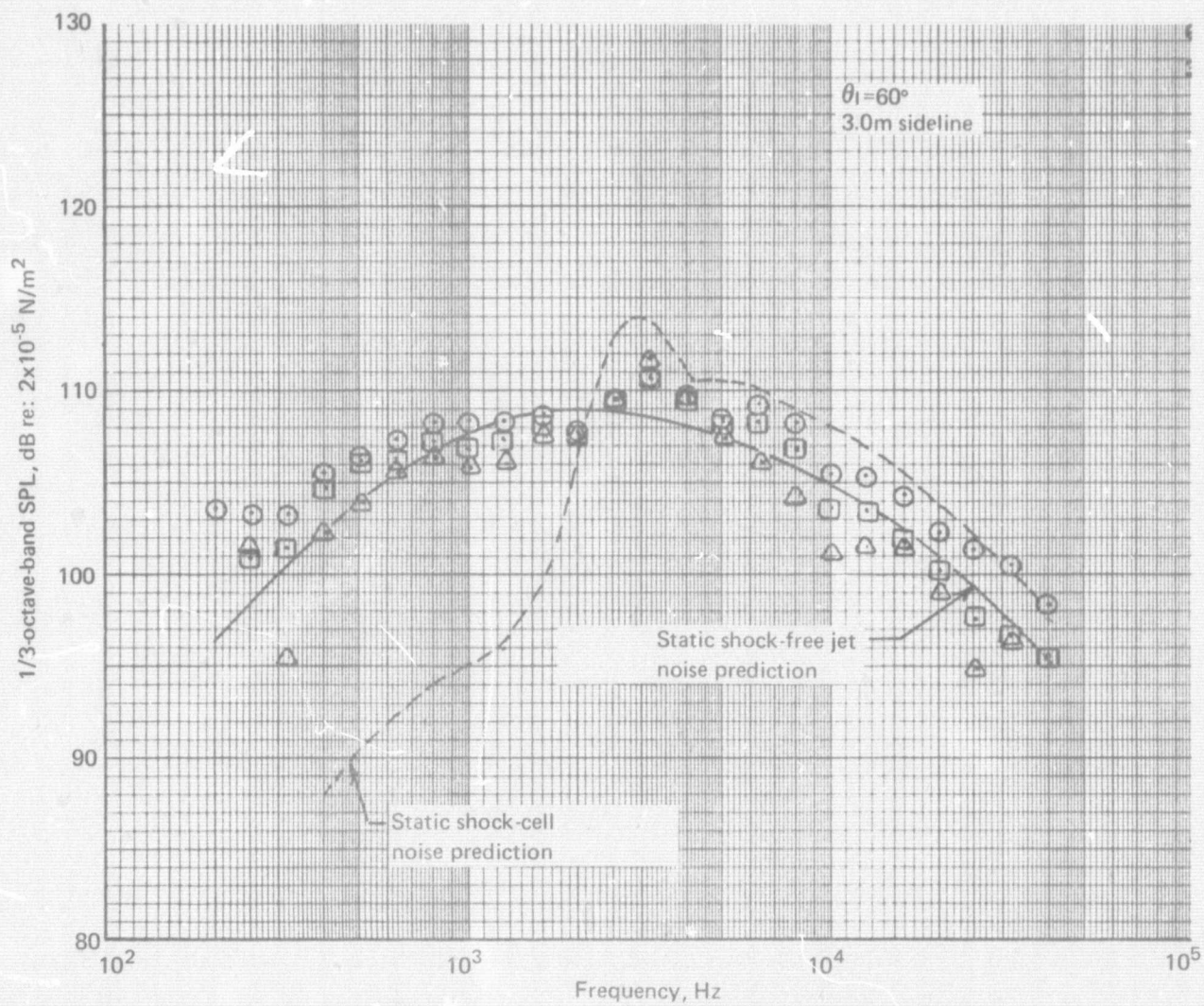


Figure 35.—(Continued)

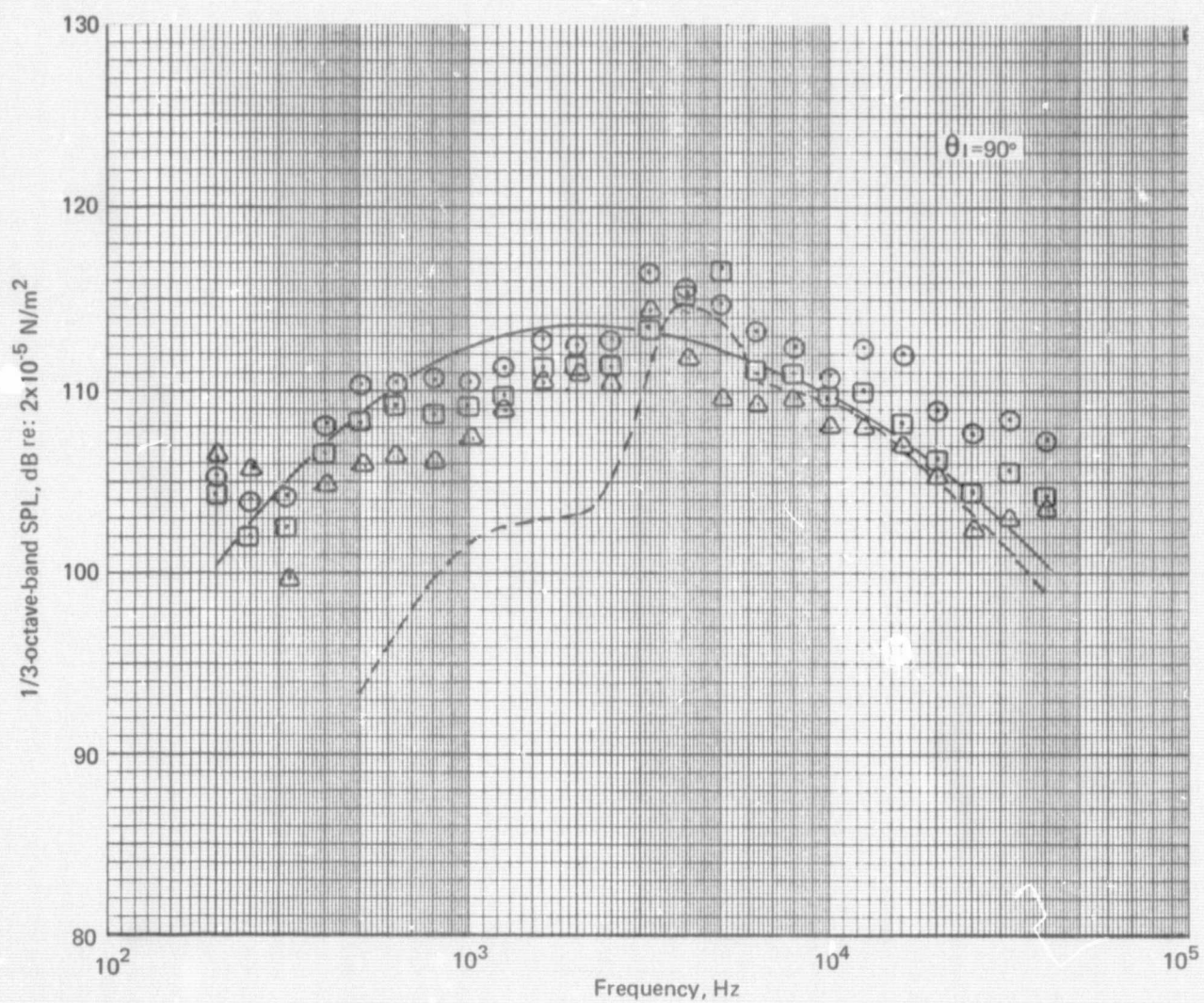


Figure 35.—(Continued)

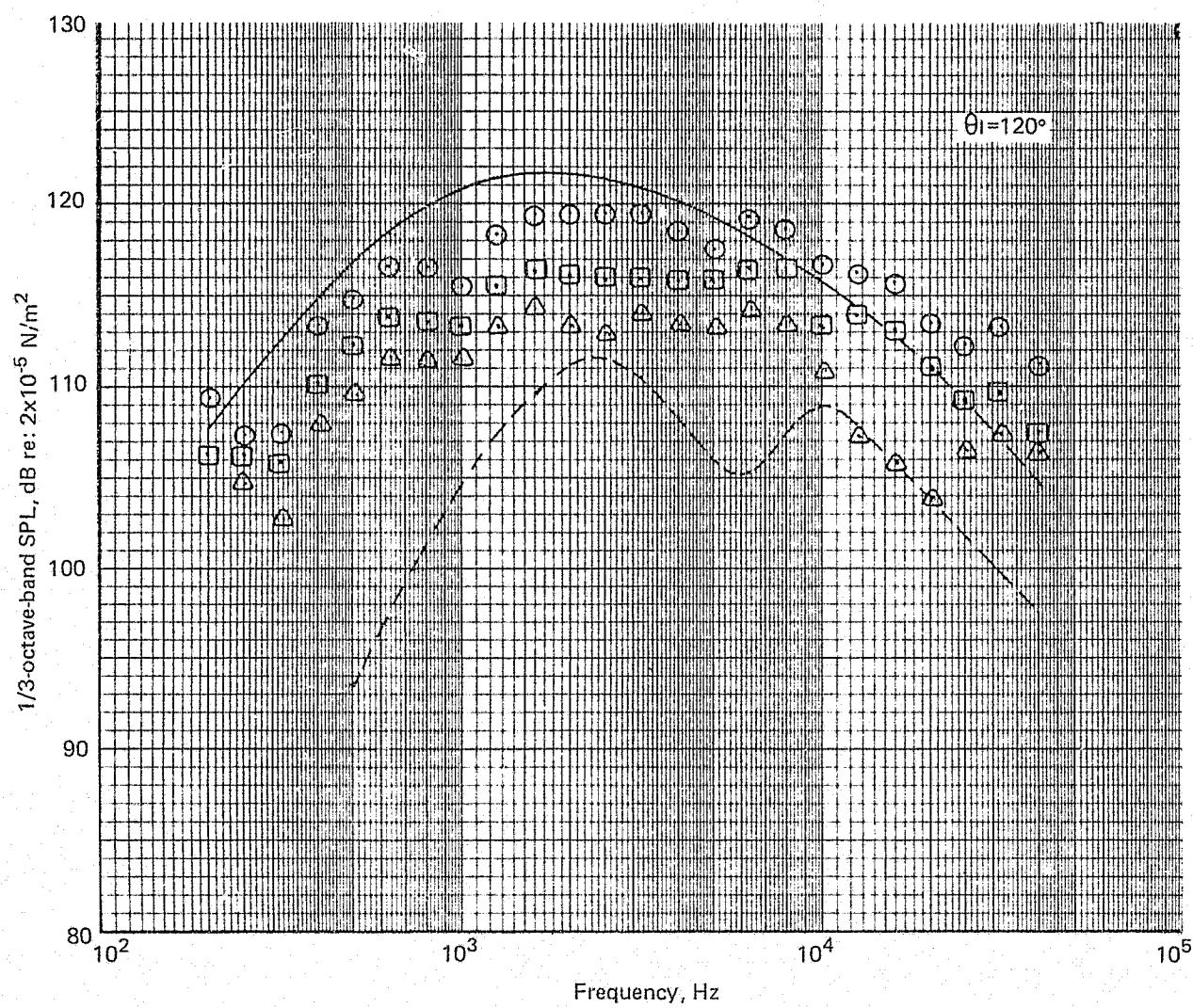


Figure 35.—(Continued)

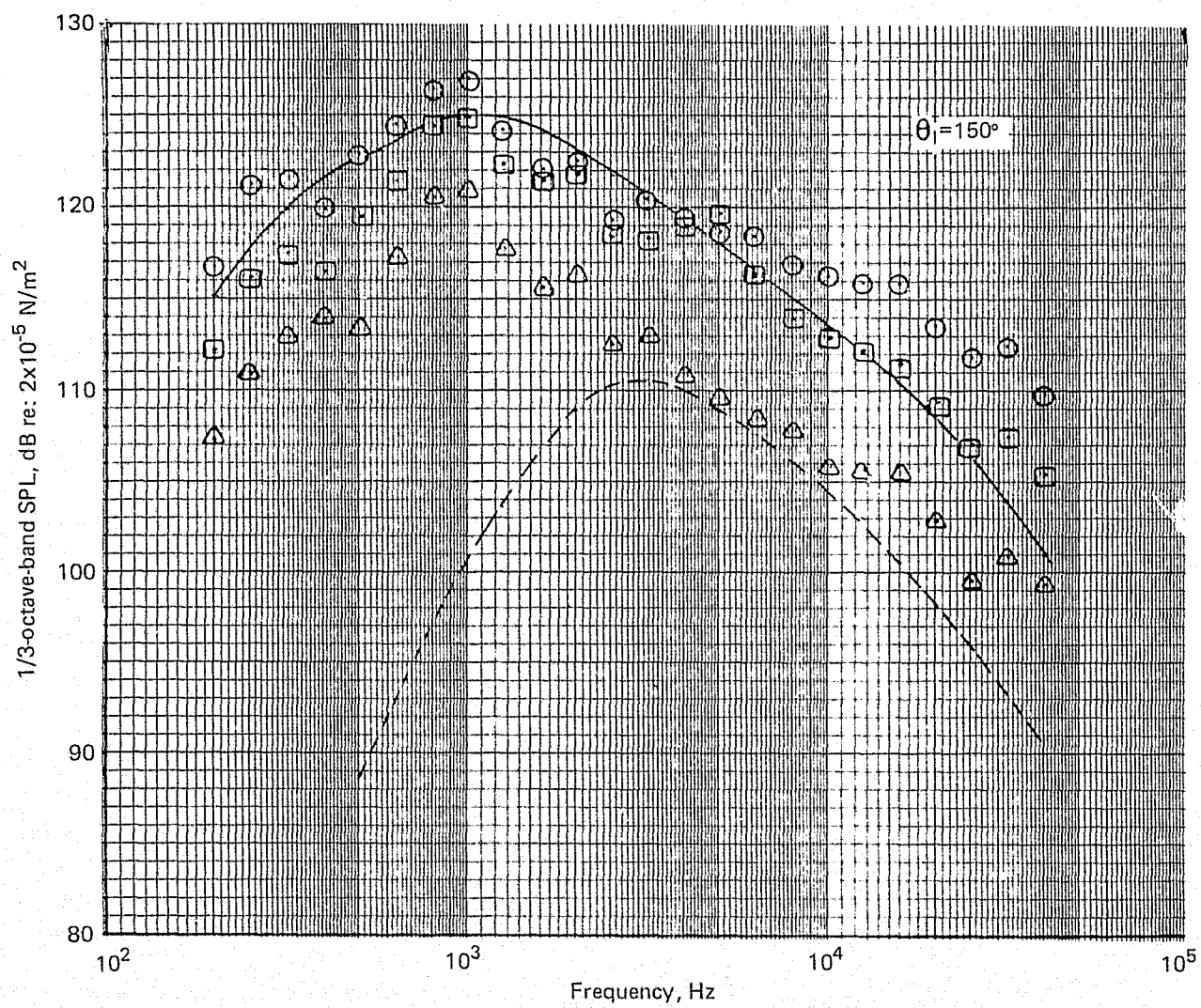


Figure 35.—(Concluded)

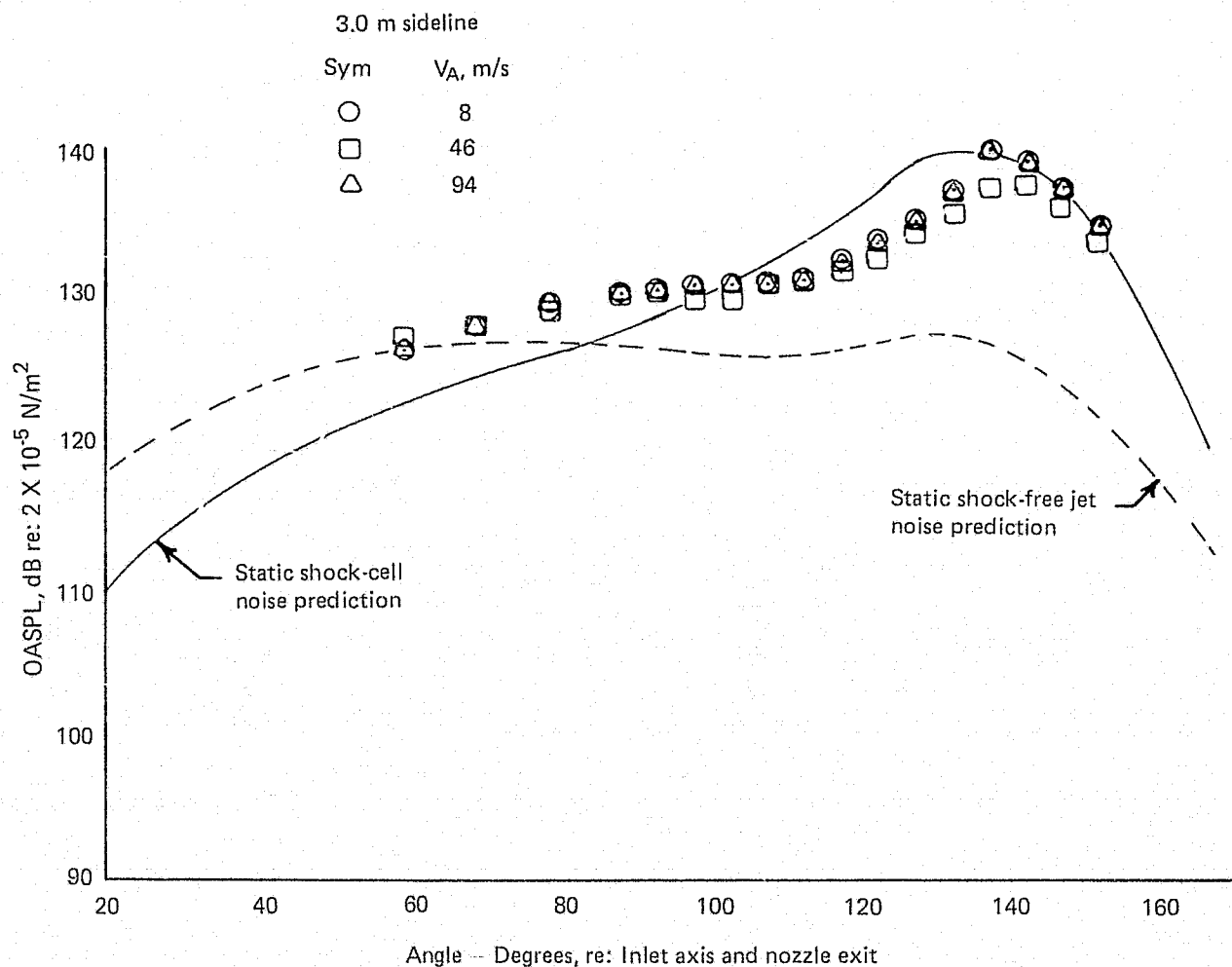


Figure 36.— Effect of Ambient Velocity on Jet Noise OASPL and 1/3-OBSPL Spectra for a 15.24 cm RC Nozzle NPR = 2.60

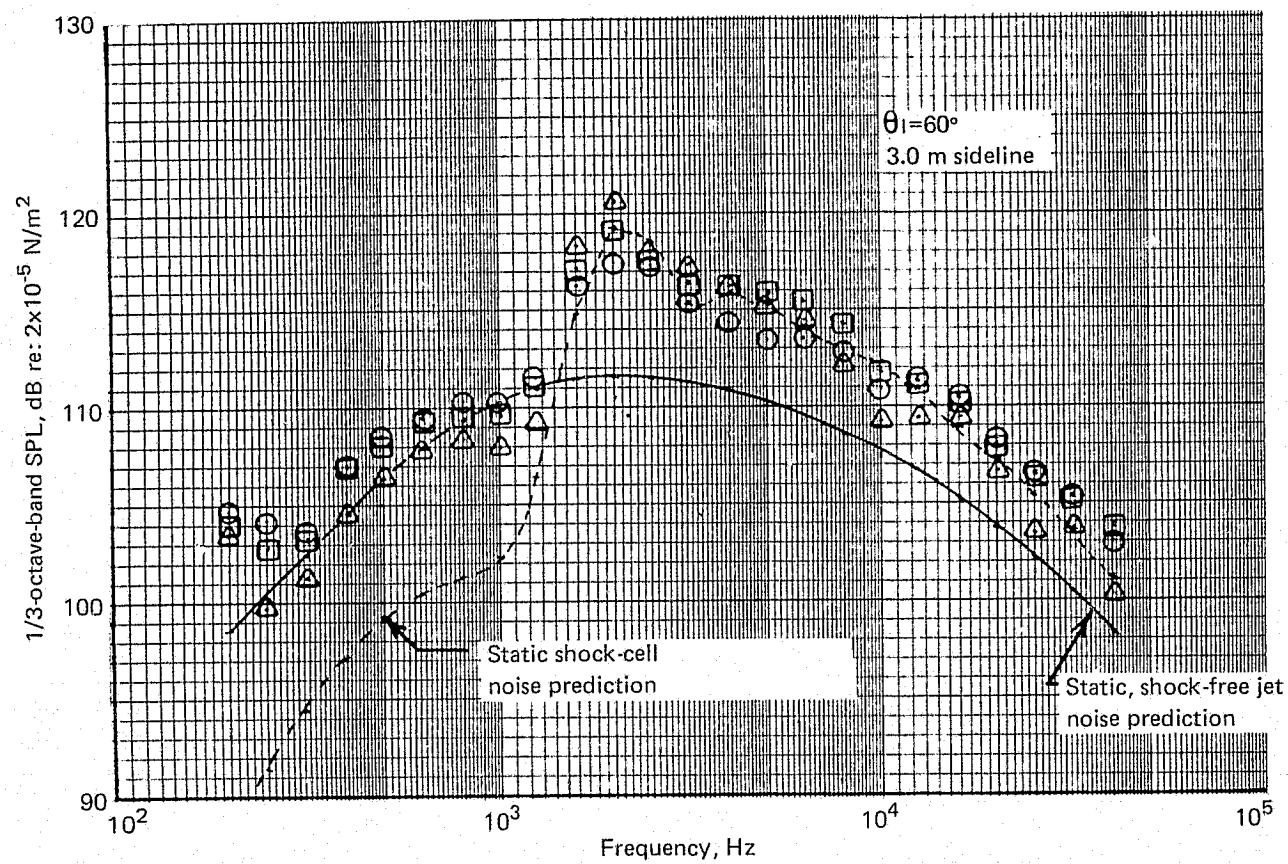


Figure 36.—(Continued)

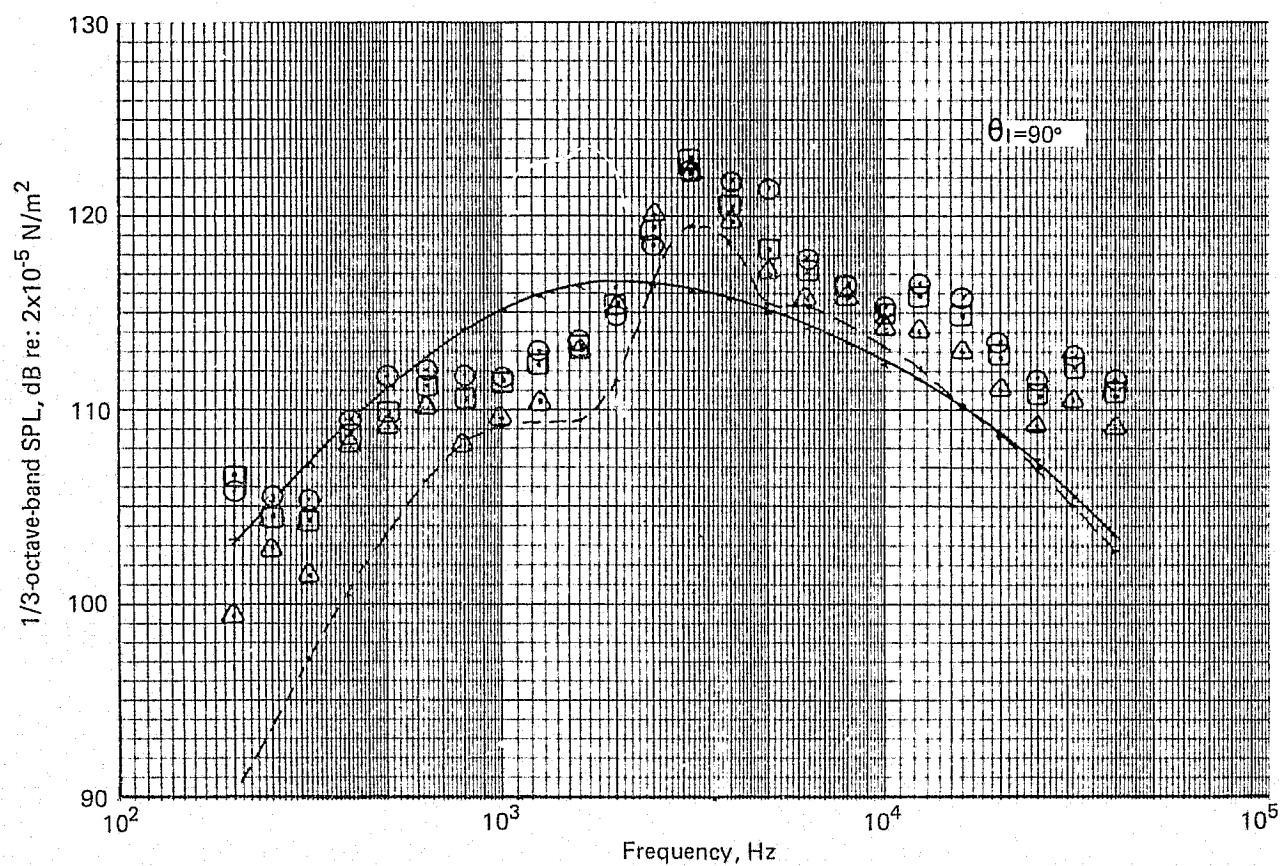


Figure 36.—(Continued)

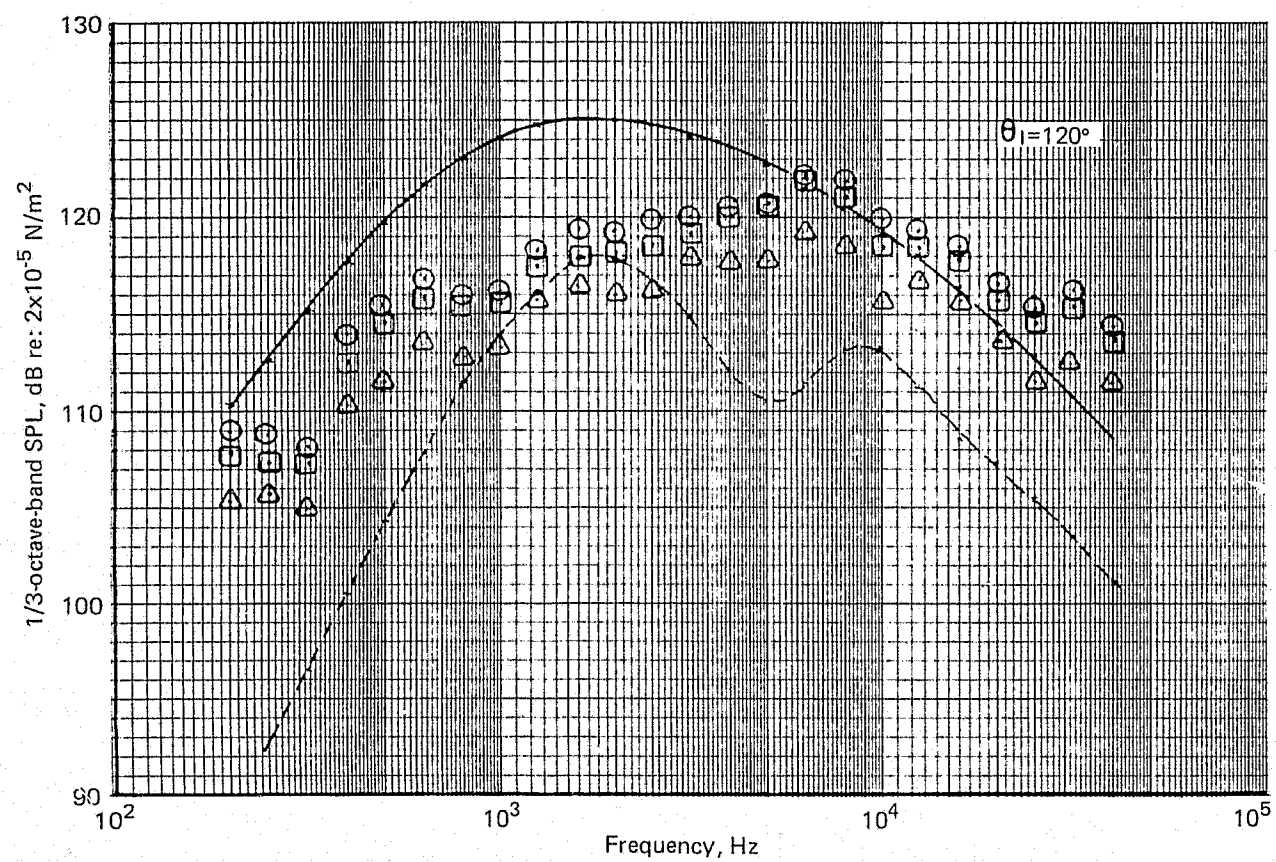


Figure 36.—(Continued)

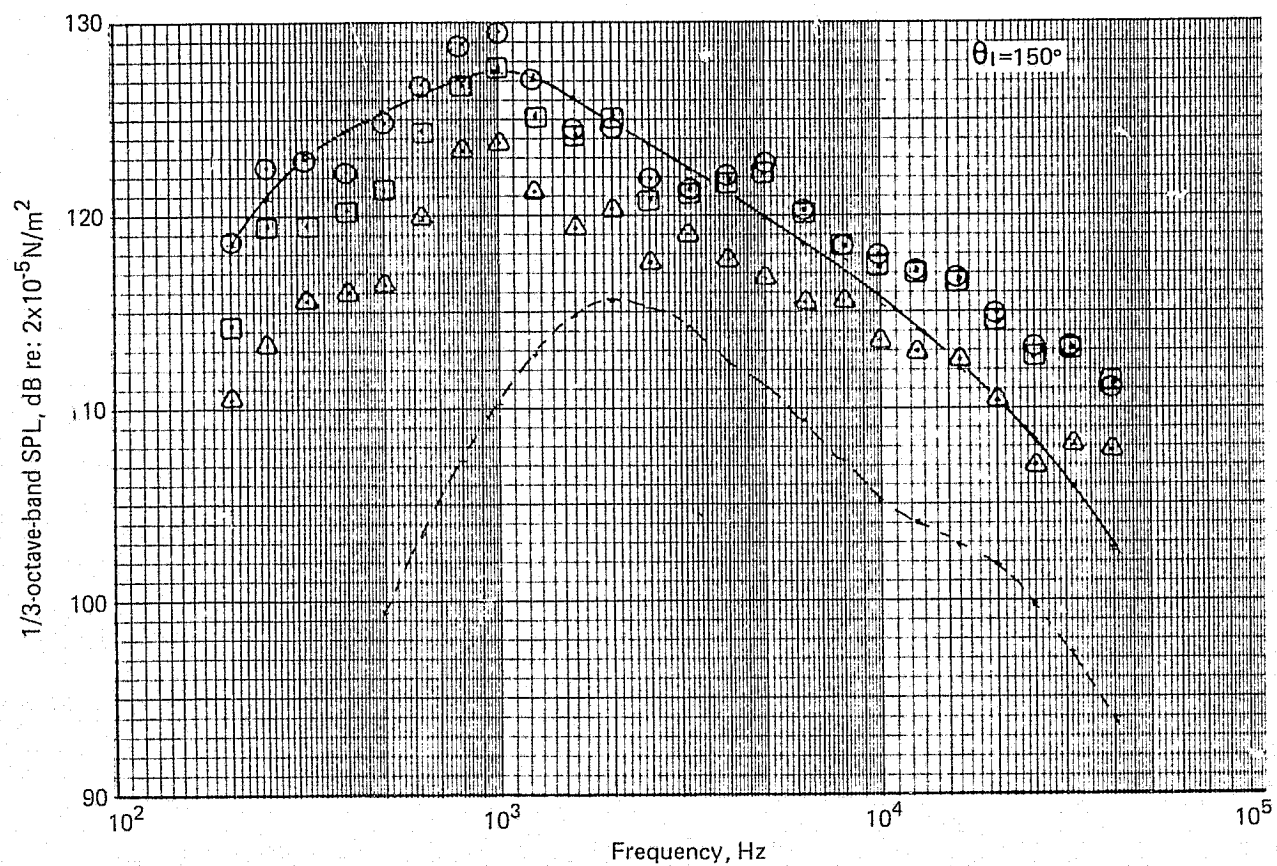


Figure 36.—(Concluded)

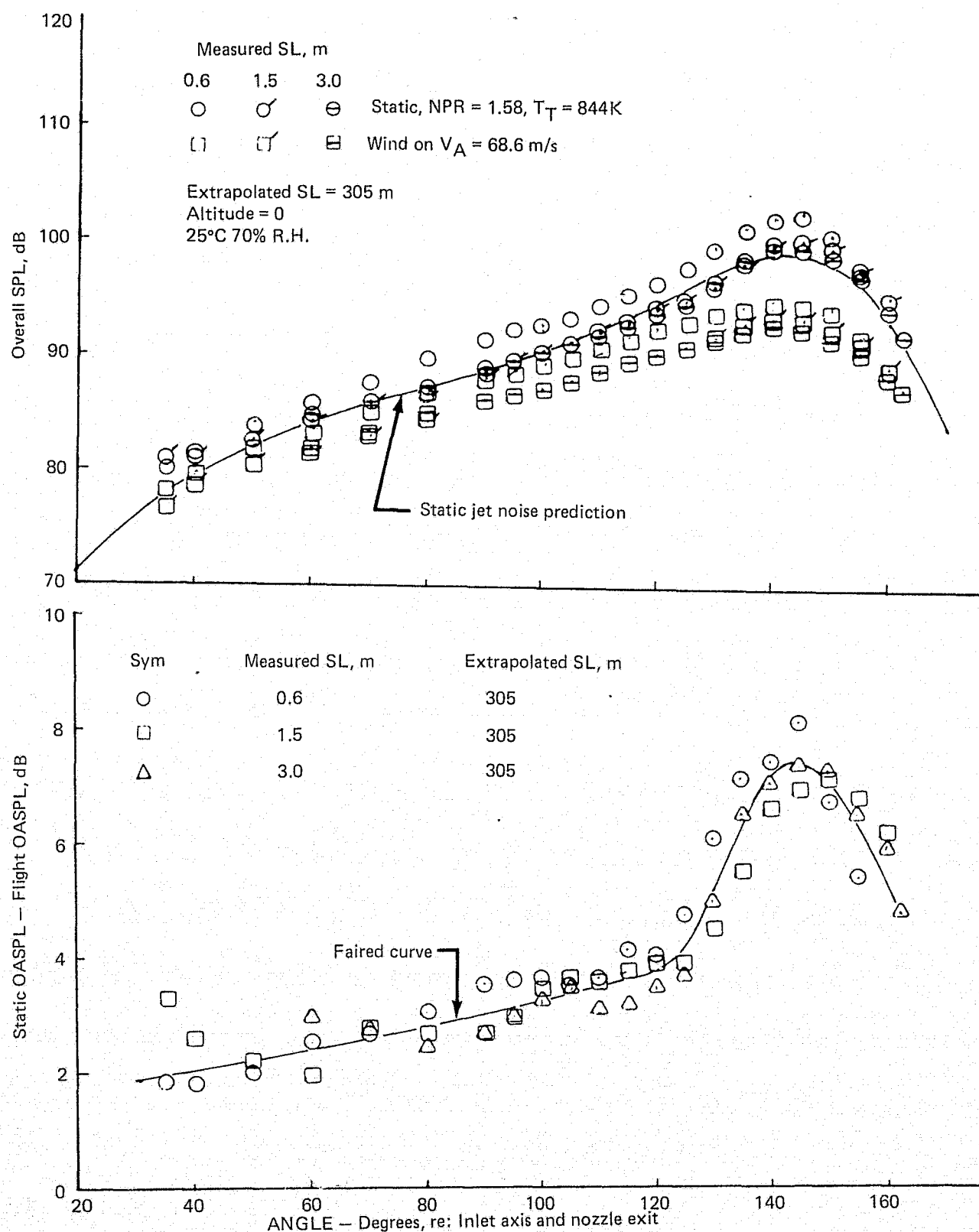


Figure 37.— 0.76 m RC Nozzle Flight Effects Based on 40 by 80 Tunnel Measurements
 $V_j = 457$ m/s $V_A = 68.6$ m/s

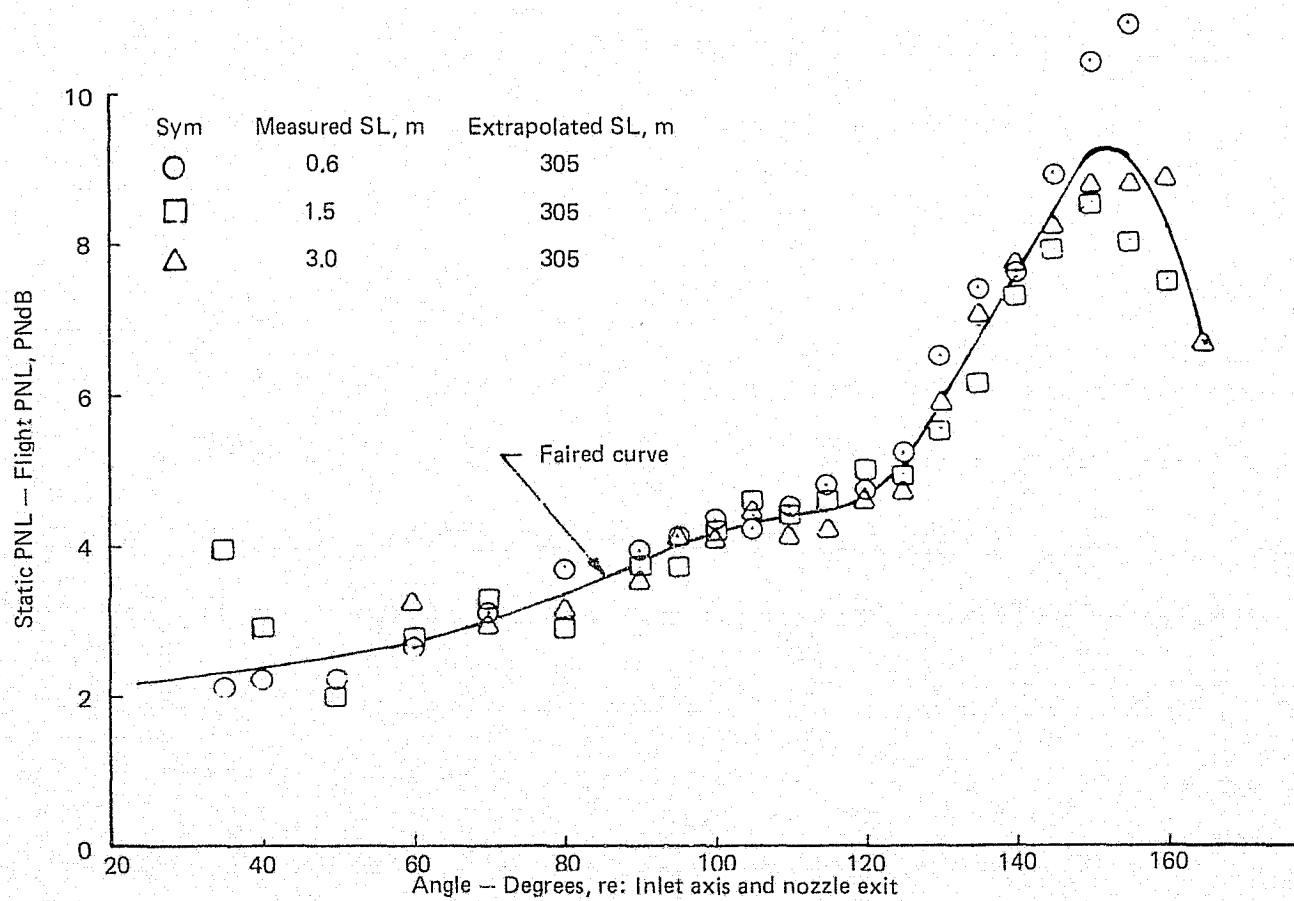
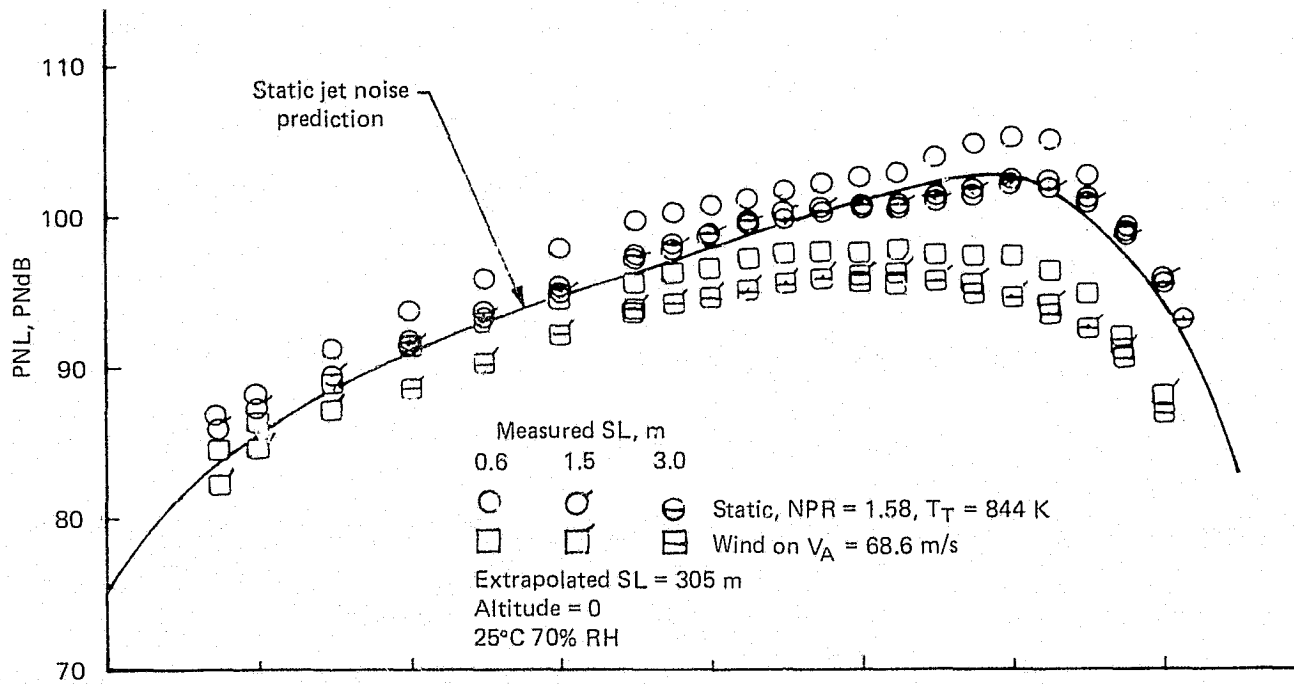


Figure 37.— (Concluded)

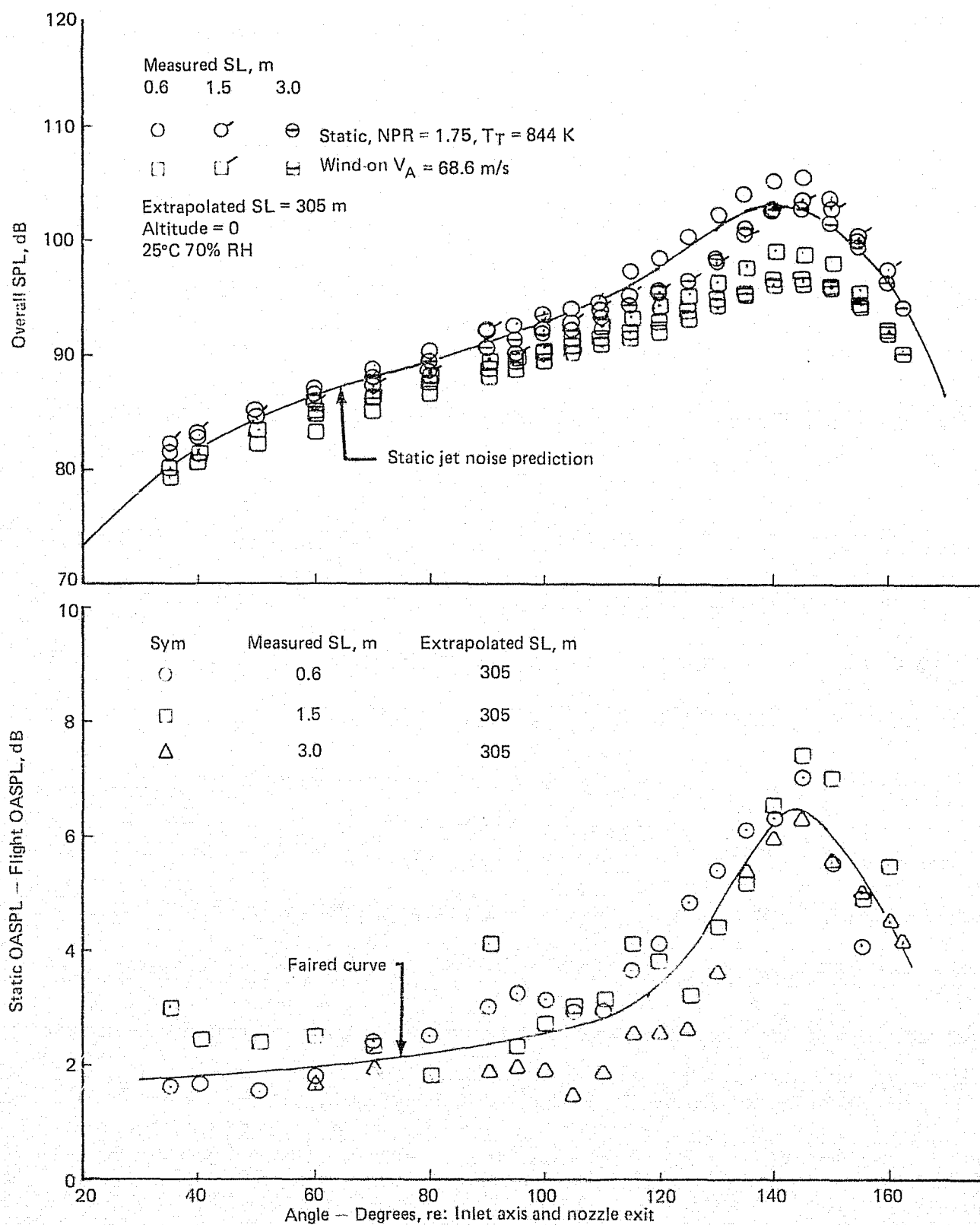


Figure 38.-- 0.76 m RC Nozzle Flight Effects Based on 40 by 80 Tunnel Measurements
 $V_j = 500$ m/s $V_A = 68.6$ m/s

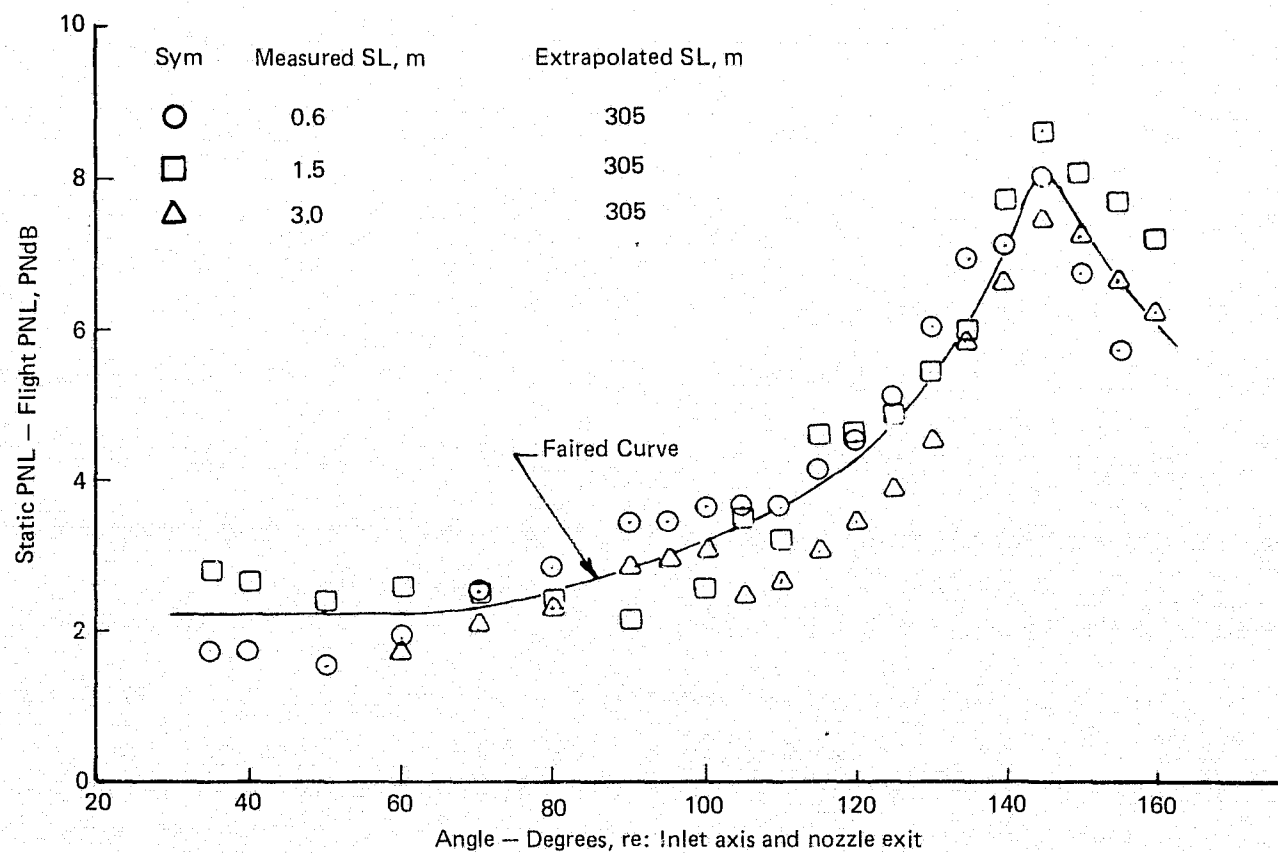
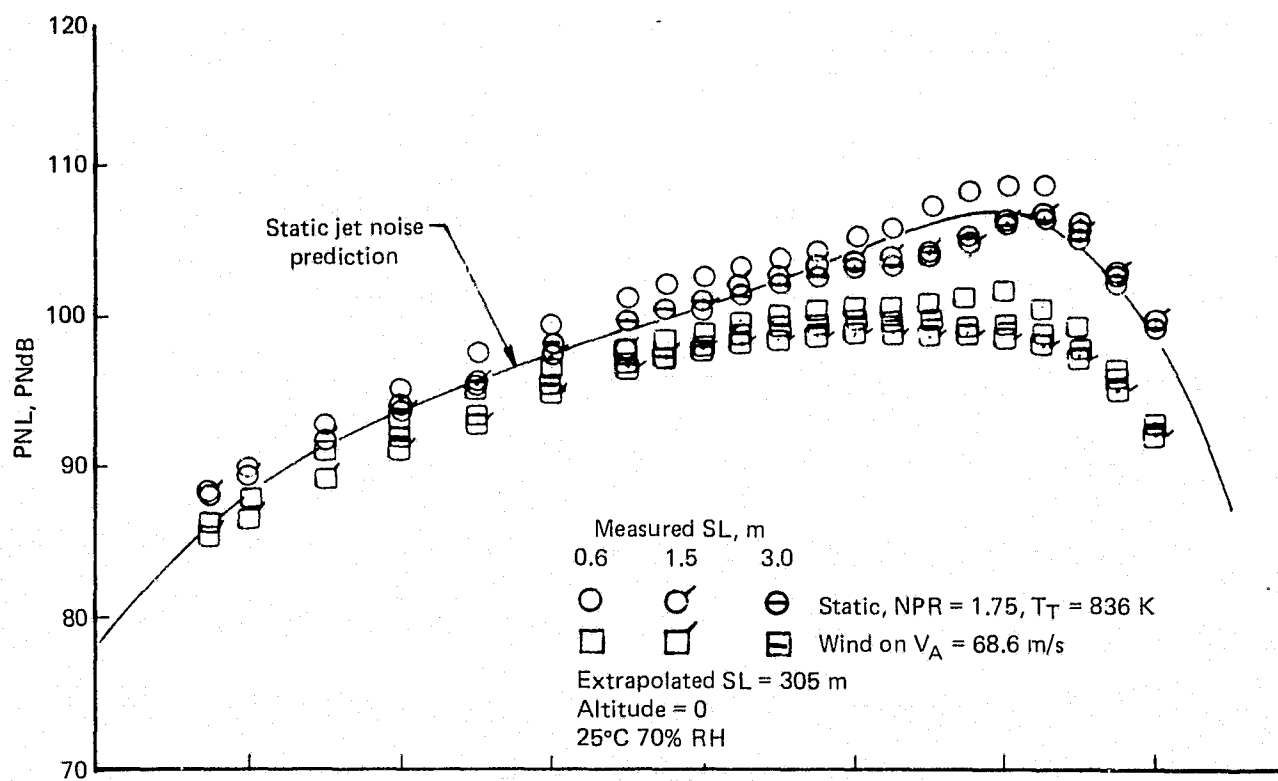


Figure 38.— (Concluded)

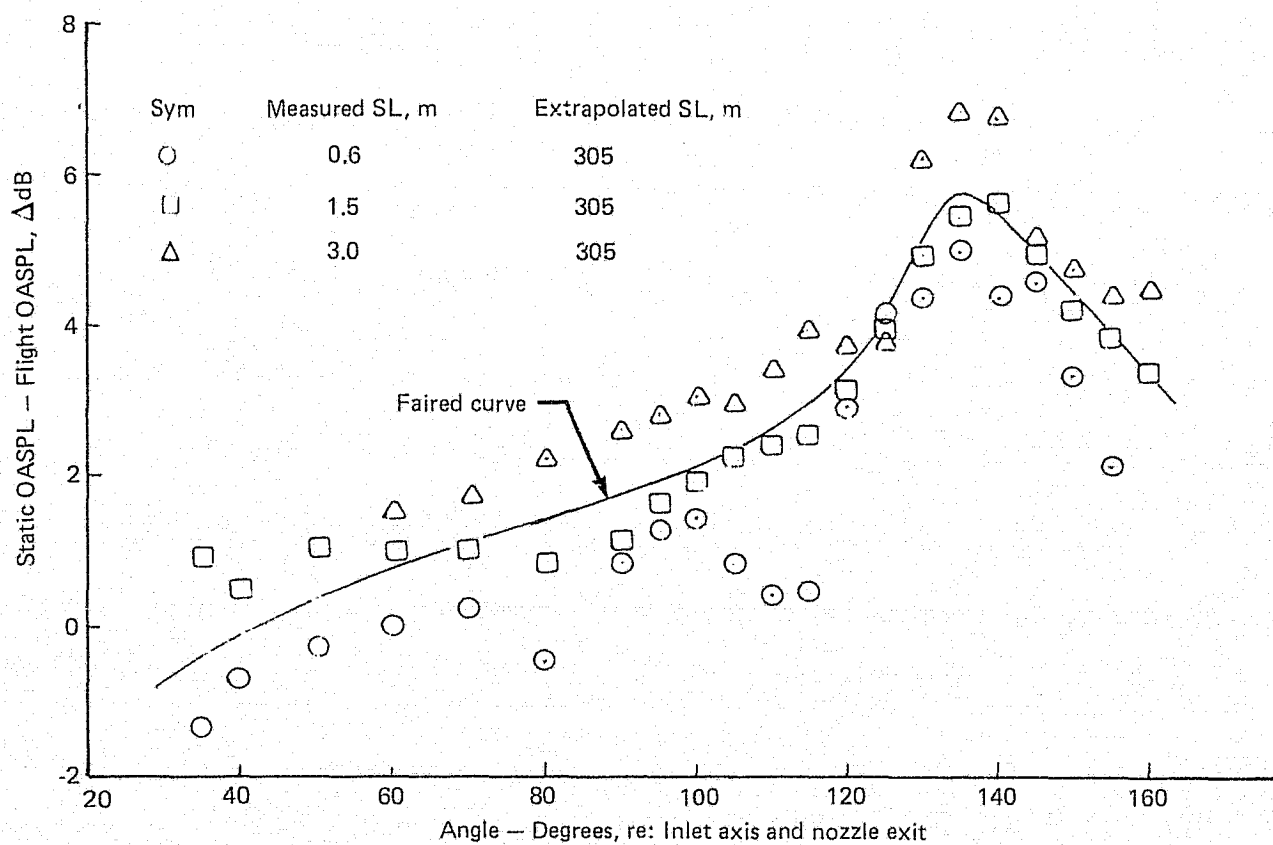
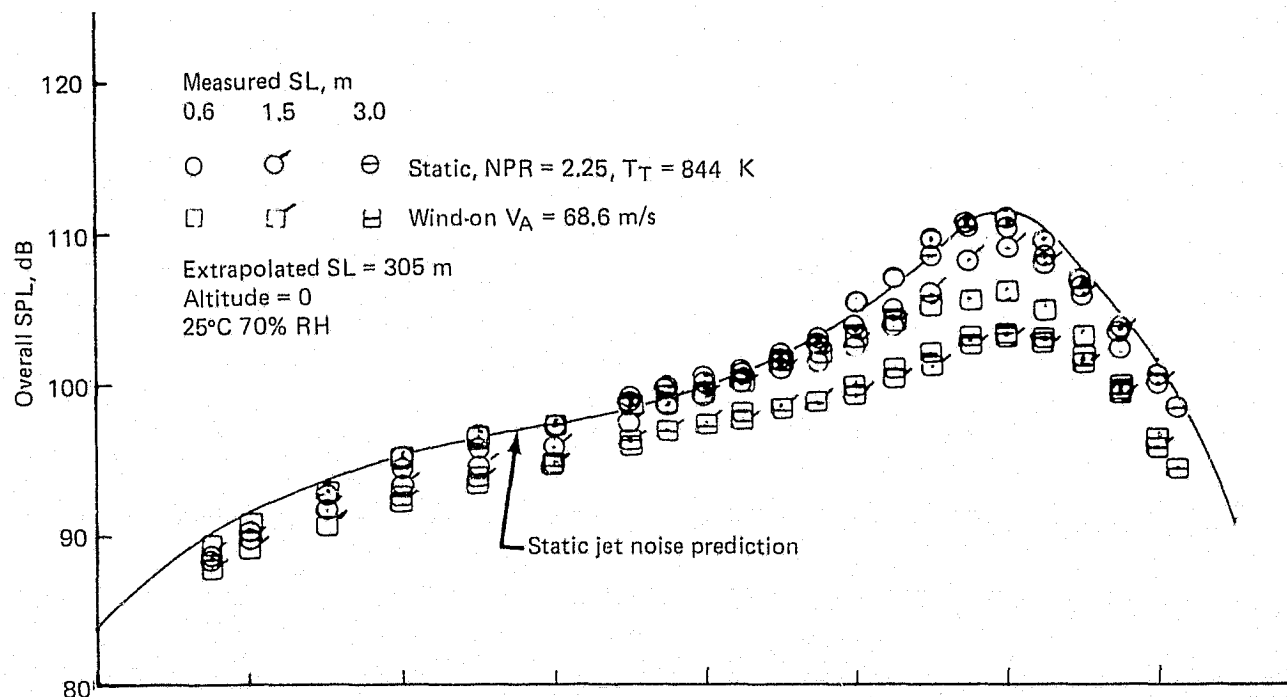


Figure 39.— 0.76 m RC Nozzle Flight Effects Based on 40 by 80 Tunnel Measurements
 $V_j = 594$ m/s $V_A = 68.6$ m/s

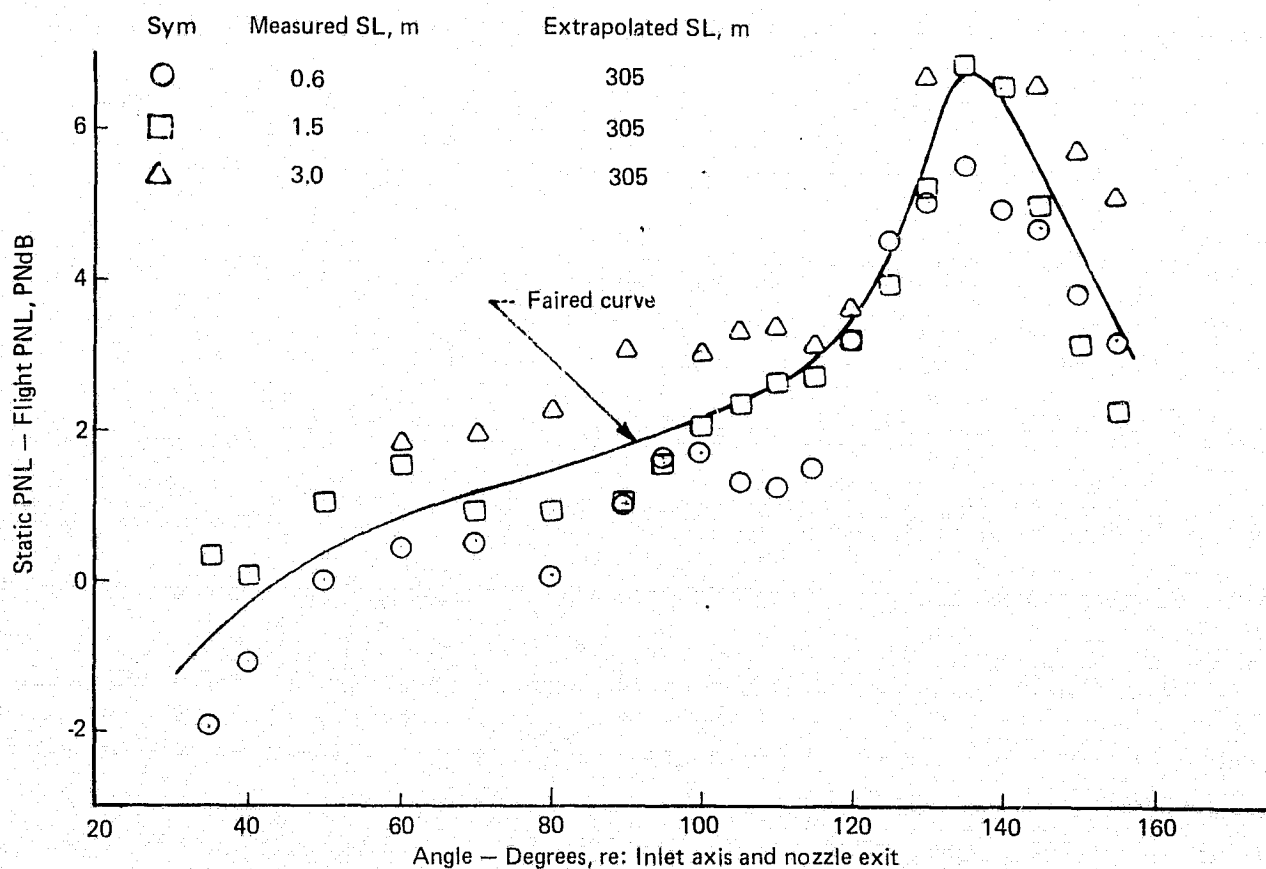
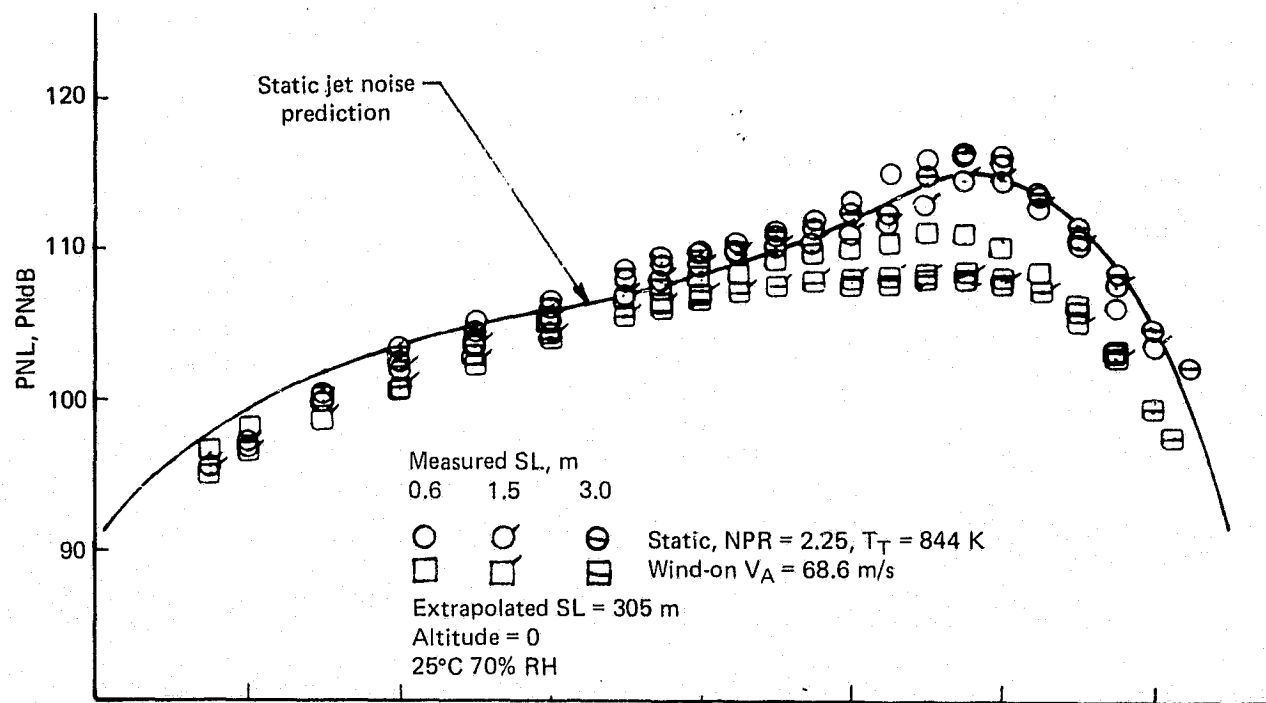


Figure 39. - (Concluded)

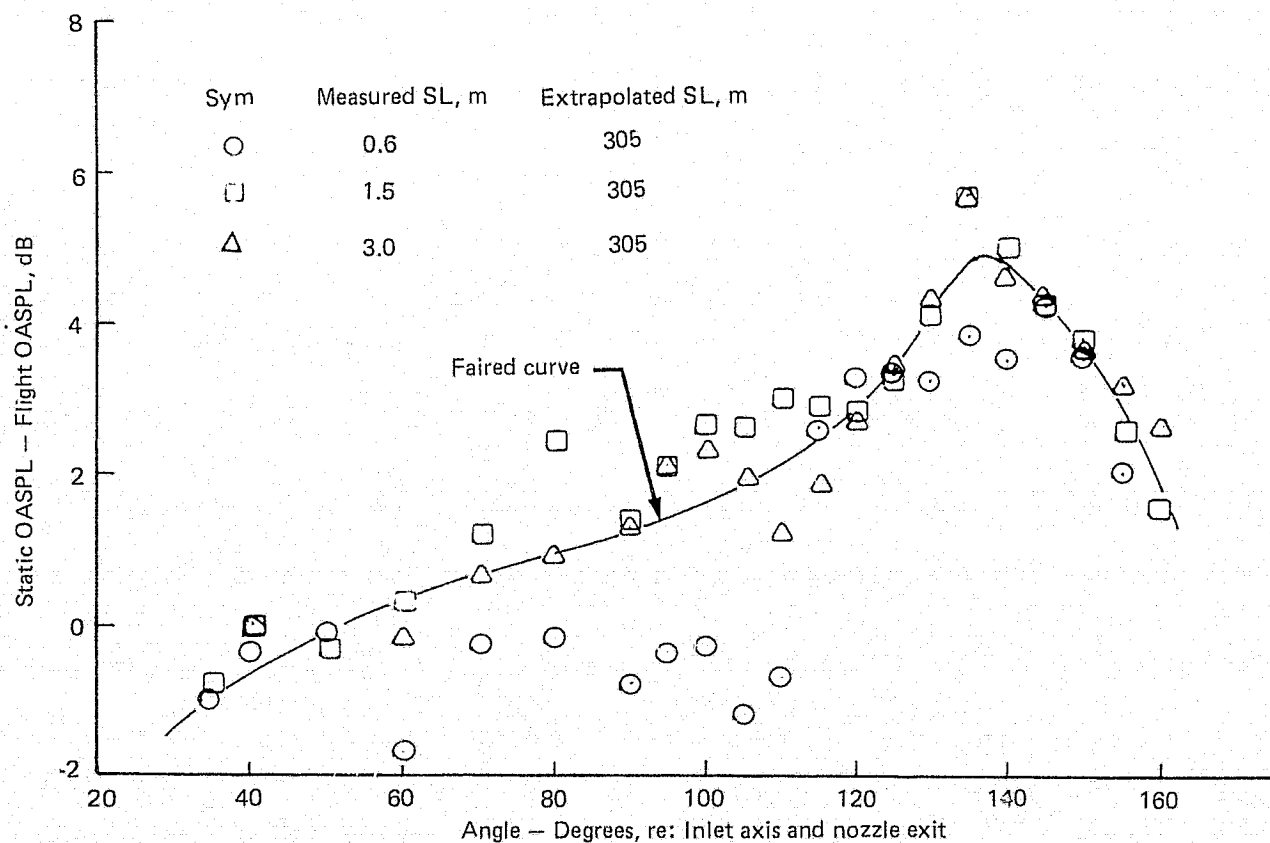
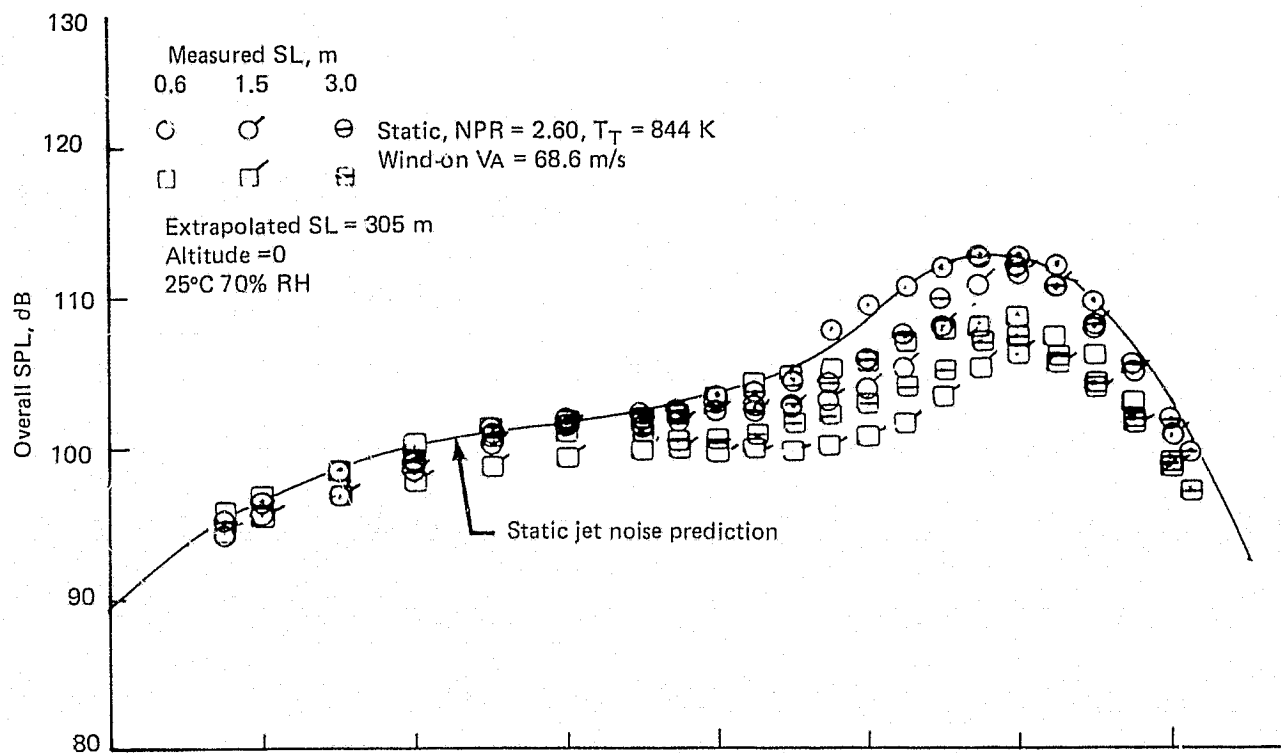


Figure 40.— 0.76 m RC Nozzle Flight Effects Based on 40 by 80 Tunnel Measurements
 $V_j = 640$ m/s $V_A = 68.6$ m/s

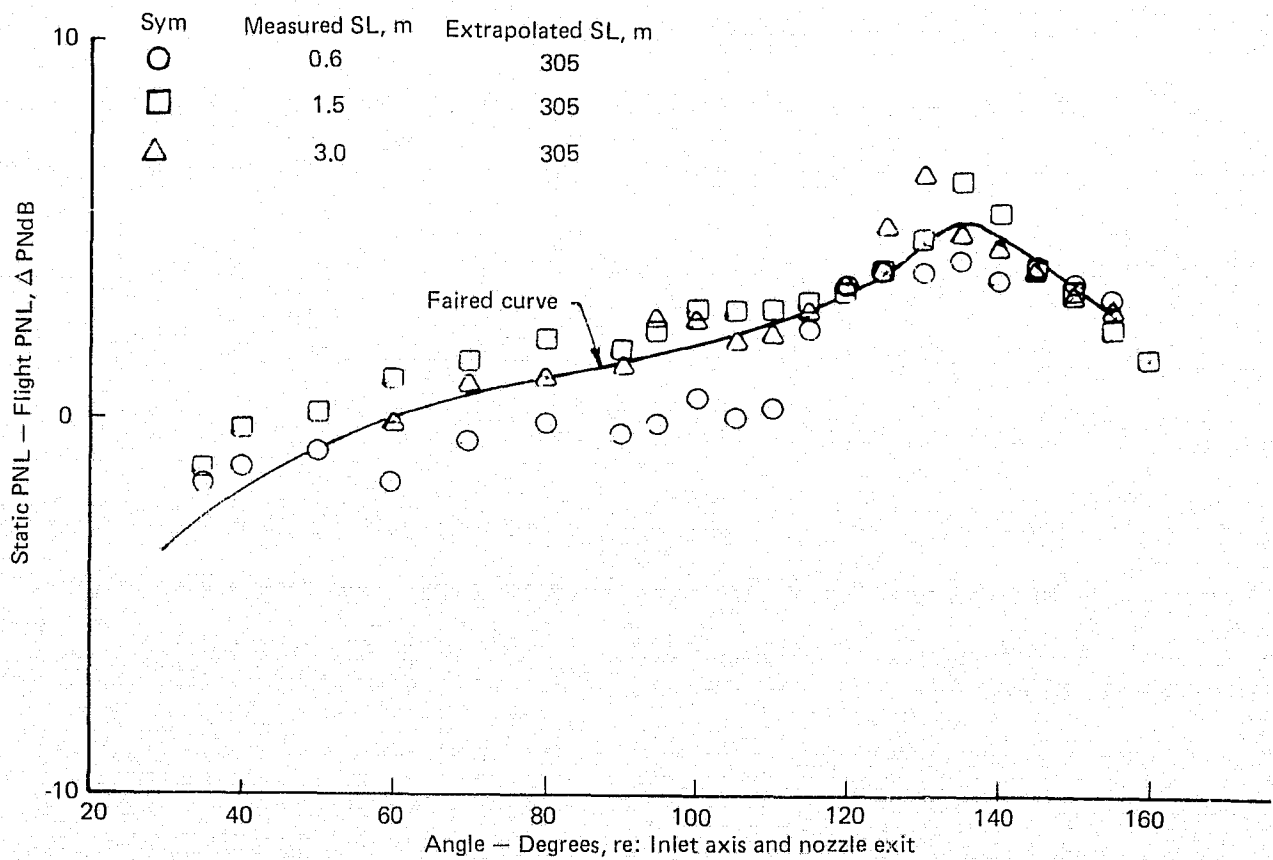
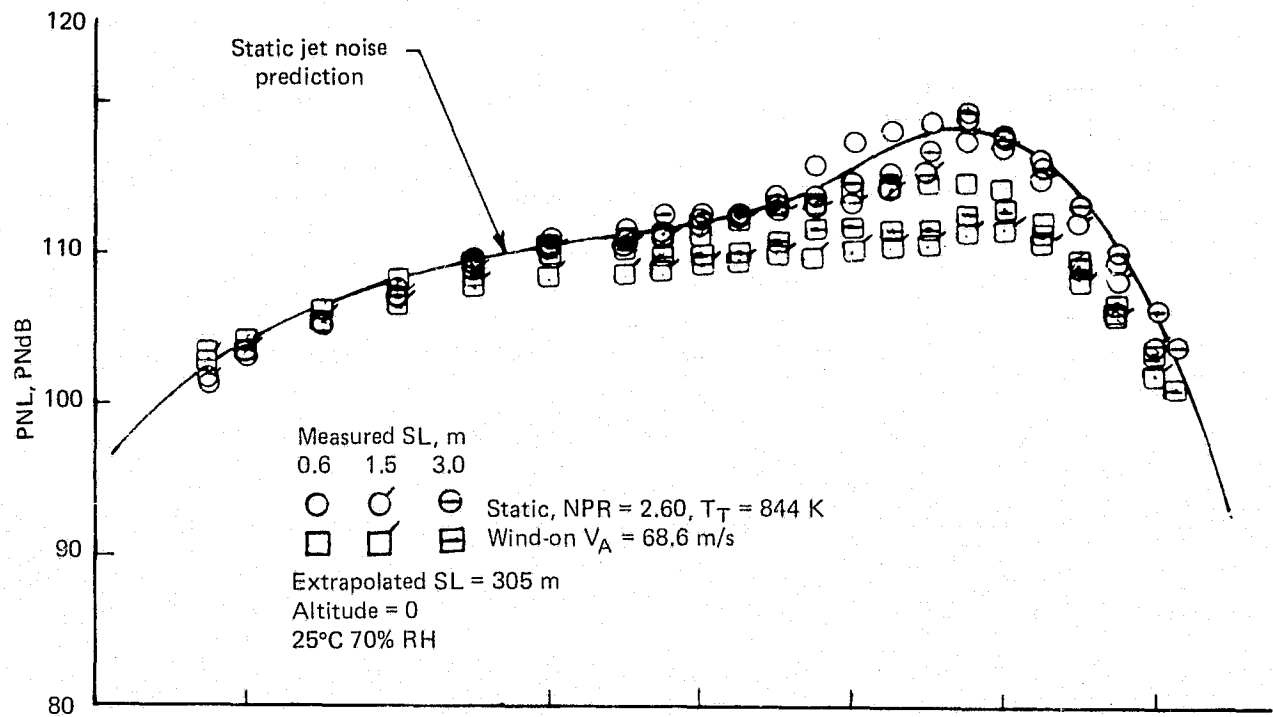


Figure 40.- (Concluded)

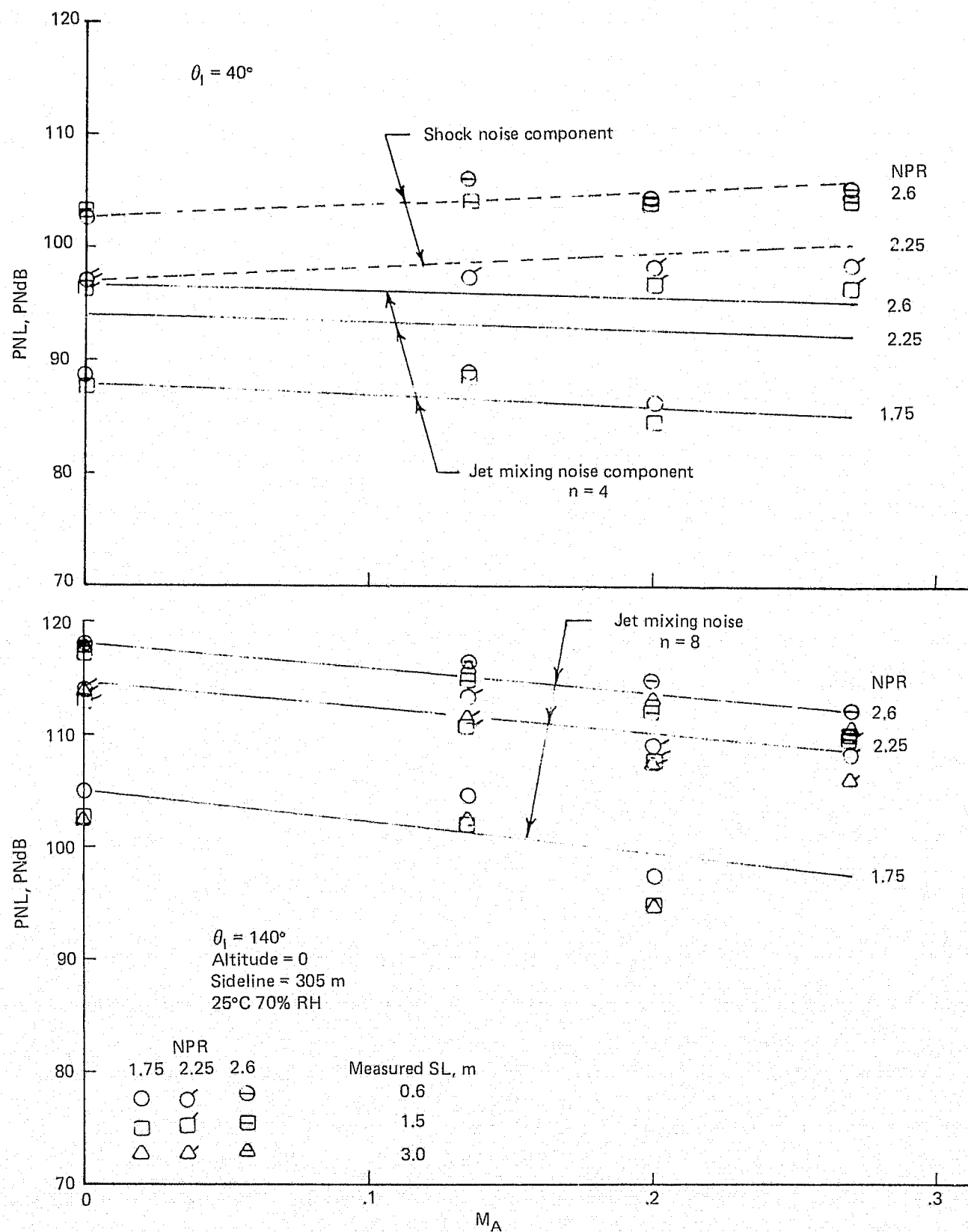


Figure 41.— Effect of Ambient Velocity on Shock-Cell Noise from an RC Nozzle

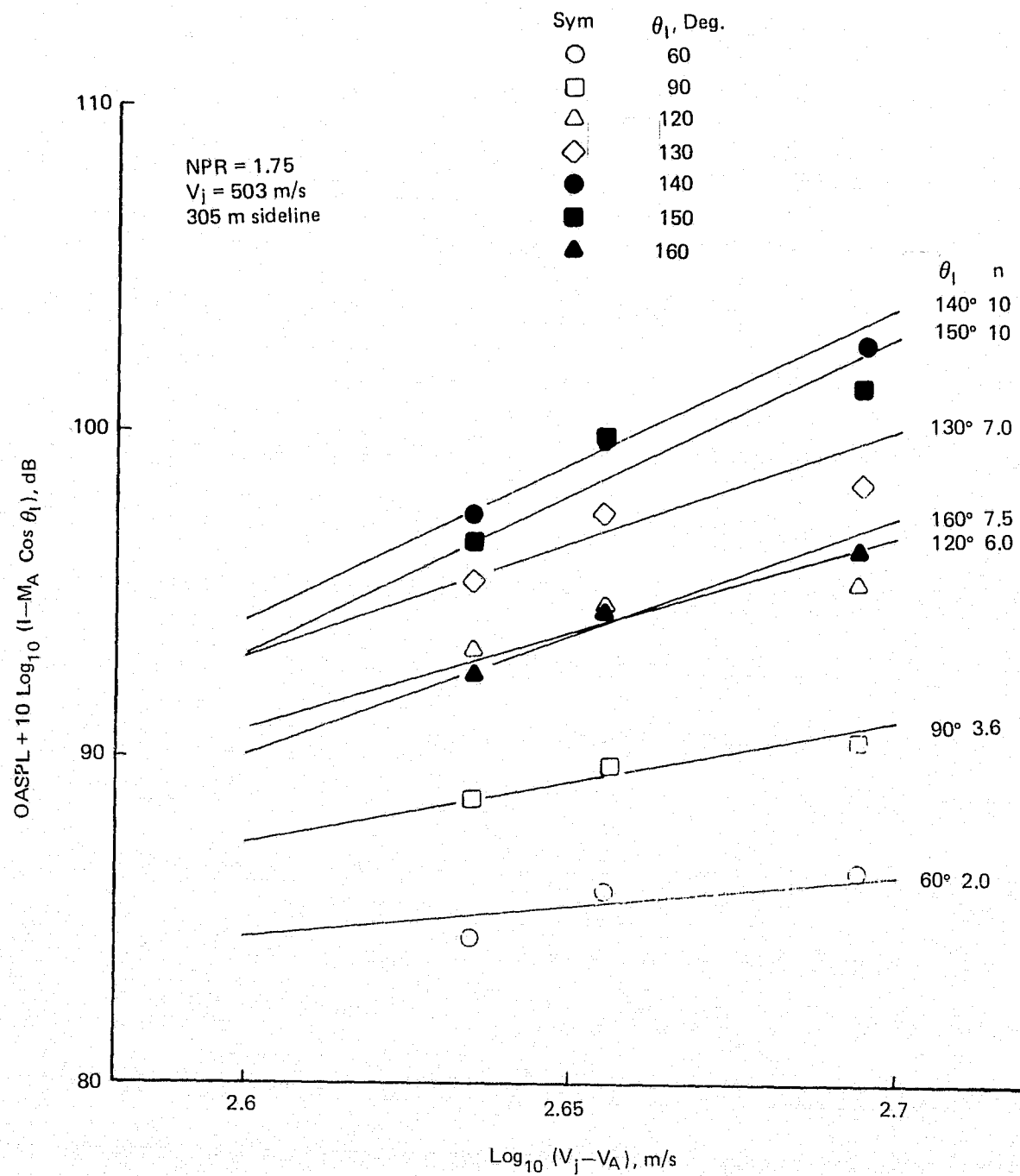


Figure 42.— Variation of OASPL and PNL with Relative Velocity for an RC Nozzle

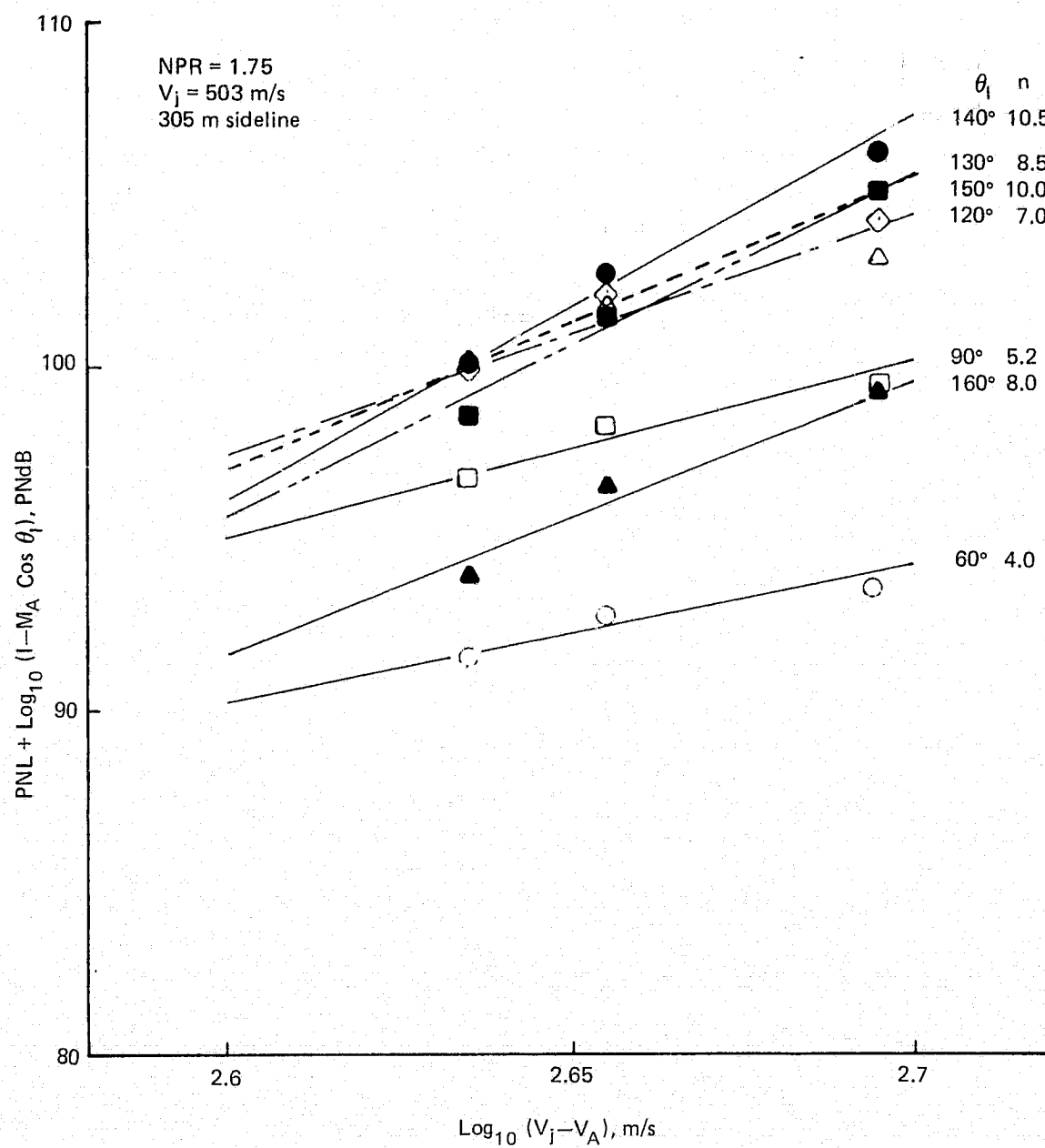


Figure 42.— (Continued)

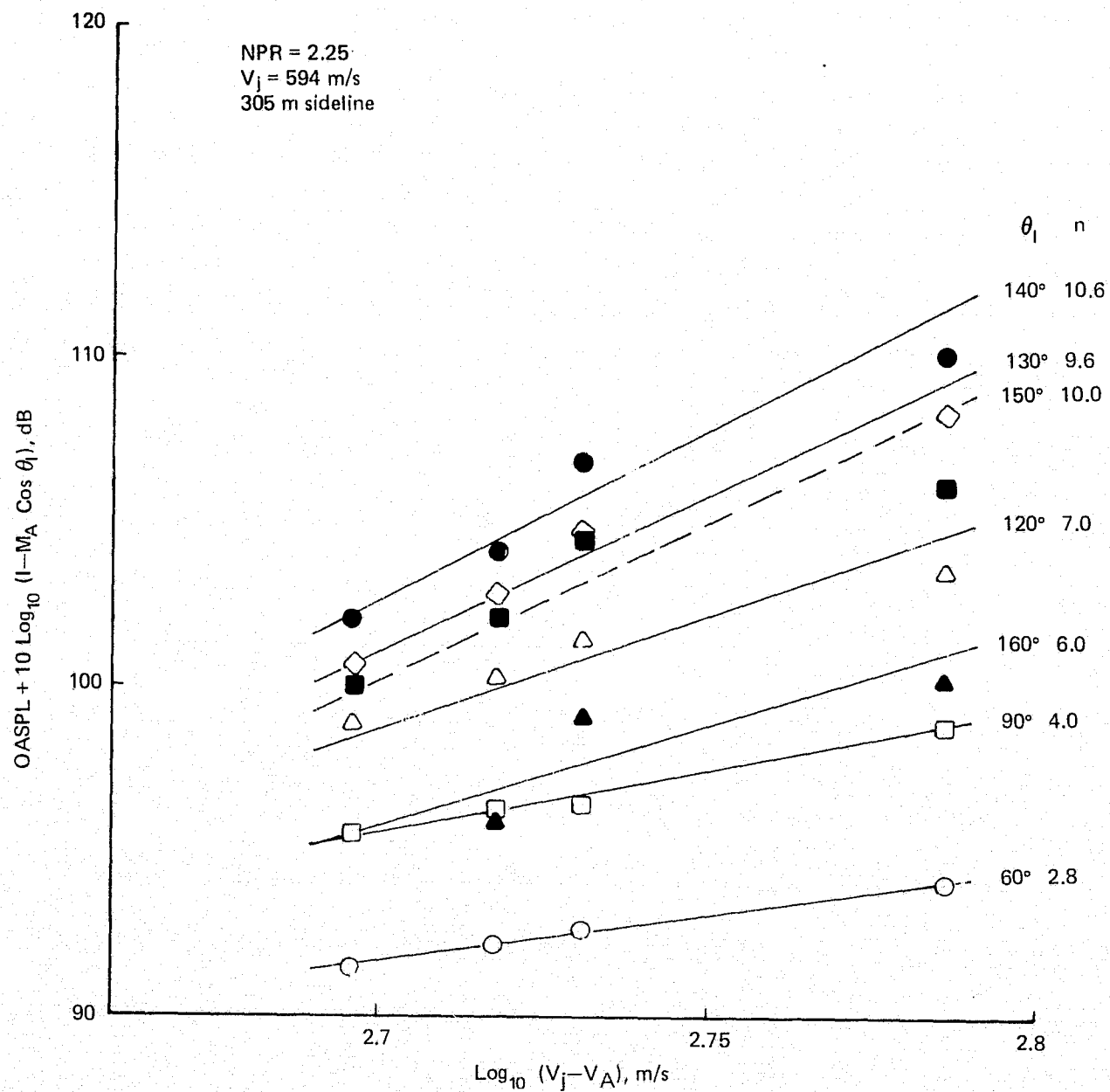


Figure 42.— (Continued)

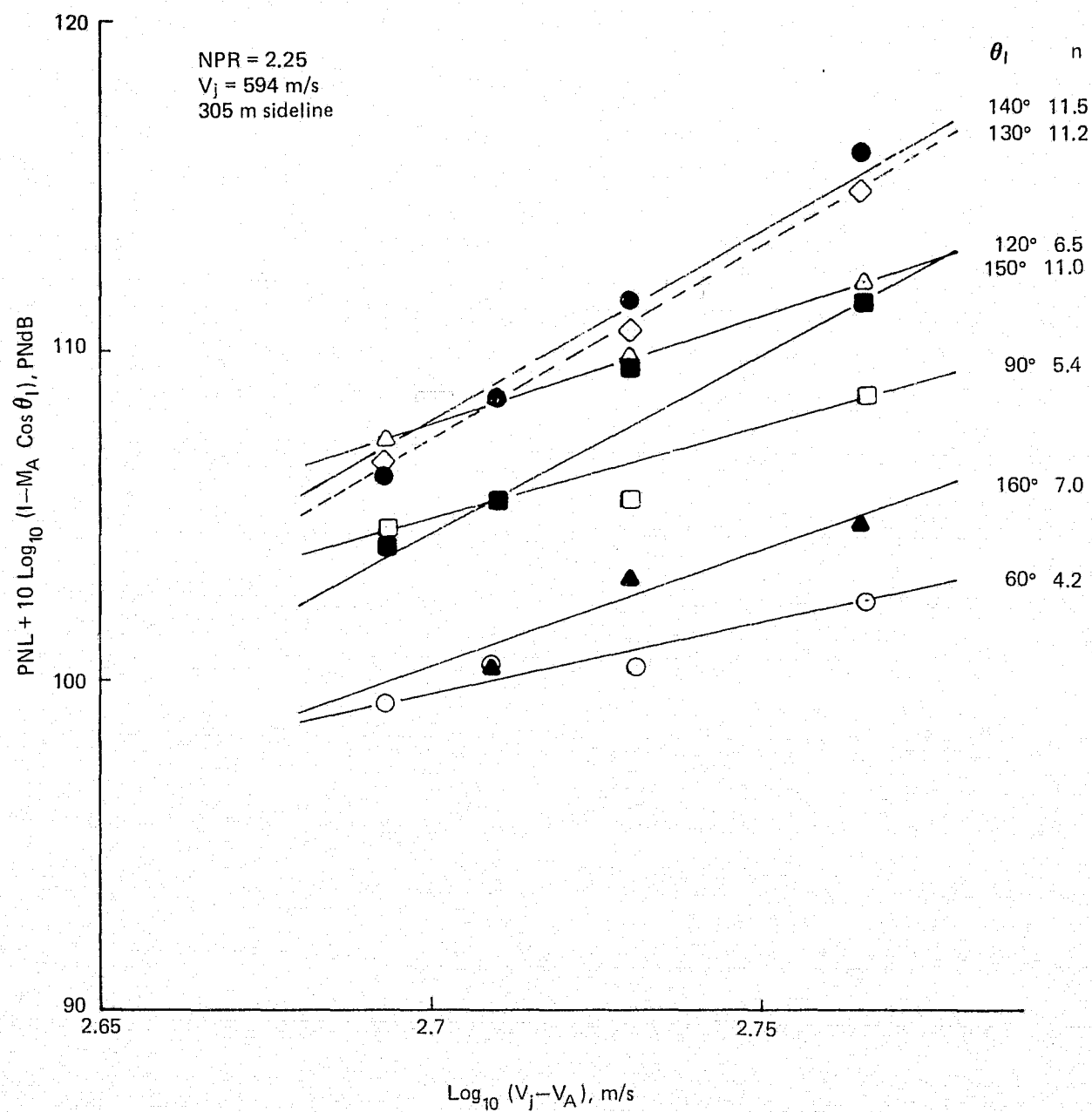


Figure 42.— (Concluded)

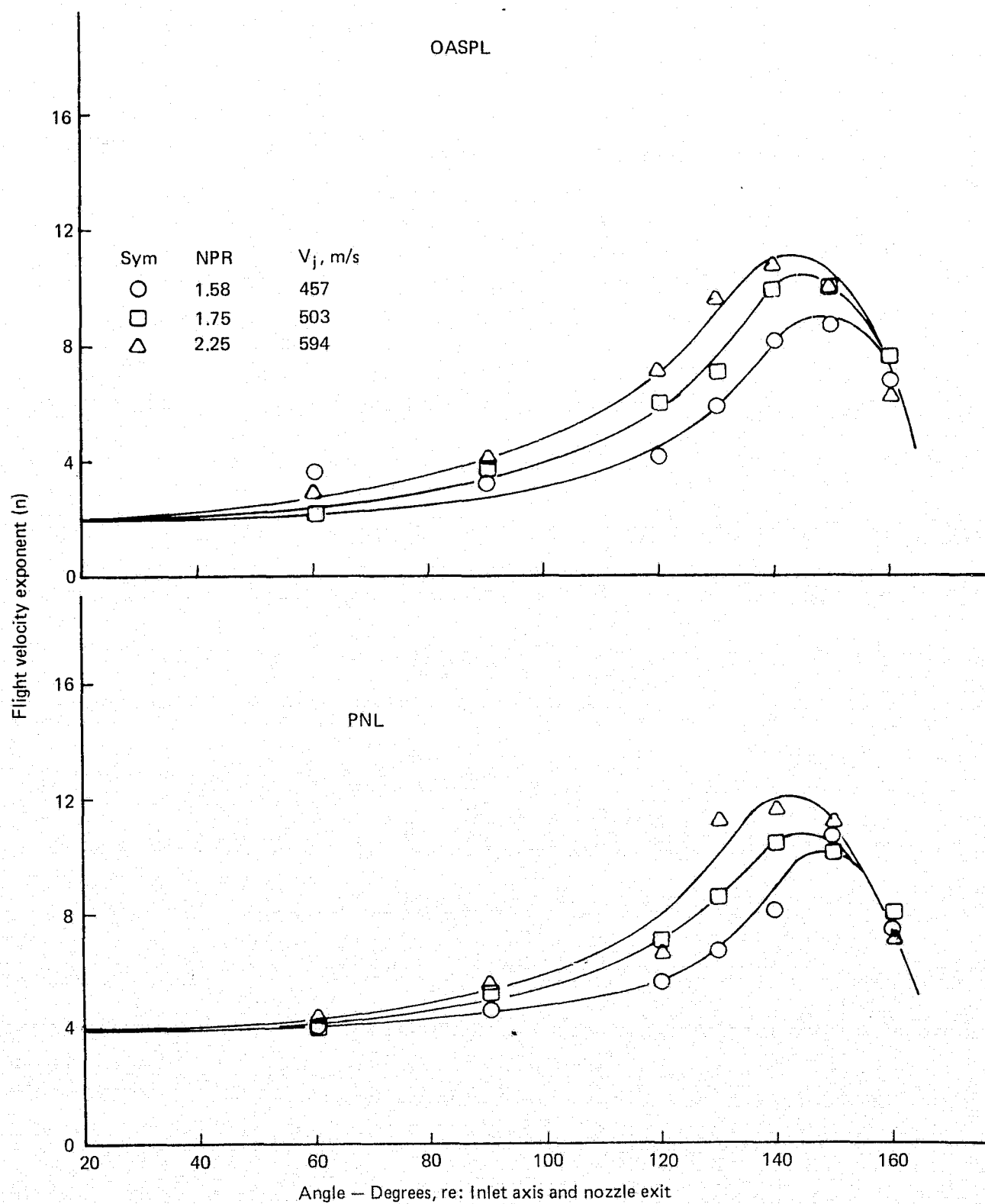


Figure 43.— RC Nozzle Flight Velocity Exponent Based on 40 by 80 Tunnel Data

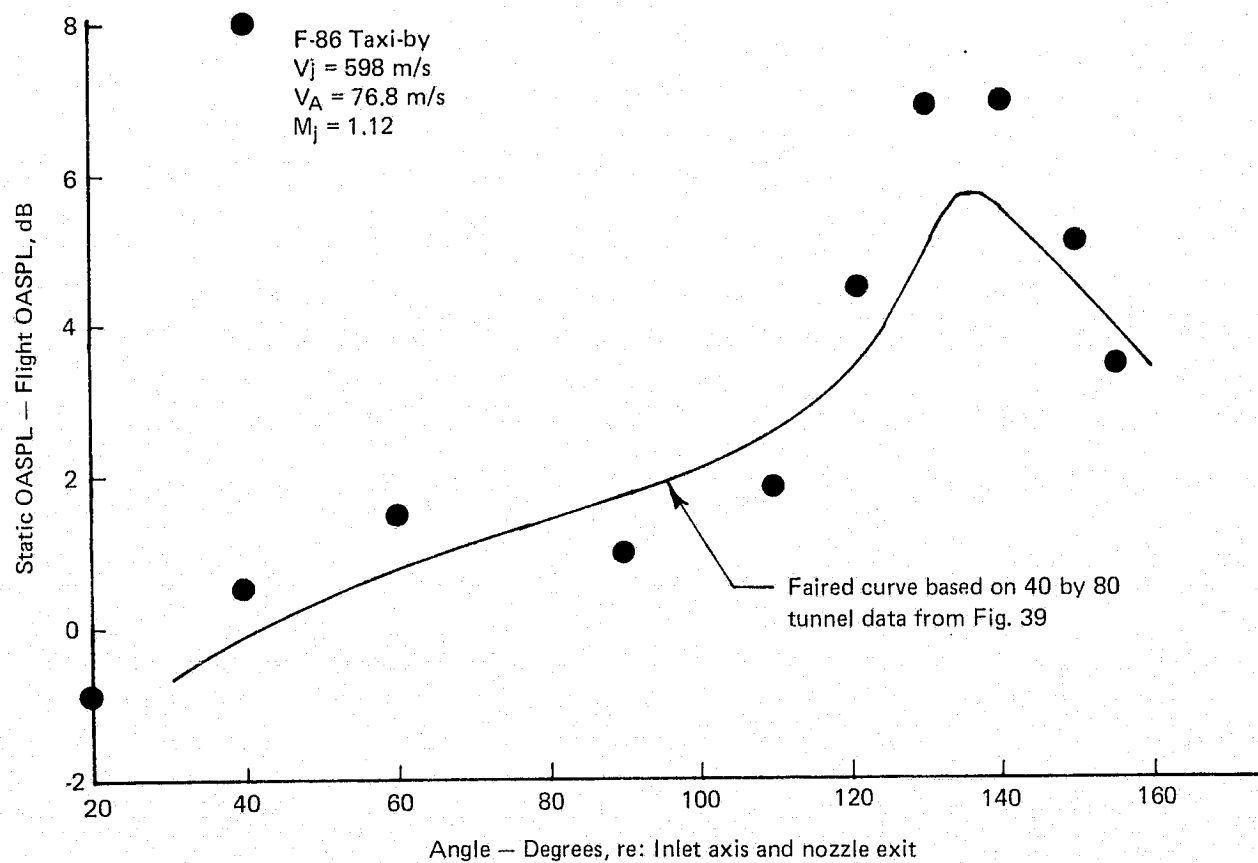


Figure 44.— Comparison of Flight Effects on OASPL Measured in the 40 by 80 Tunnel with F-86 Taxi-By Results

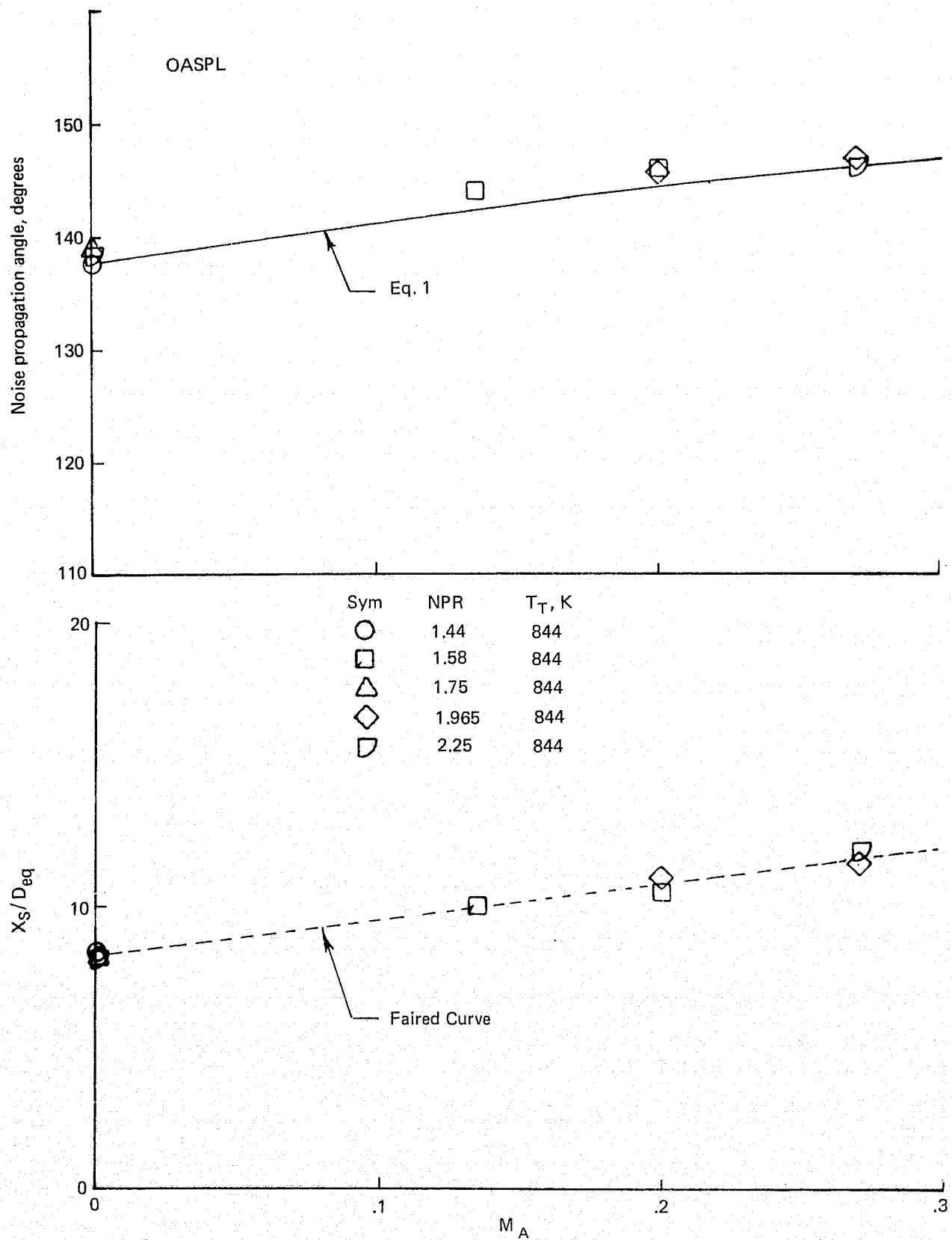


Figure 45.— Peak Noise Source Locations and Noise Propagation Angles for the Annular Nozzle

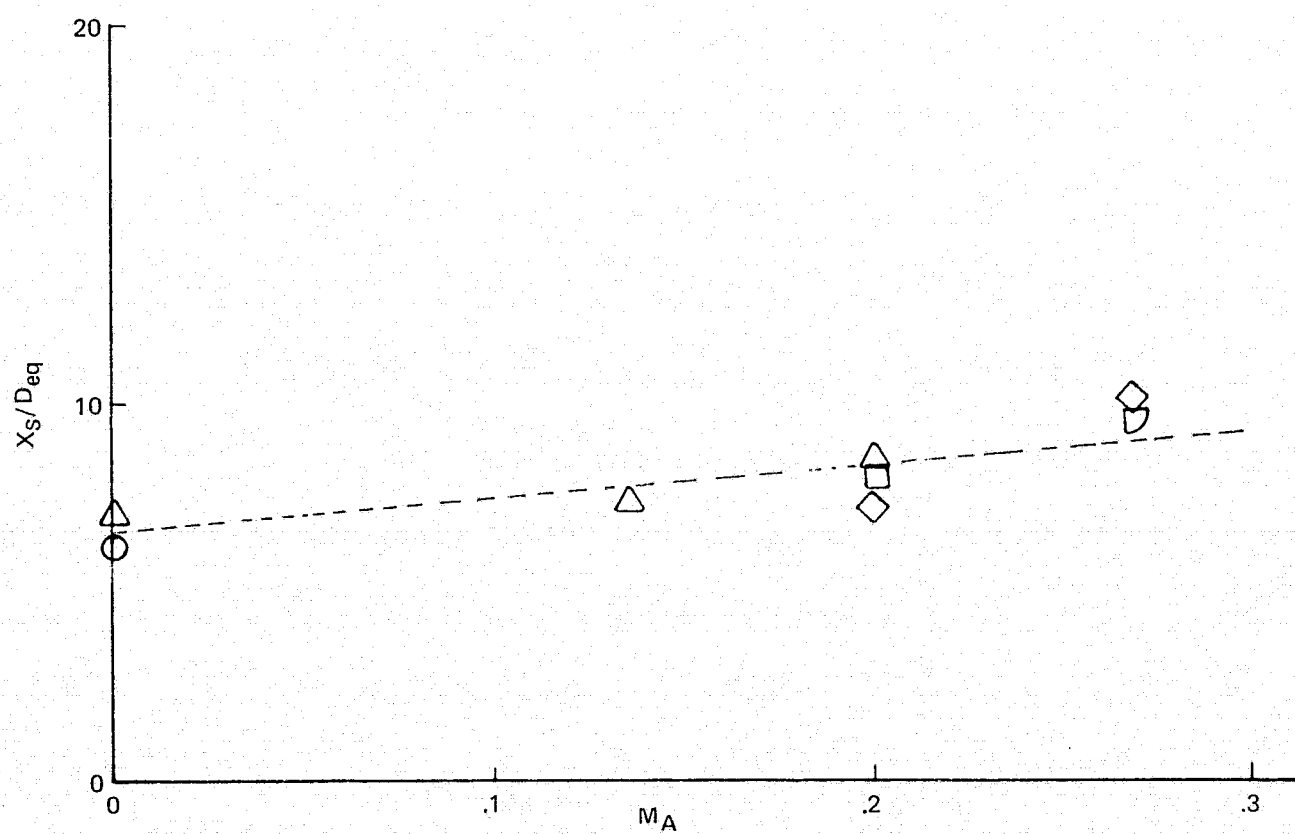
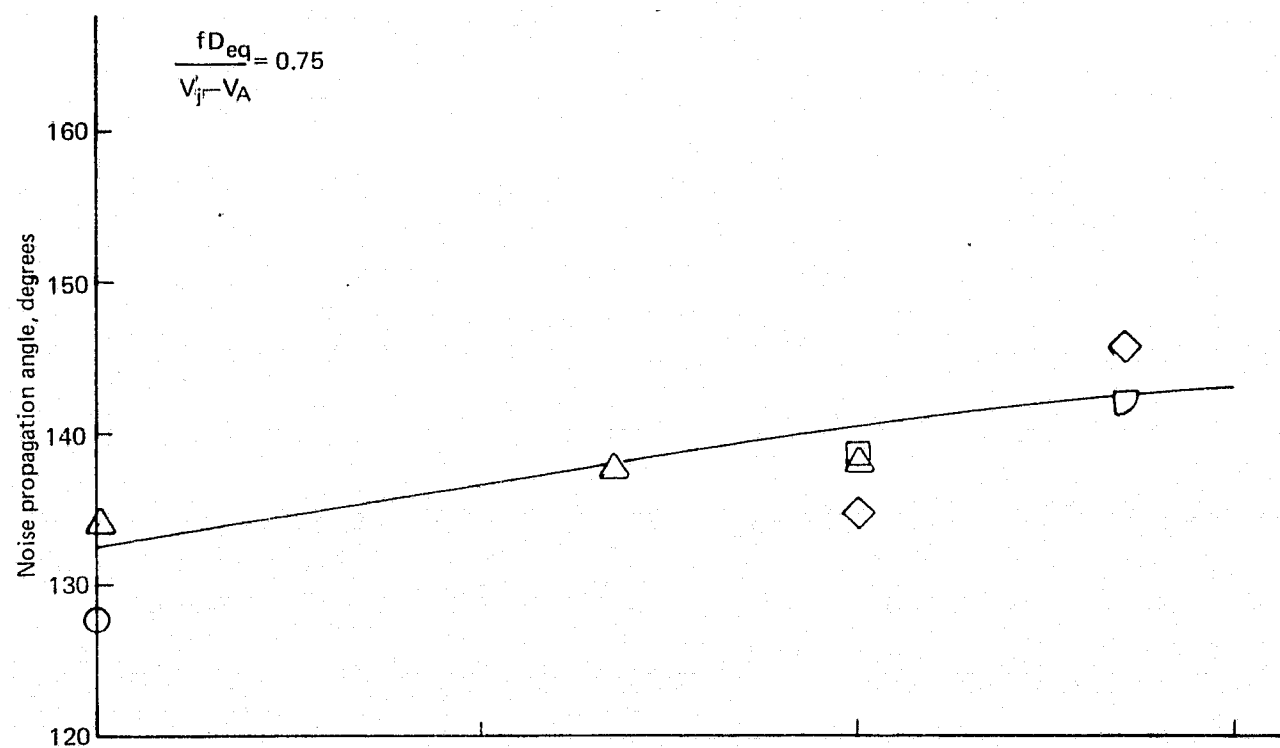


Figure 45.— (Continued)

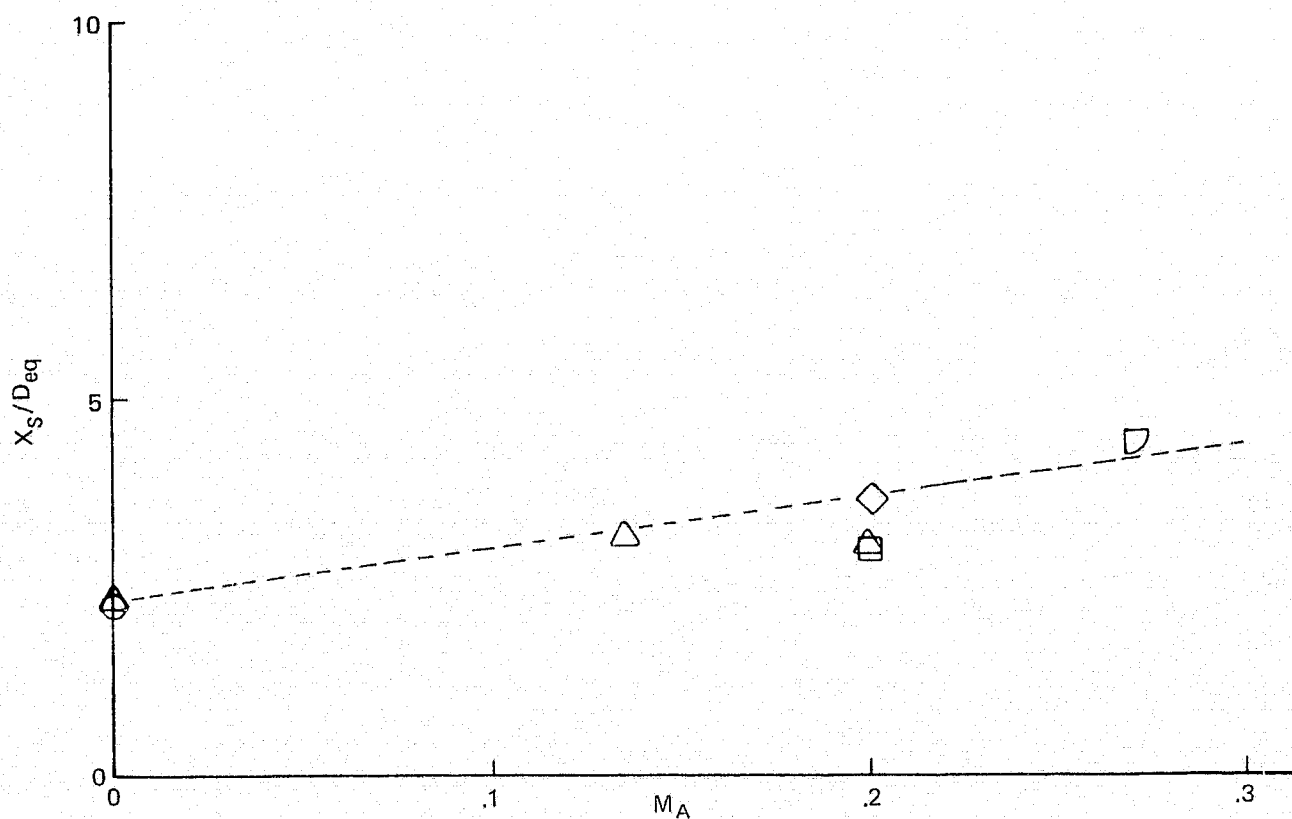
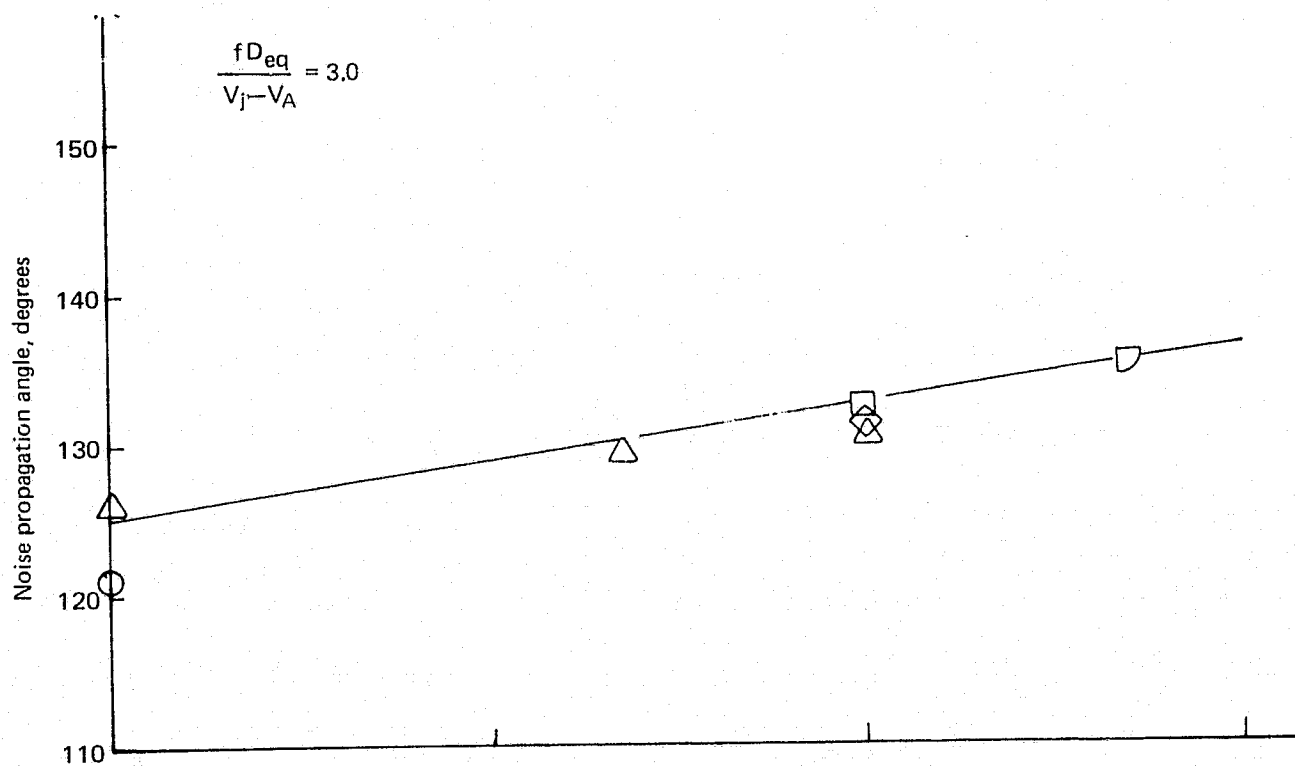


Figure 45.— (Continued)

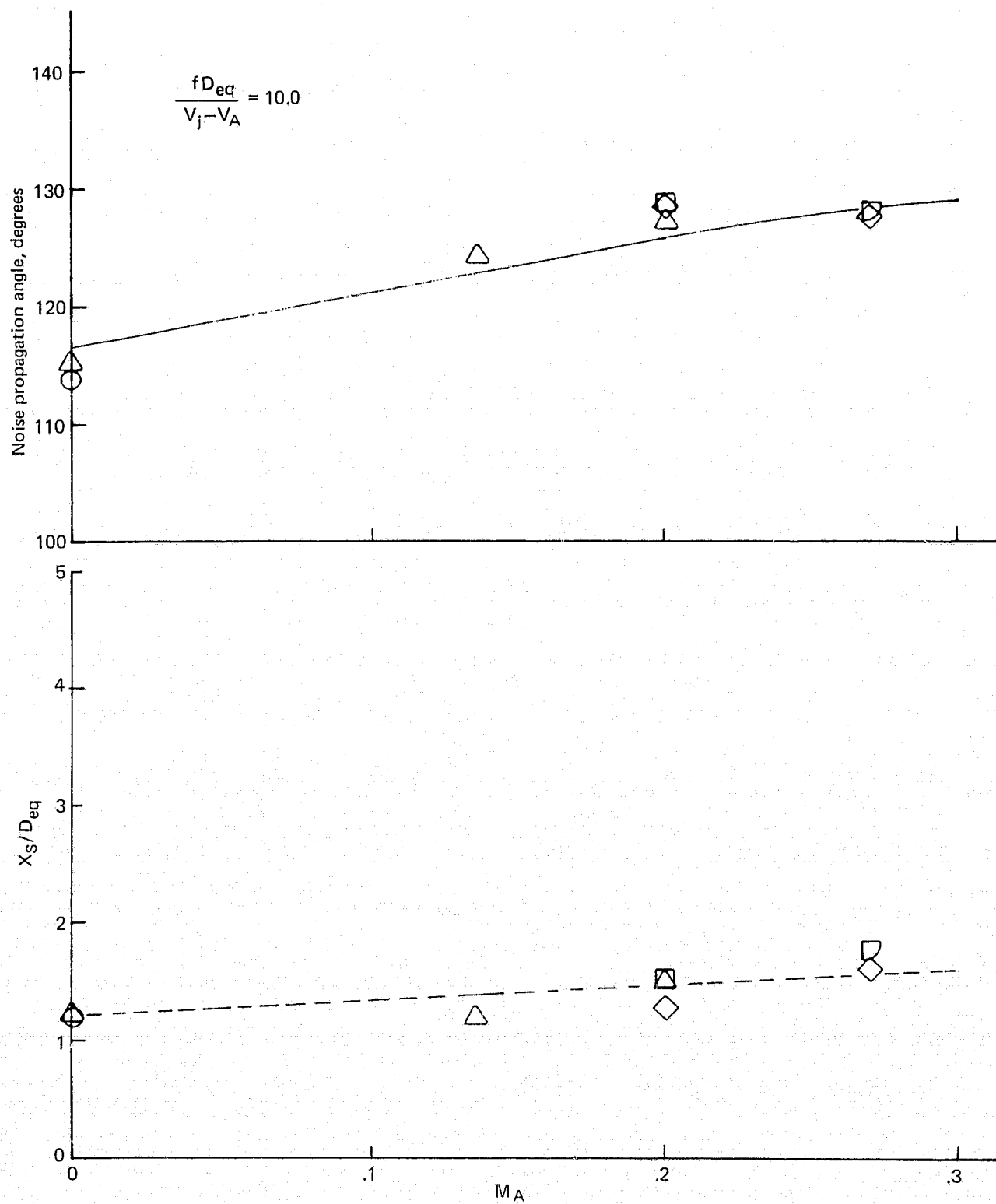


Figure 45.— (Concluded)

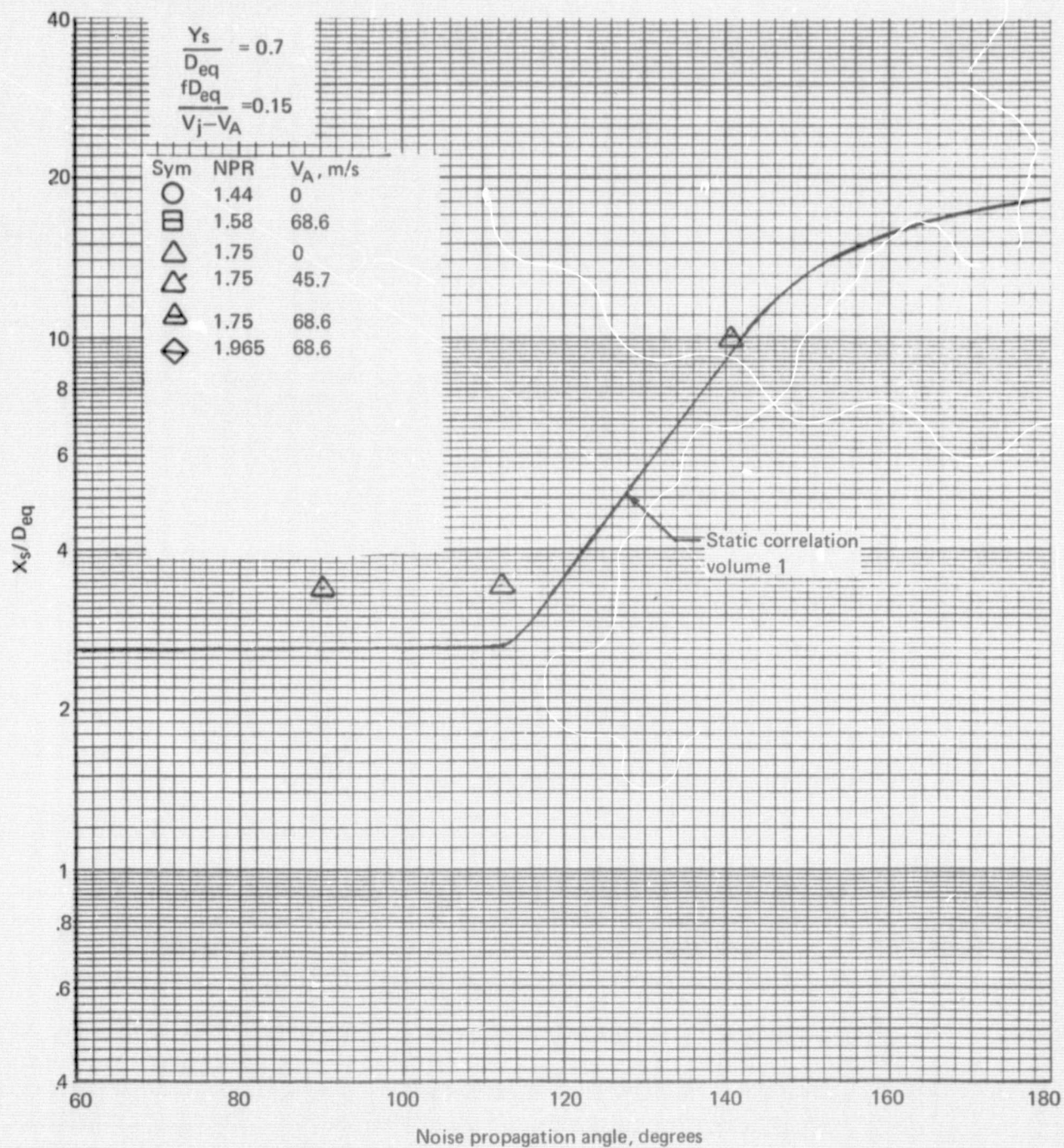


Figure 46.—Effect of Ambient Velocity on the Distributed Noise Source Locations for an Annular Nozzle

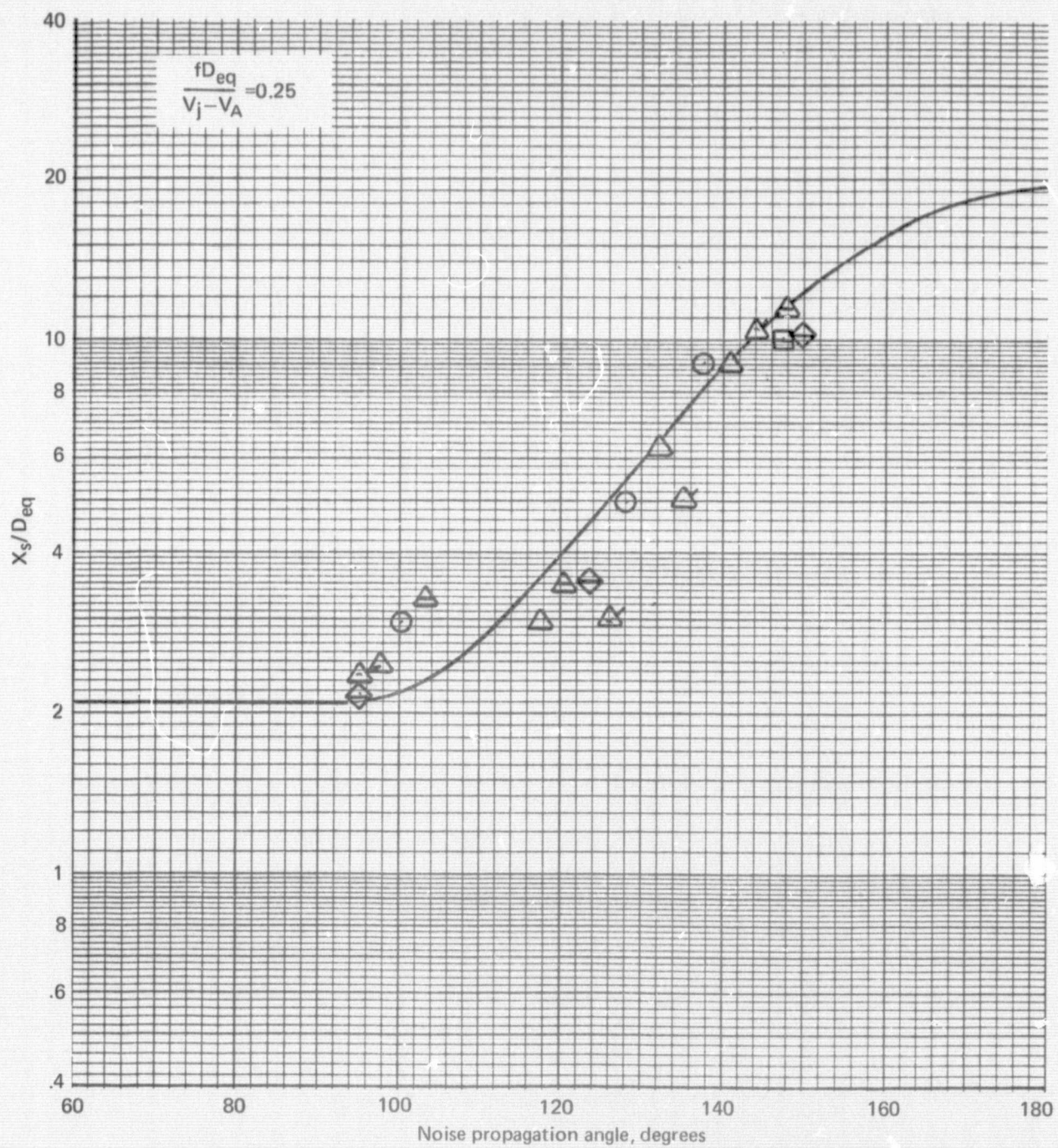


Figure 46.—(Continued)

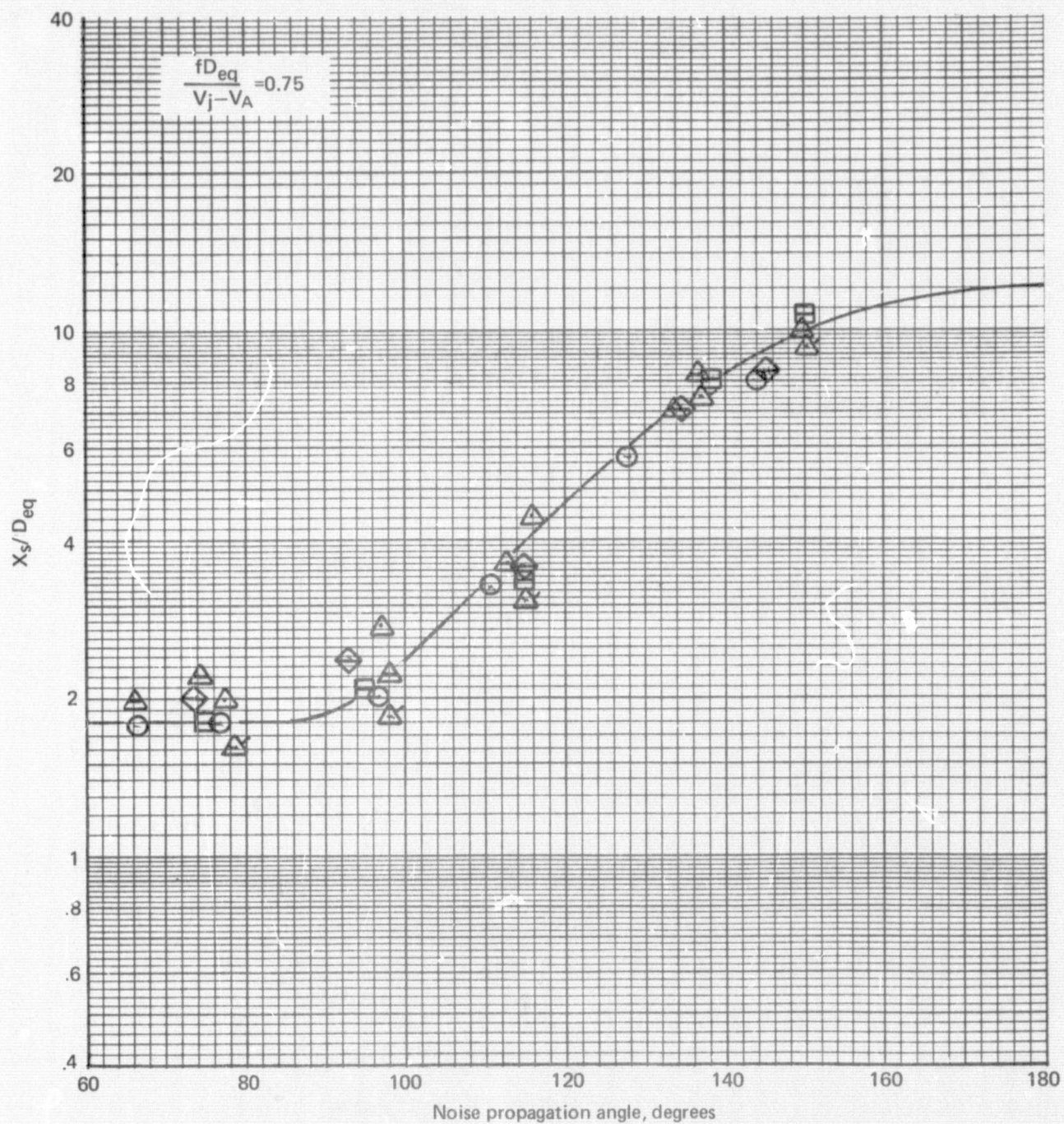


Figure 46.—(Continued)

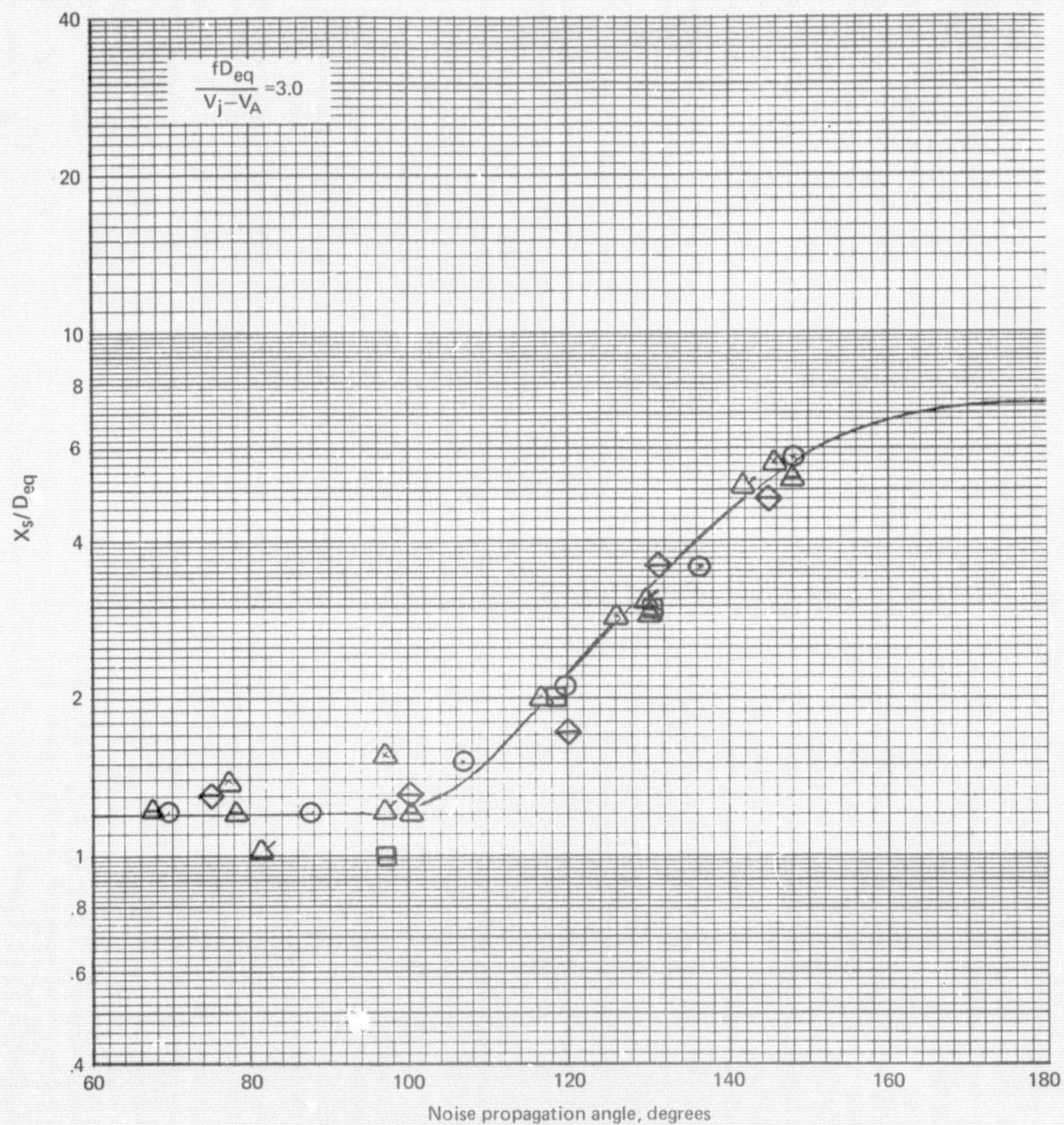


Figure 46.—(Continued)

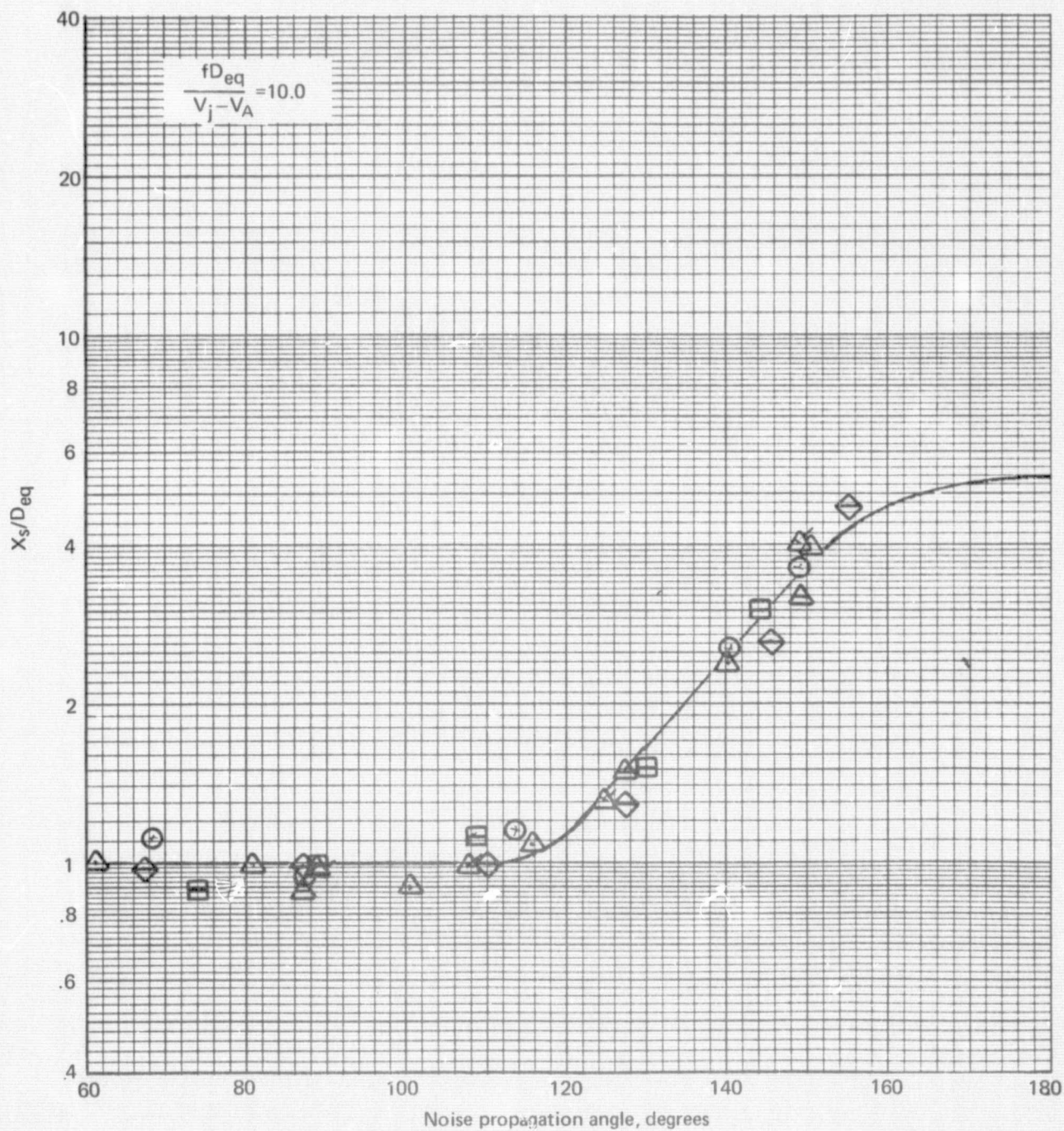


Figure 46.—(Concluded)

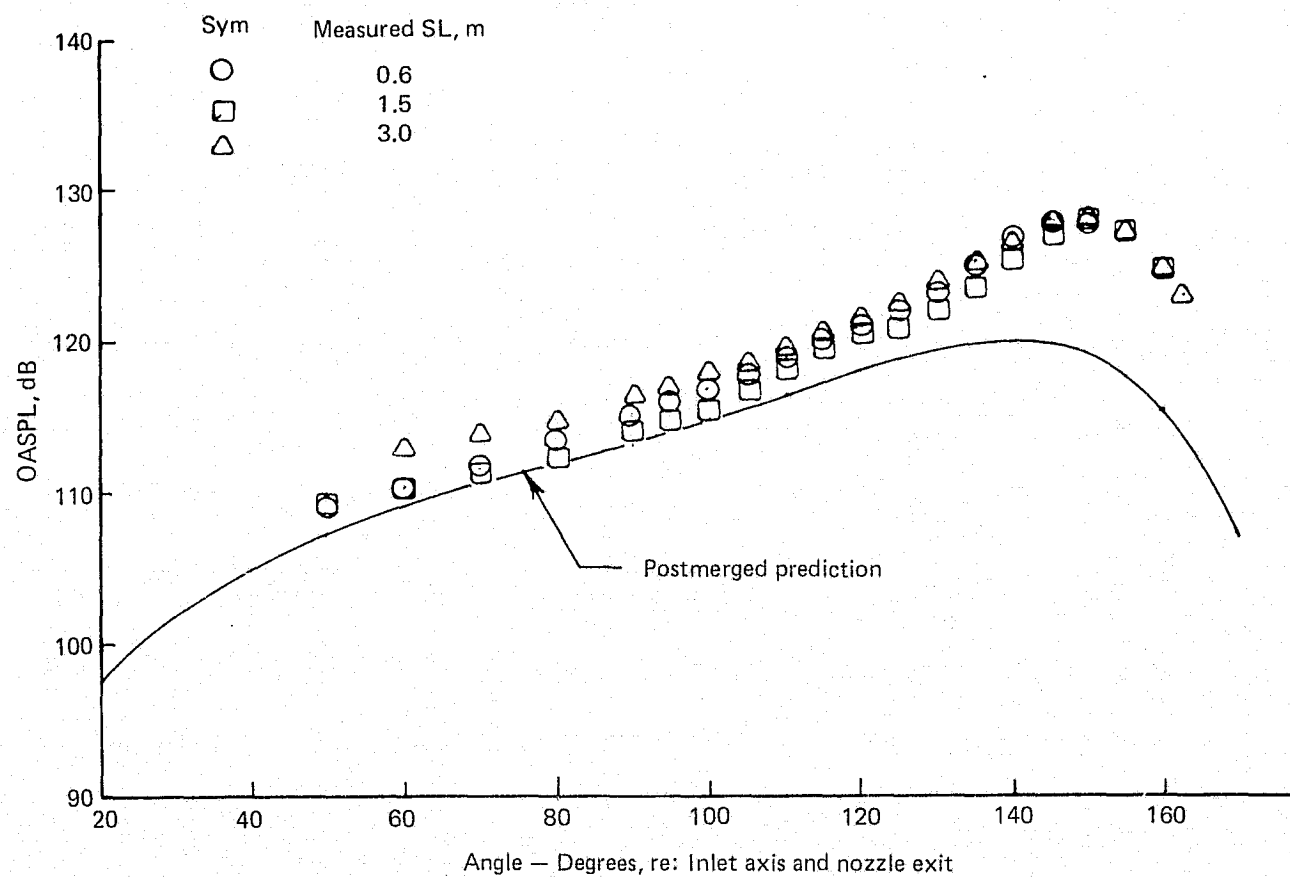


Figure 47.— OASPL Directivity and Jet Noise Spectra for an Annular Nozzle Extrapolated to a 3.0 m Sideline, $NPR = 1.75$, $V_A = 0$ m/s

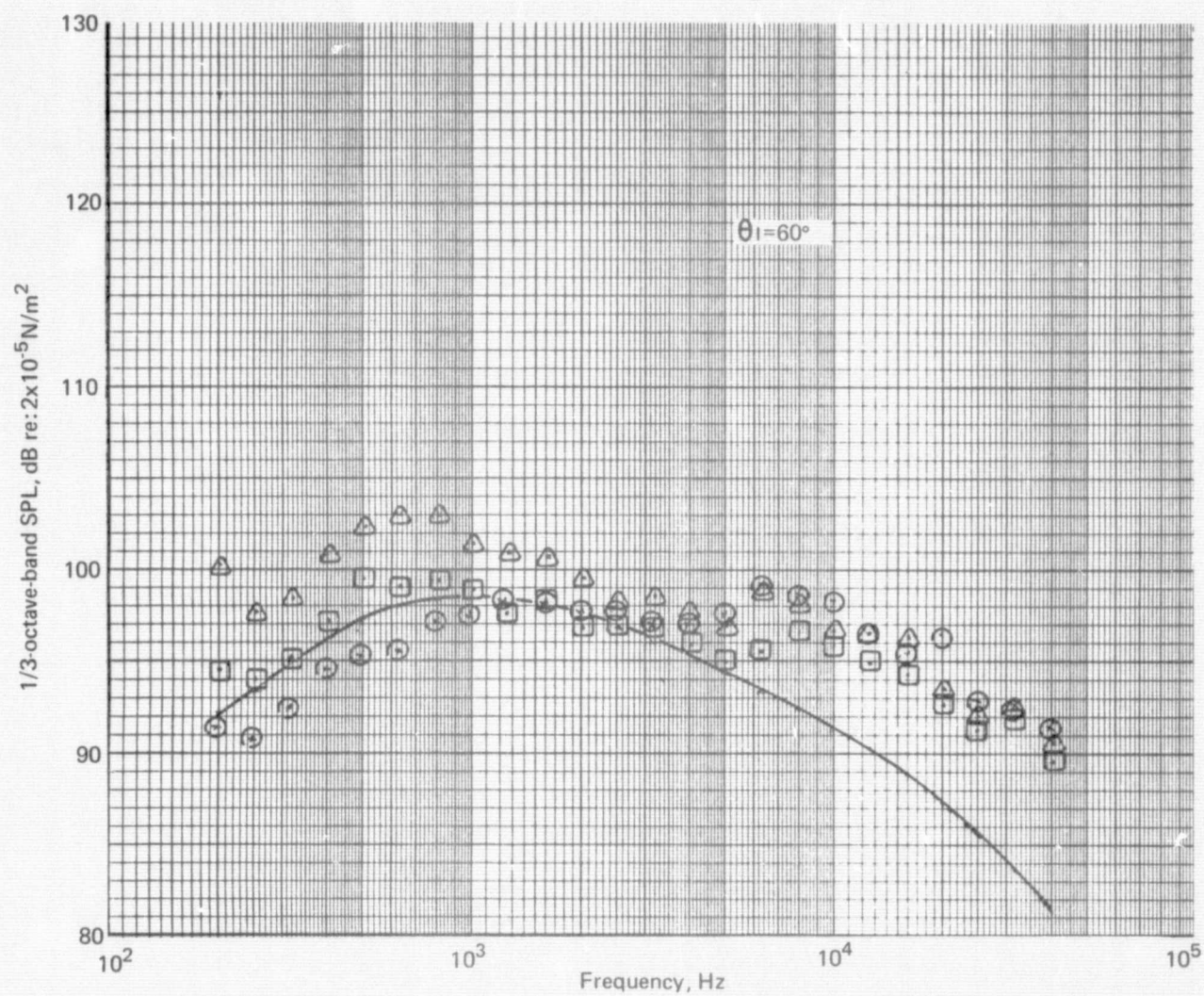


Figure 47.—(Continued)

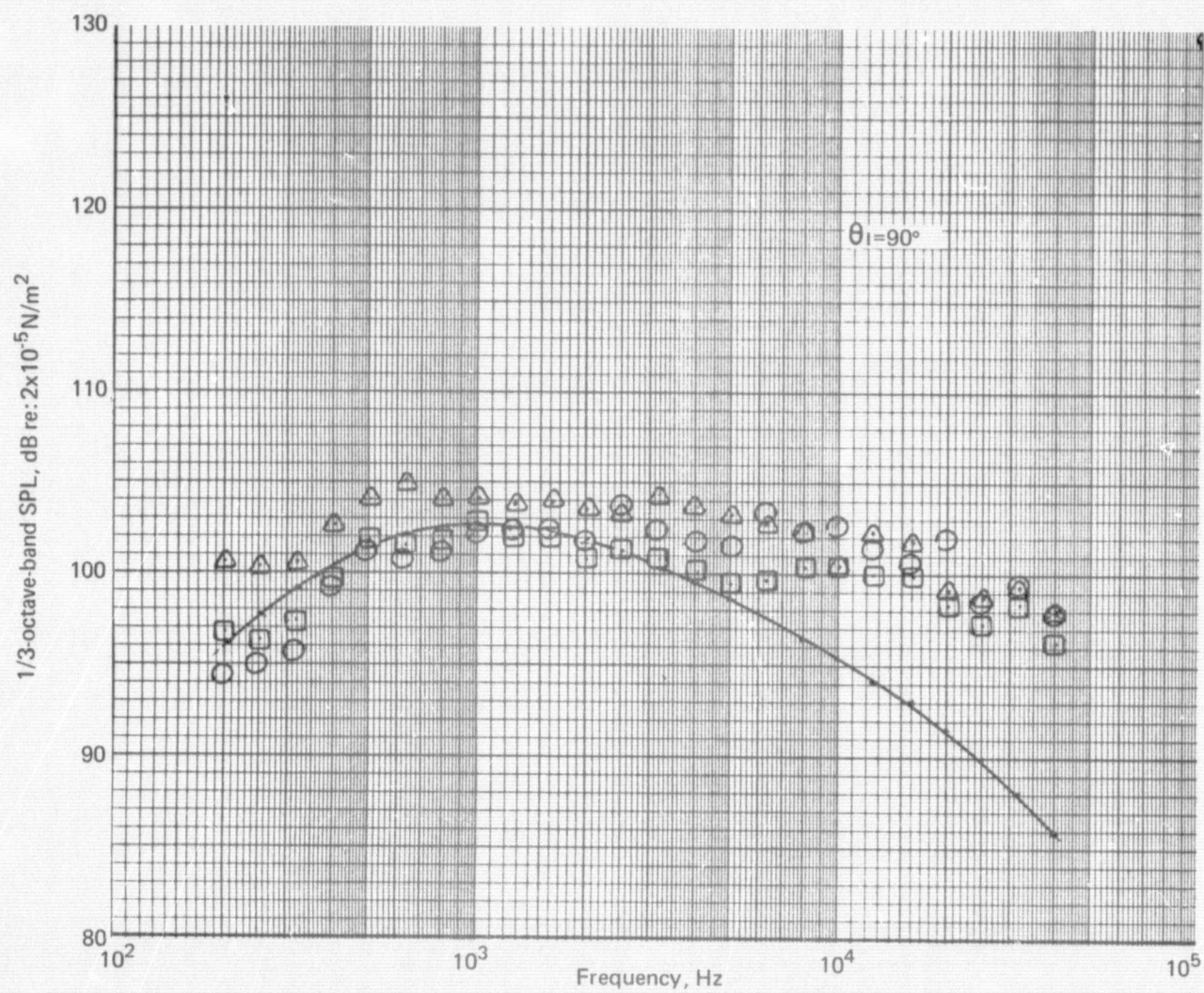


Figure 47.—(Continued)

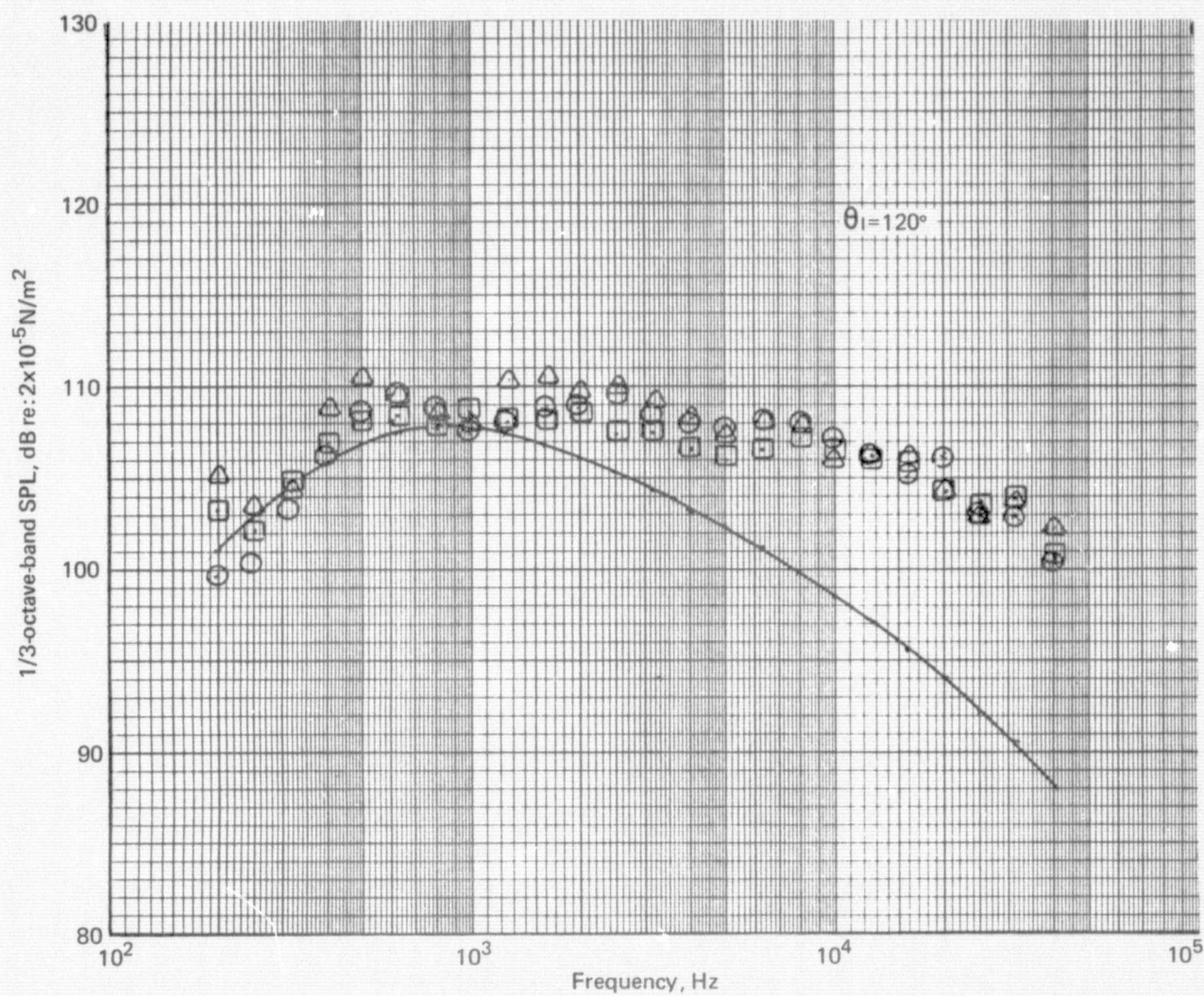


Figure 47.—(Continued)

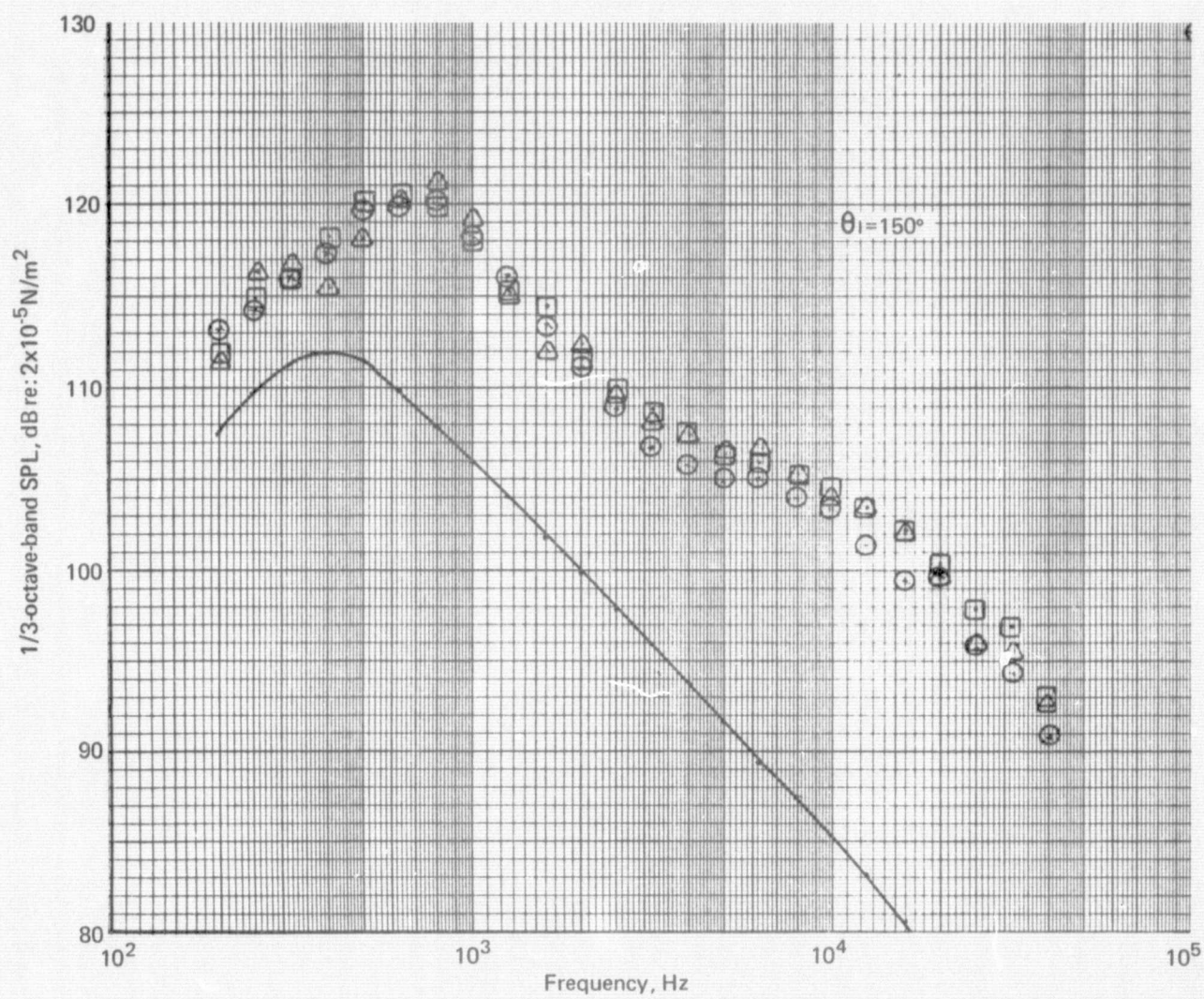


Figure 47.—(Concluded)

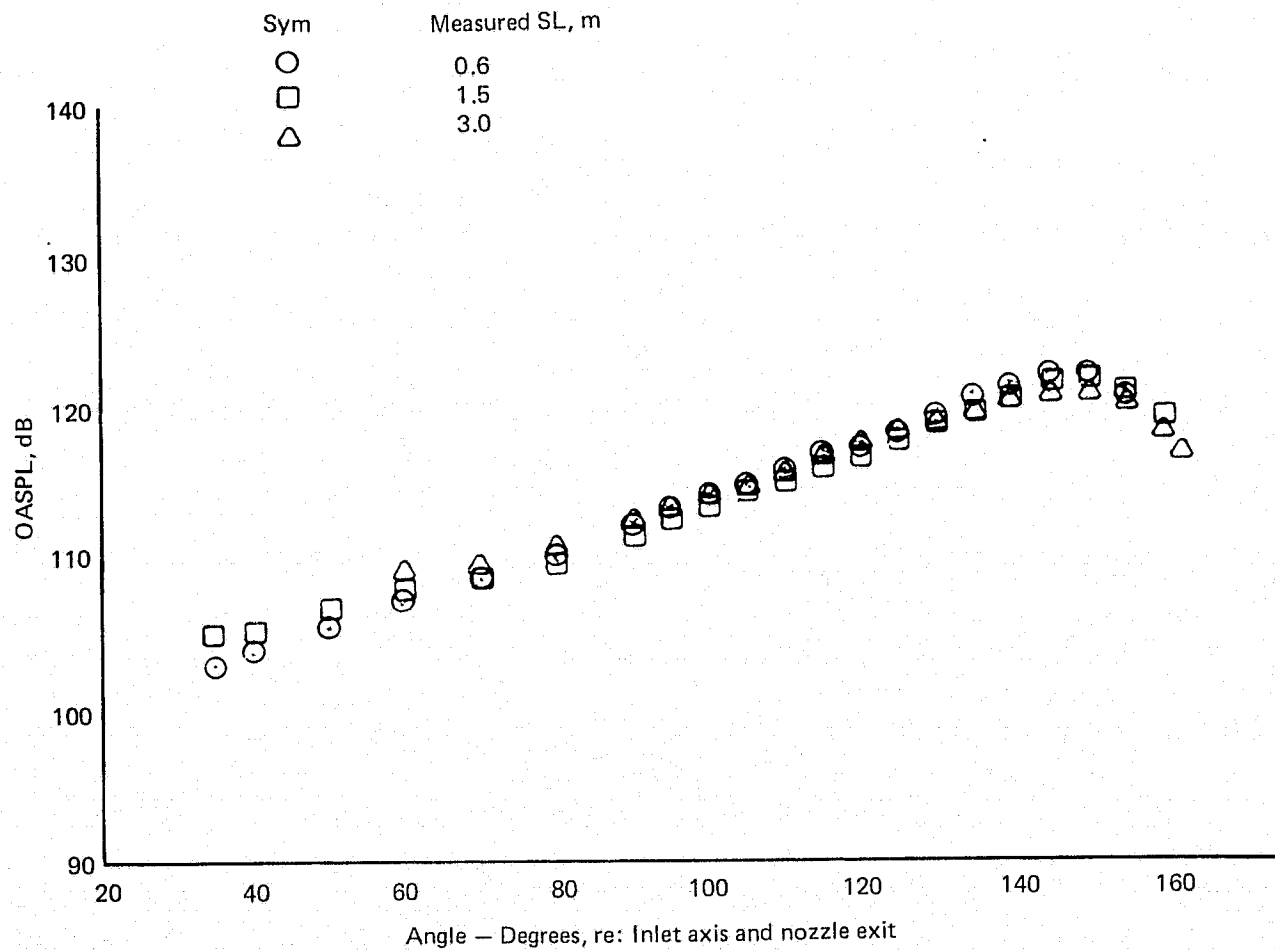


Figure 48.— OASPL Directivity and Jet Noise Spectra for an Annular Nozzle Extrapolated to a 3.0 m Sideline, $NPR = 1.75$, $V_A = 68.5$ m/s

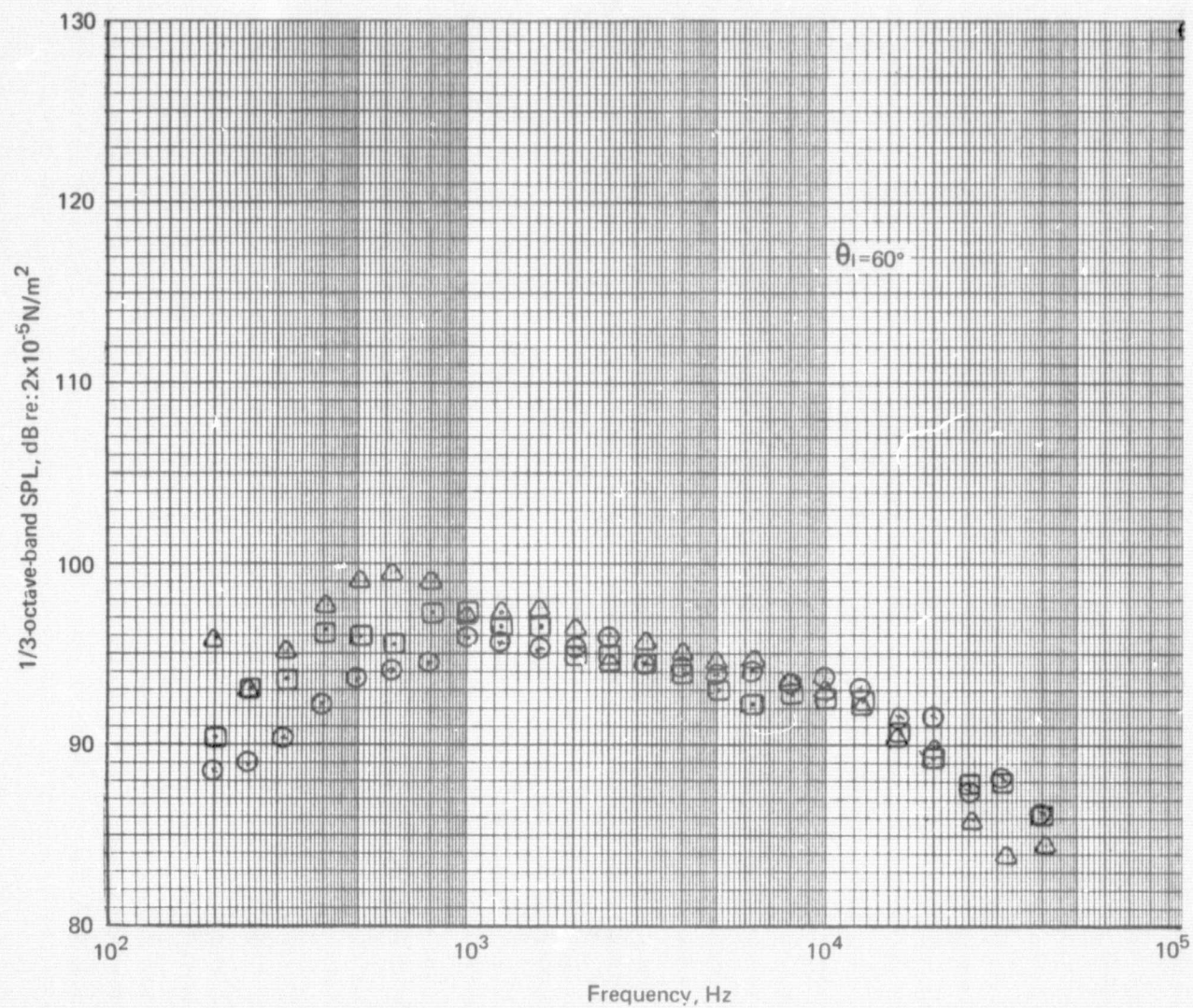


Figure 48.—(Continued)

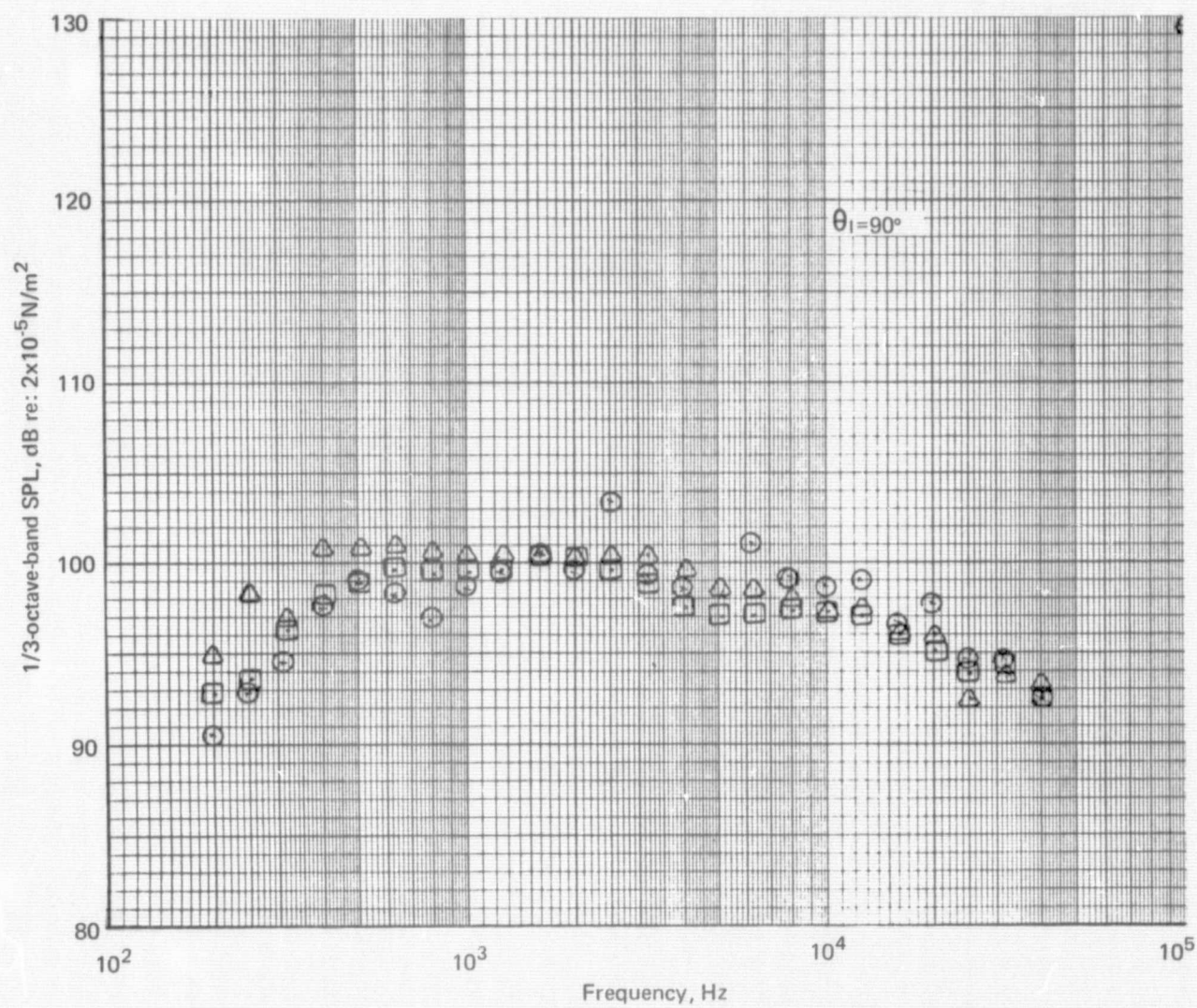


Figure 48.—(Continued)

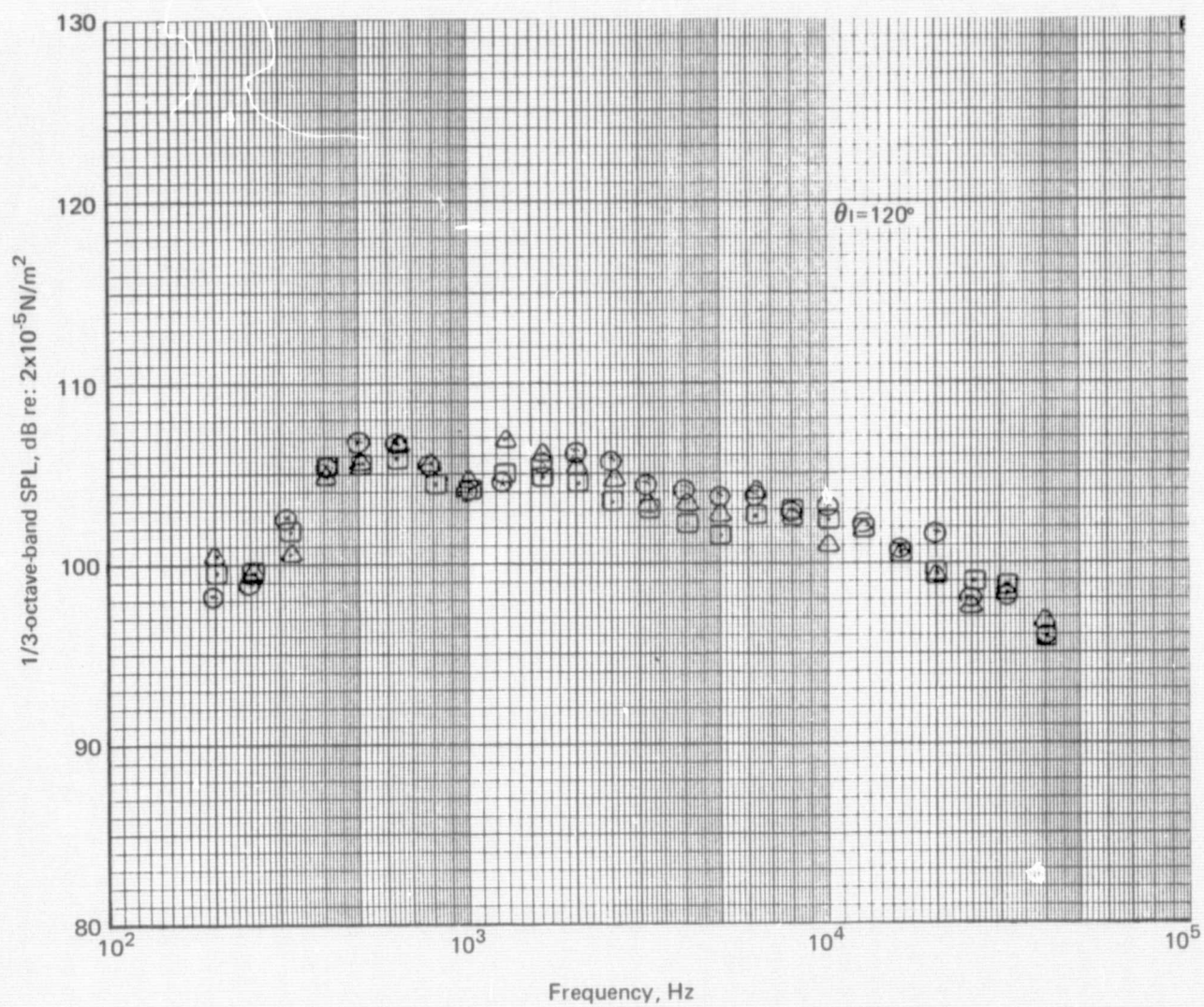


Figure 48.—(Continued)

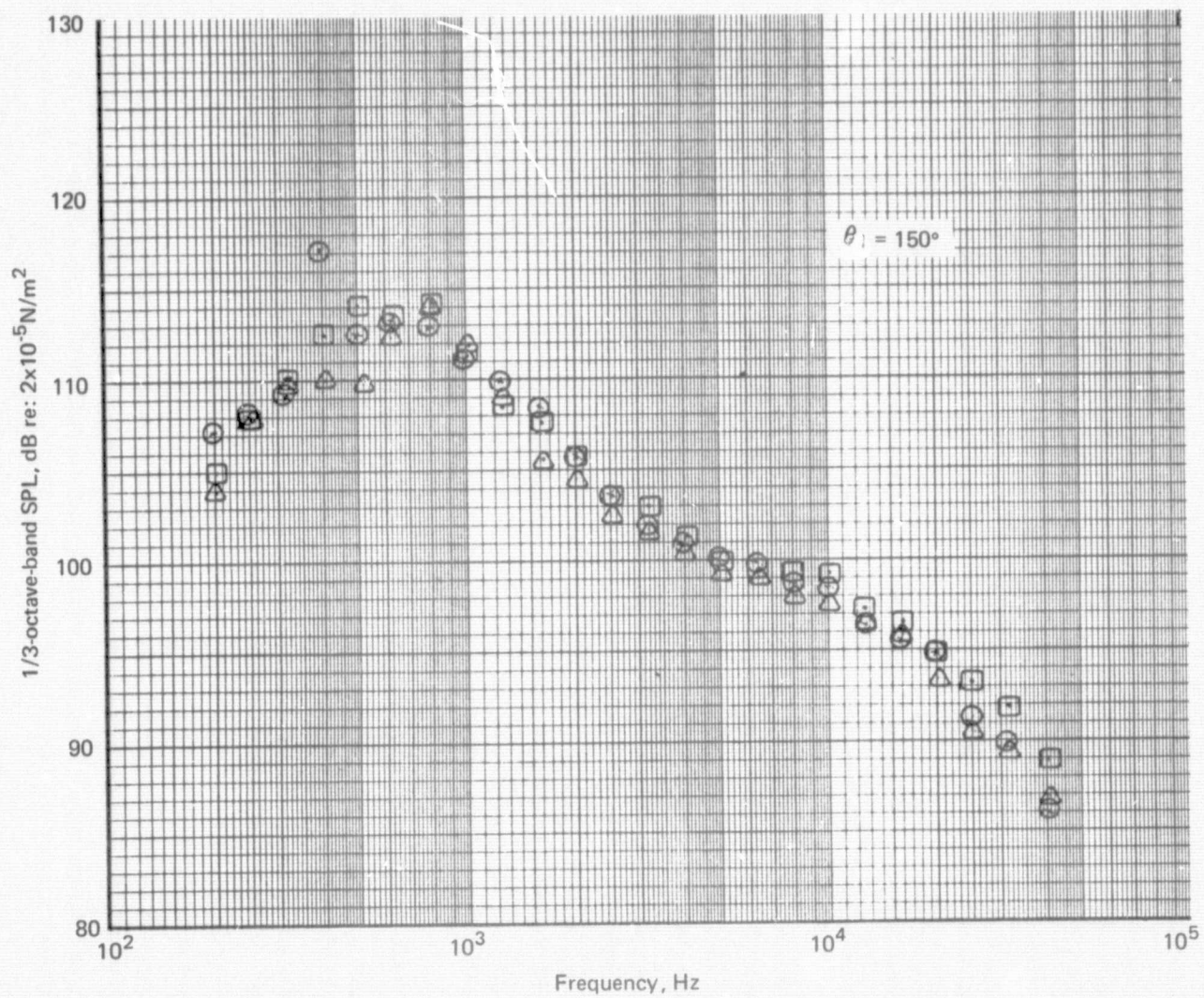


Figure 48.—(Concluded)

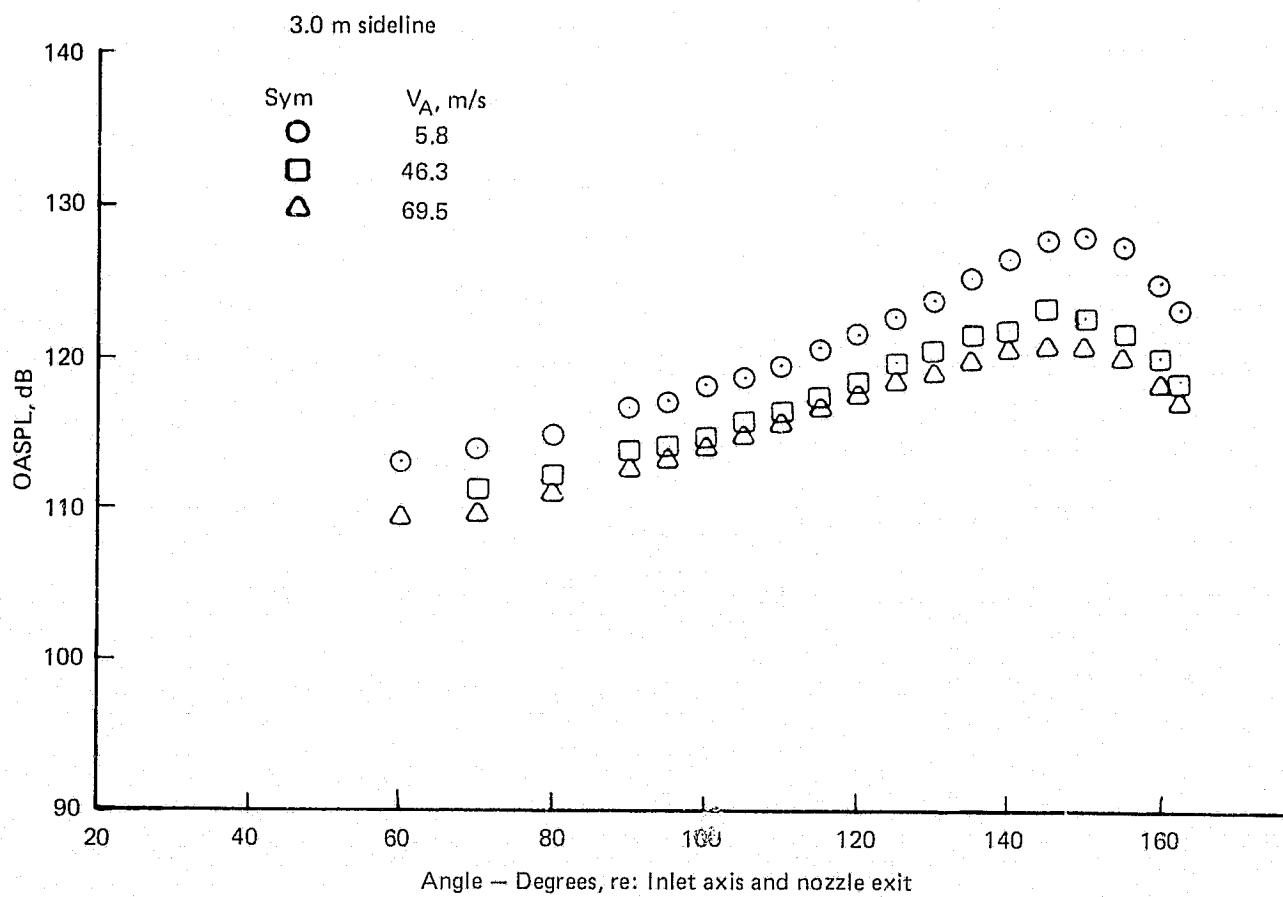


Figure 49.— Effect of Ambient Velocity on Jet Noise OASPL and 1/3-OBSPL Spectra for an Annular Nozzle NPR = 1.75

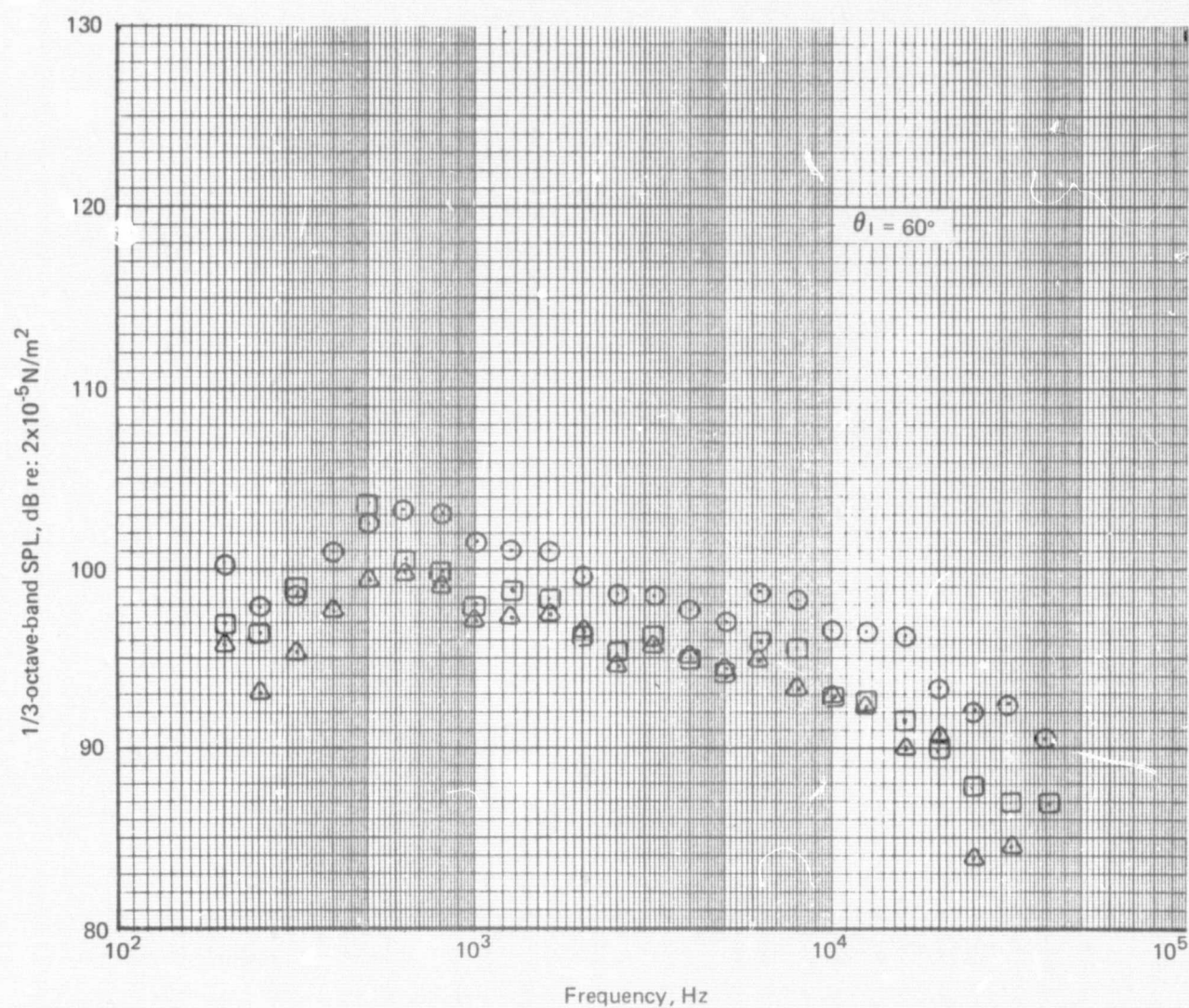


Figure 49.—(Continued)

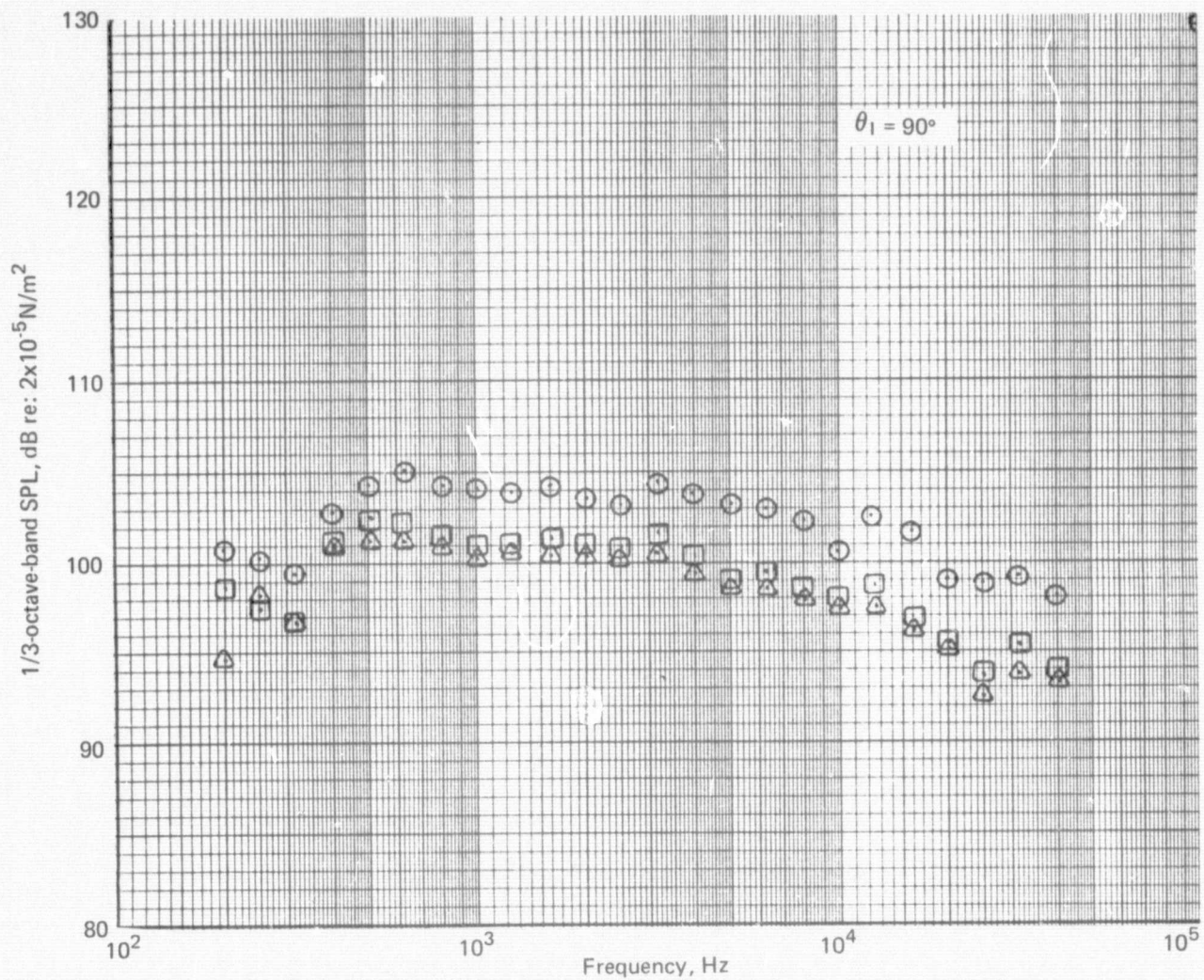


Figure 49.—(Continued)

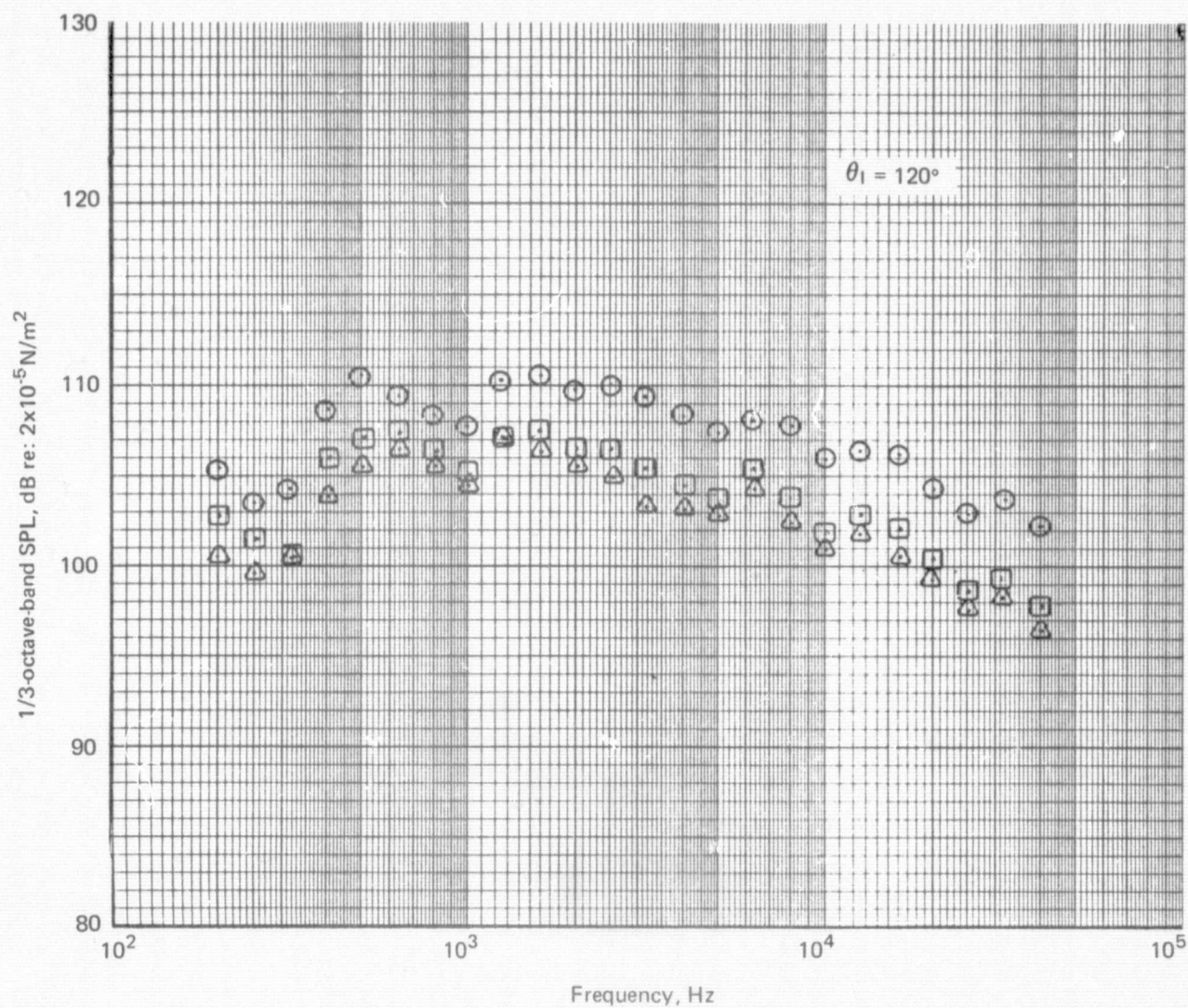


Figure 49.—(Continued)

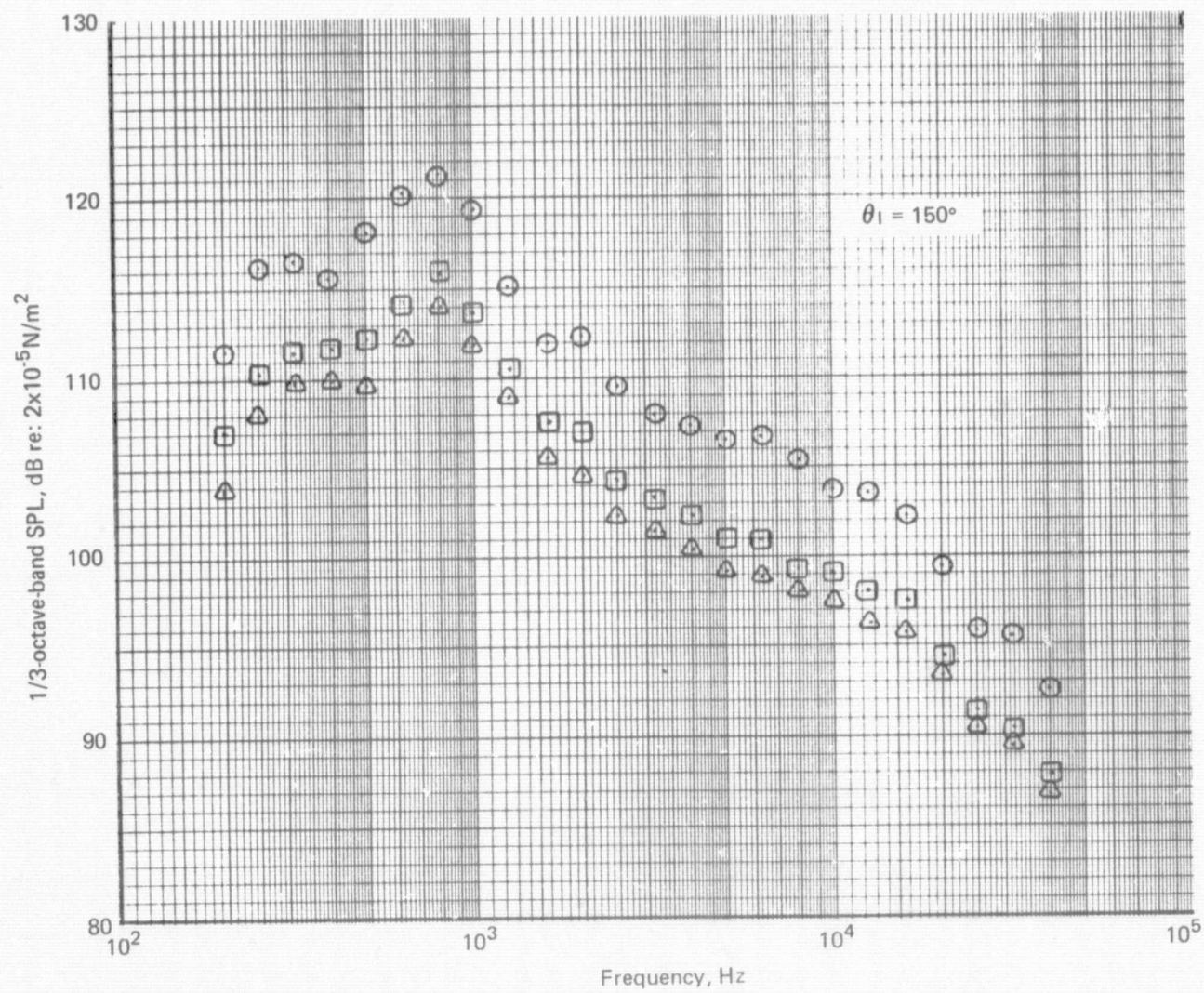


Figure 49.—(Concluded)

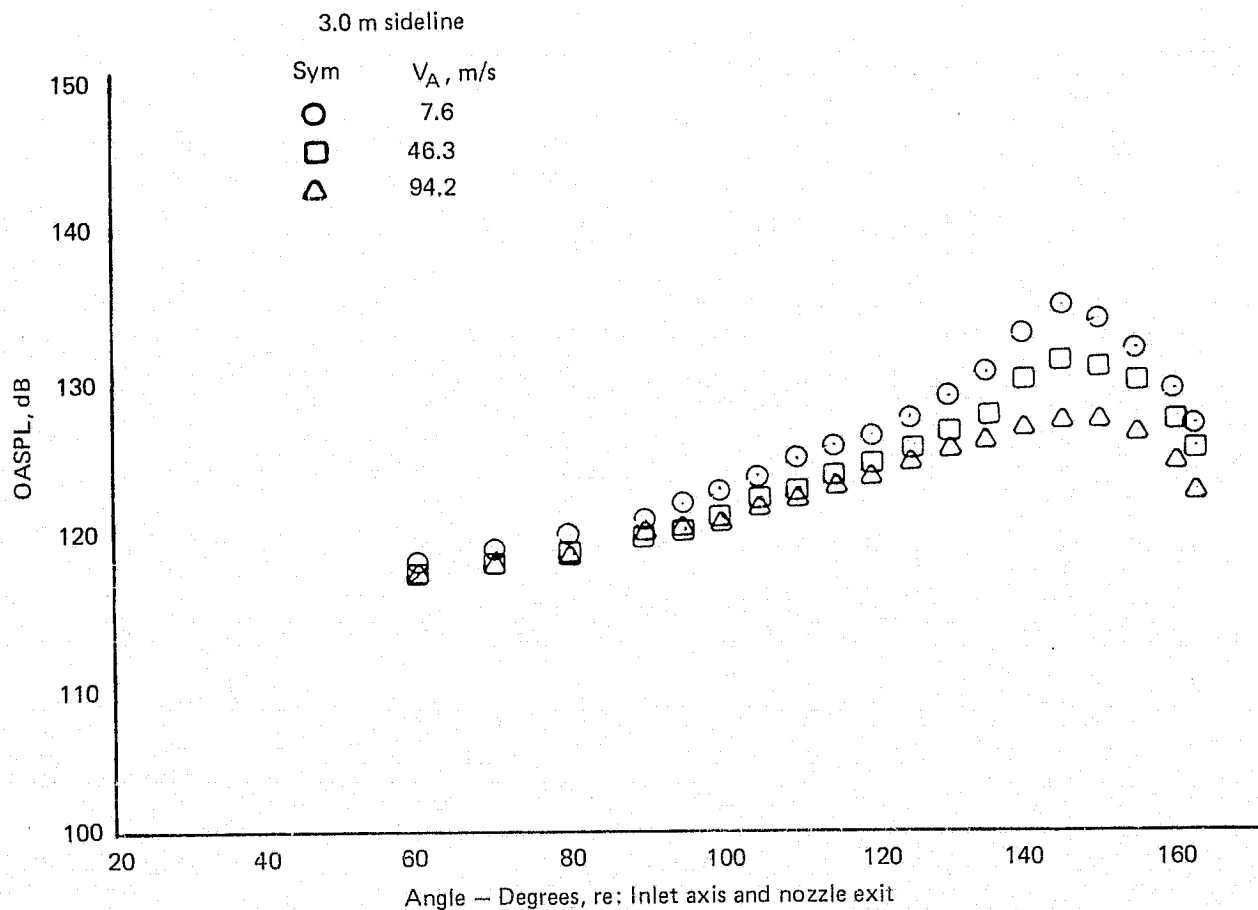


Figure 50.— Effect of Ambient Velocity on Jet Noise OASPL and 1/3-OB SPL Spectra, NPR = 2.25

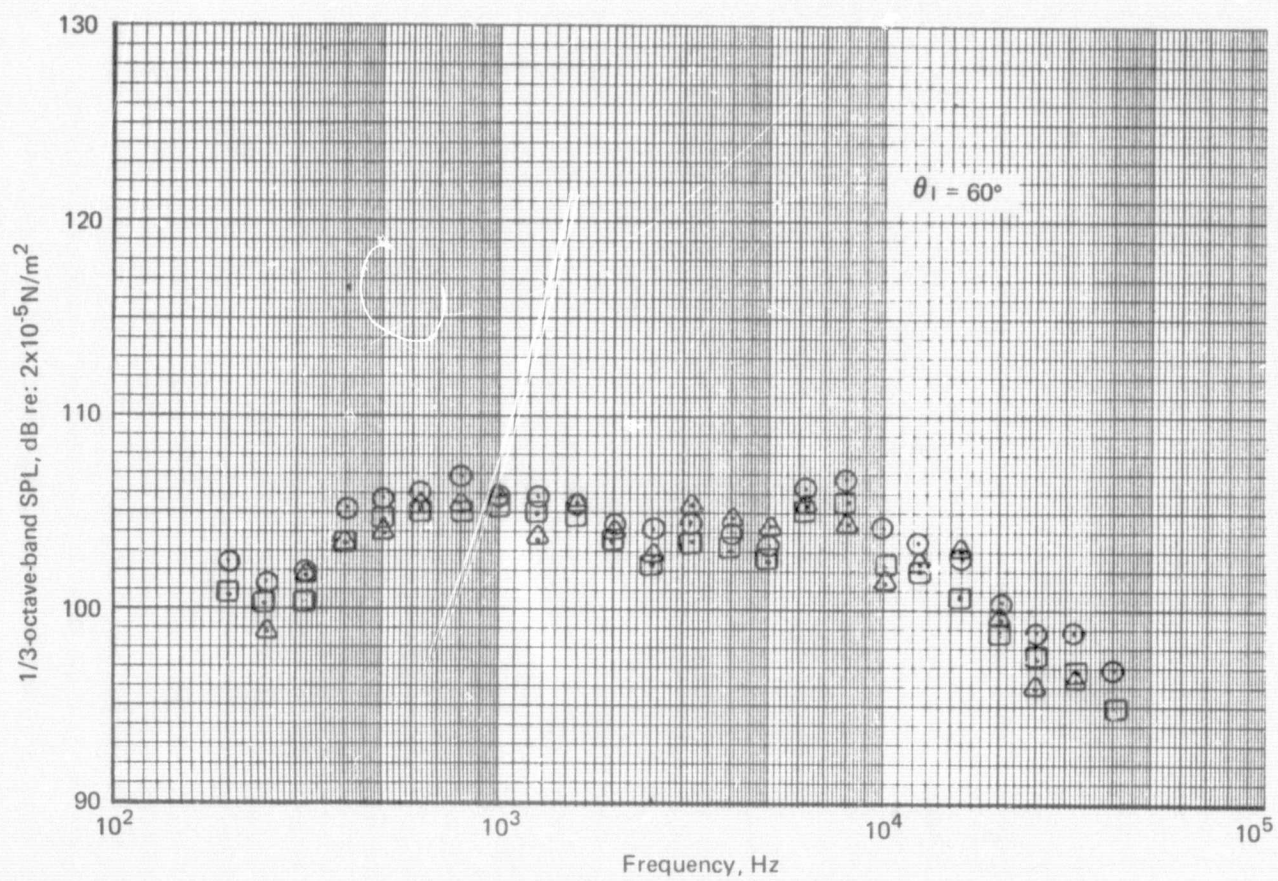


Figure 50.—(Continued)

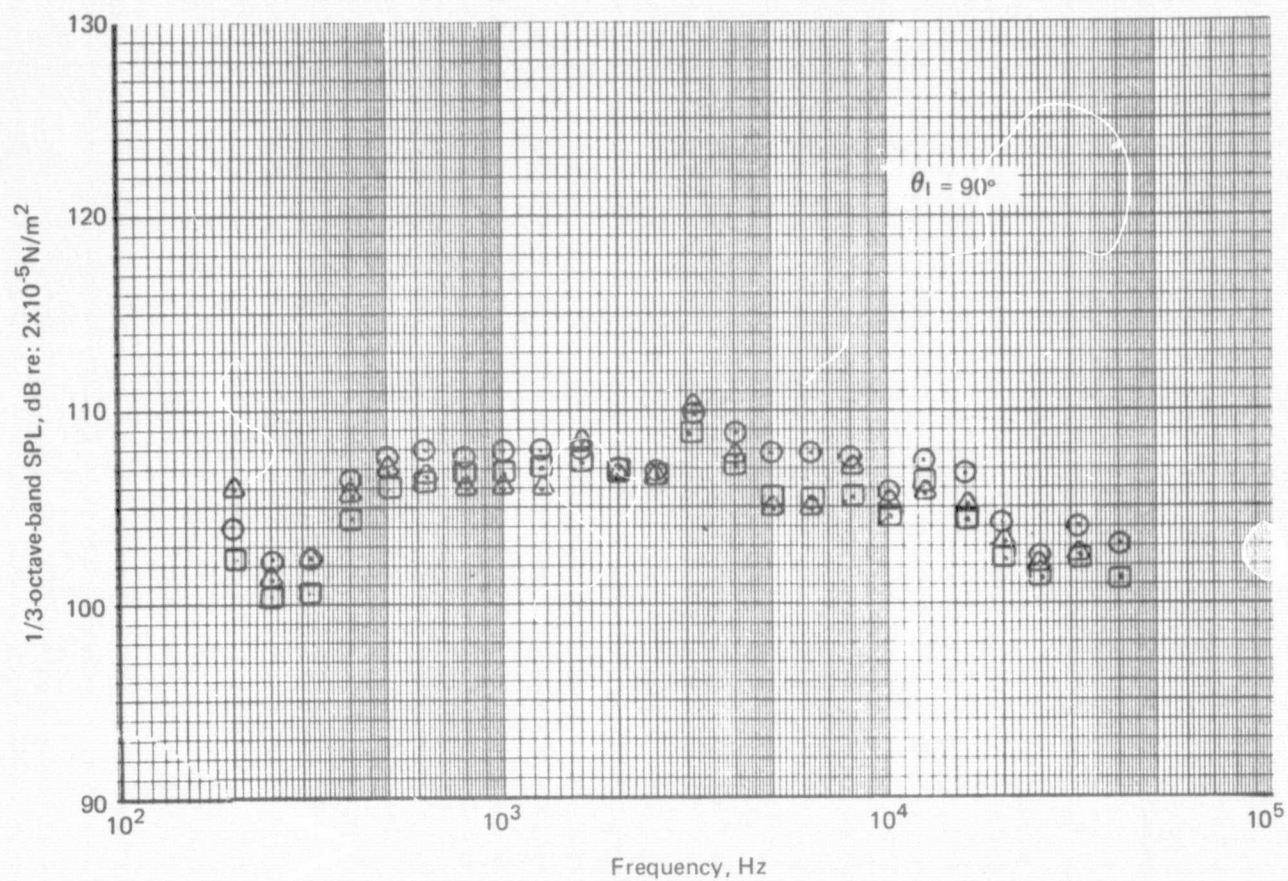


Figure 50.—(Continued)

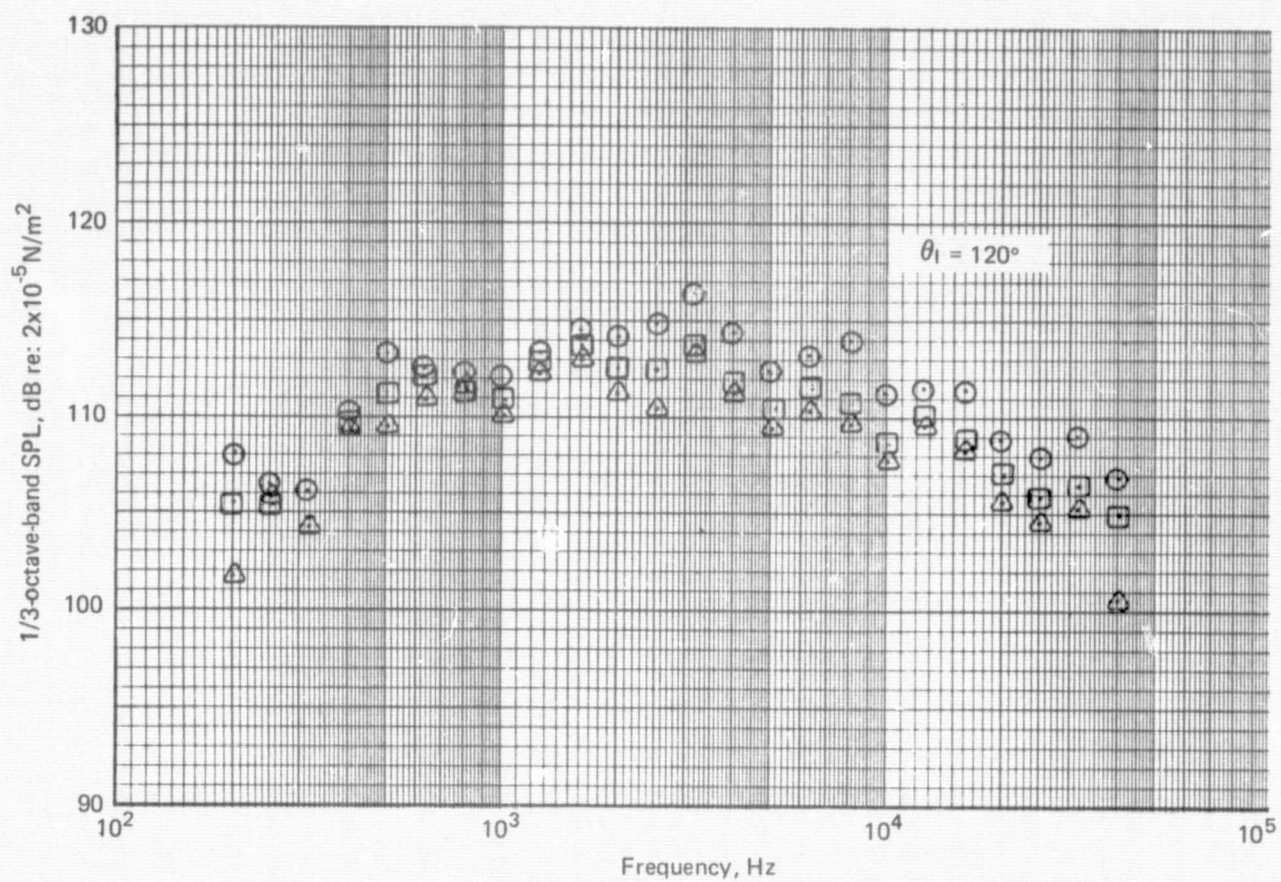


Figure 50.—(Continued)

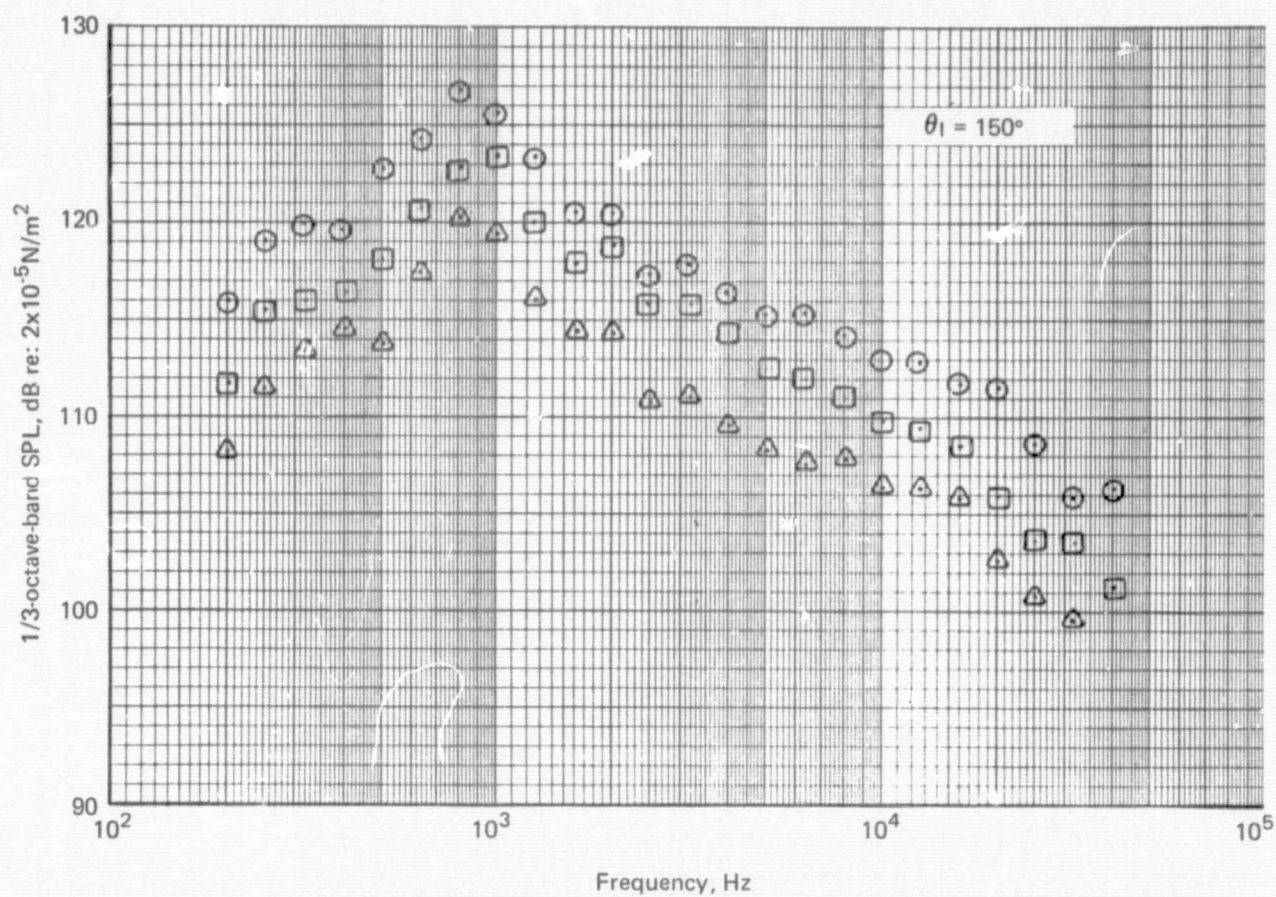


Figure 50.--(Concluded)

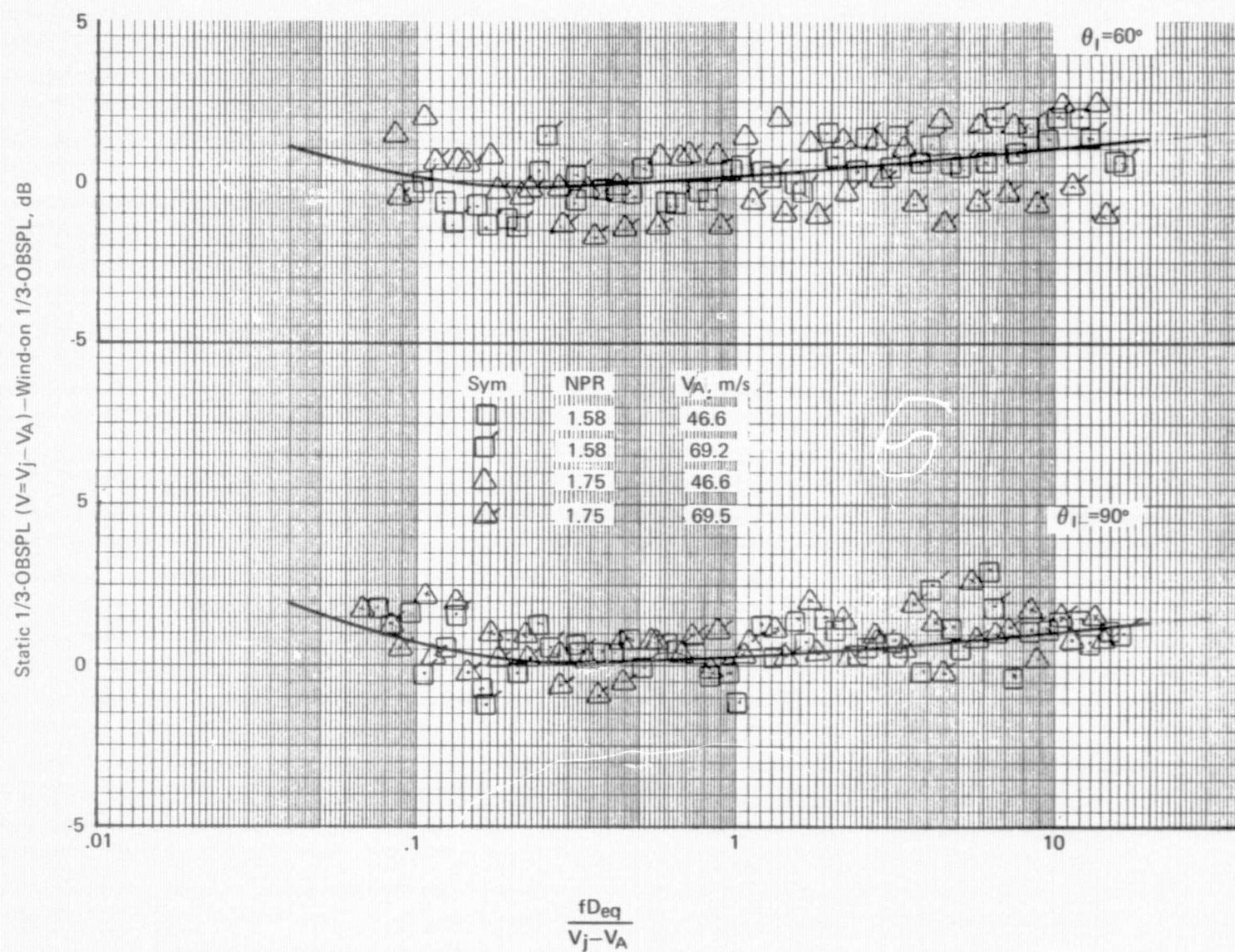


Figure 51.—Effect of Ambient Velocity on Subsonic Jet Noise Spectra of an Annular Nozzle Referenced to the Static Case Where $V=V_j-V_A$, $T_T=844K$, 3.0 m Sideline

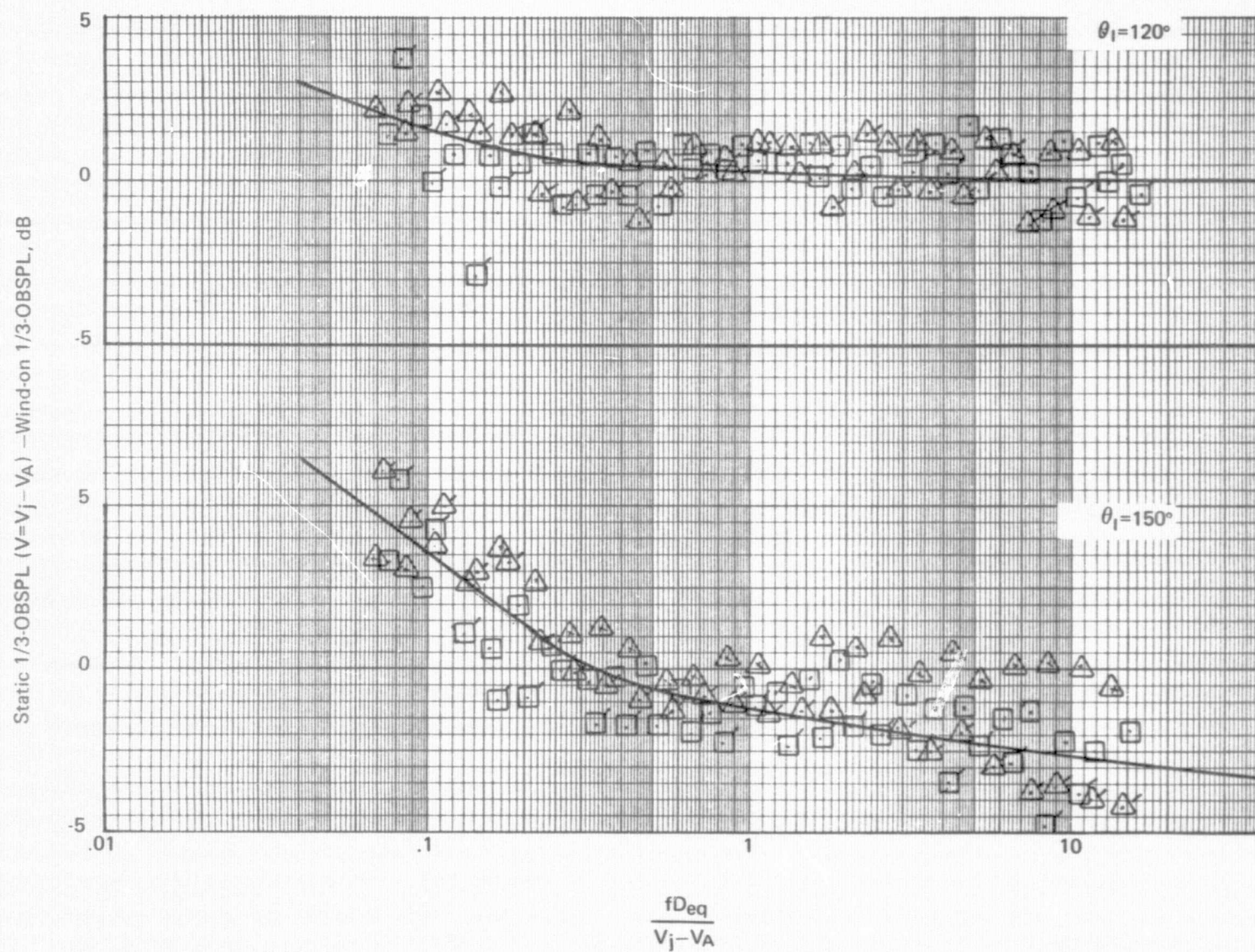


Figure 51.—(Concluded)

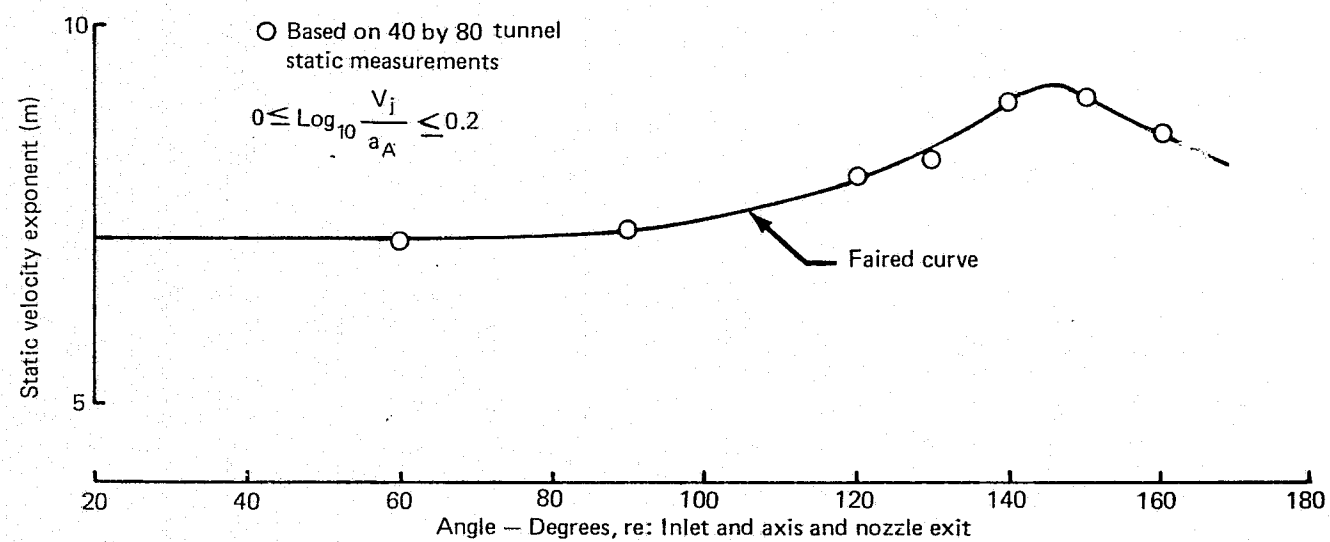


Figure 52.— Static Velocity for an Annular Nozzle

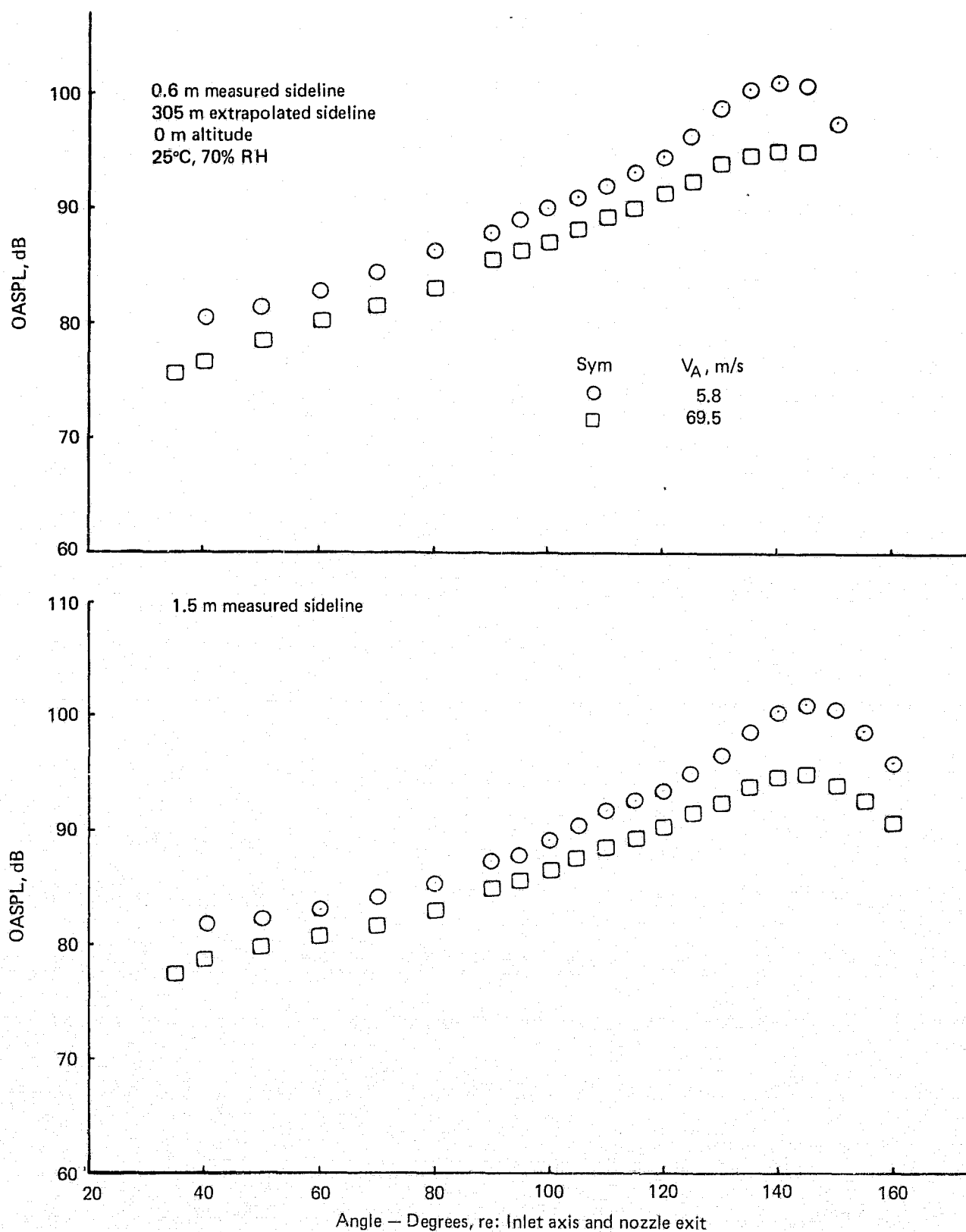


Figure 53.— Flight Effects on OASPL of an Annular Nozzle $NPR = 1.75$, $V_j = 503$ m/s

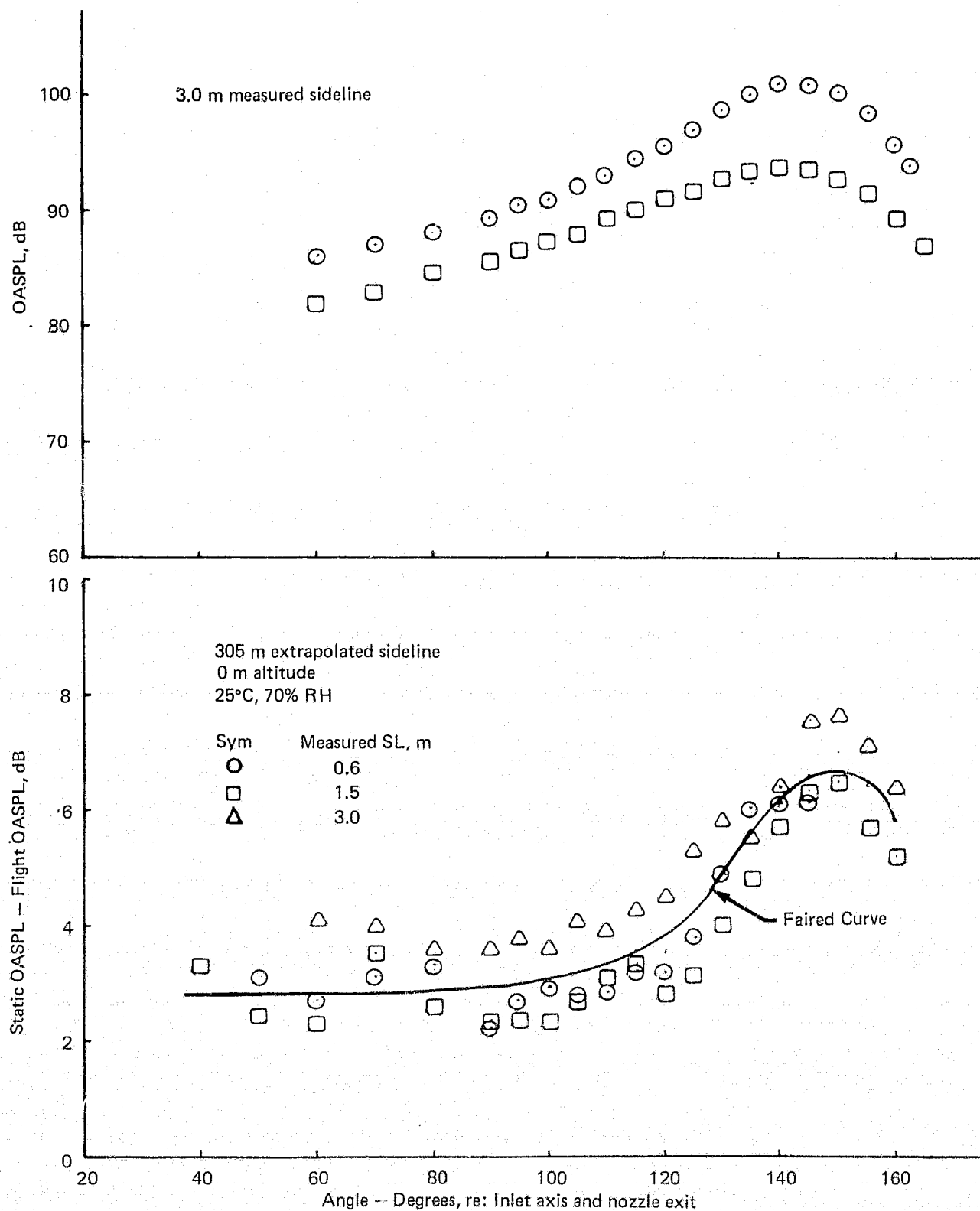


Figure 53.— (Concluded)

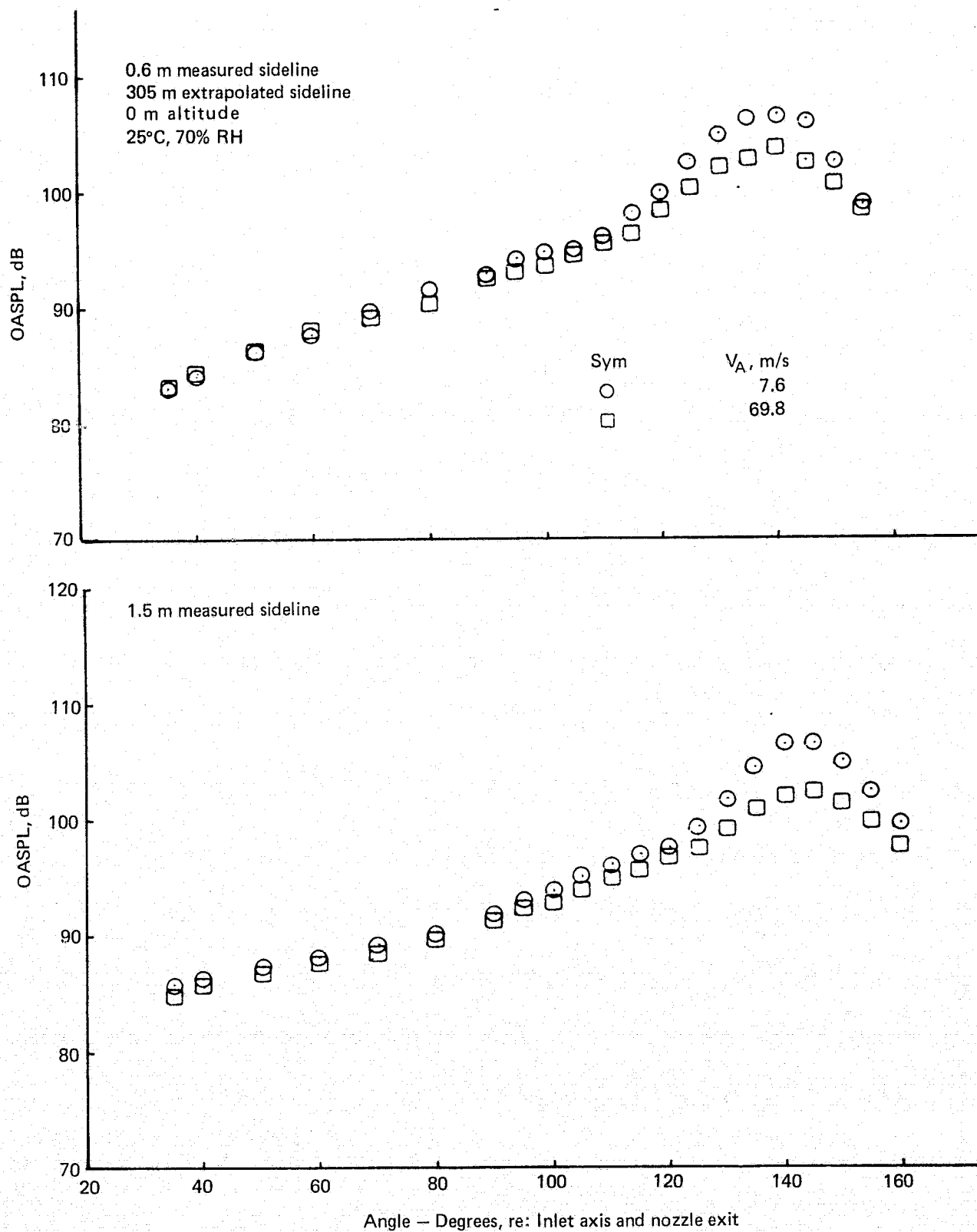


Figure 54.— Flight Effects on OASPL of an Annular Nozzle $NPR = 2.25$, $V_j = 594$ m/s

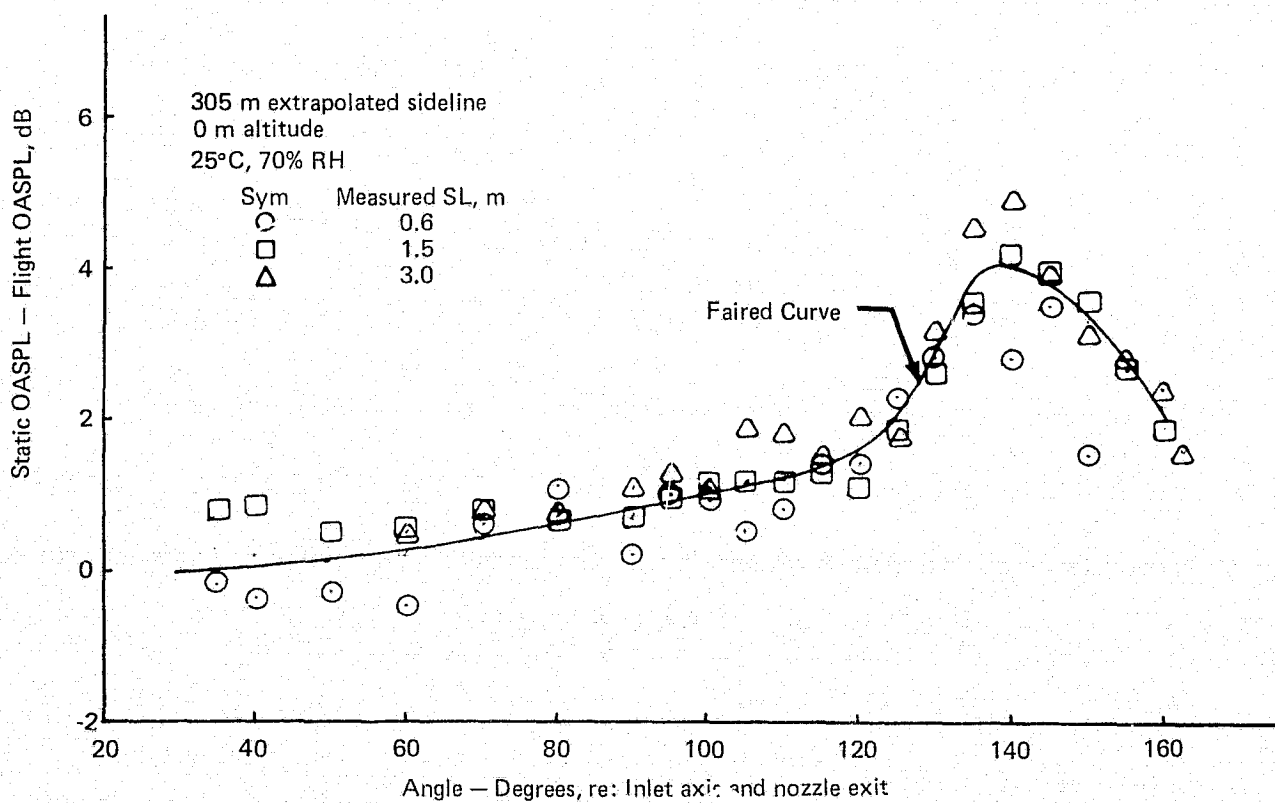
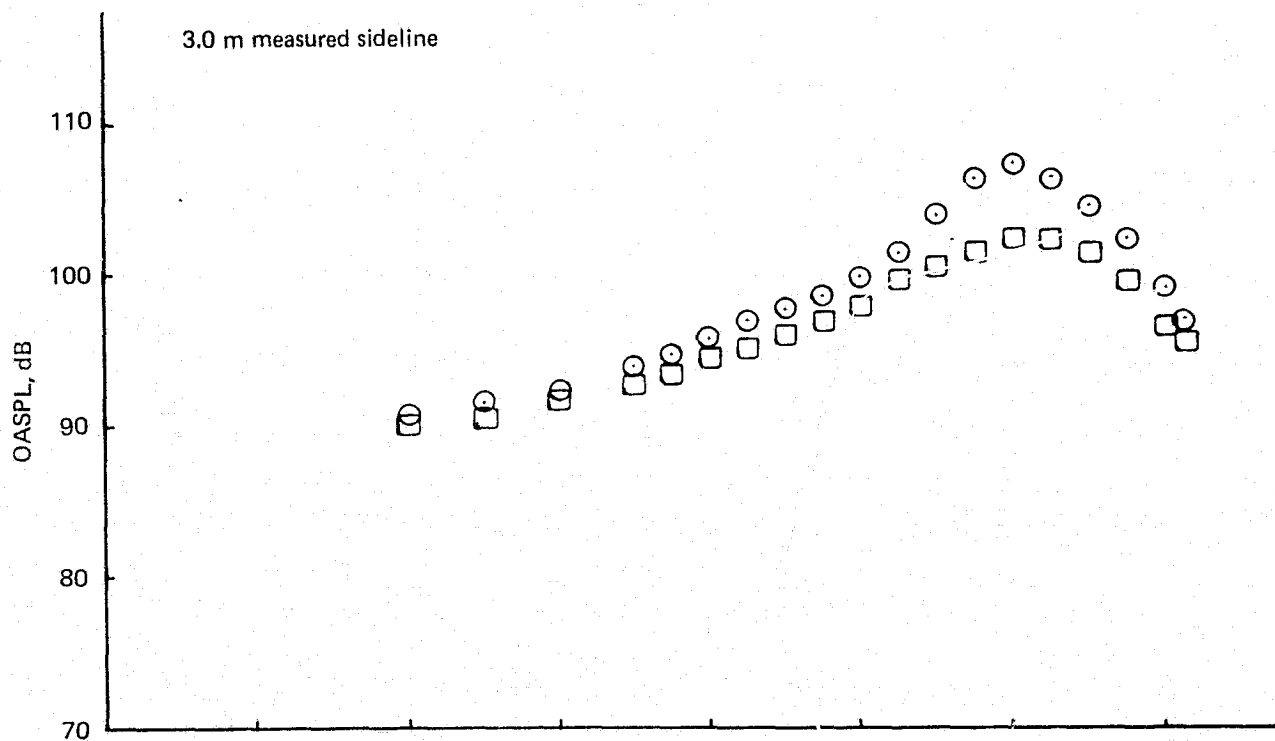


Figure 54.— (Concluded)

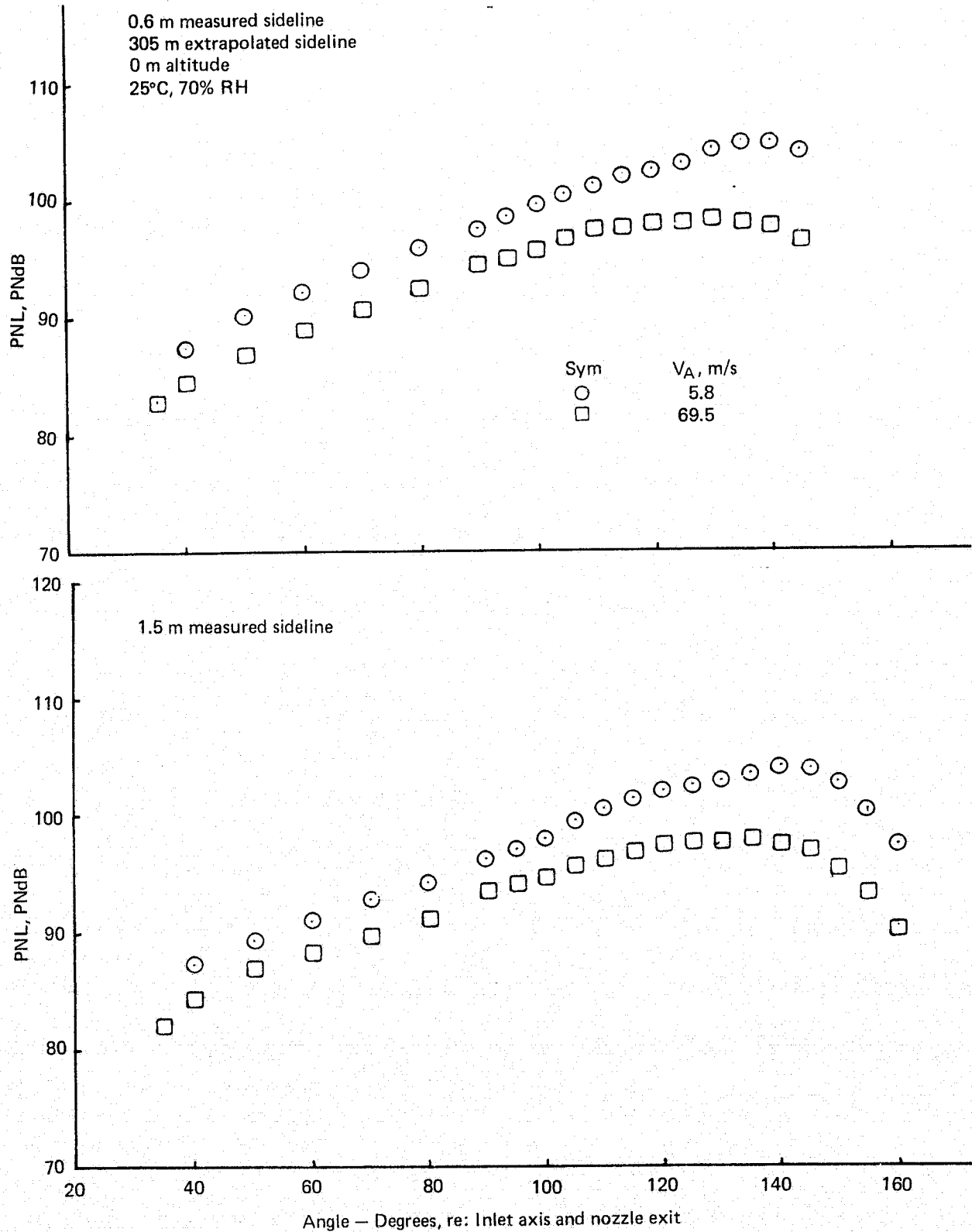


Figure 55.— Flight Effects on PNL of an Annular Nozzle $NPR = 1.75$, $V_j = 503$ m/s

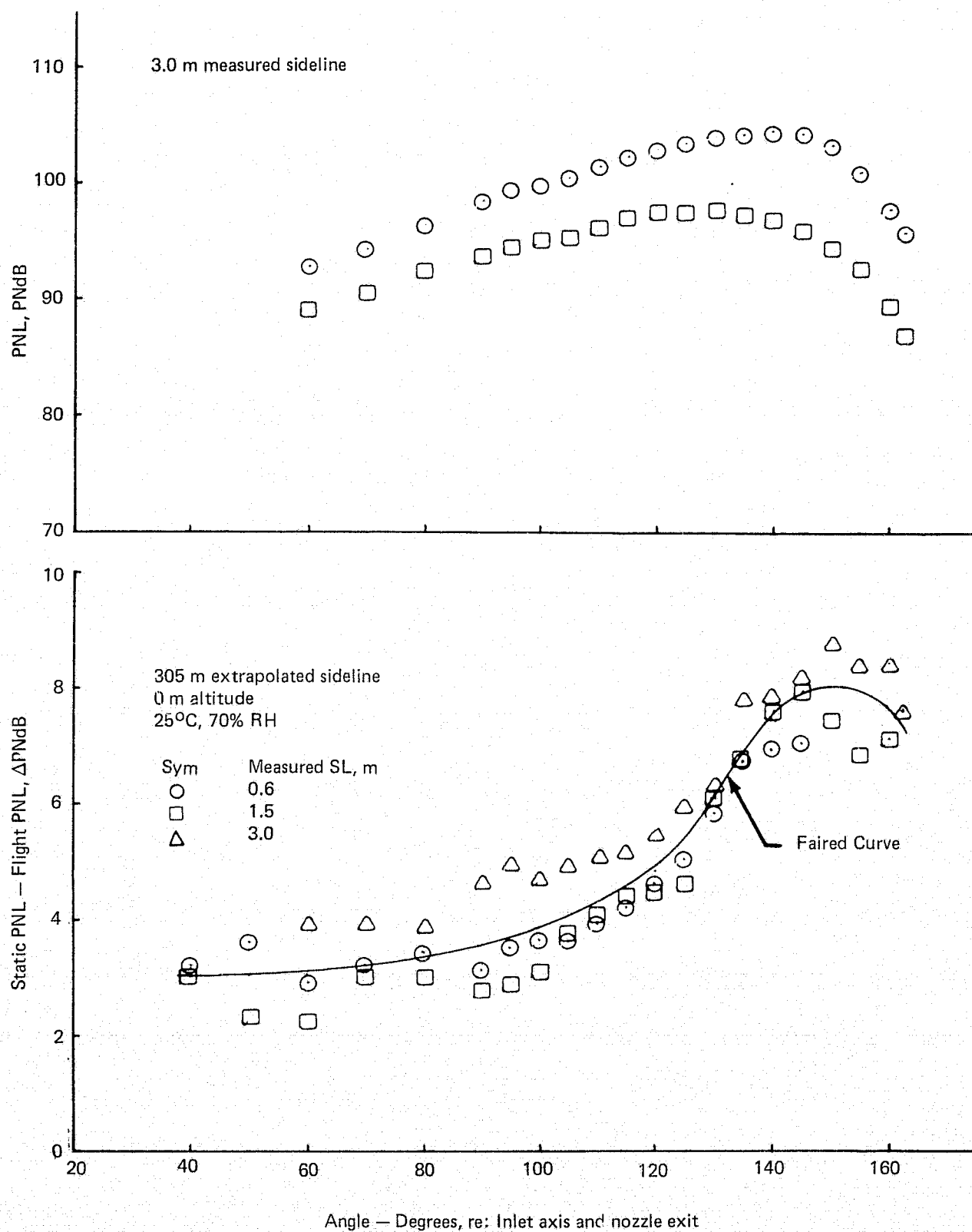


Figure 55.— (Concluded)

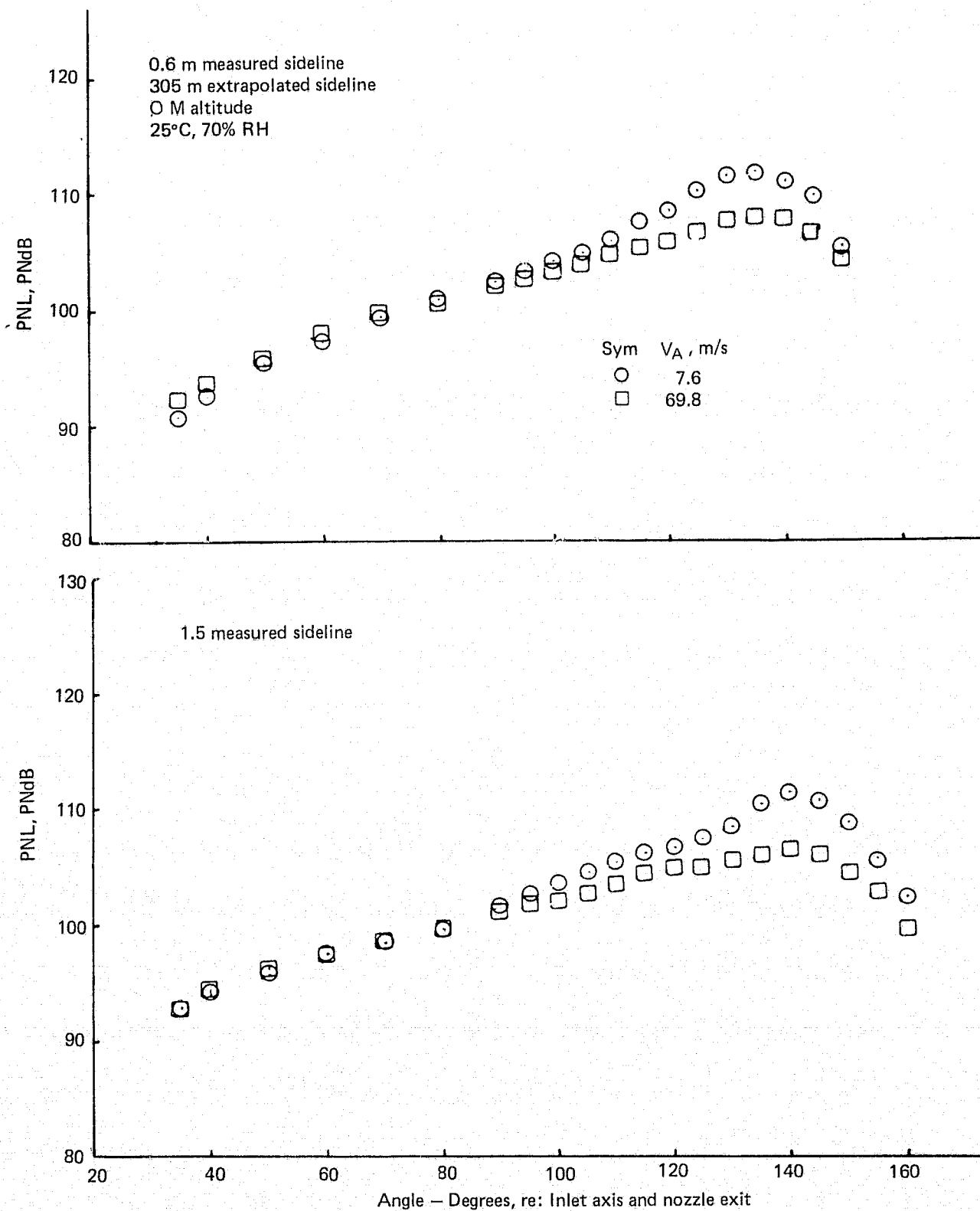


Figure 56.— Flight Effects on PNL of an Annular Nozzle $NPR = 2.25$, $V_i = 594$ m/s

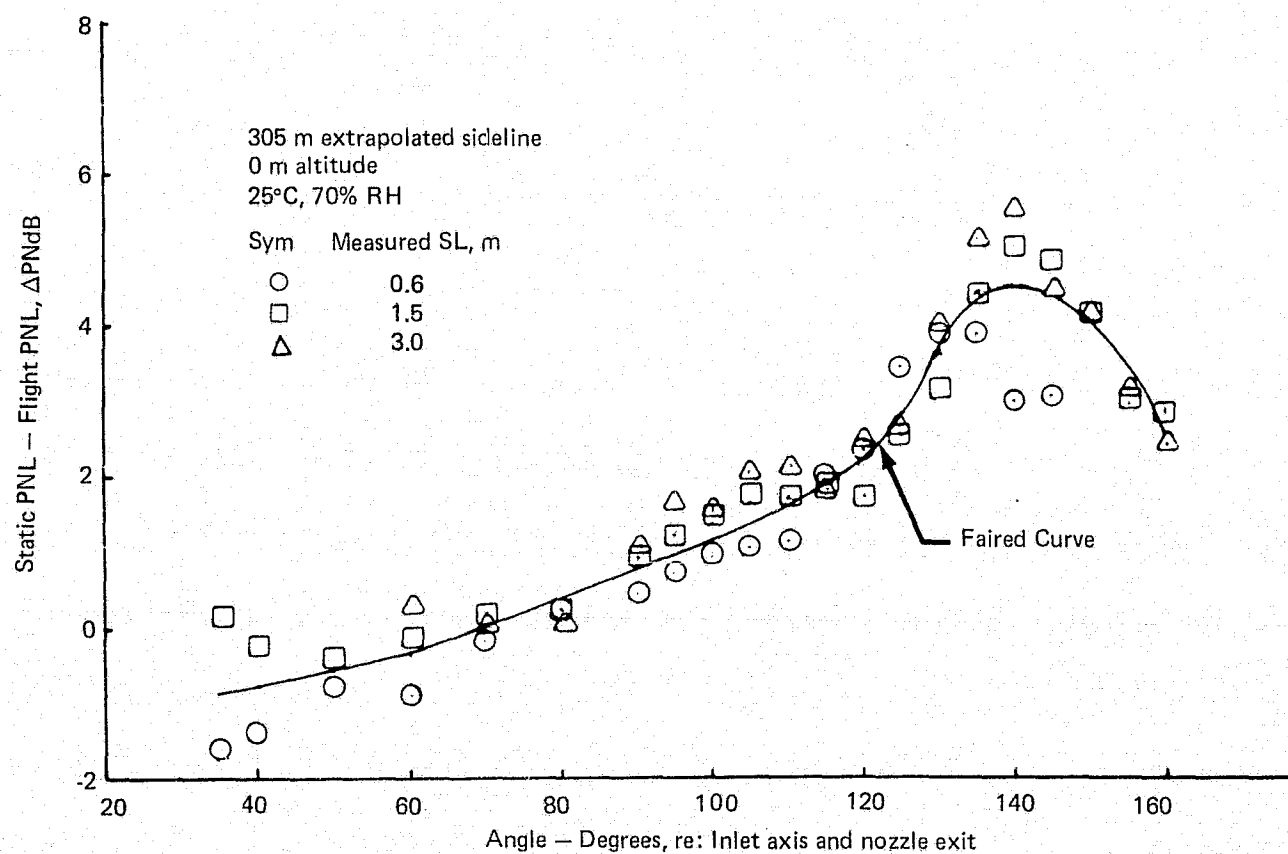
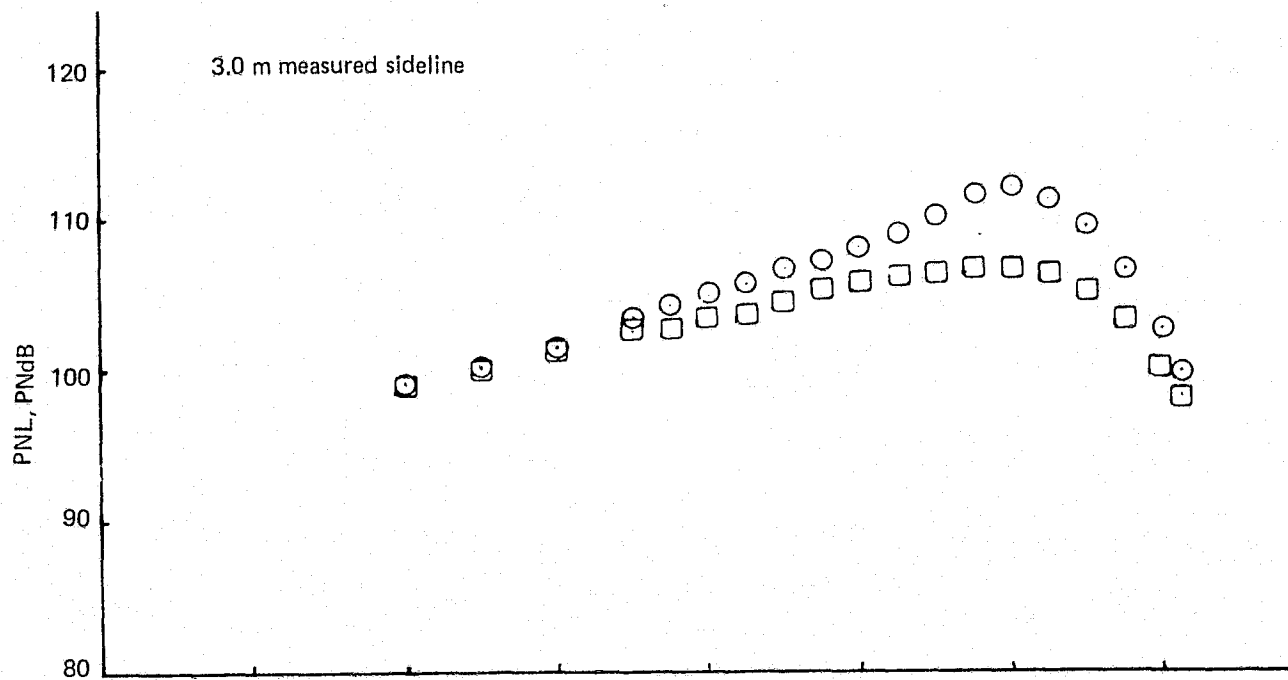


Figure 56.— (Concluded)

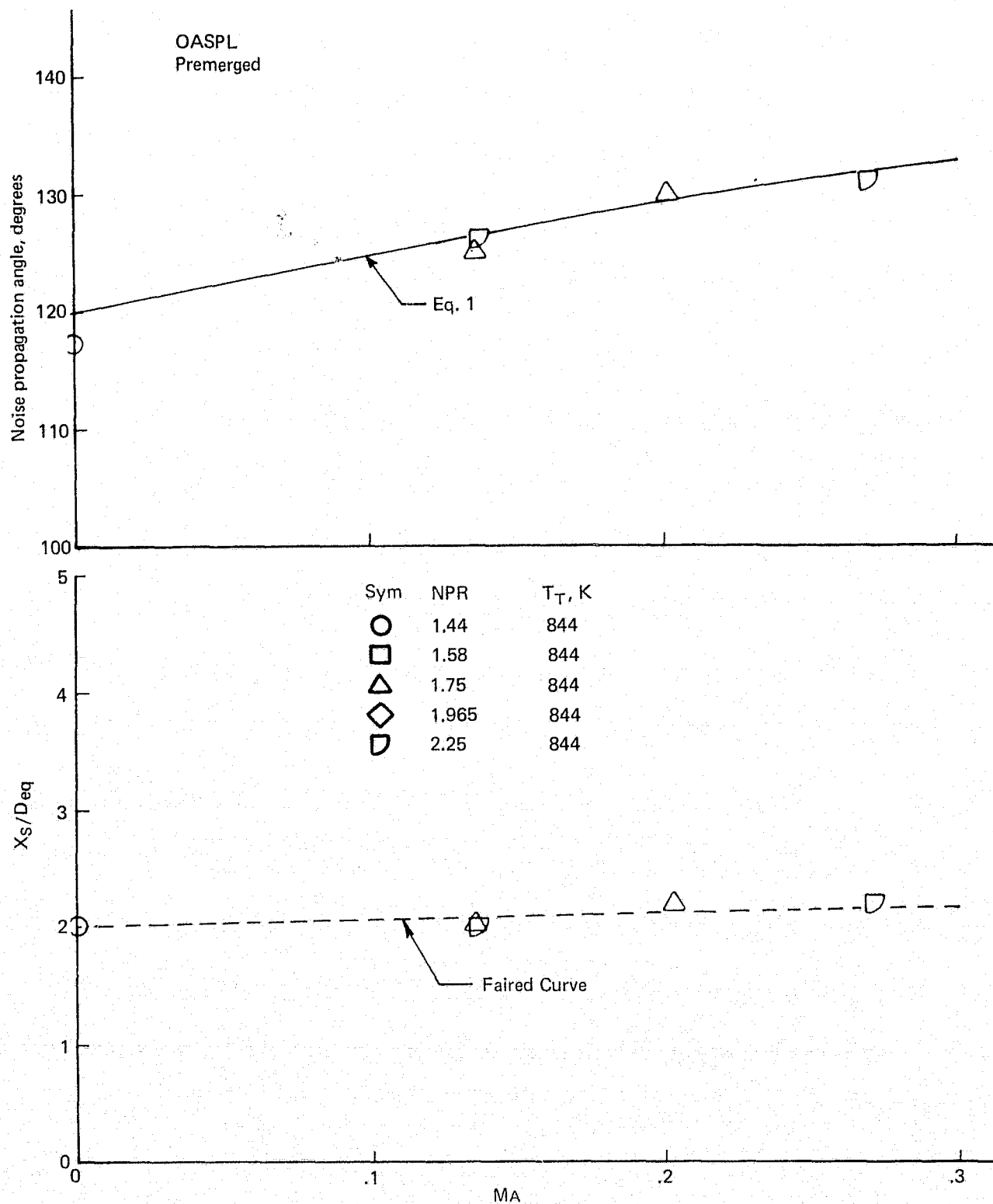


Figure 57.—Peak Noise Source Locations and Noise Propagation Angles for the Bare 20-Lobe Nozzle

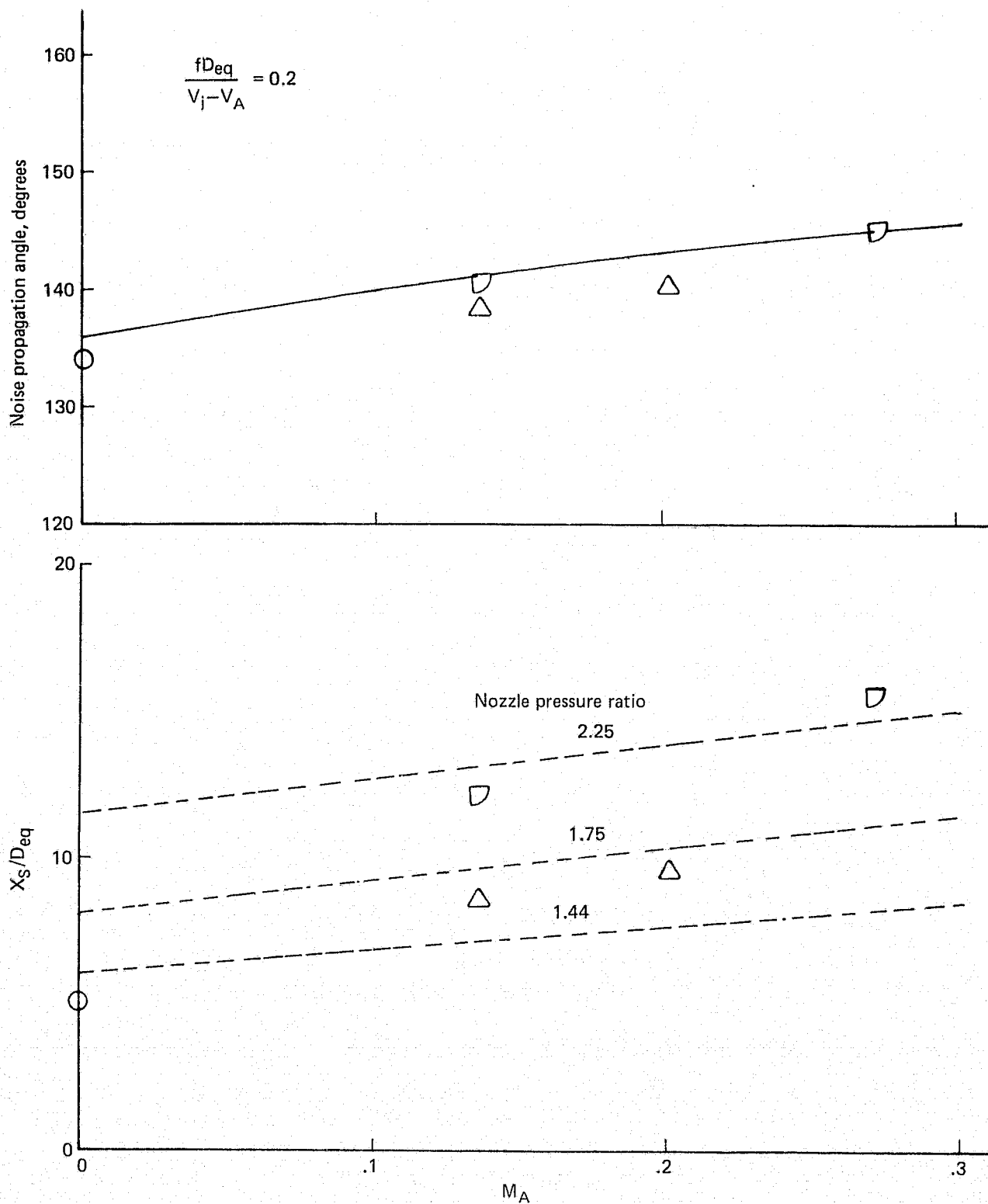


Figure 57.— (Continued)

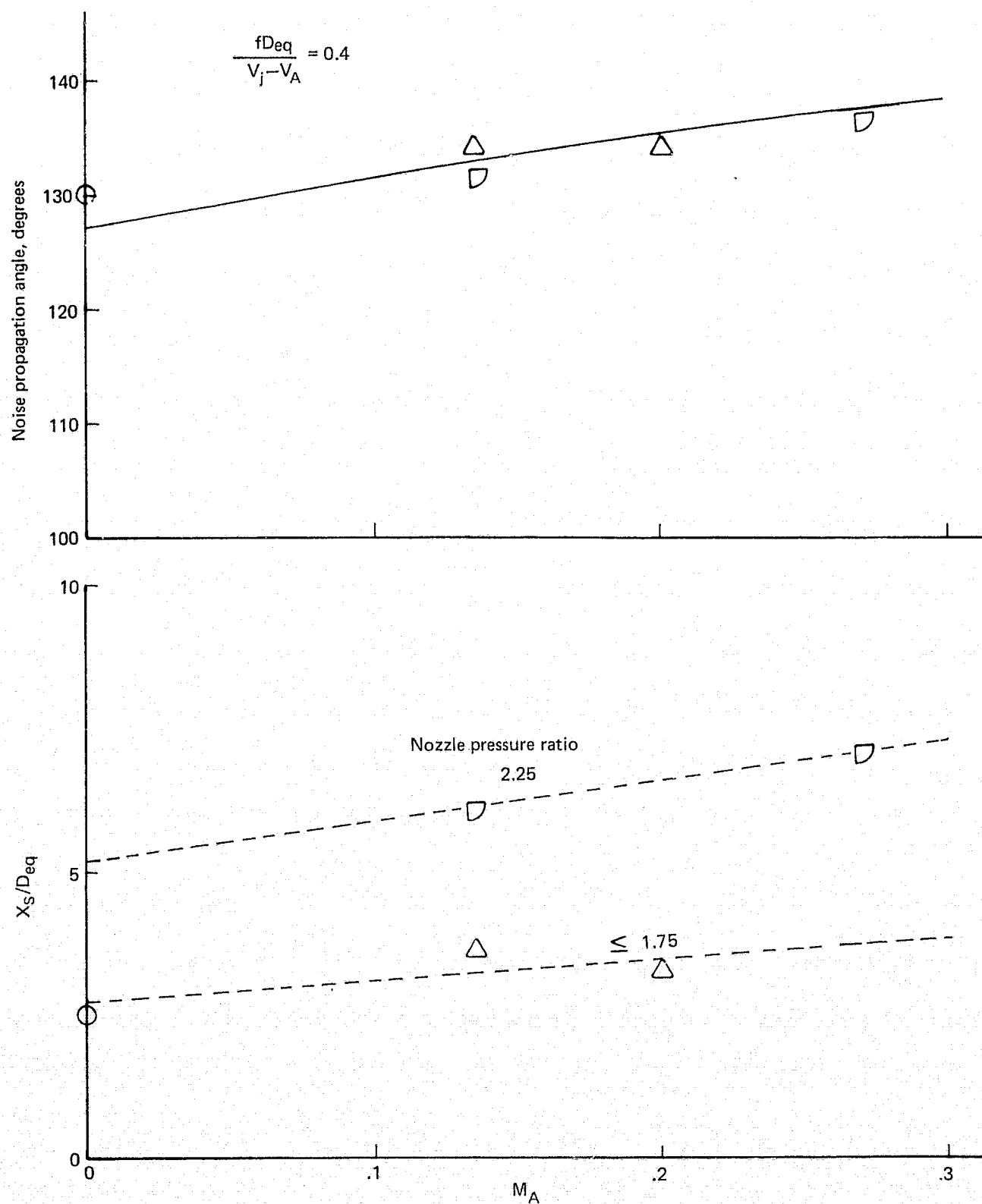


Figure 57.— (Continued)

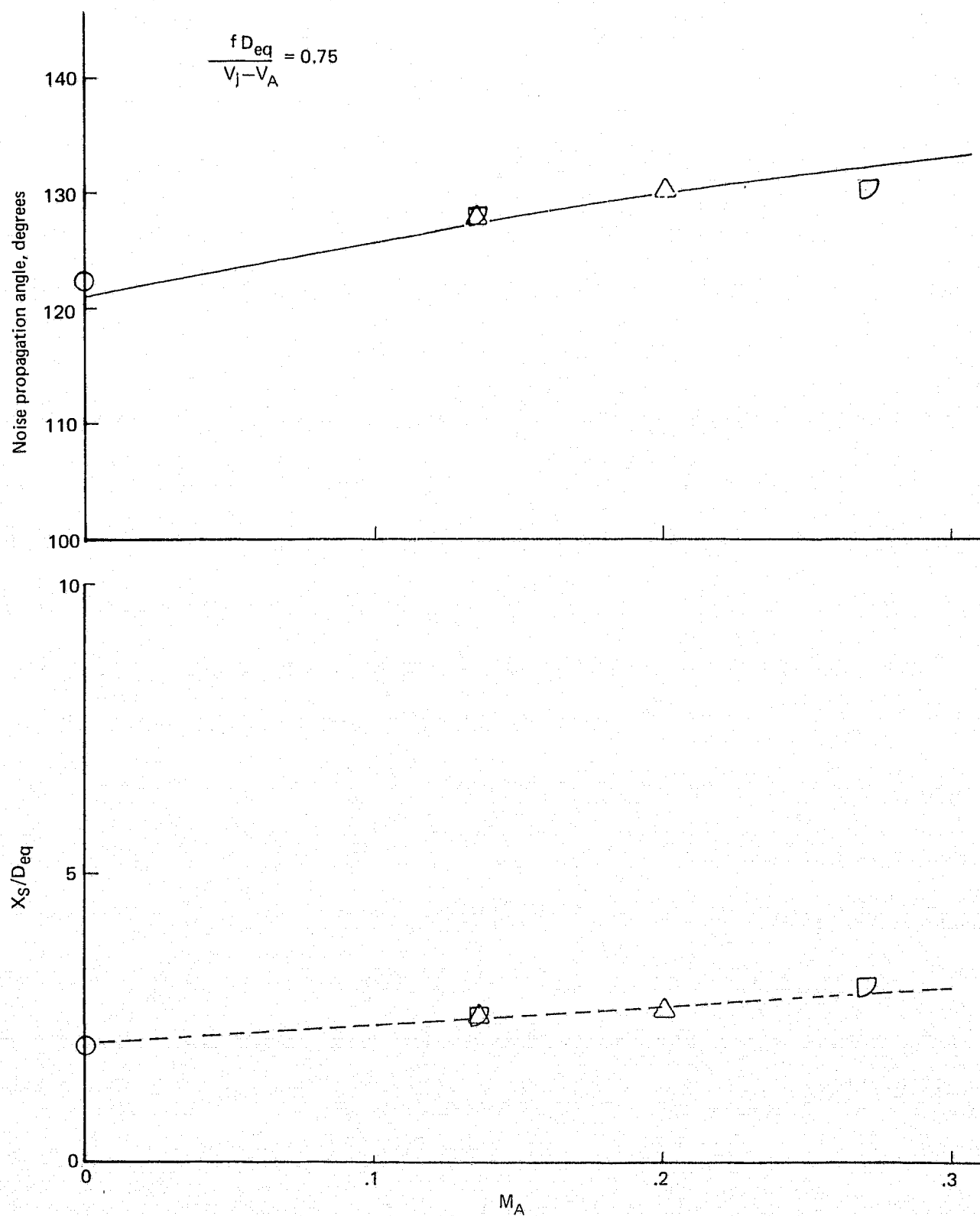


Figure 57.— (Continued)

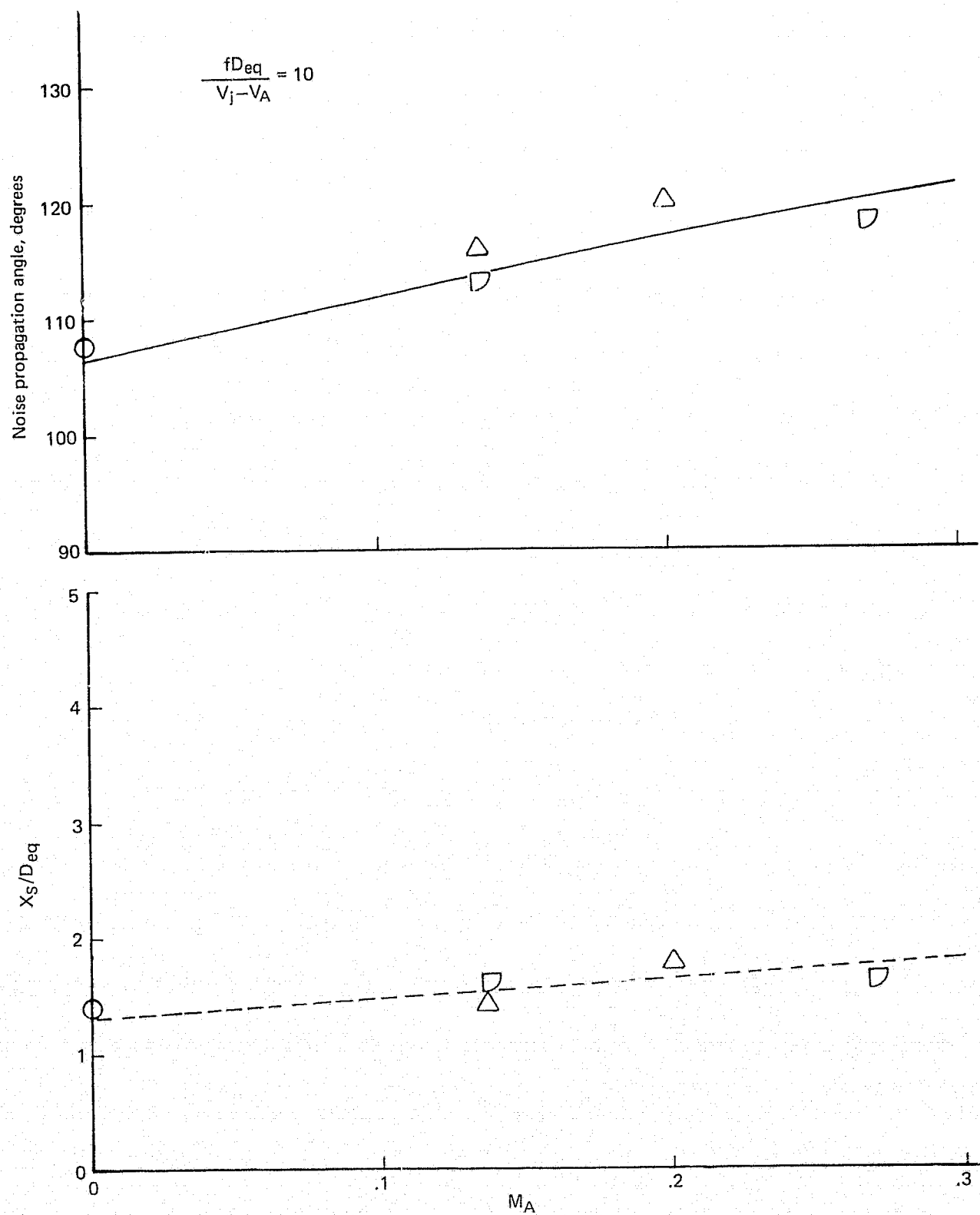


Figure 57.— (Concluded)

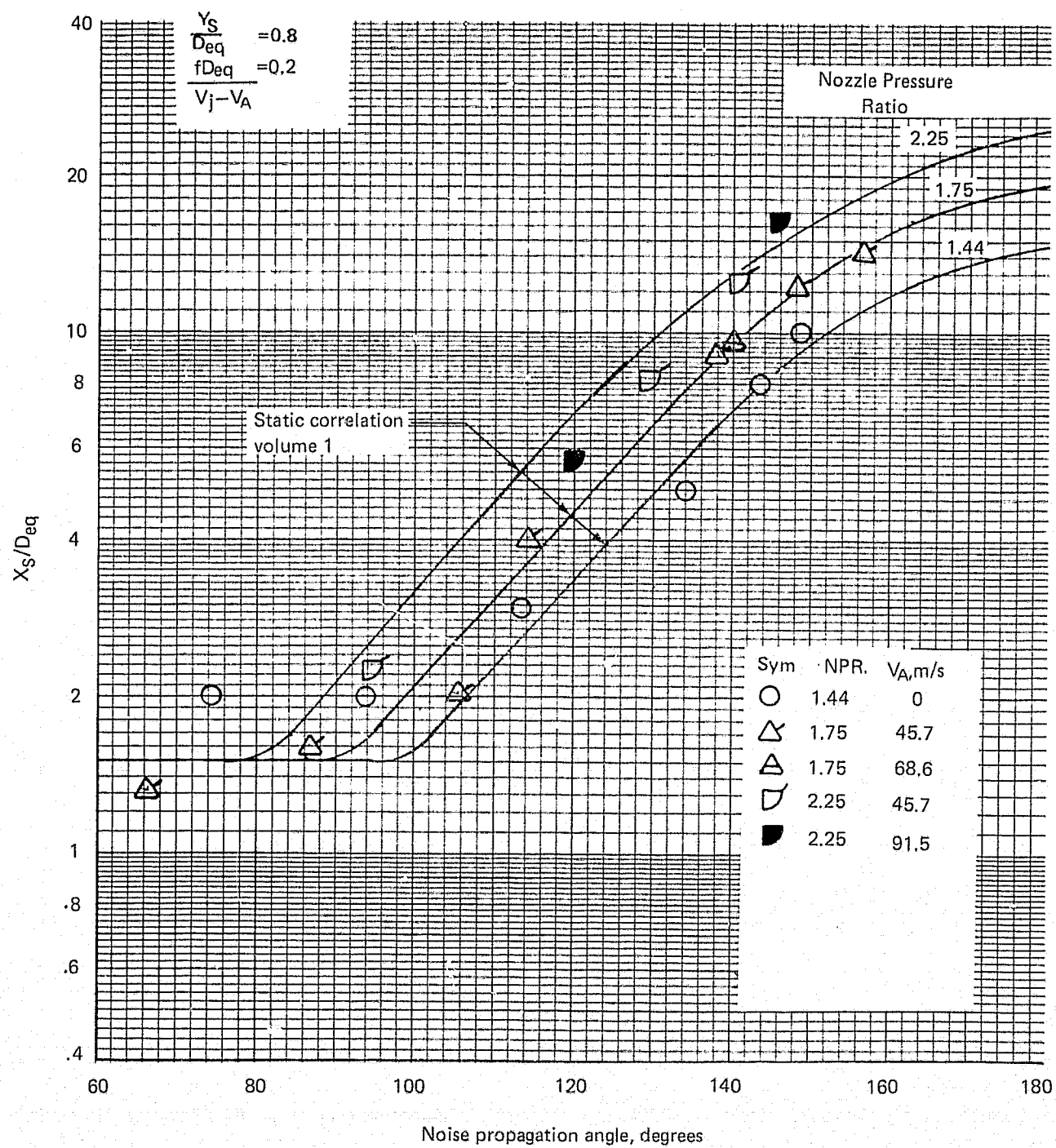


Figure 58.—Effect of Ambient Velocity on the Distributed Noise Source Locations for a 20-Lobe Nozzle

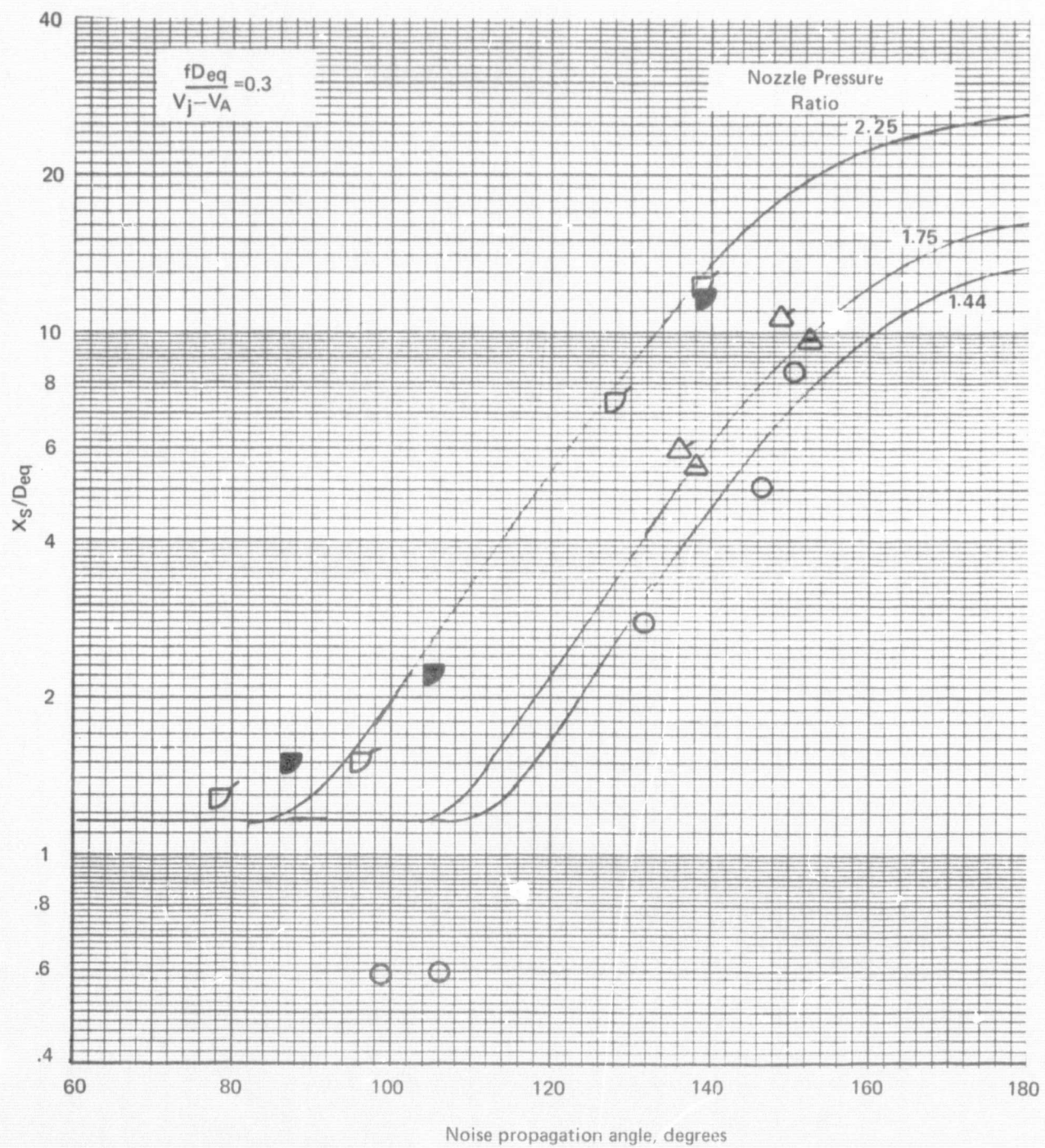


Figure 58.—(Continued)

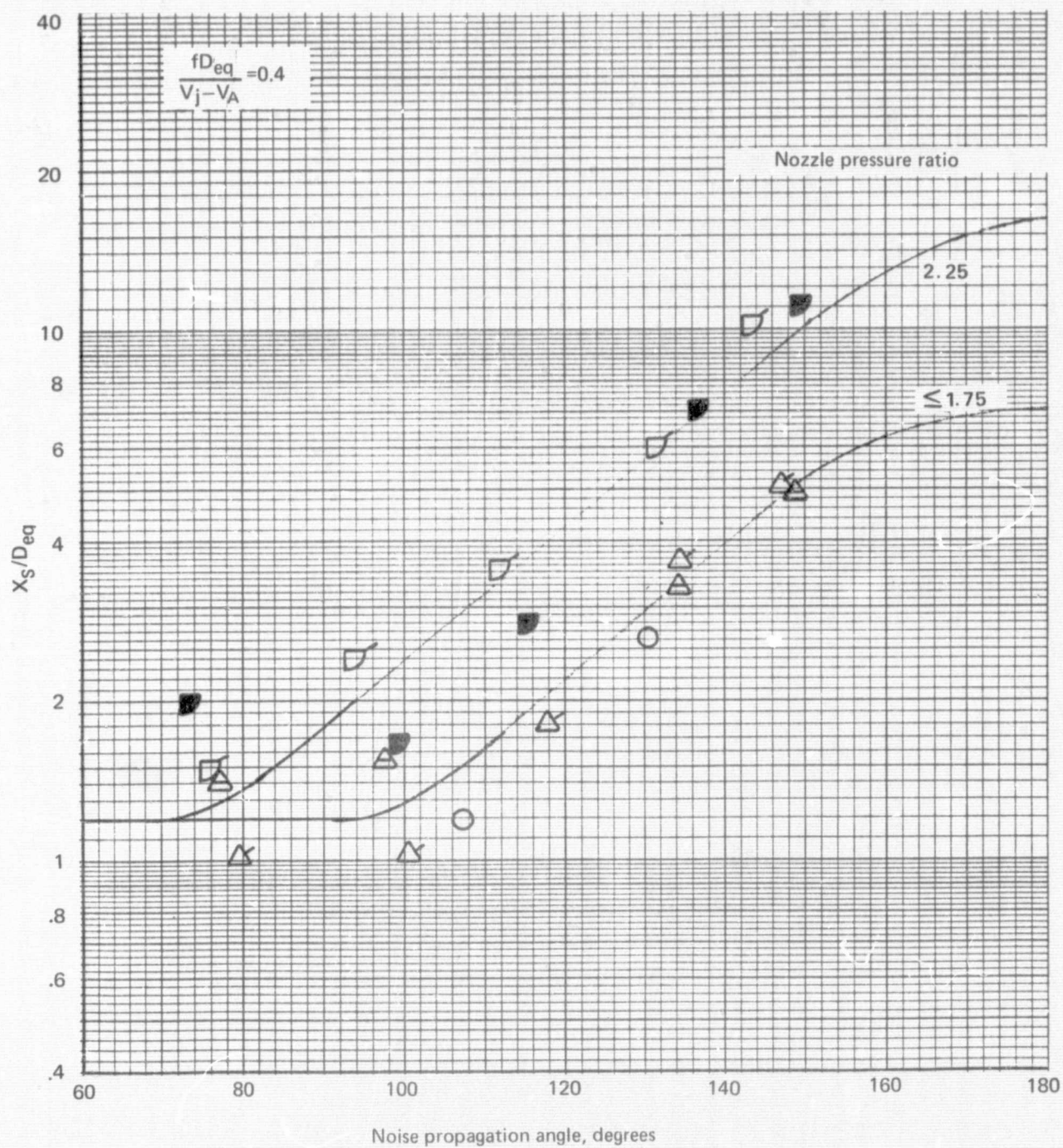


Figure 58.—(Continued)

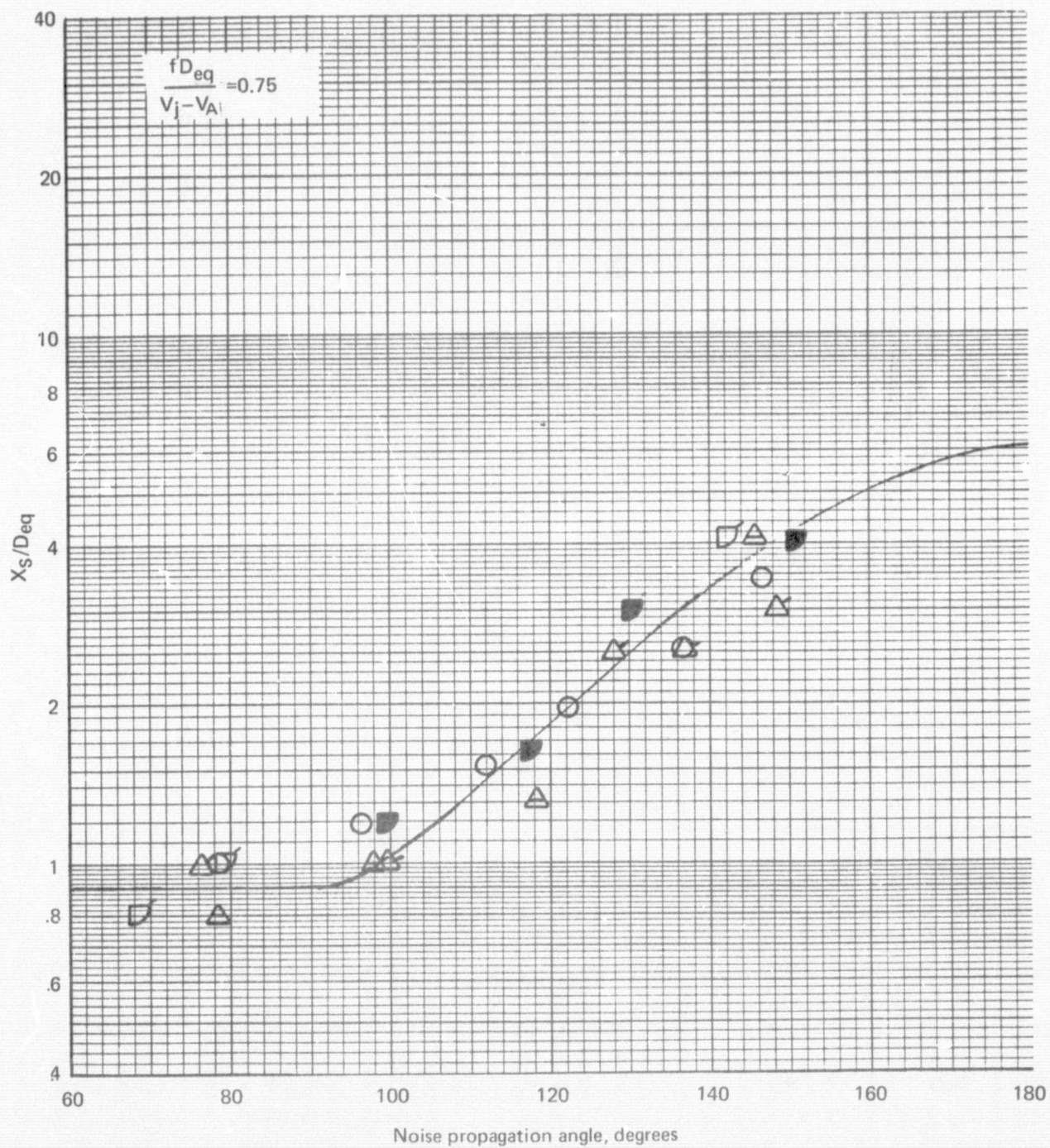


Figure 58.—(Continued)

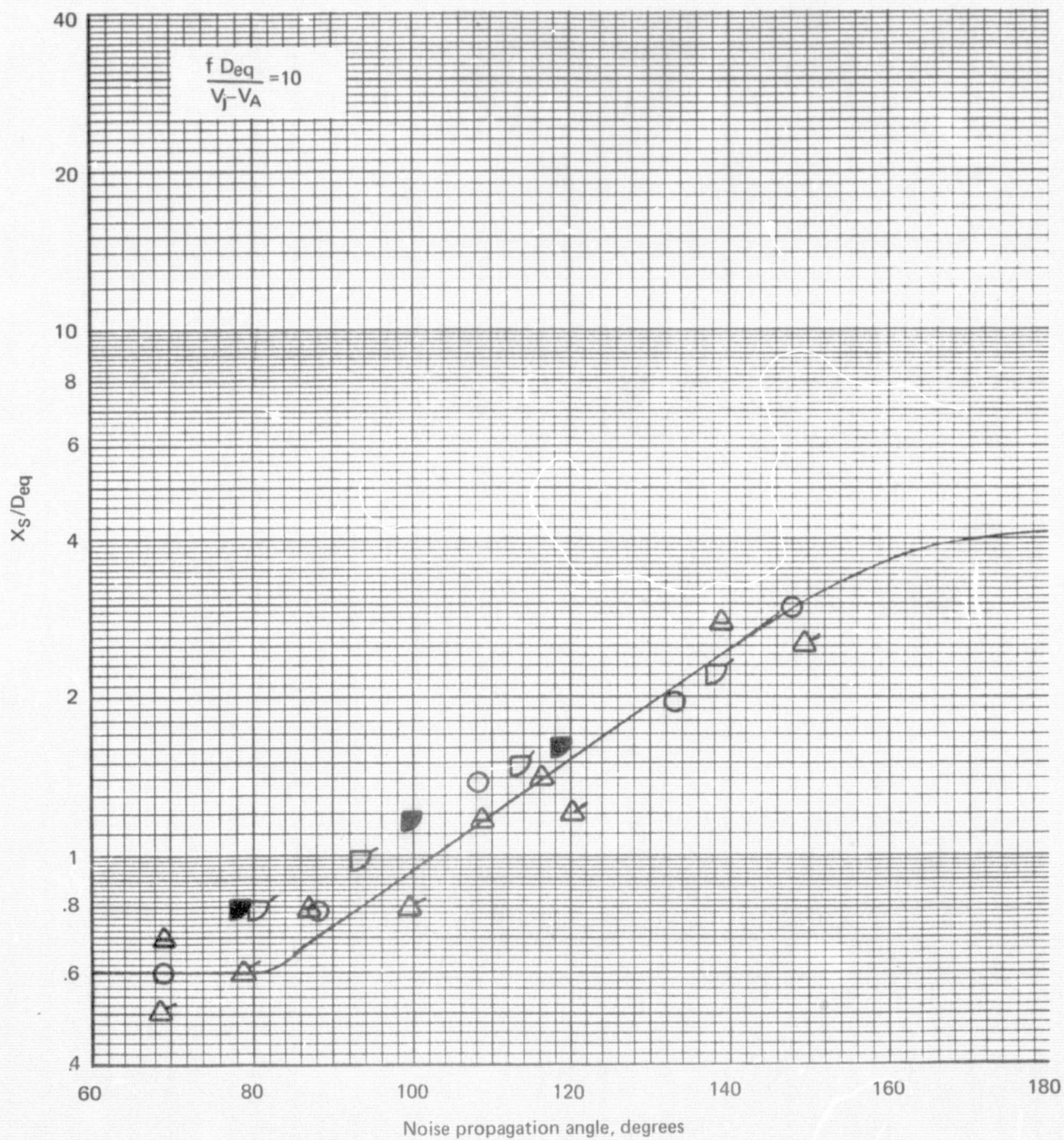


Figure 58.—(Concluded)

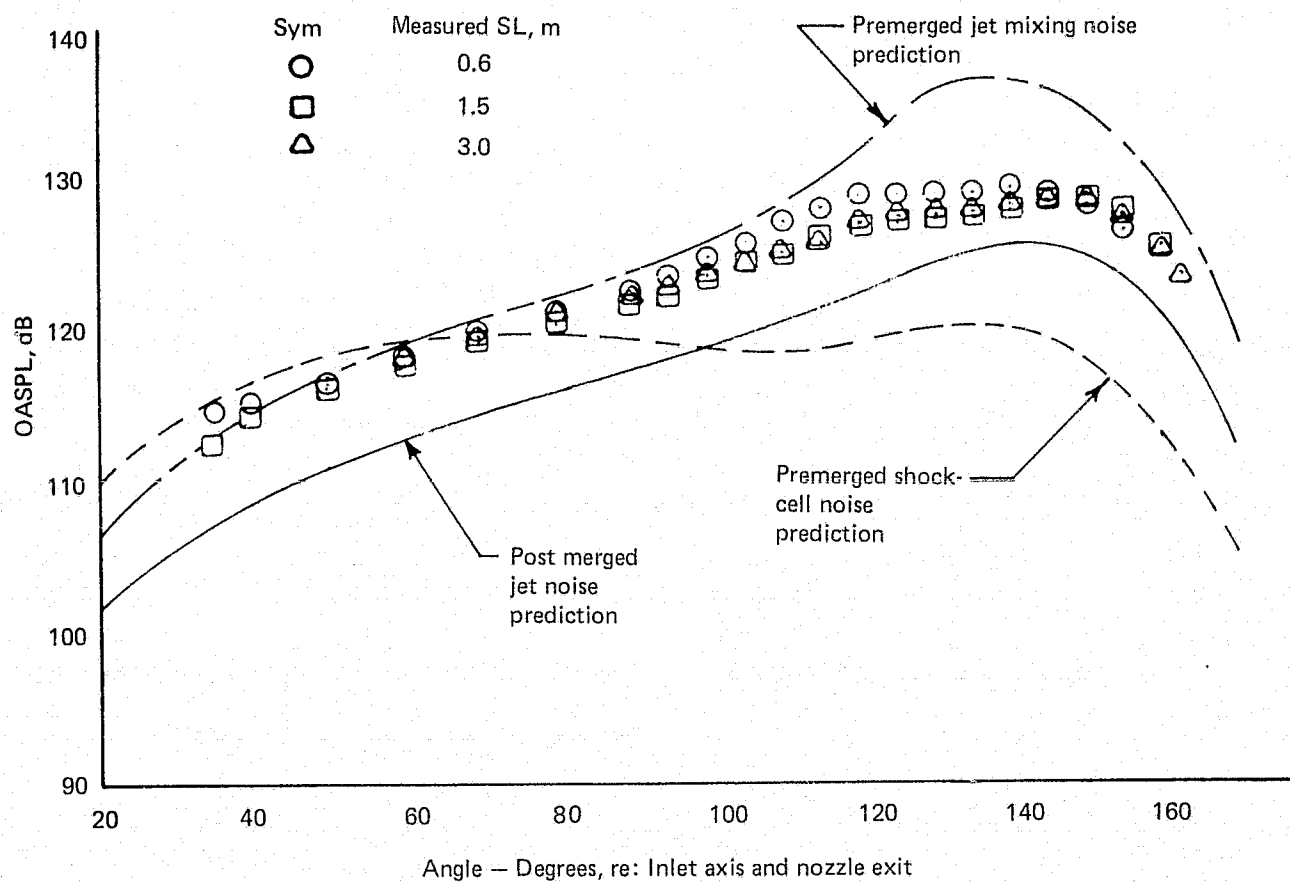


Figure 59.— OASPL Directivity and Jet Noise Spectra for the 20-Lobe Nozzle Extrapolated to a 3.0 m Sideline, $NPR = 2.25$, $V_A = 0$ m/s

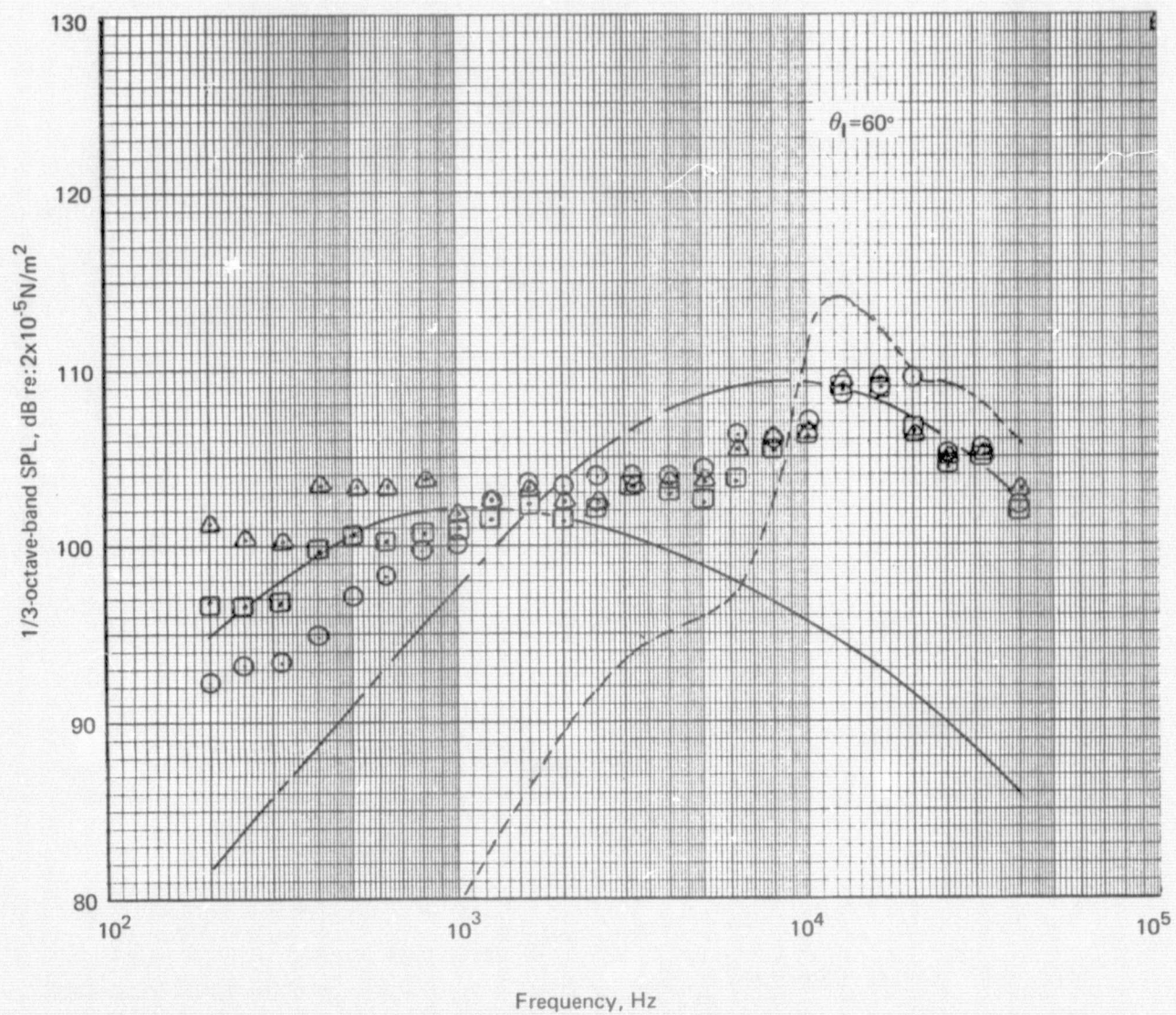


Figure 59.—(Continued)

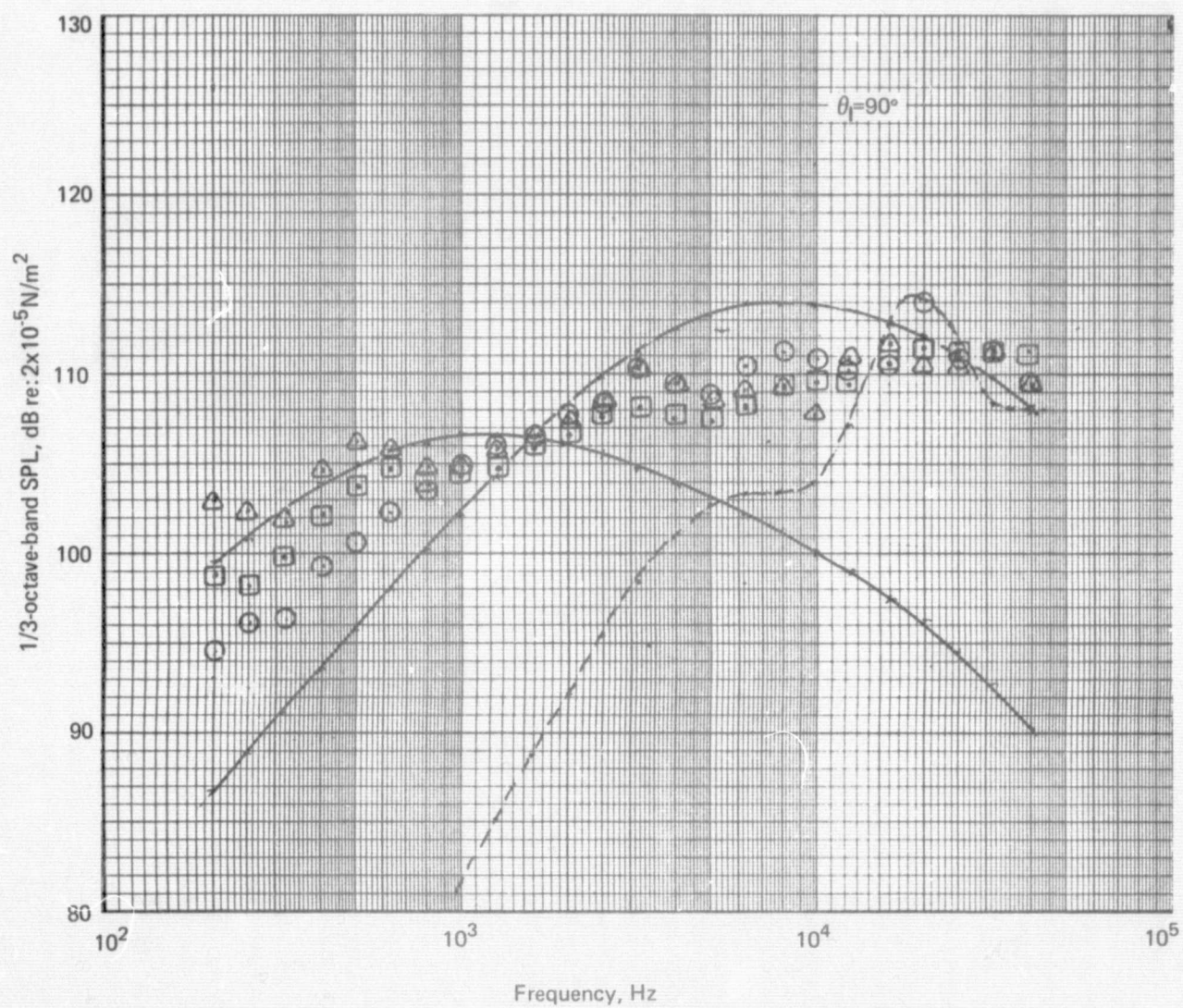


Figure 59.—(Continued)

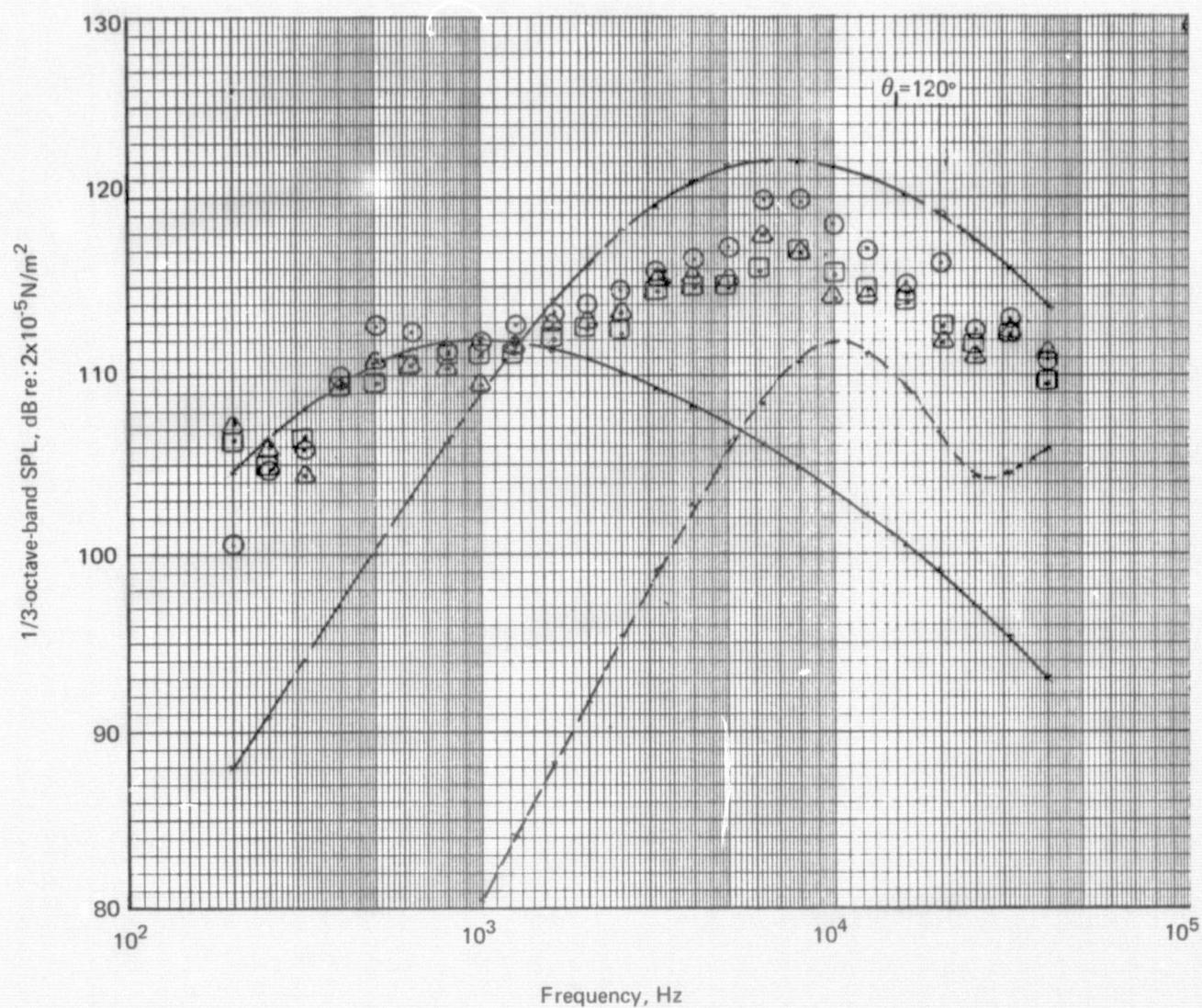


Figure 59.—(Continued)

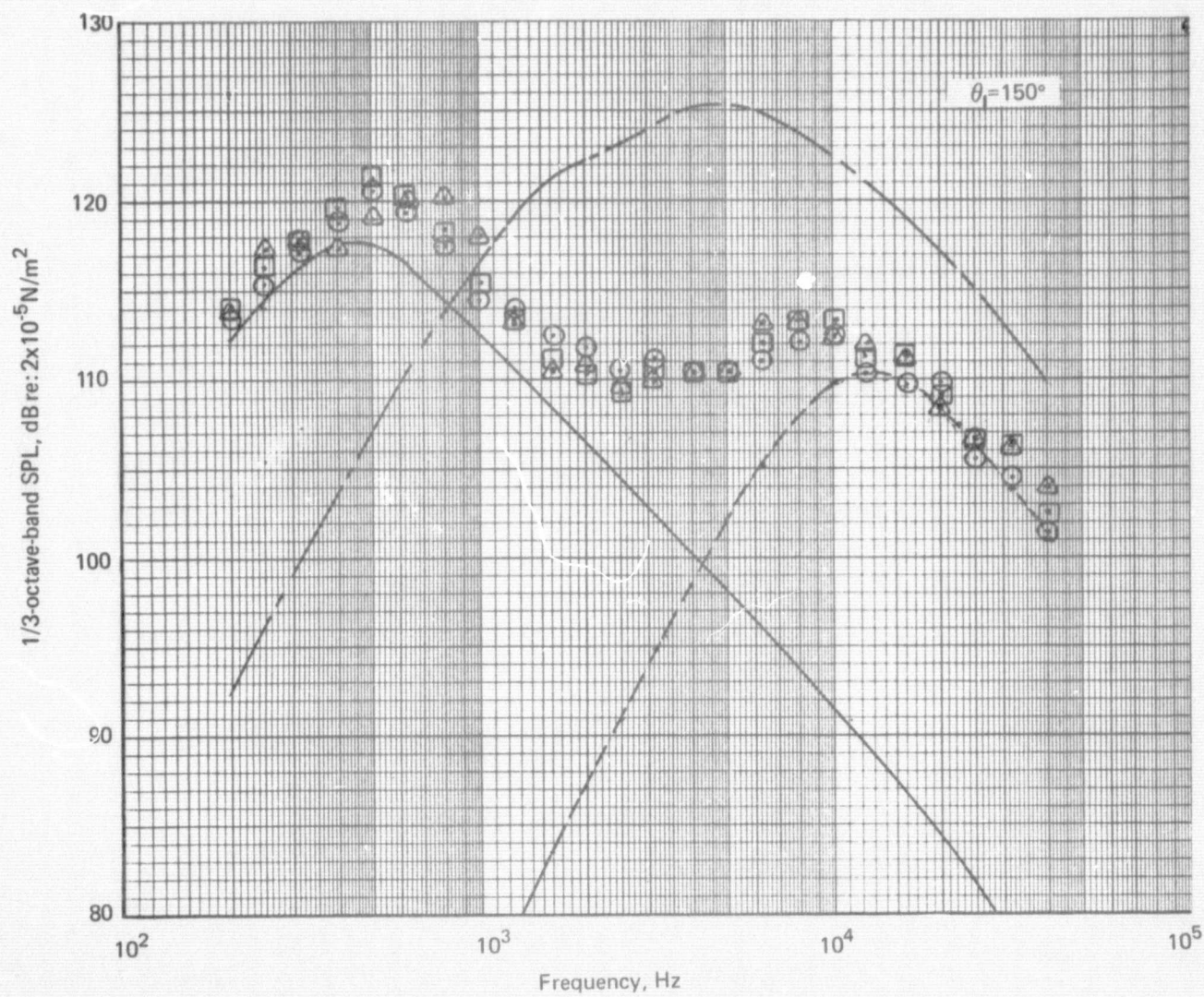


Figure 59.—(Concluded)

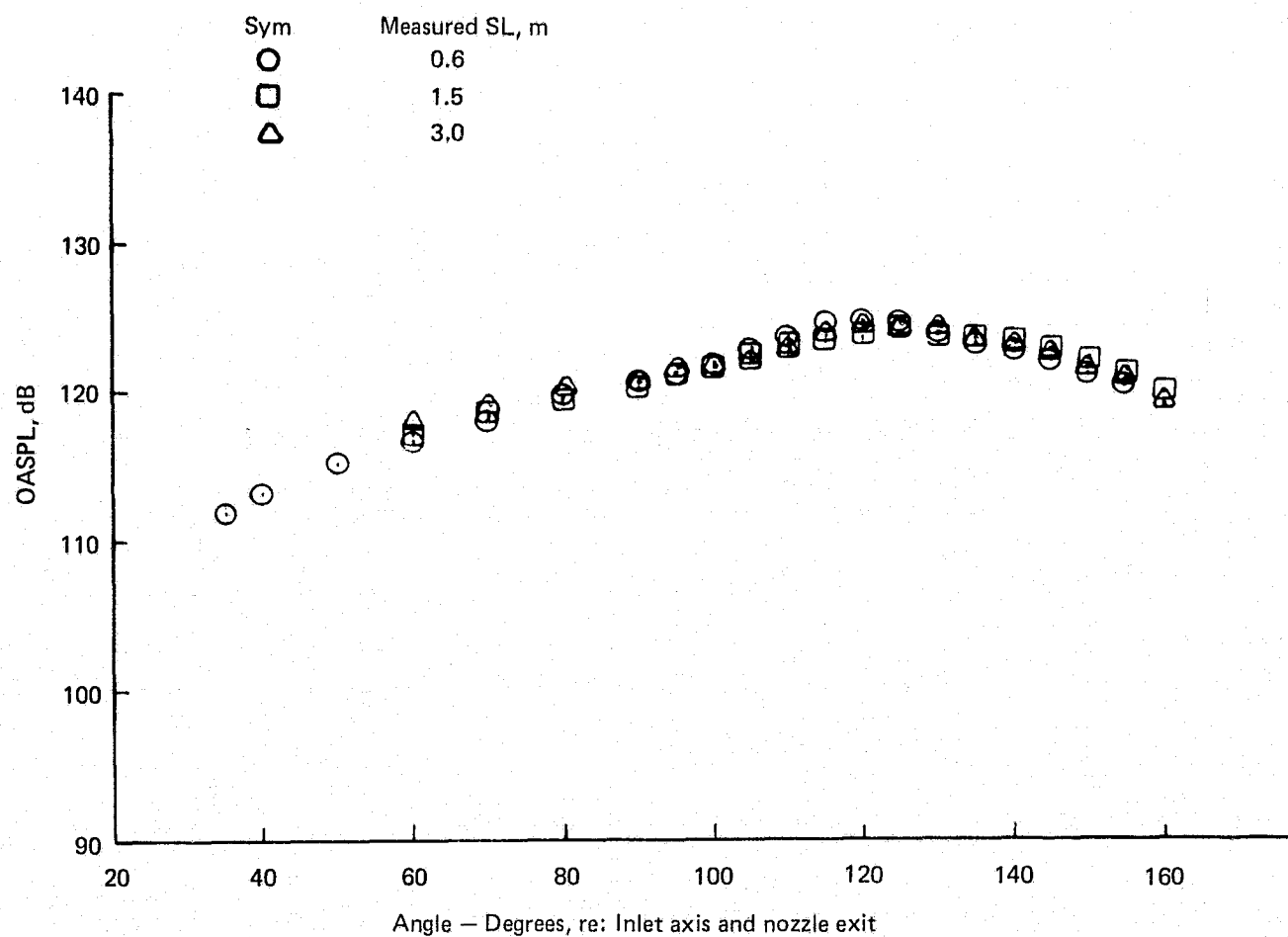


Figure 60.— OASPL Directivity and Jet Noise Spectra for the 20-Lobe Nozzle to a 3.0 m Sideline, $NPR = 2.25$, $V_A = 93.9$ m/s

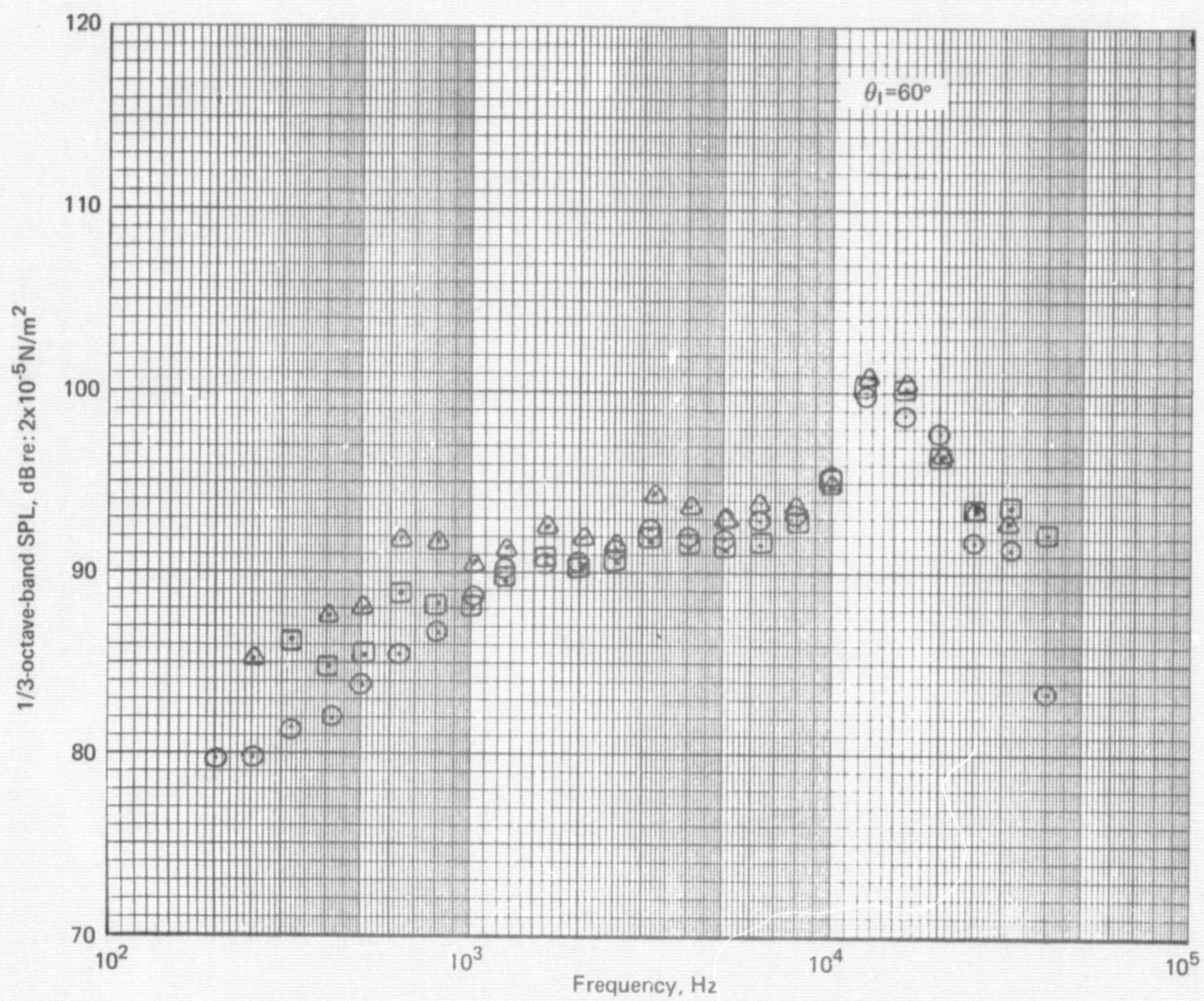


Figure 60.—(Continued)

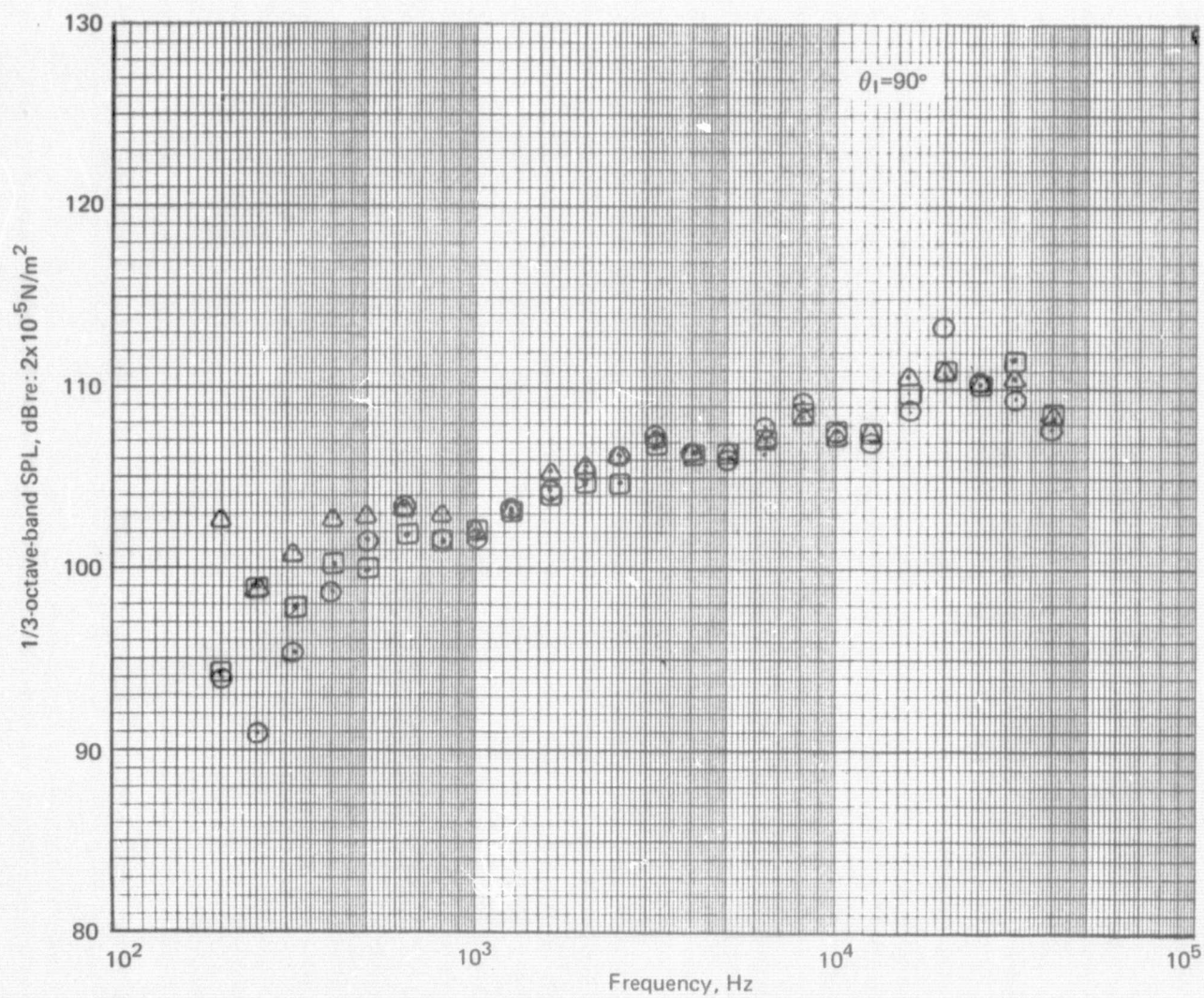


Figure 60.—(Continued)

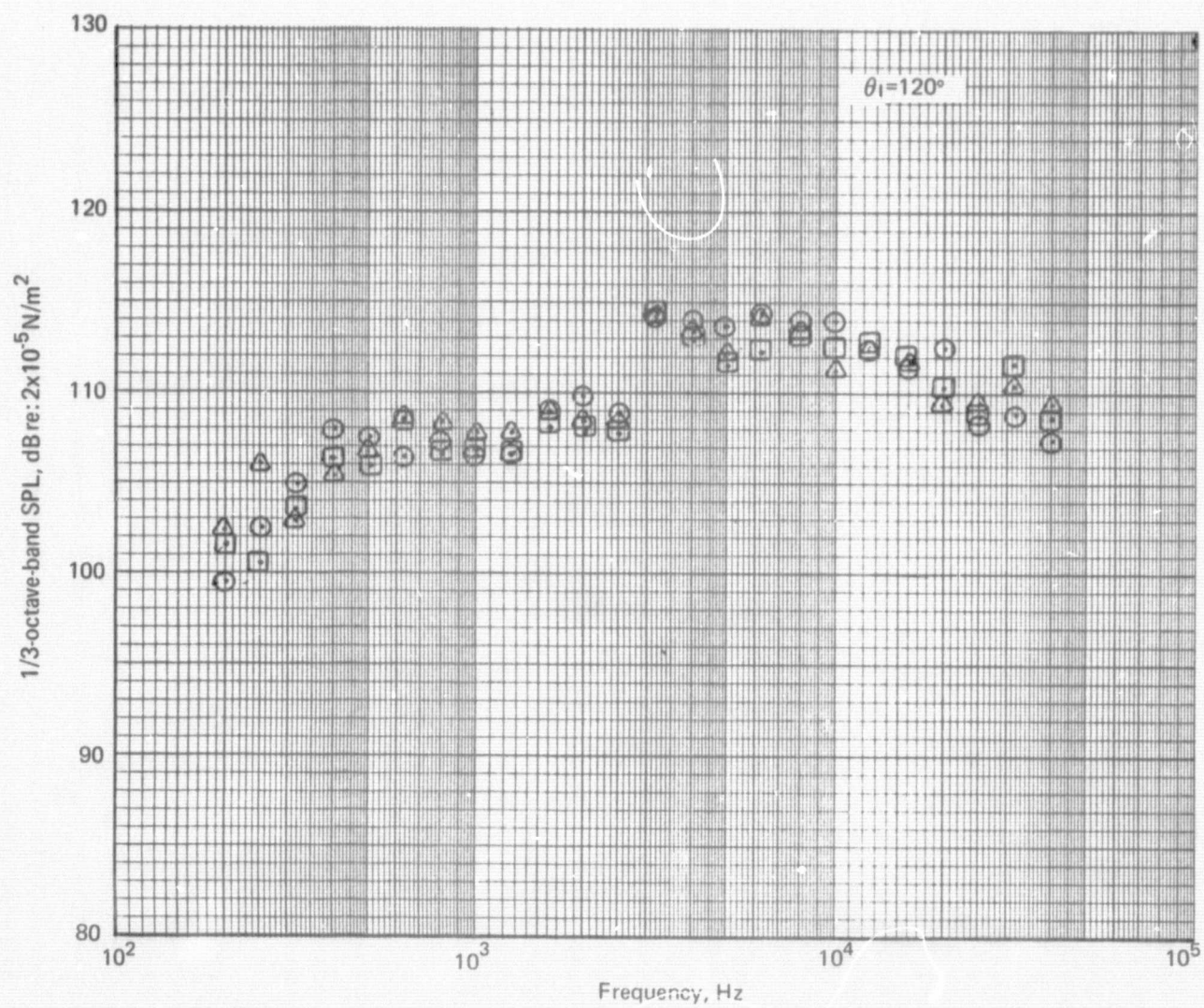


Figure 60.—(Continued)

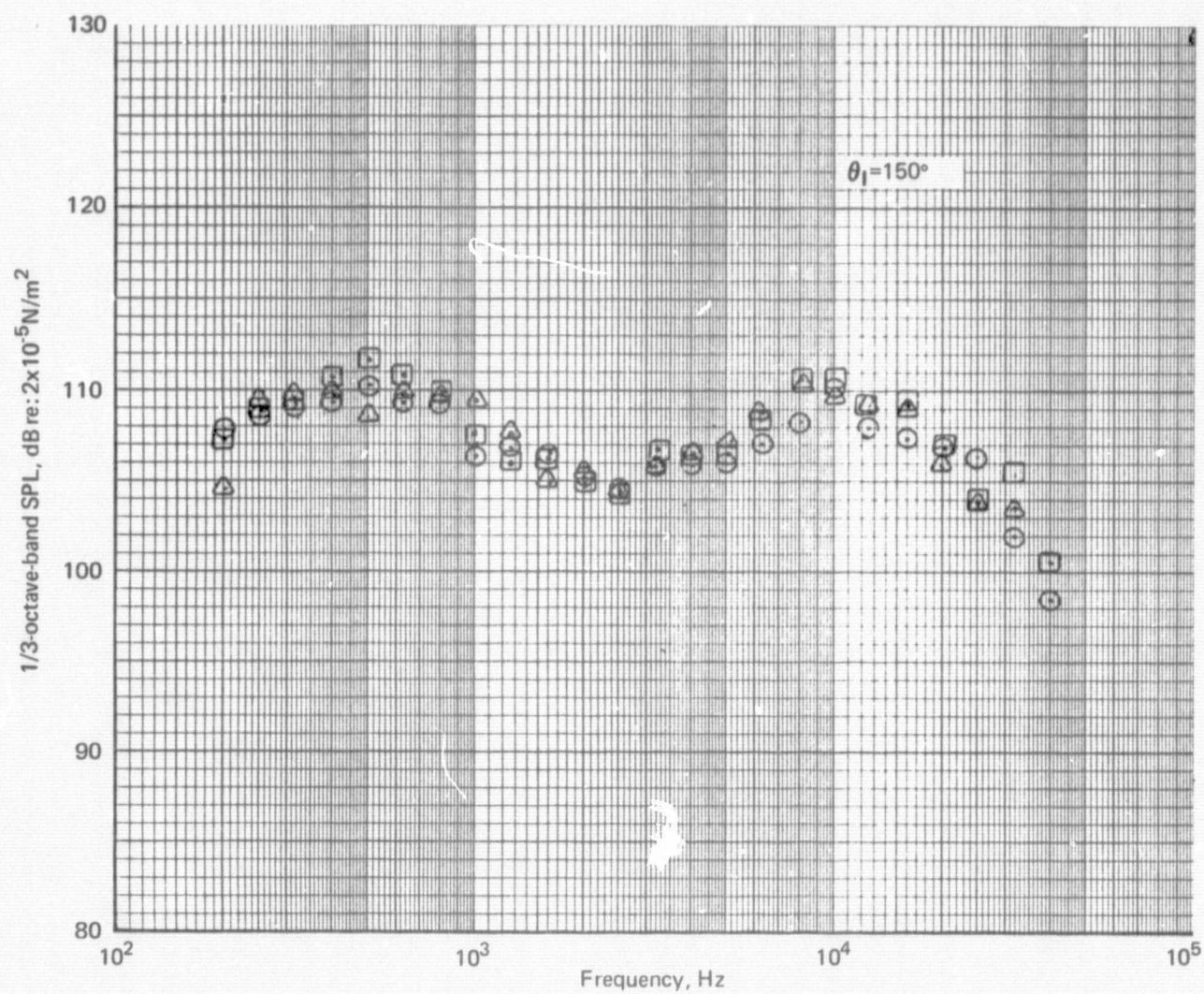


Figure 60.—(Concluded)

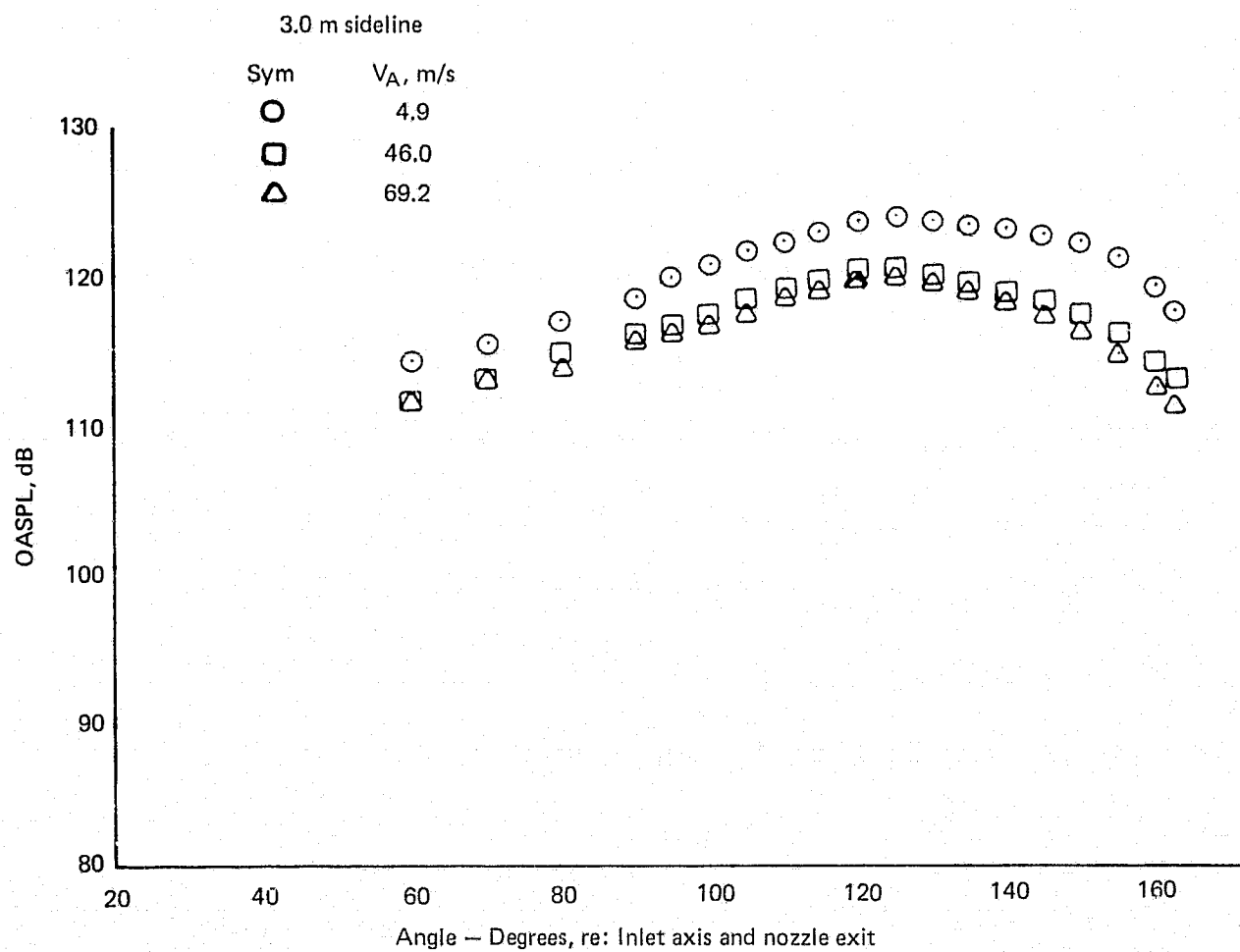


Figure 61.— Effect of Ambient Velocity on Jet Noise OASPL and 1/3-OBSPL Spectra for the 20-Lobe Nozzle NPR = 1.75

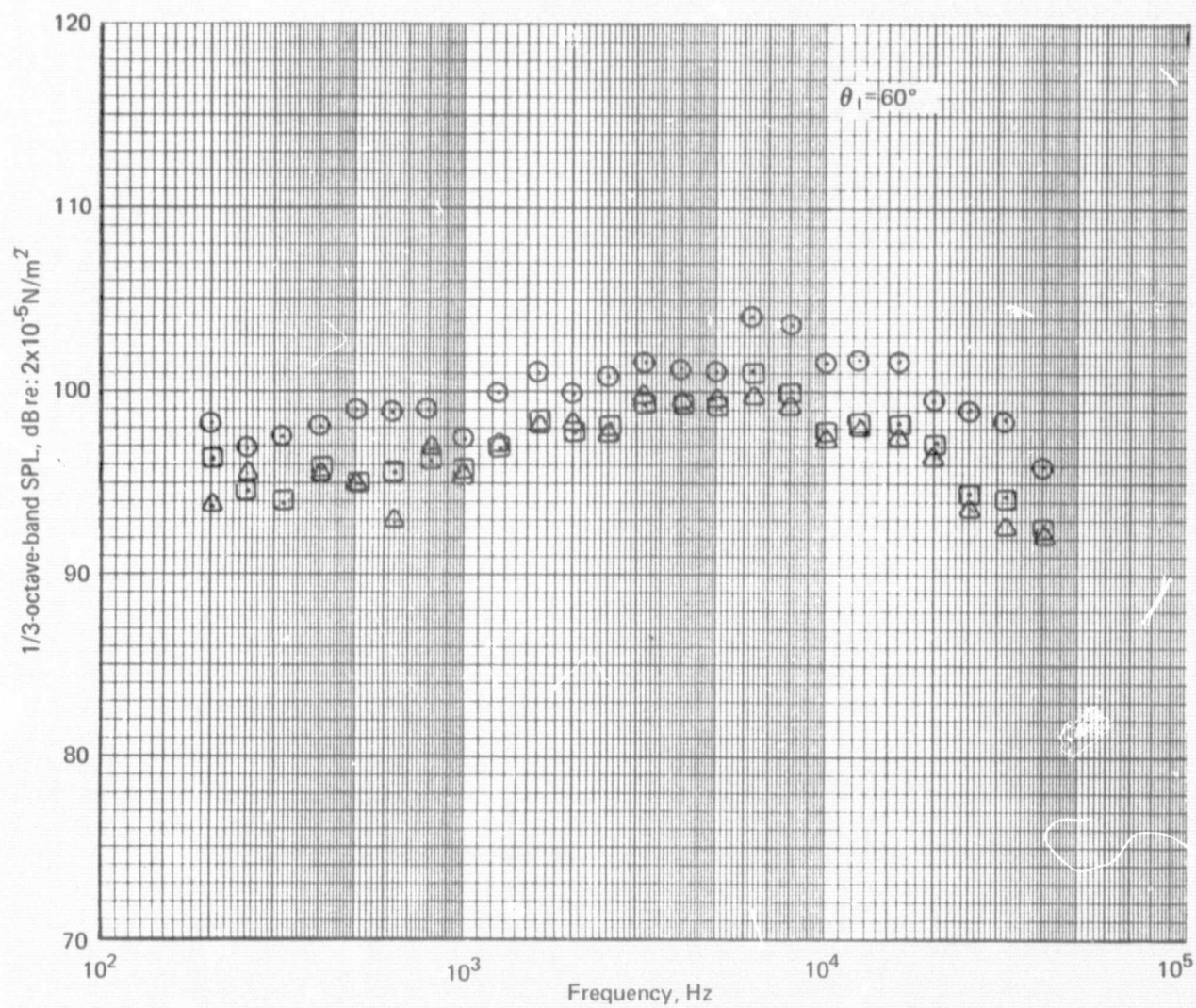


Figure 61.—(Continued)

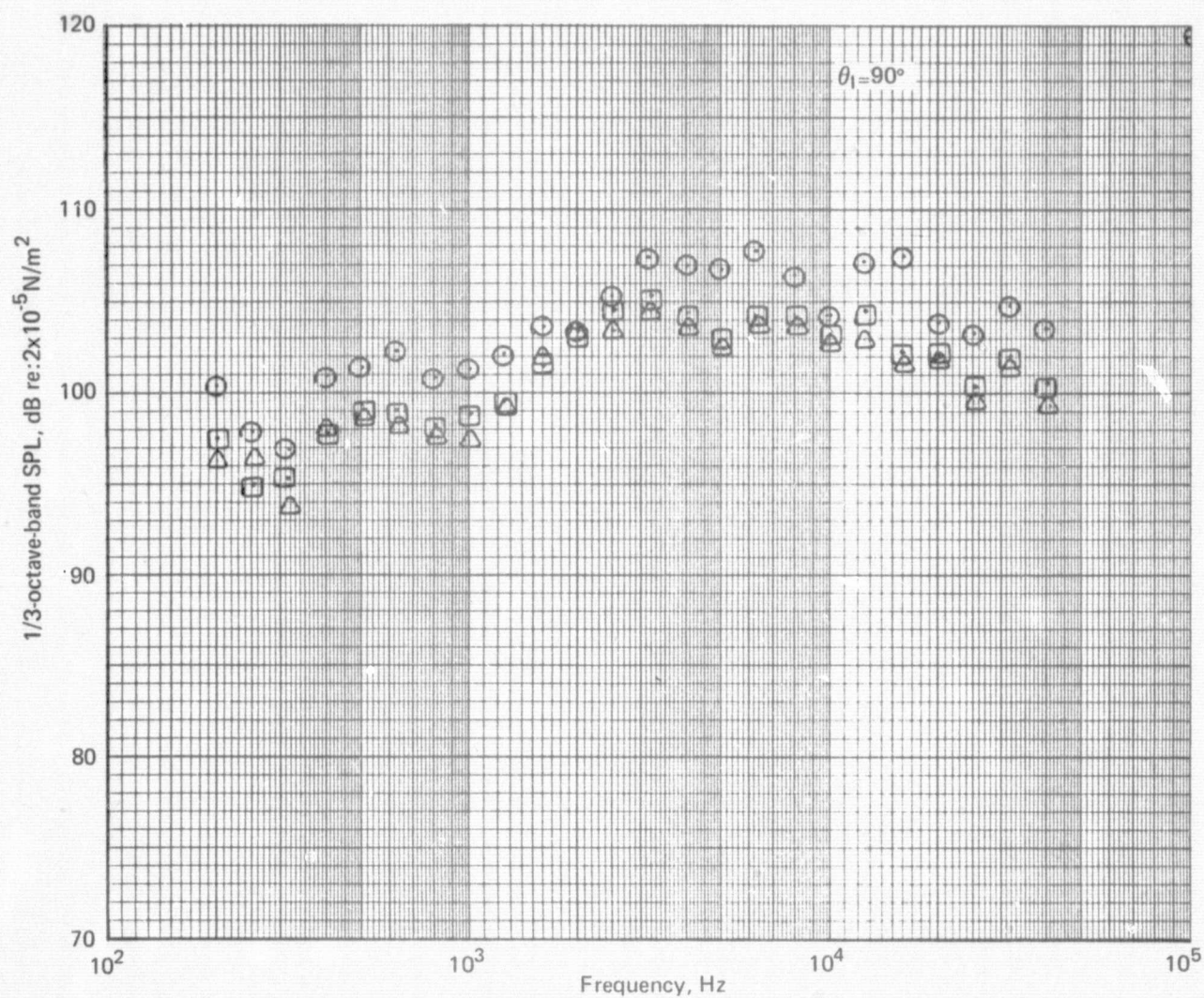


Figure 61.—(Continued)

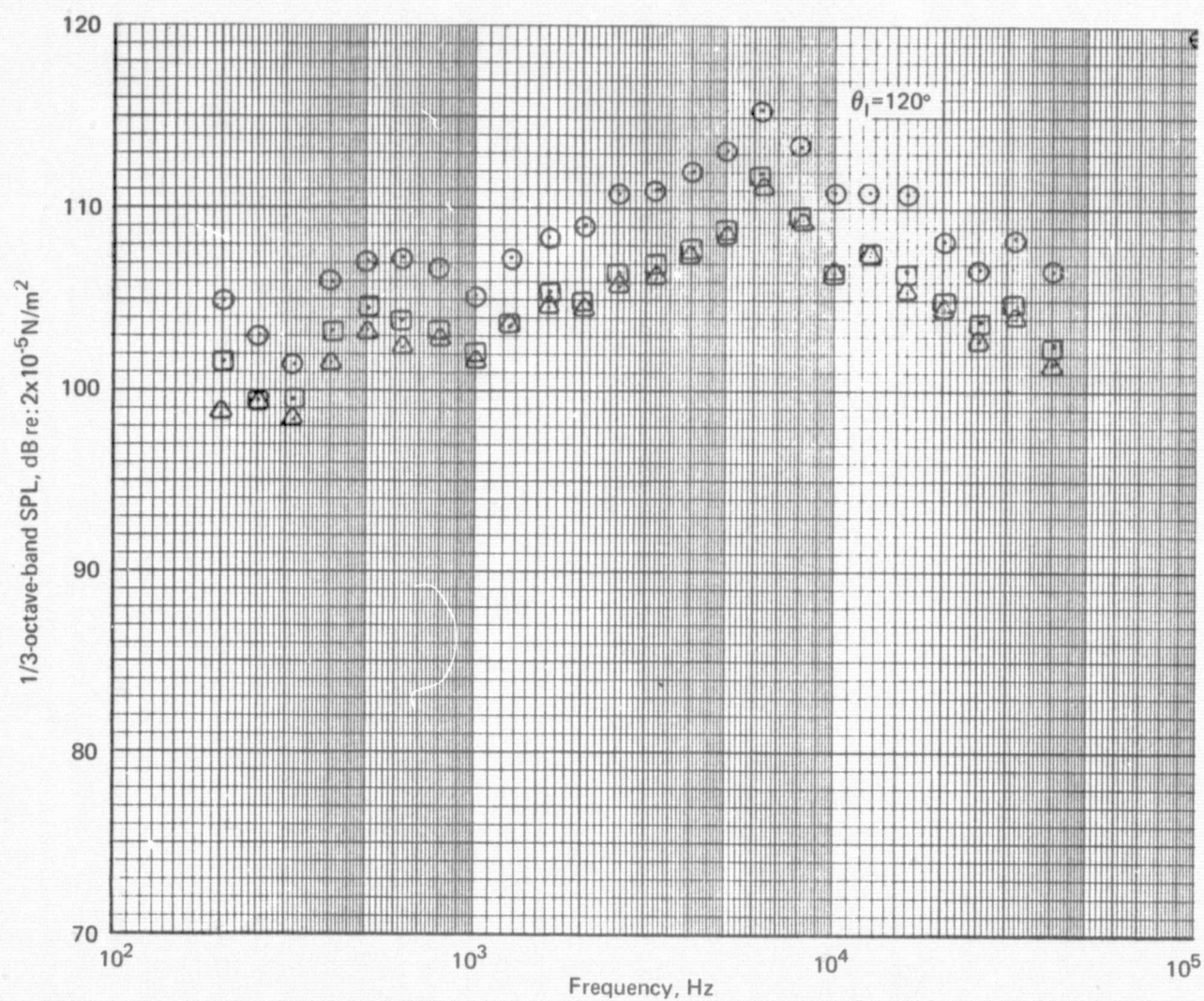


Figure 61.—(Continued)

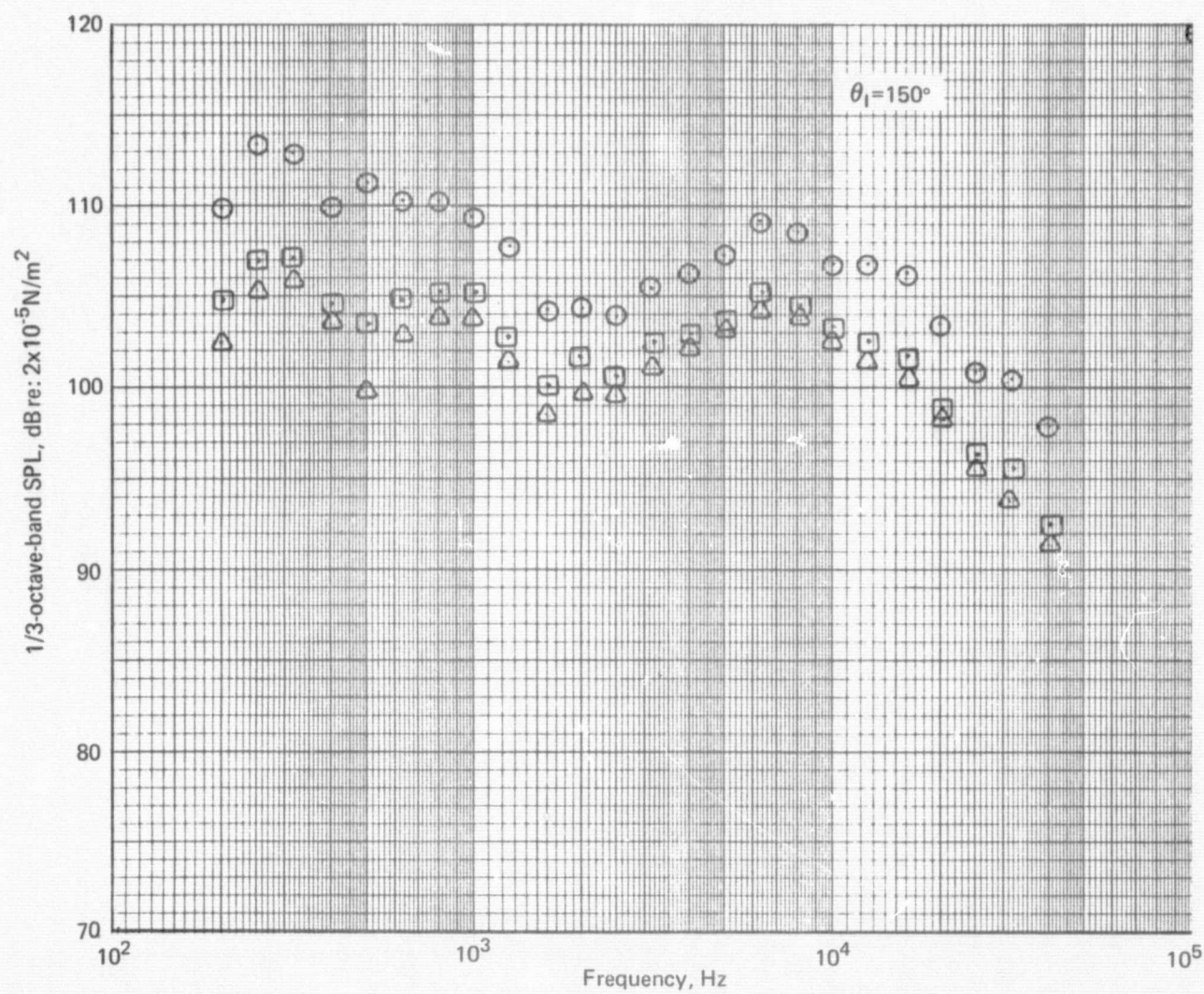


Figure 61.—(Concluded)

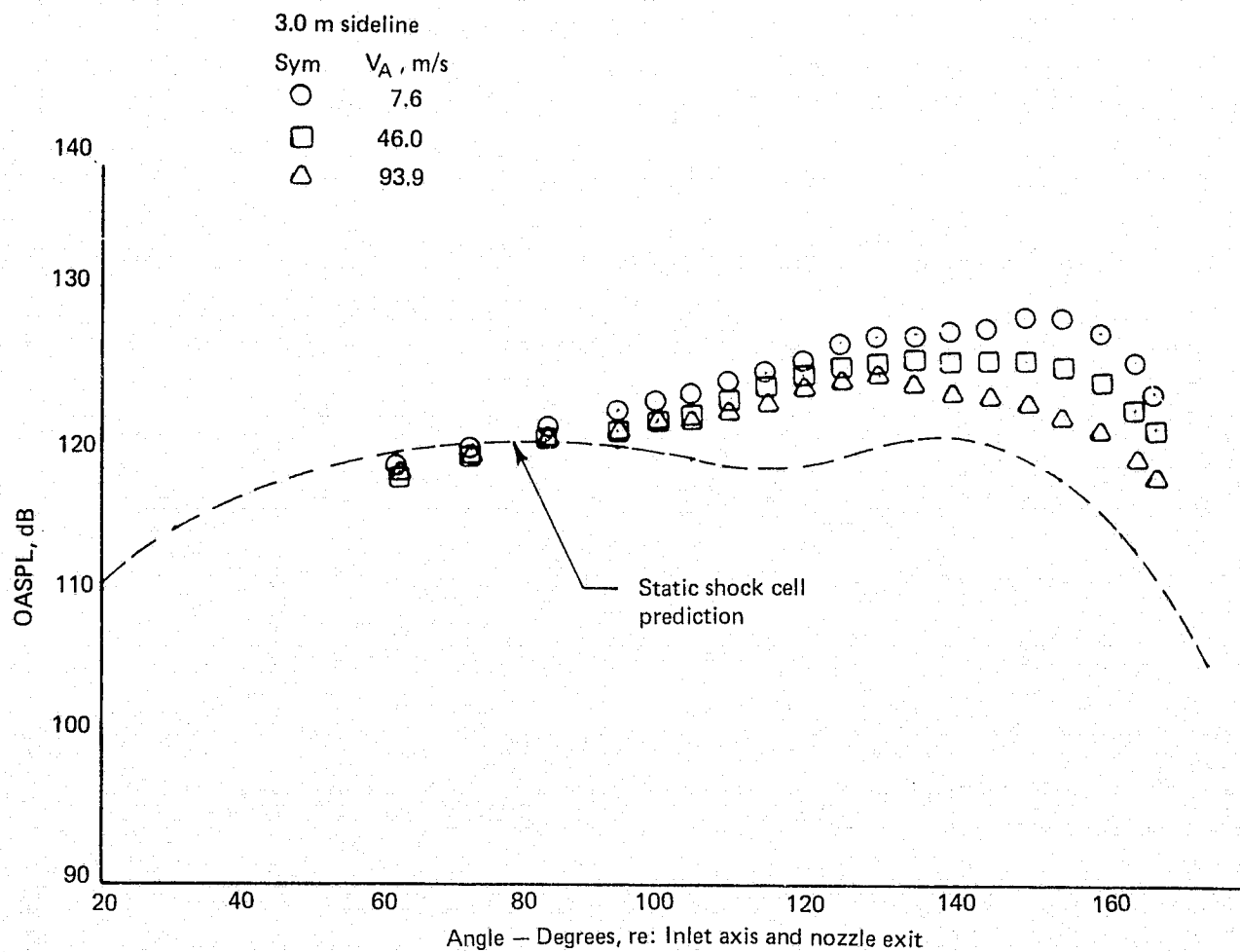


Figure 62.— Effect of Ambient Velocity on Jet Noise OASPL and 1/3-OB SPL Spectra for the 20-Lobe Nozzle NPR = 2.25

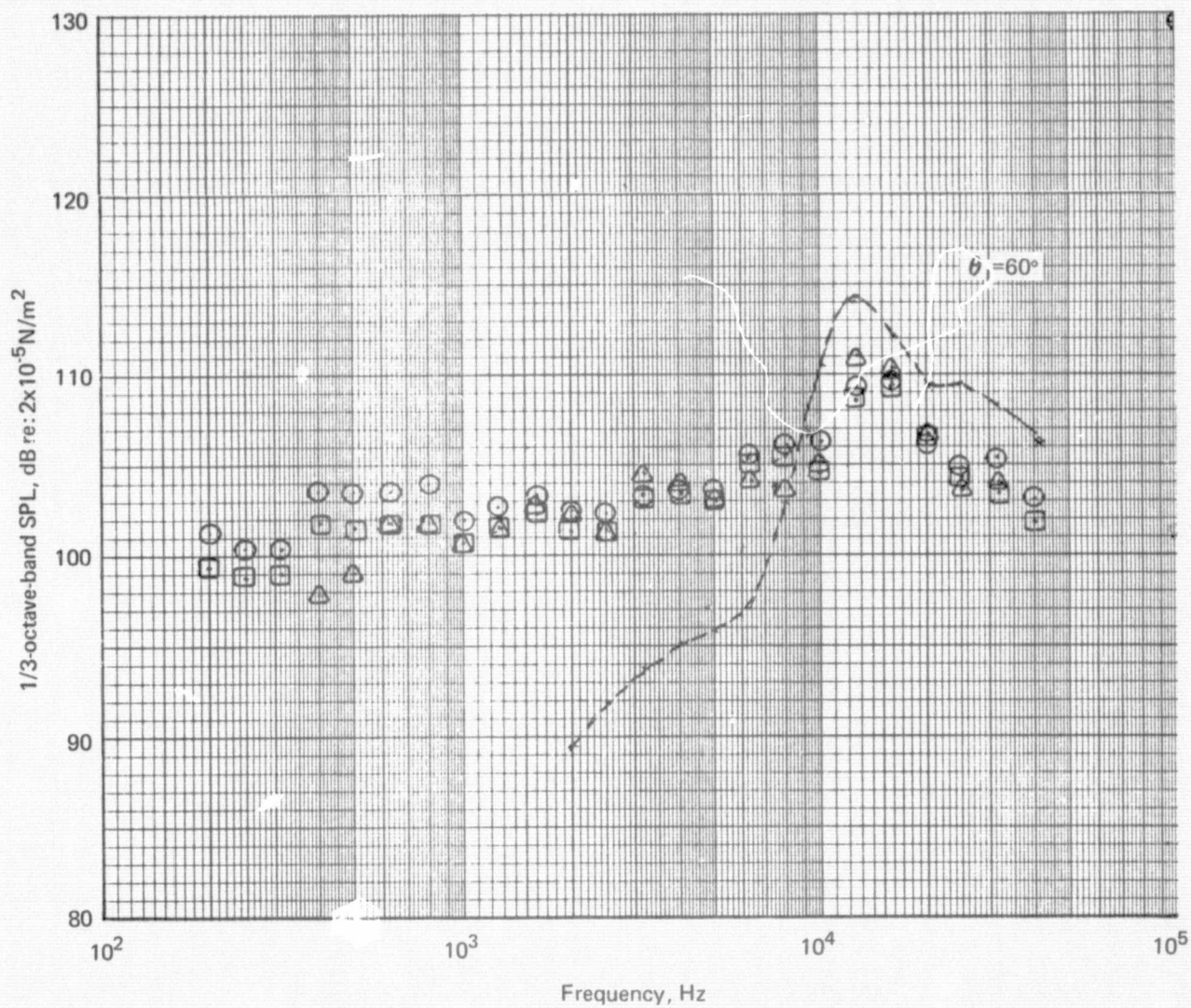


Figure 62.—(Continued)

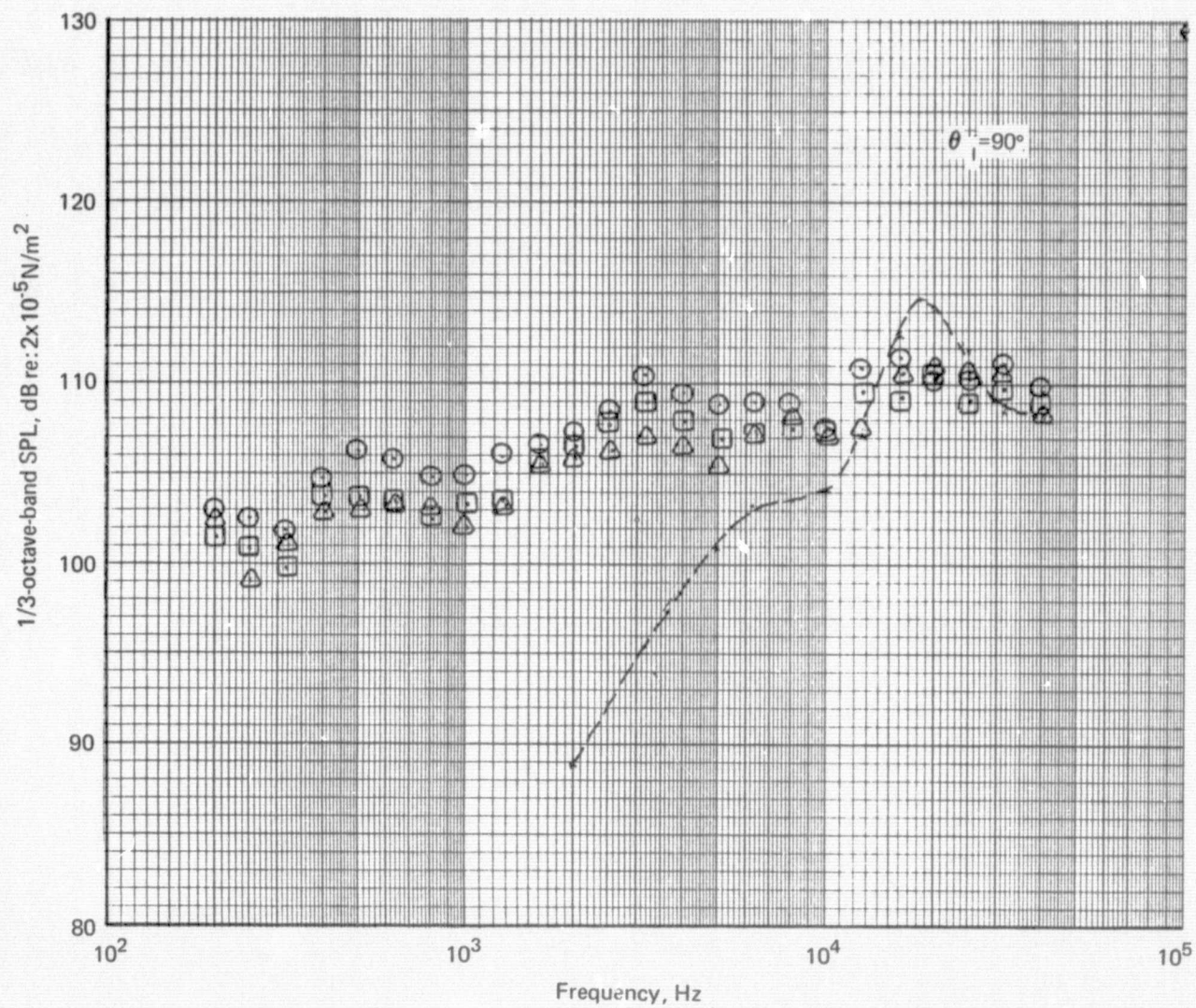


Figure 62.—(Continued)

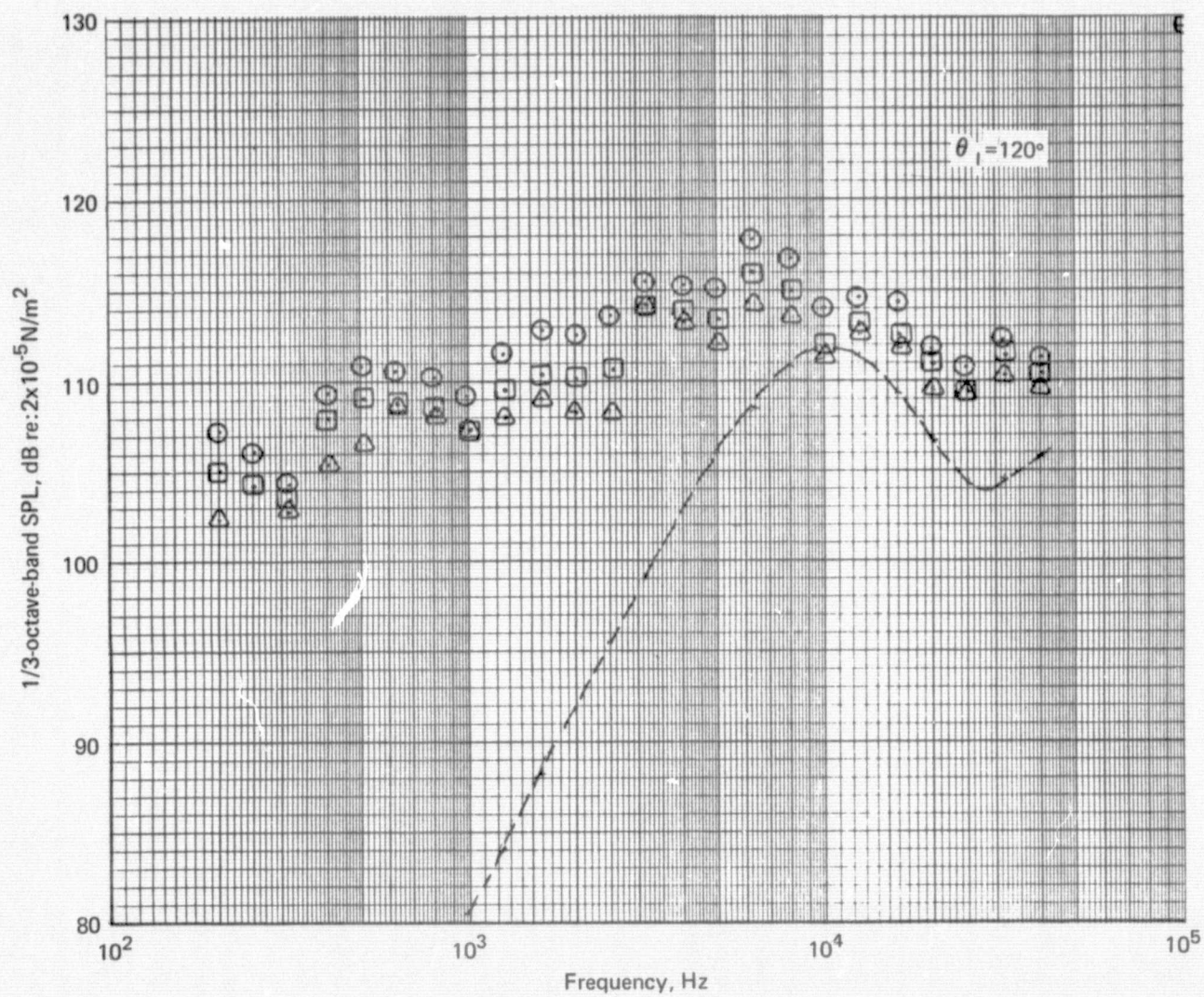


Figure 62.—(Continued)

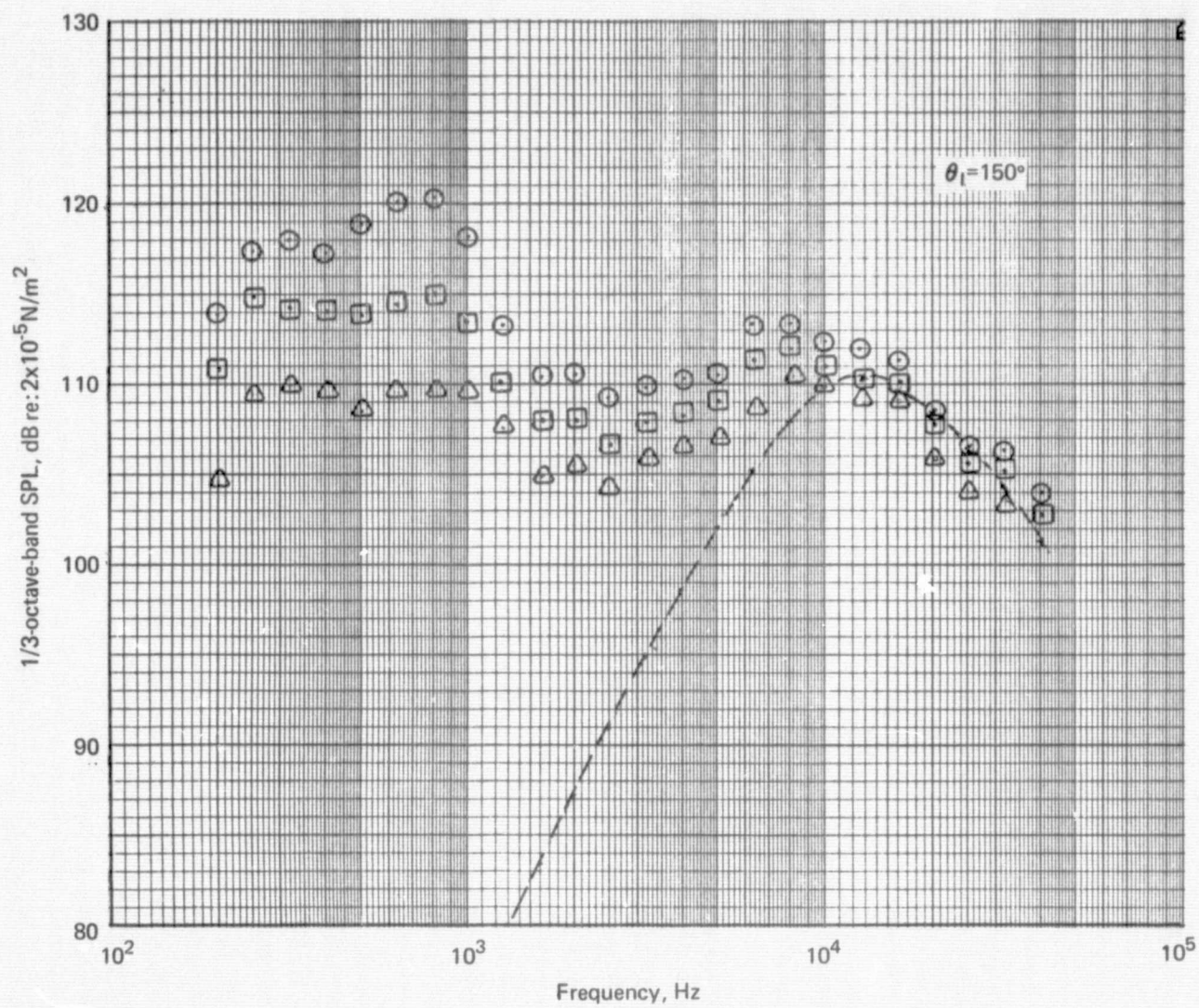


Figure 62.—(Concluded)

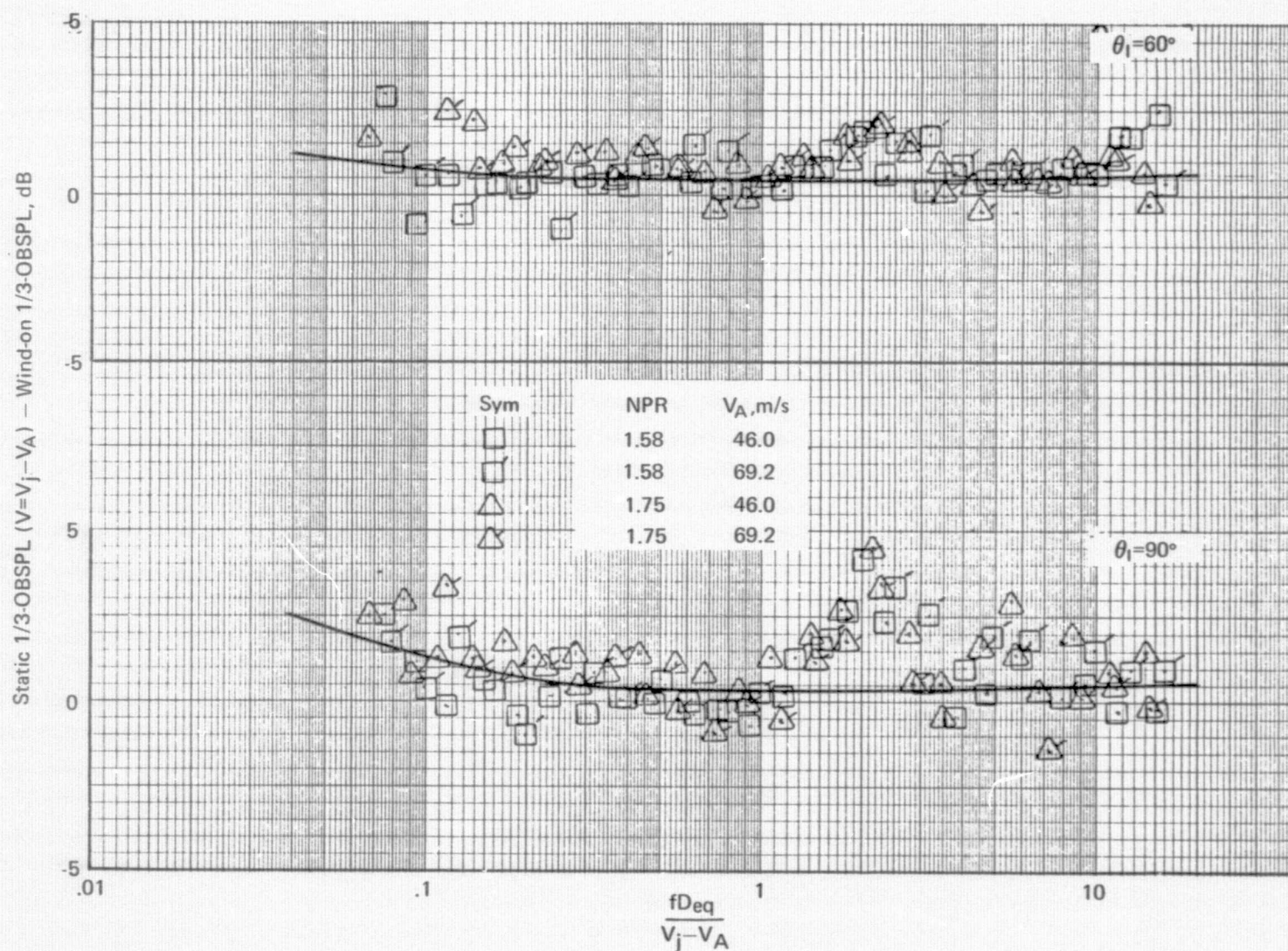


Figure 63.—Effect of Ambient Velocity on Subsonic Jet Noise Spectra of a 20-Lobe Nozzle Referenced to the Static Case Where $V=V_j-V_A$, $T_T=844\text{K}$, 3.0 m Sideline

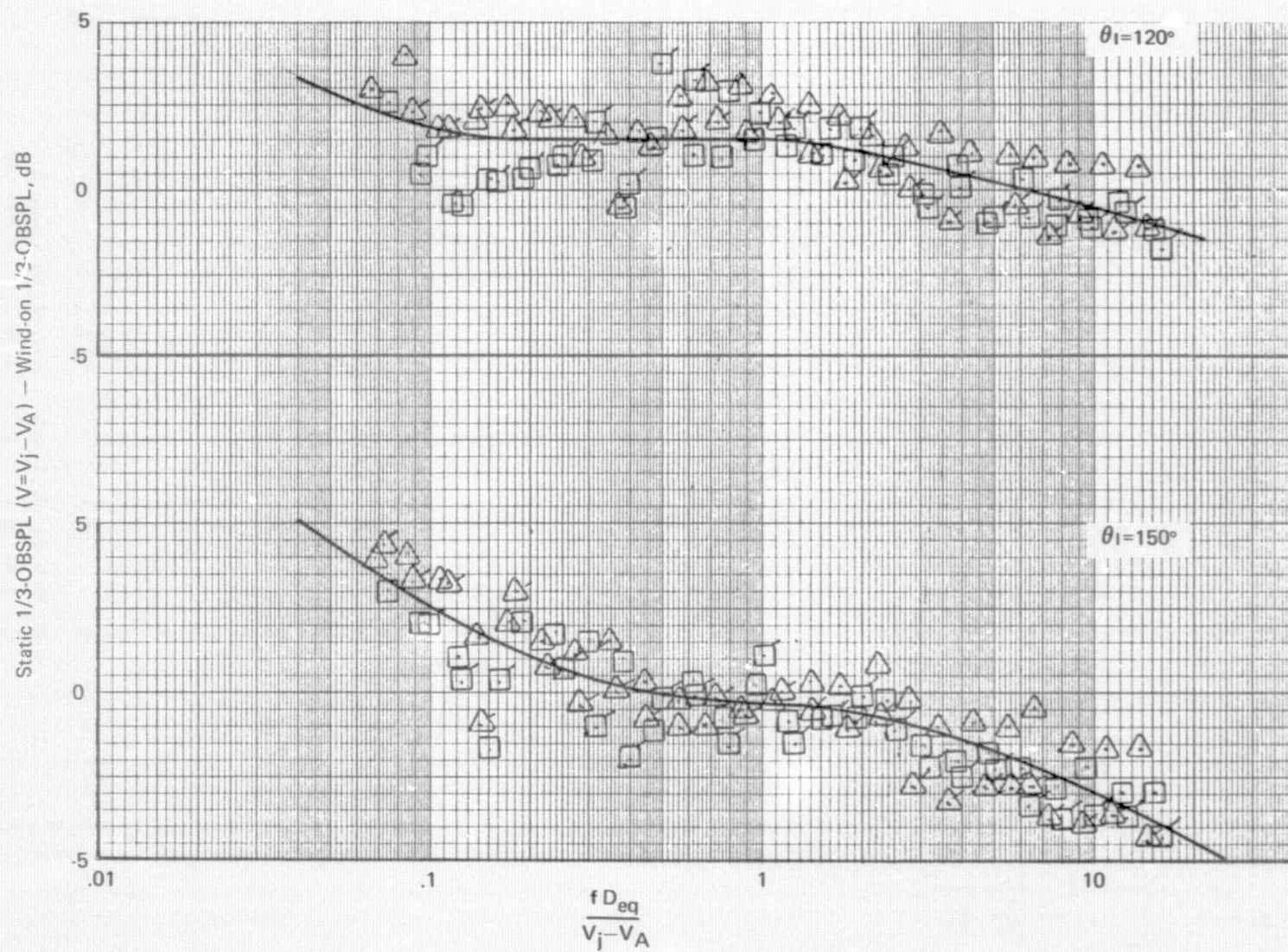


Figure 63.—(Concluded)

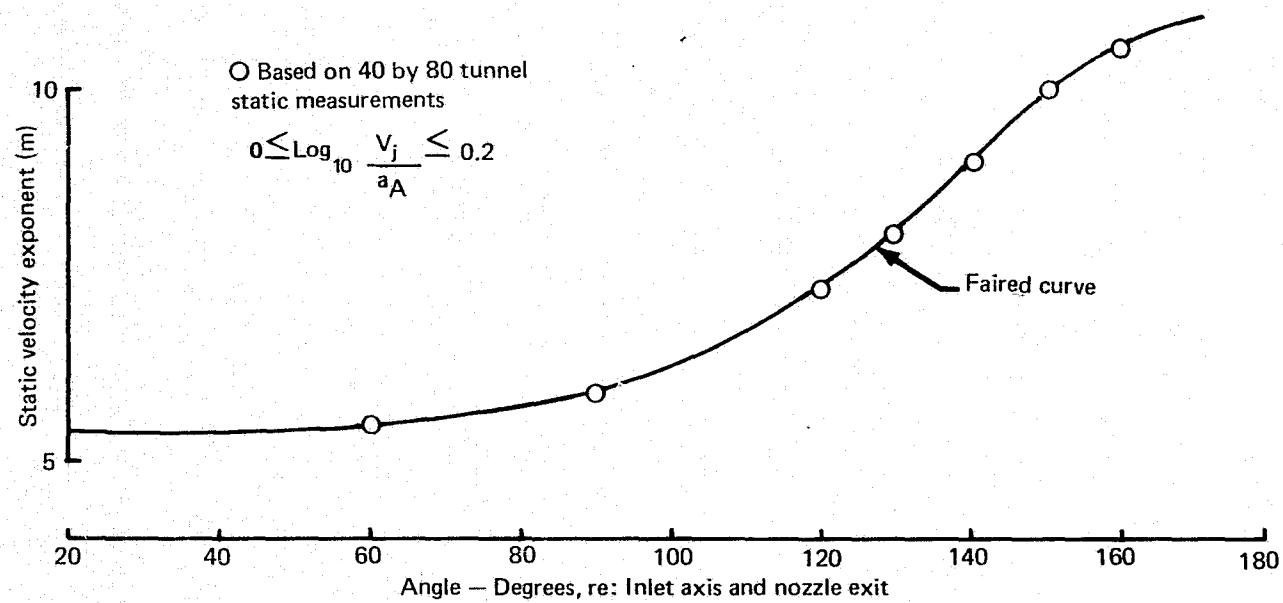


Figure 64.— Static Velocity Exponent for a 20-Lobe Nozzle

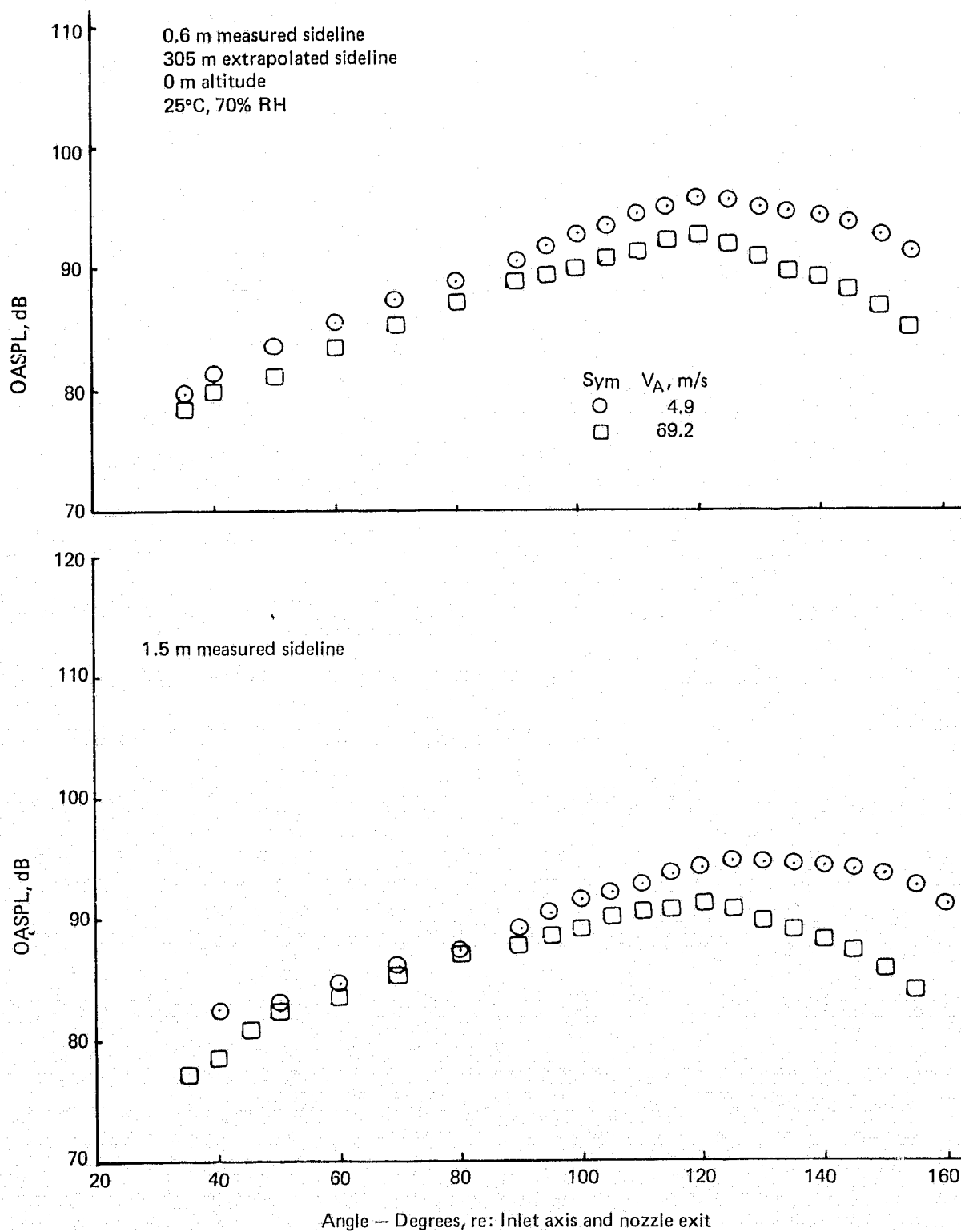


Figure 65.— Flight Effects on OASPL of a 20-Lobe Nozzle $NPR = 1.75$, $V_j = 503$ m/s

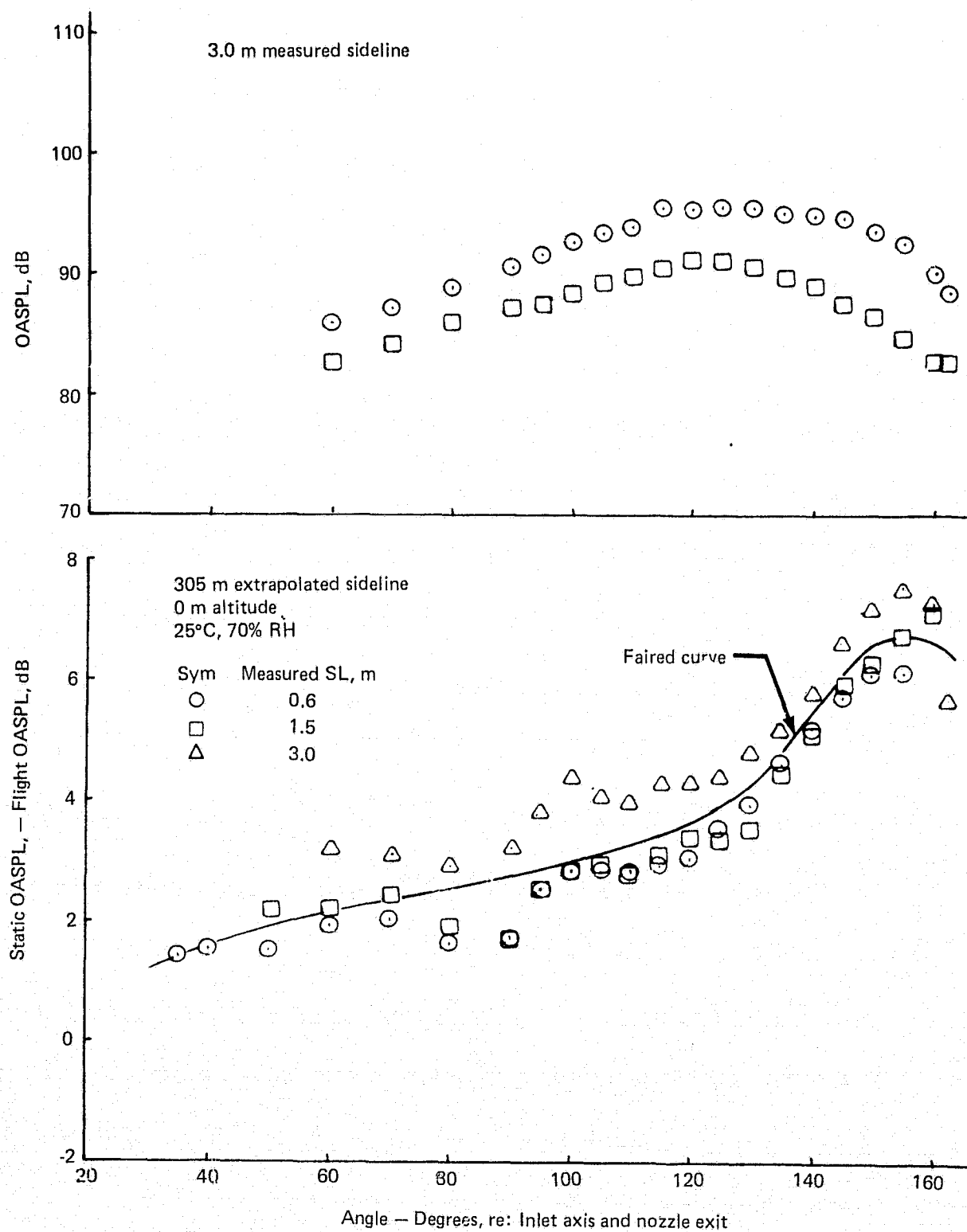


Figure 65.— (Concluded)

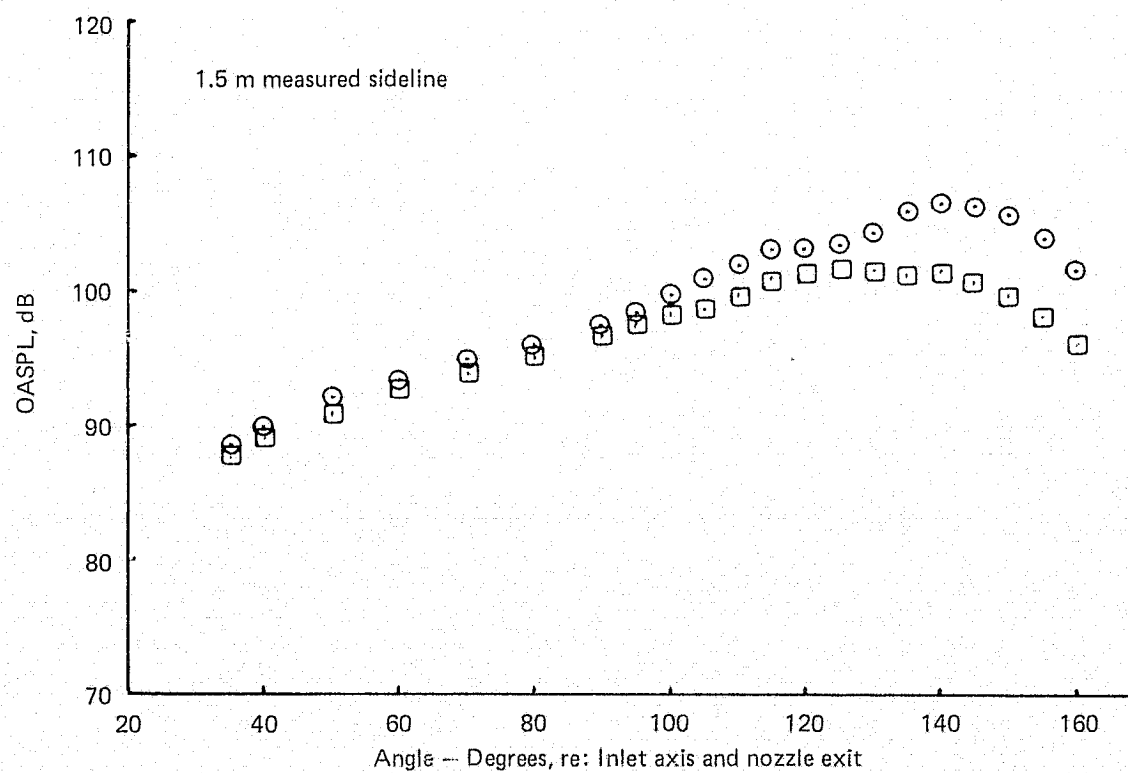
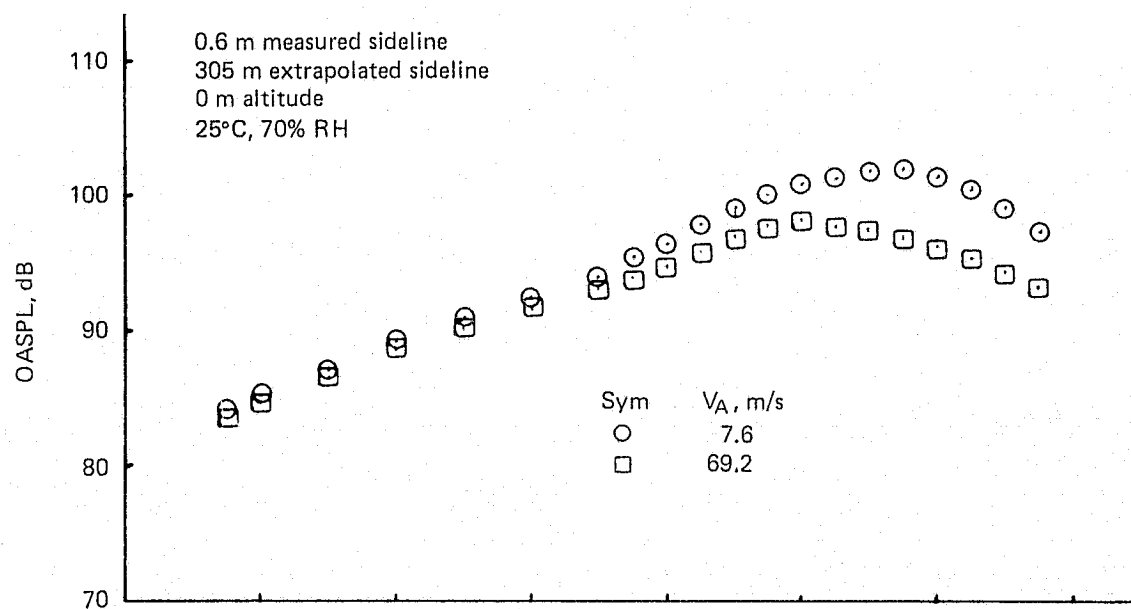


Figure 66.— Flight Effects on OASPL of a 20-Lobe Nozzle $NPR = 2.25$, $V_j = 594$ m/s

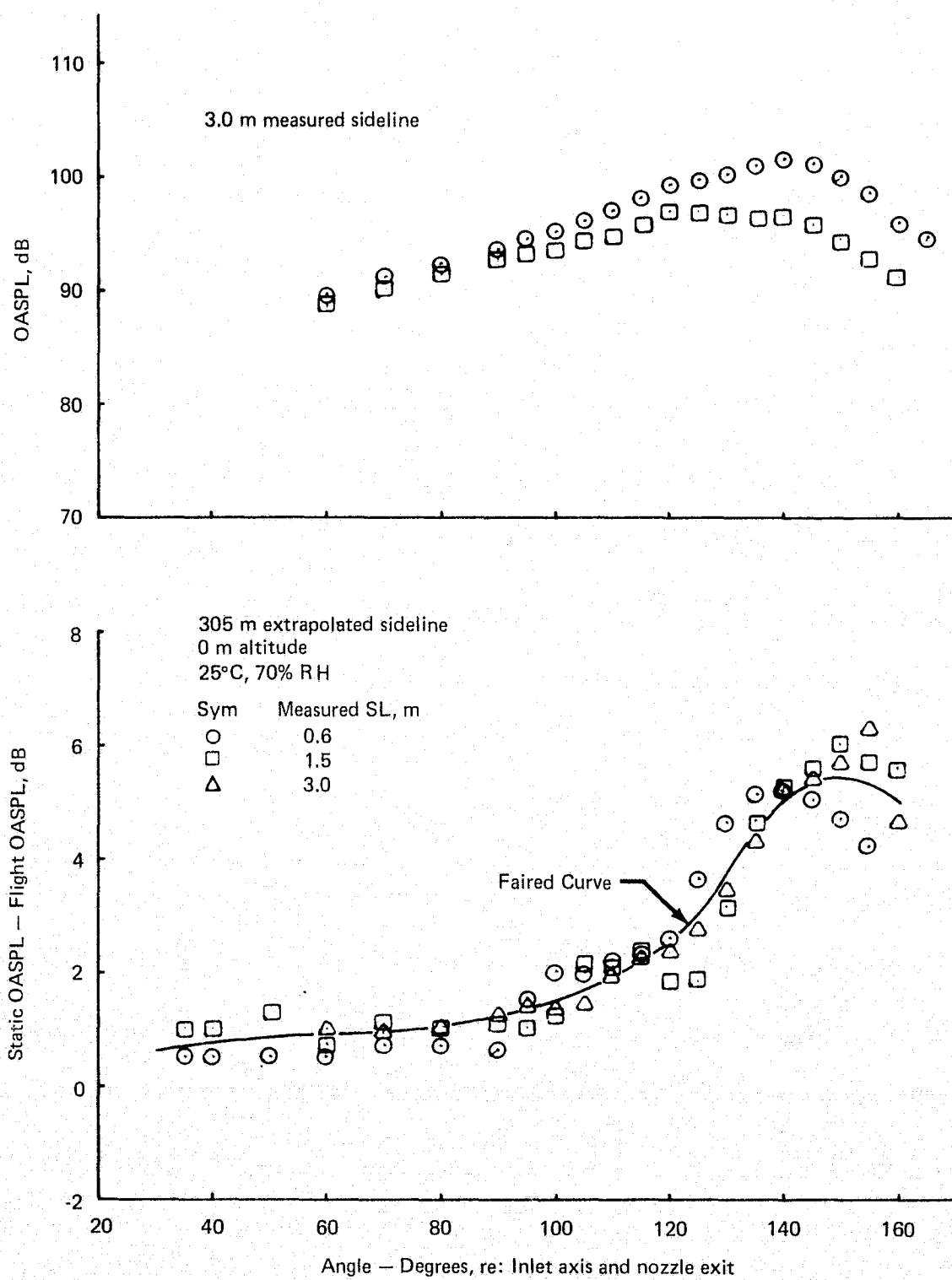


Figure 66.— (Concluded)

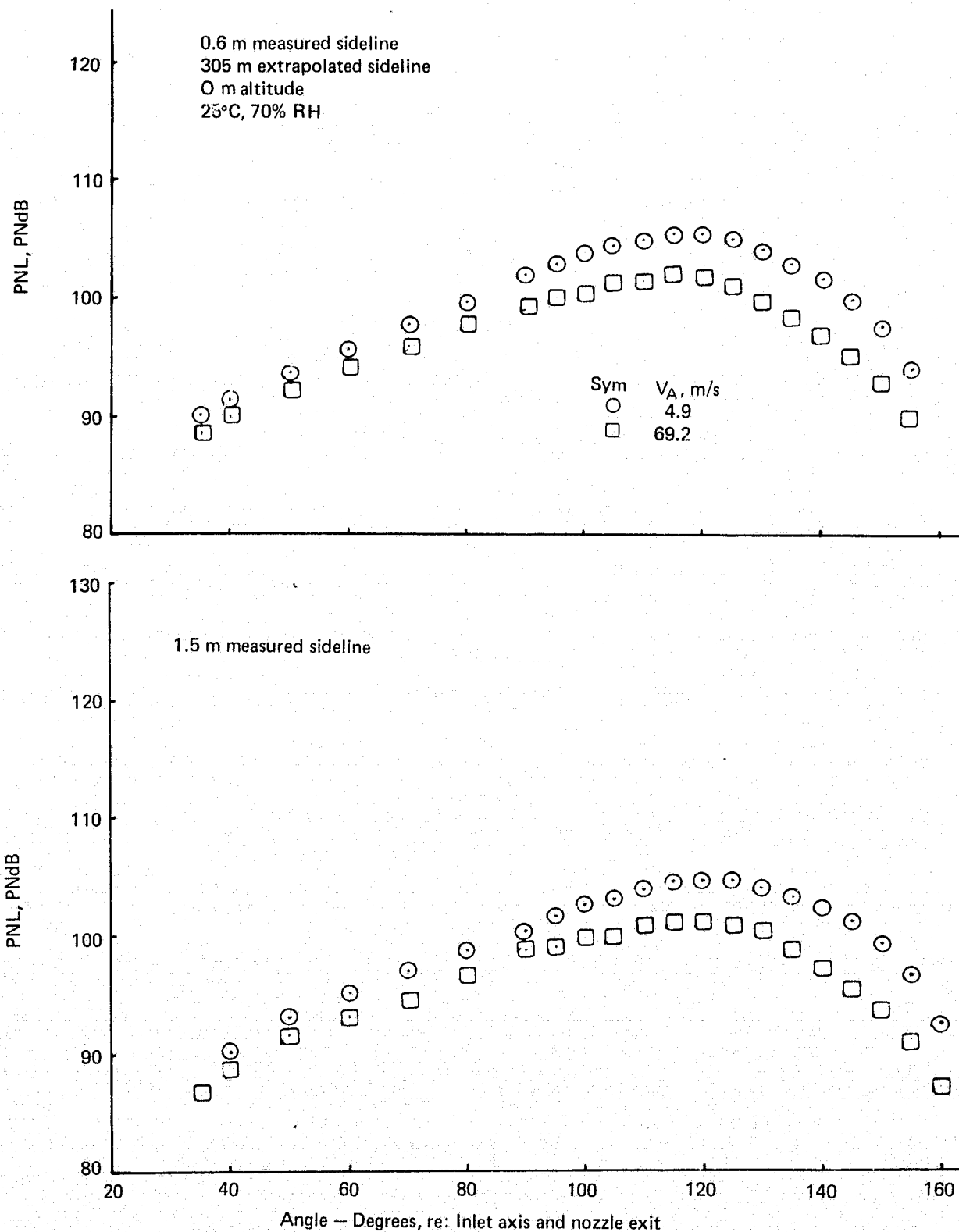


Figure 67.— Flight Effects on PNL of a 20-Lobe Nozzle $NPR = 1.75$, $V_i = 503$ m/s

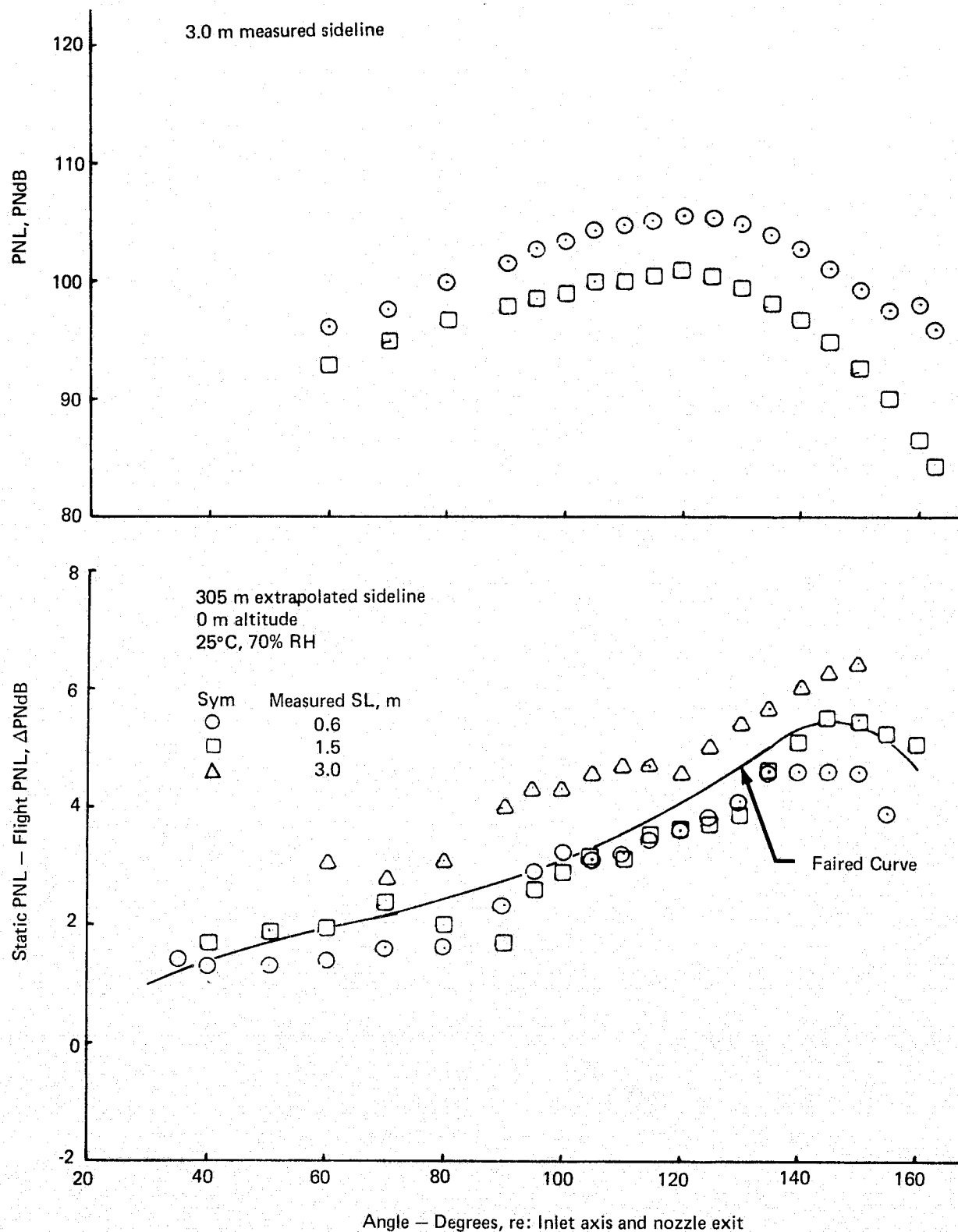


Figure 67.— (Concluded)

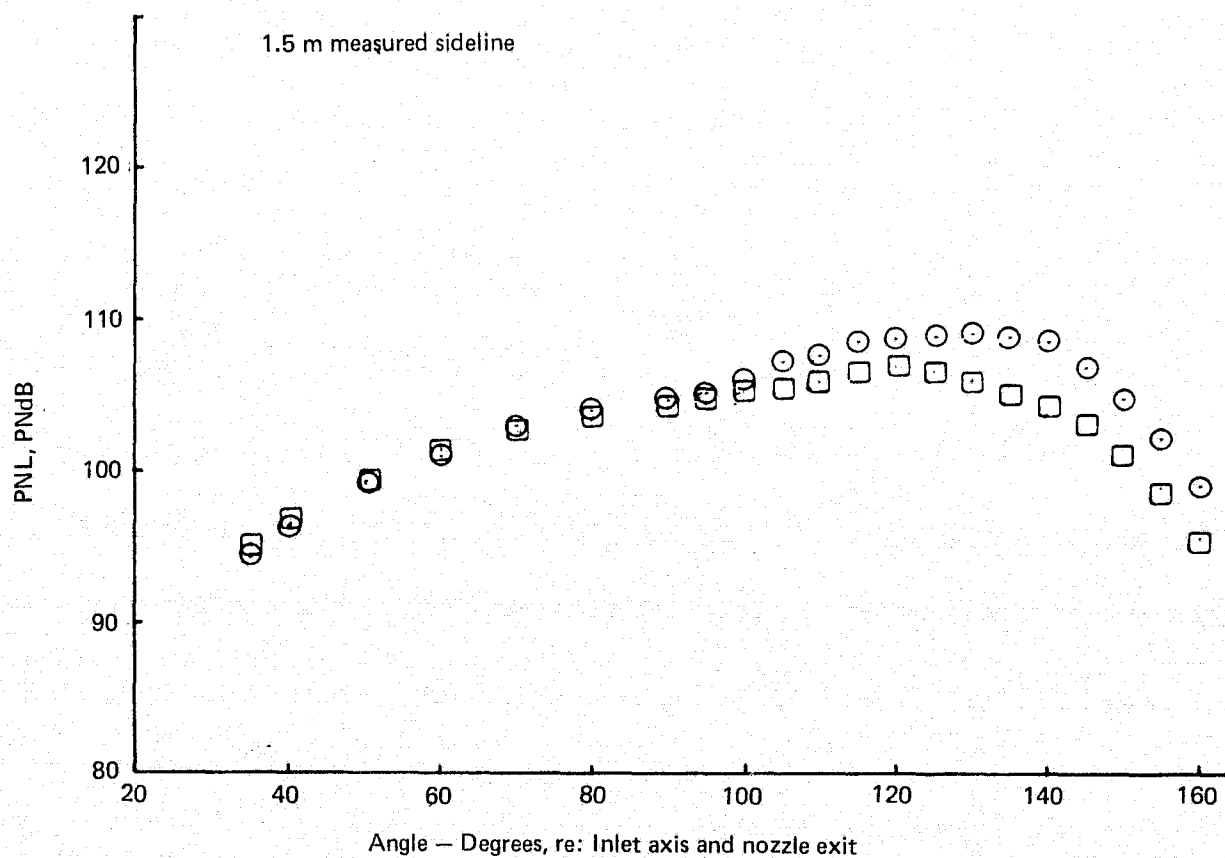
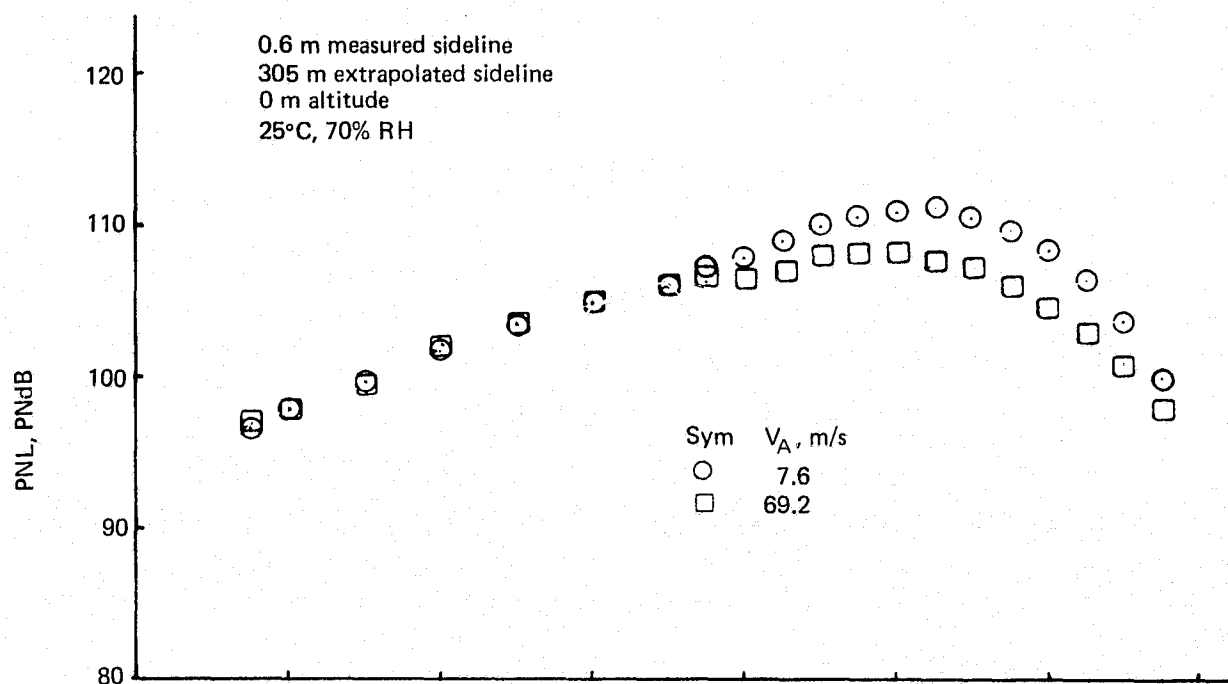


Figure 68.— Flight Effects on PNL of a 20-Lobe Nozzle $NPR = 2.25$, $V_j = 594$ m/s

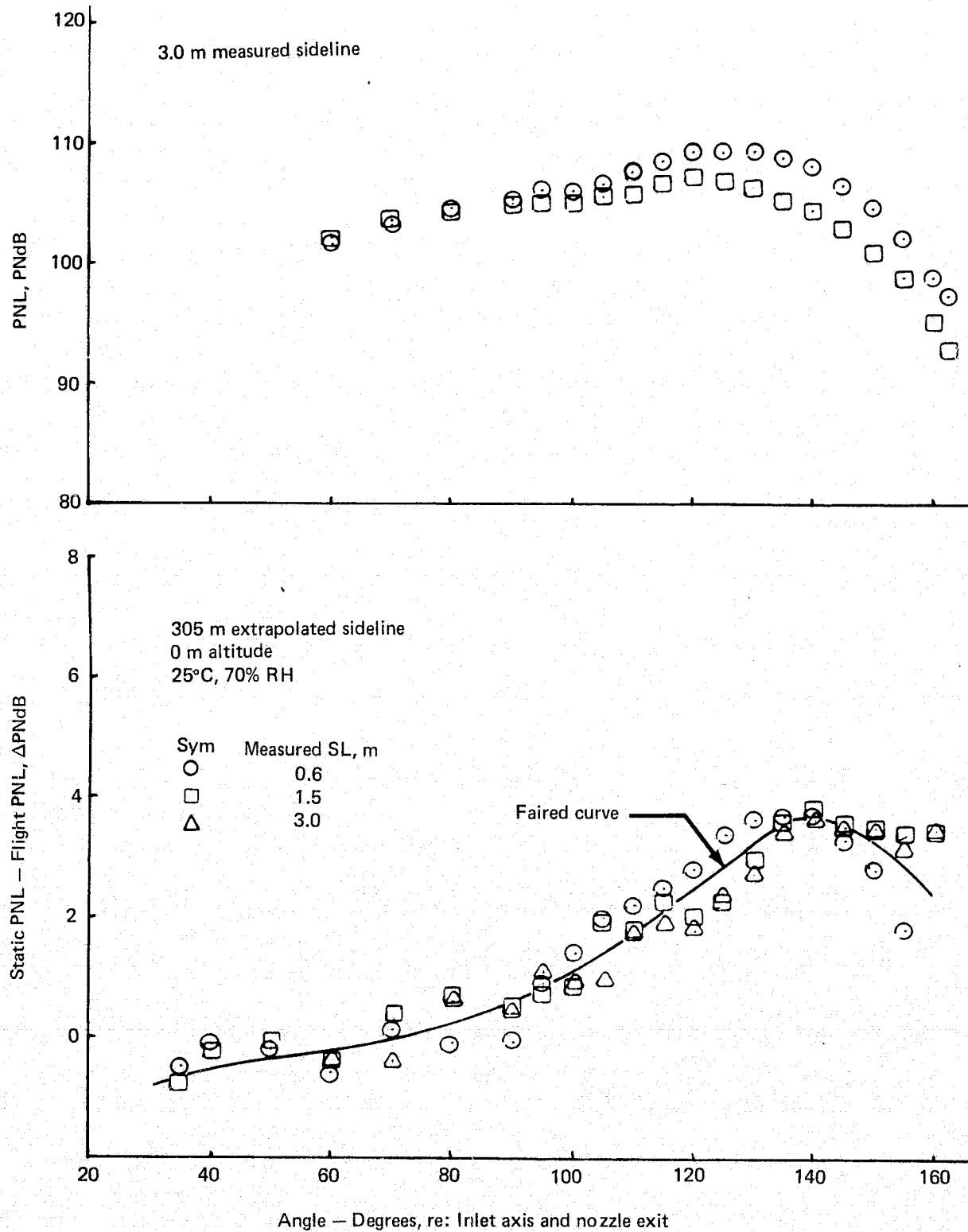


Figure 68.— (Concluded)

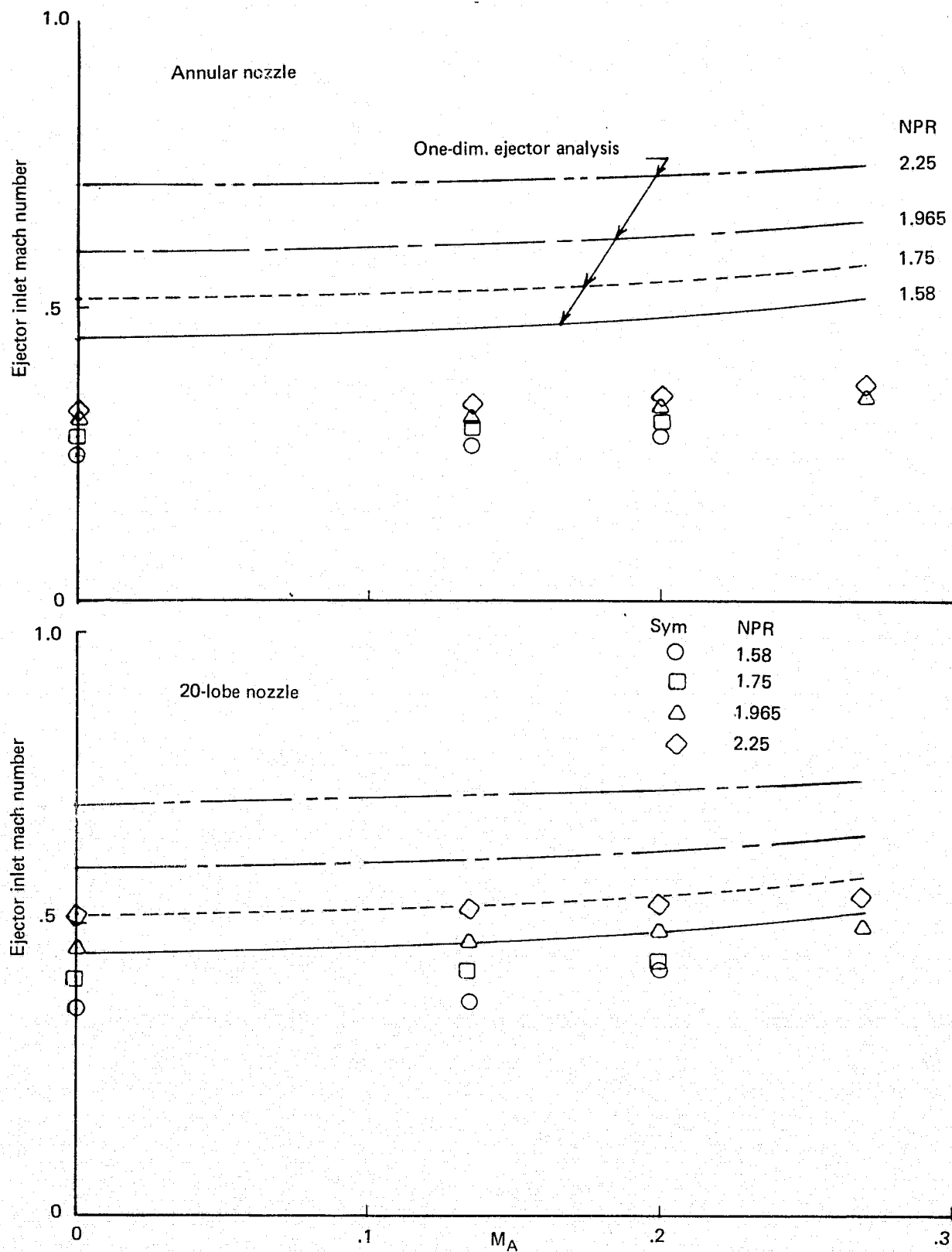
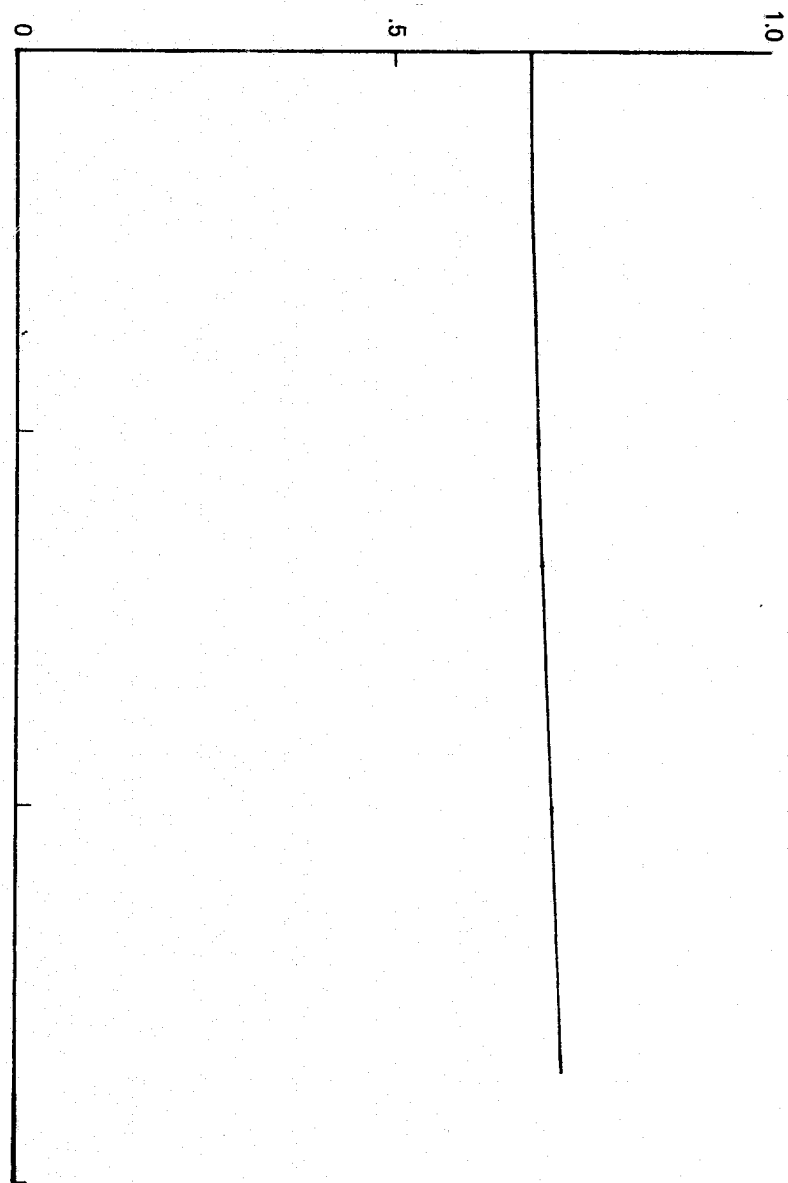


Figure 69.— Ejector Performance with Annular and 20-Lobe Nozzles

Ratio of fully-mixed ejector exit
velocity to the jet velocity



Ratio of fully-mixed ejector exit
total temp. to the amb. total temp.

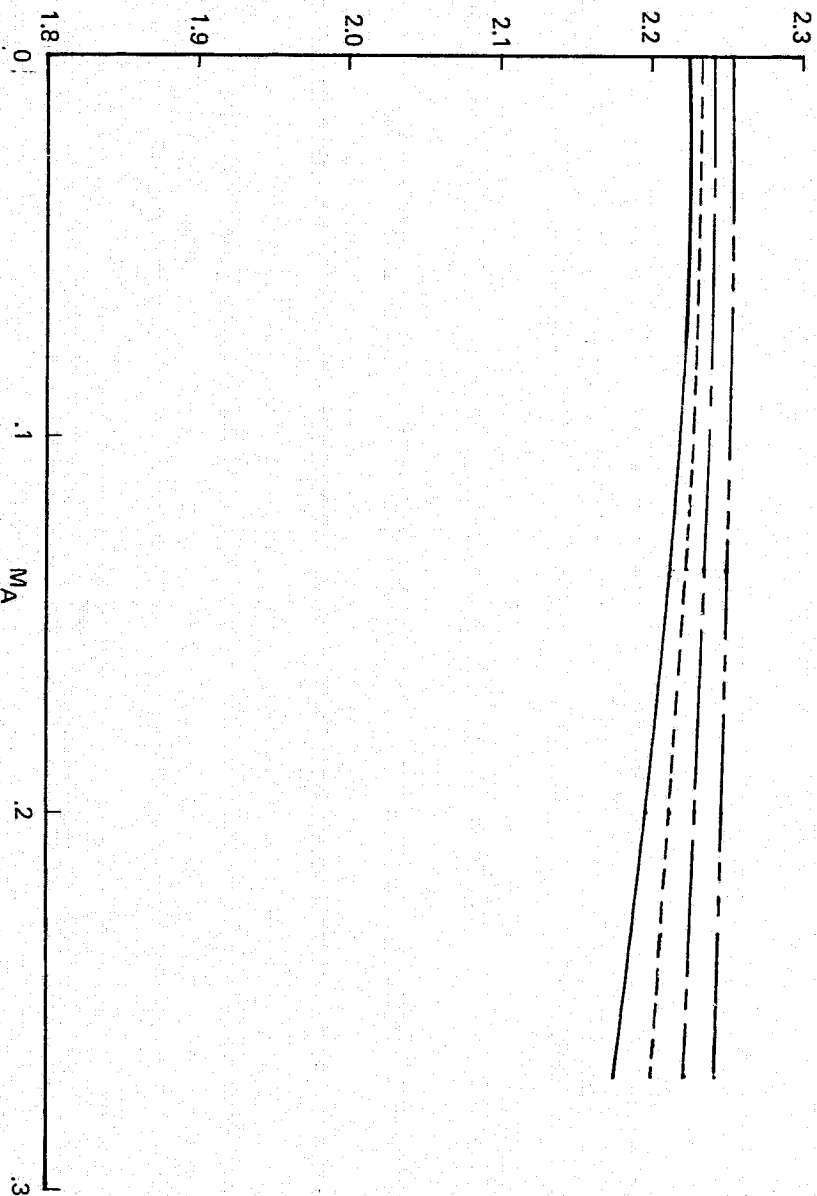


Figure 69.—(Continued)

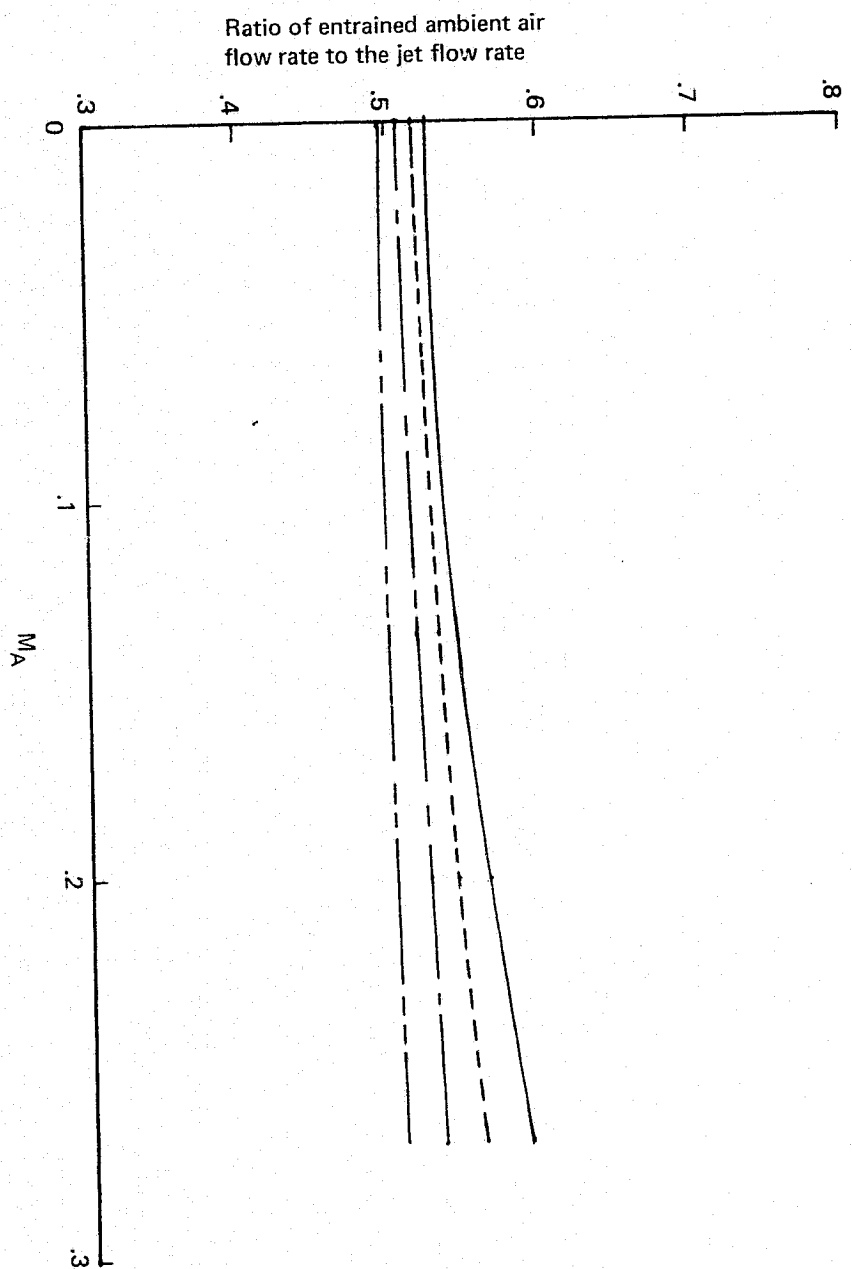


Figure 69. — (Concluded)

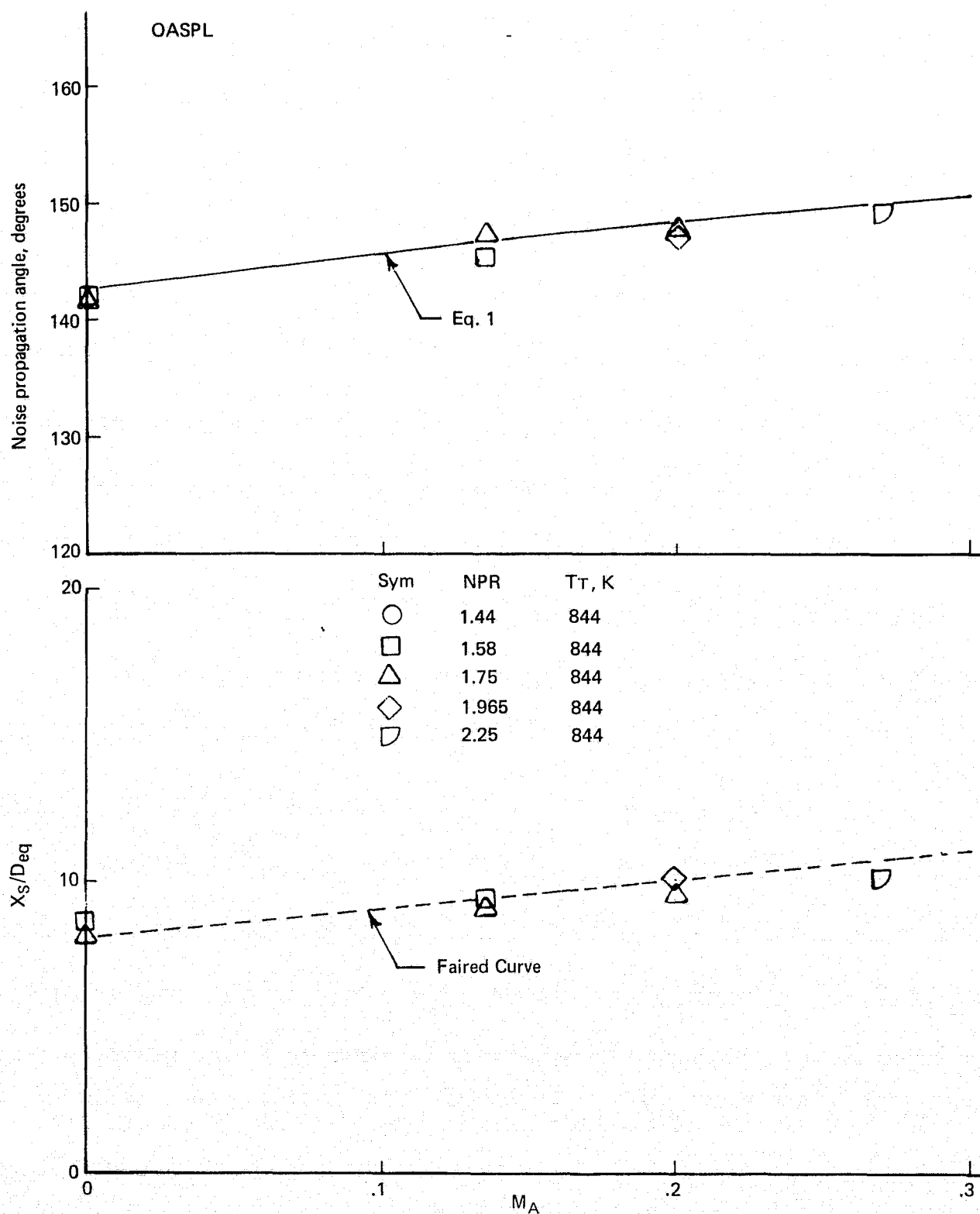


Figure 70.— Peak Noise Source Locations and Noise Propagation Angles for the Annular Nozzle with Lined Ejector

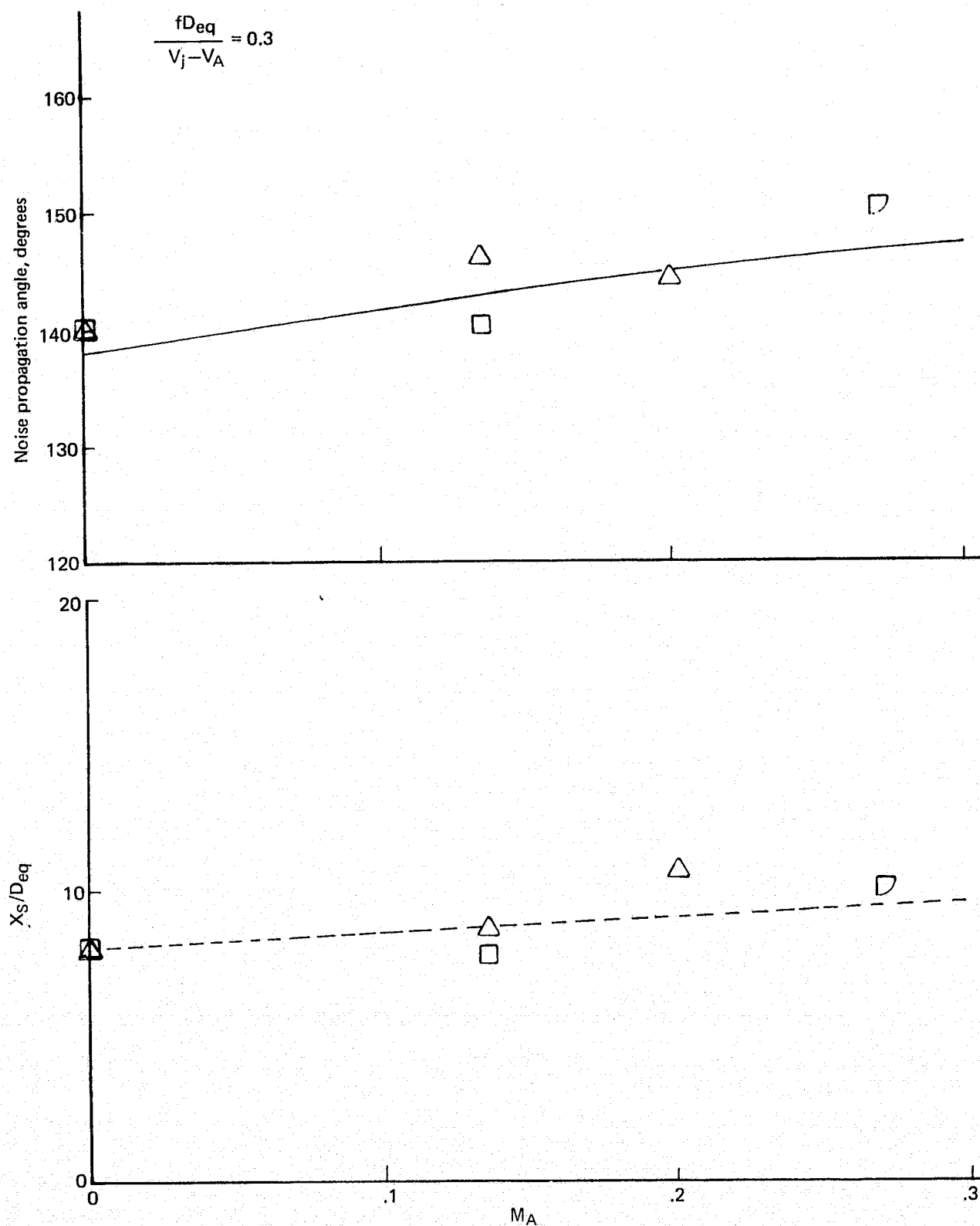


Figure 70.— (Continued)

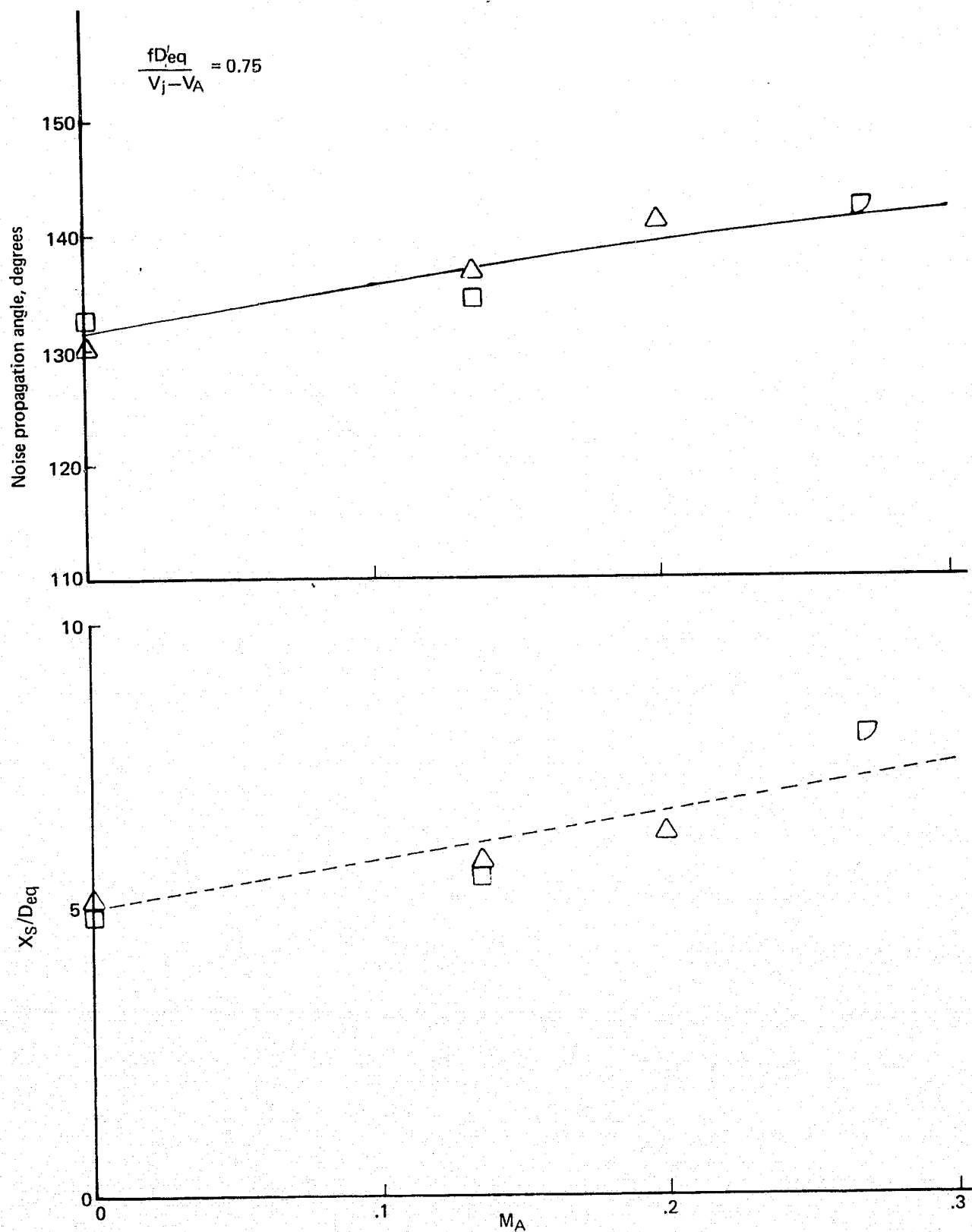


Figure 70.— (Continued)

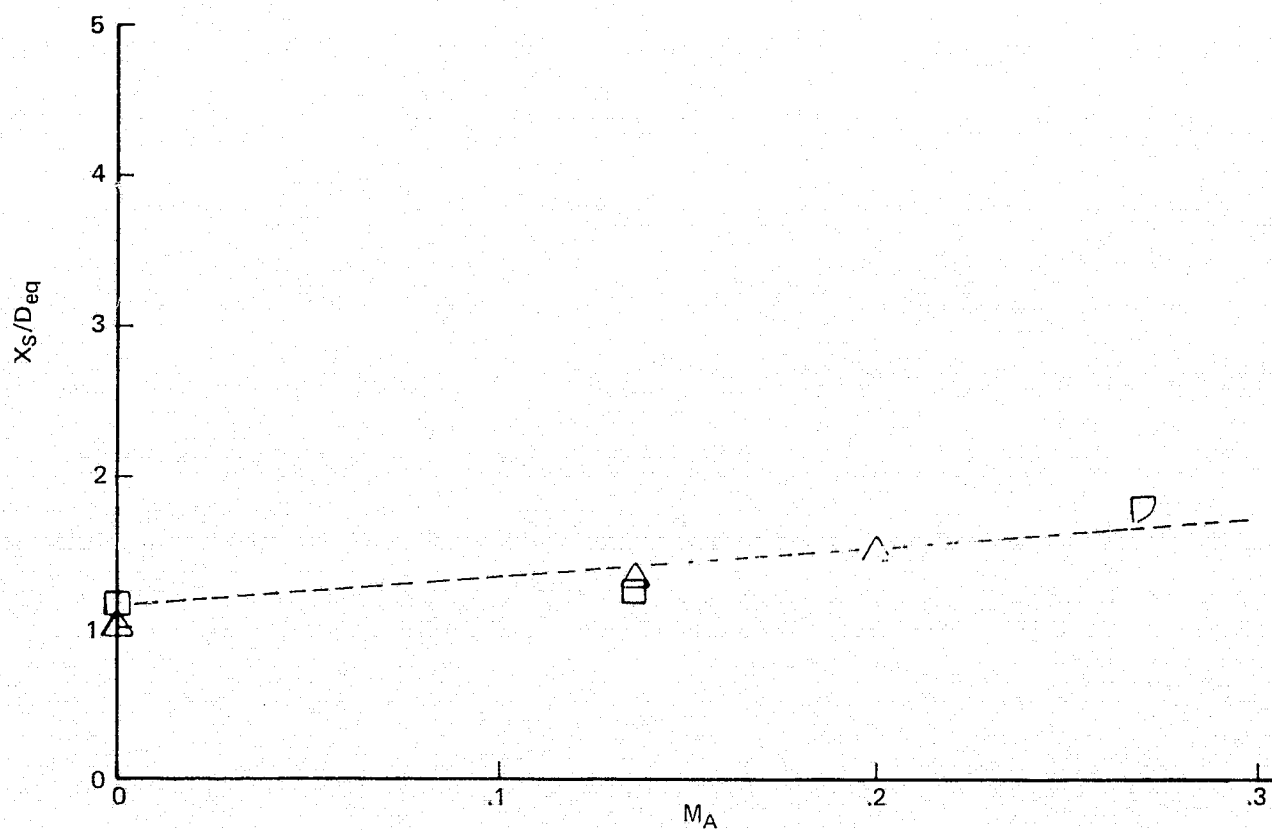
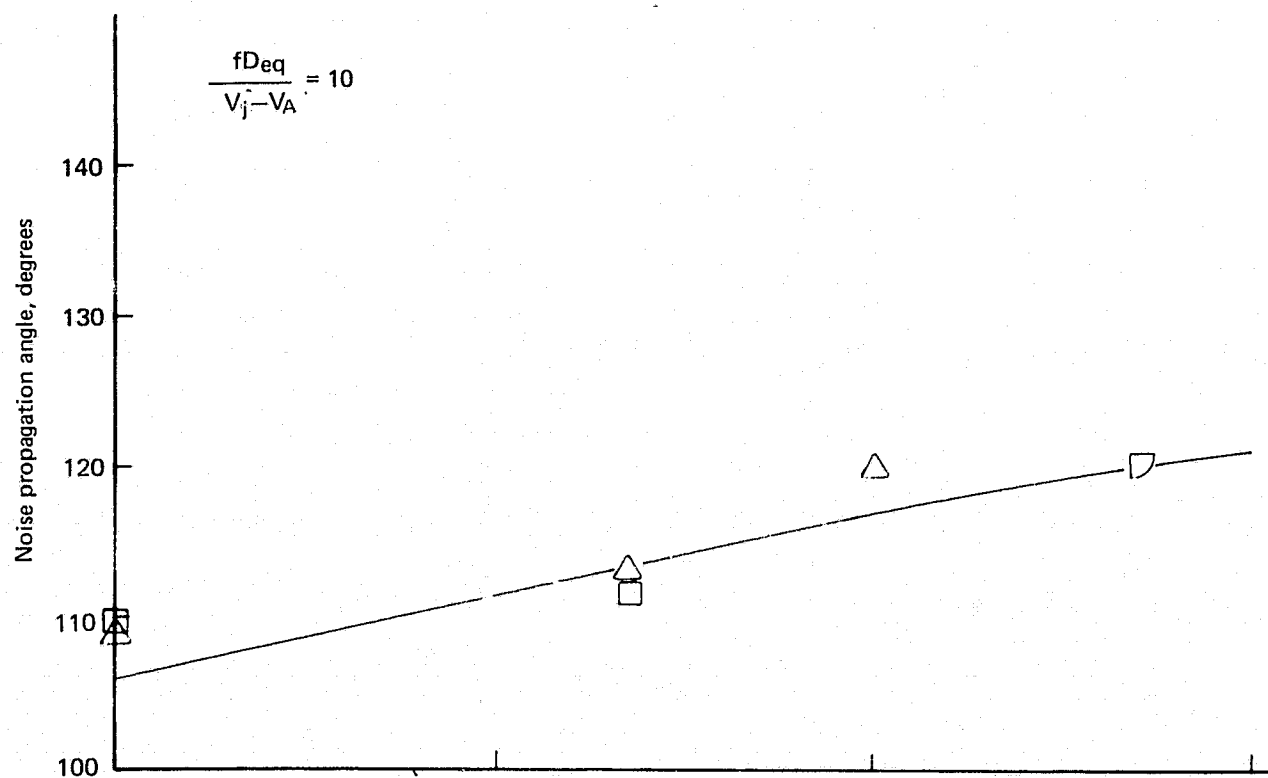


Figure 70.— (Concluded)

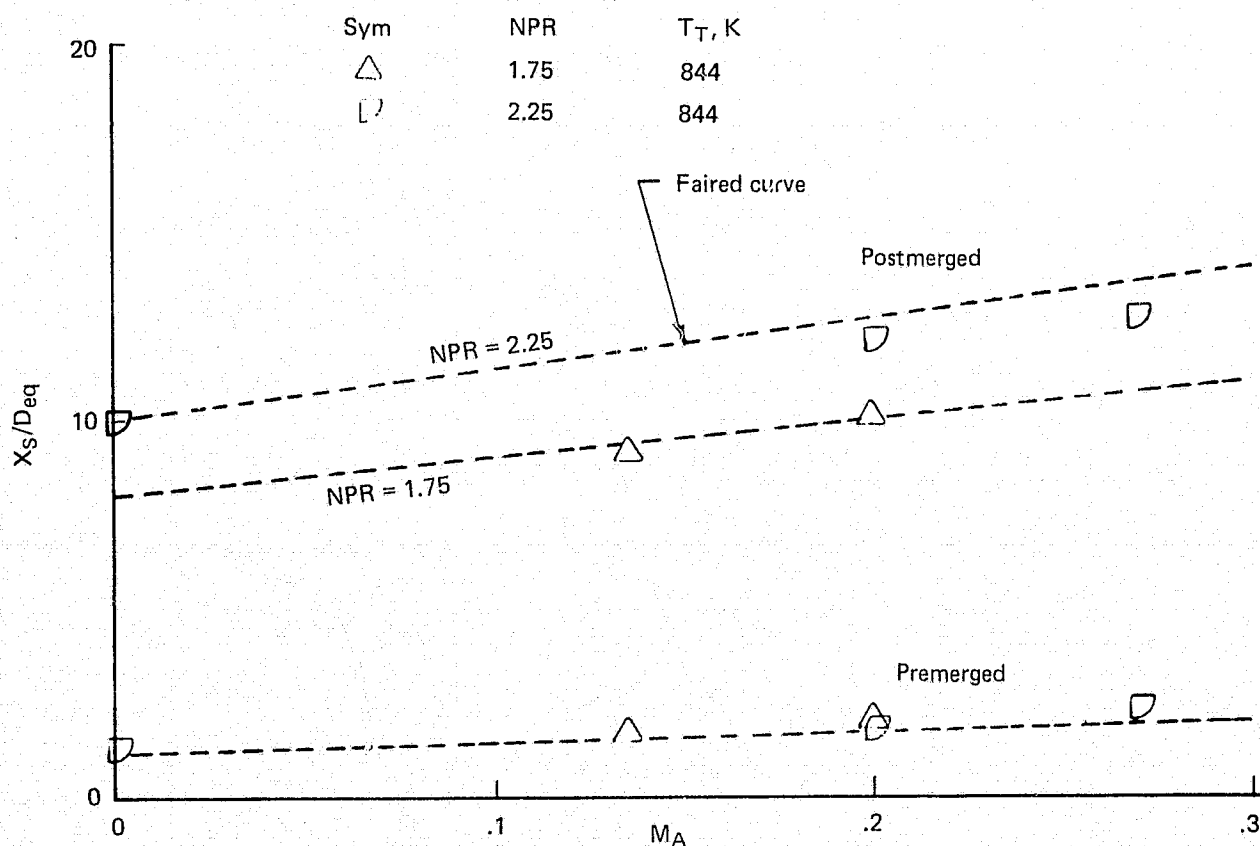
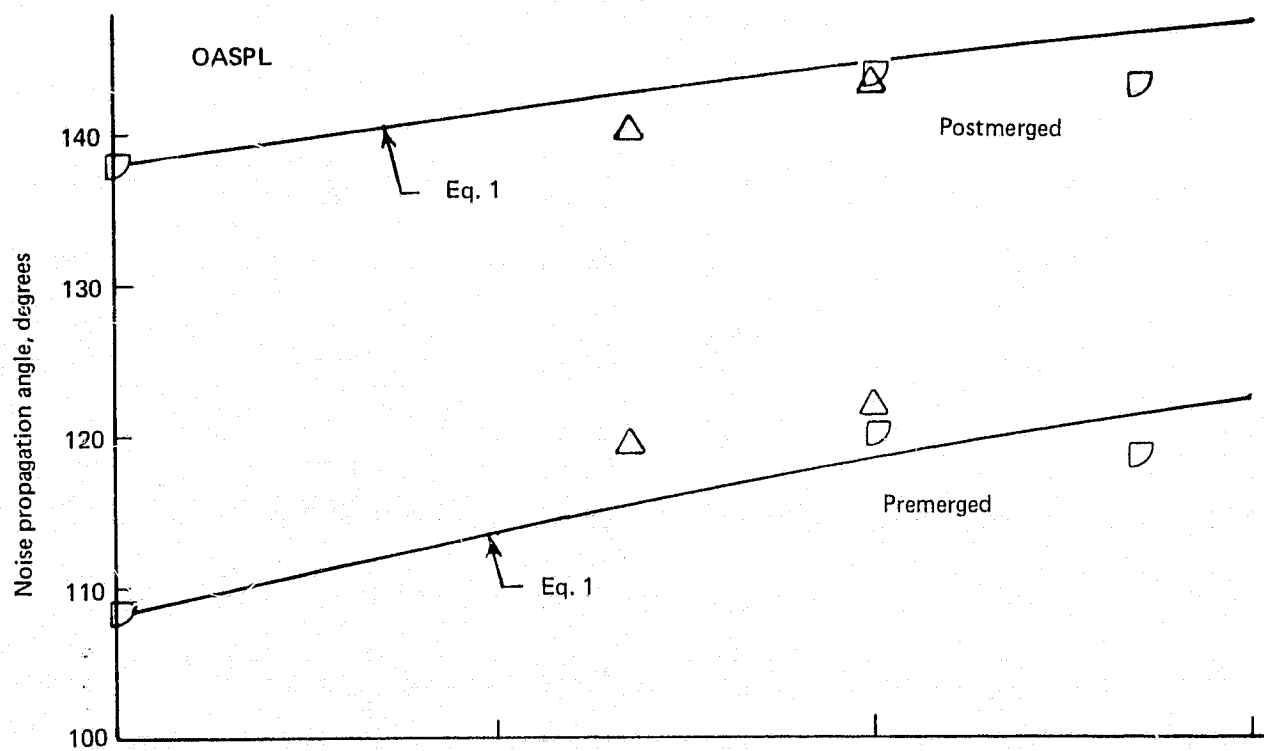


Figure 71.— Peak Noise Source Locations and Noise Propagation Angles for the 20-Lobe Nozzle With Lined Ejector

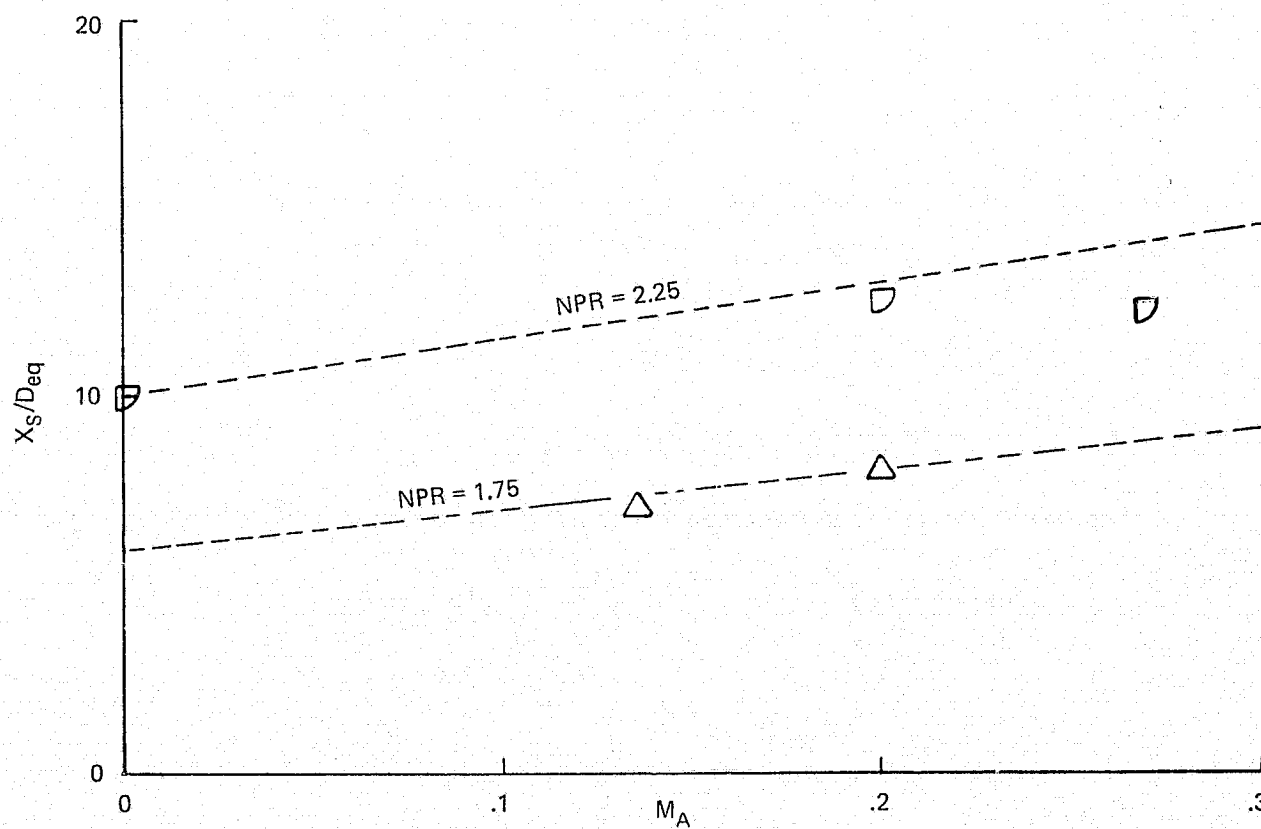
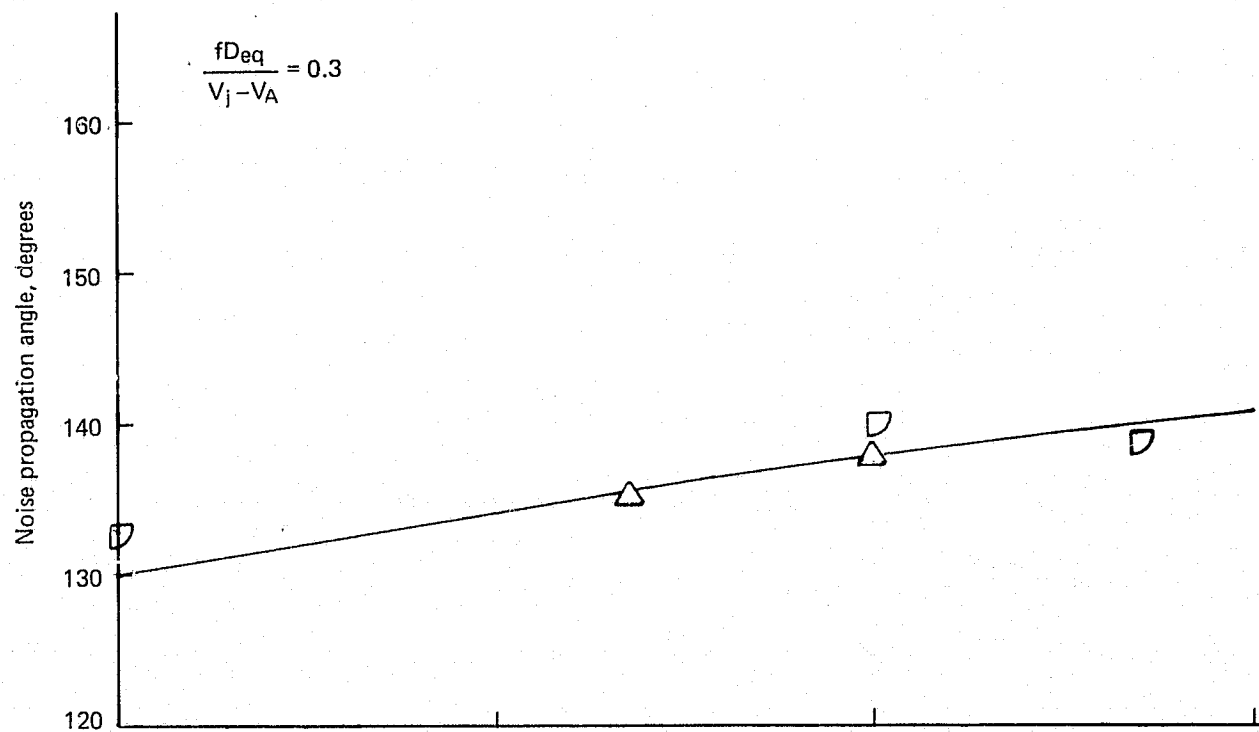


Figure 71.— (Continued)

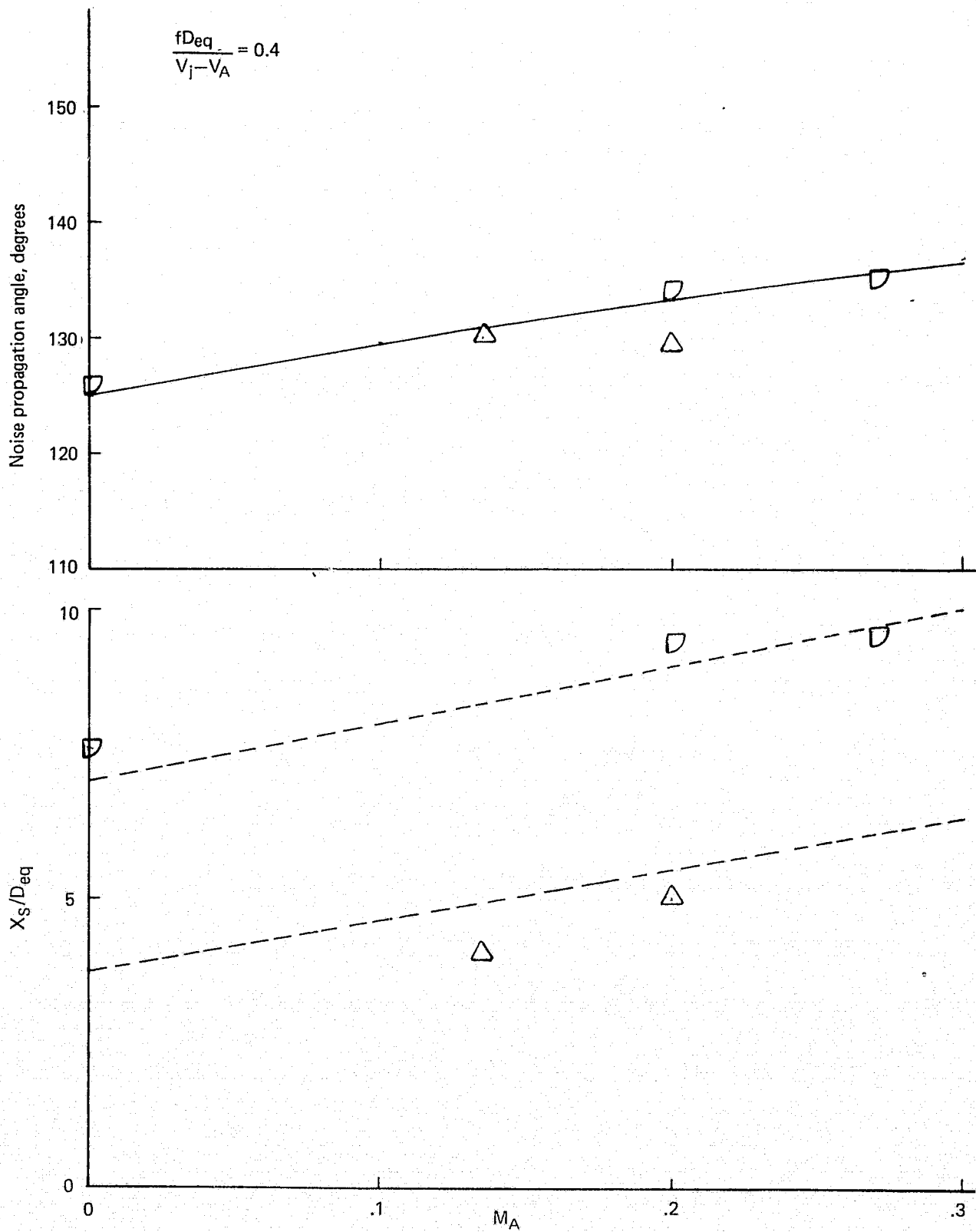


Figure 71.— (Continued)

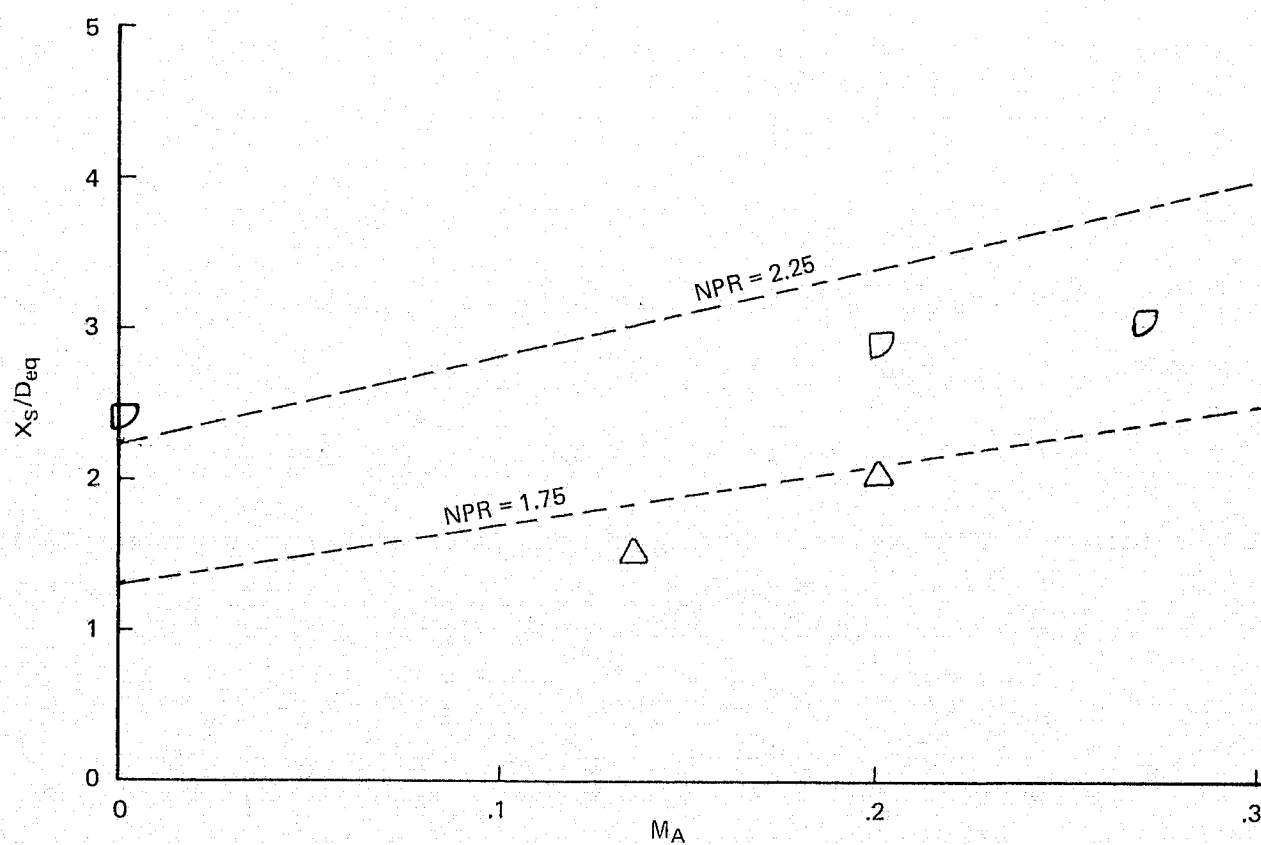
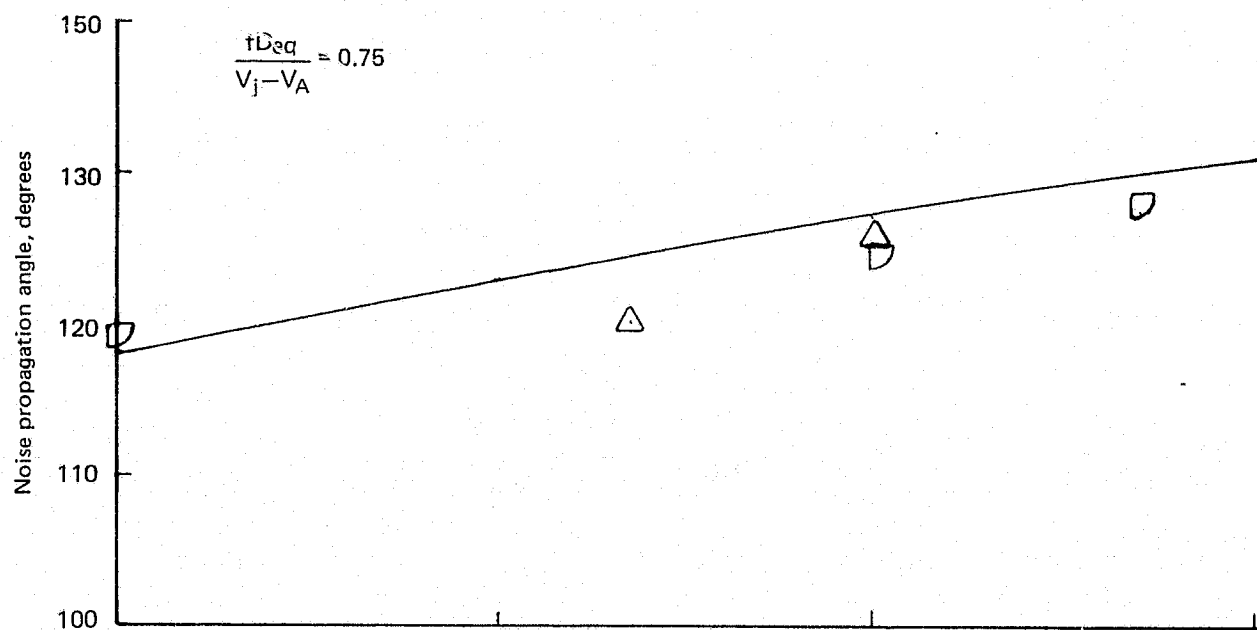


Figure 71.— (Continued)

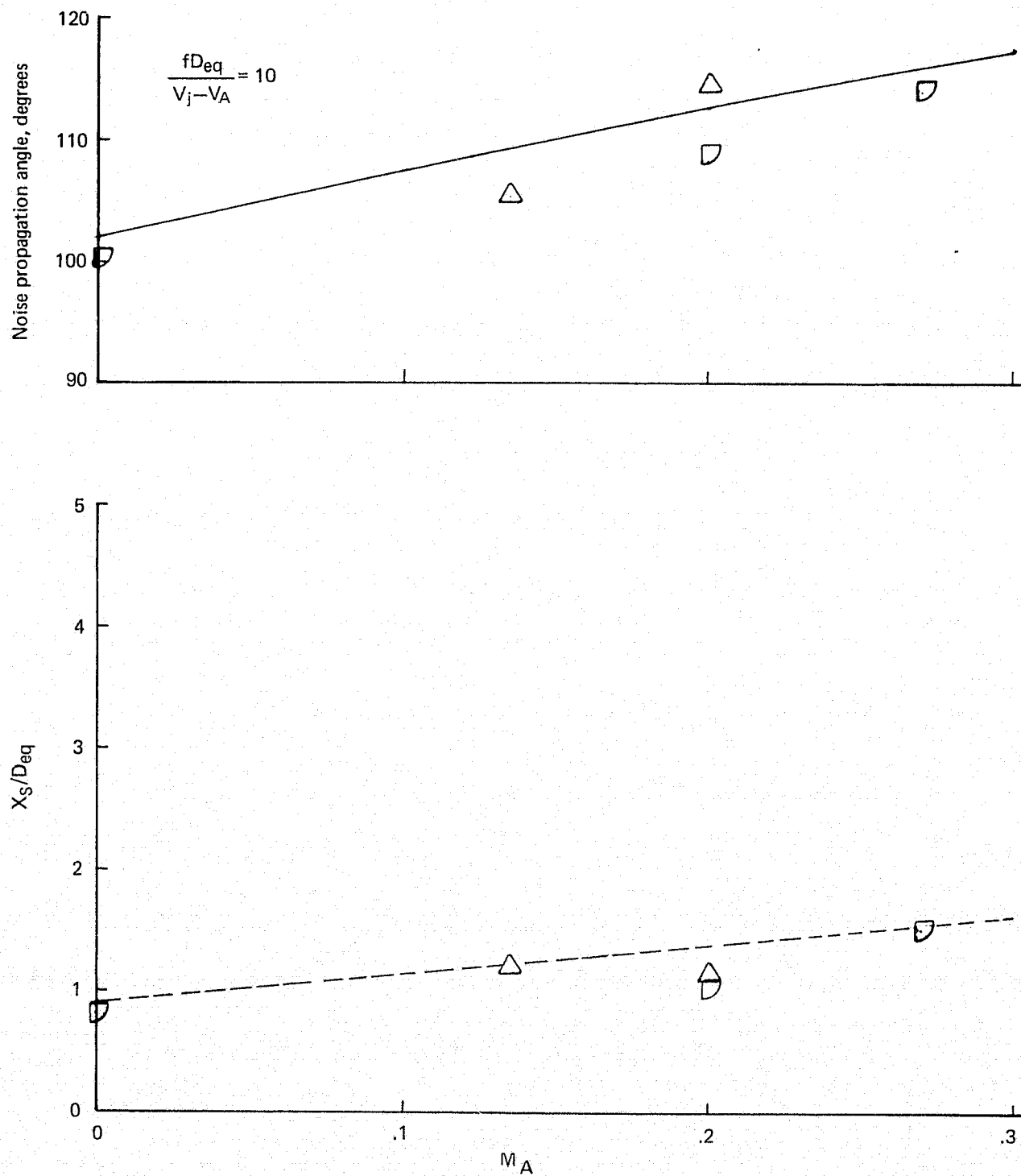


Figure 71.— (Concluded)

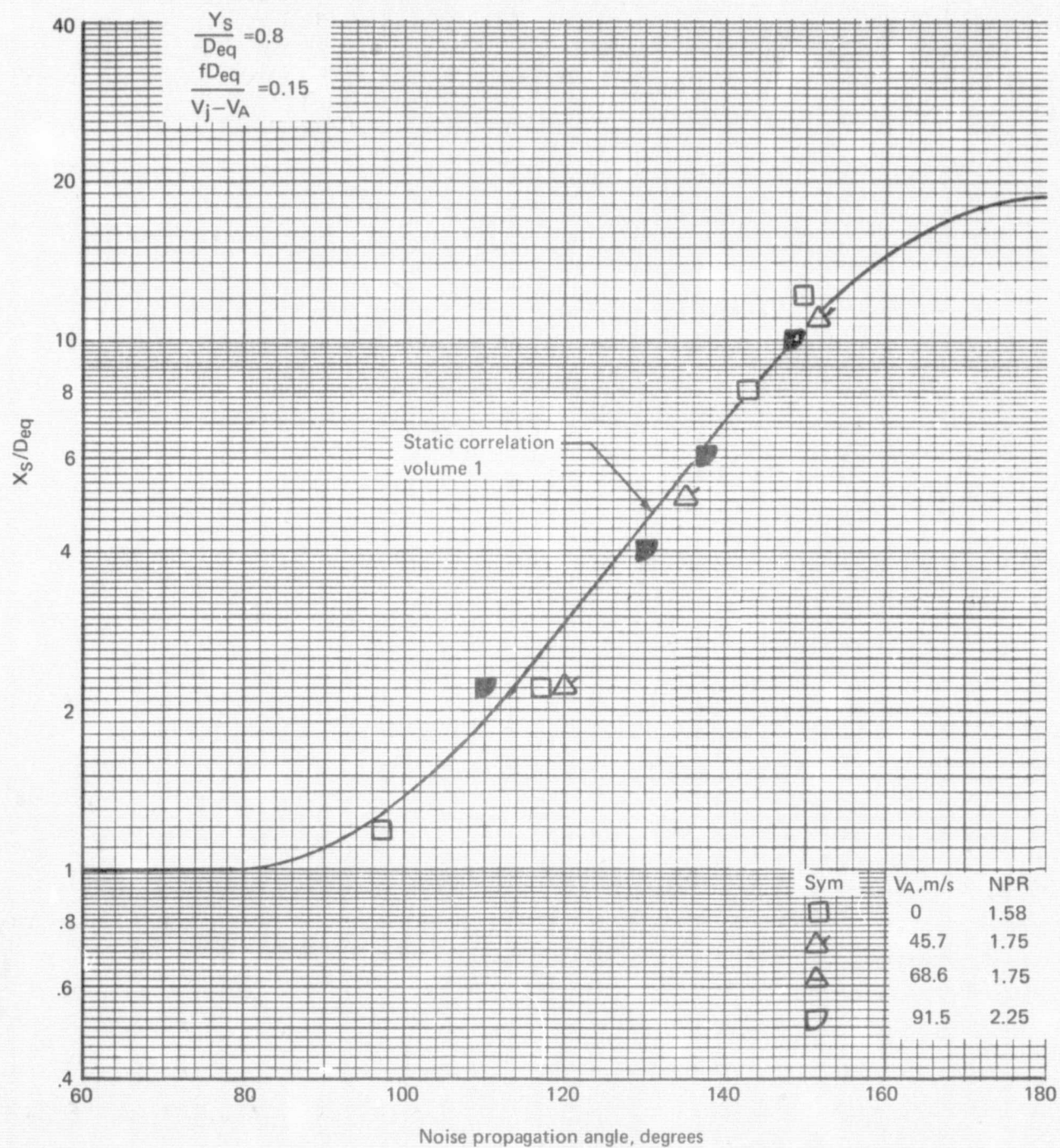


Figure 72.—Effect of Ambient Velocity on the Distributed Source Locations for the Annular Nozzle with Lined Ejector

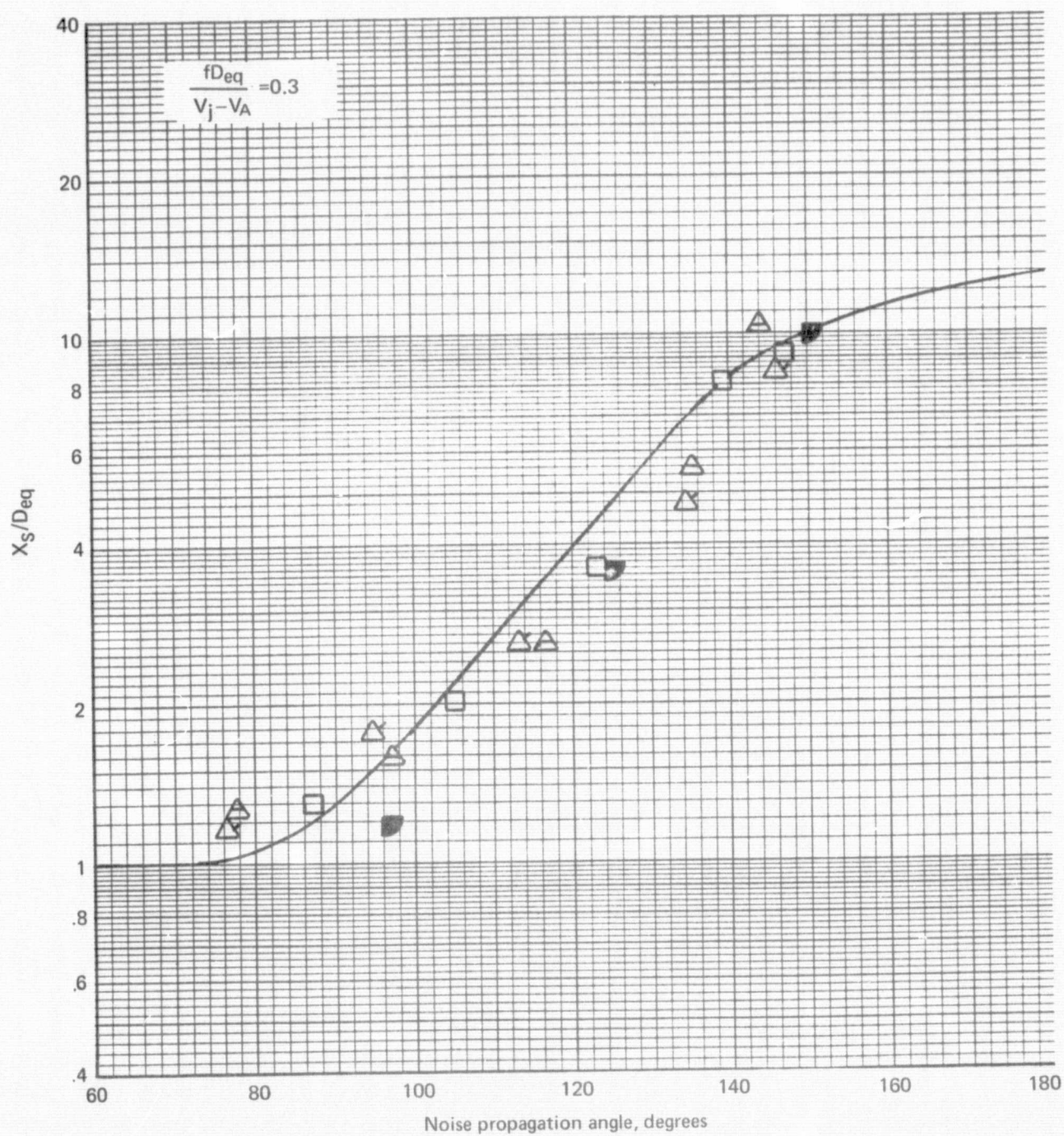


Figure 72.—(Continued)

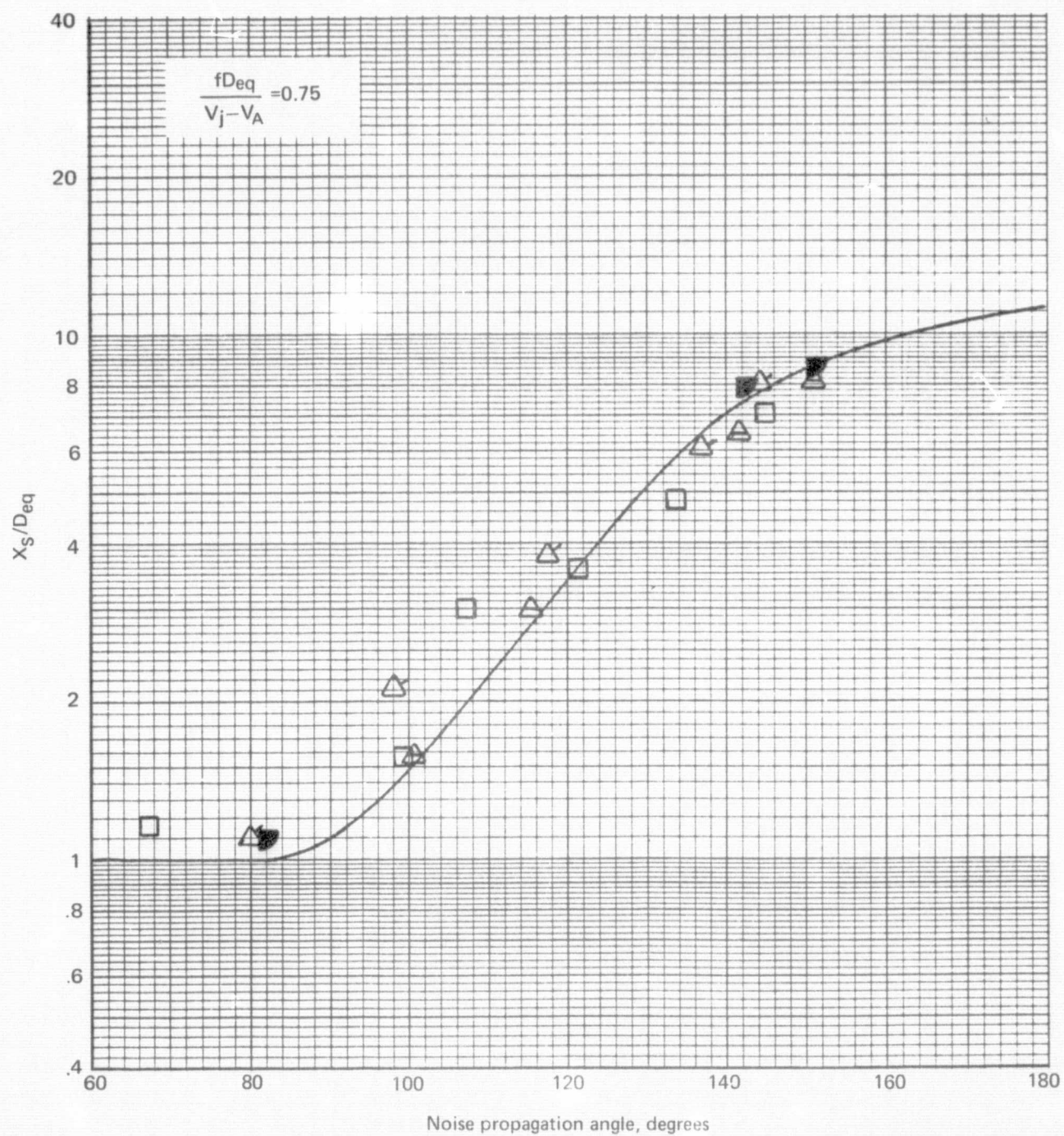


Figure 72.—(Continued)

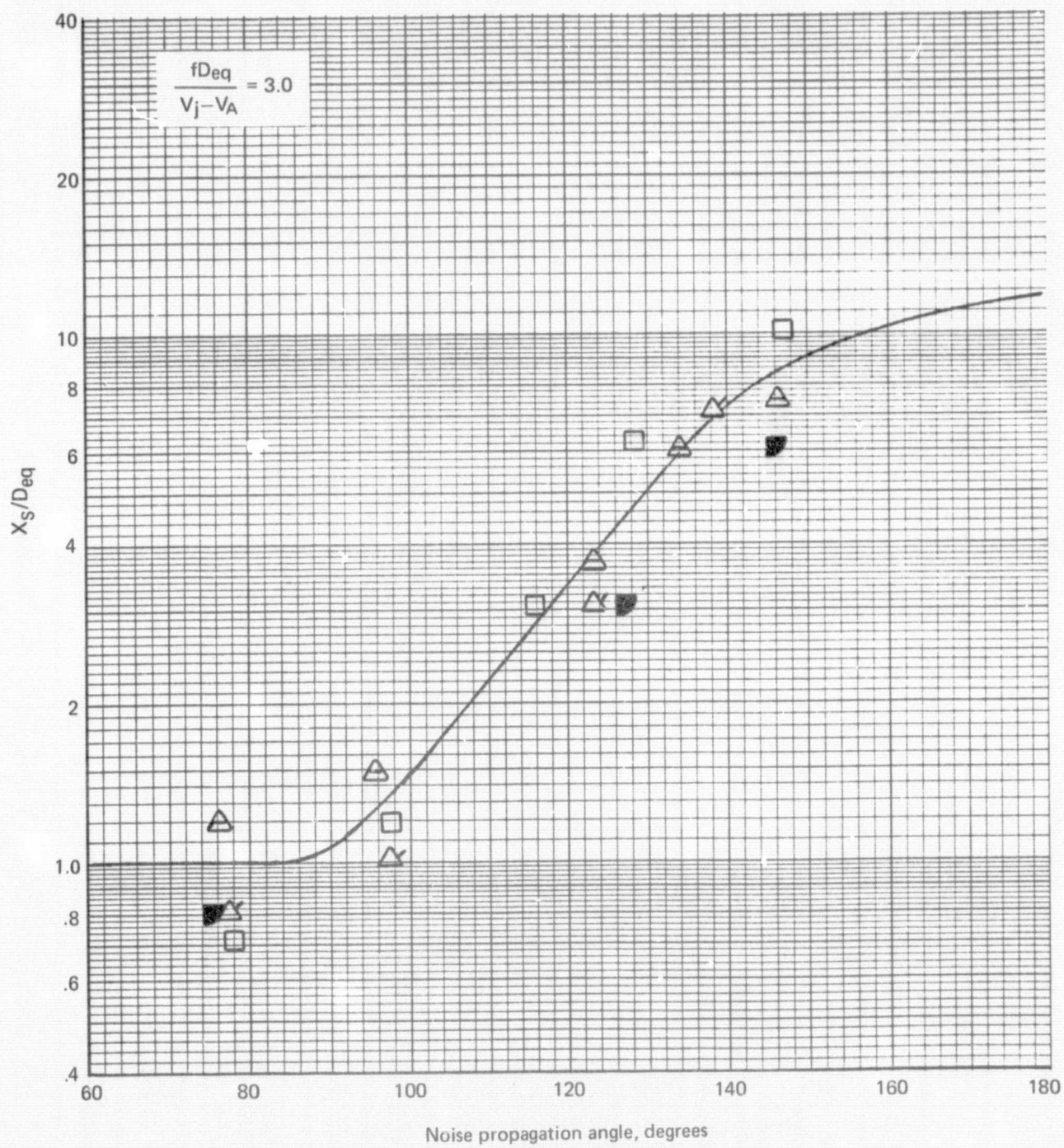


Figure 72.—(Continued)

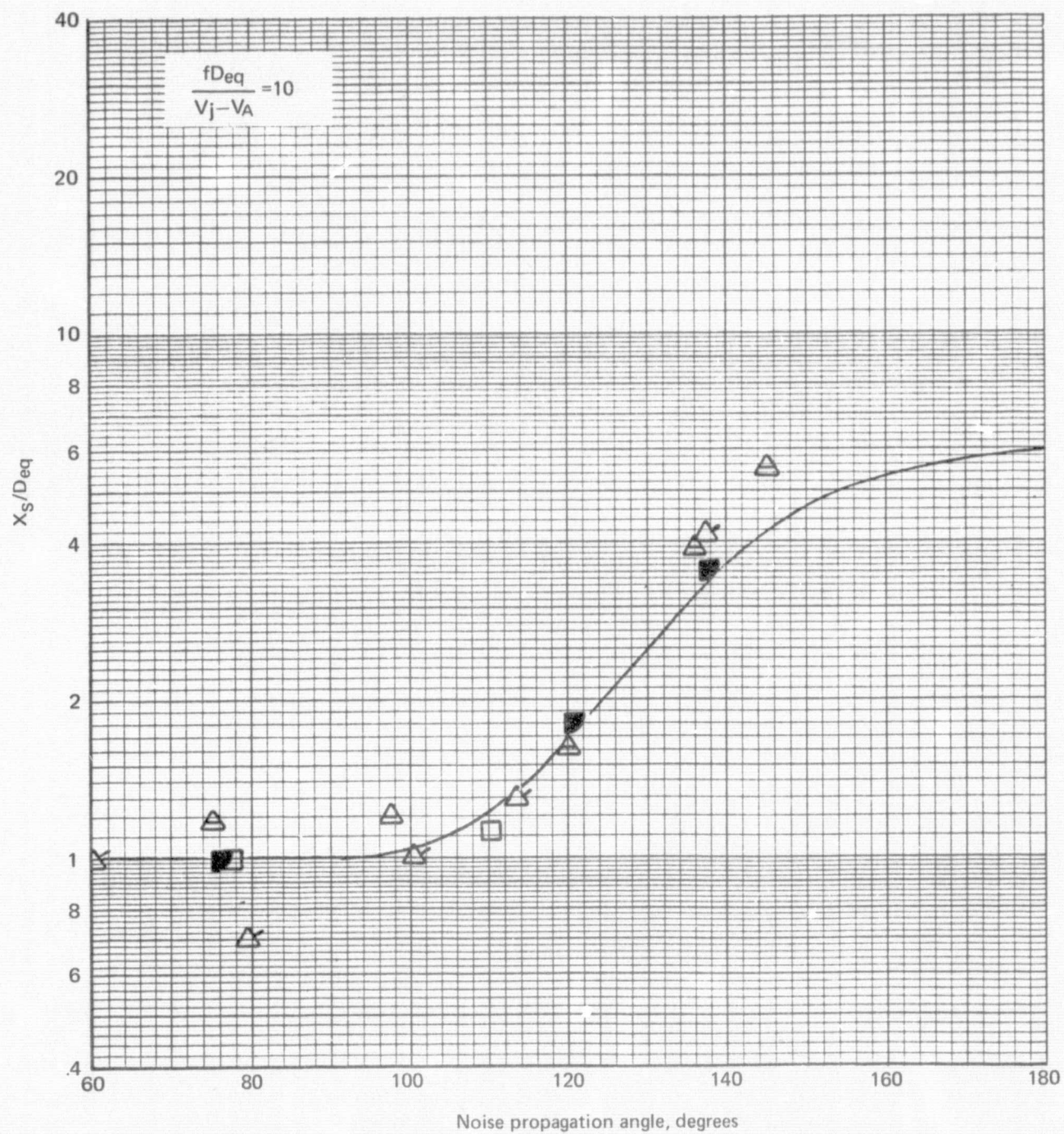


Figure 72.—(Concluded)

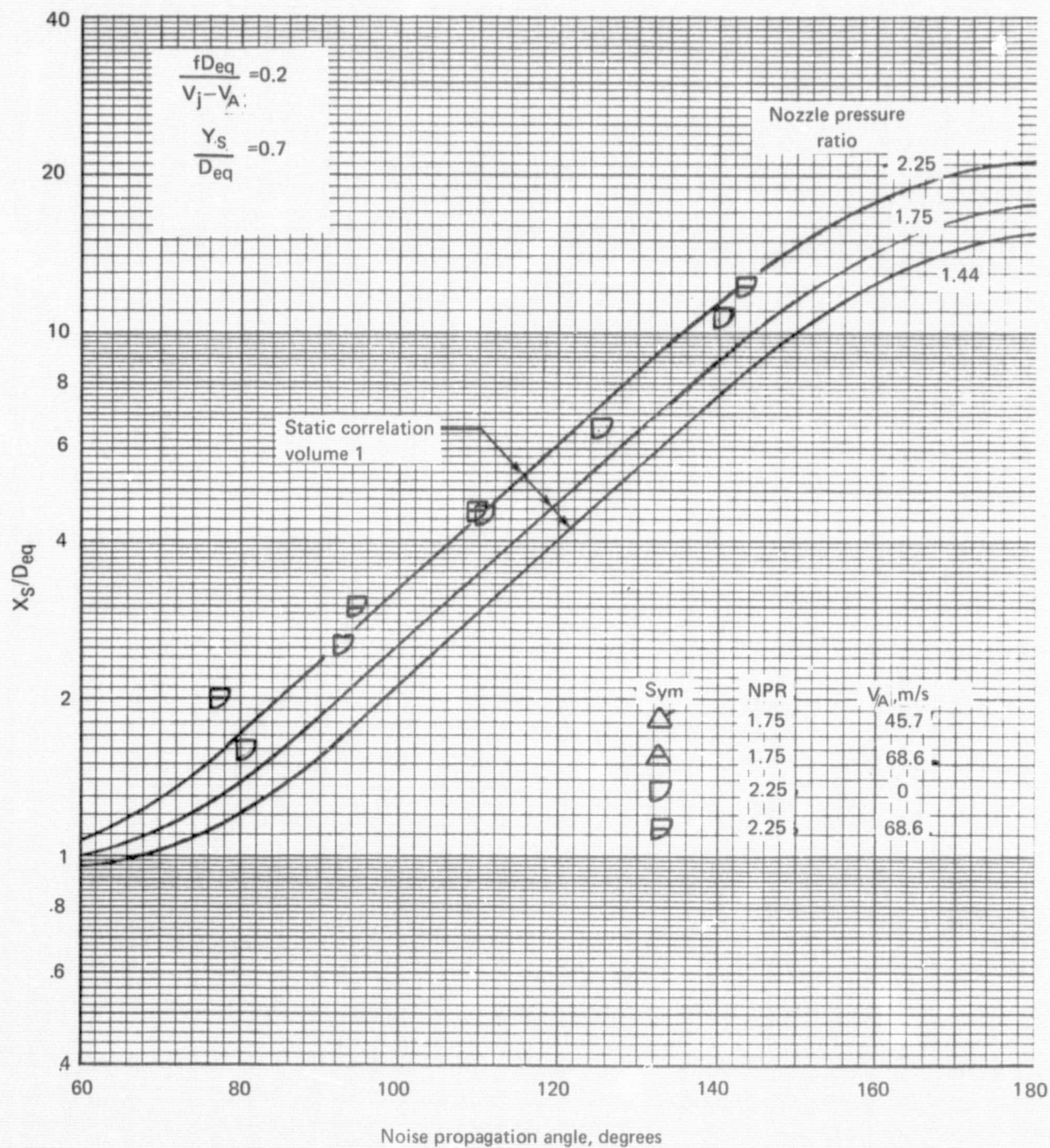


Figure 73.—Effect of Ambient Velocity on the Distributed Noise Source Locations for a 20-Lobe Nozzle with Lined Ejector

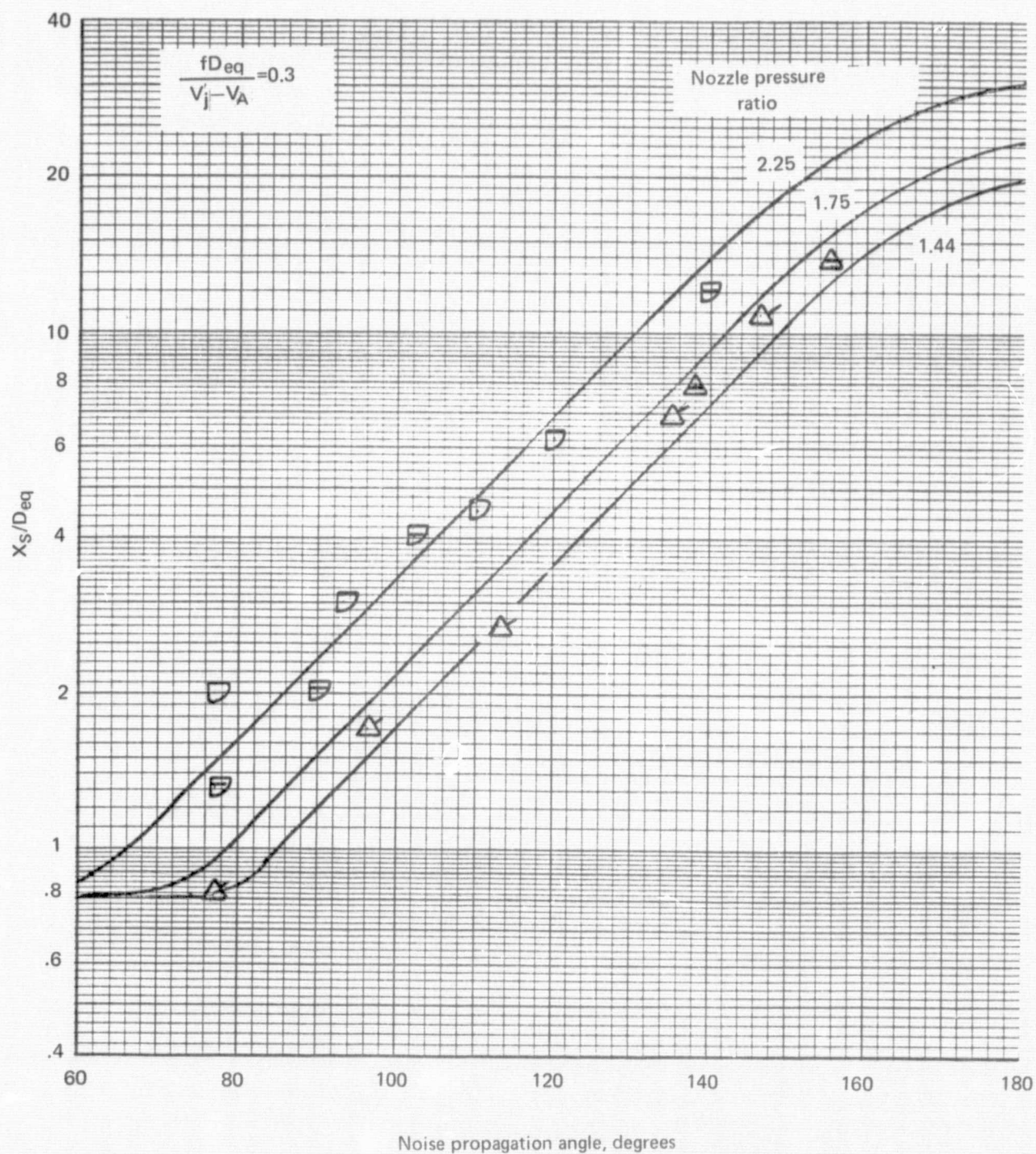


Figure 73.—(Continued)

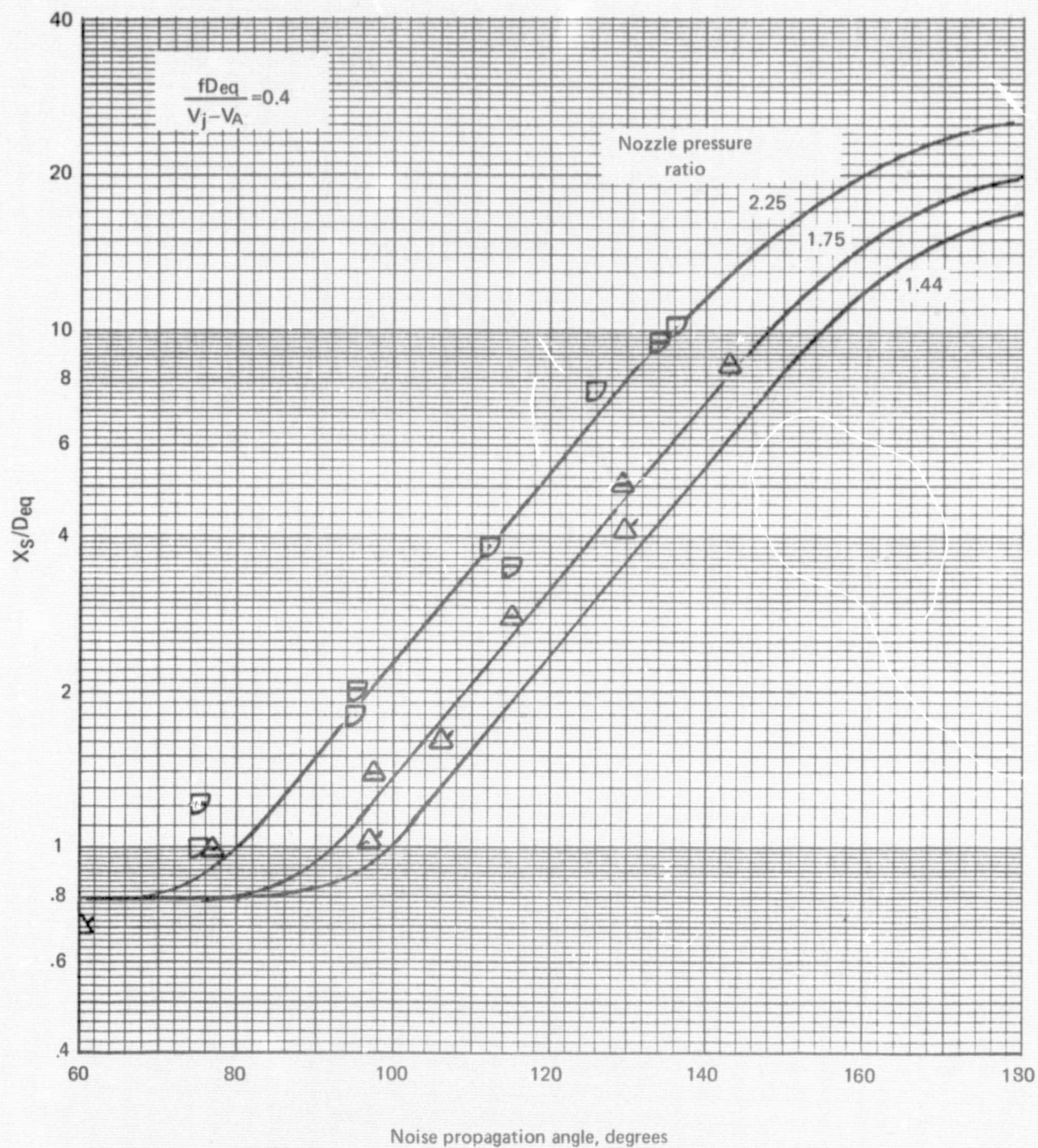


Figure 73.—(Continued)

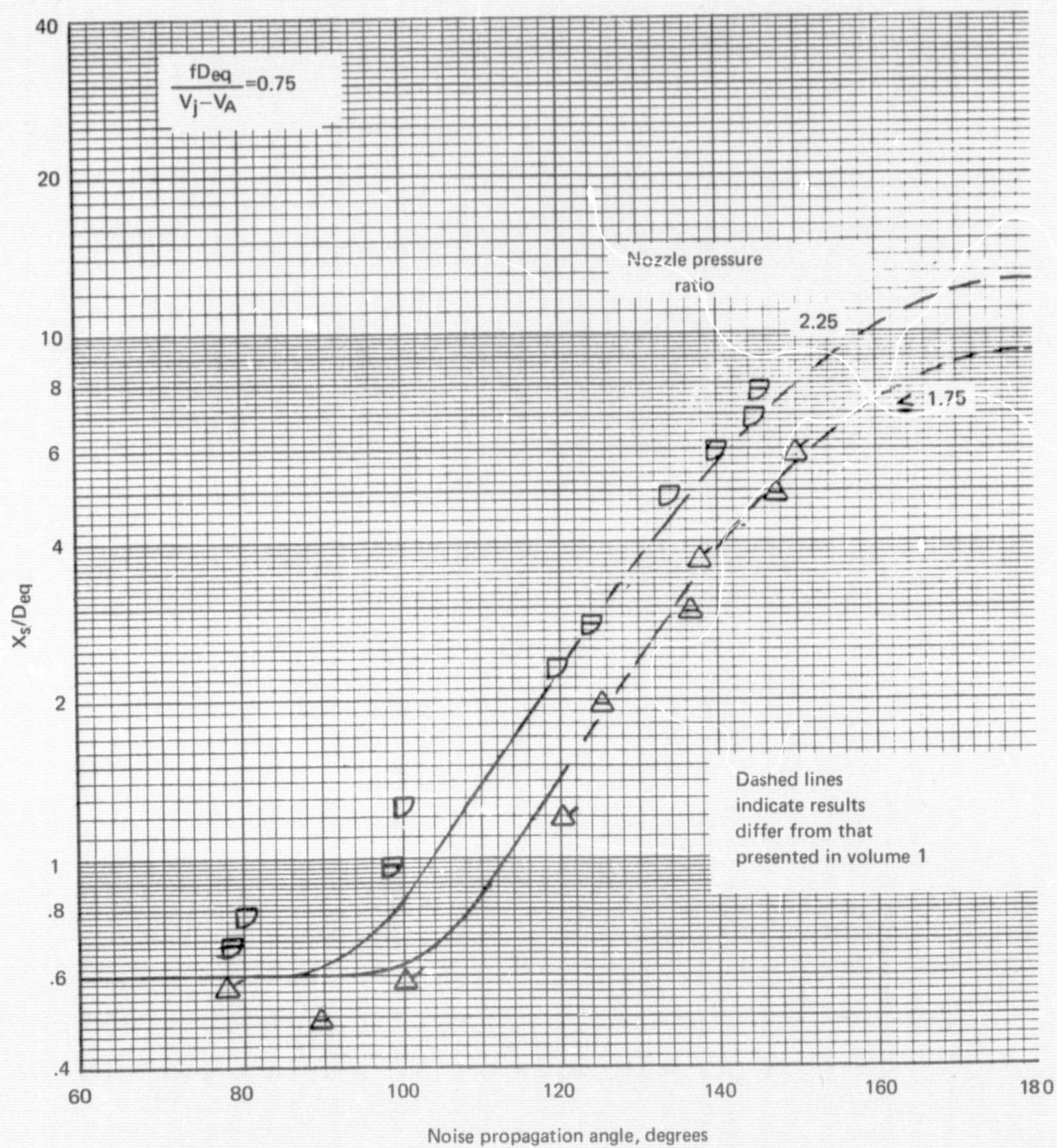


Figure 13.—(Continued)

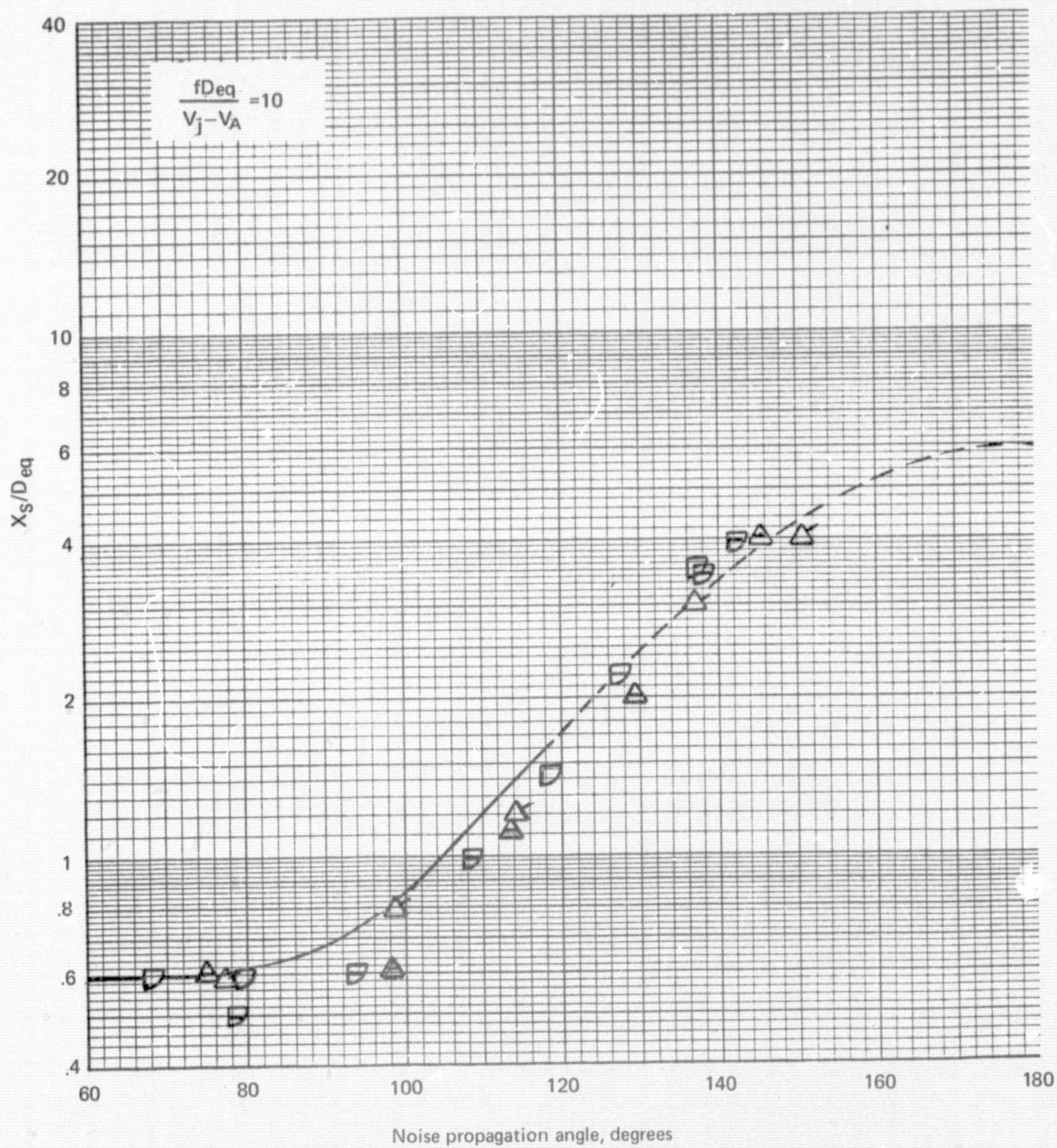


Figure 73.—(Concluded)

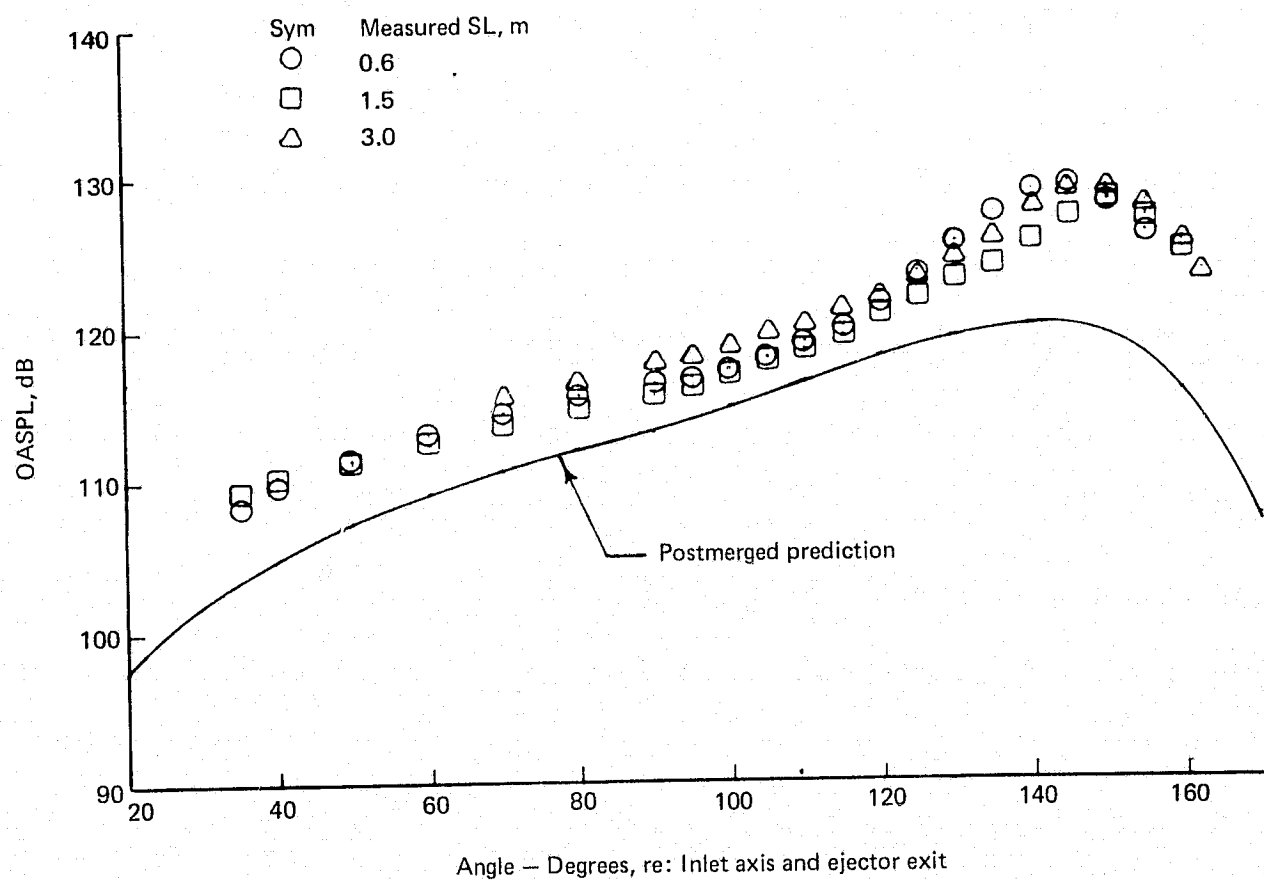


Figure 74.— OASPL Directivity and Jet Noise Spectra for the Annular Nozzle with Lined Ejector Extrapolated to a 3.0 m Sideline $NPR = 1.76$, $V_A = 3.3$ m/s

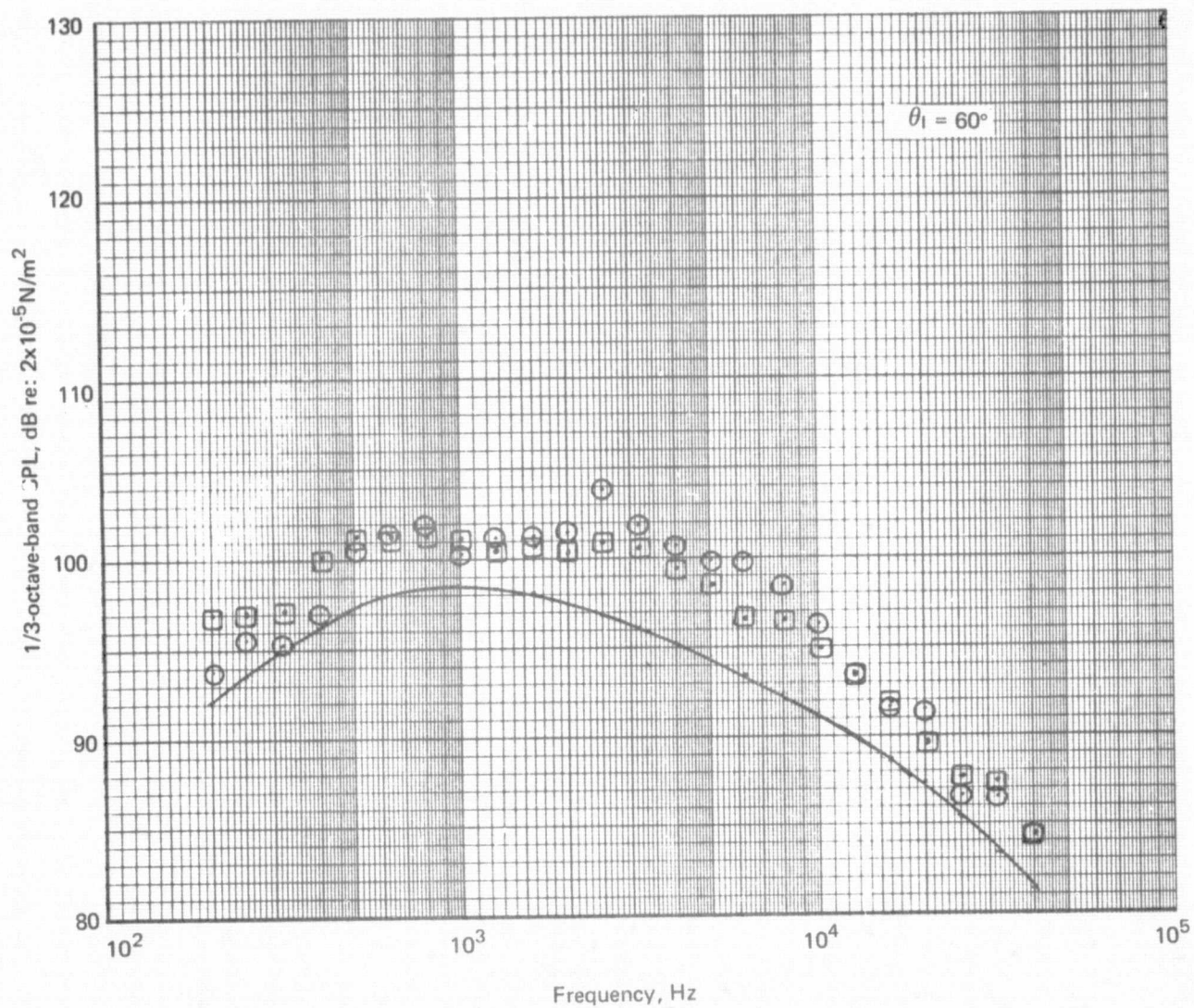


Figure 74.--(Continued)

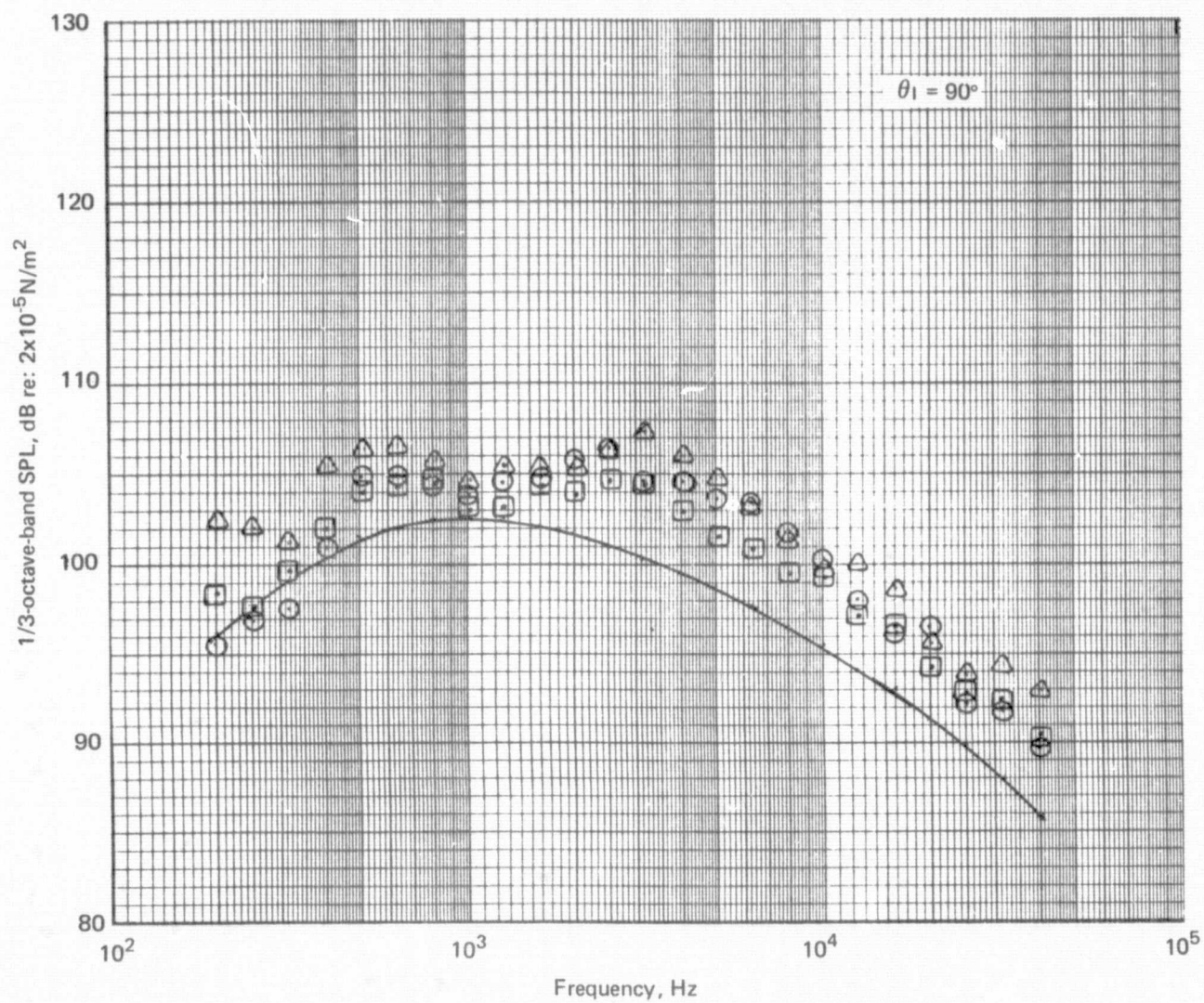


Figure 74.—(Continued)

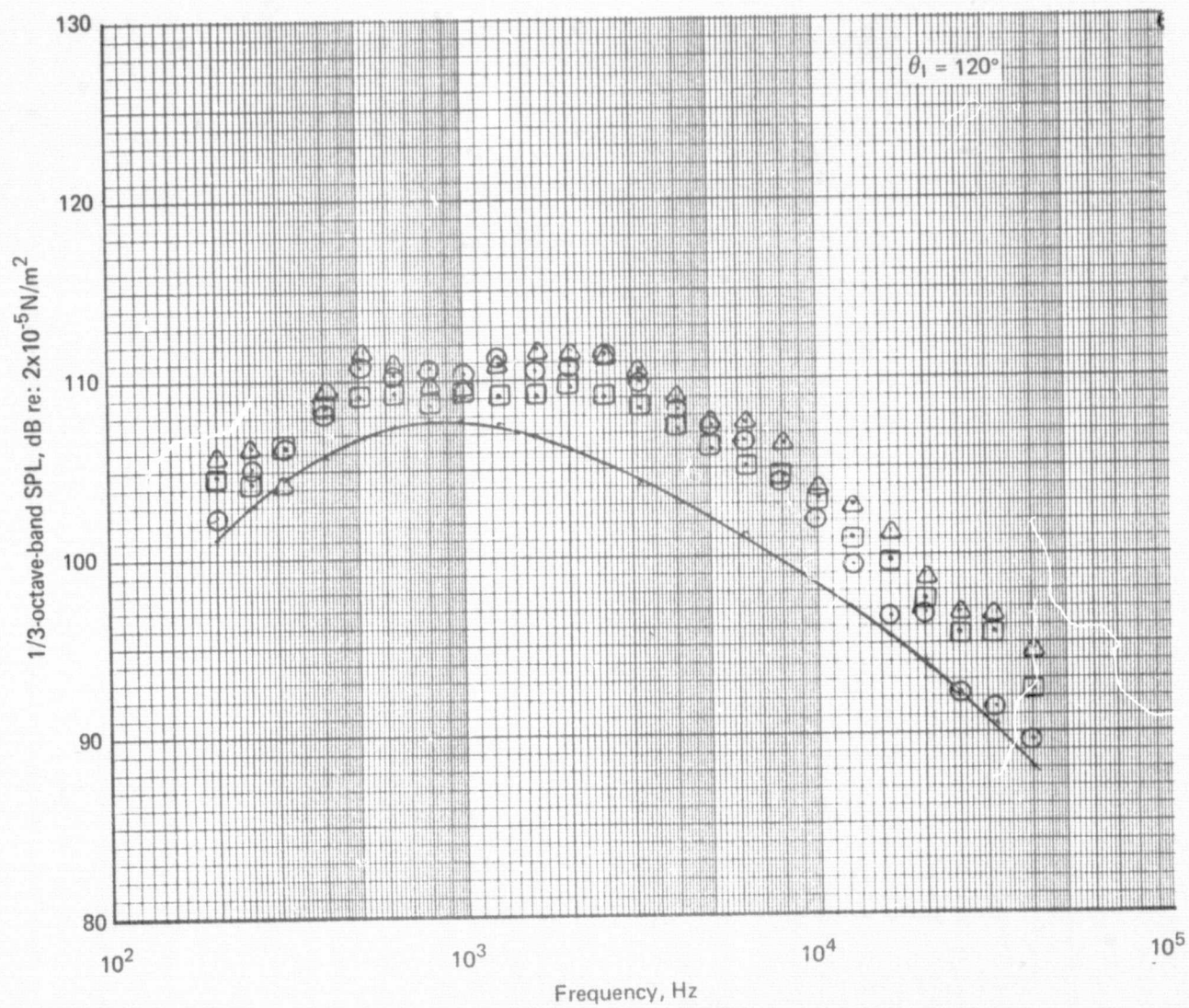


Figure 74.--(Continued)

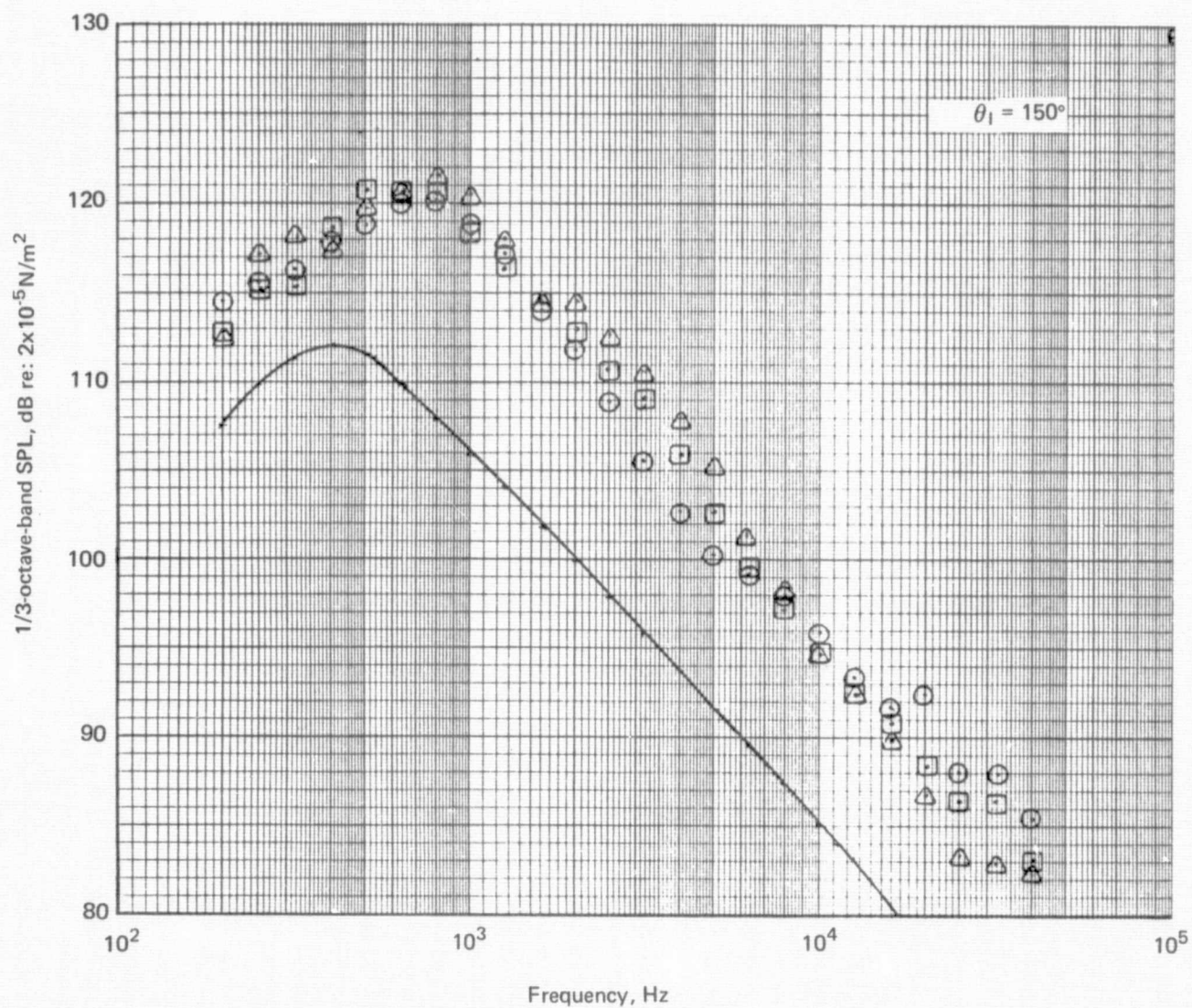


Figure 74.—(Concluded)

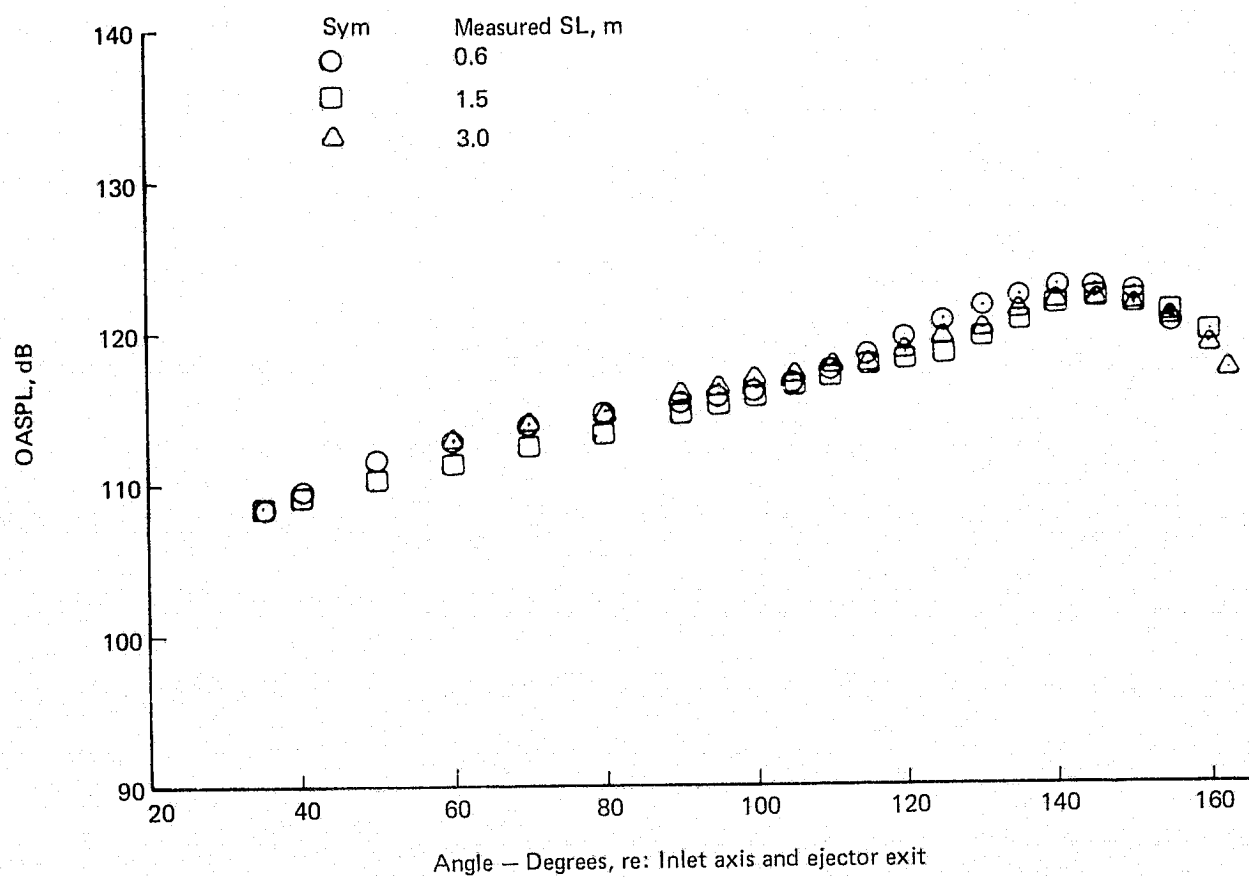


Figure 75.— OASPL Directivity and Jet Noise Spectra for the Annular Nozzle with Lined Ejector Extrapolated to a 3.0 m Sideline NPR = 1.766, $V_A = 69.5$ m/s

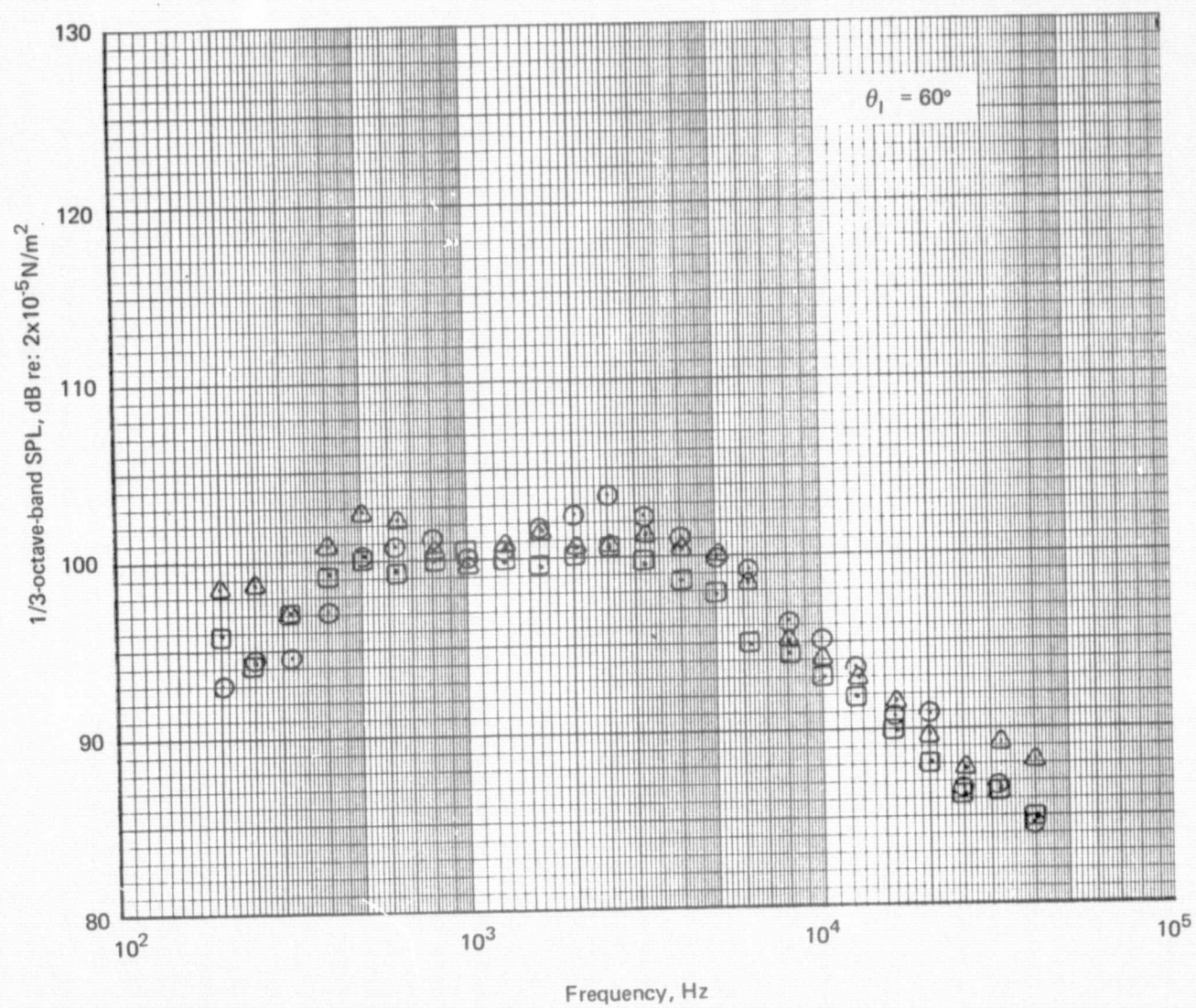


Figure 75.—(Continued)

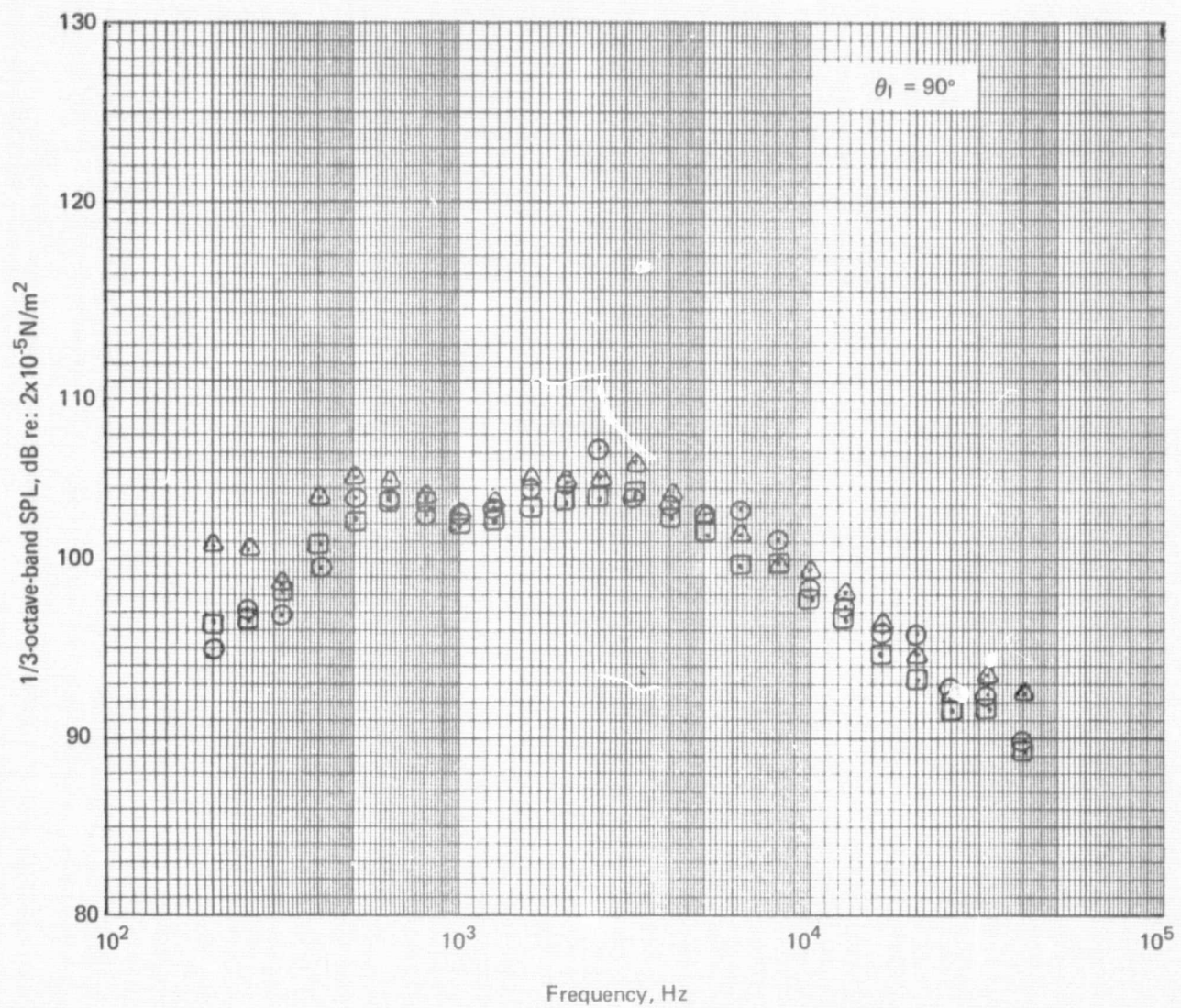


Figure 75.—(Continued)

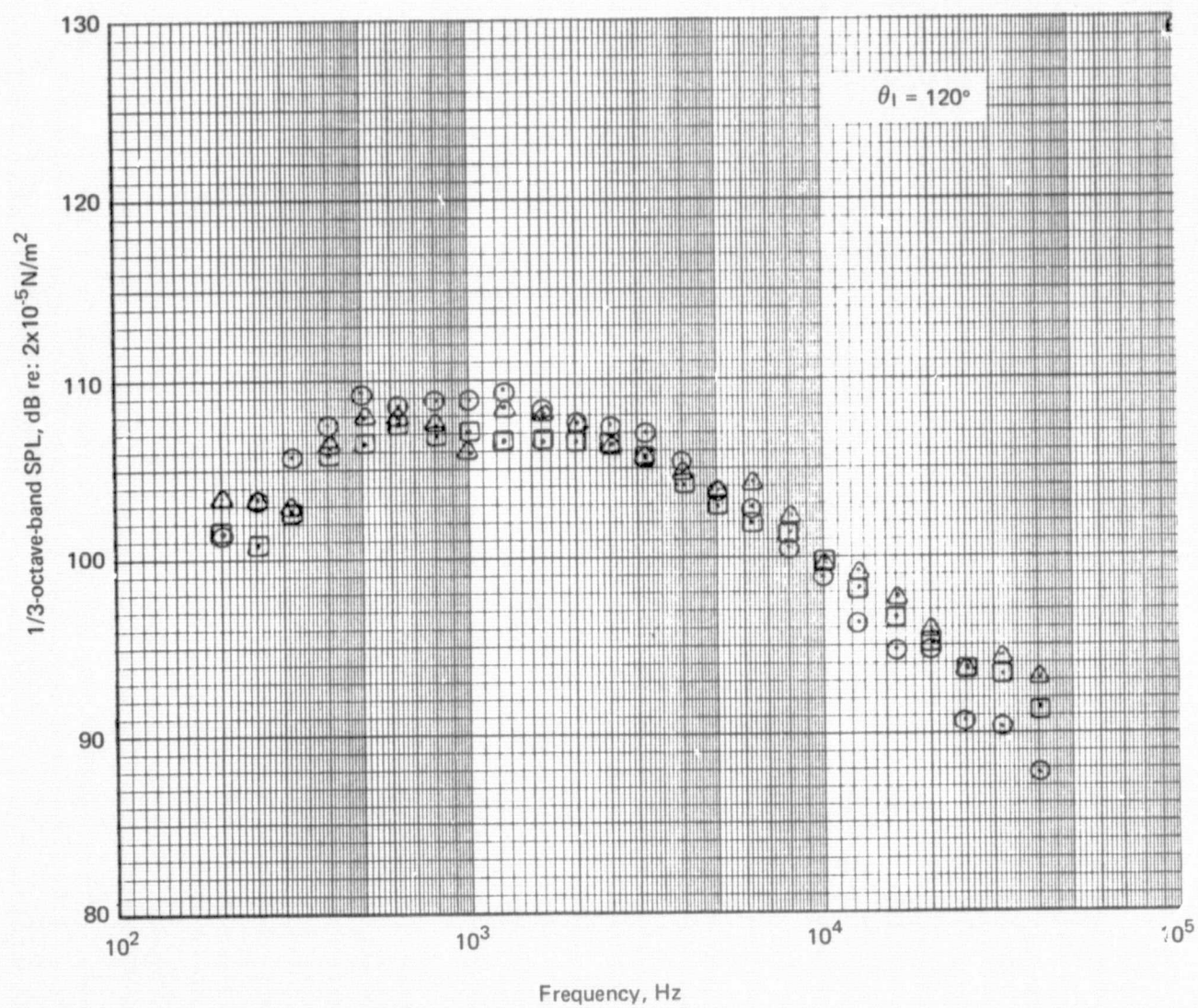


Figure 75.—(Continued)

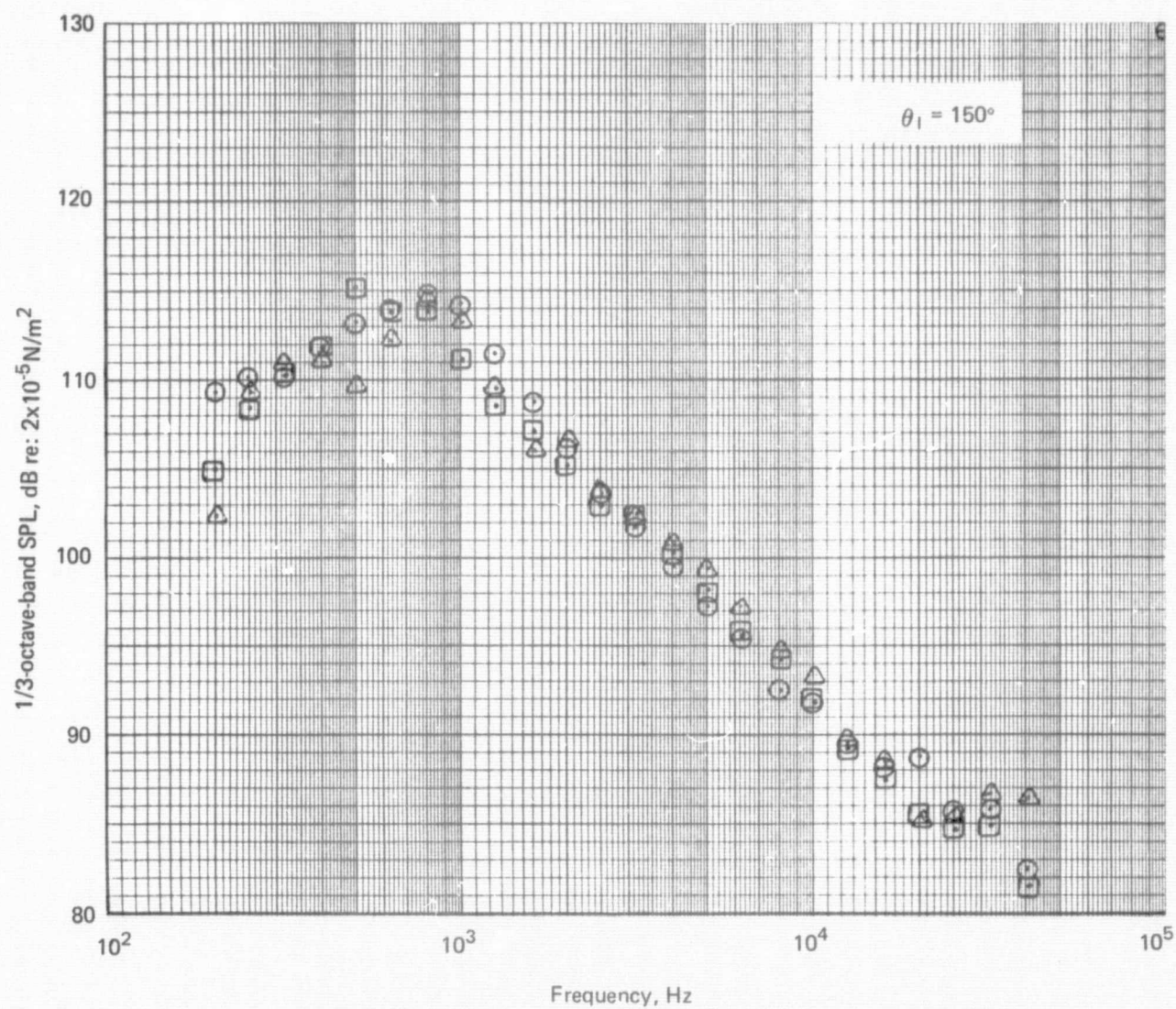


Figure 75.—(Concluded)

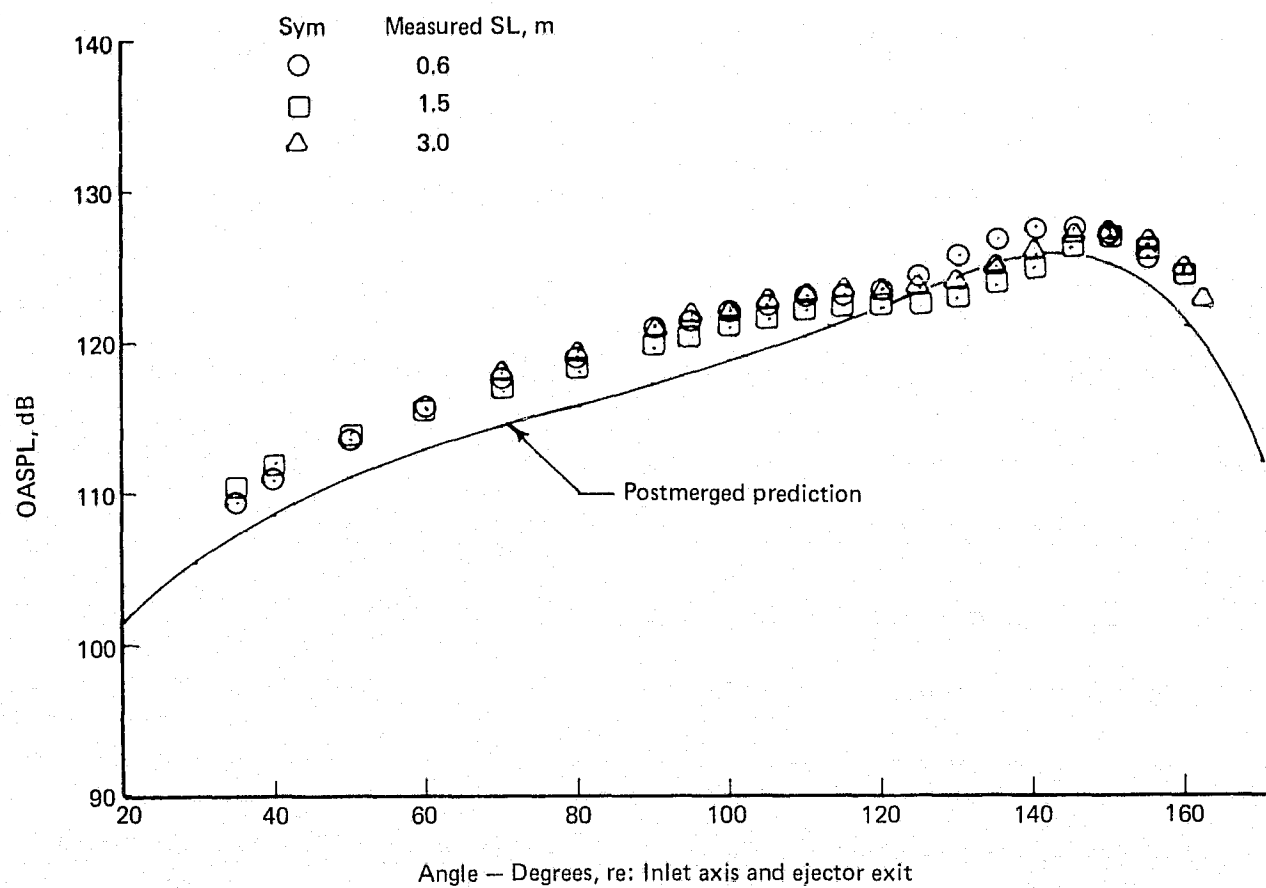


Figure 76.— OASPL Directivity and Jet Noise Spectra for the 20-Lobe Nozzle with Lined Ejector Extrapolated to a 3.0 m Sideline, $NPR = 2.26$, $V_A = 5.8$ m/s

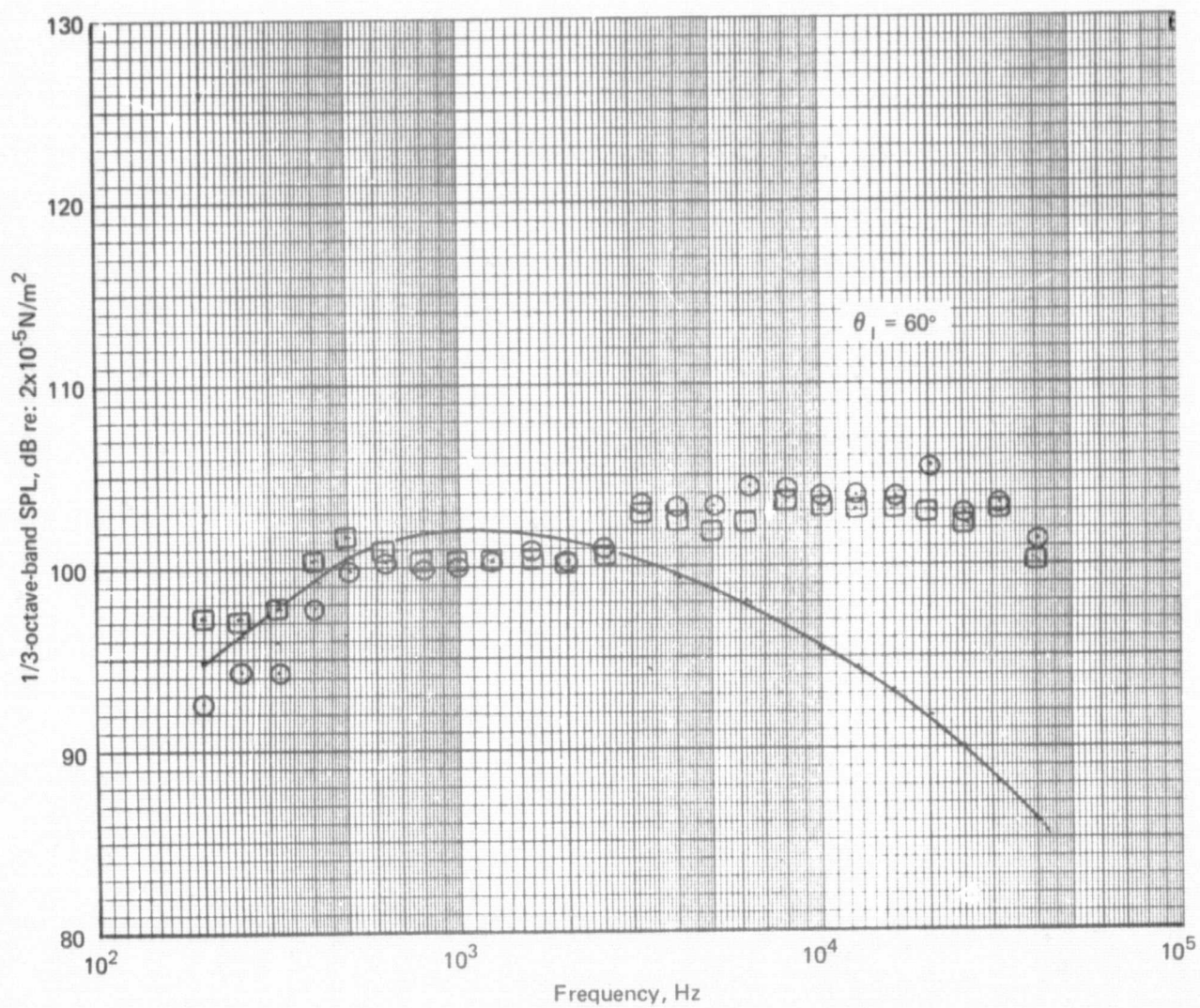


Figure 76.—(Continued)

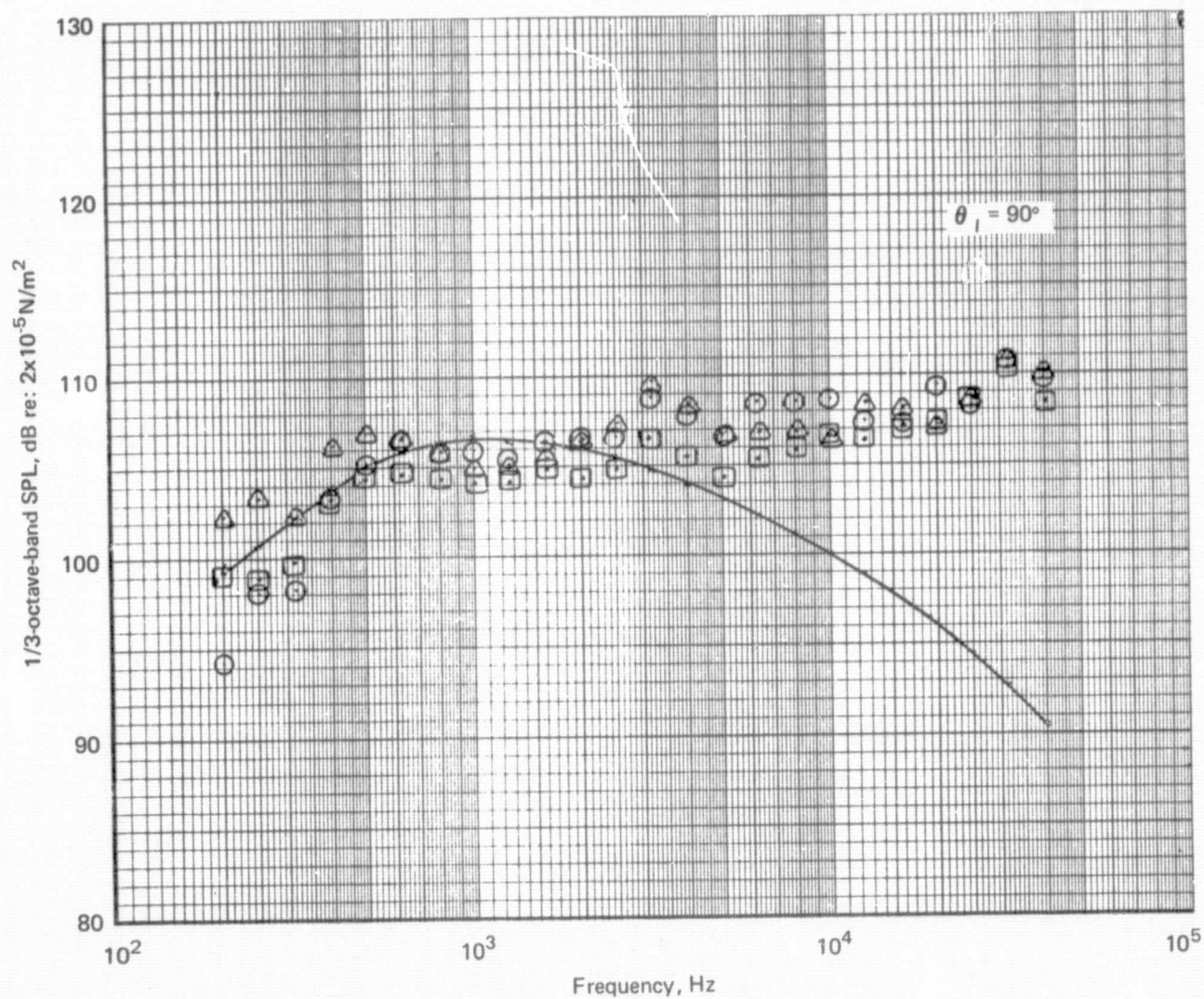


Figure 76.—(Continued)

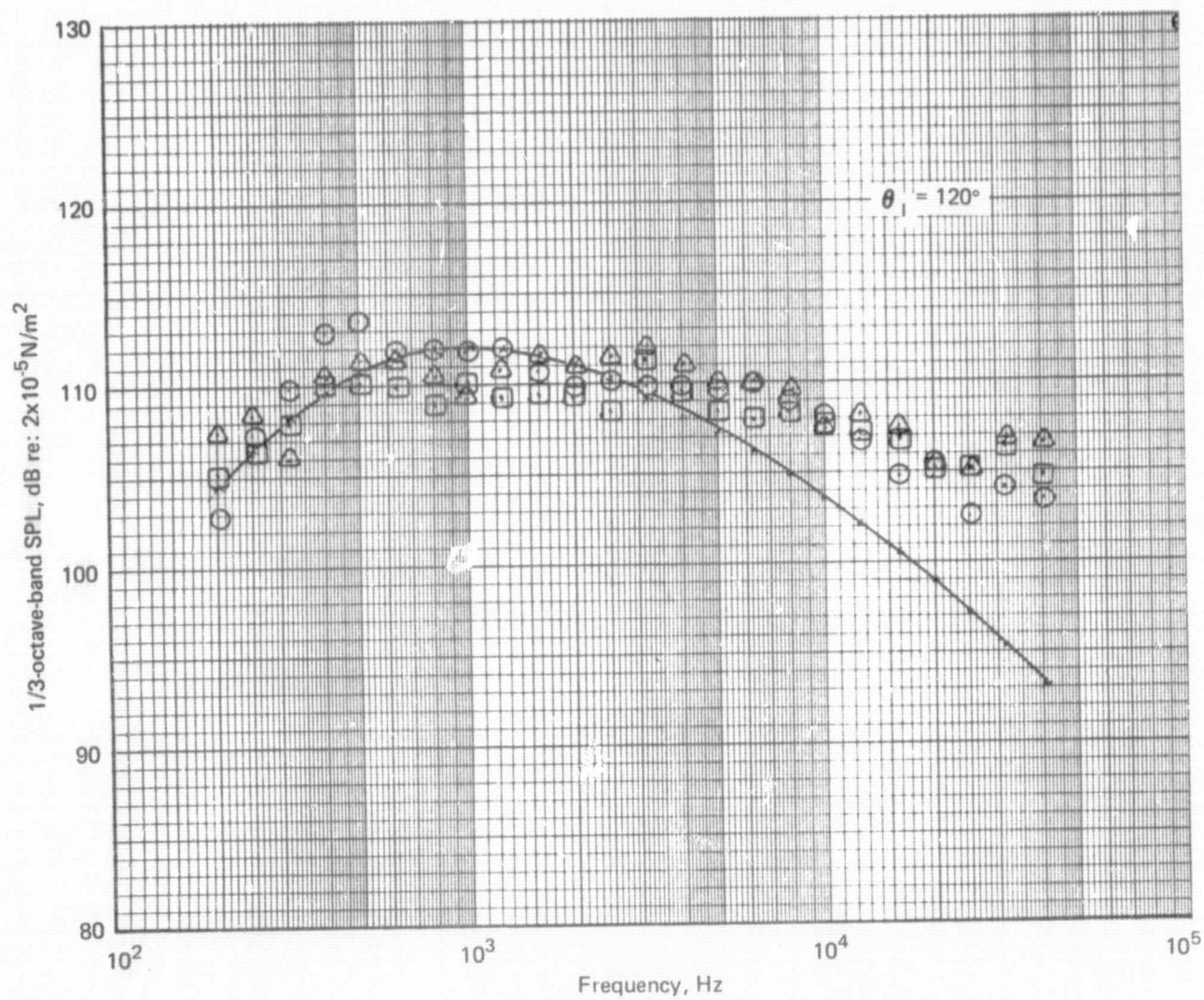


Figure 76.—(Continued)

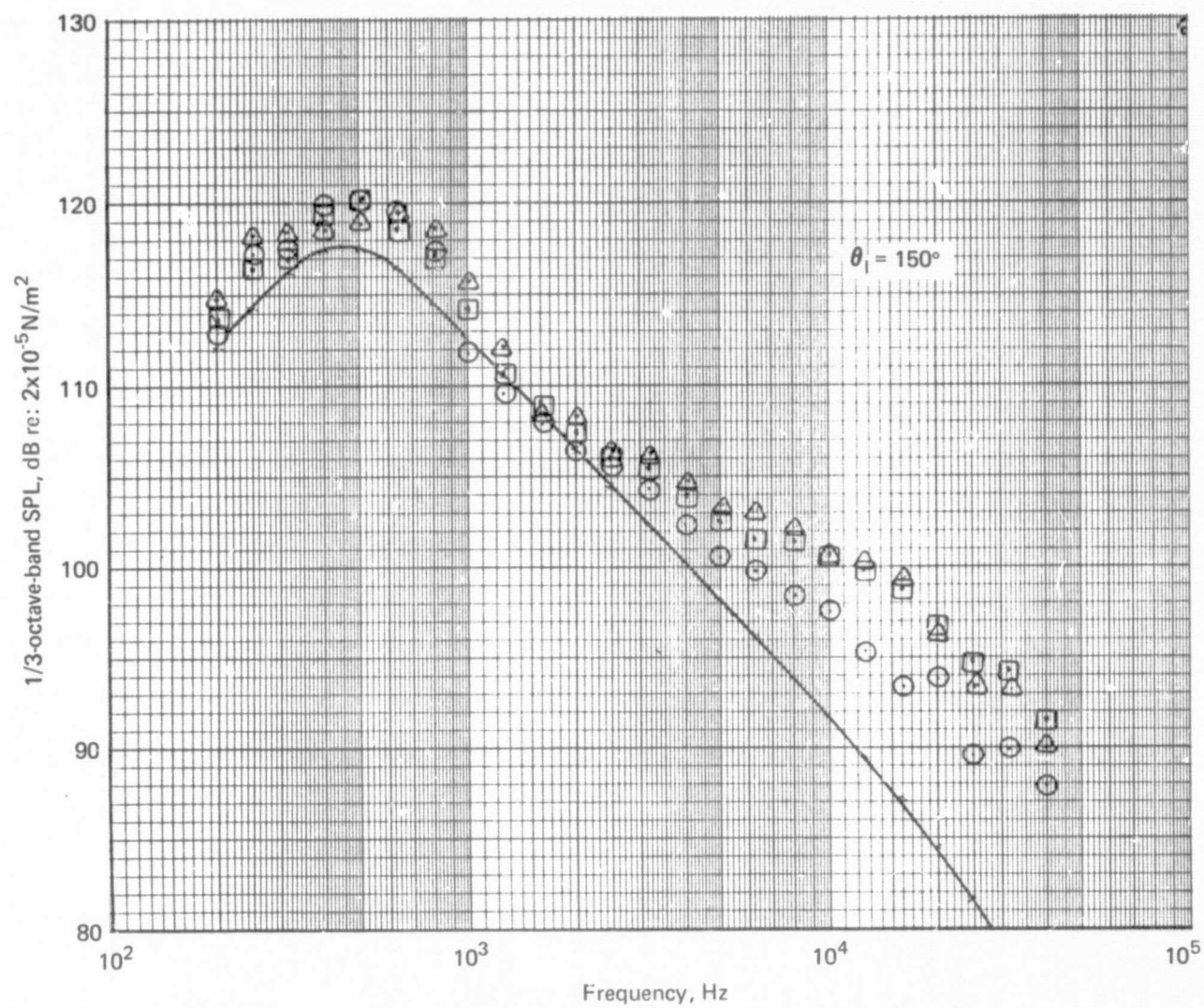


Figure 76.—(Concluded)

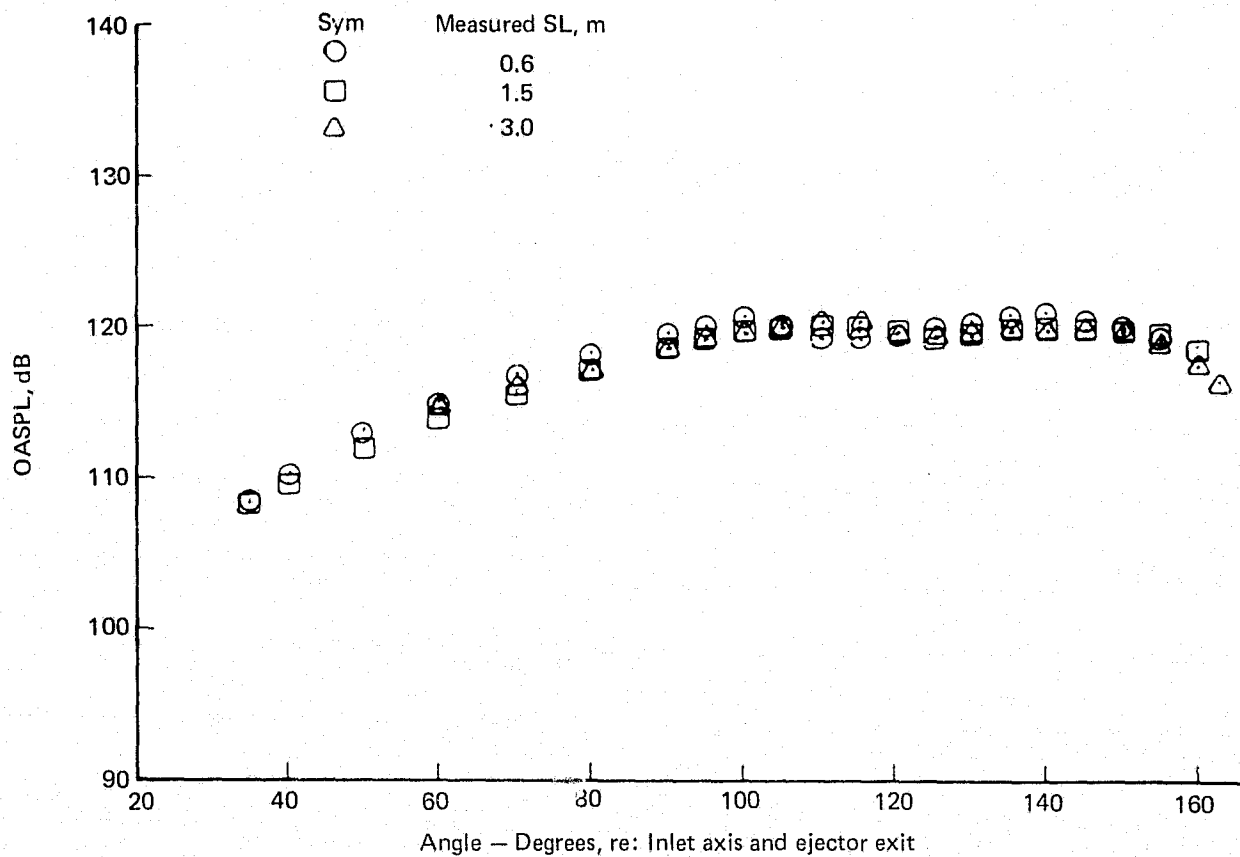


Figure 77.— OASPL Directivity and Jet Noise Spectra for the 20-Lobe Nozzle with Lined Ejector Extrapolated to a 3.0 m Sideline, $NPR = 2.22$, $V_A = 69.2$ m/s

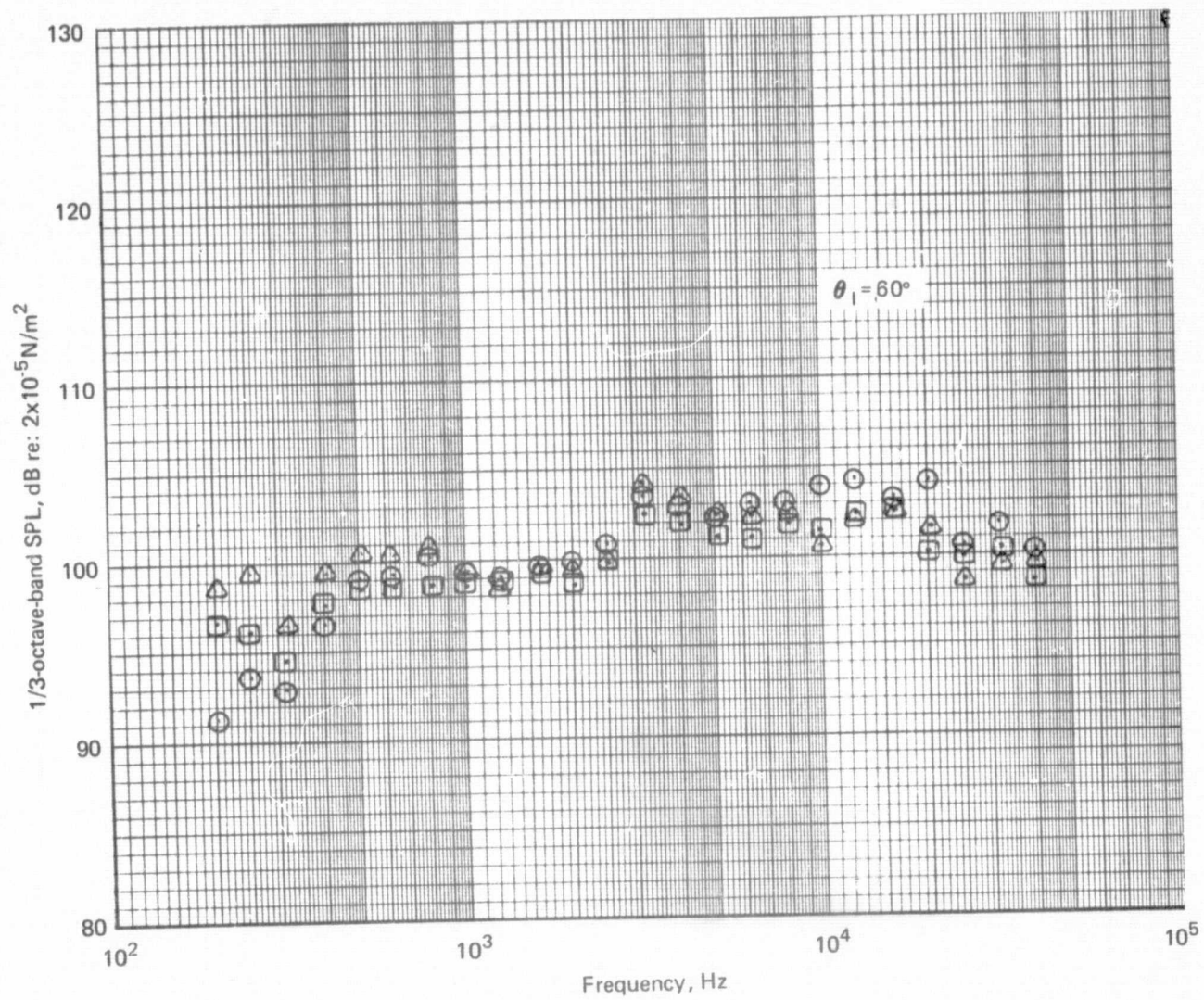


Figure 77.—(Continued)

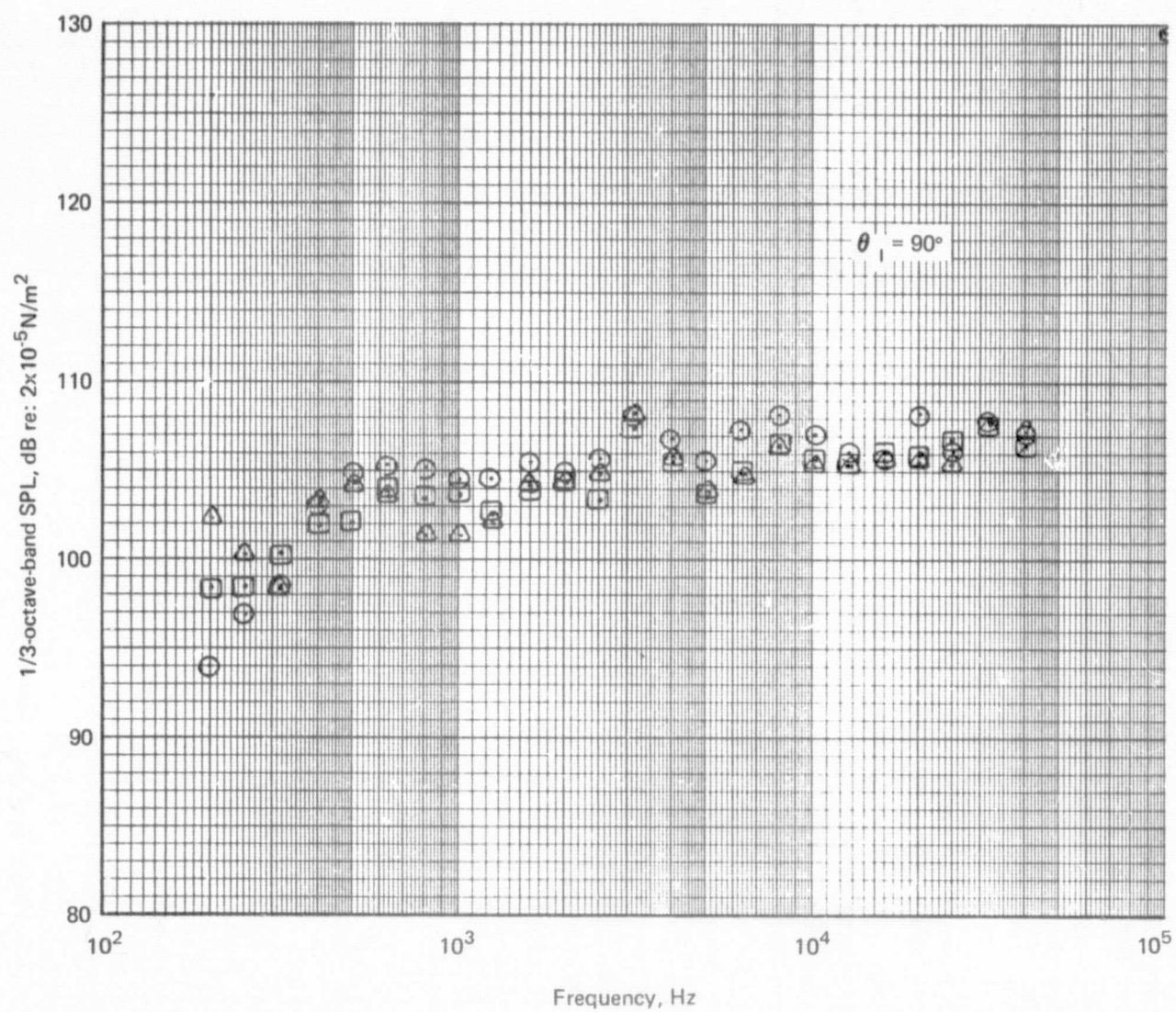


Figure 77.—(Continued)

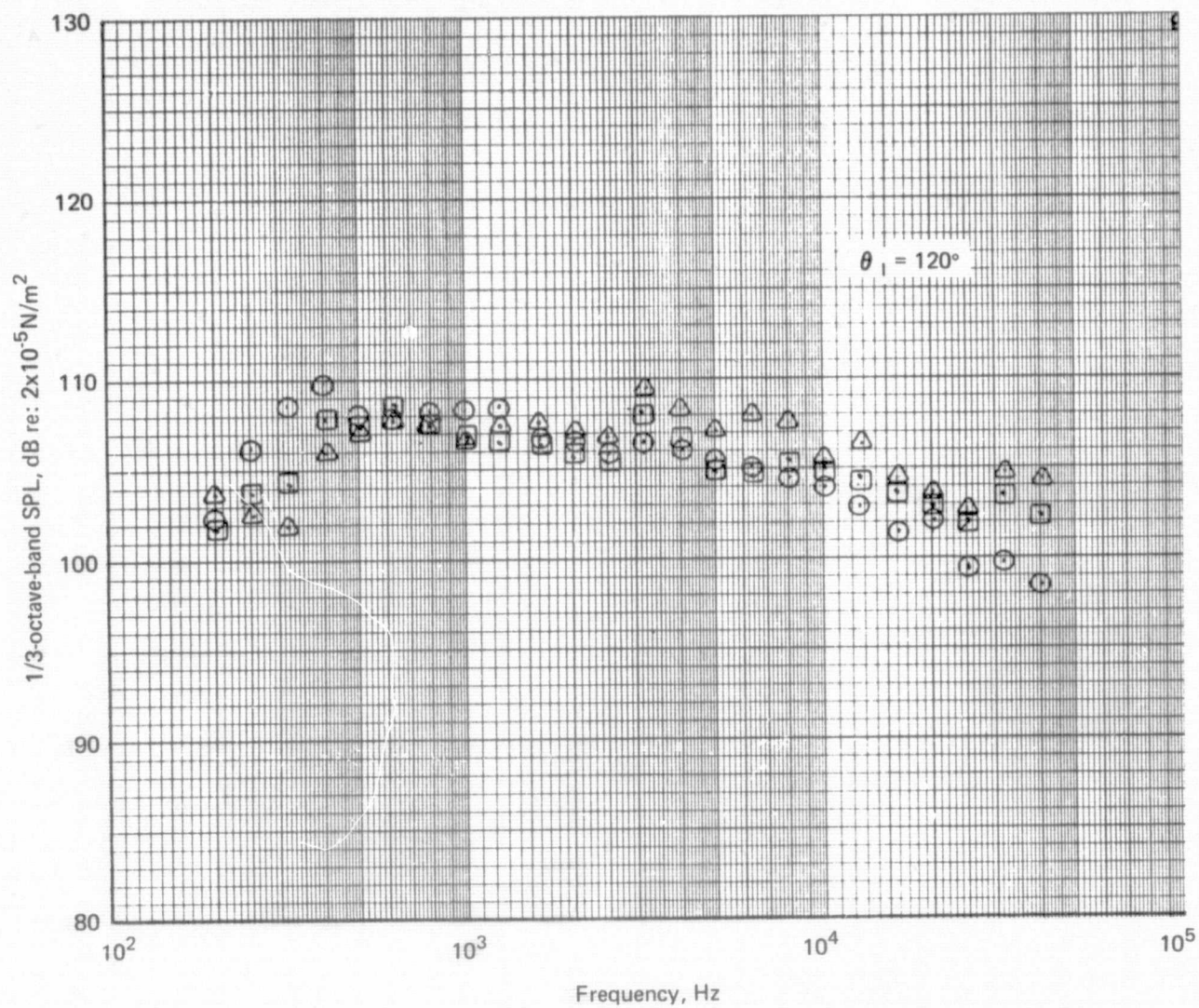


Figure 77.—(Continued)

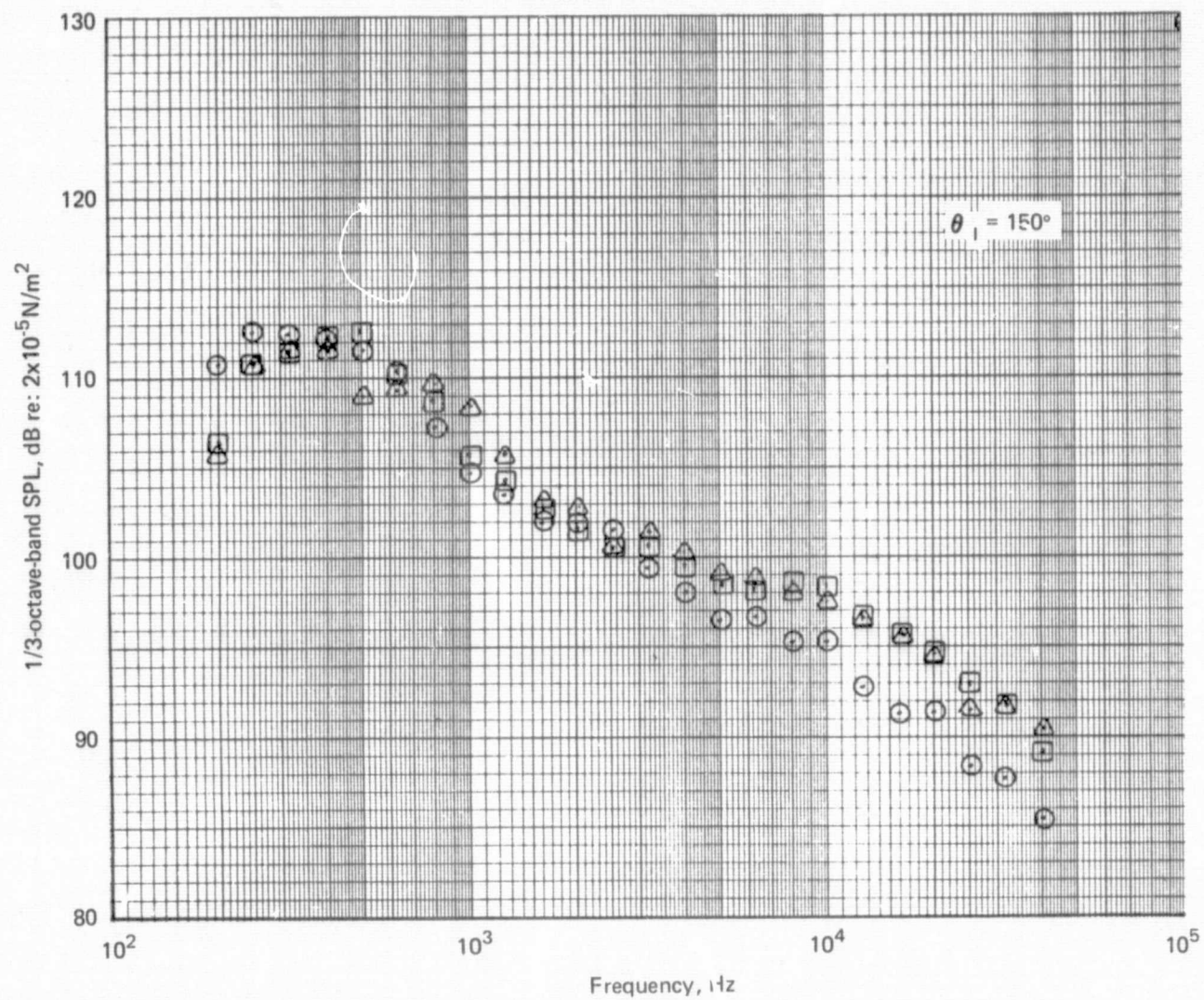


Figure 77.—(Concluded)

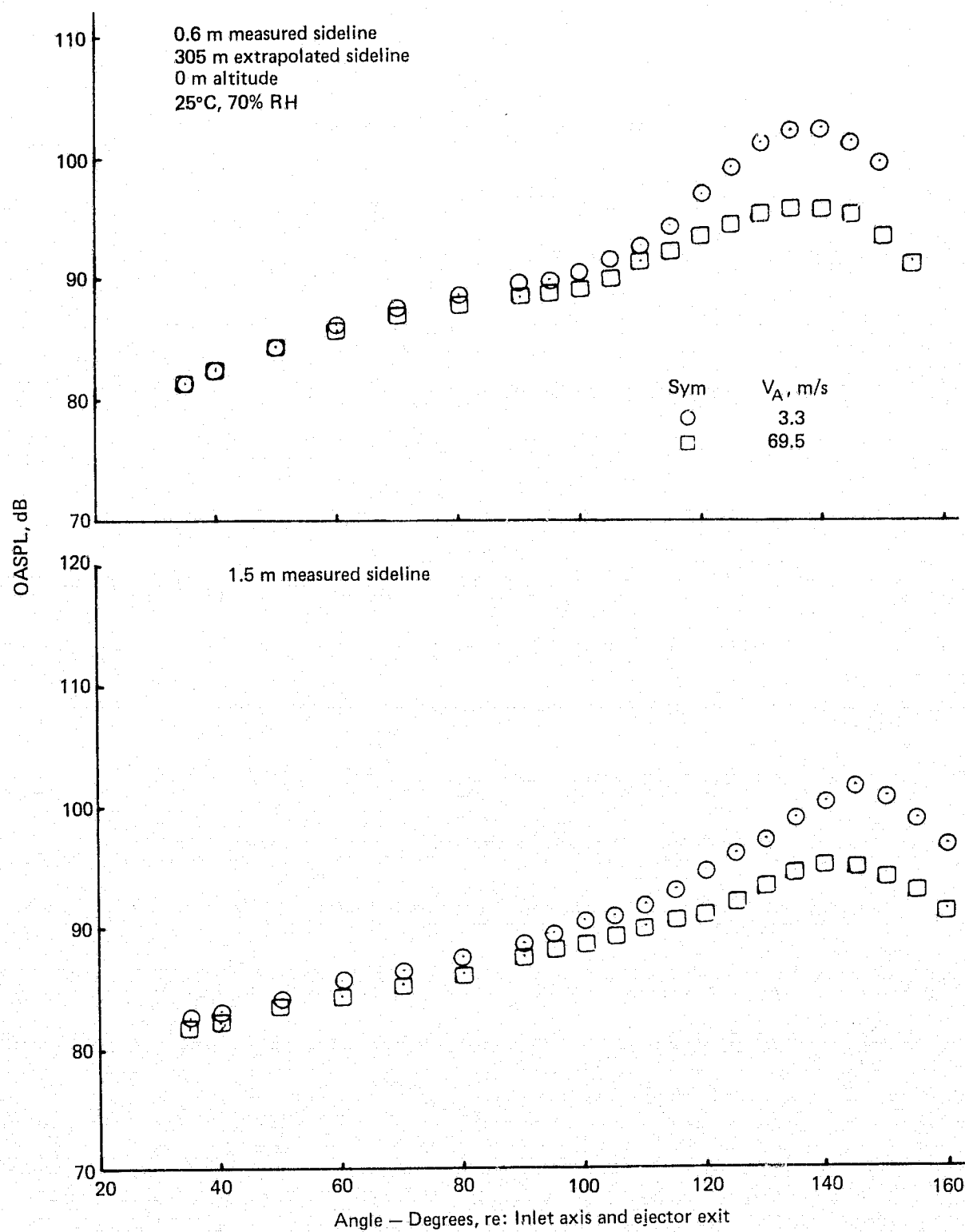


Figure 78.— Flight Effects on OASPL of an Annular Nozzle with Lined Ejector
NPR = 1.75, $V_j = 503$ m/s

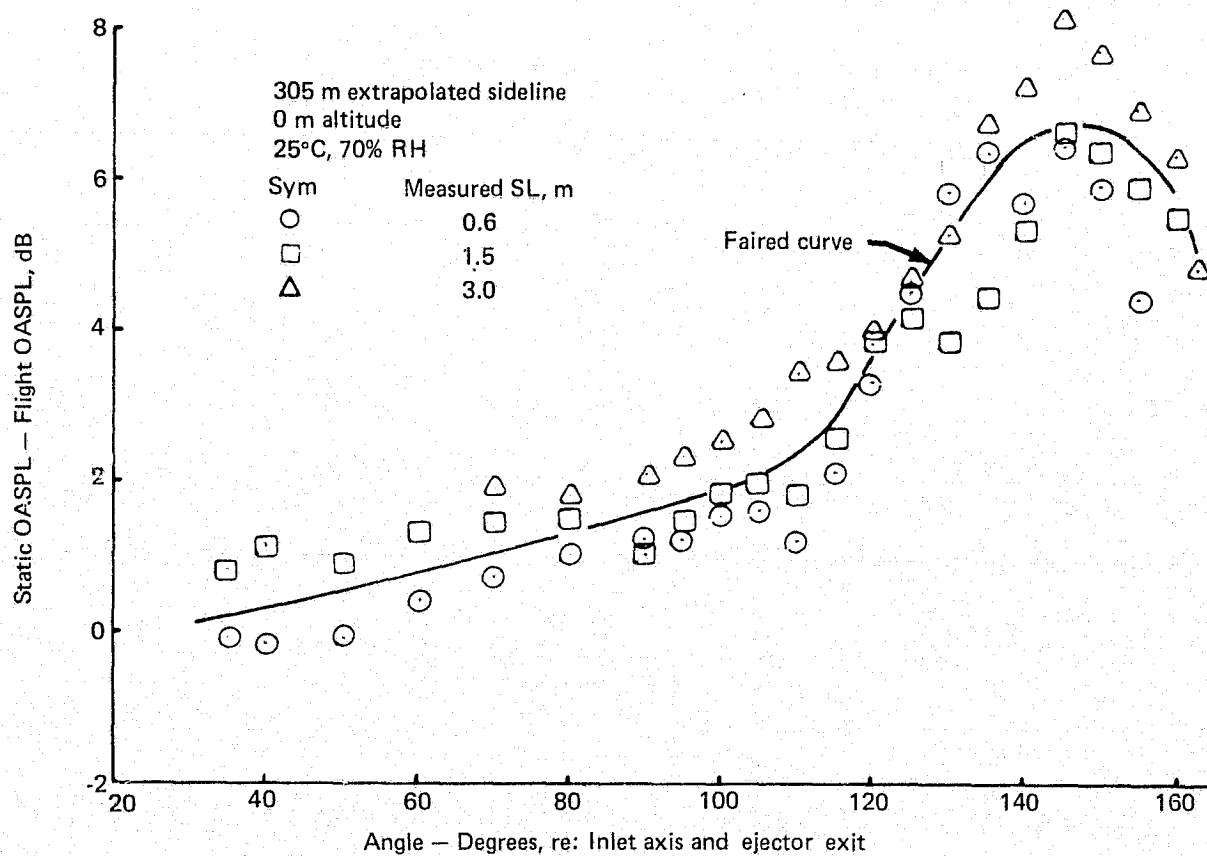
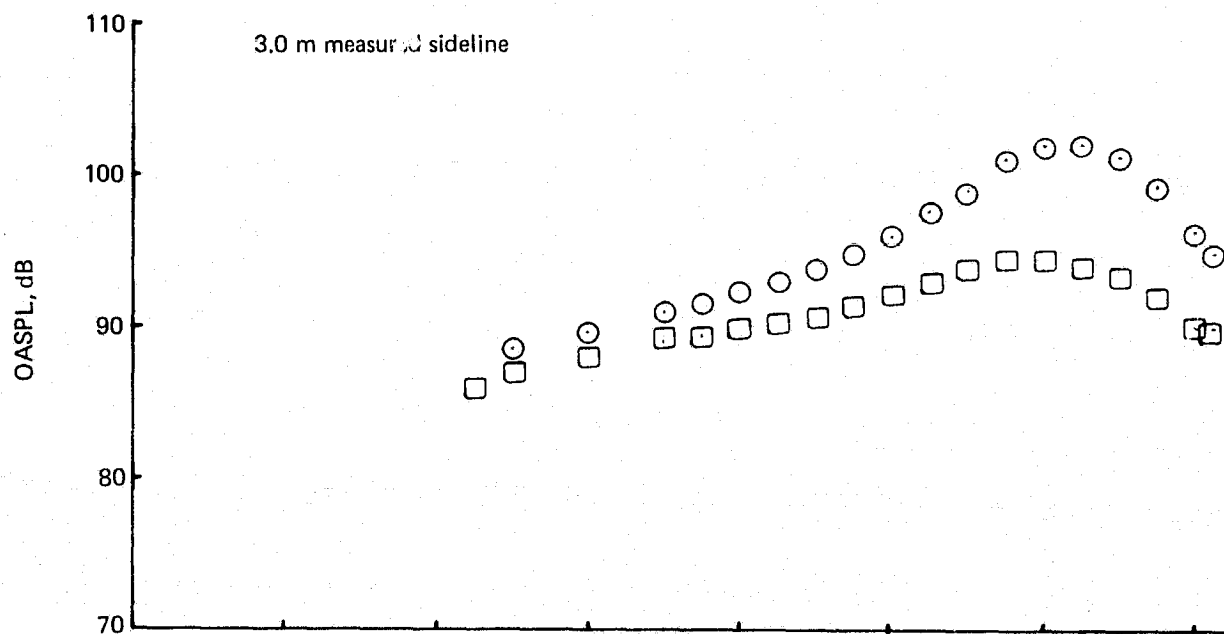


Figure 78. - (Concluded)

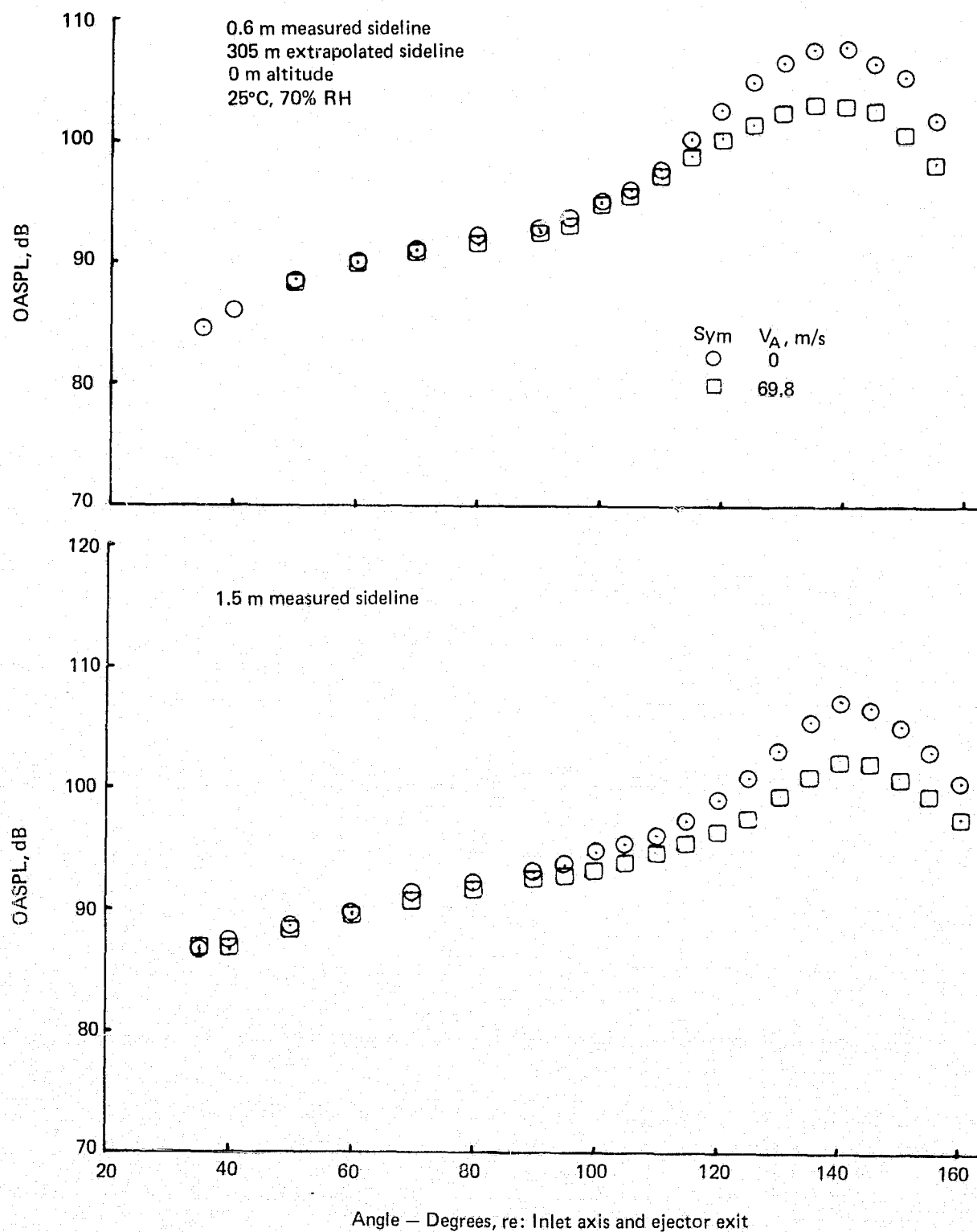


Figure 79.— Flight Effects on OASPL of an Annular Nozzle with Lined Ejector
NPR = 2.25, $V_f = 594$ m/s

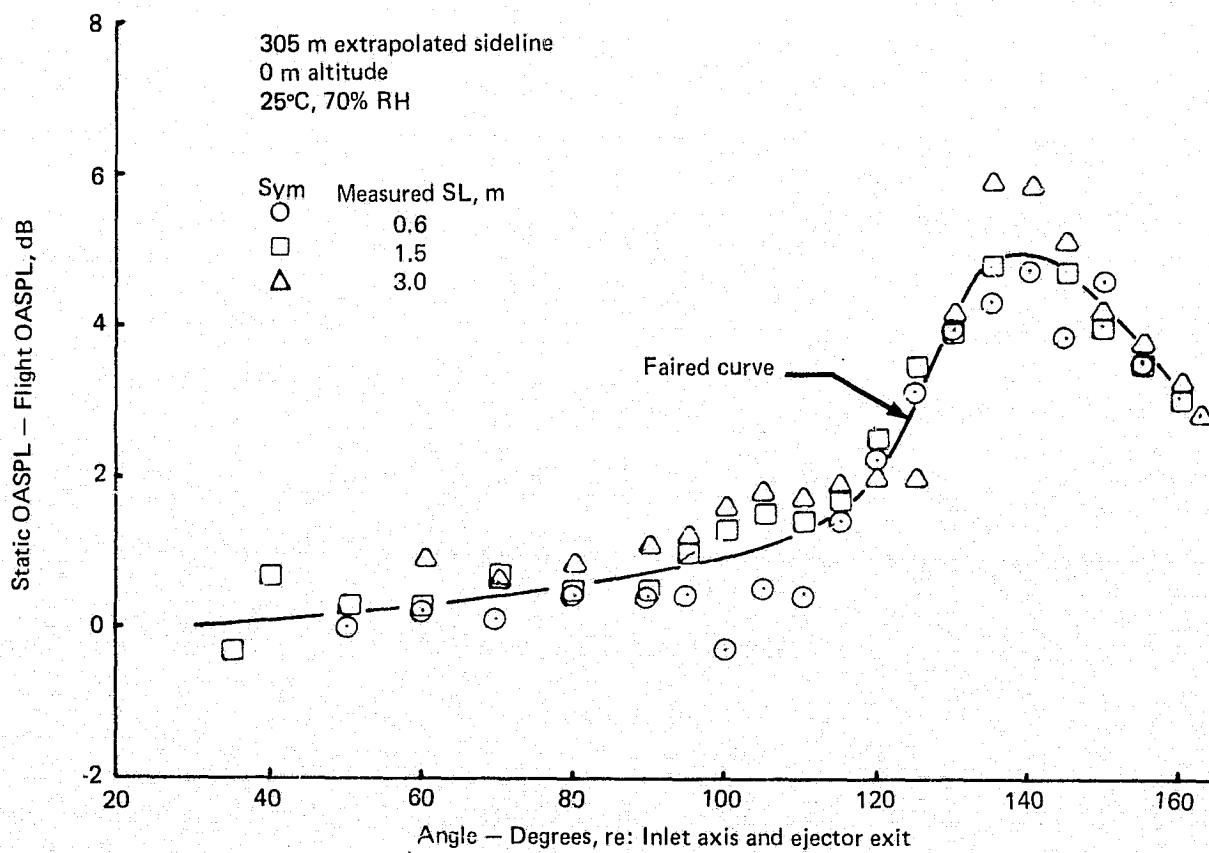
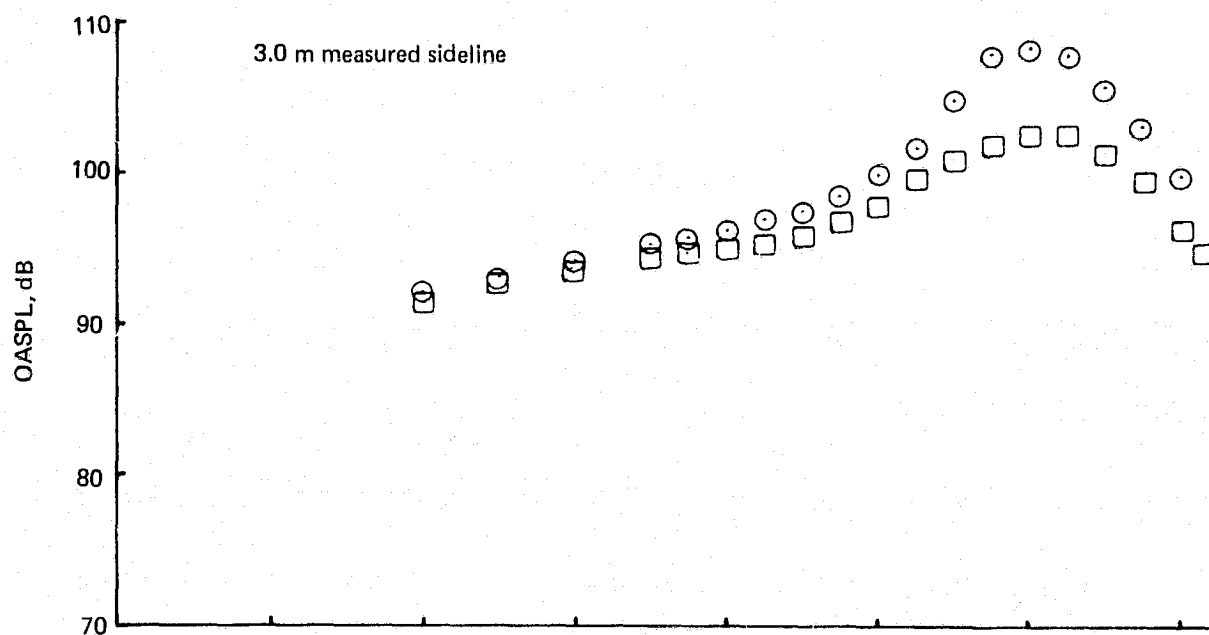


Figure 79.— (Concluded)

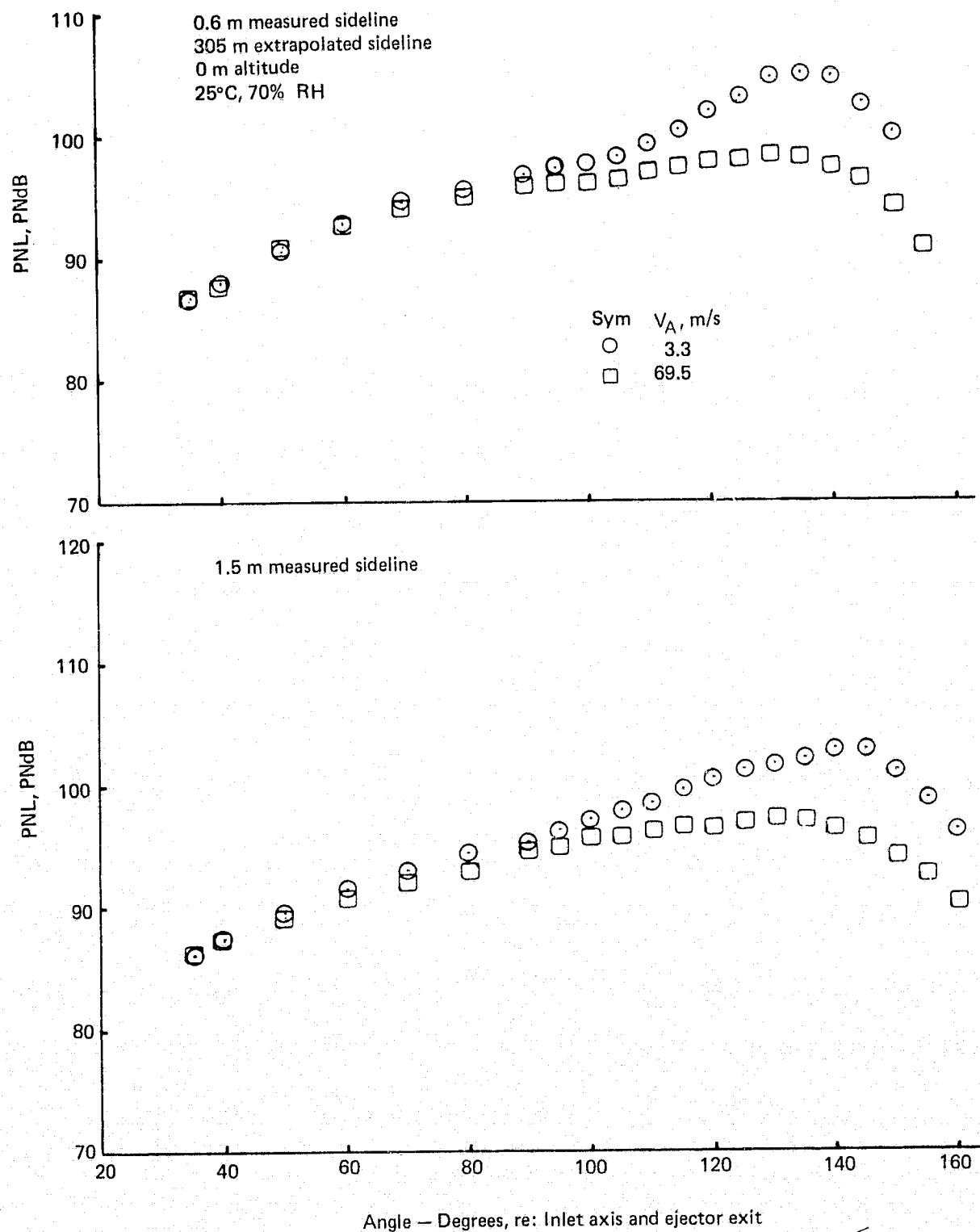


Figure 80.— Flight Effects on PNL of an Annular Nozzle with Lined Ejector
 $NPR = 1.75$, $V_j = 503$ m/s

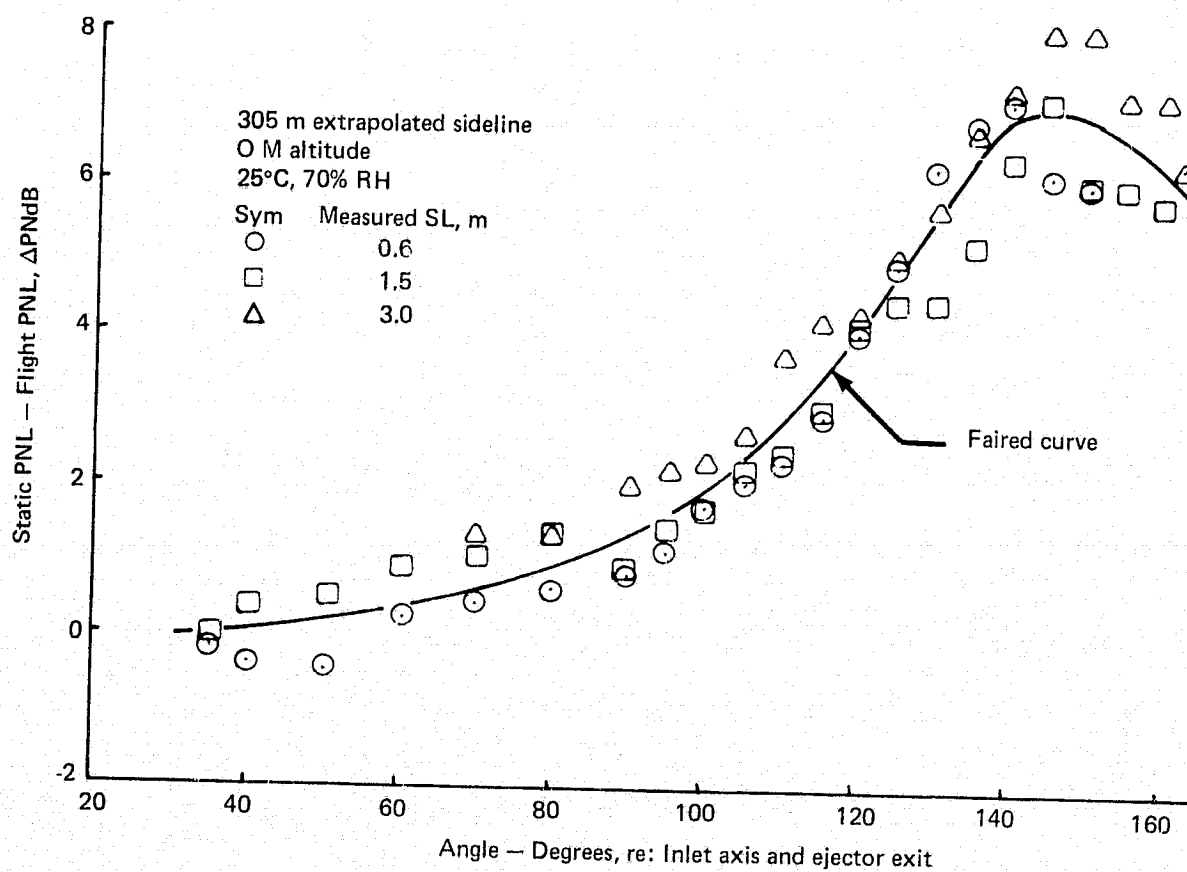
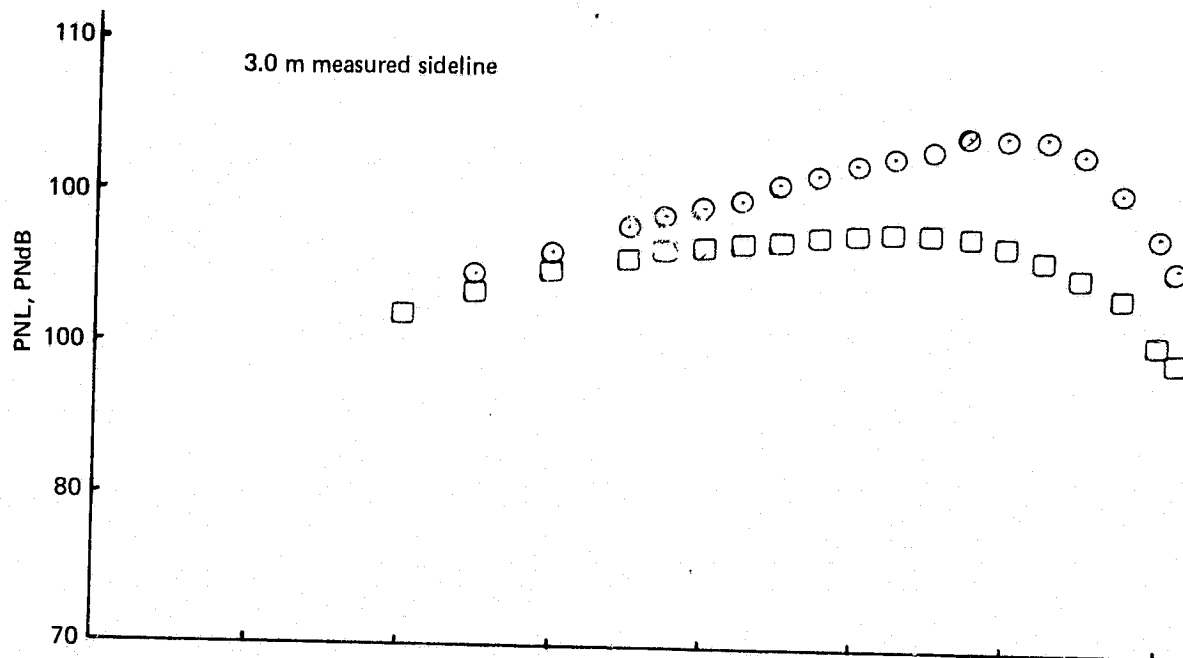


Figure 80.— (Concluded)

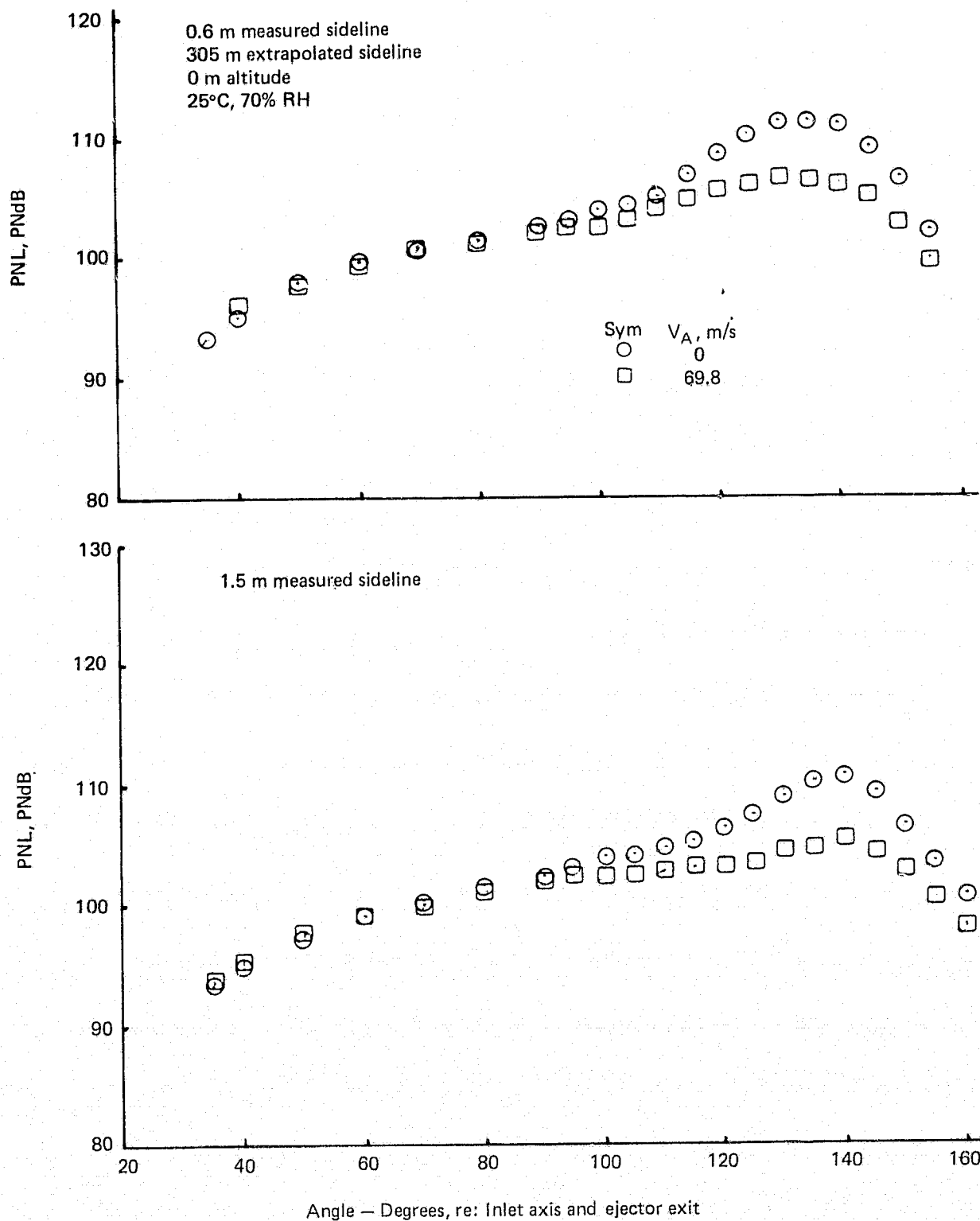


Figure 81.— Flight Effects on PNL of an Annular Nozzle with Lined Ejector
 $NPR = 2.25$, $V_j = 594 \text{ m/s}$

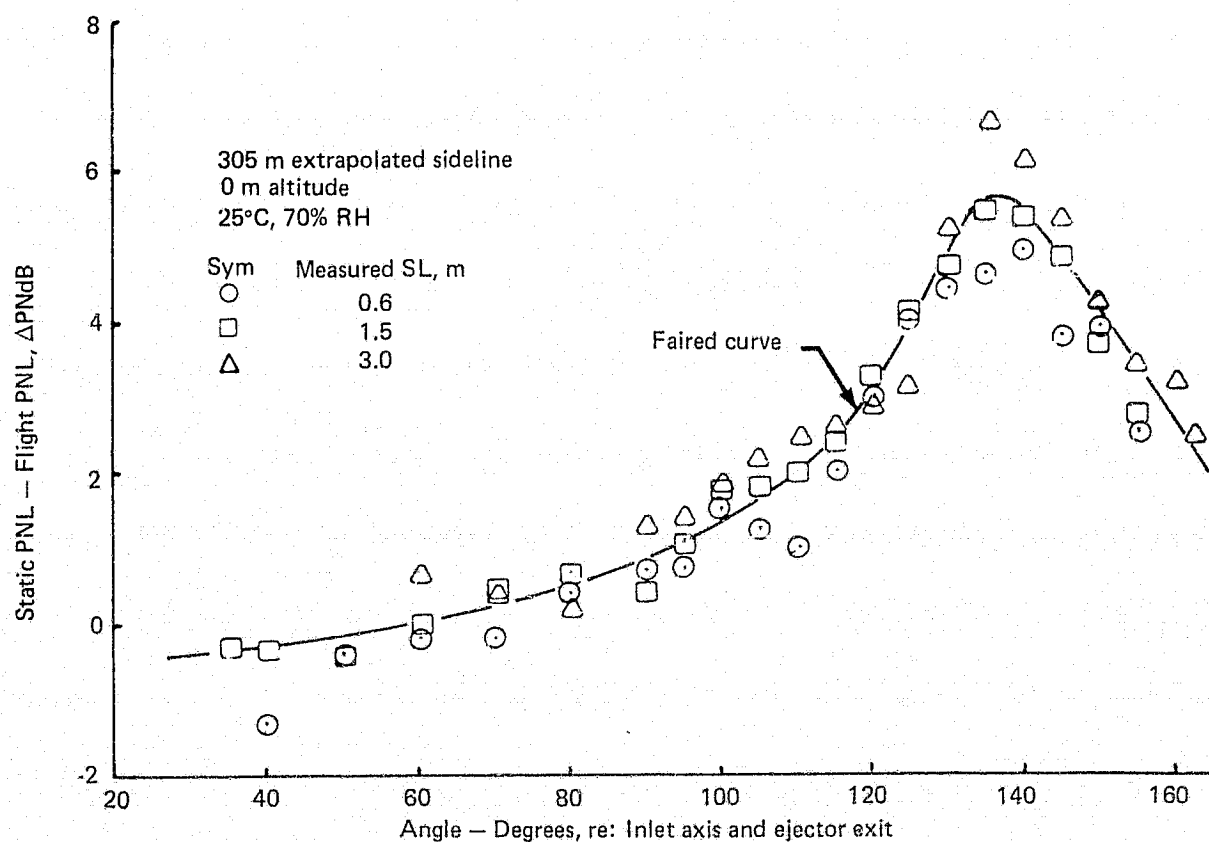
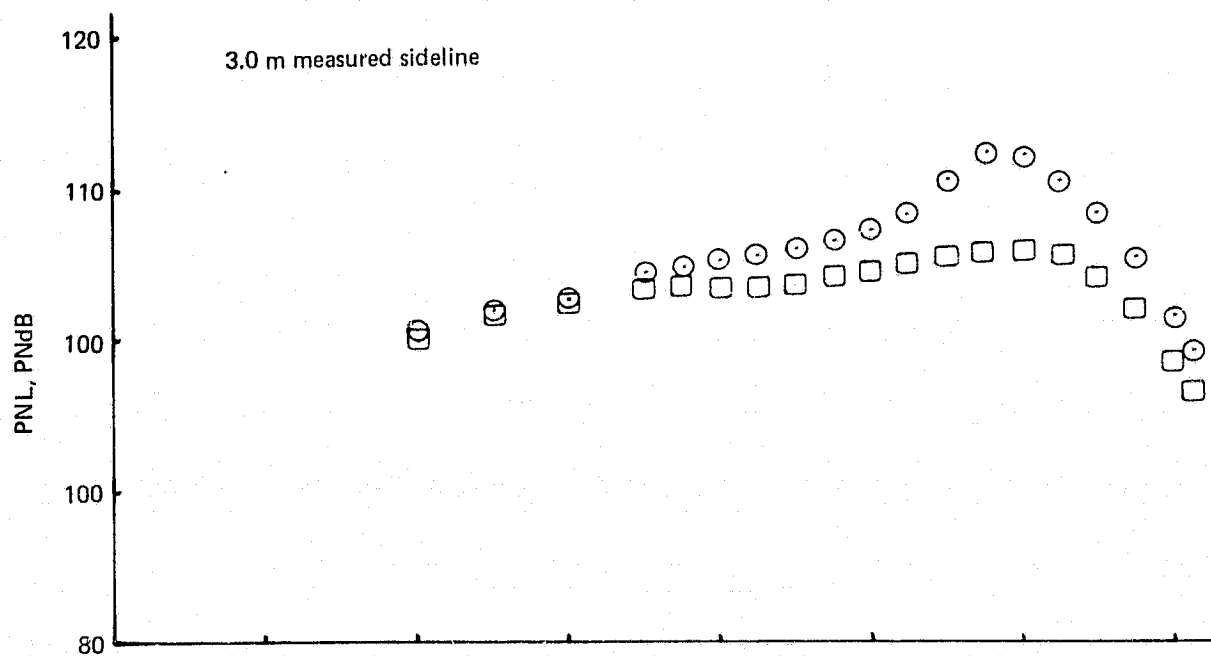


Figure 81.— (Concluded)

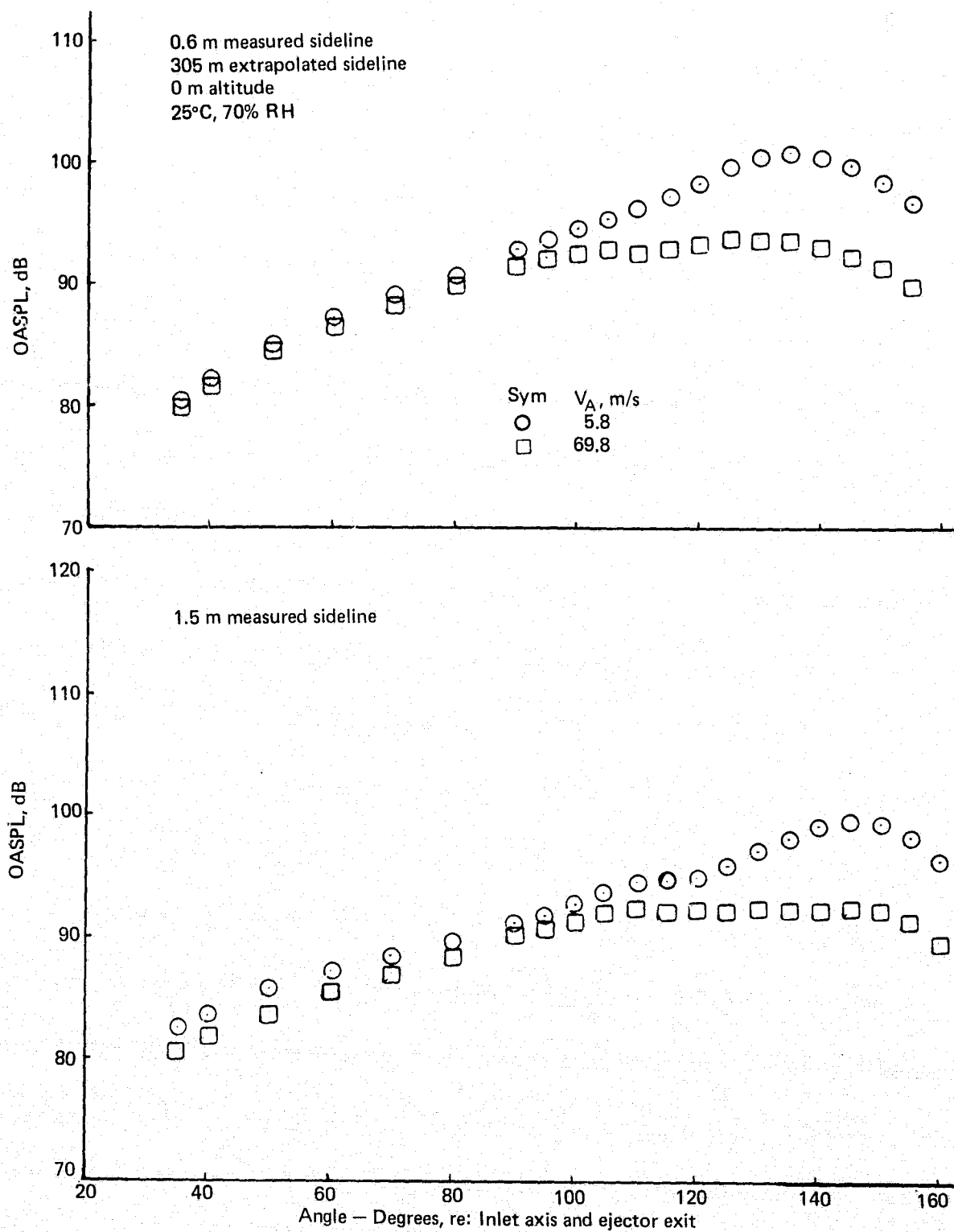


Figure 82.— Flight Effects on OASPL of a 20-Lobe Nozzle with Ejector
NPR = 1.75 $V_i = 503$ m/s

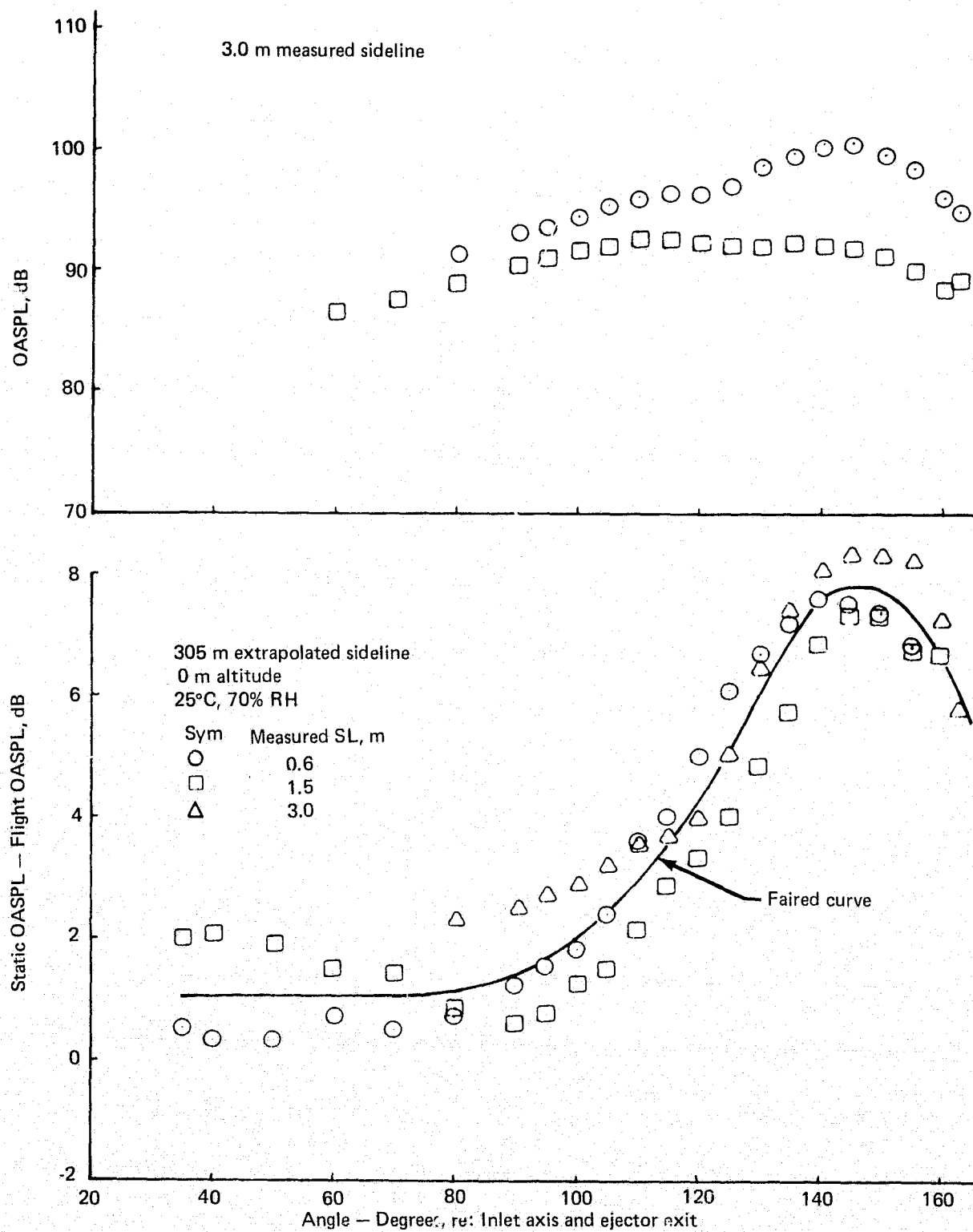


Figure 82.— (Concluded)

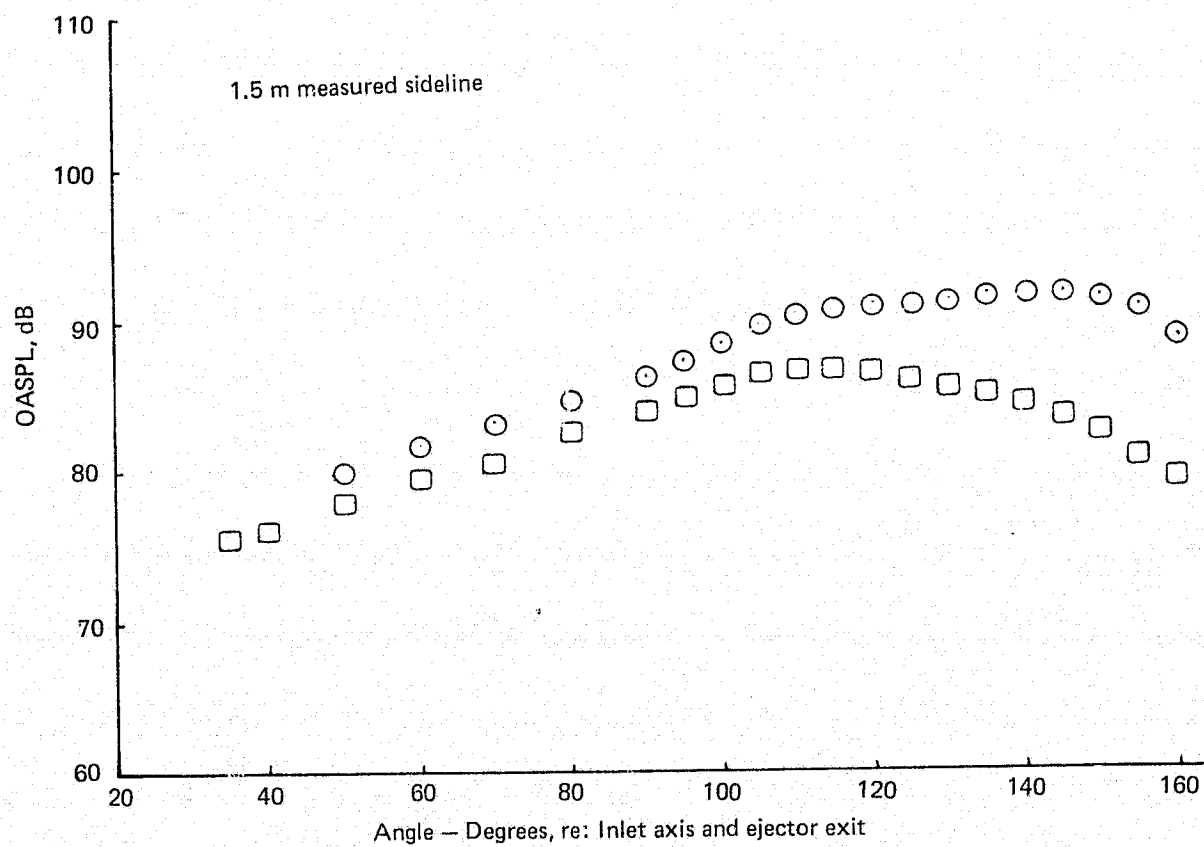
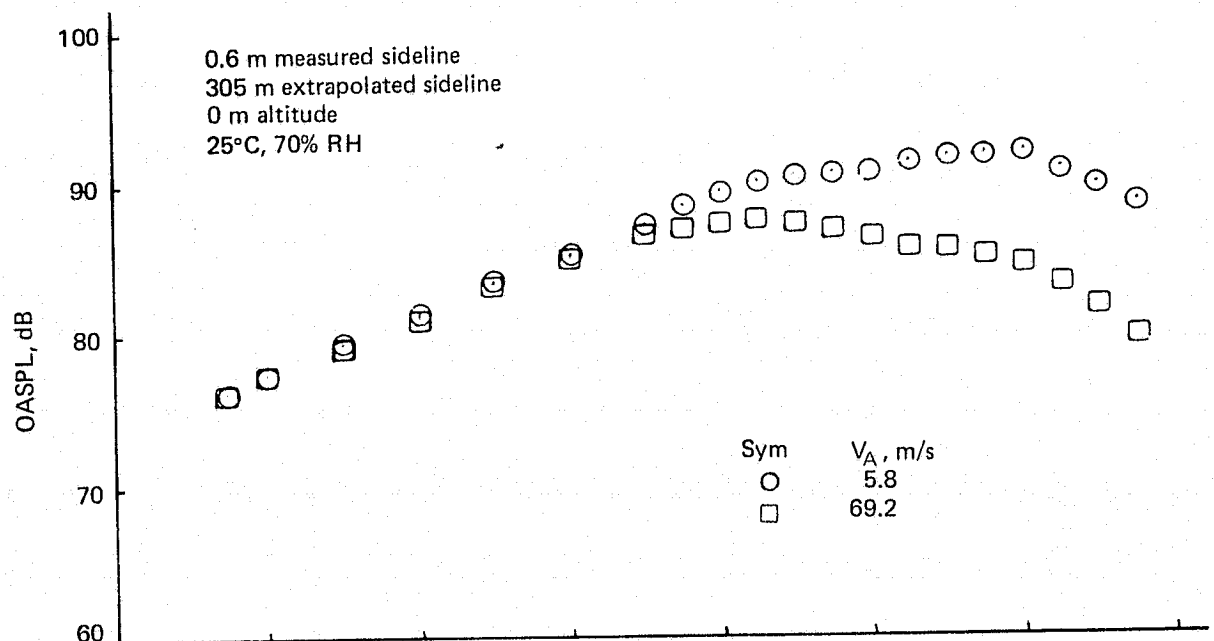


Figure 83.— Flight Effects on OASPL of a 20-Lobe Nozzle with Ejector
 $NPR = 2.25$ $V_j = 594$ m/s

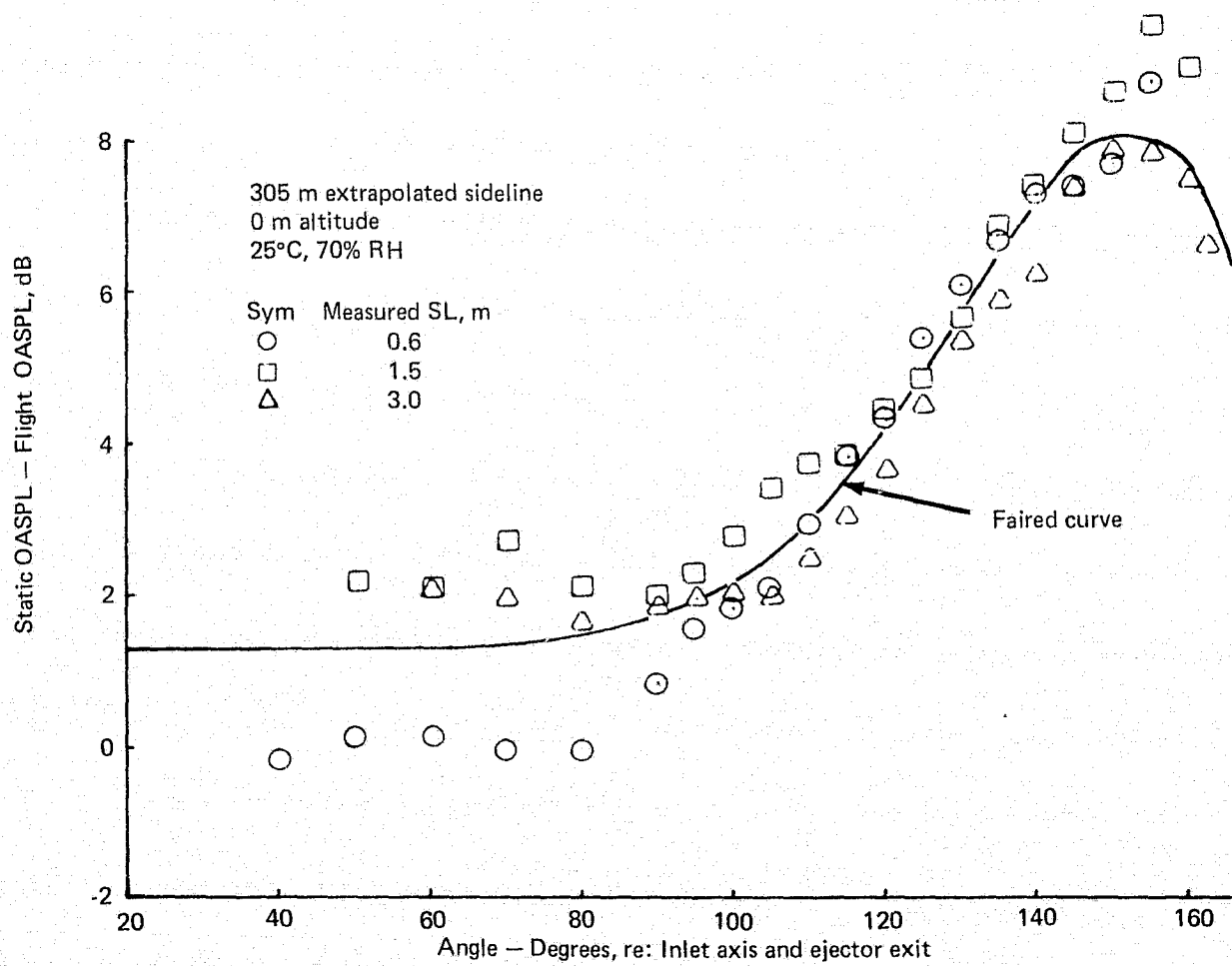
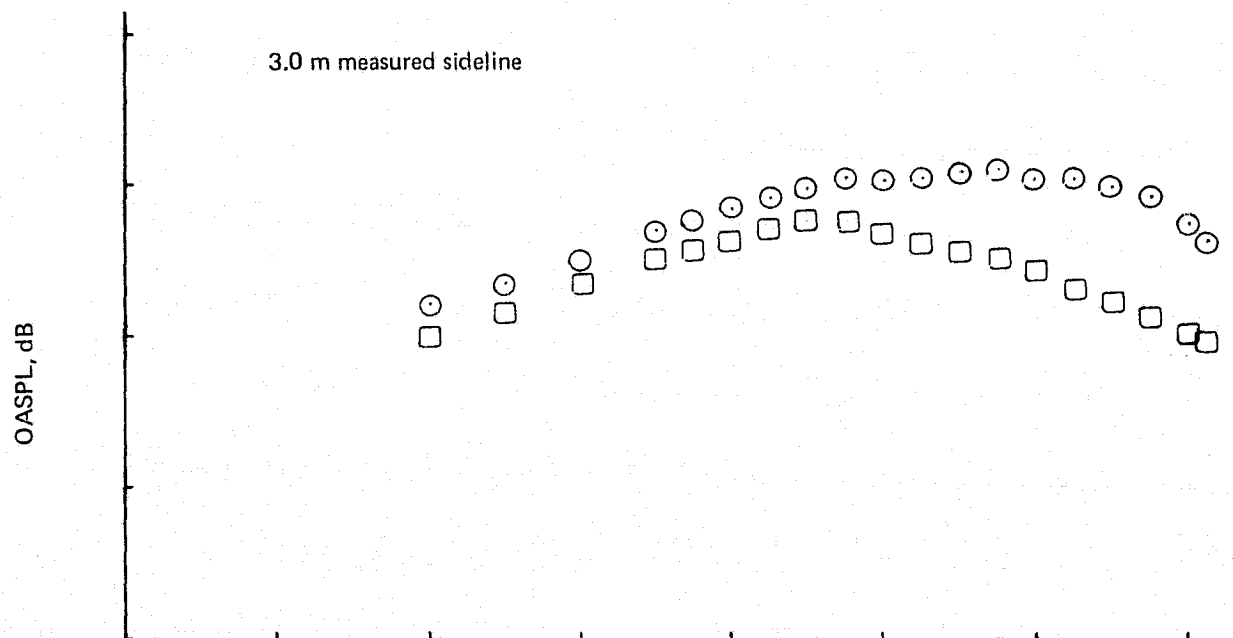


Figure 83.- (Concluded)

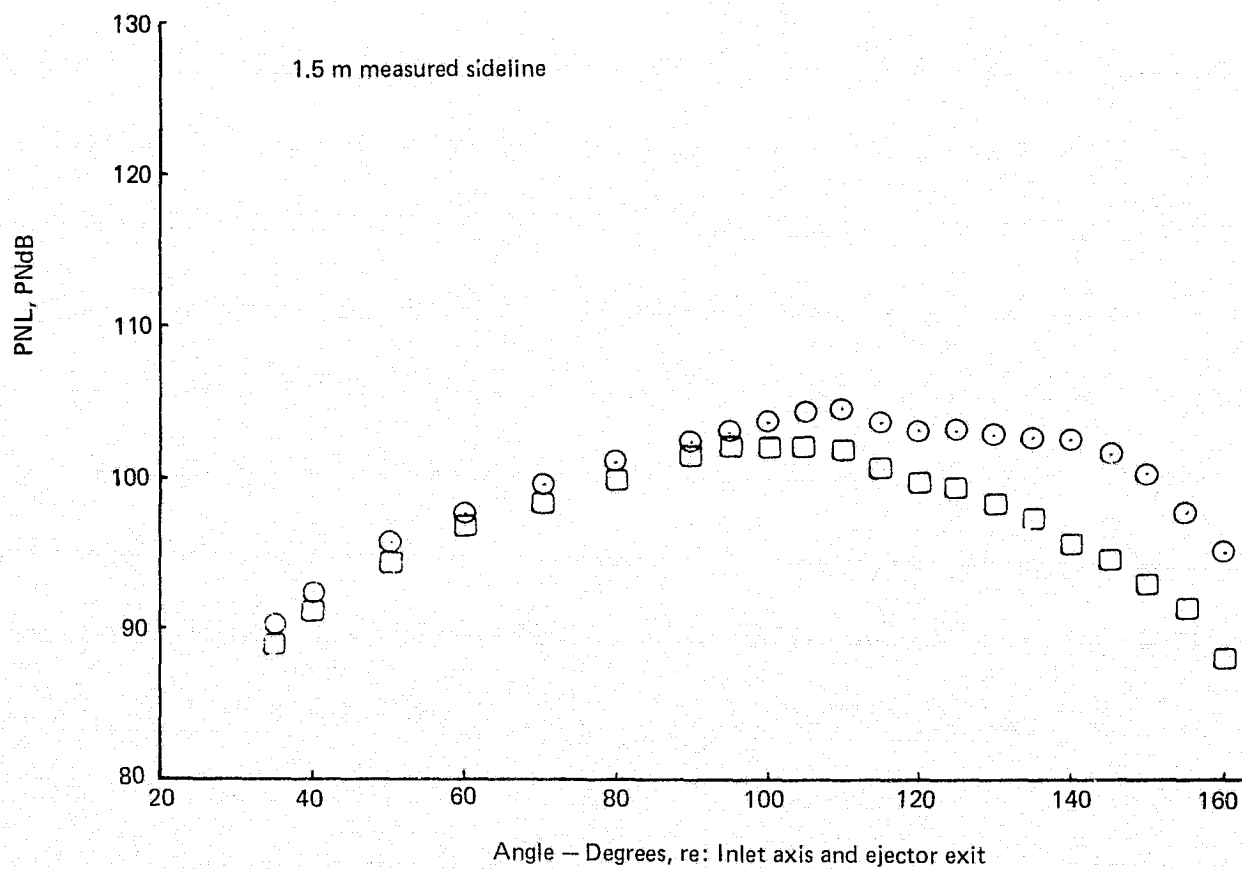
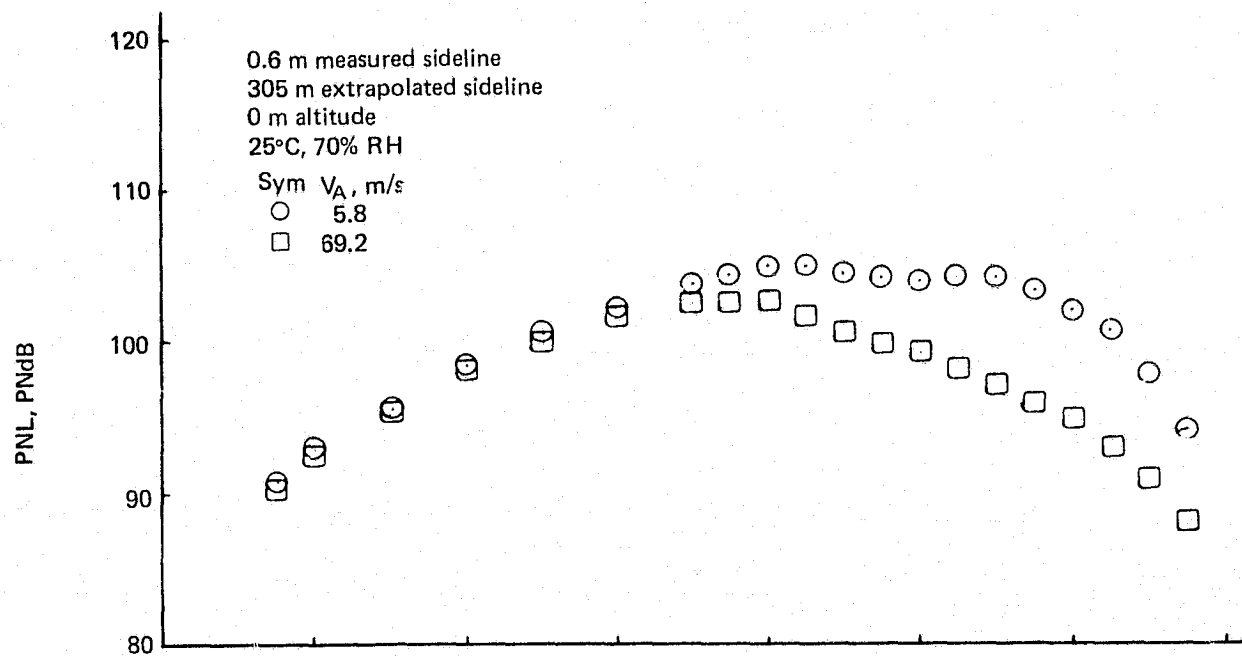


Figure 84.— Flight Effects on PNL of a 20-Lobe Nozzle with Ejector
 $NPR = 1.75$ $V_j = 503$ m/s

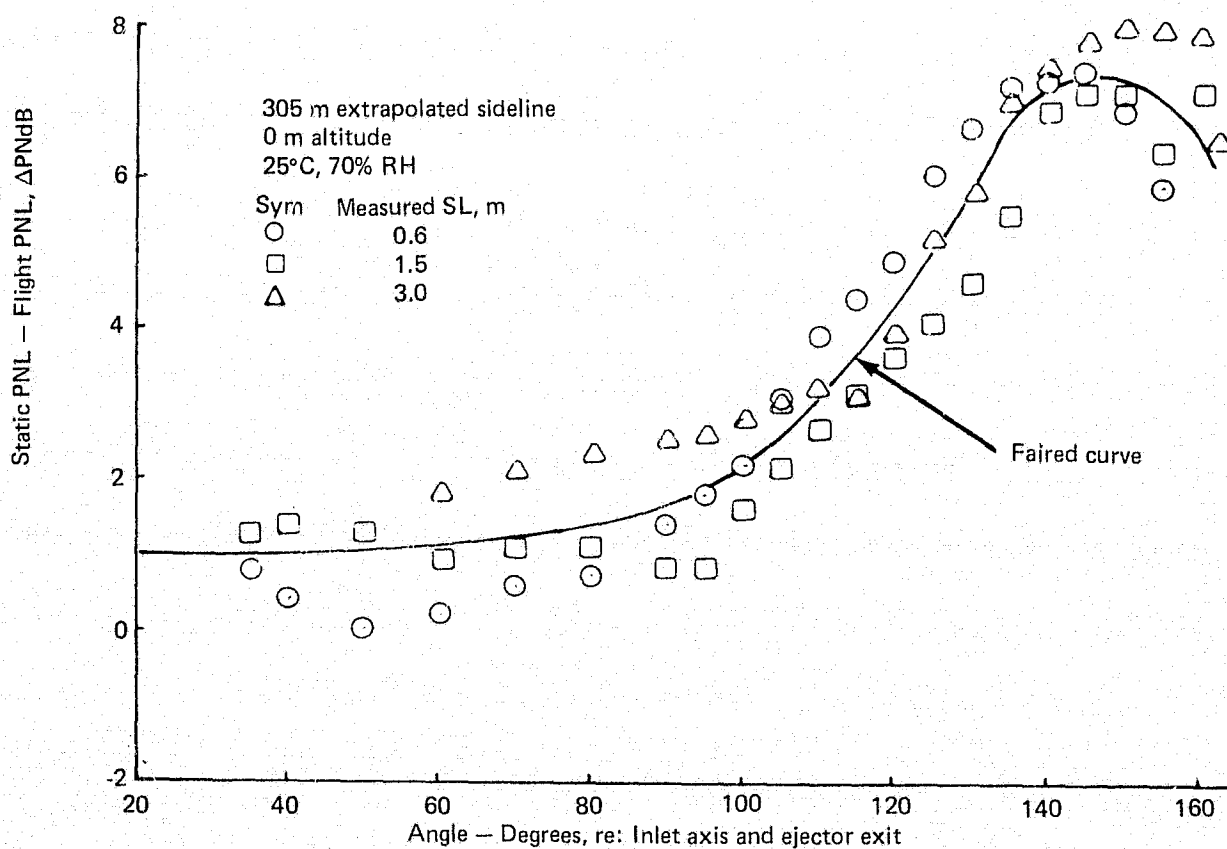
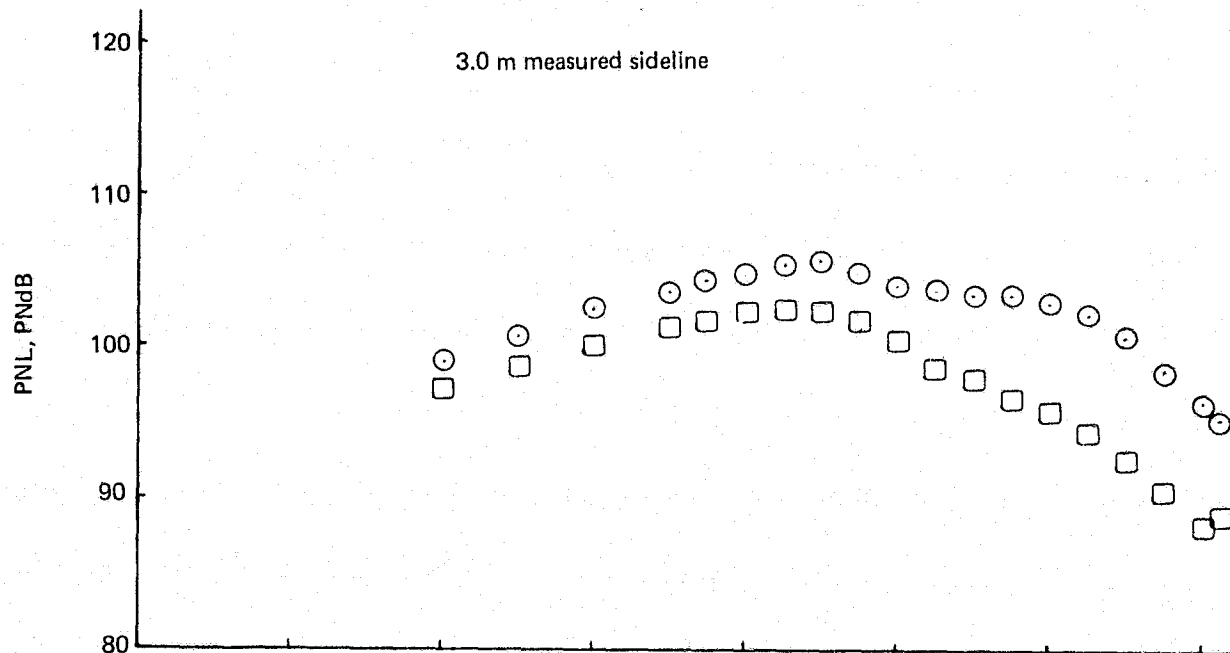


Figure 84.— (Concluded)

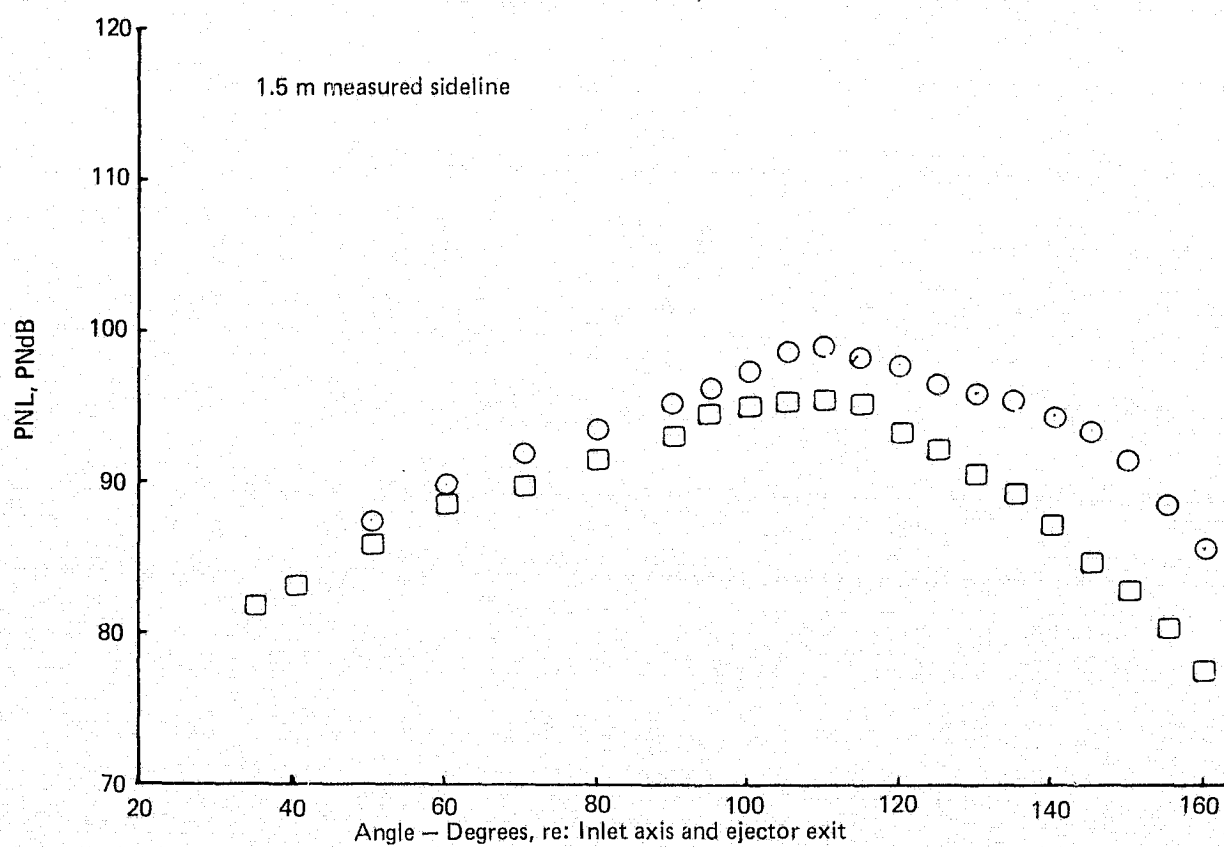
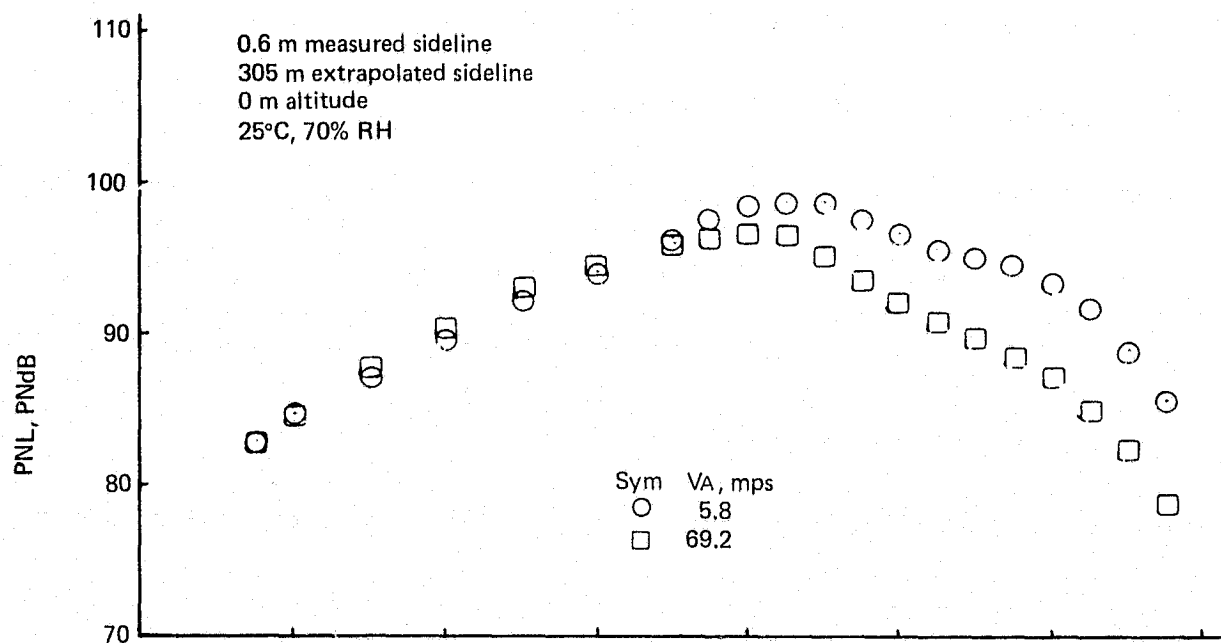


Figure 85.— Flight Effects on PNL of a 20-Lobe Nozzle with Ejector
NPR = 2.25 $V_j = 594$ m/s

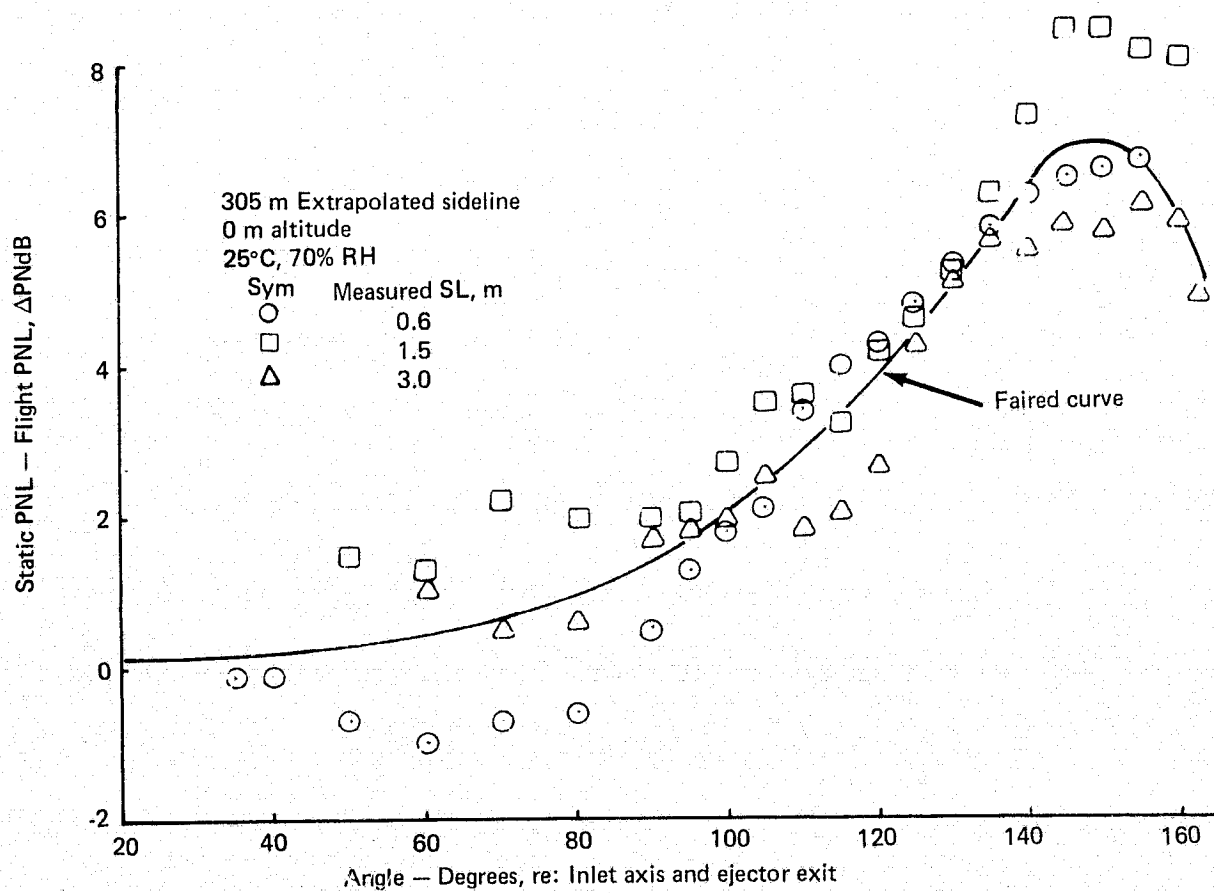
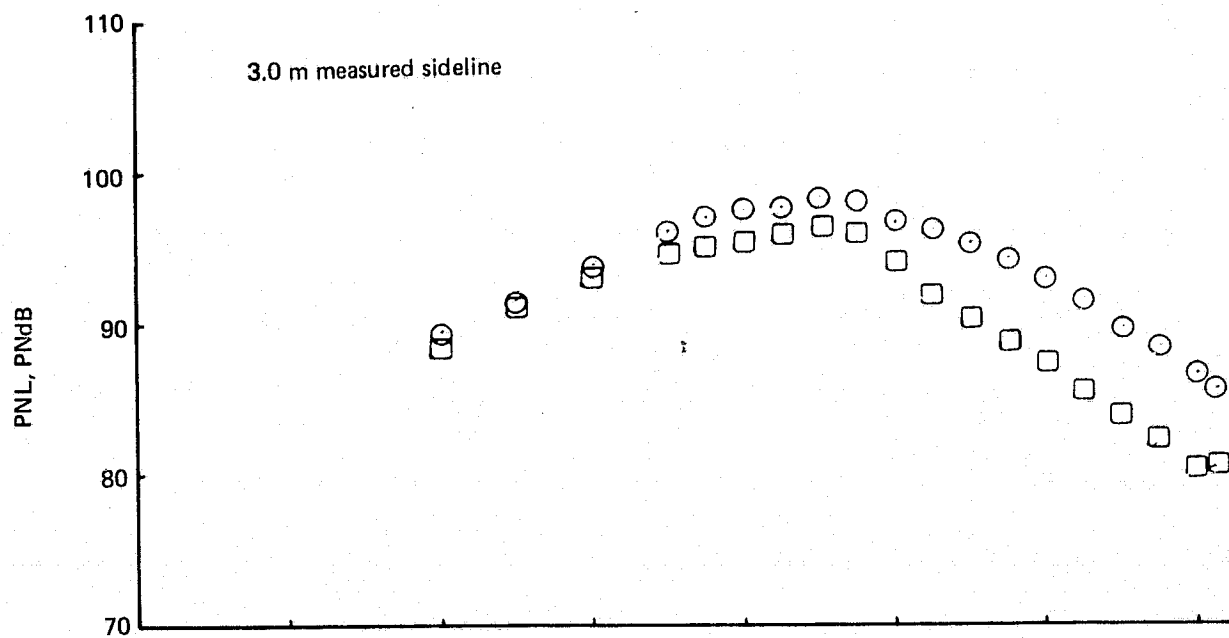


Figure 85.— (Concluded)

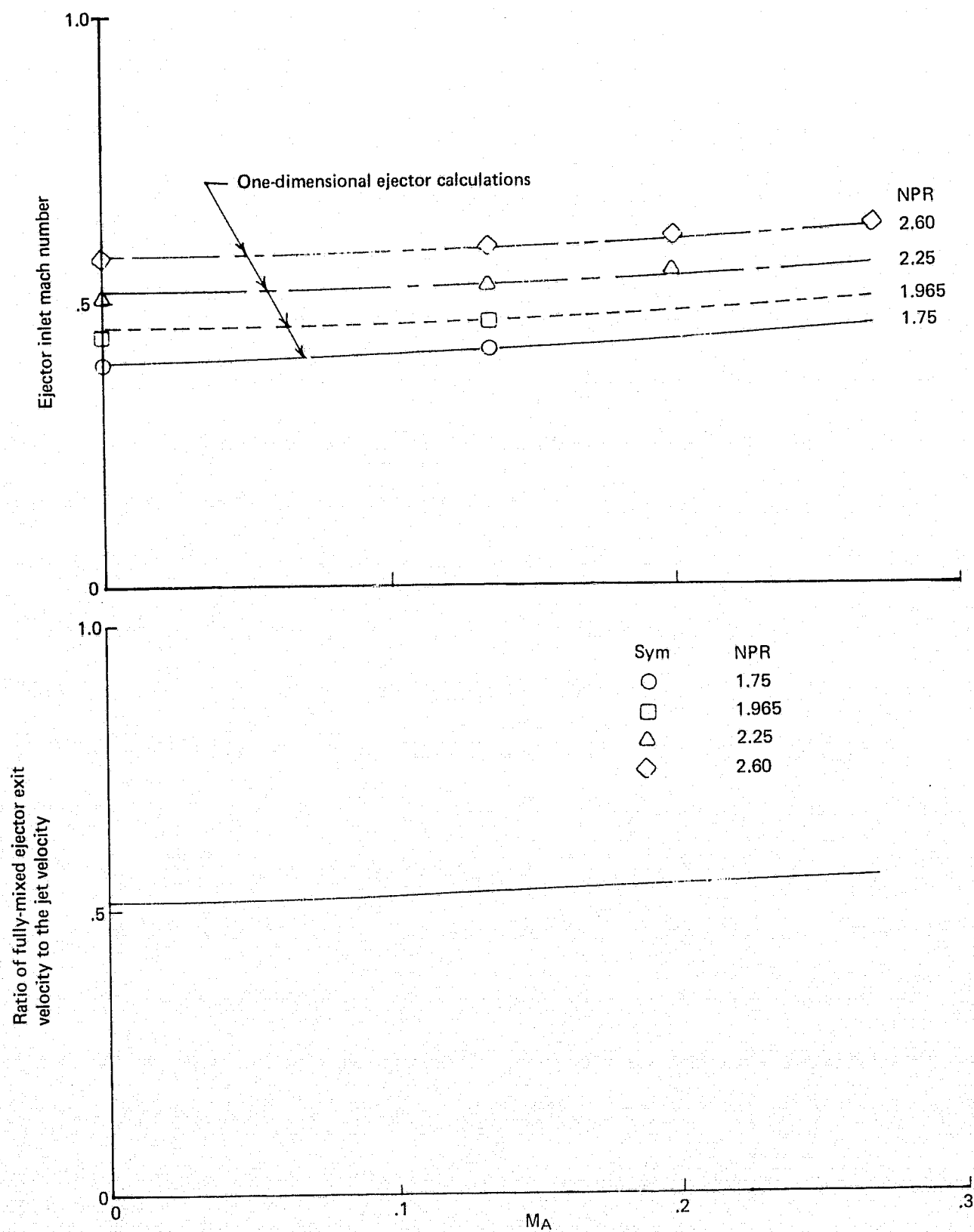


Figure 86.— Ejector Performance with the 57-Tube Nozzle

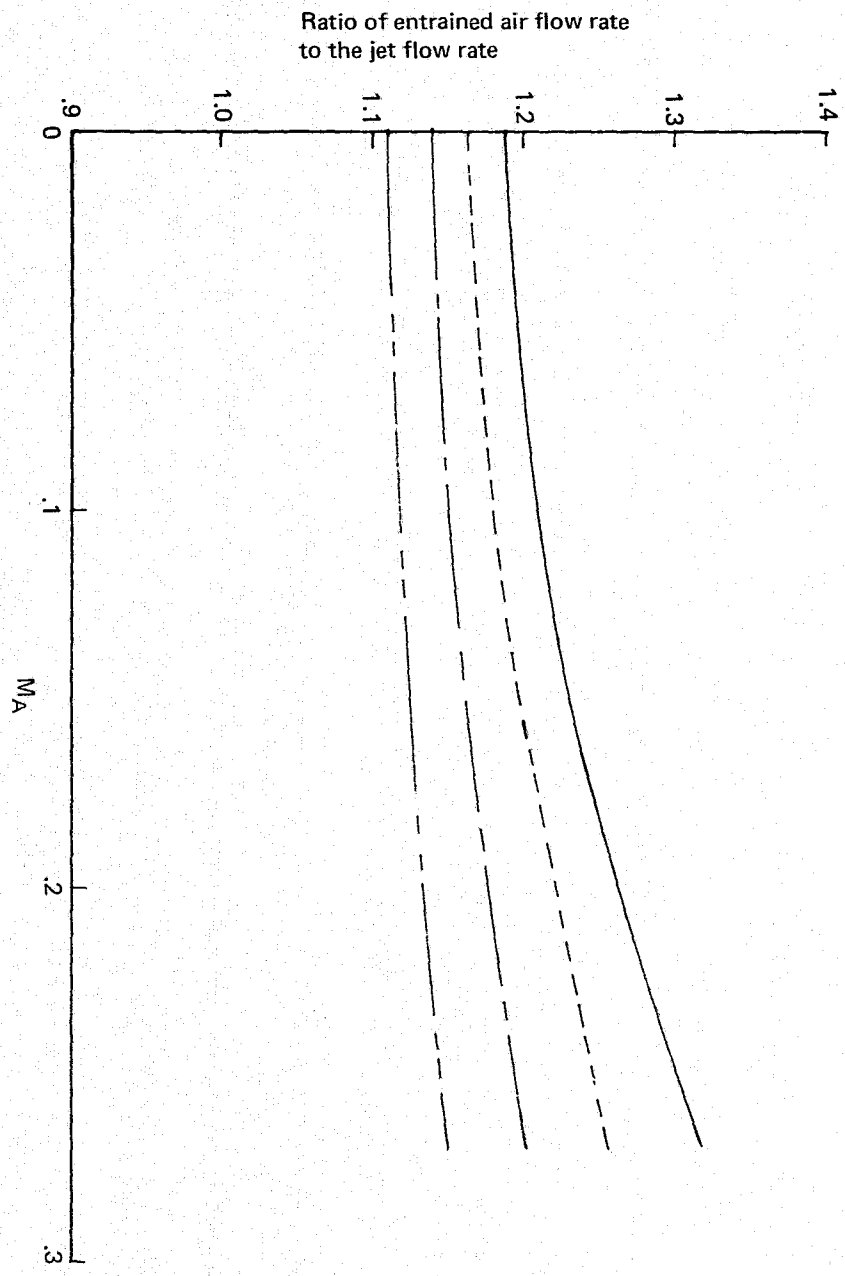
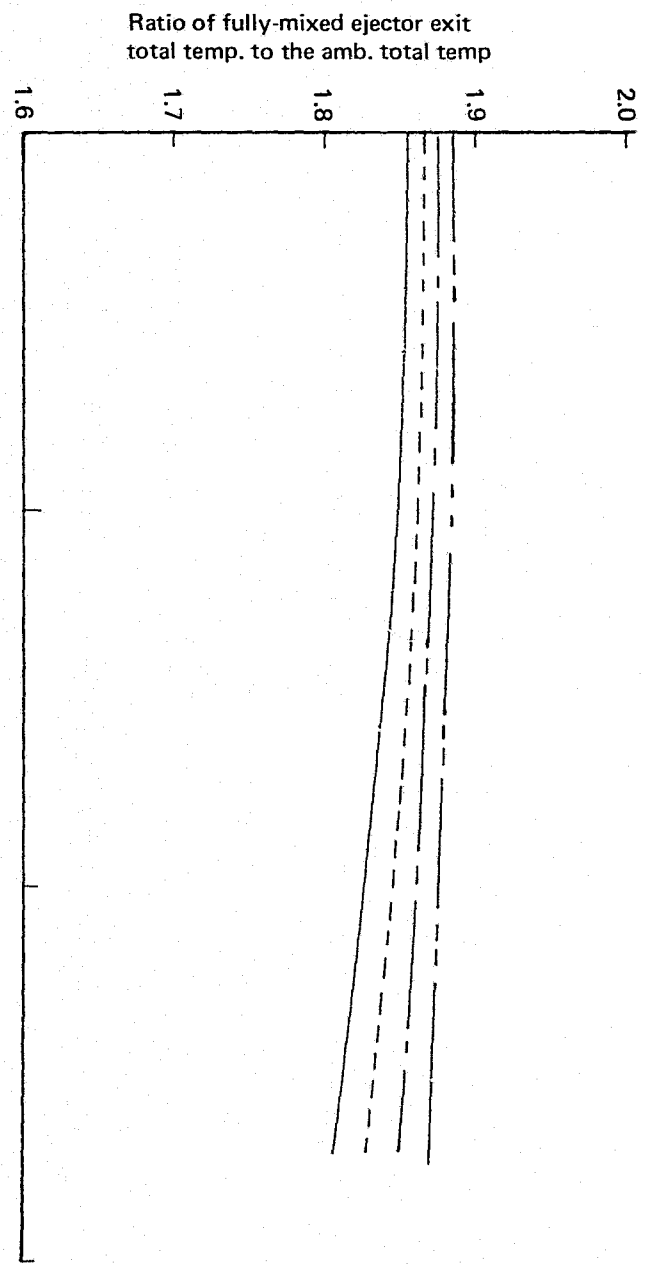


Figure 86.— (Concluded)

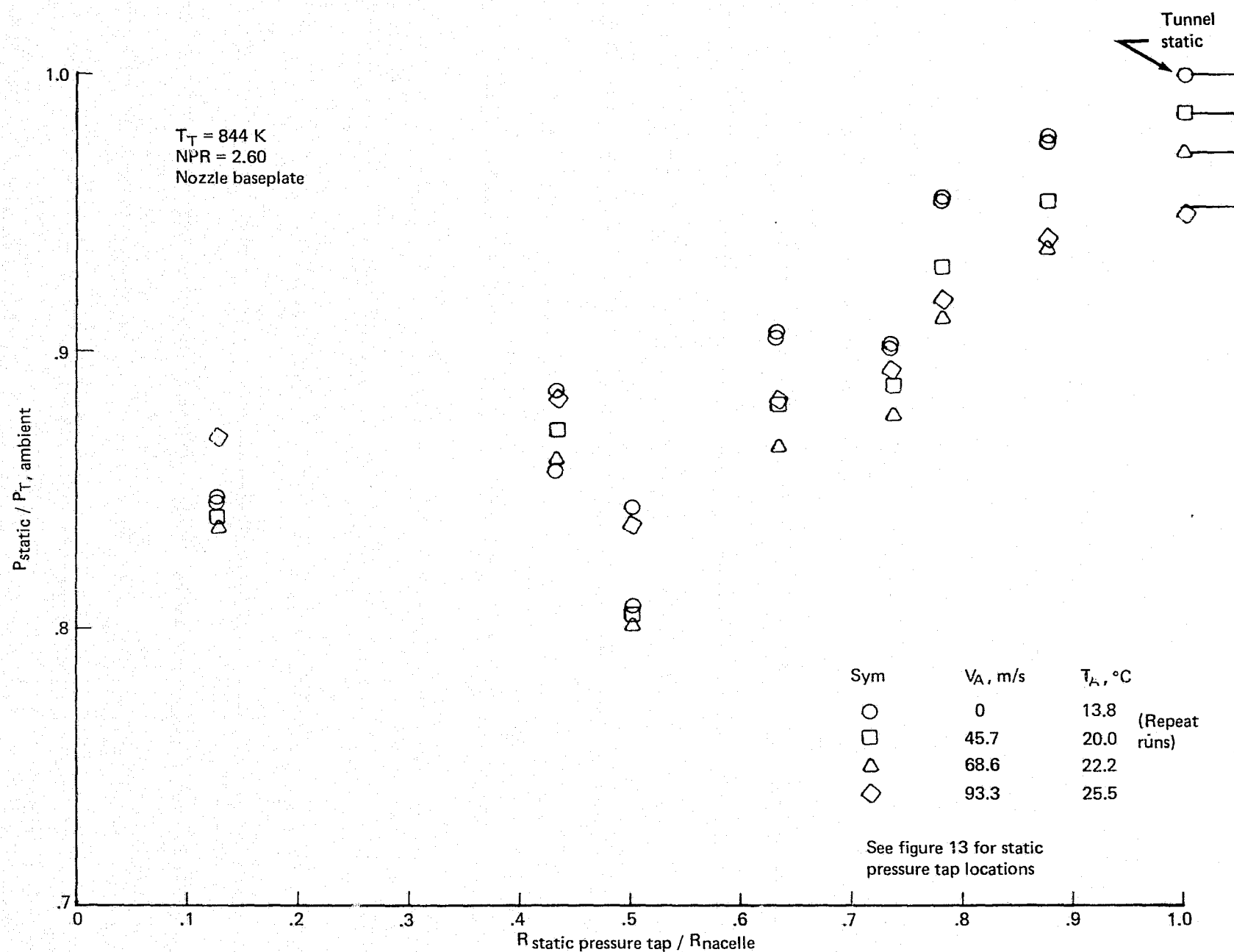


Figure 87.— 57-Tube Nozzle Base and Ejector Lip Pressure Distributions

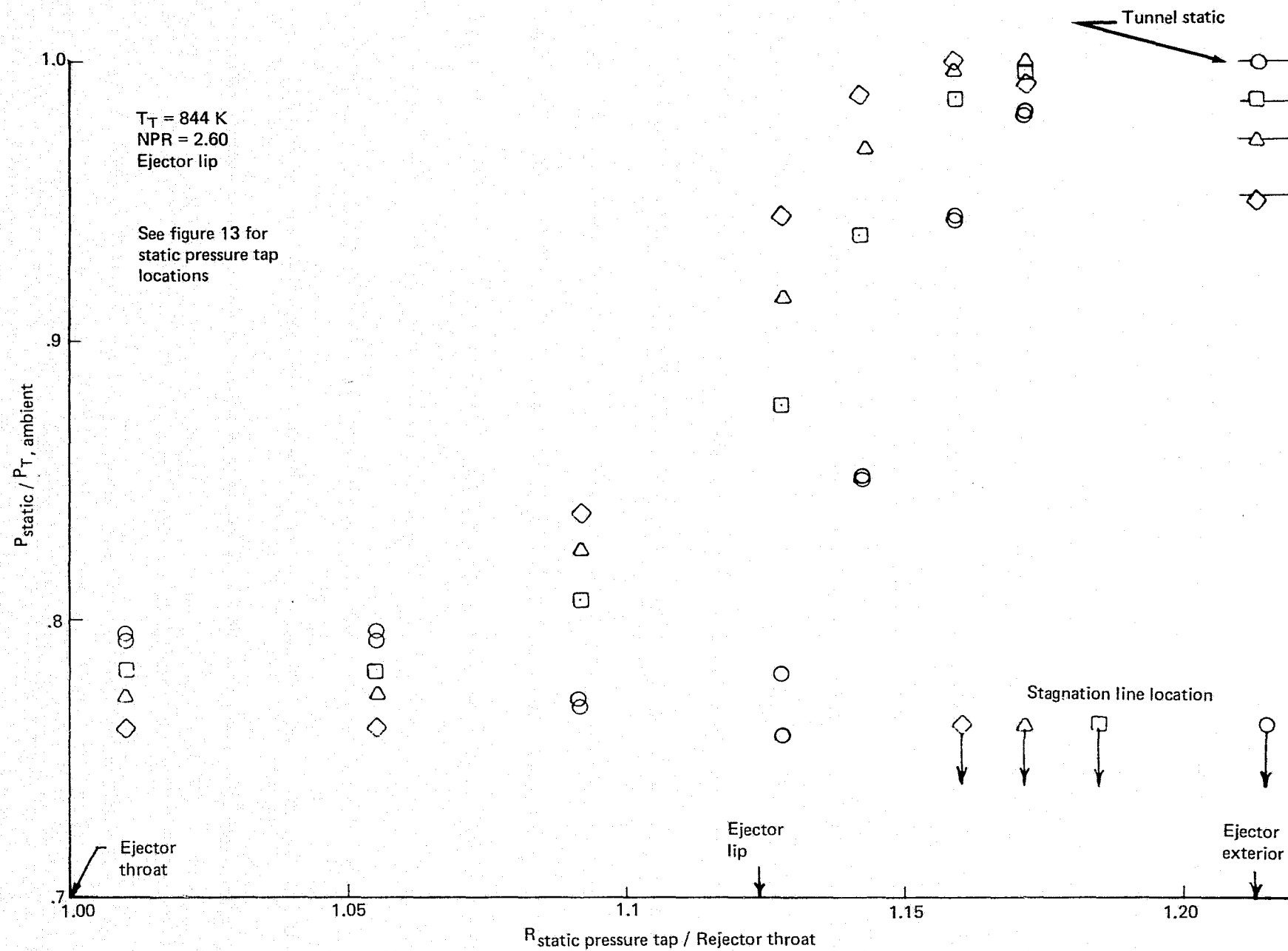


Figure 87.— (Concluded)

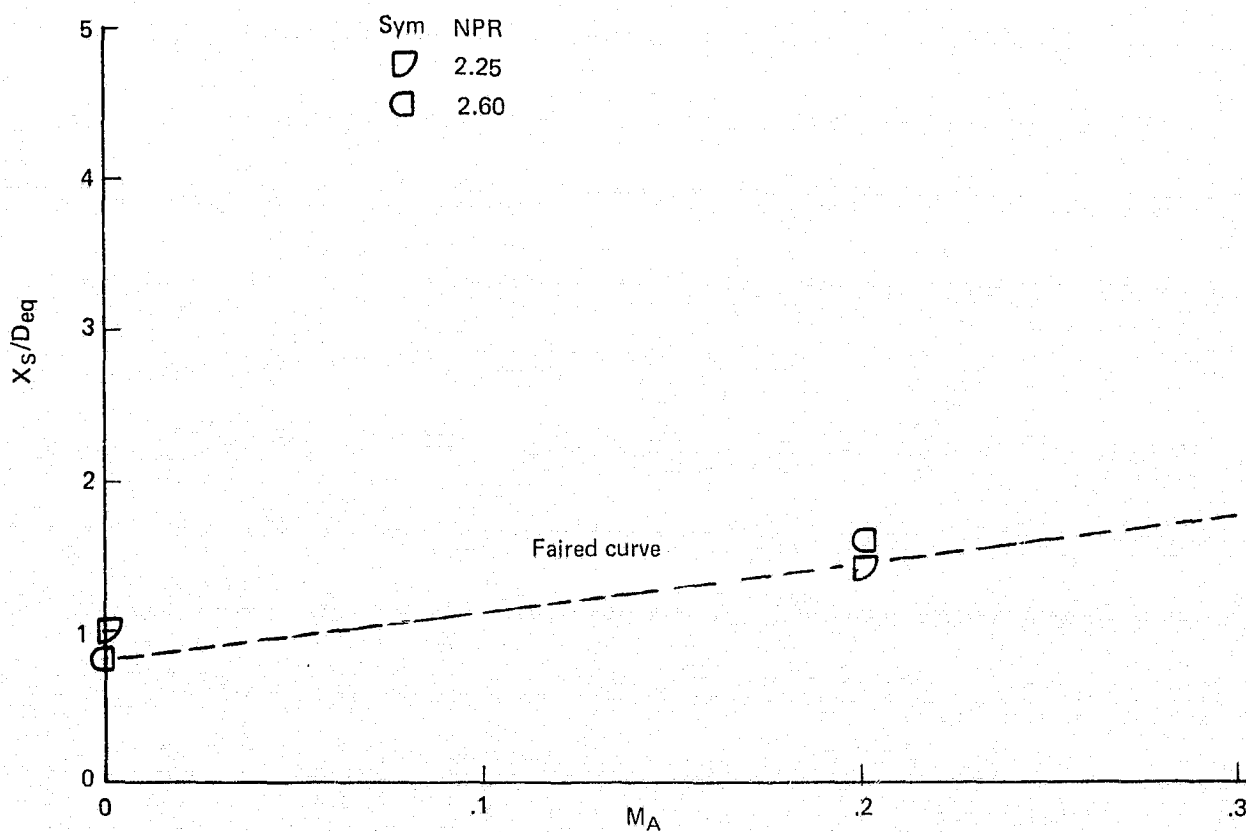
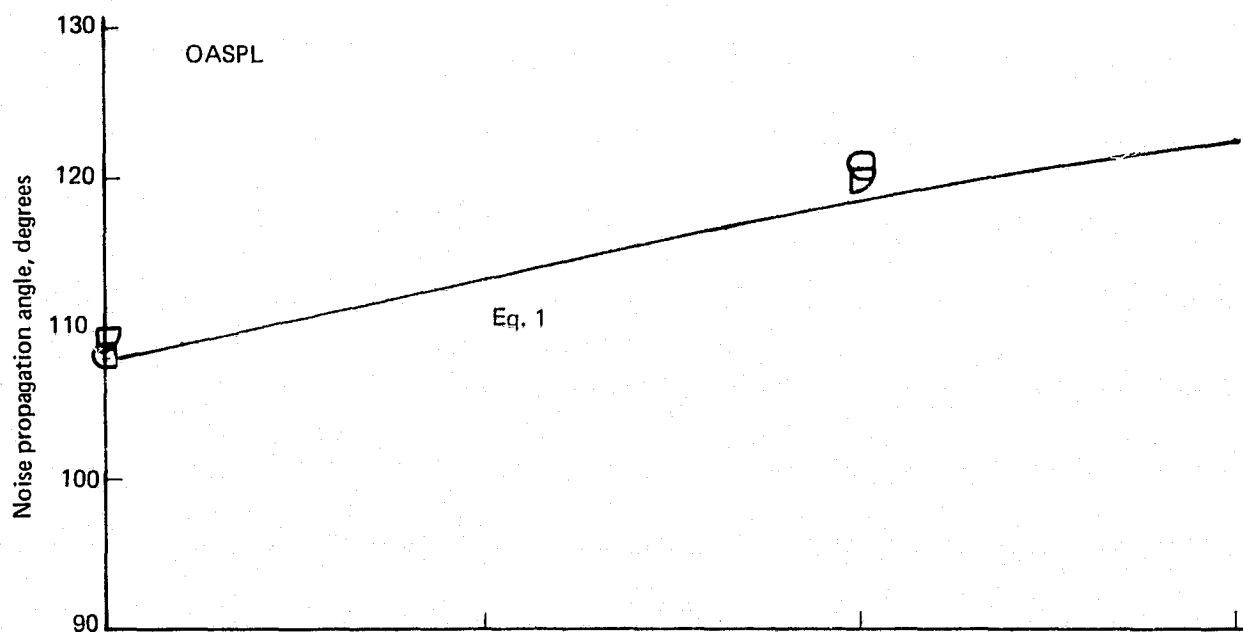


Figure 88.— Peak Noise Source Locations and Noise Propagation Angles for the 57-Tube Nozzle with Lined Ejector

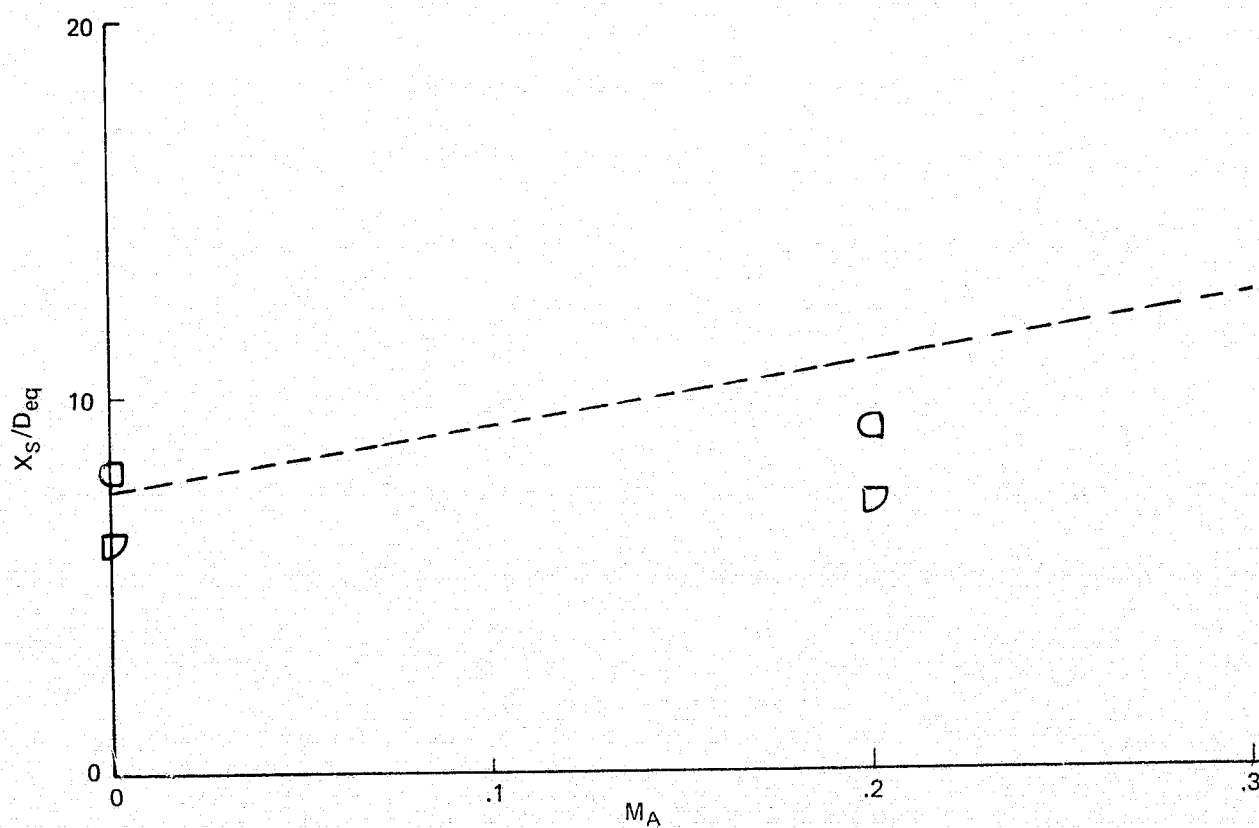
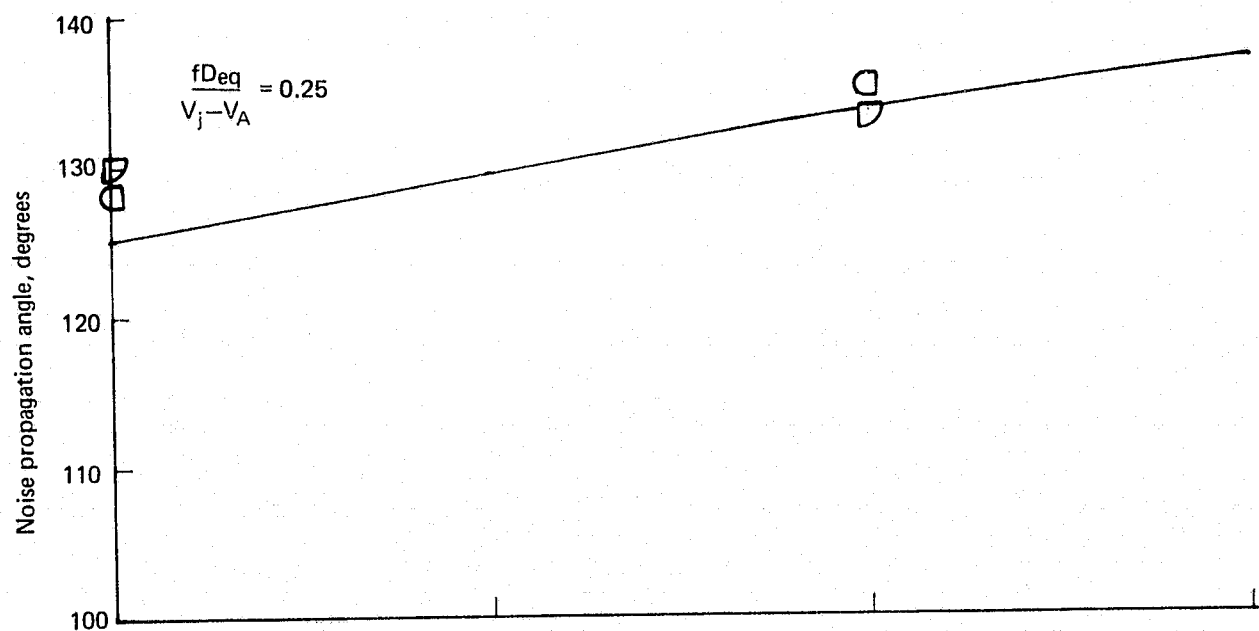


Figure 88.— (Continued)

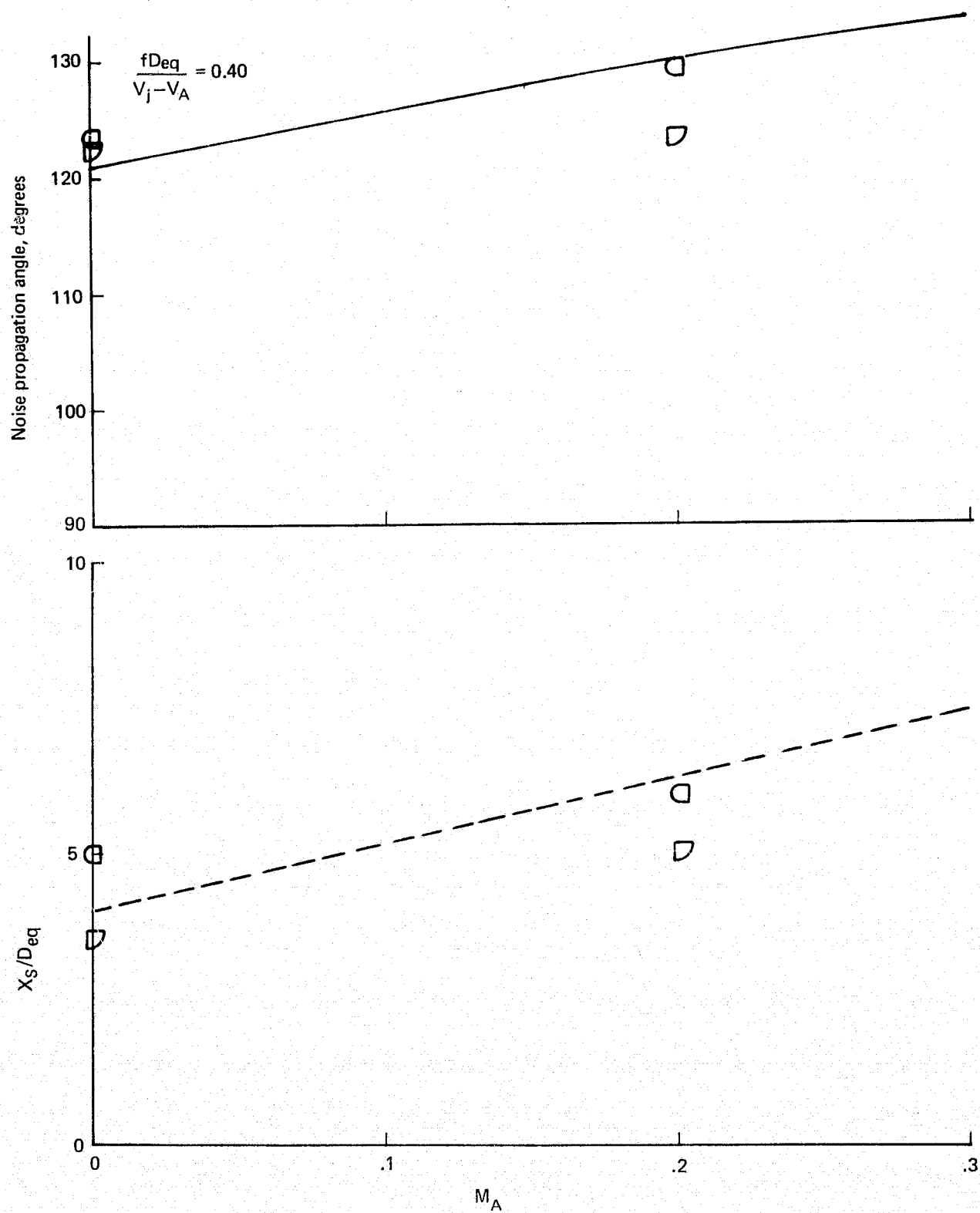


Figure 88.— (Continued)

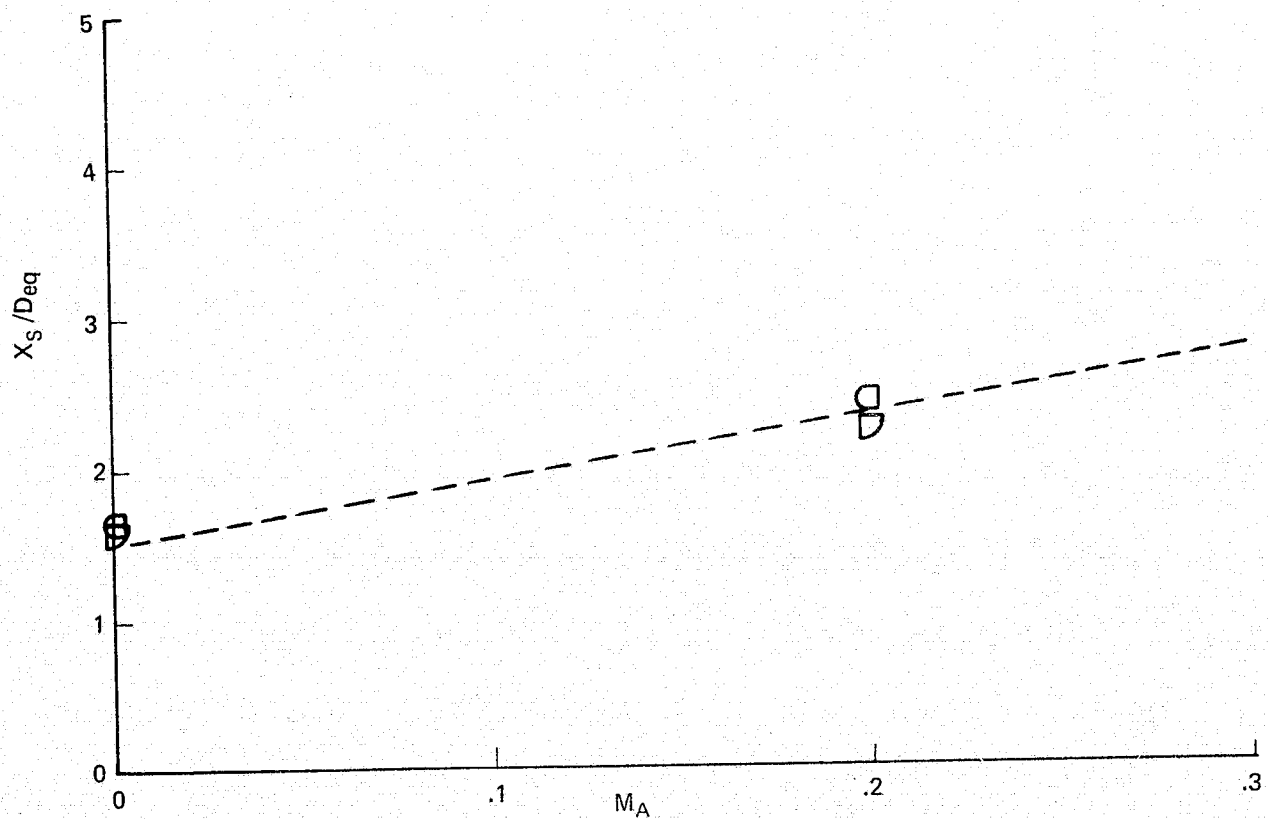
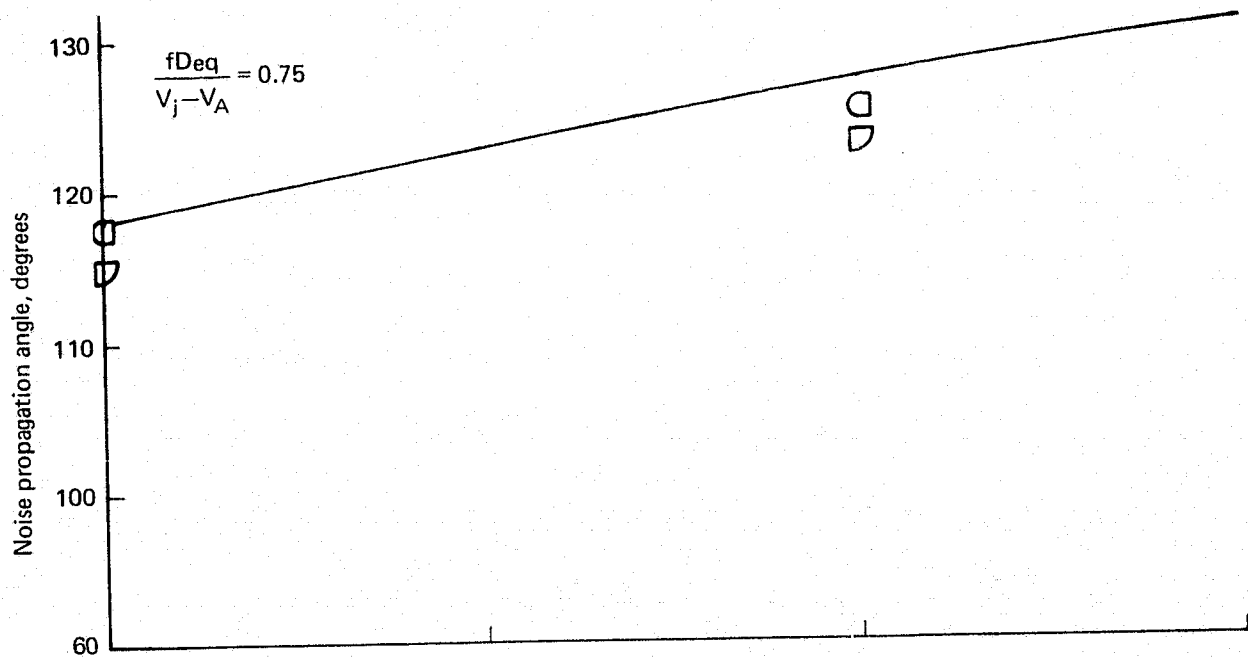


Figure 88.— (Continued)

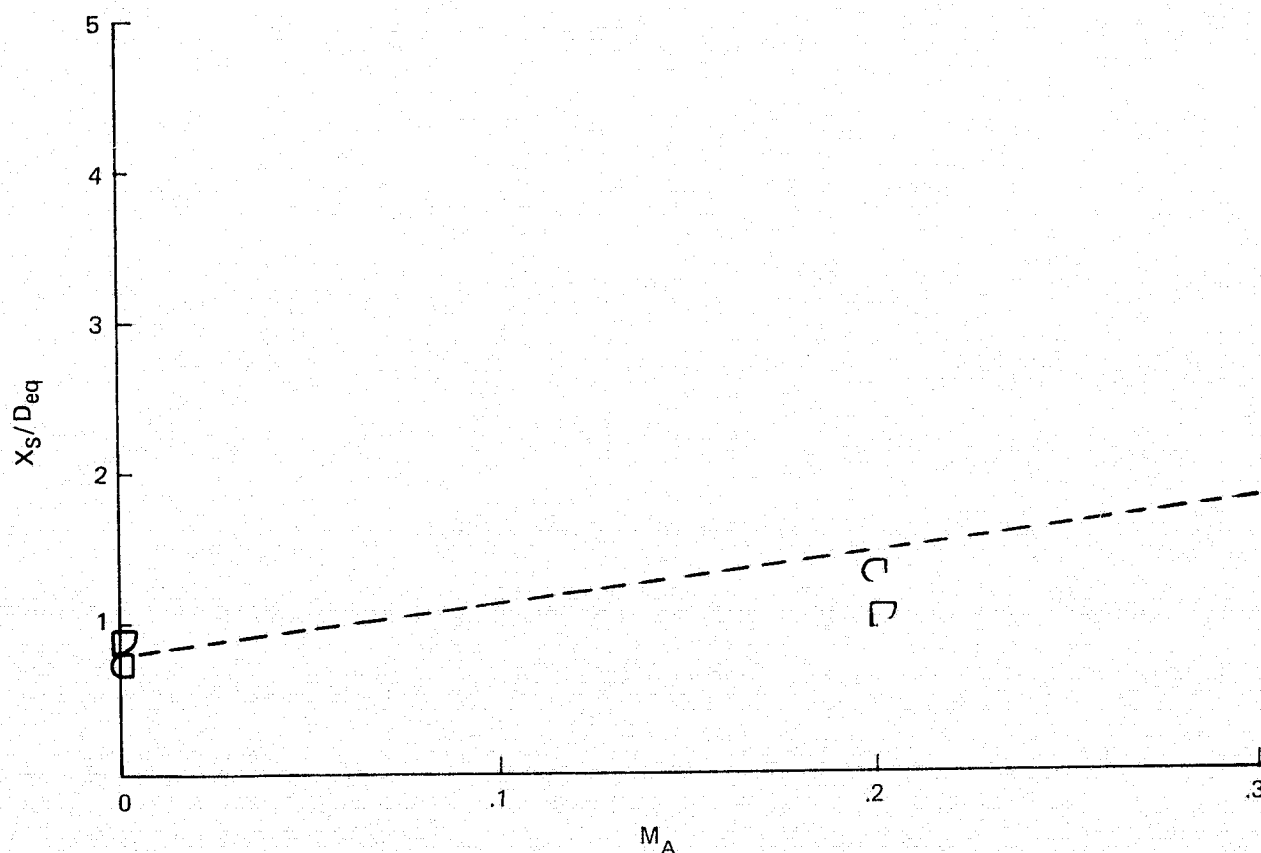
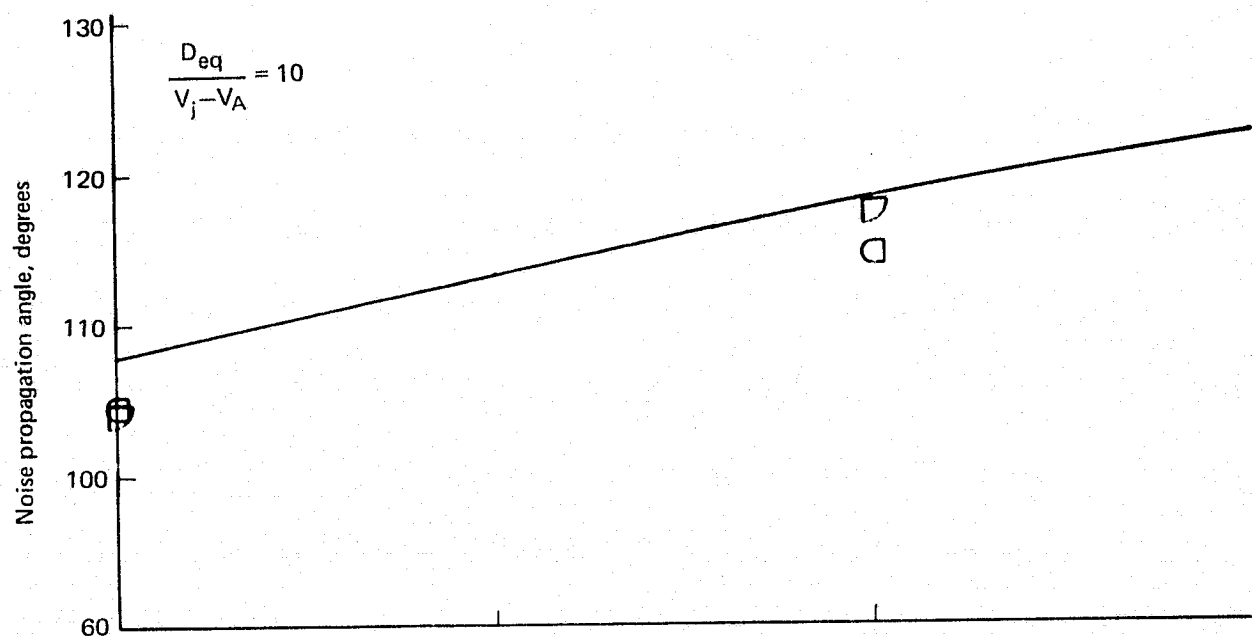


Figure 88.— (Concluded)

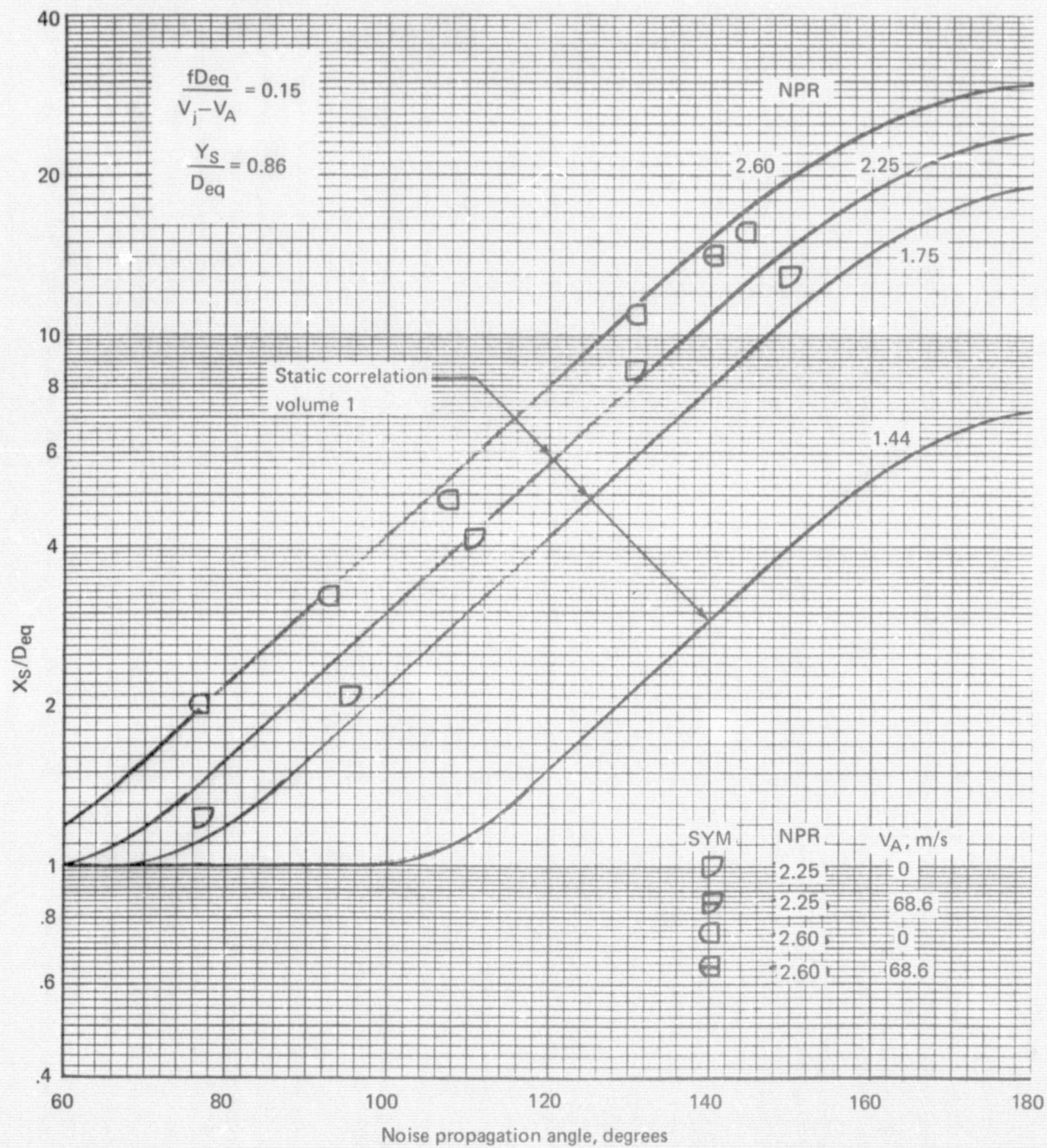


Figure 89.—Effect of Ambient Velocity on Distributed Noise Source Locations for the 57-Tube Nozzle with Lined Ejector

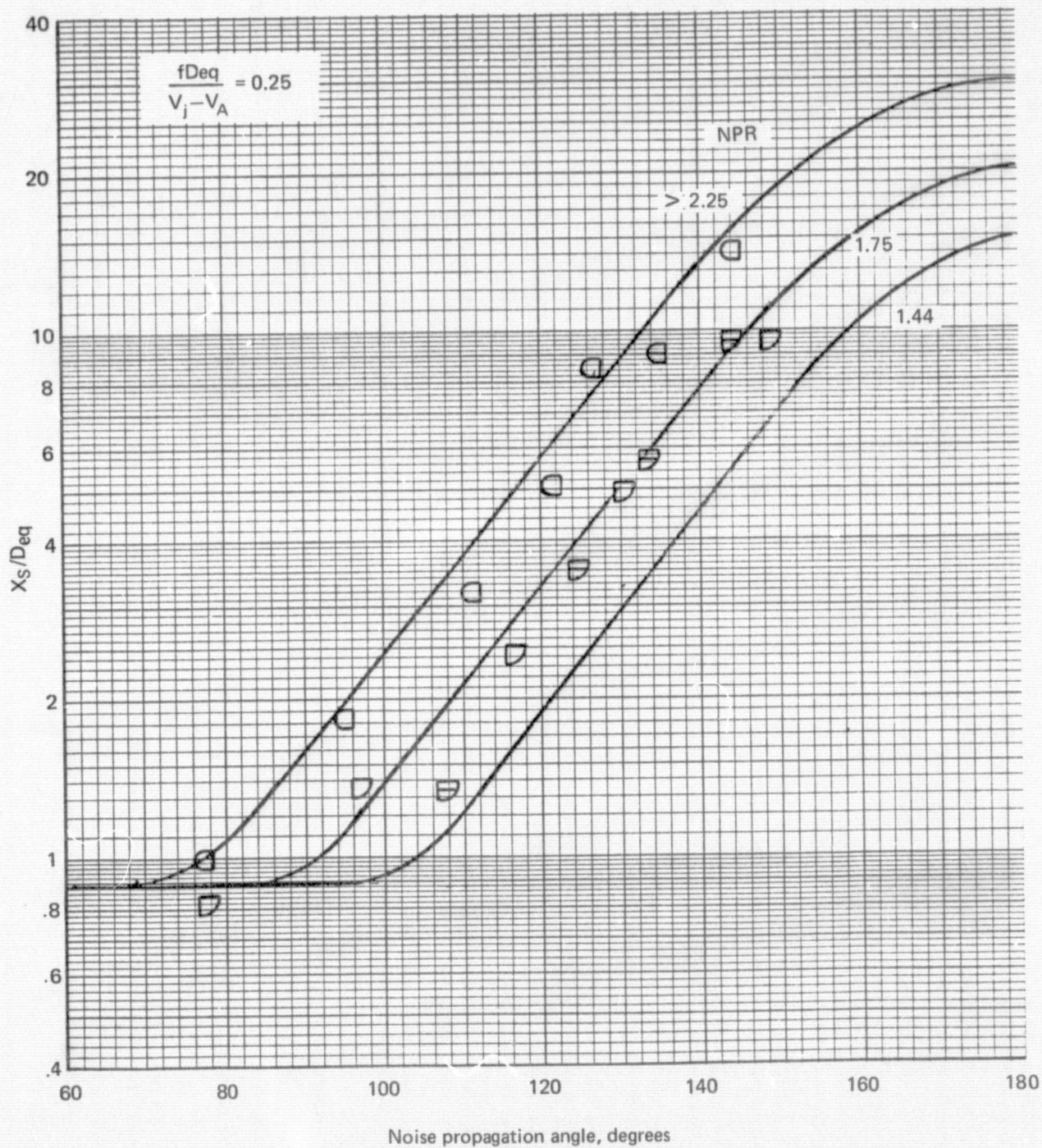


Figure 89.—(Continued)

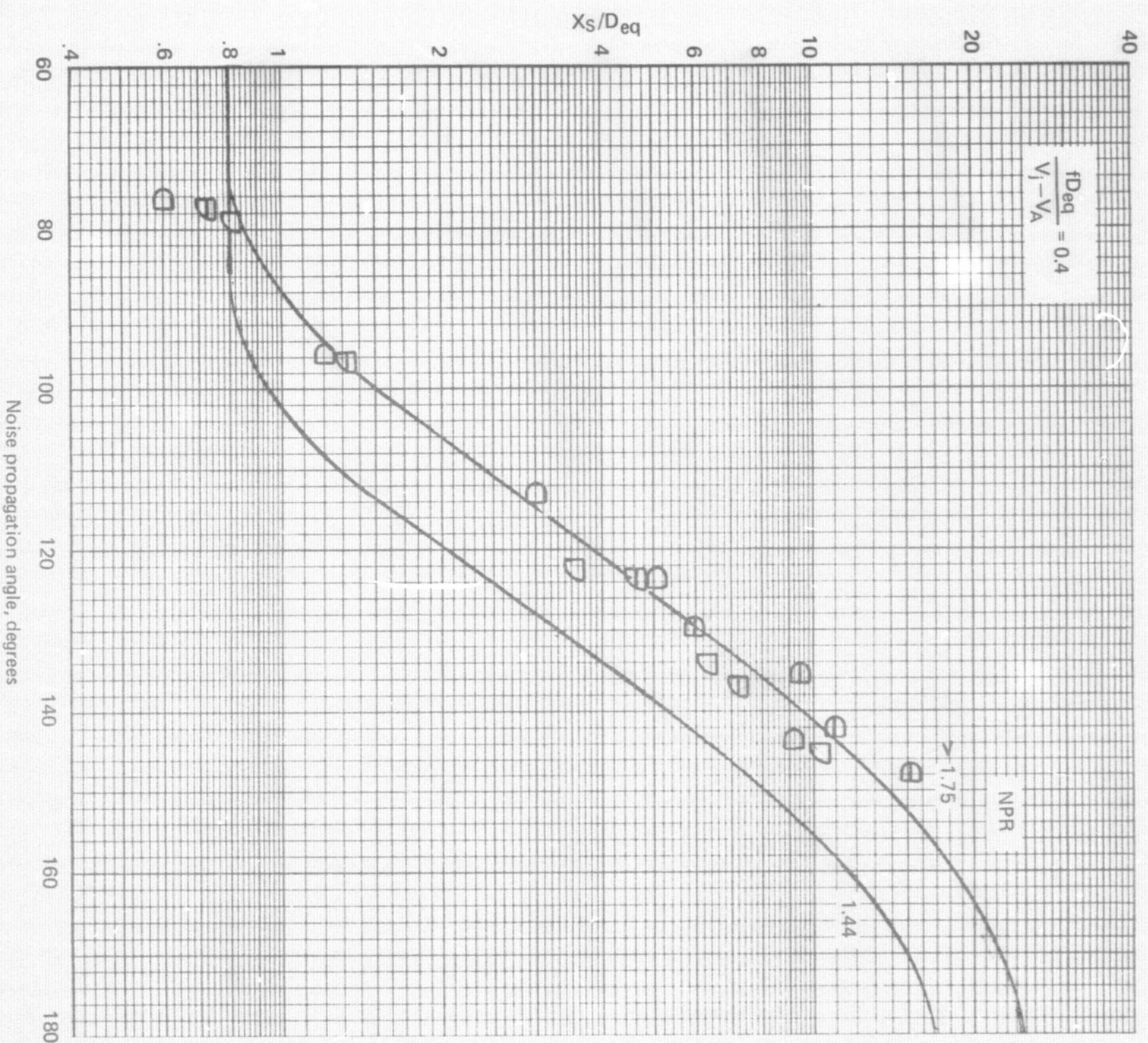


Figure 89.—(Continued)

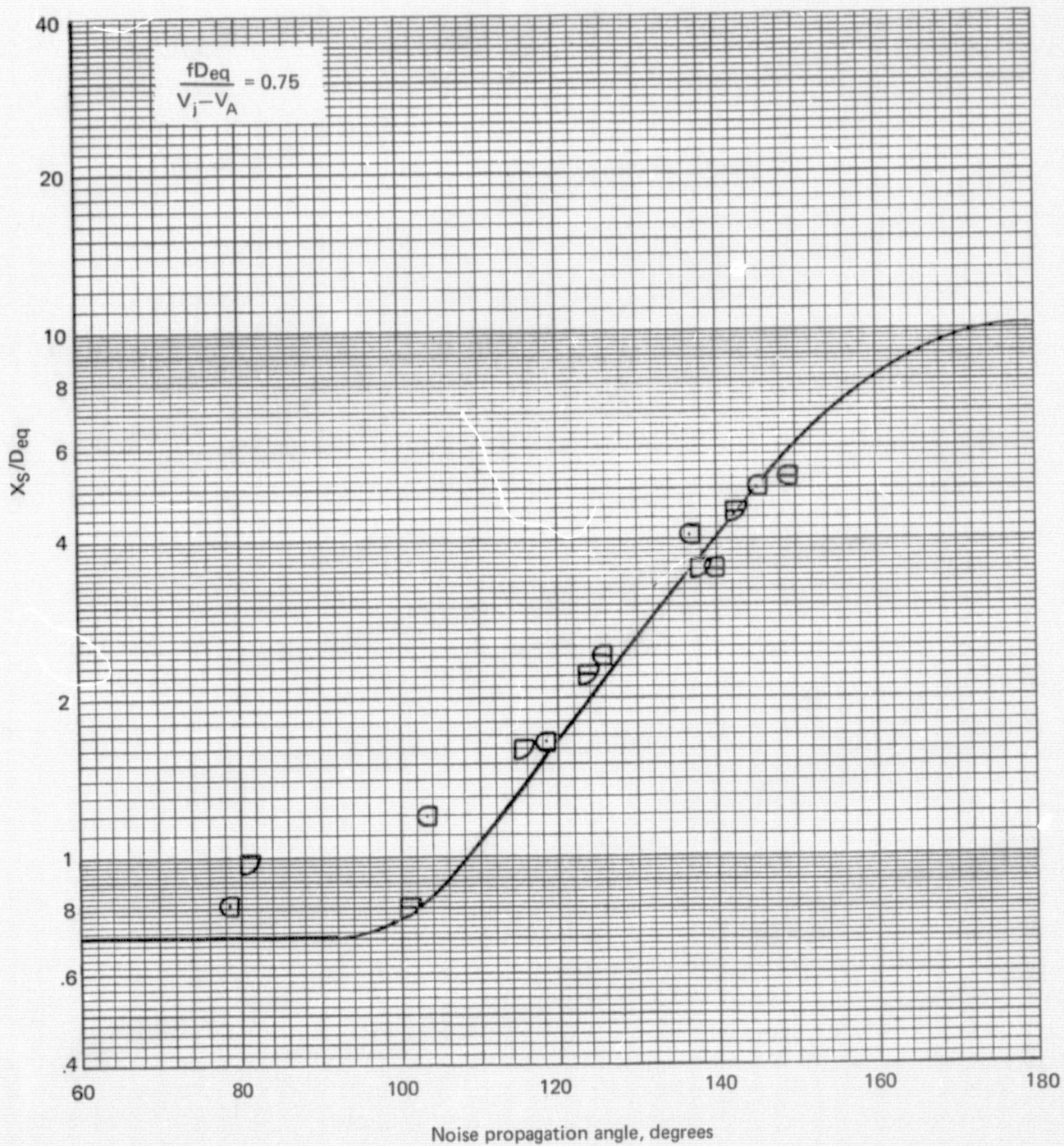


Figure 89.—(Continued)

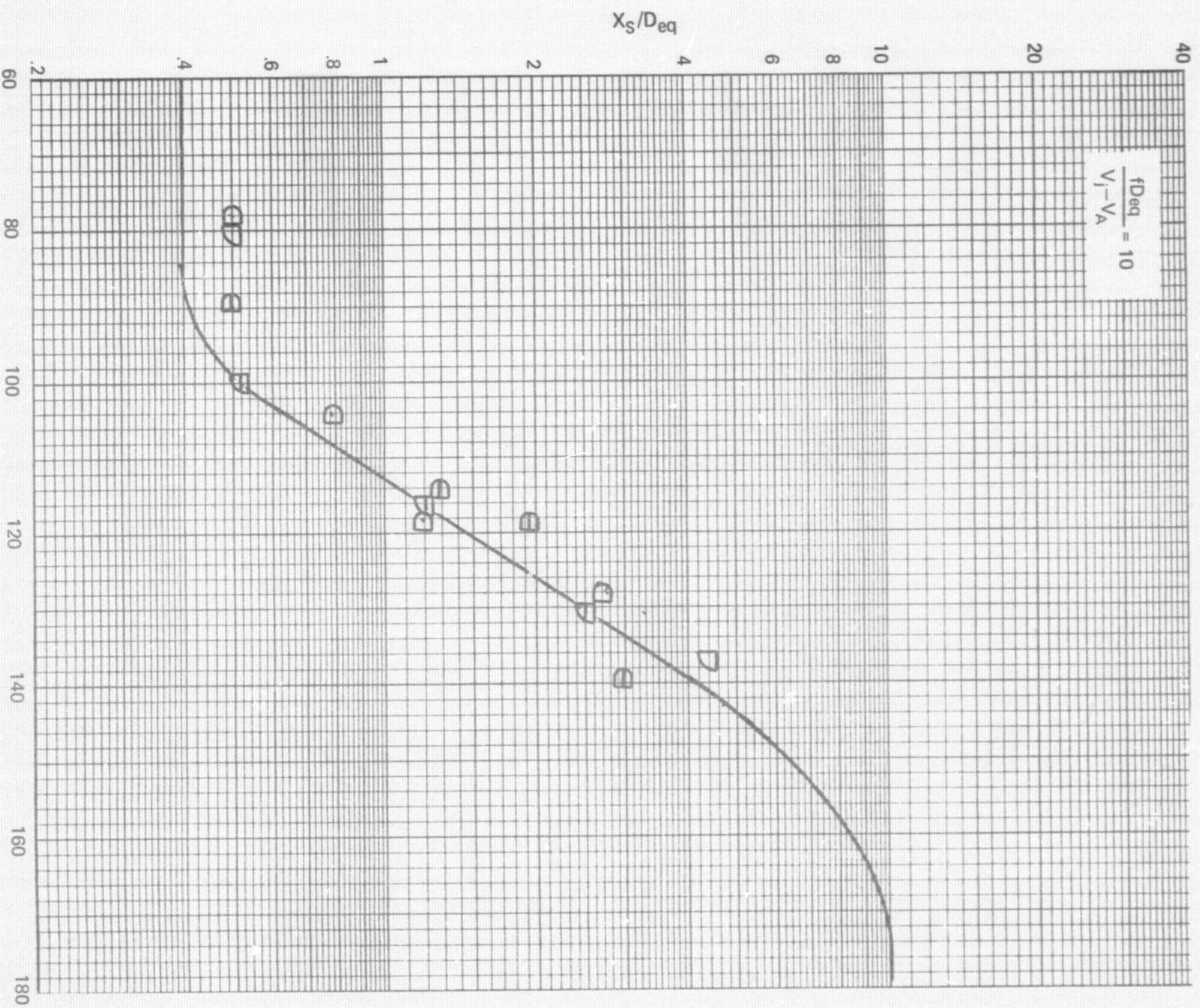


Figure 89.—(Concluded)

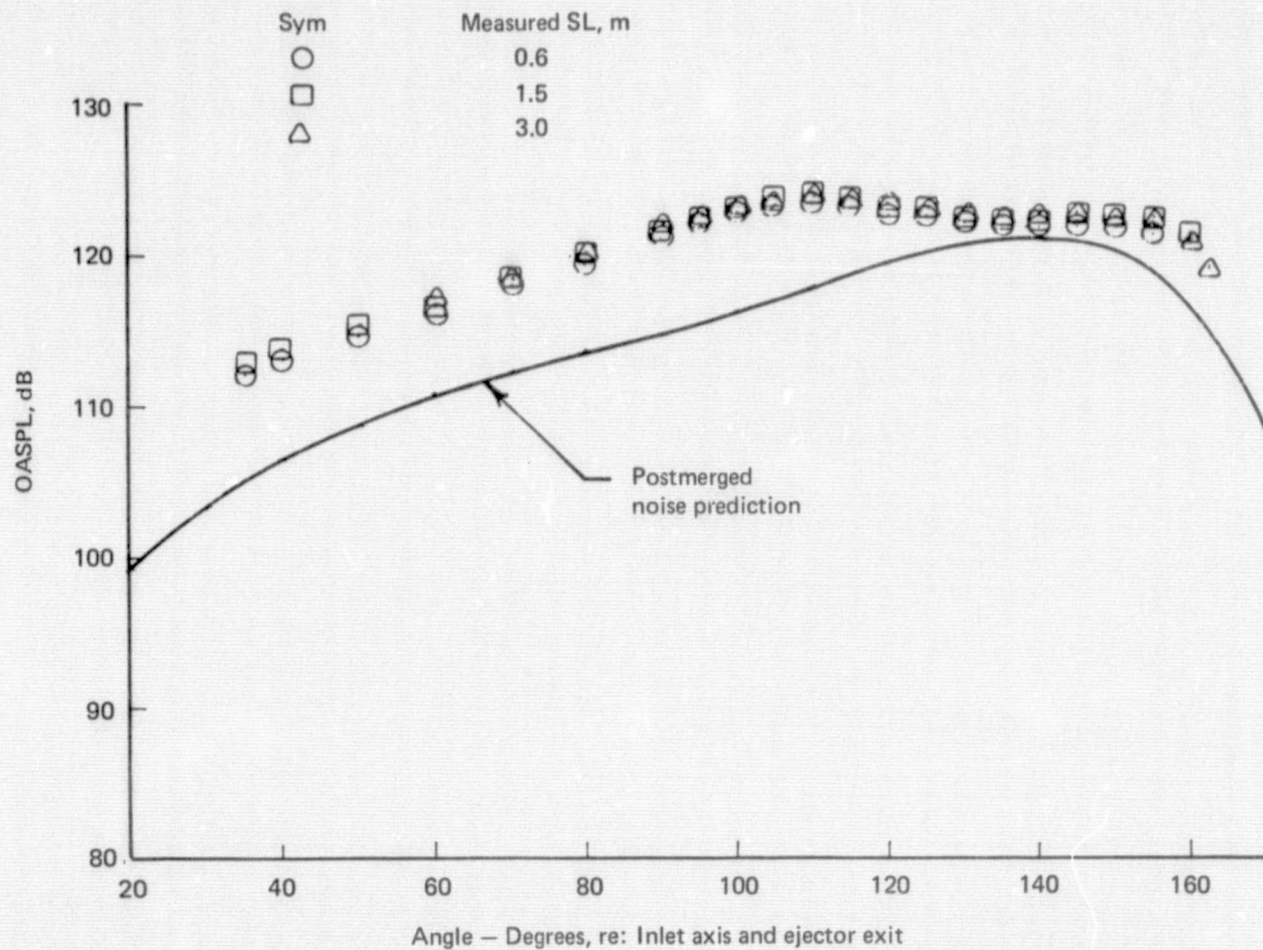


Figure 90.— OASPL Directivity and Jet Noise Spectra for the 57-Tube Nozzle with Lined Ejector Extrapolated to a 3.0 m Sideline NPR = 2.61, $V_A = 3.3$ m/s

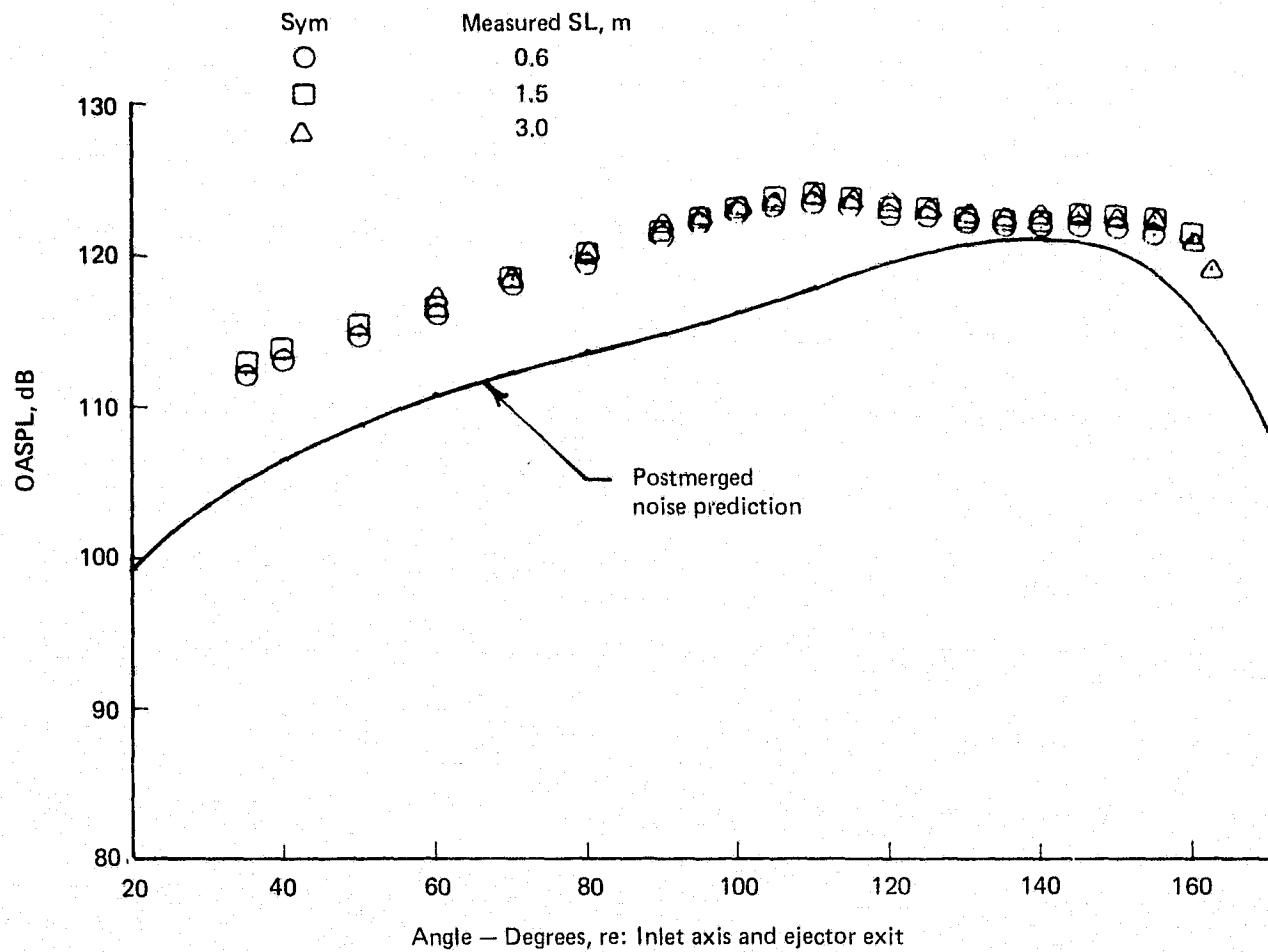


Figure 90.— OASPL Directivity and Jet Noise Spectra for the 57-Tube Nozzle with Lined Ejector Extrapolated to a 3.0 m Sideline NPR = 2.61, $V_A = 3.3$ m/s

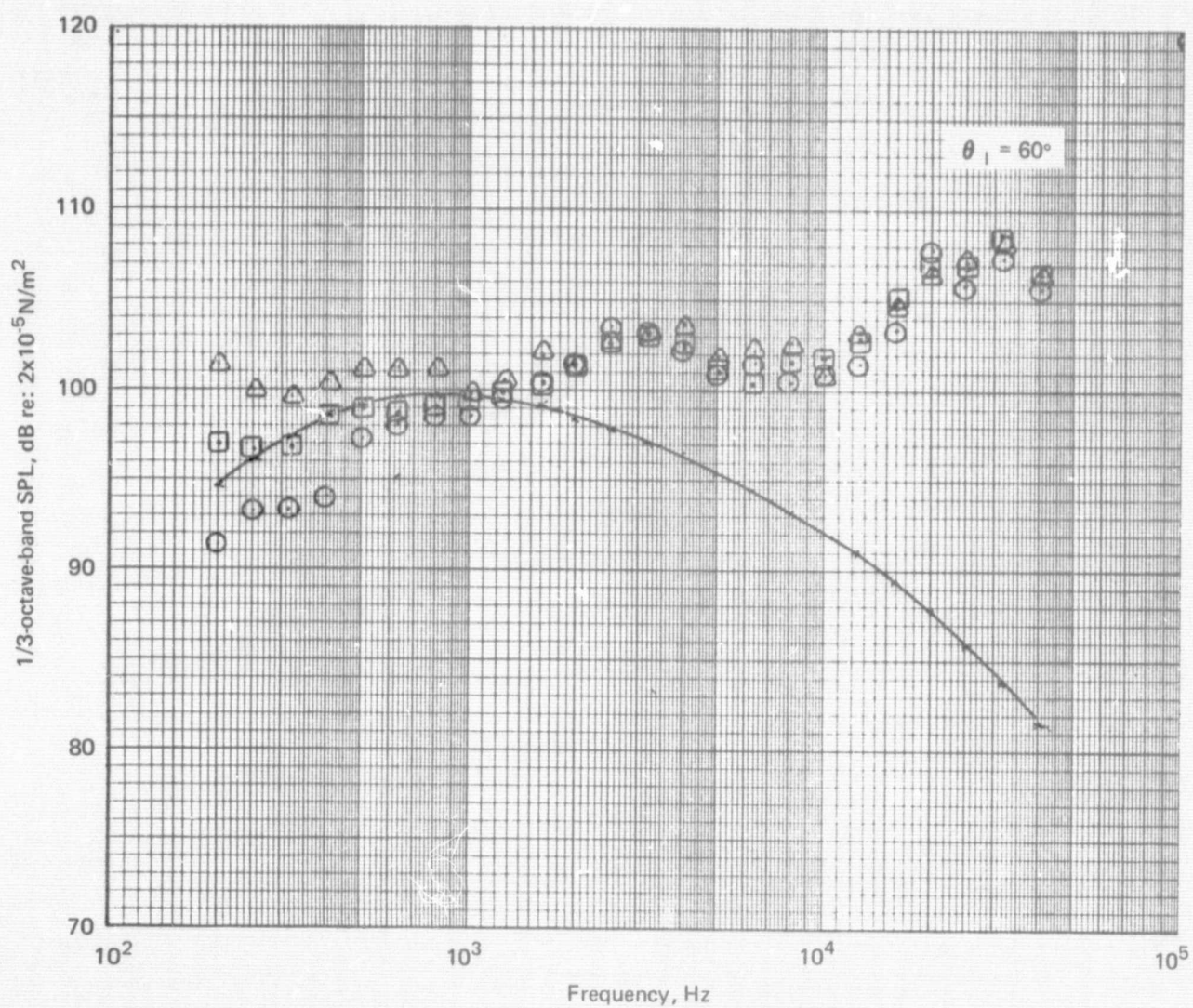


Figure 90.—(Continued)

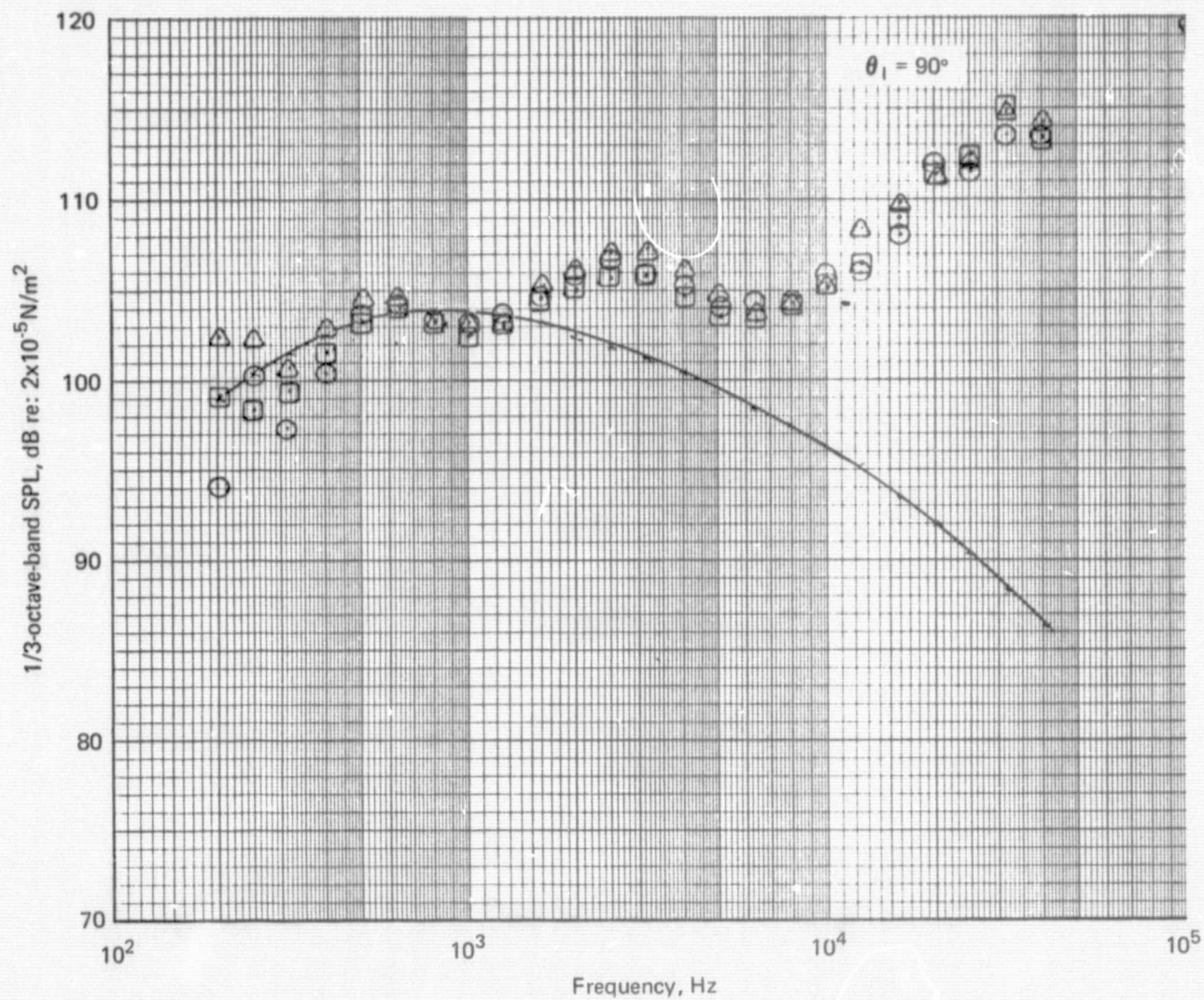


Figure 90.—(Continued)

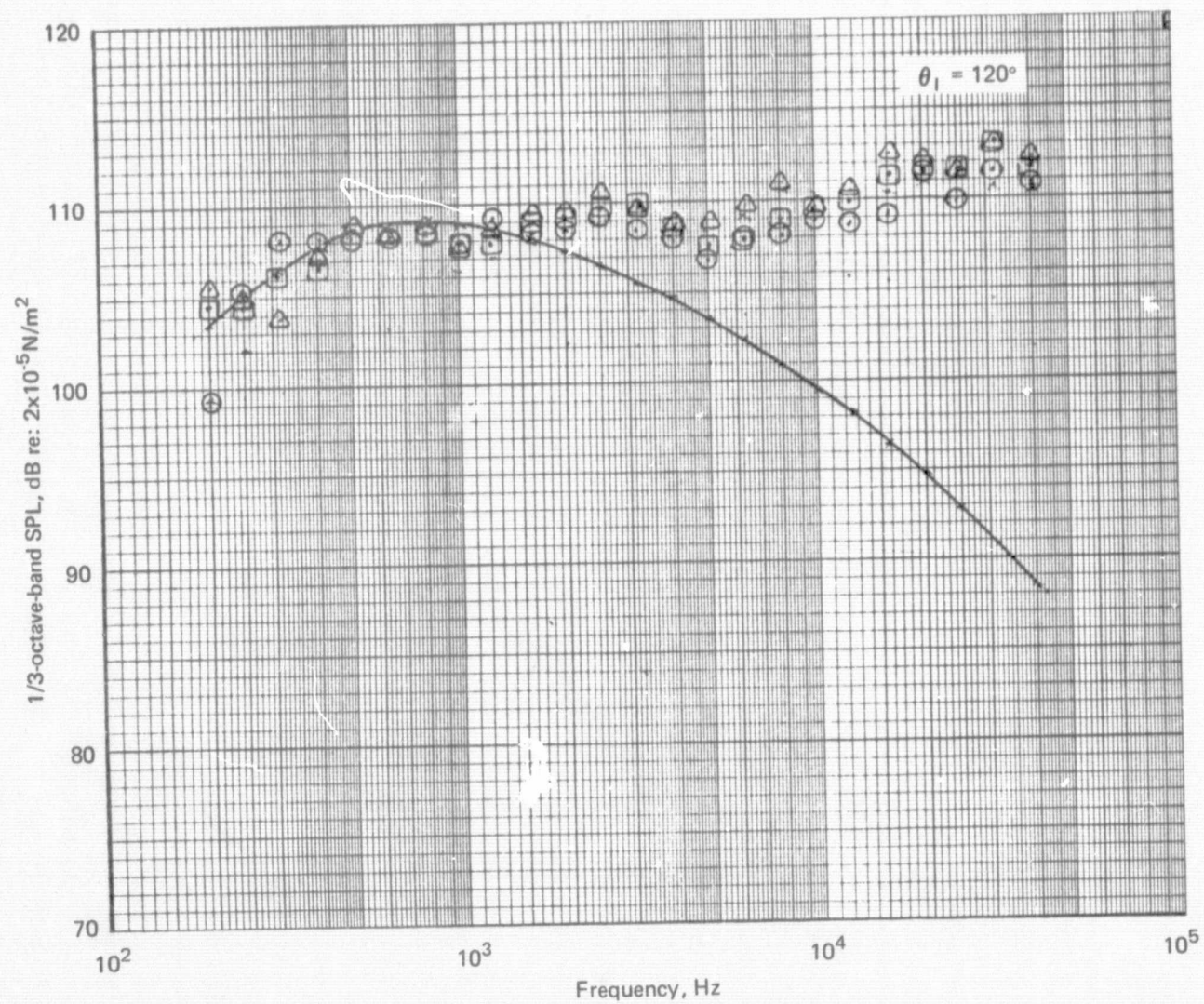


Figure 90.—(Continued)

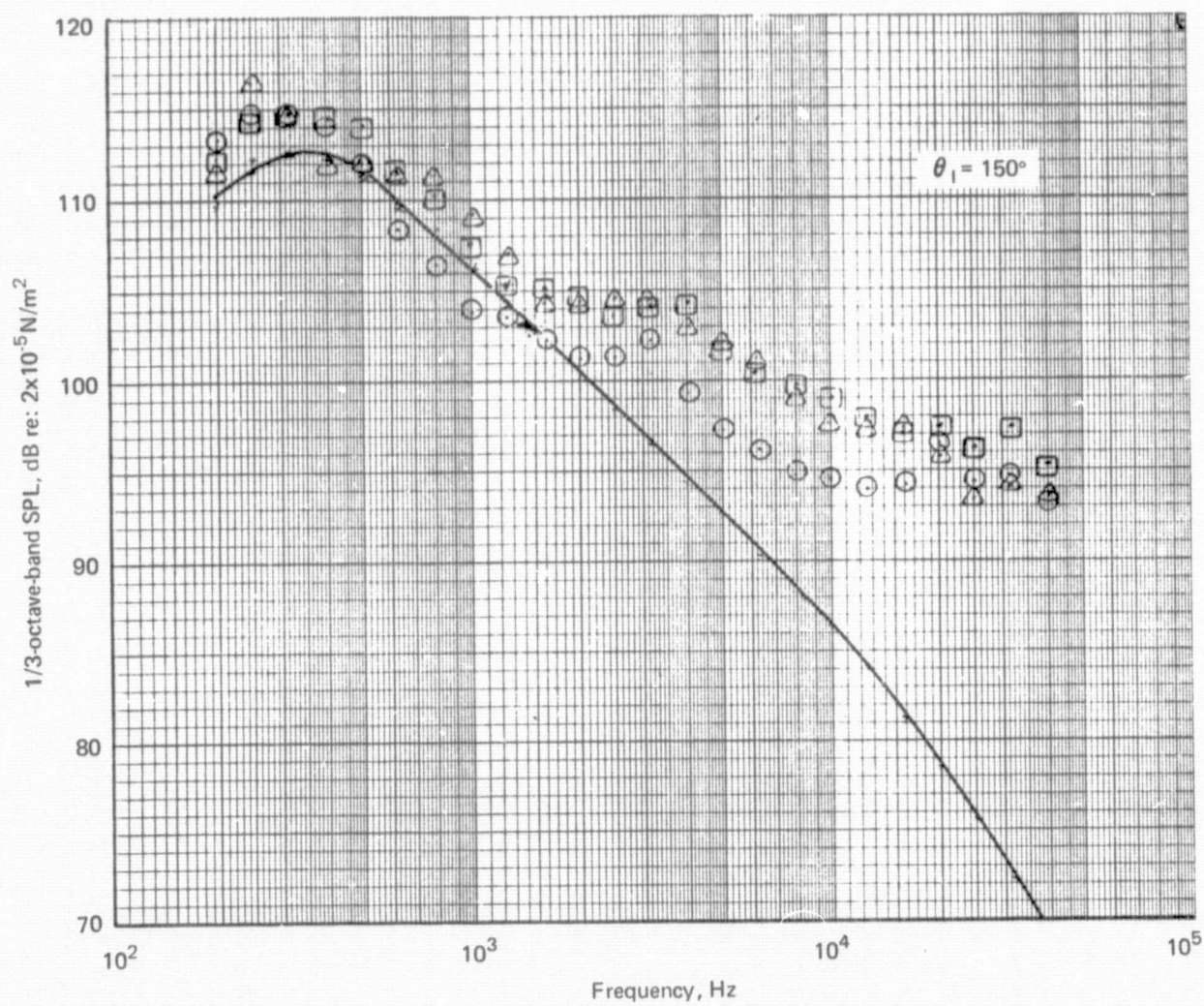


Figure 90.—(Concluded)

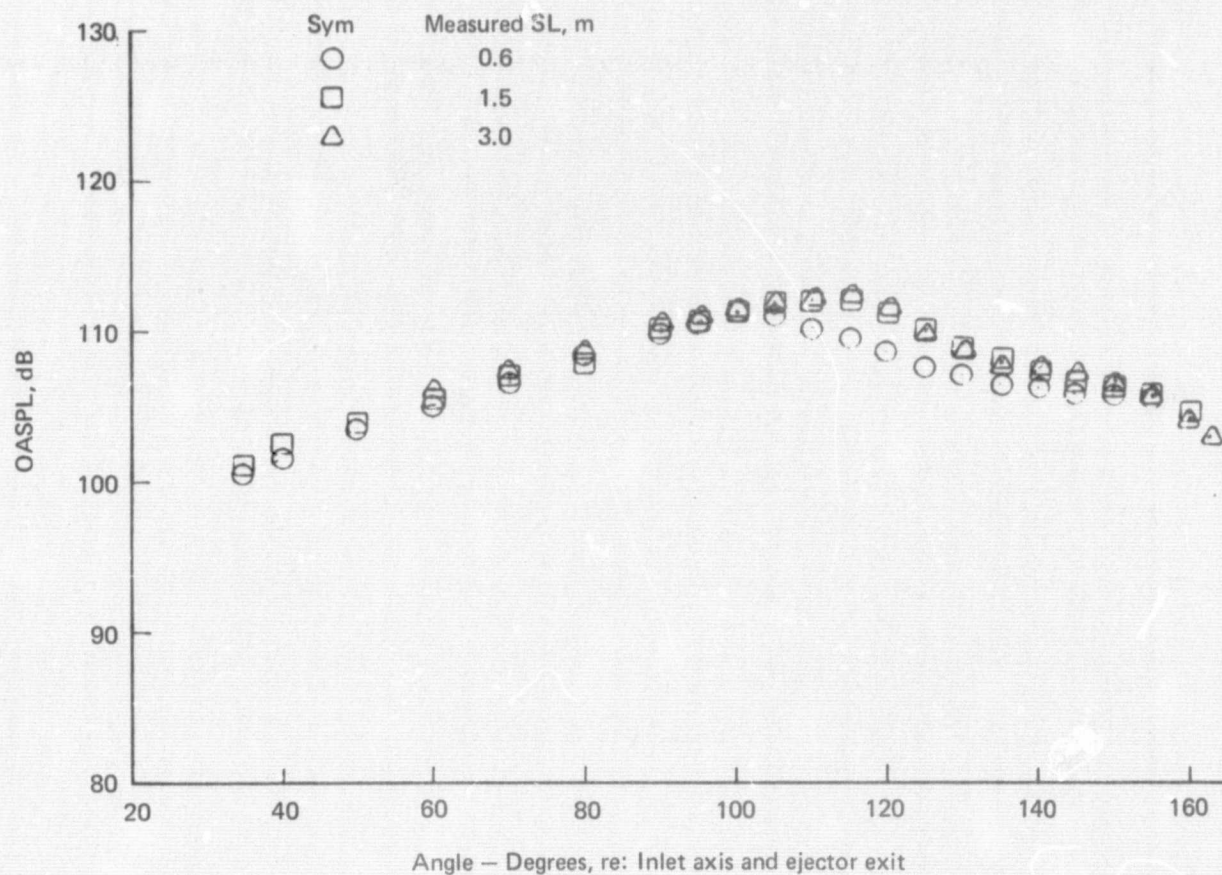


Figure 91.— OASPL Directivity and Jet Noise Spectra for the 57-Tube Nozzle with Lined Ejector Extrapolated to a 3.0 m Sideline NPR = 2.60, $V_A = 68.6$ m/s

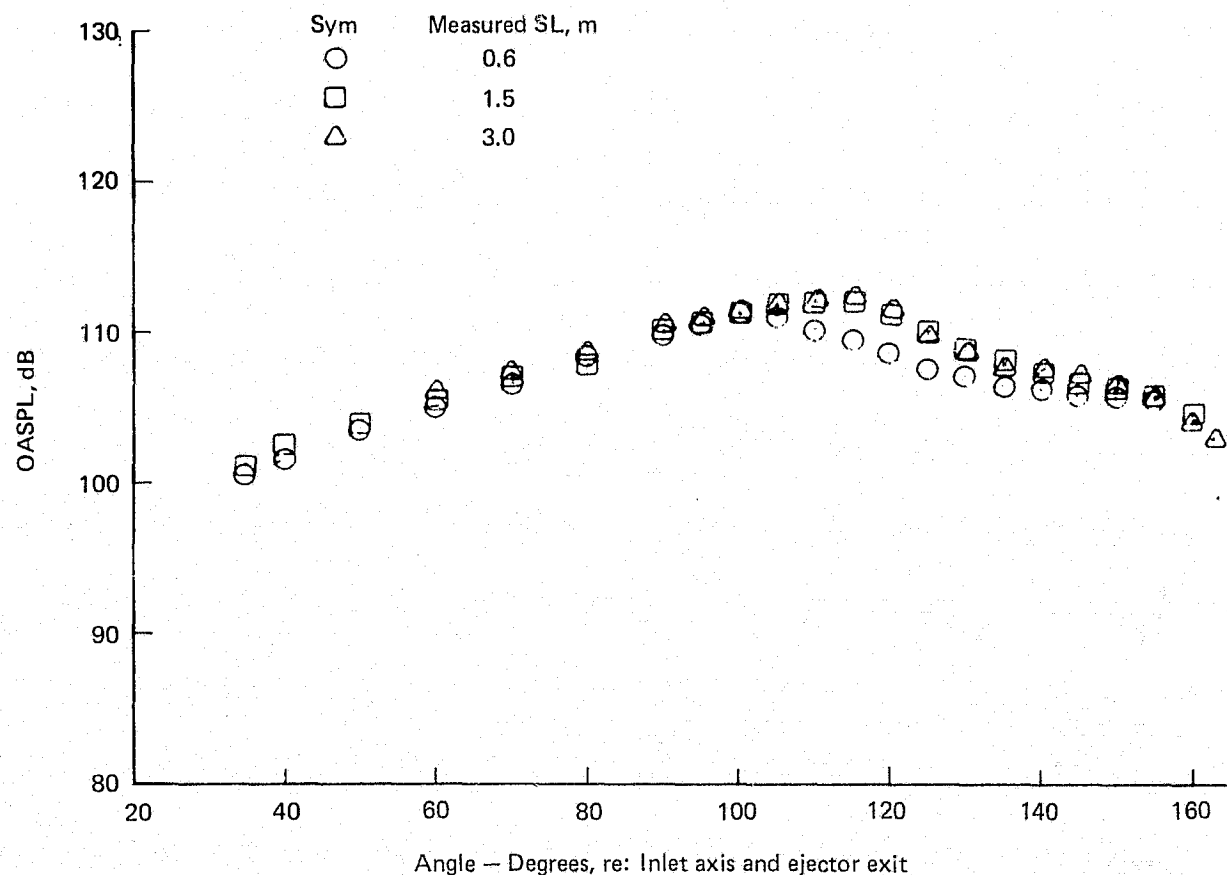


Figure 91.— OASPL Directivity and Jet Noise Spectra for the 57-Tube Nozzle with Lined Ejector Extrapolated to a 3.0 m Sideline NPR = 2.60, $V_A = 68.6$ m/s

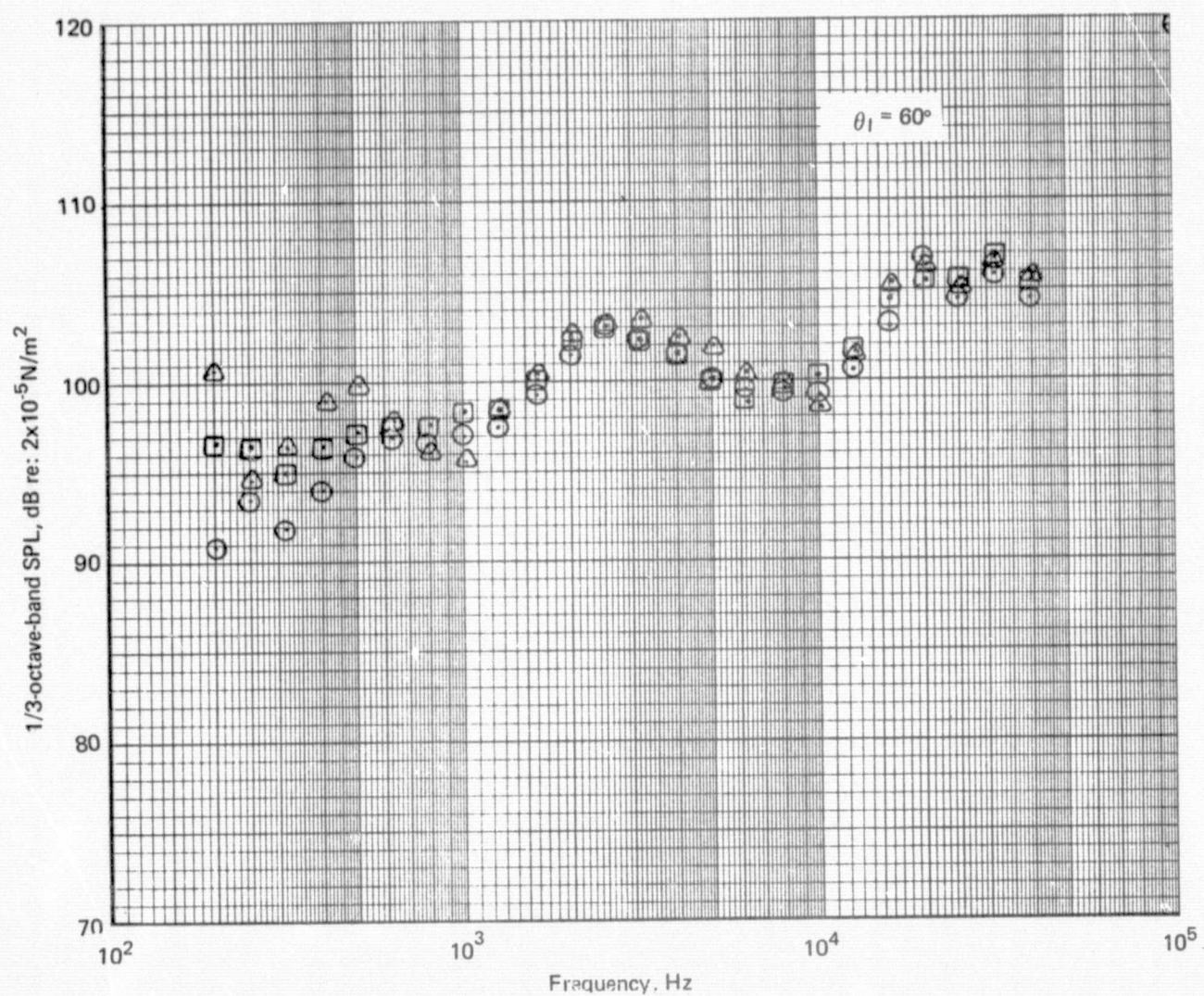


Figure 90.—(Continued)

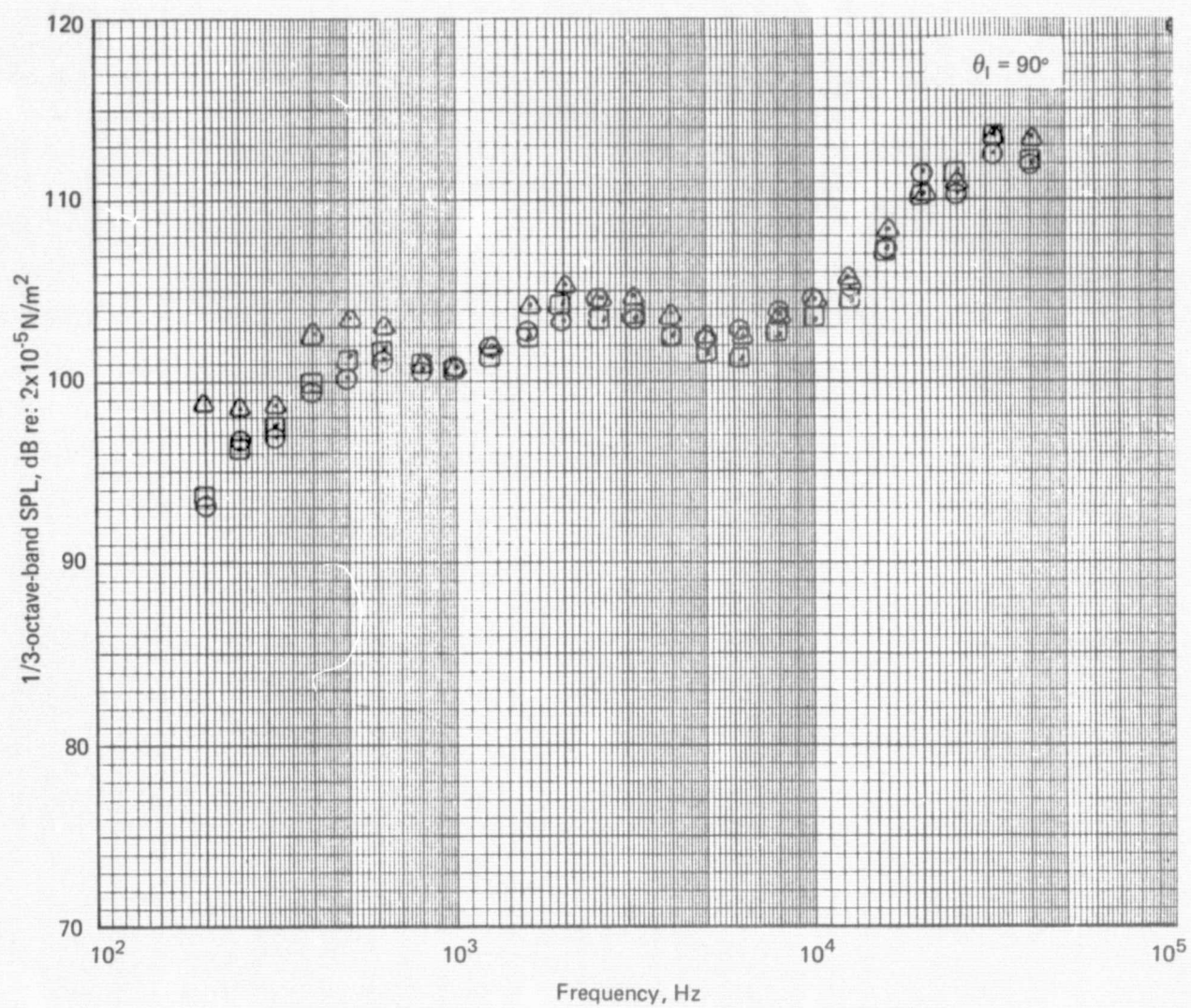


Figure 91.—(Continued)

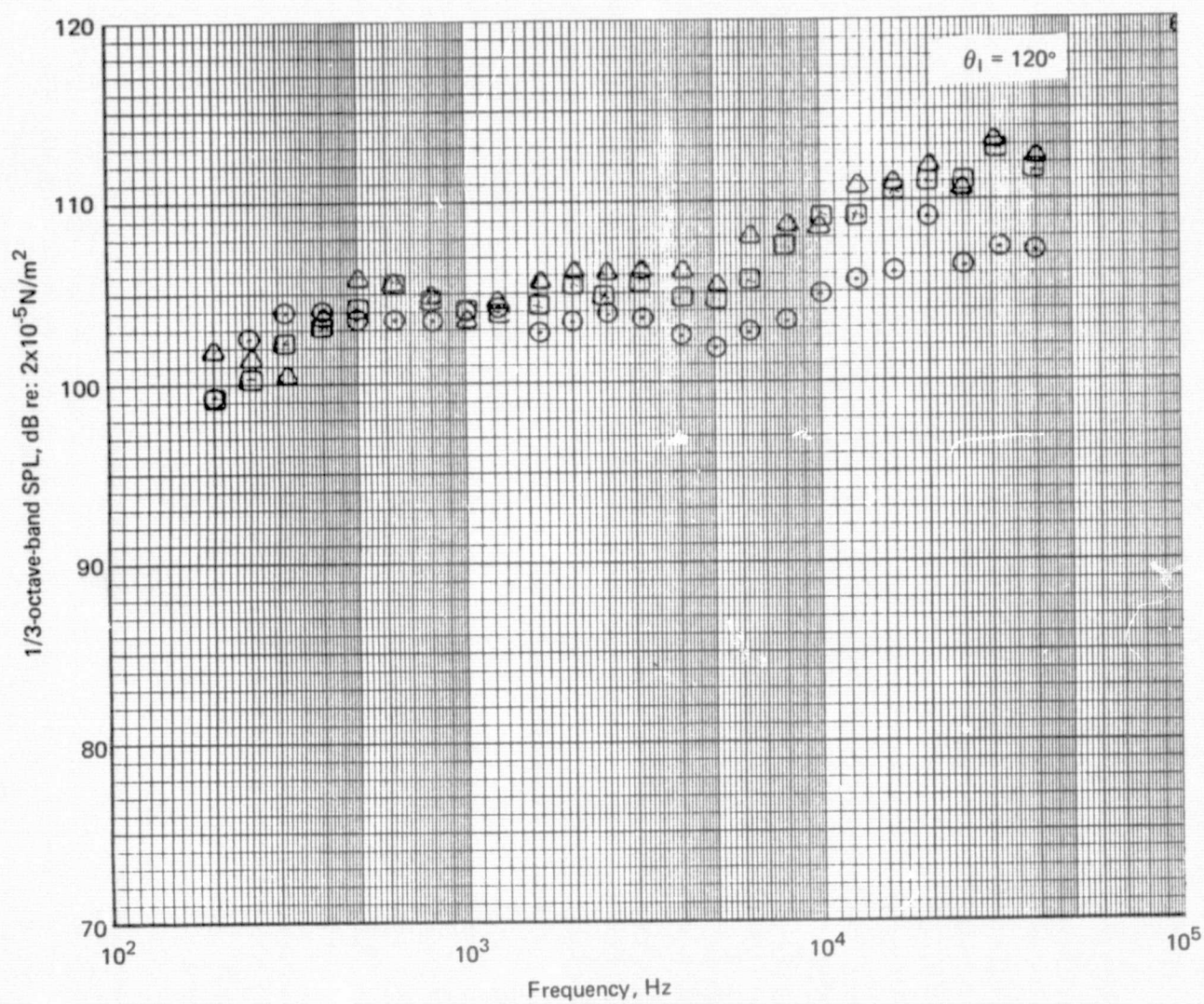


Figure 91.--(Continued)

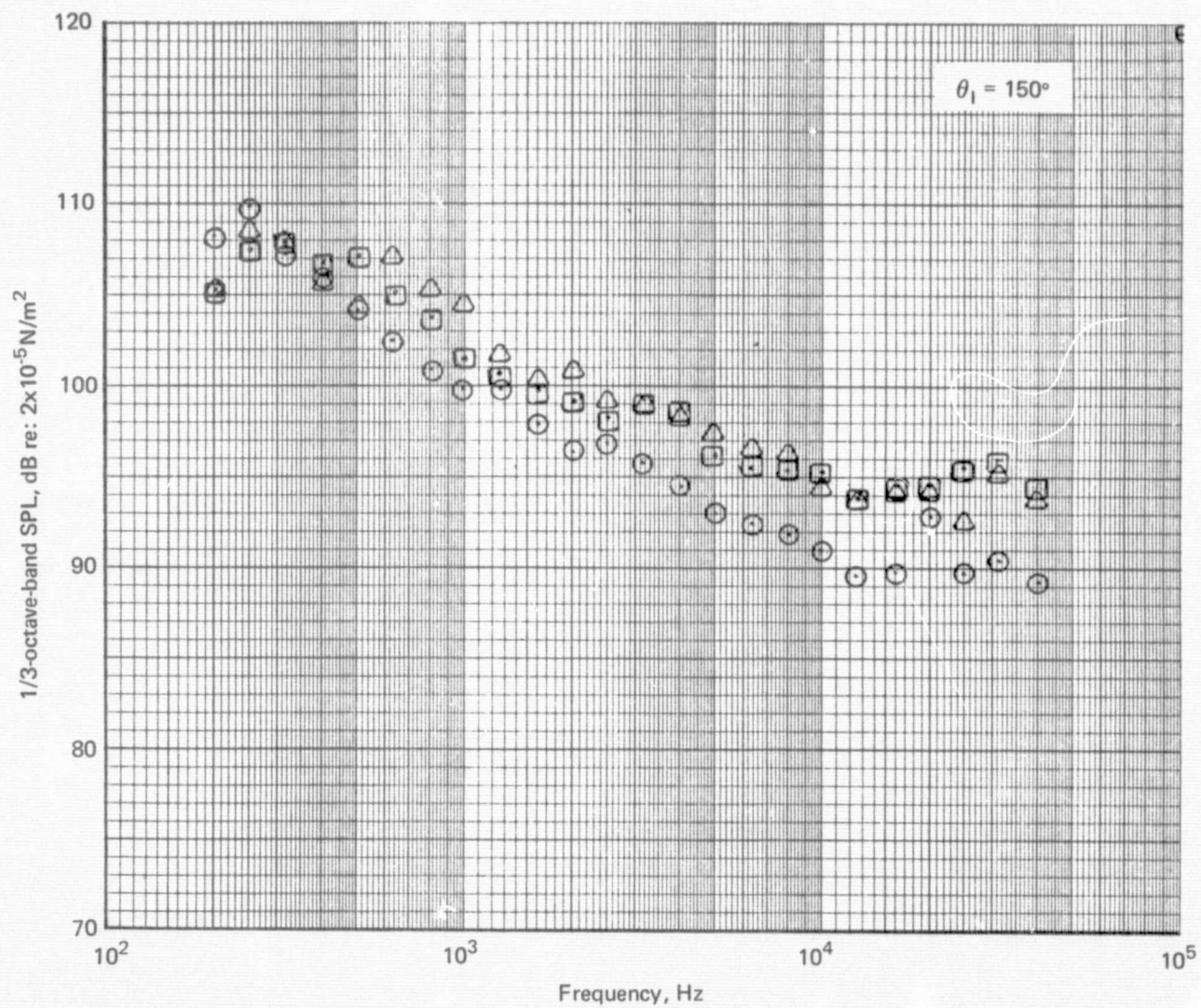


Figure 91.—(Concluded)

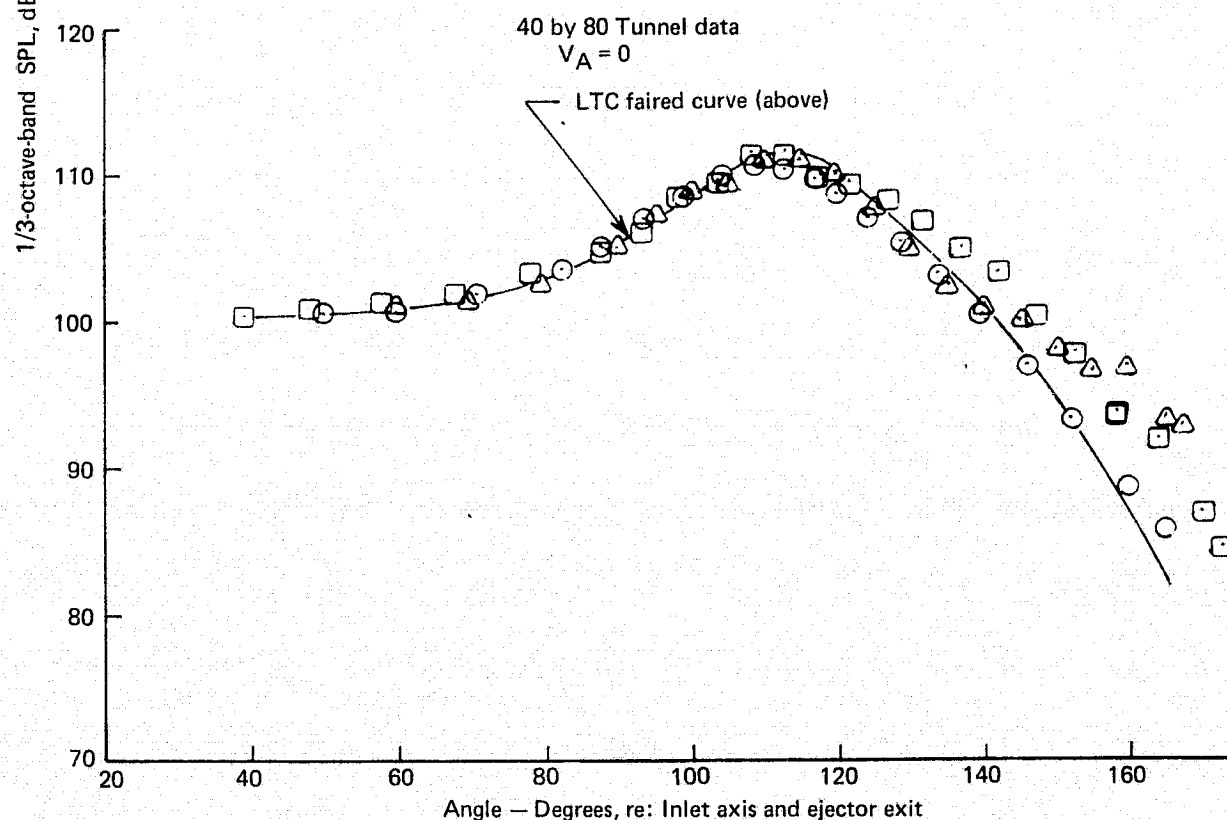
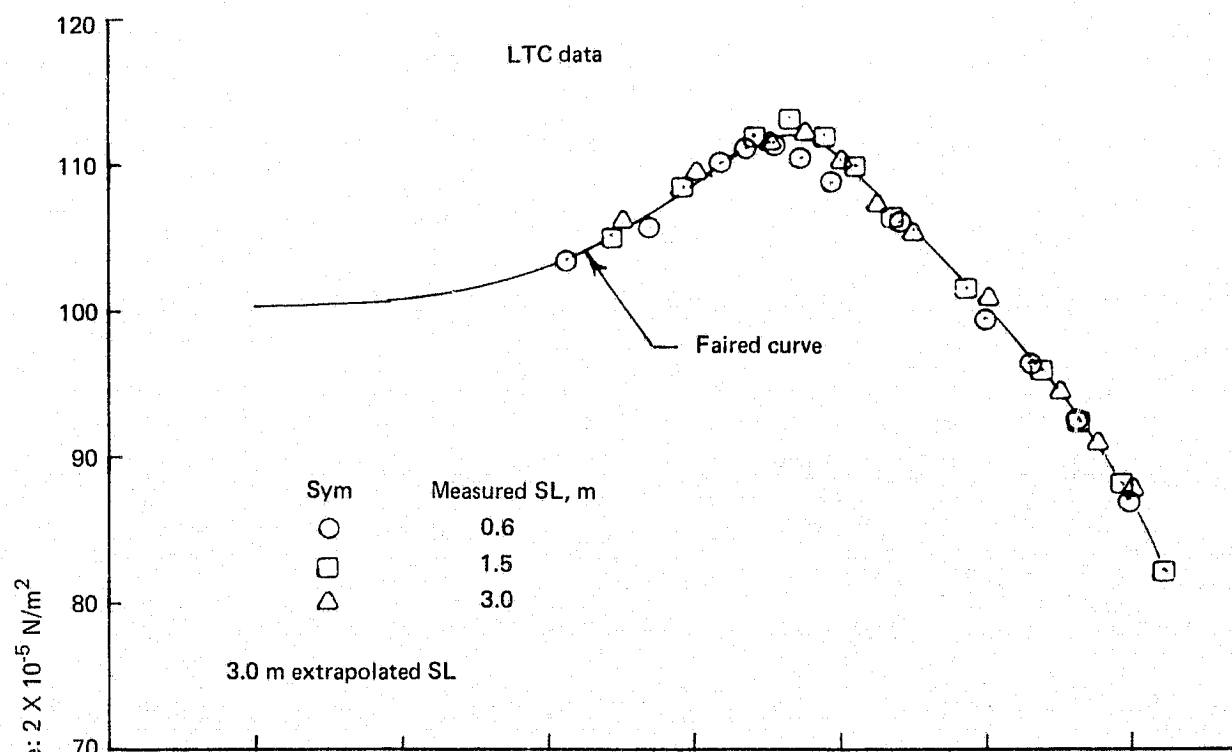


Figure 92.— 10 kHz 1/3-OBSPL Directivity Comparisons for the 57-Tube Nozzle with Ejector

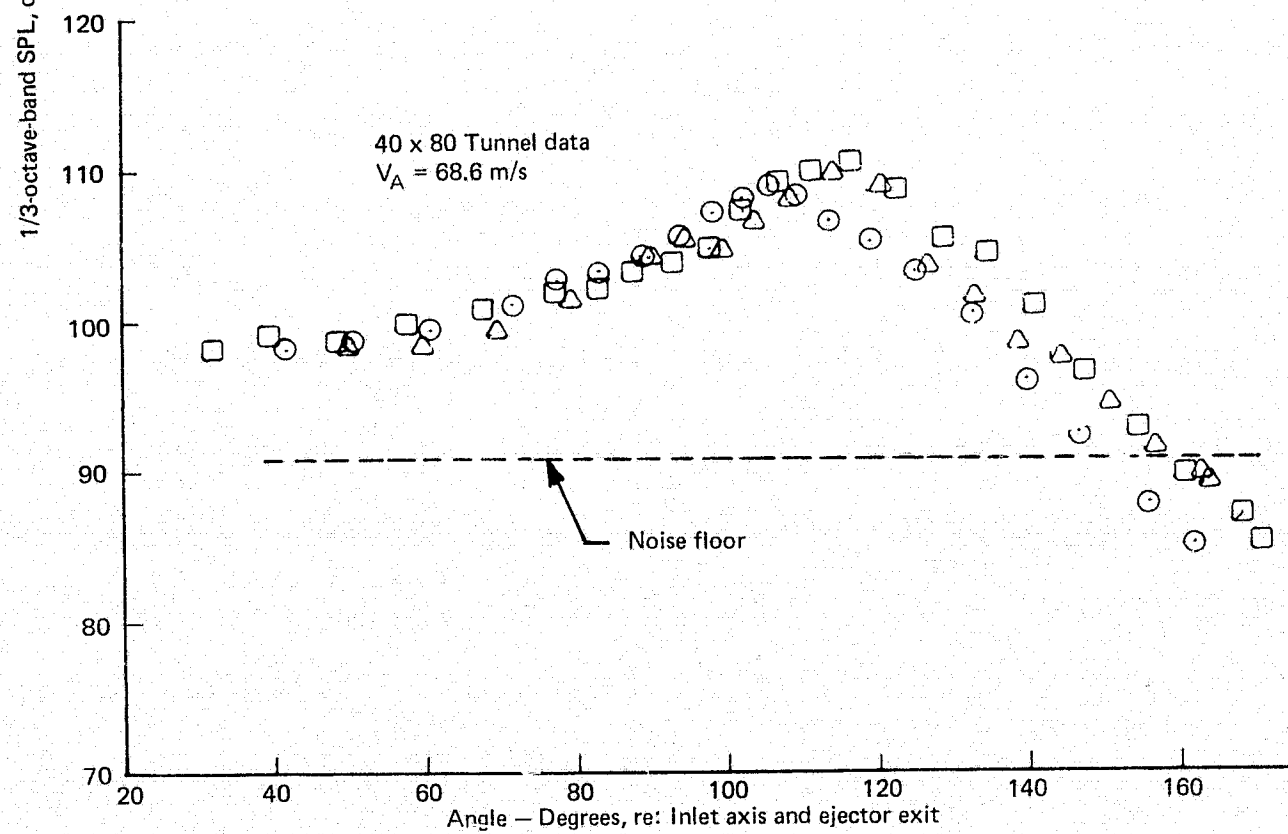
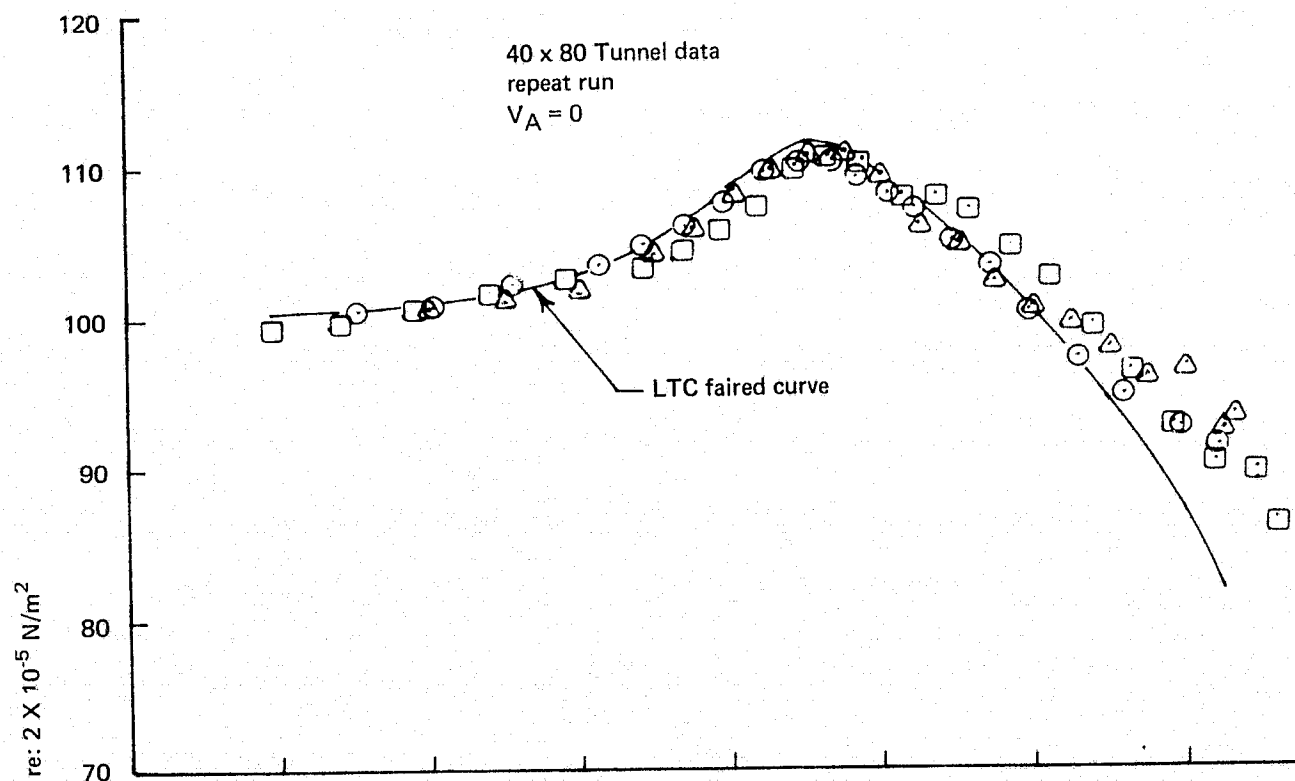


Figure 92.— (Concluded)

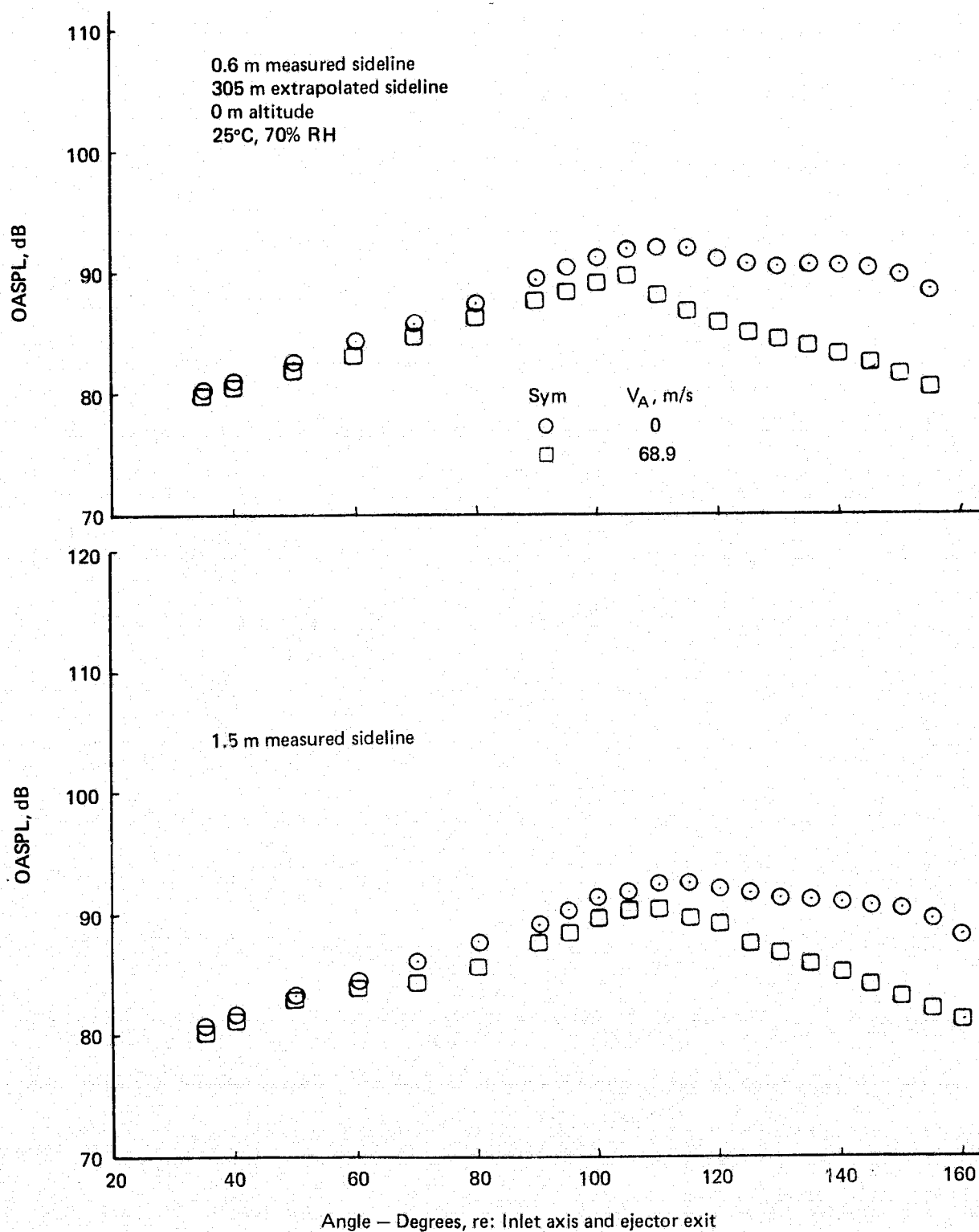


Figure 93.— Flight Effects on OASPL of a 57-Tube Nozzle with Ejector
NPR = 2.25 $V_j = 594$ m/s

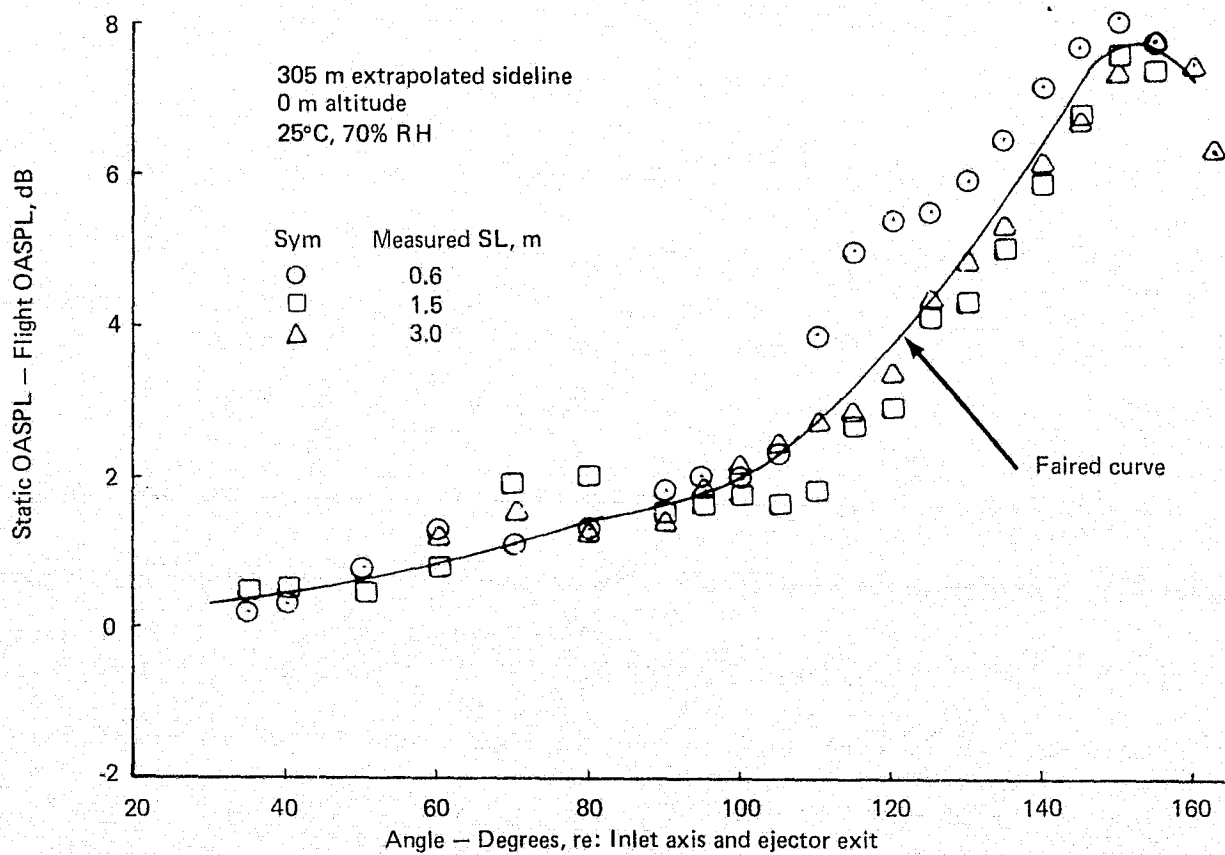
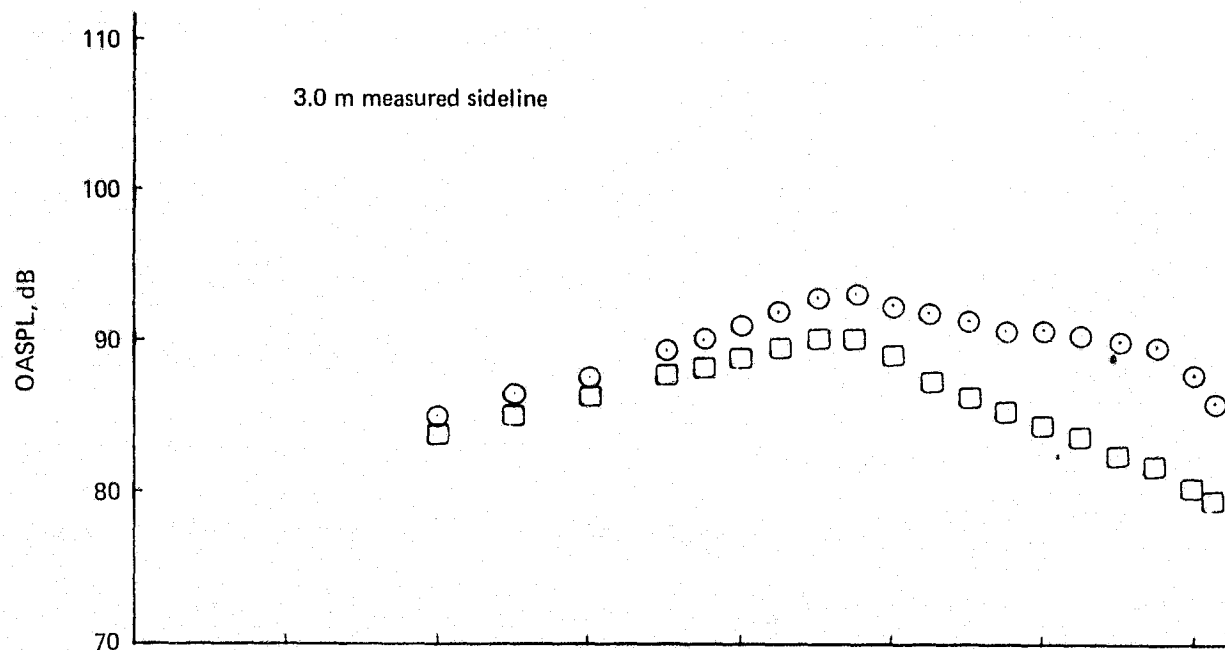
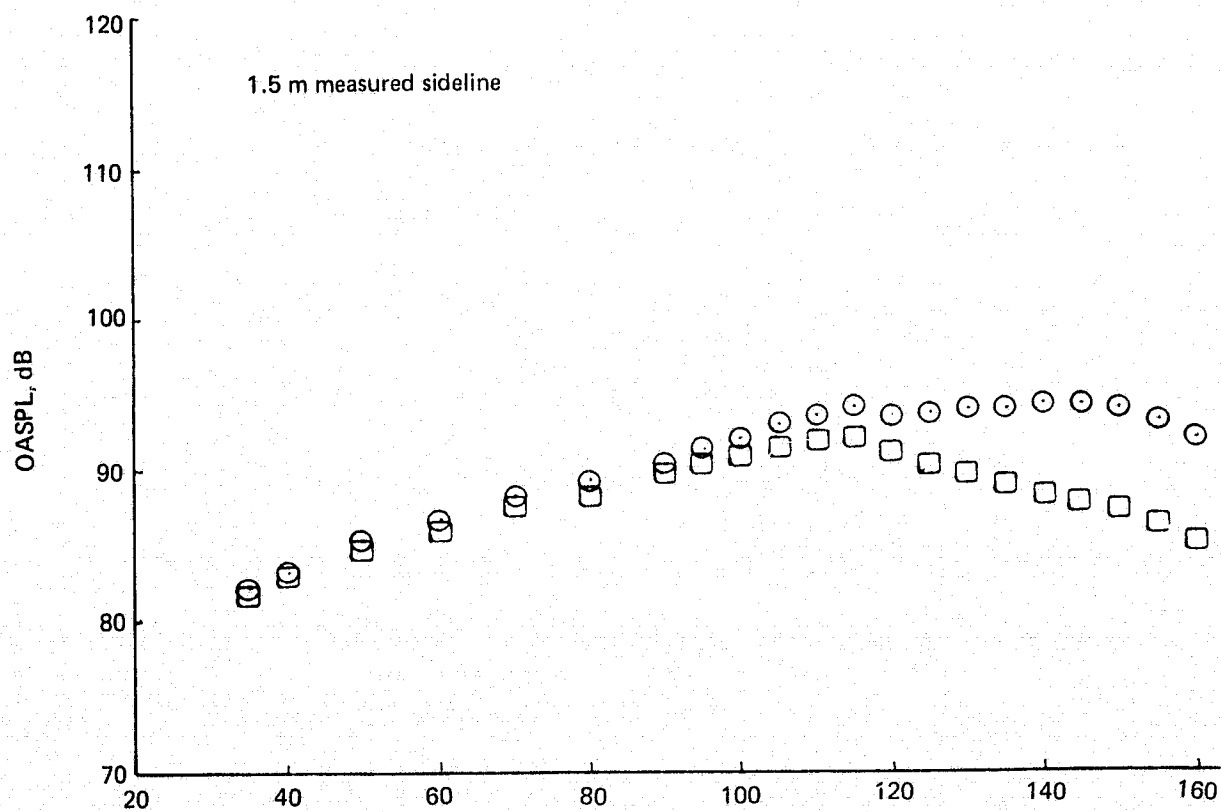
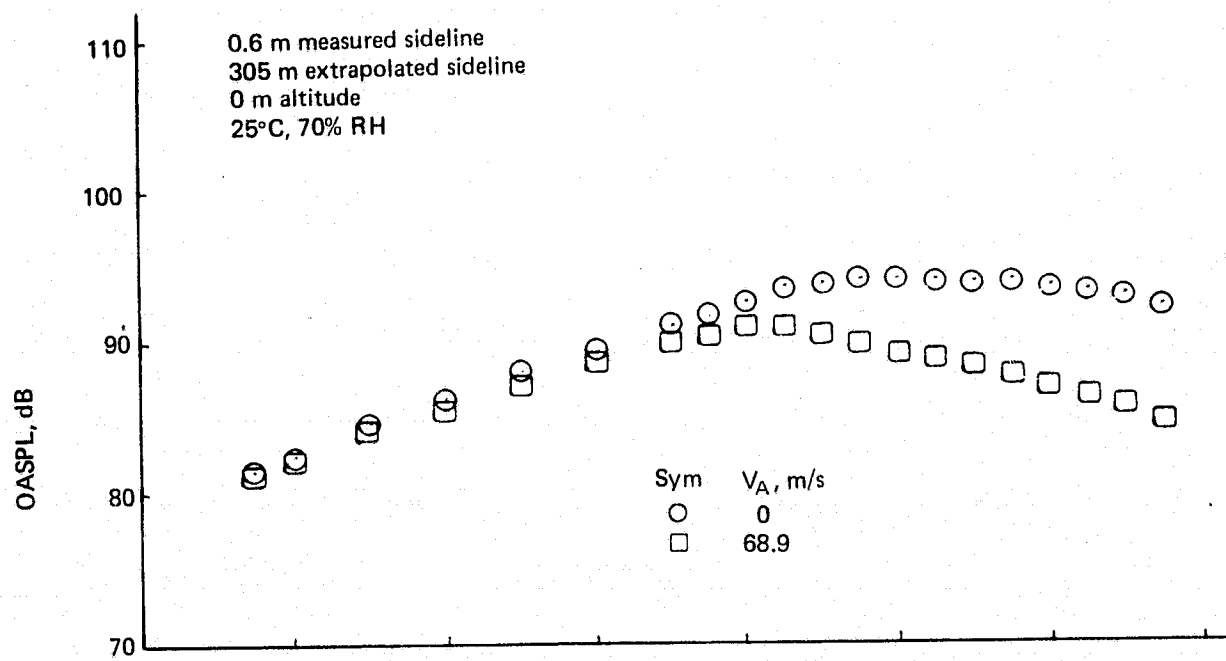


Figure 93.— (Concluded)



Angle — Degrees, re: Inlet axis and ejector exit

Figure 94.— Flight Effects on OASPL of a 57-Tube Nozzle with Ejector
 $NPR = 2.6$ $V_j = 640$ m/s

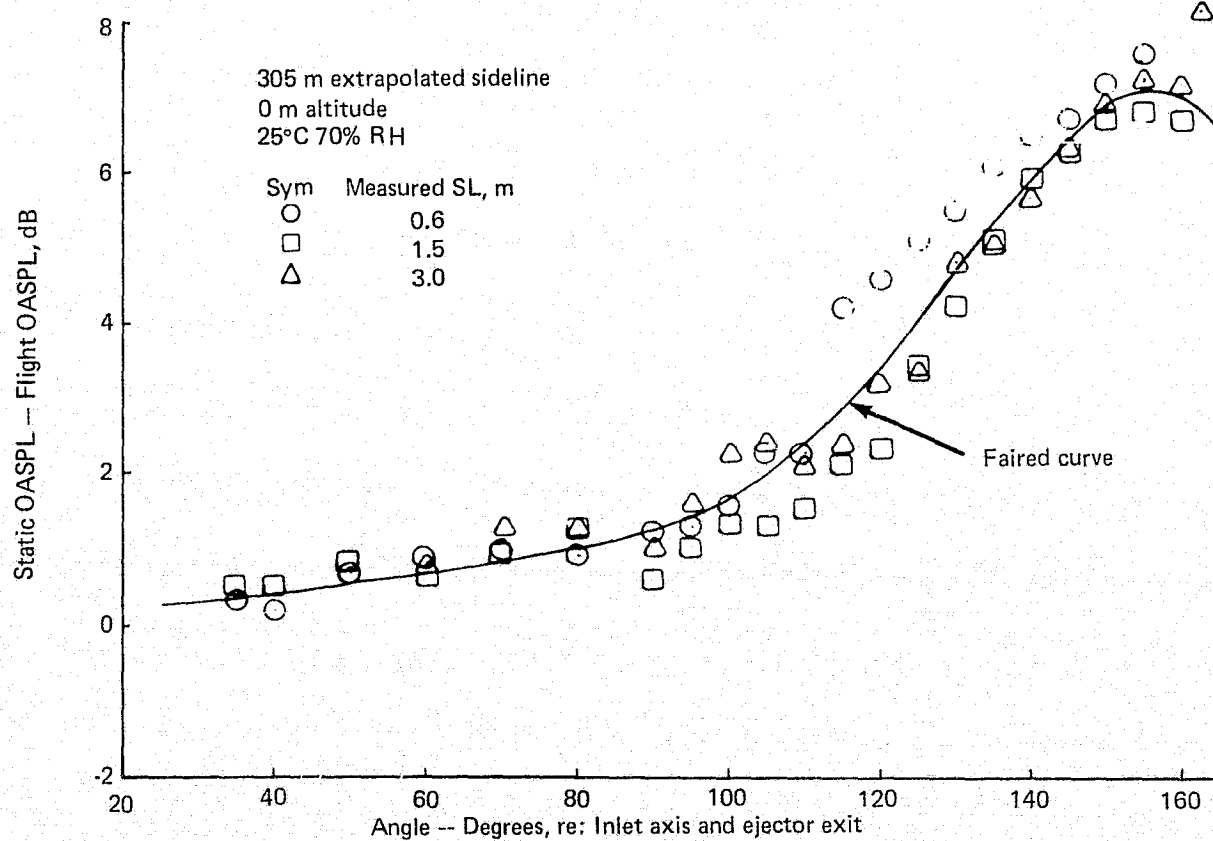
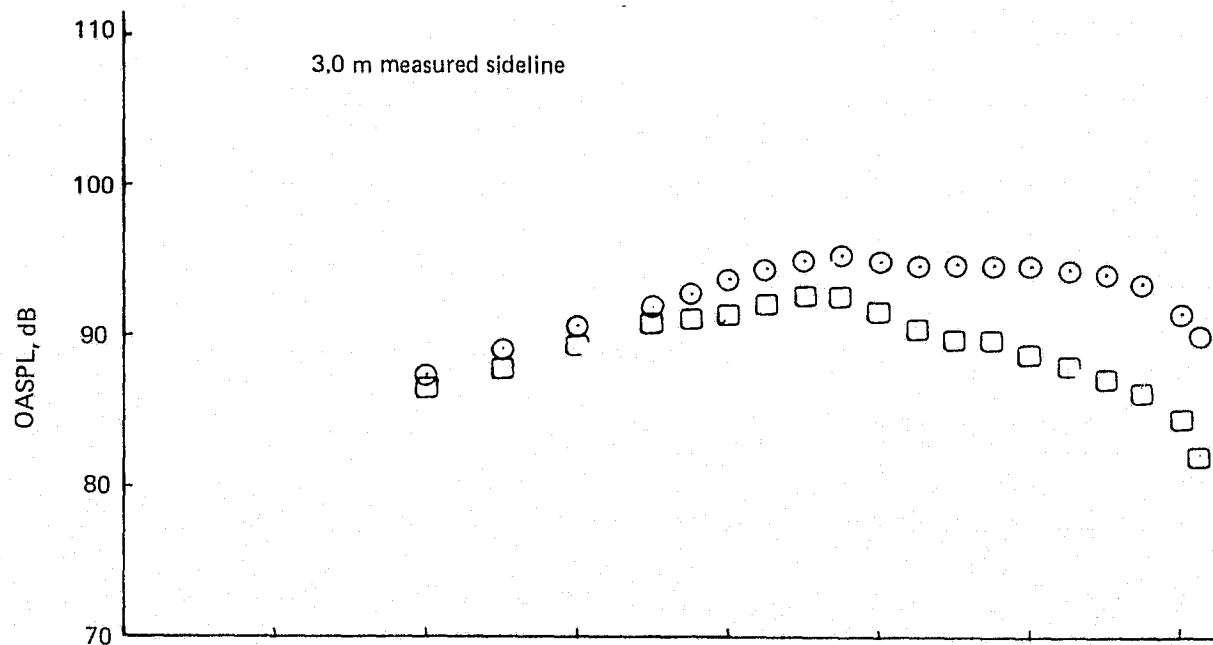


Figure 94.-- (Concluded)

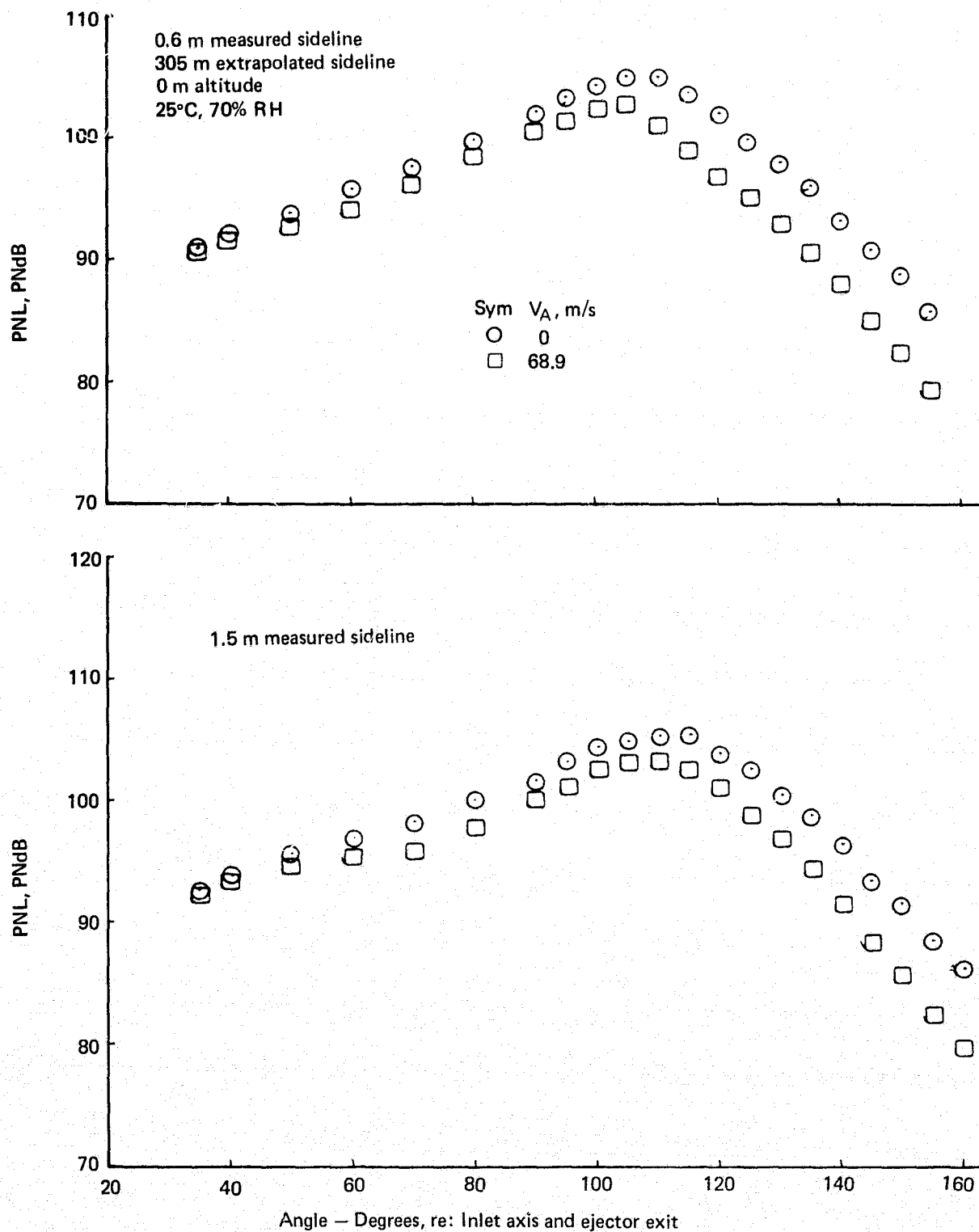


Figure 95.— Flight Effects on PNL of a 57-Tube Nozzle with Ejector
NPR = 2.25 V_j = 594 m/s

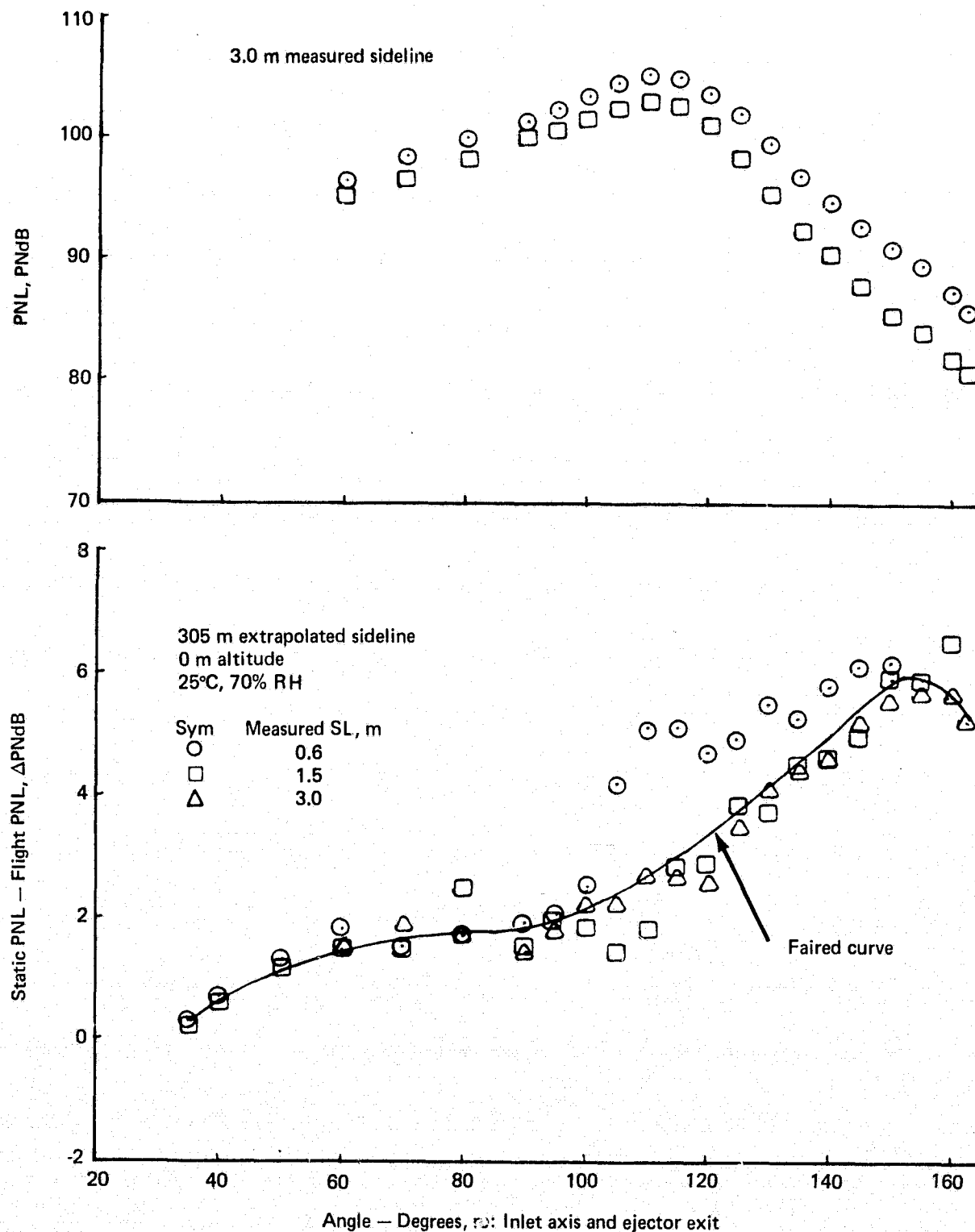


Figure 95.— (Concluded)

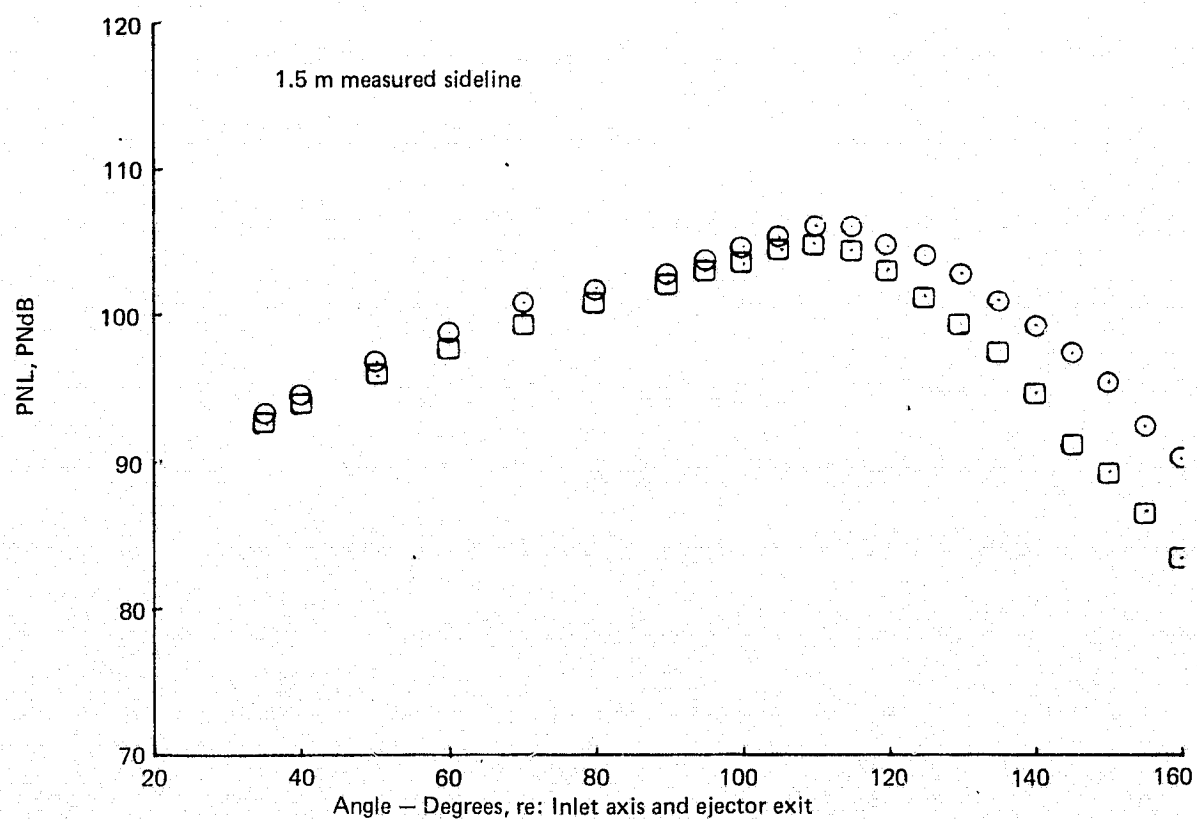
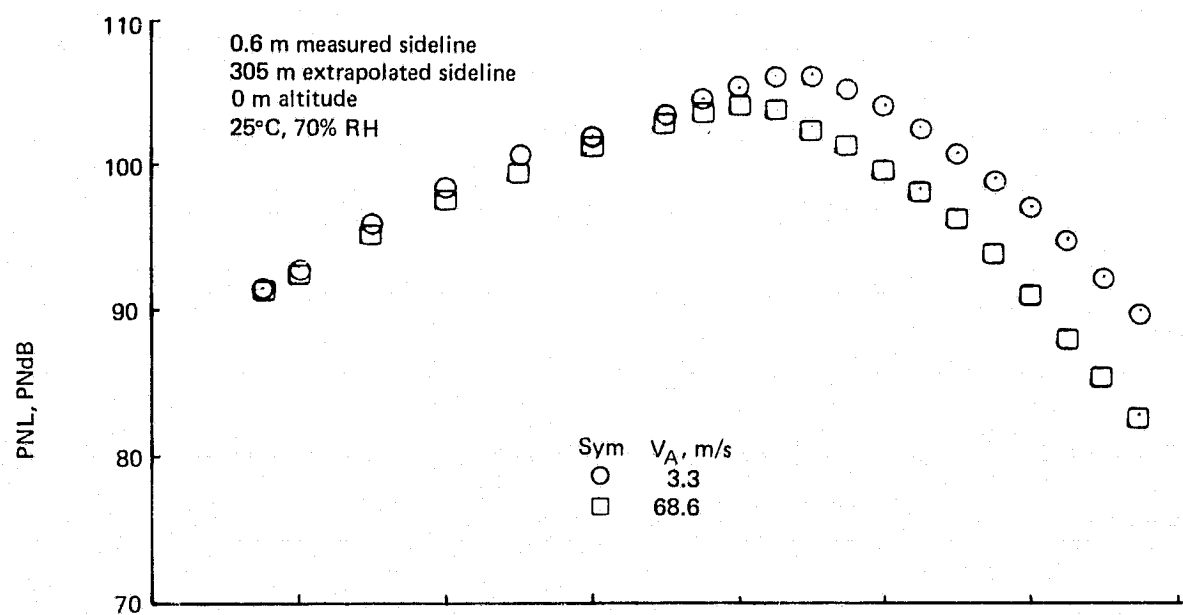


Figure 96.— Flight Effects on PNL of A 57-Tube Nozzle with Ejector
 $NPR = 2.6$ $V_j = 640$ m/s

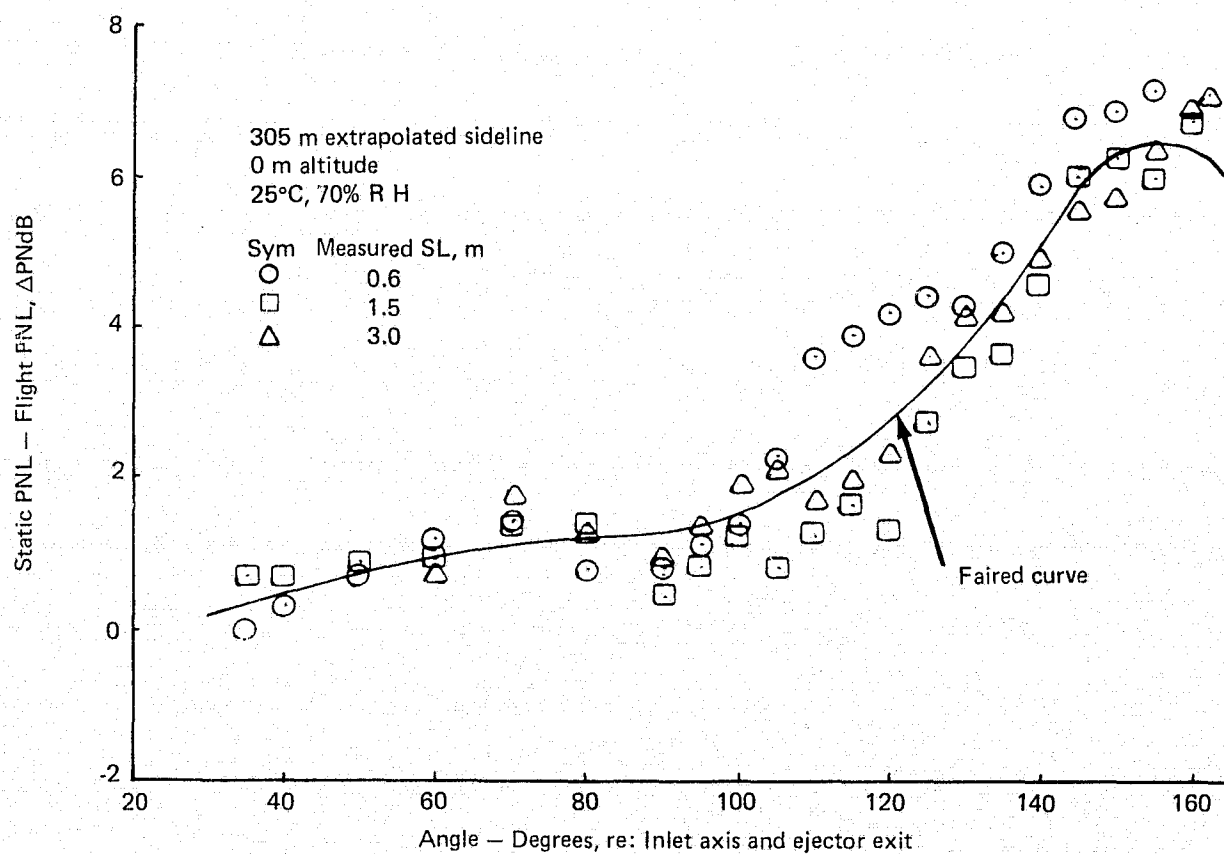
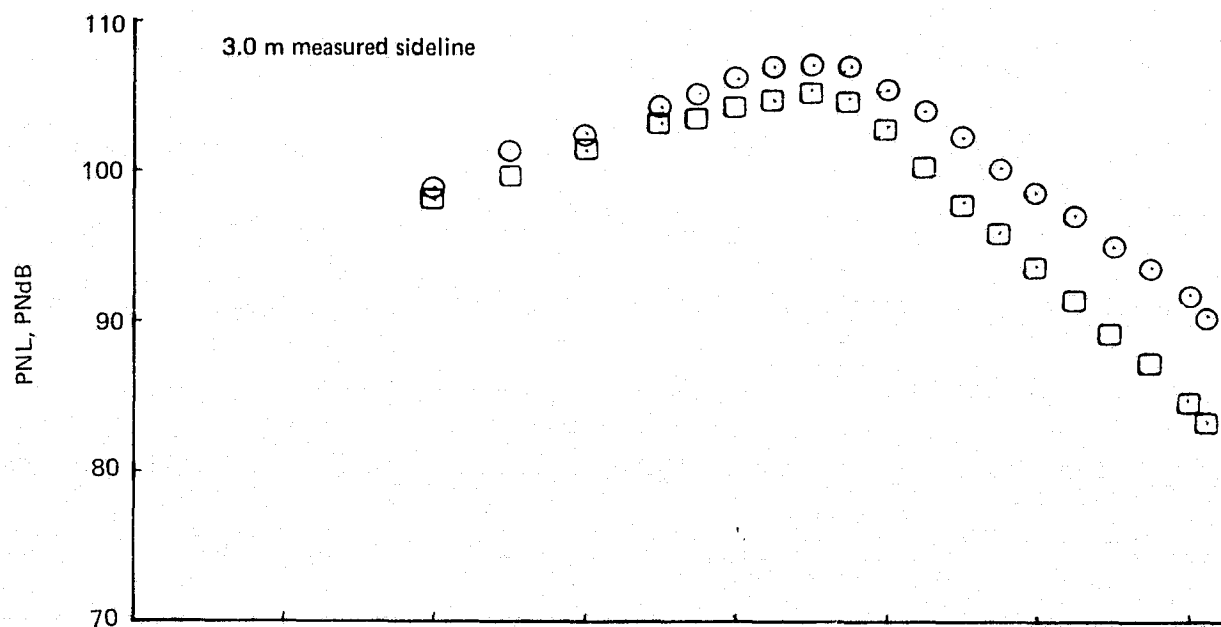


Figure 96.- (Concluded)

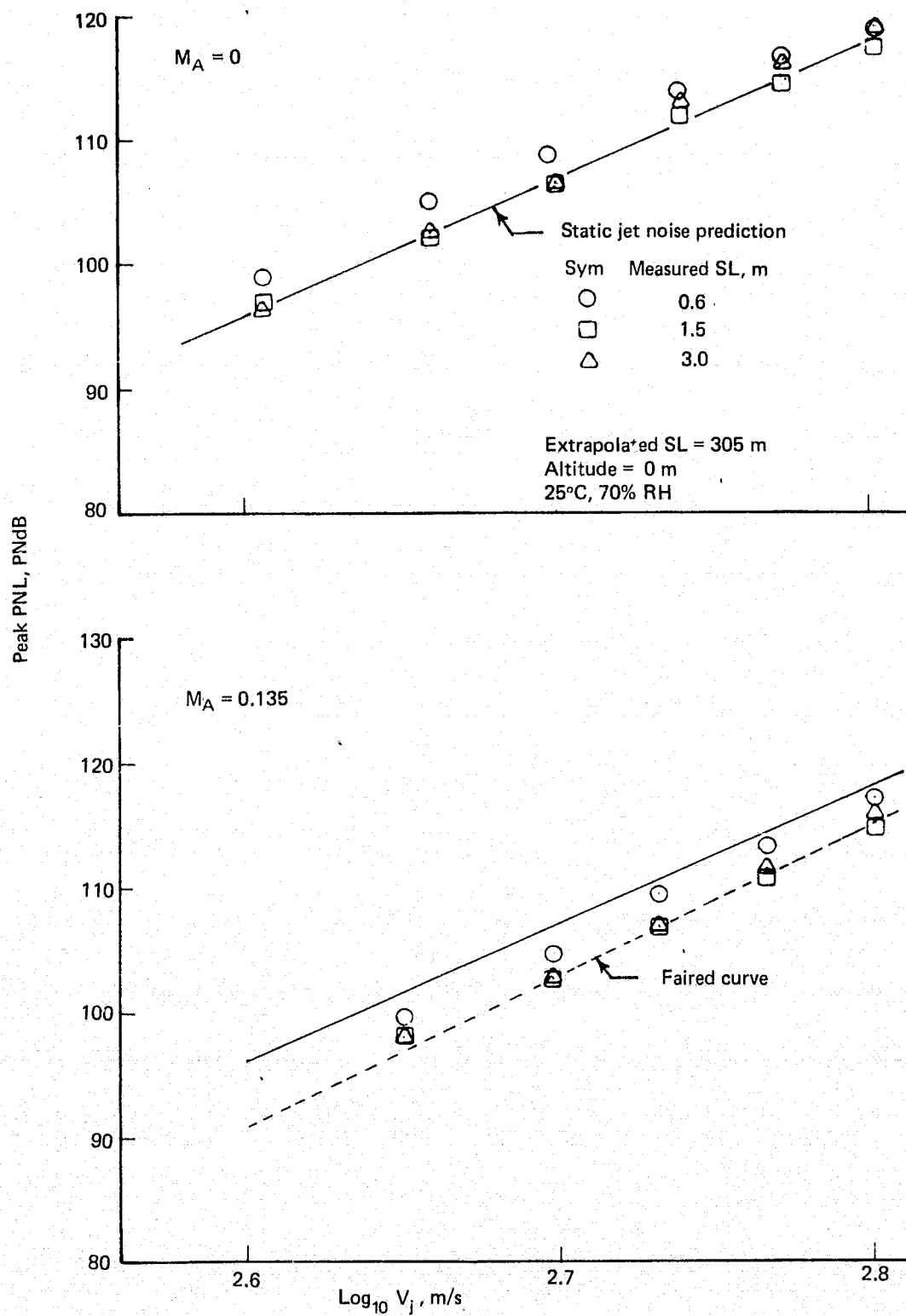


Figure 97.— Effect of Ambient Velocity on Peak PNL of an RC Nozzle

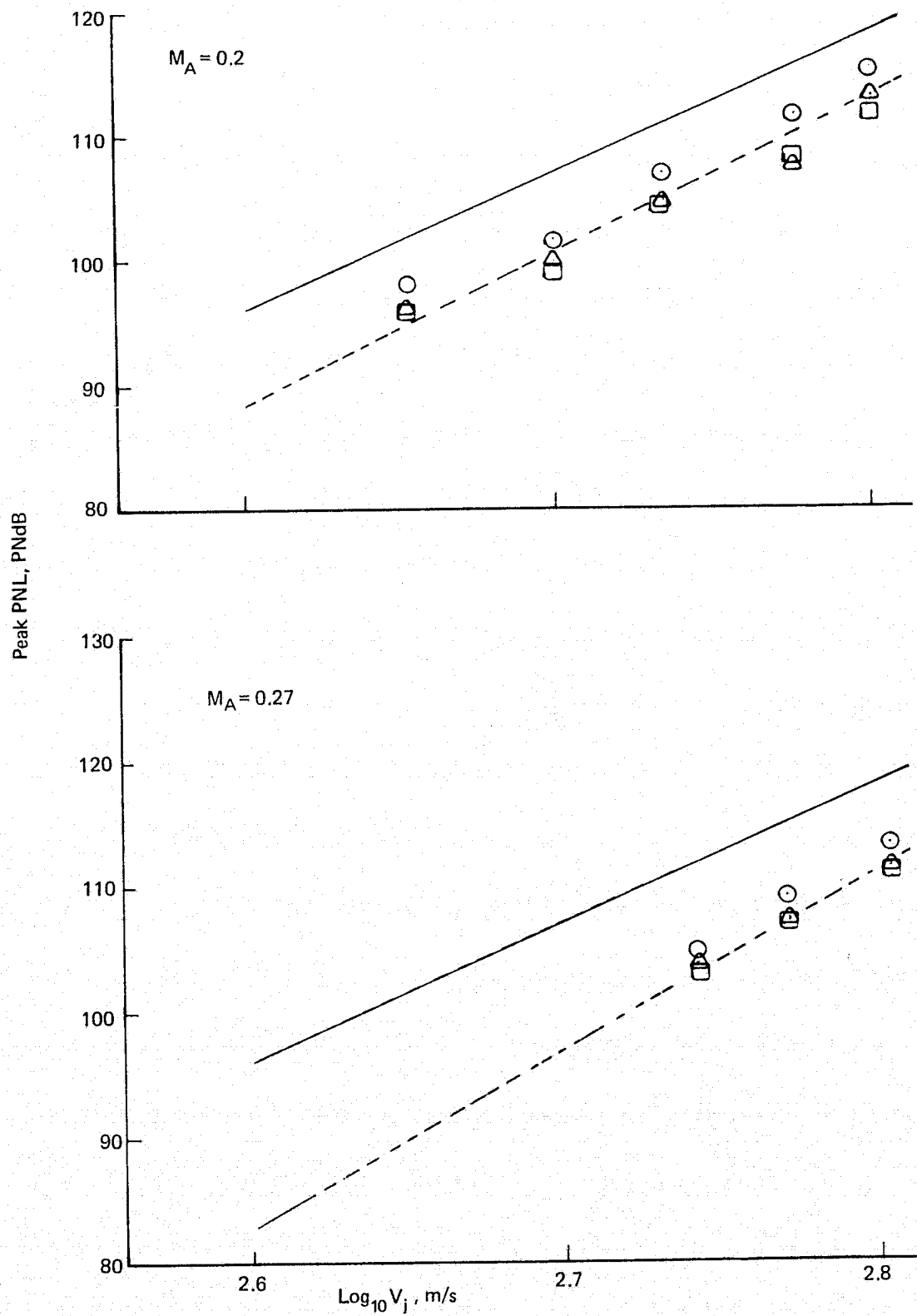


Figure 97.— (Concluded)

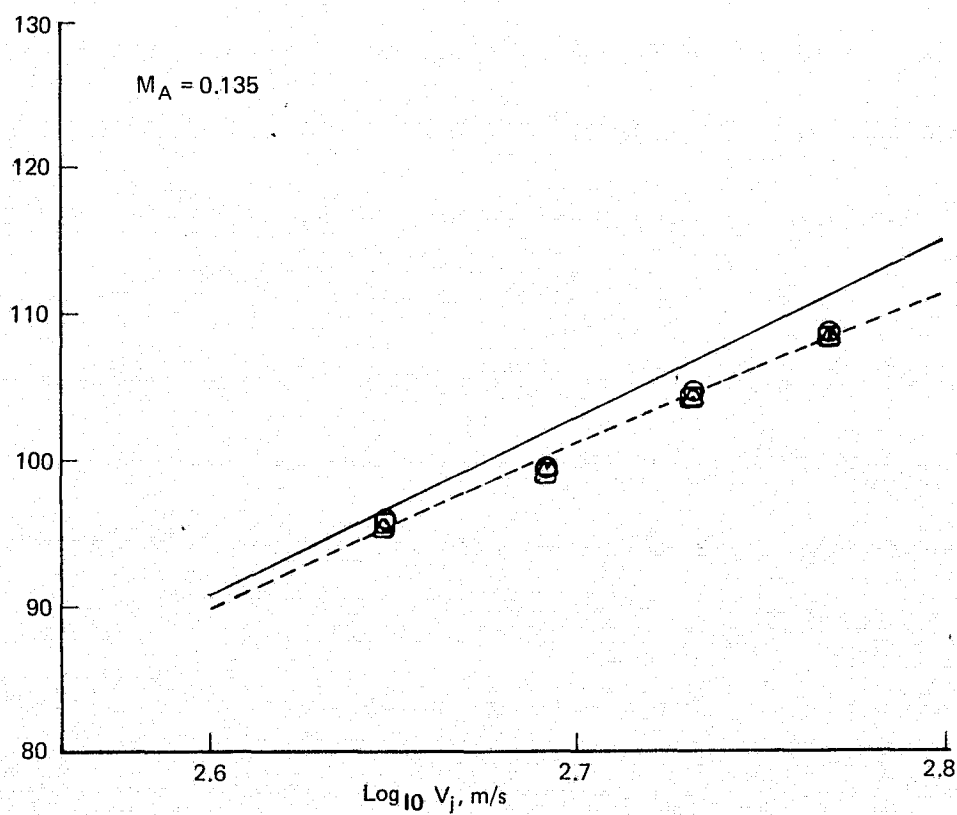
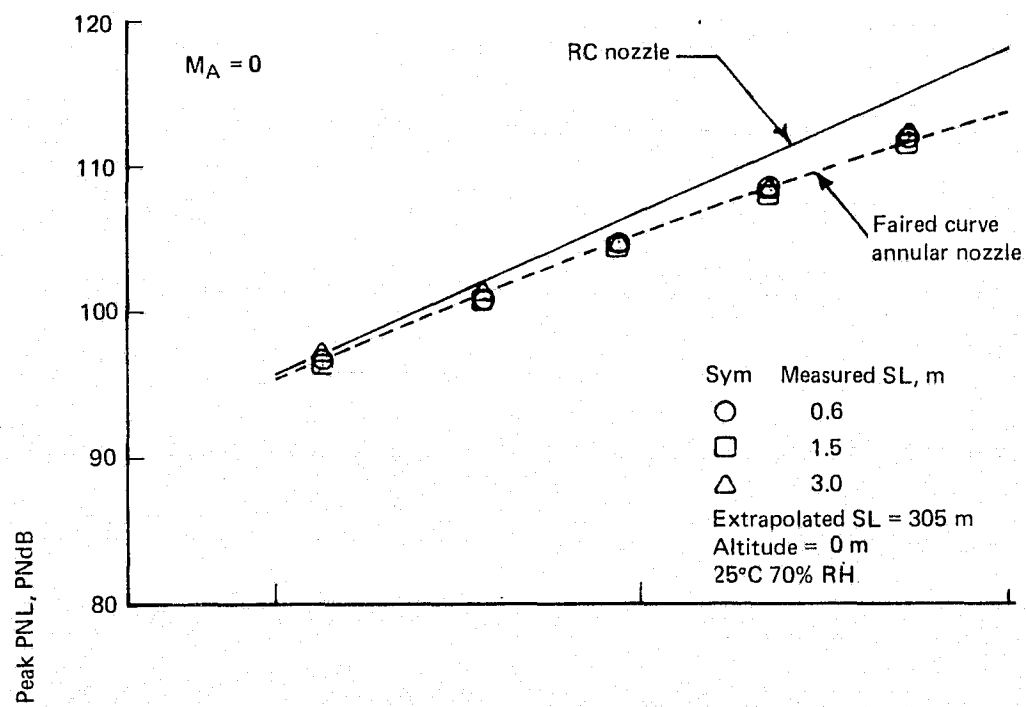


Figure 98.— Effect of Ambient Velocity on Peak PNL of an Annular Nozzle

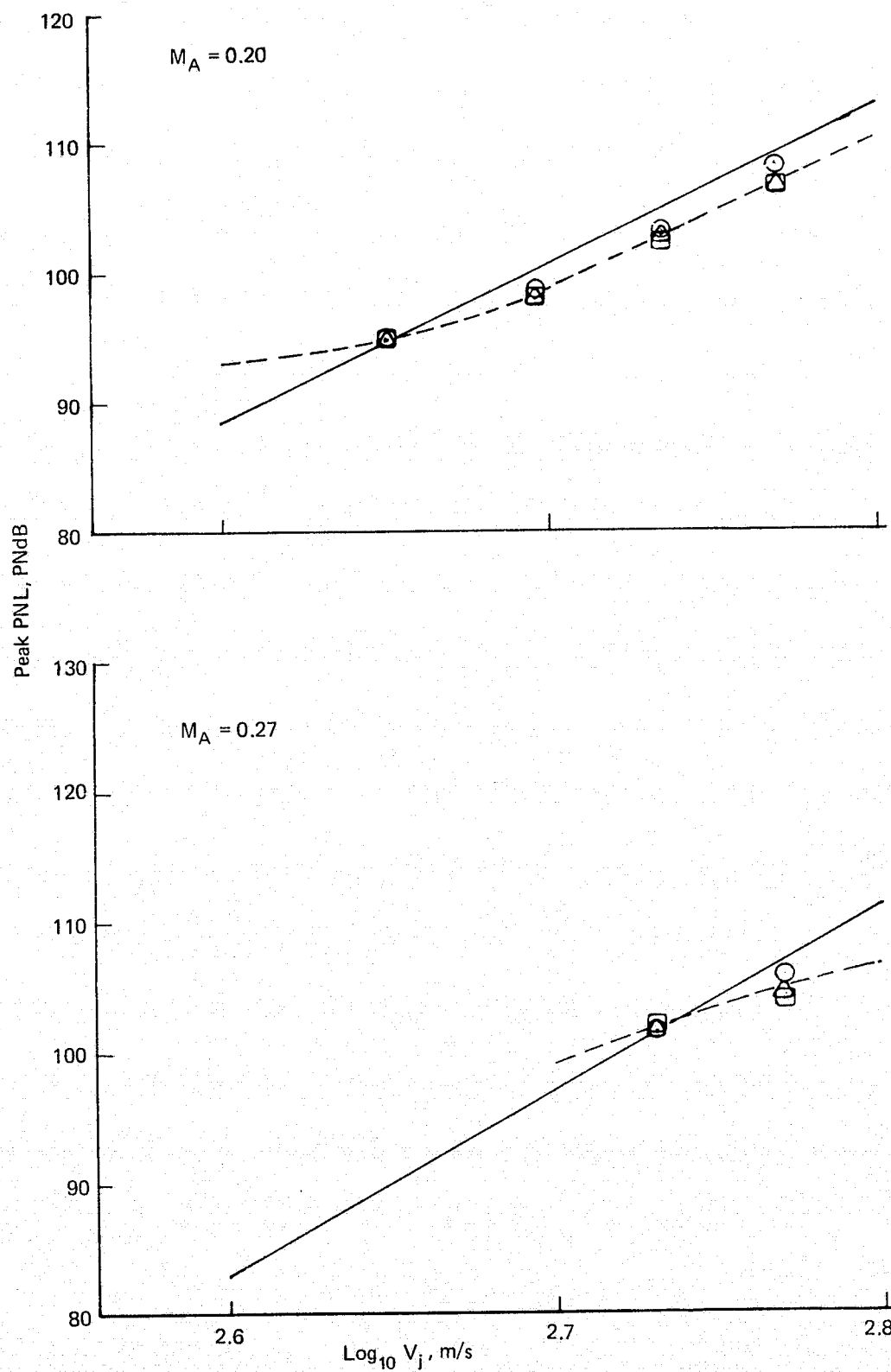


Figure 98.— (Concluded)

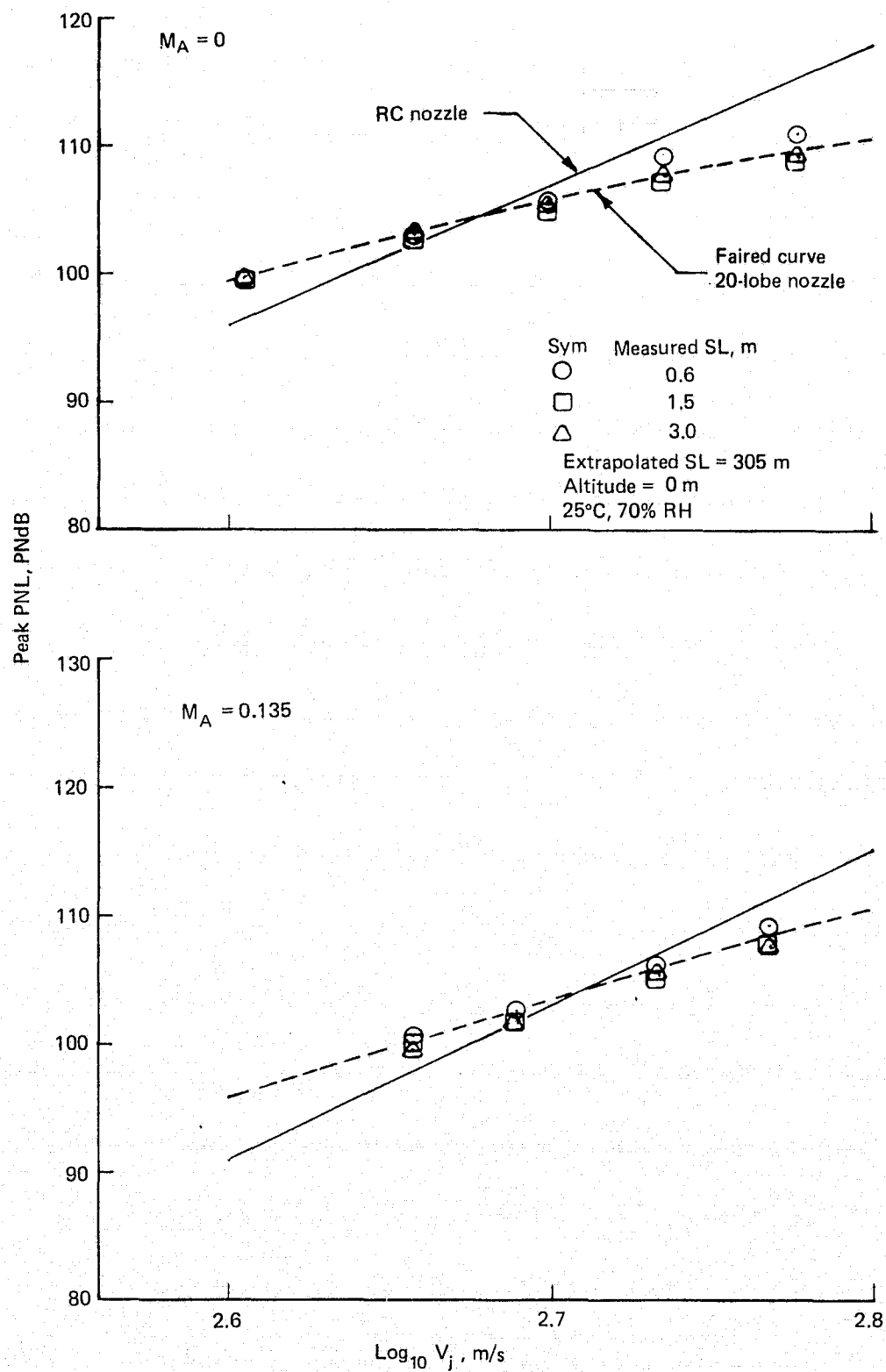


Figure 99.— Effect of Ambient Velocity on Peak PNL of a 20-Lobe Nozzle

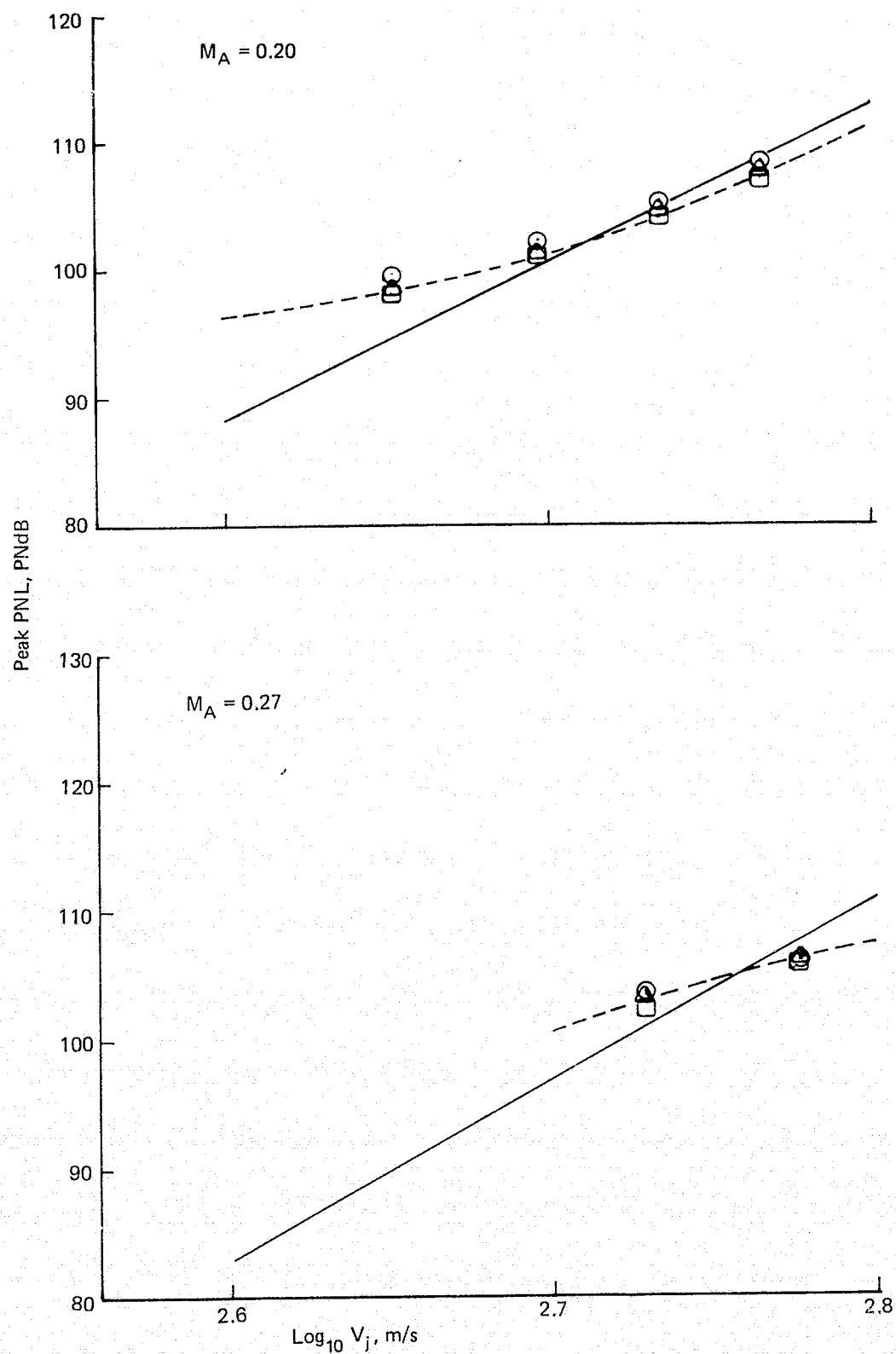


Figure 99.— (Concluded)

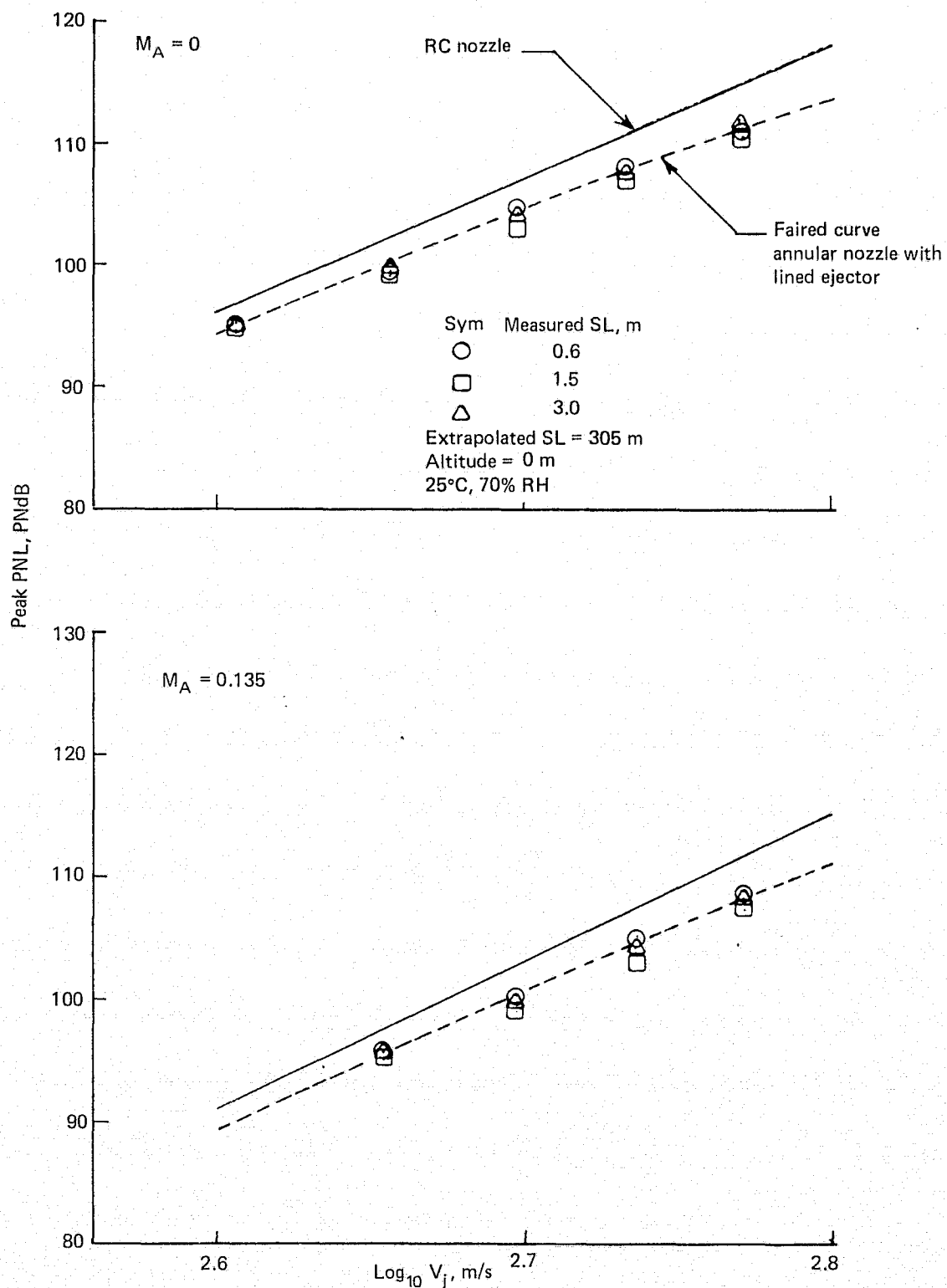


Figure 100.— Effect of Ambient Velocity on Peak PNL of an Annular Nozzle with Lined Ejector

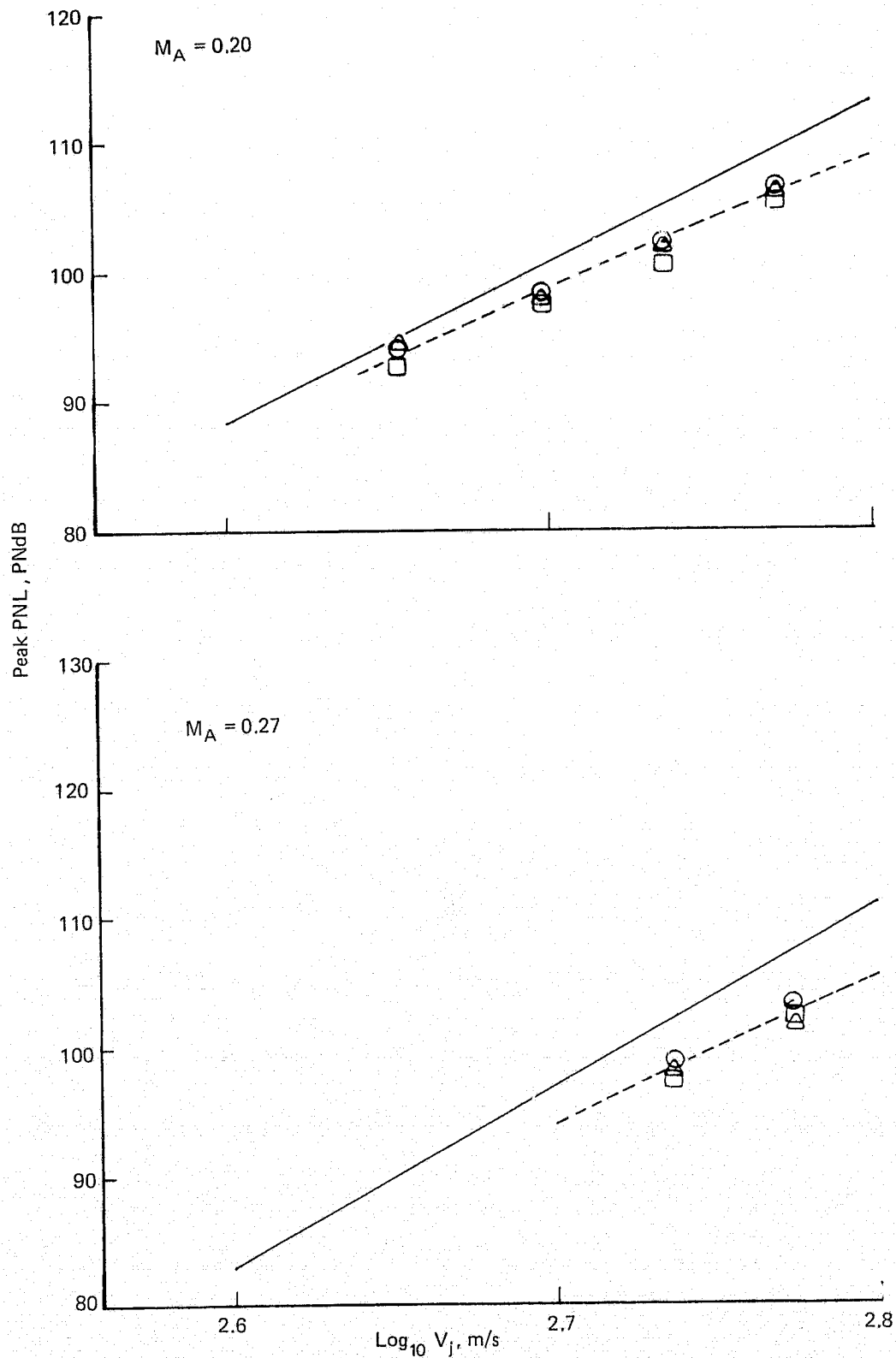


Figure 100.— (Concluded)

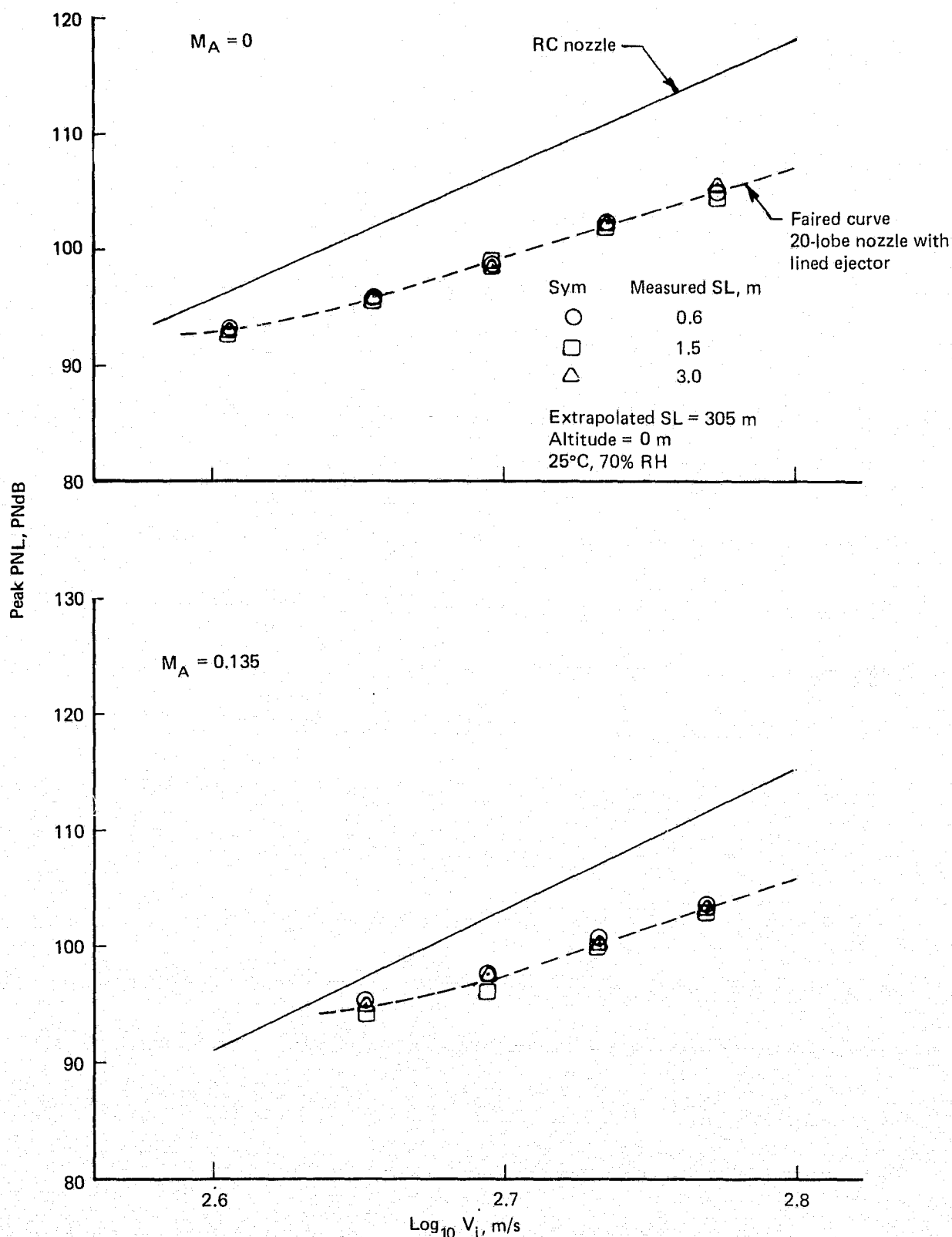


Figure 101.— Effect of Ambient Velocity on Peak PNL of a 20-Lobe Nozzle with Lined Ejector

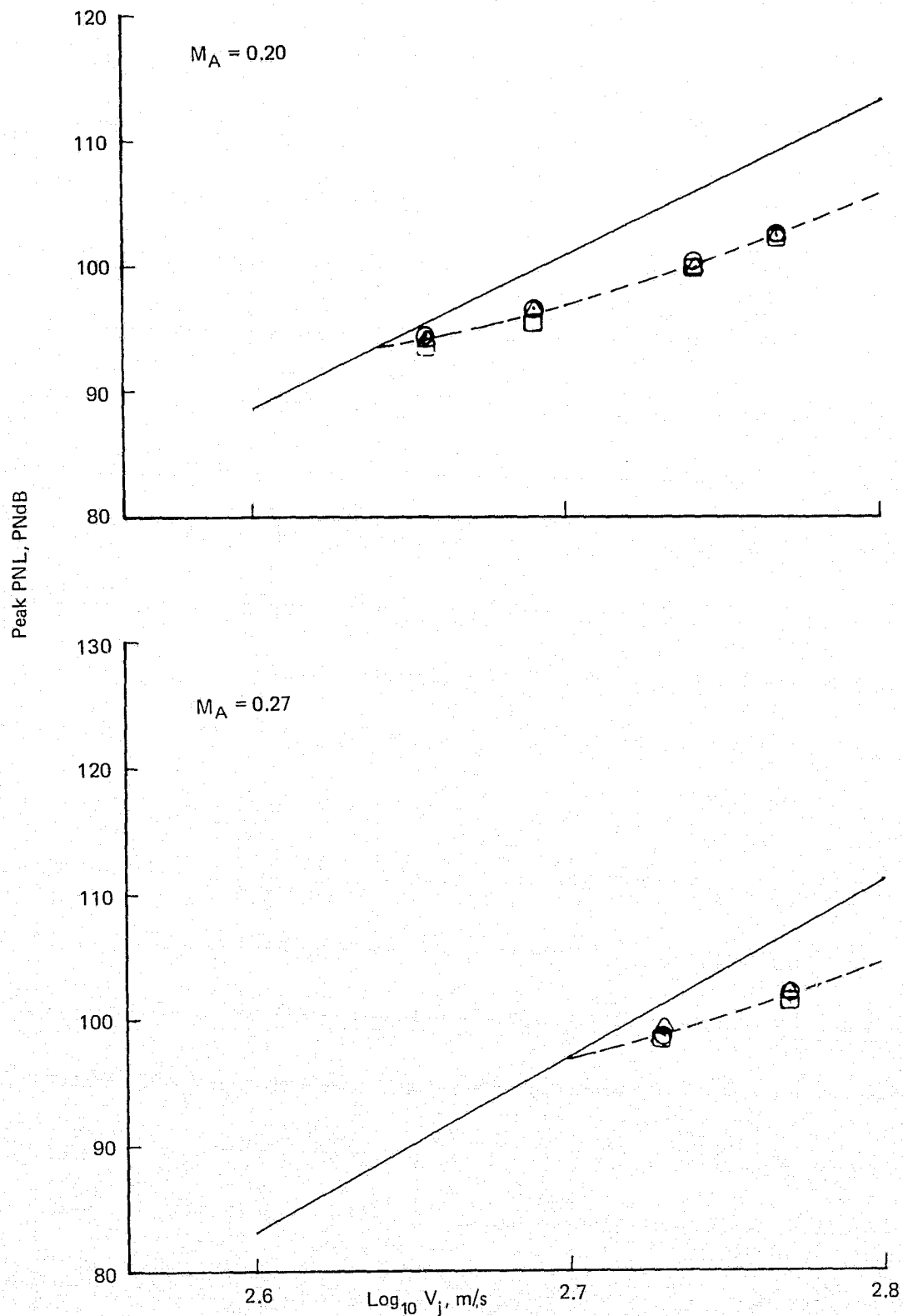


Figure 101.— Effect of Ambient Velocity on Peak PNL of a 20-Lobe Nozzle with Lined Ejector

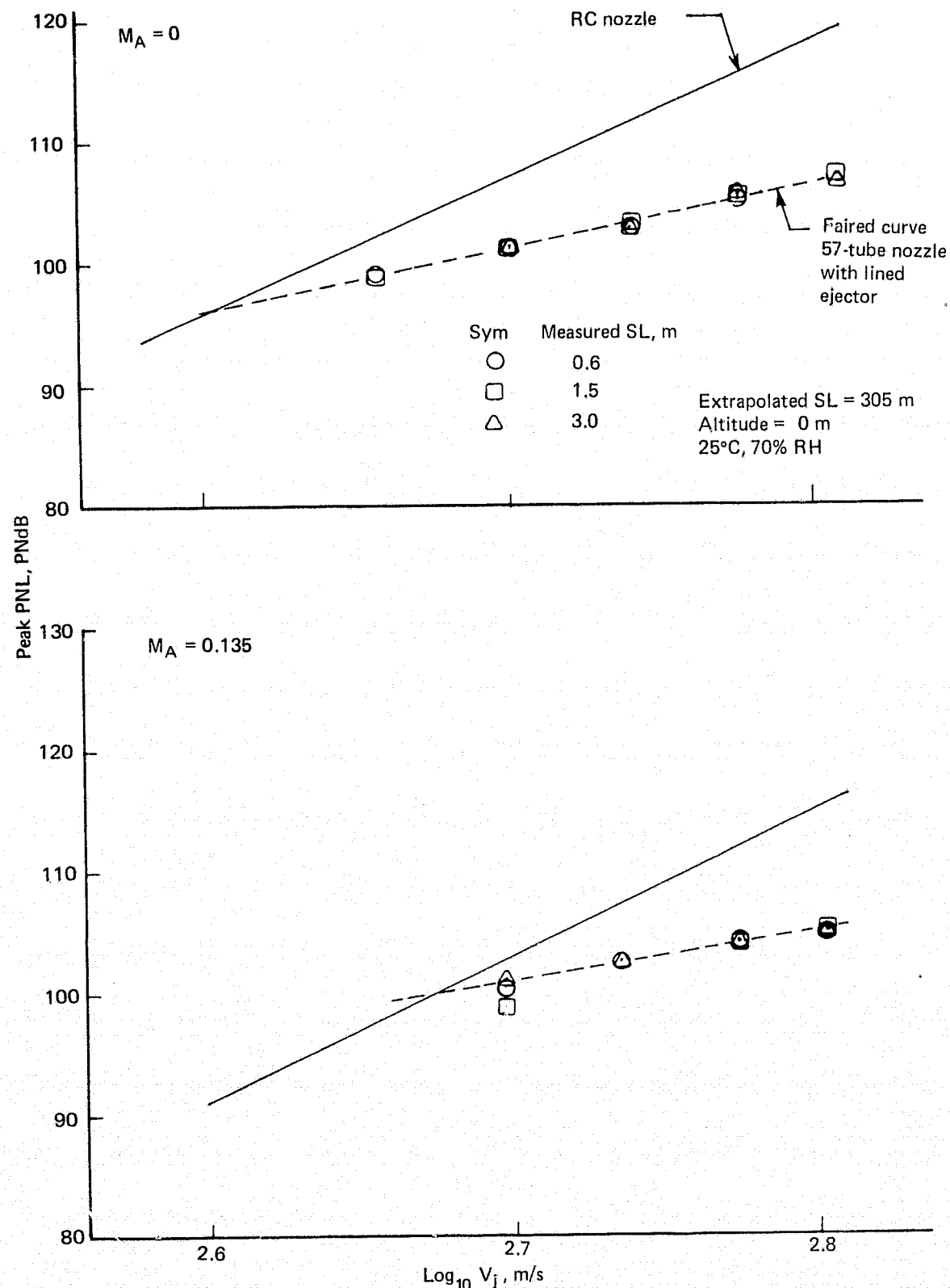


Figure 102.— Effect of Ambient Velocity on Peak PNL of a 57-Tube Nozzle with Lined Ejector

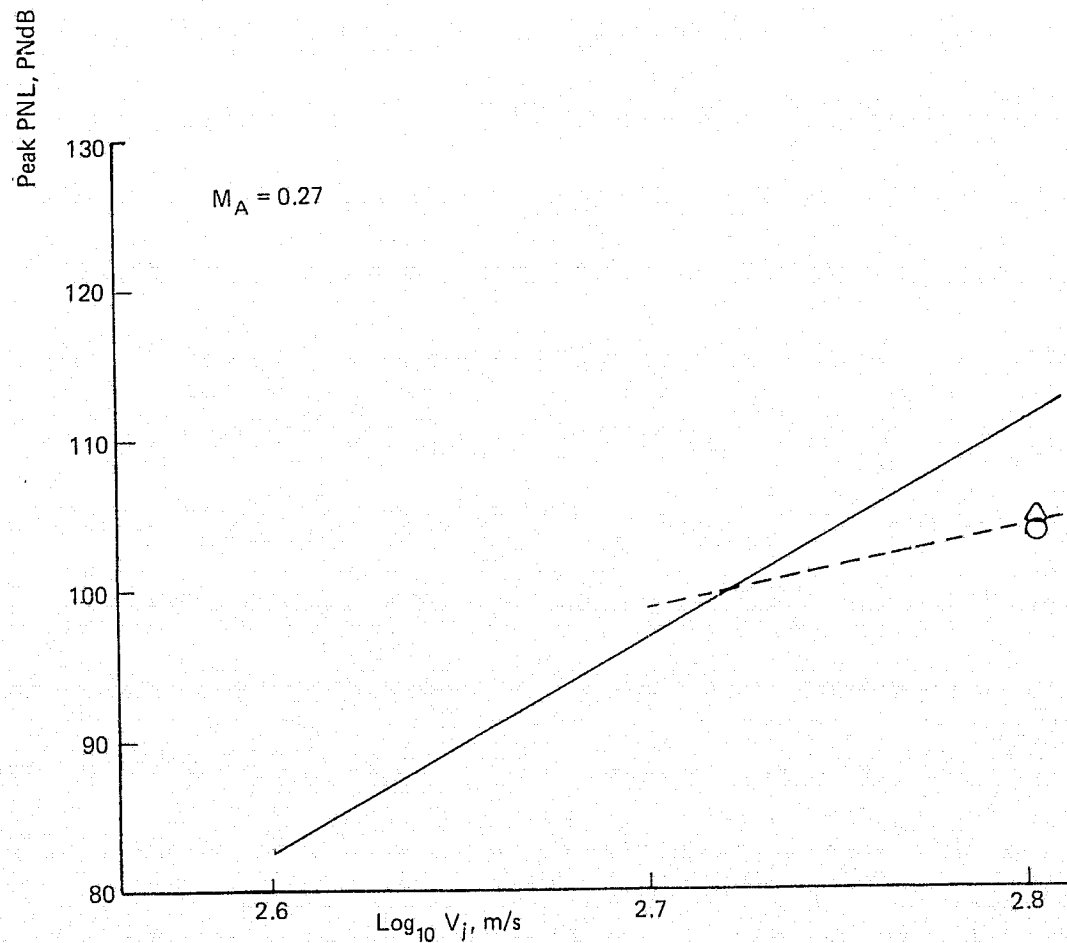
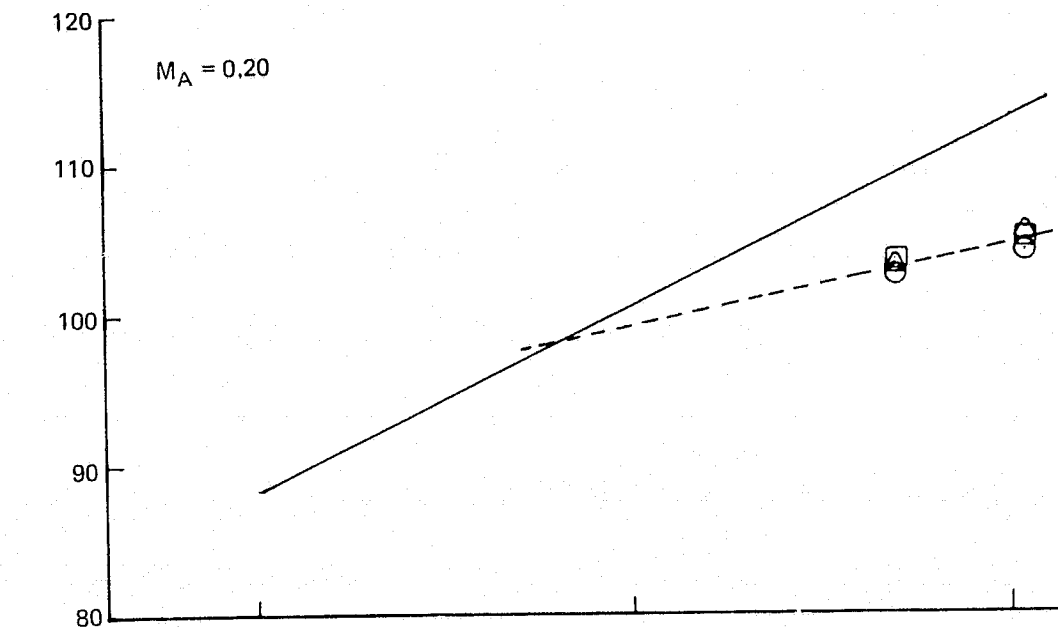


Figure 102.— (Concluded)

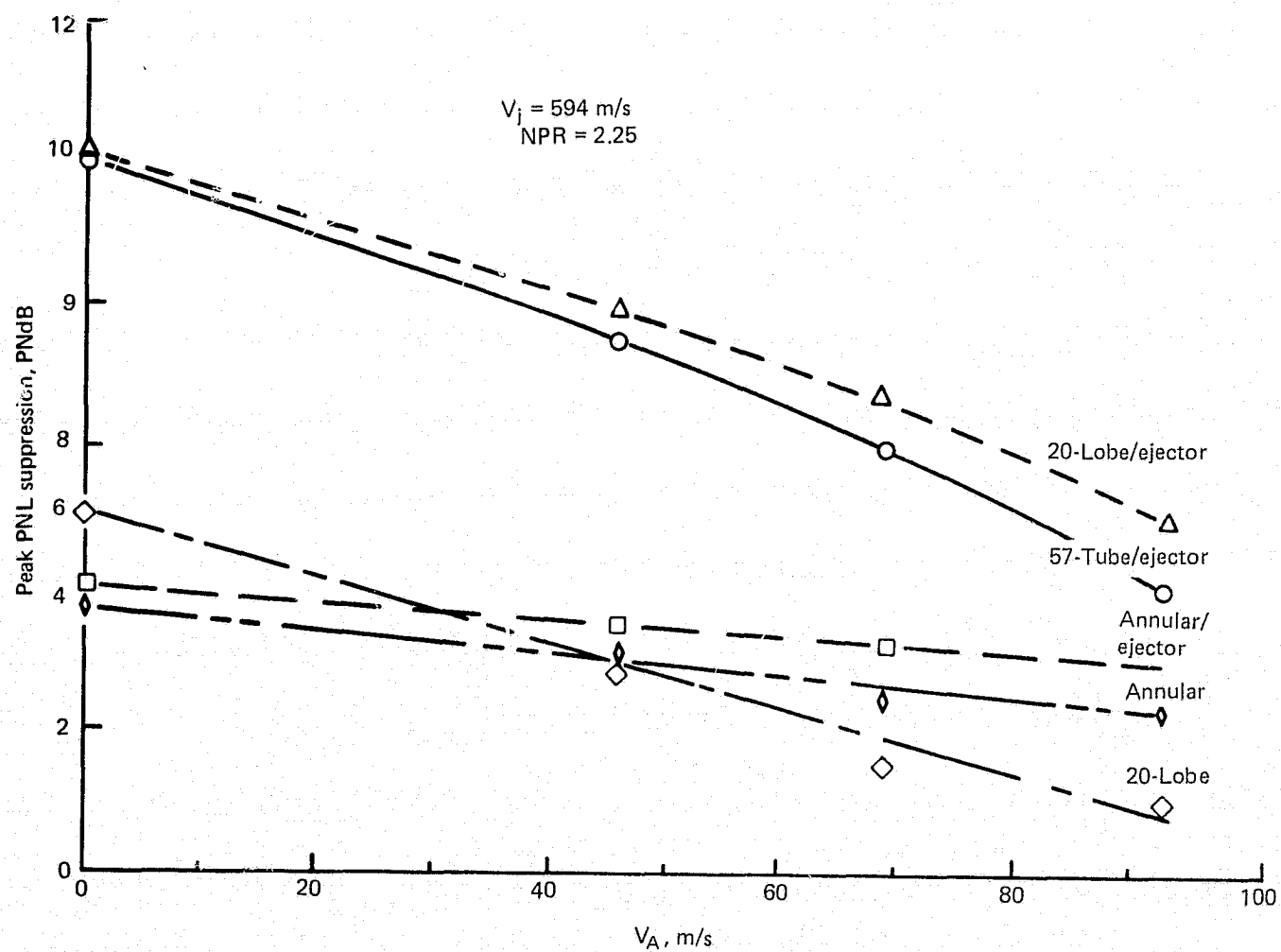


Figure 103.— Peak PNL Suppression Characteristics

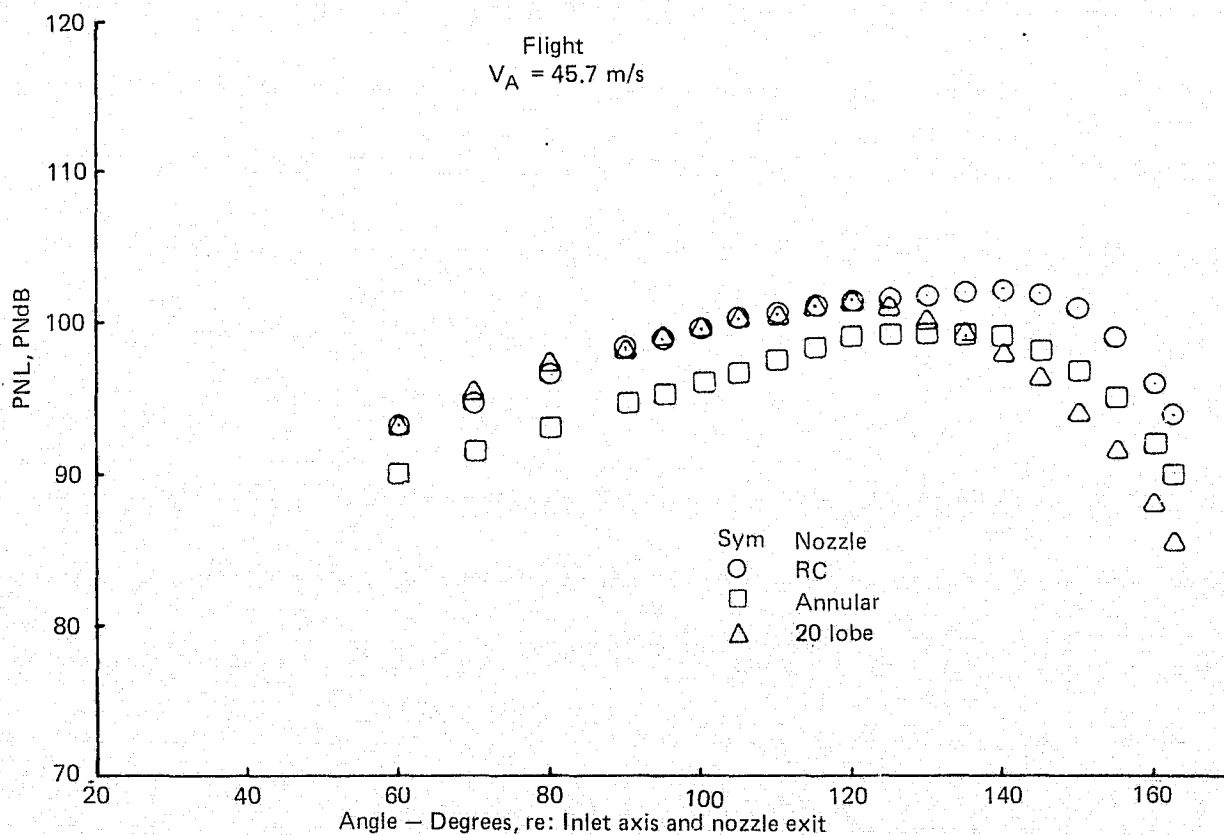
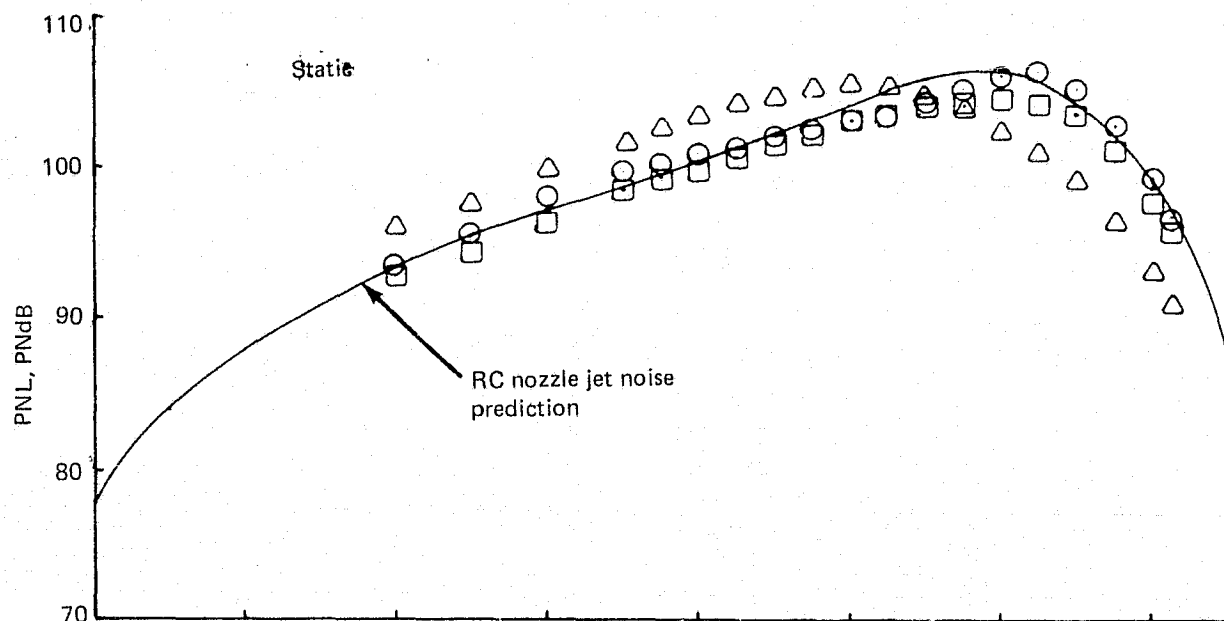


Figure 104.— Comparison of Baseline and Suppressor Nozzles on Basis of PNL Directivity
 $NPR = 1.75$ $V_j = 503 \text{ m/s}$

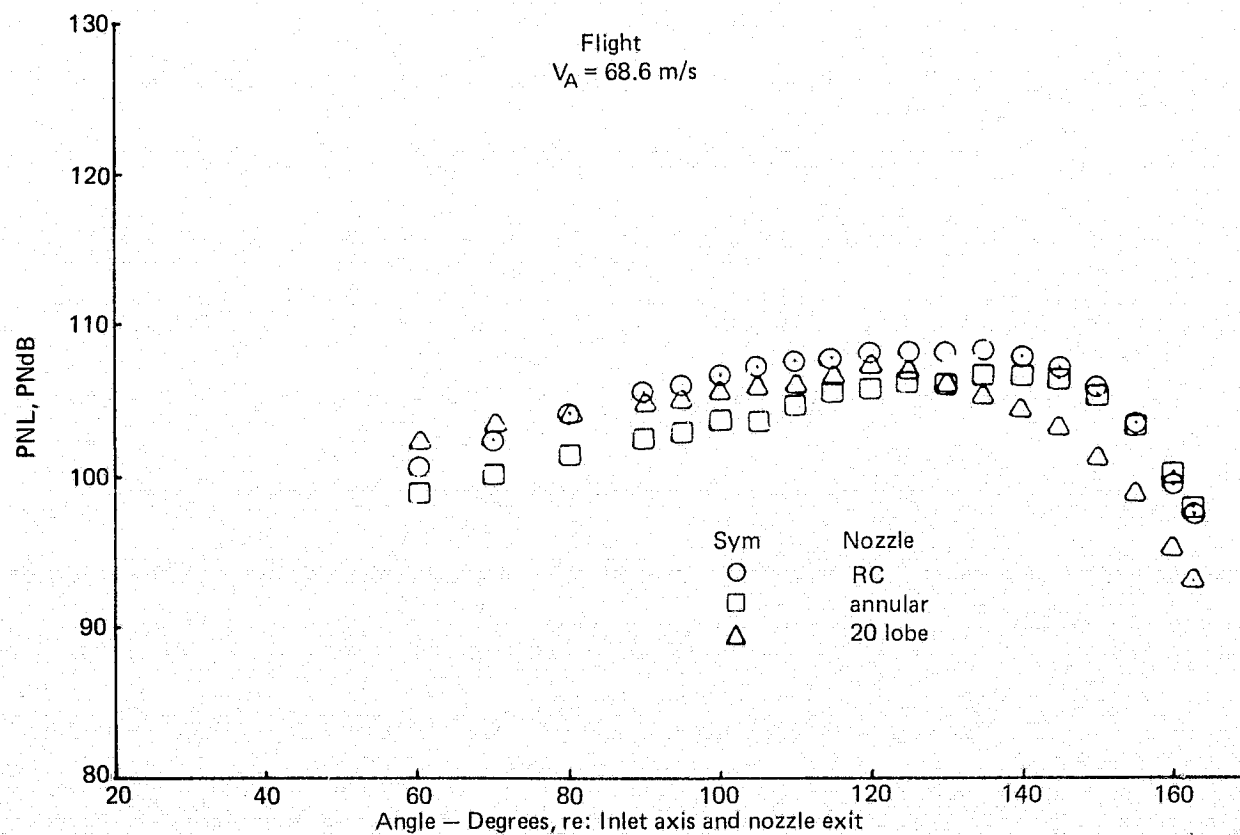
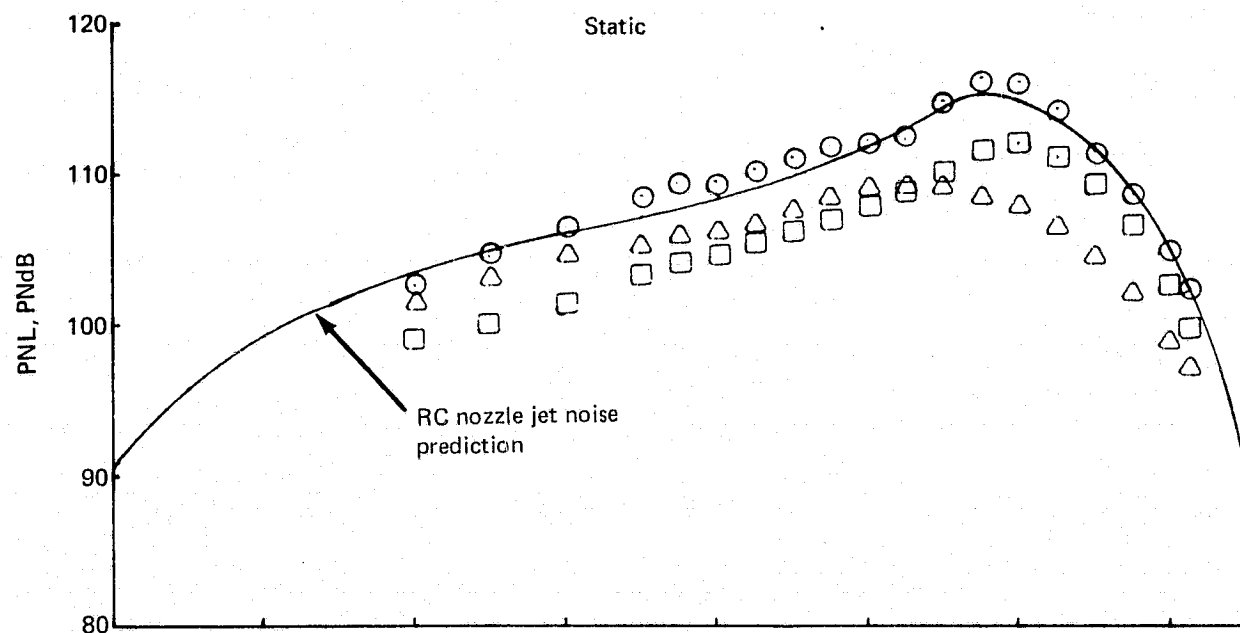


Figure 105.— Comparison of Baseline and Suppressor Nozzle on Basis of PNL Directivity
 $NPR = 2.25$ $V_j = 594 \text{ m/s}$

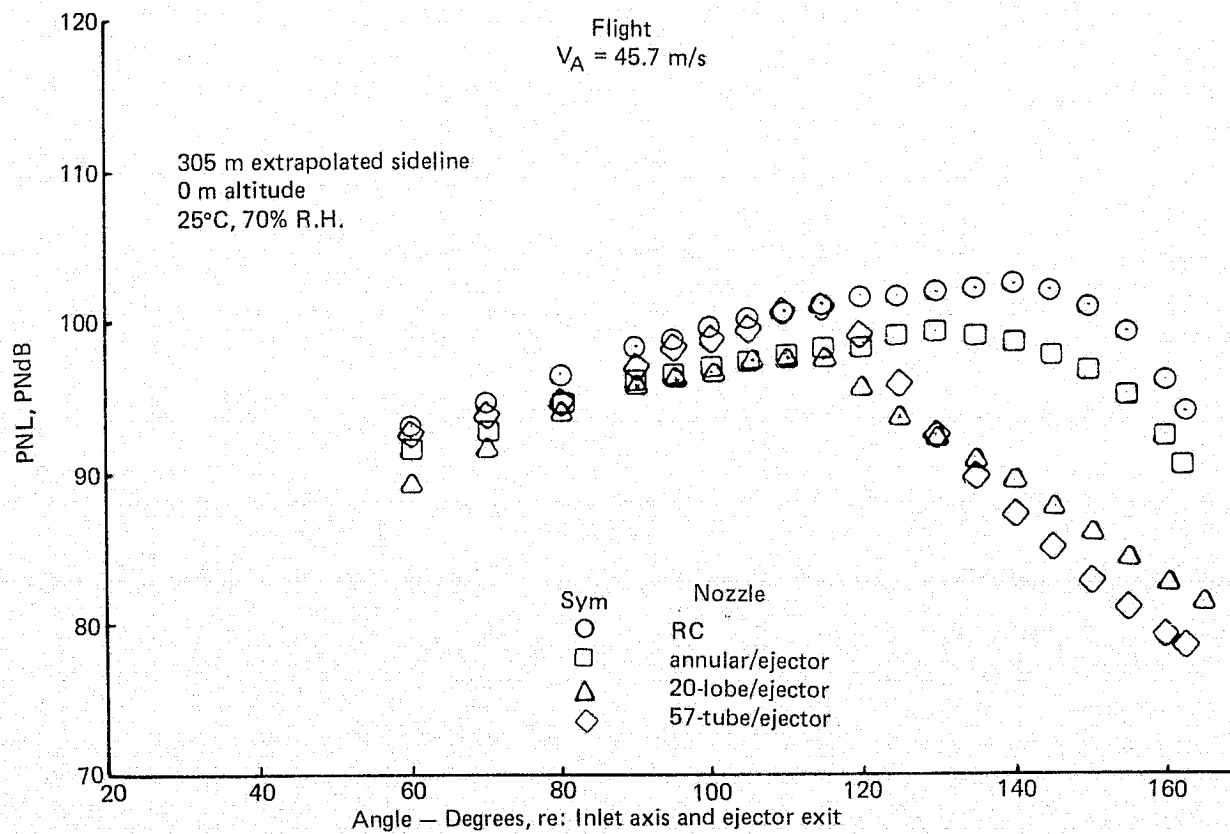
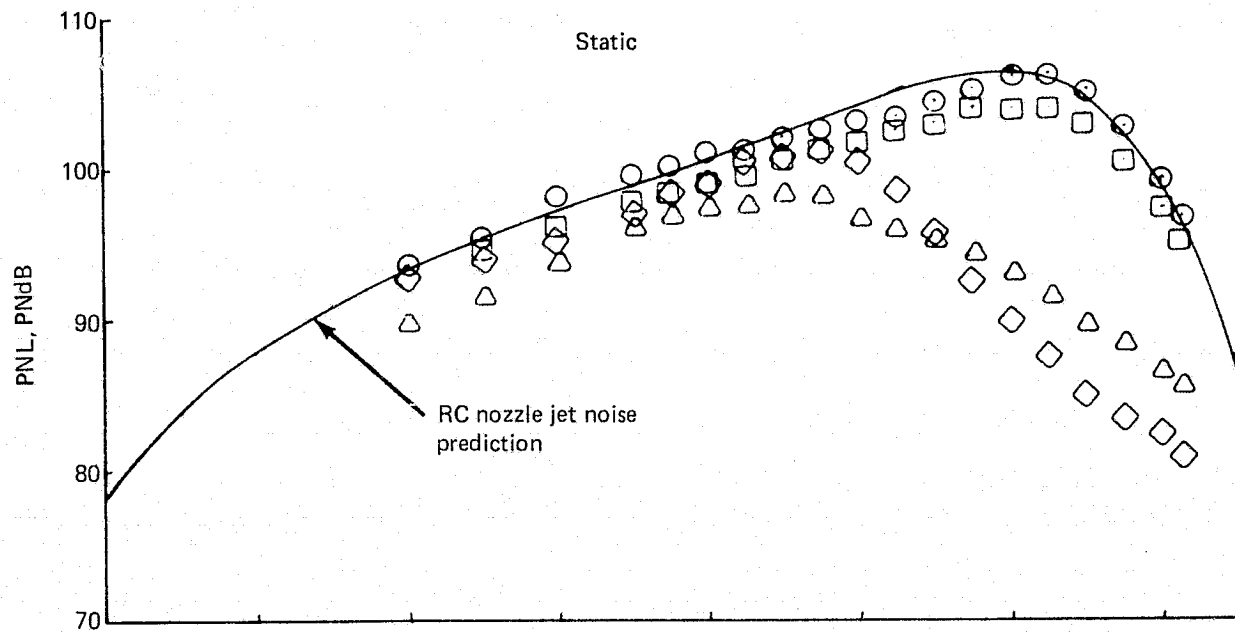


Figure 106.— Comparison of Baseline Nozzle and Suppressor Ejector Configurations on Basis of PNL Directivity $NPR = 1.75$ $V_j = 503 \text{ m/s}$

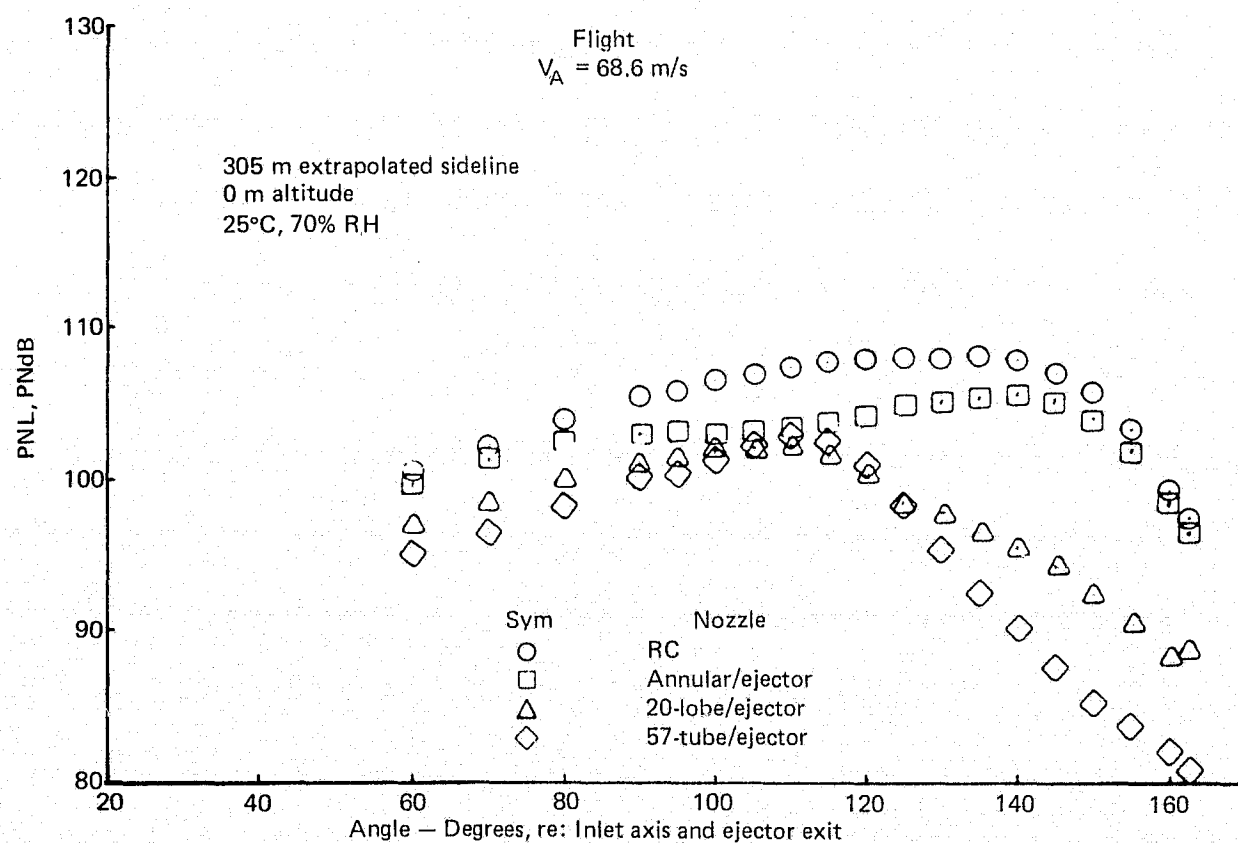
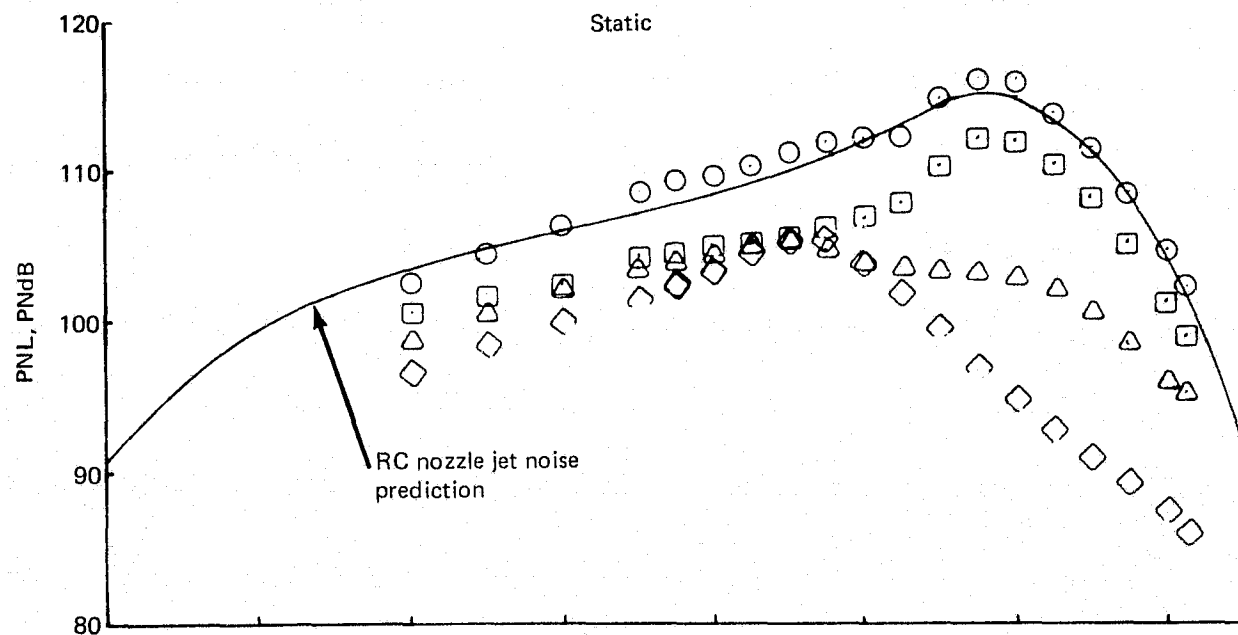


Figure 107.— Comparison of Baseline Nozzle and Suppressor Ejector Configurations on Basis of PNL Directivity NPR = 2.25 $V_j = 594 \text{ m/s}$

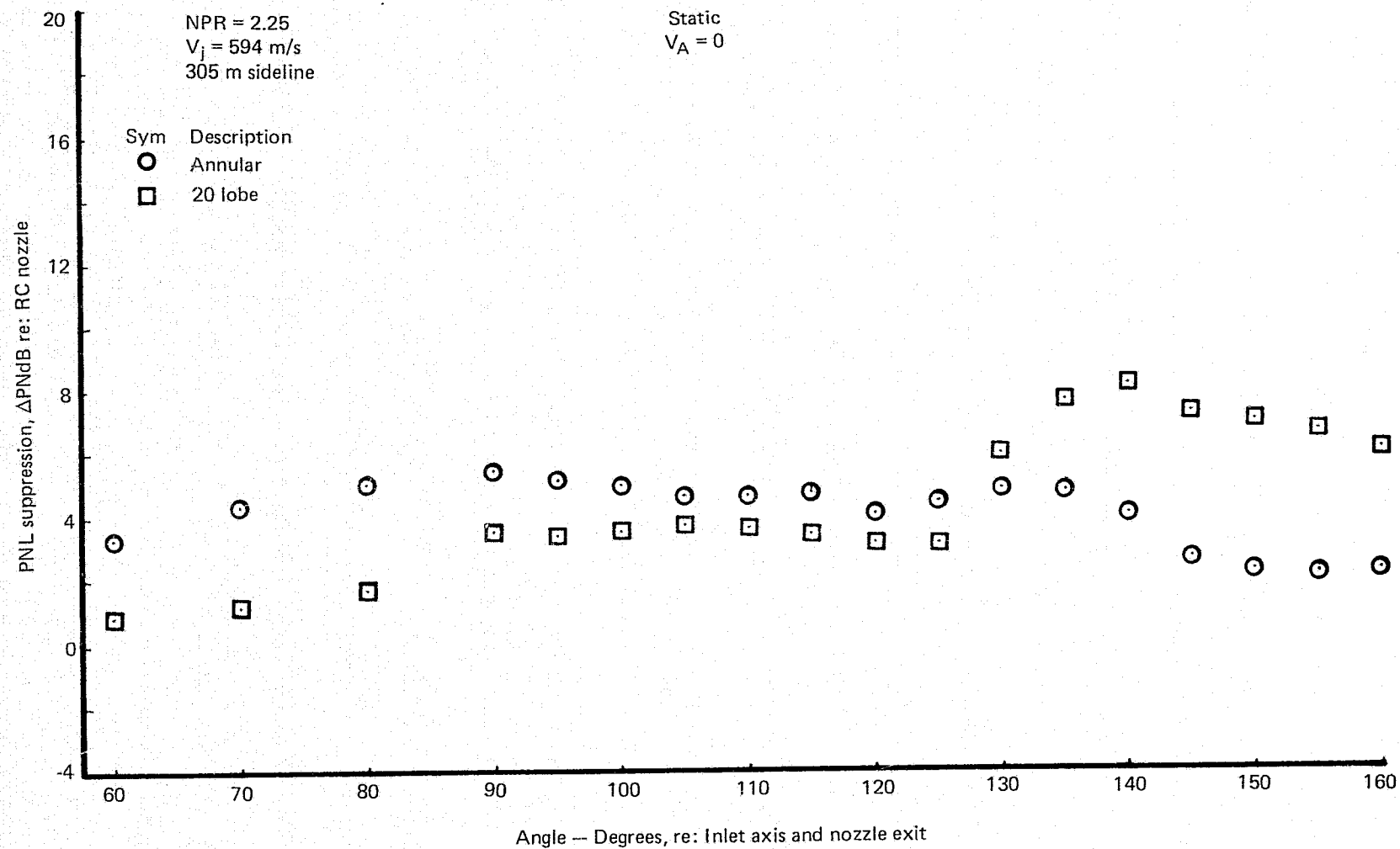


Figure 108.— PNL Suppression for the Suppressor Nozzles

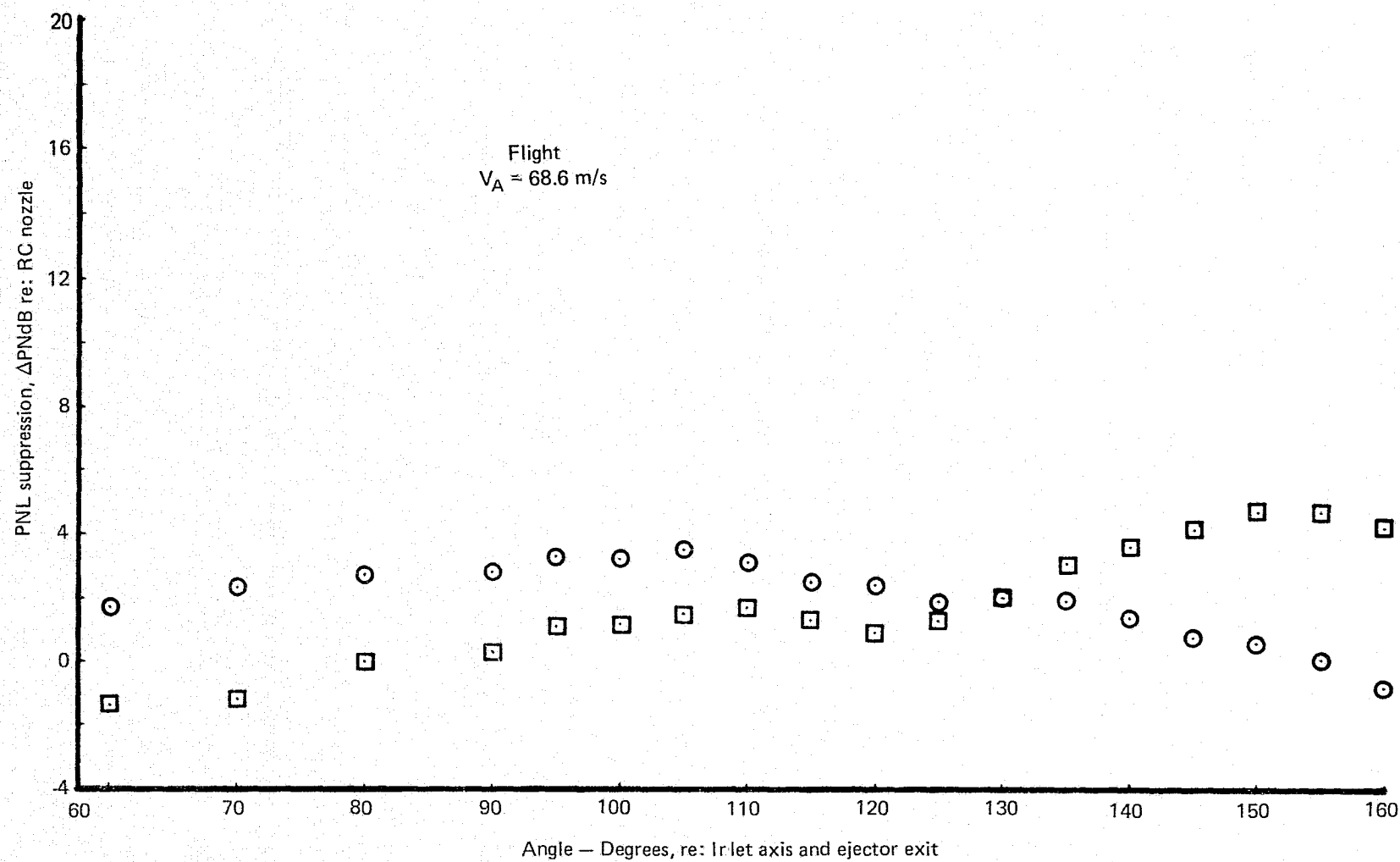


Figure 108.— (Concluded)

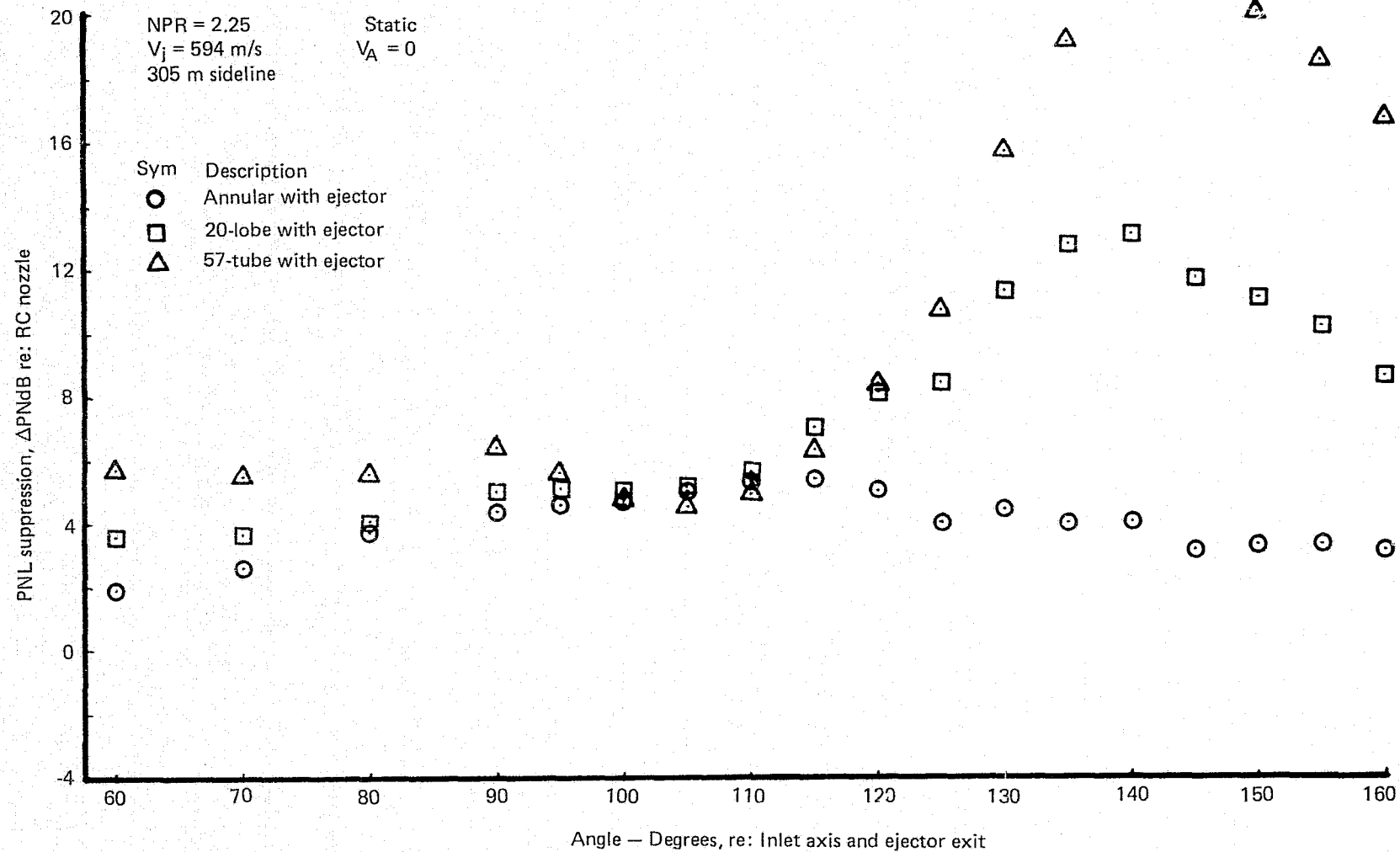
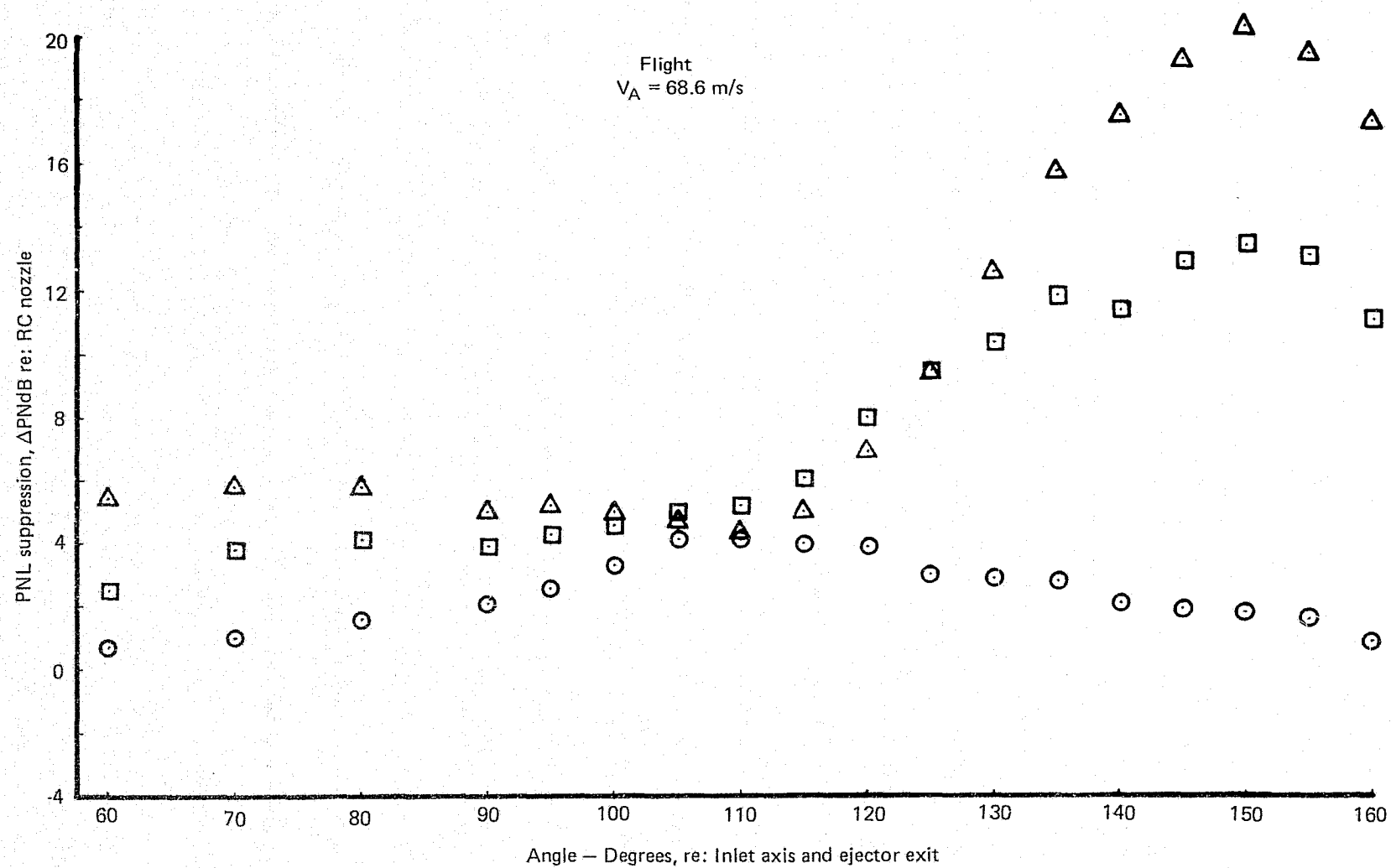


Figure 109.— PNL Suppression for the Suppressor Ejector Configurations

*Figure 109.— (Concluded)*

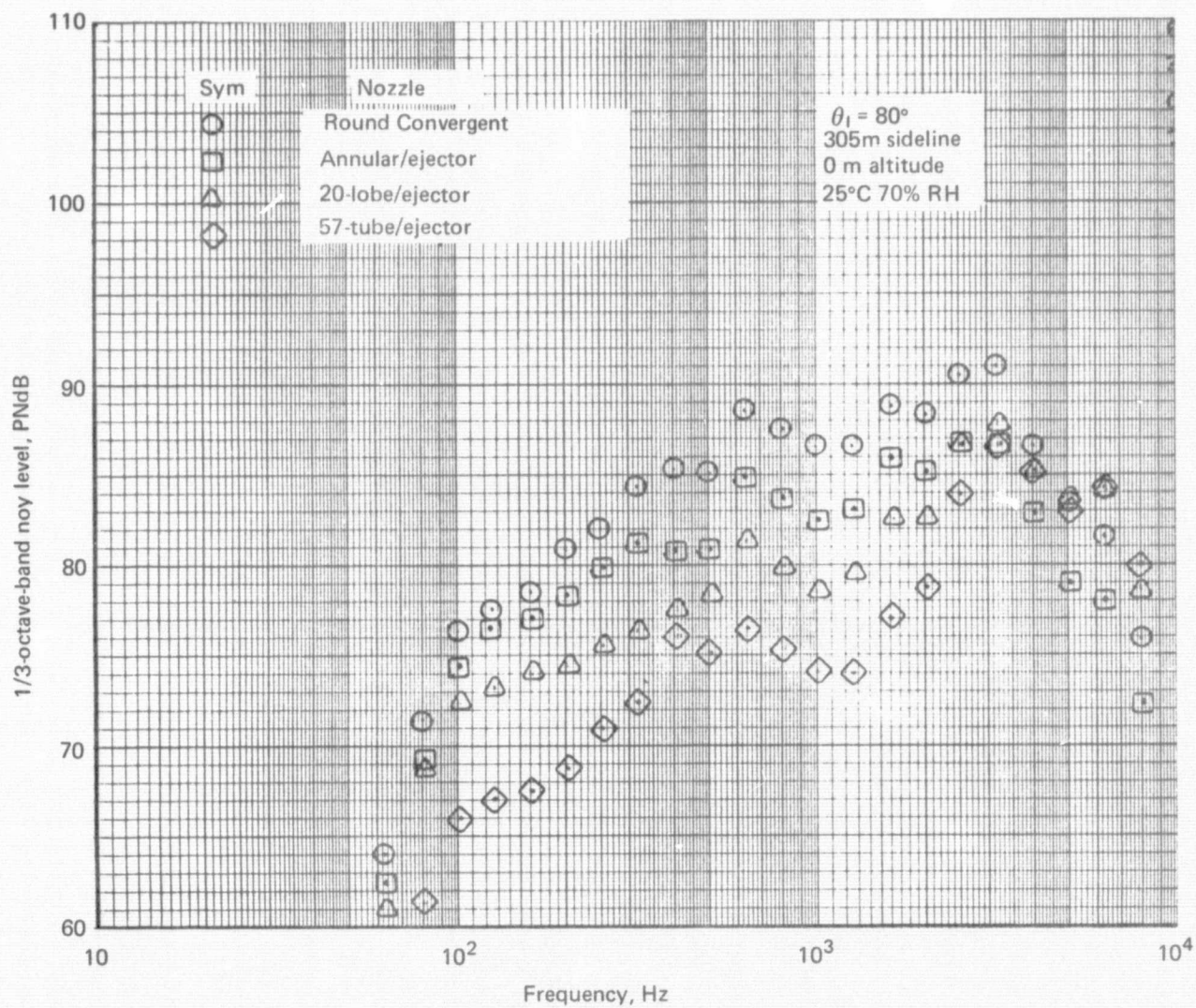


Figure 110.—Comparison of Static Noy Weighted Jet Noise Spectra for the Baseline and Suppressor Ejector Nozzles $NPR = 2.25$, $V_j = 594$ m/s, $V_A = 0$ M m/s

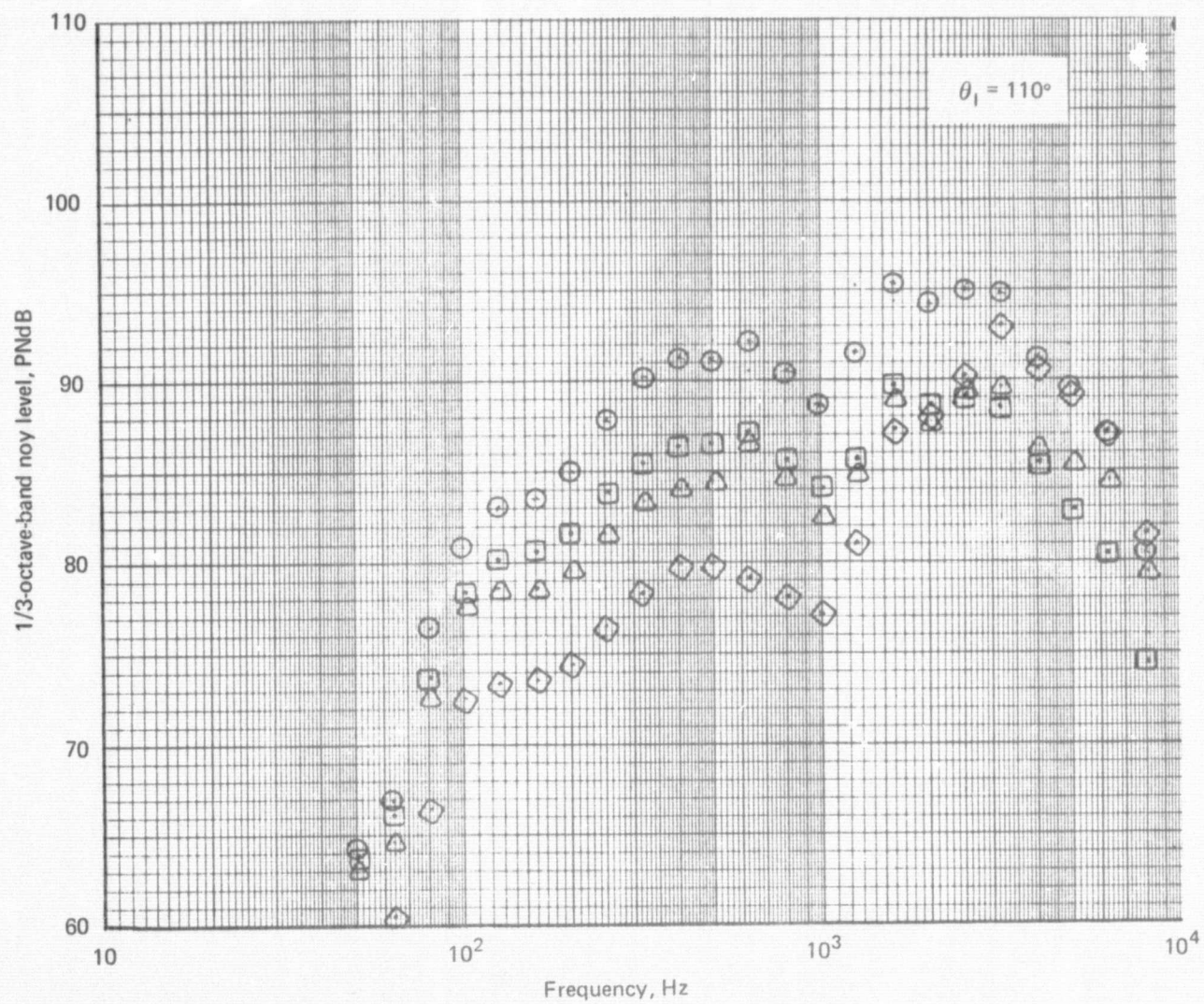


Figure 110.—(Continued)

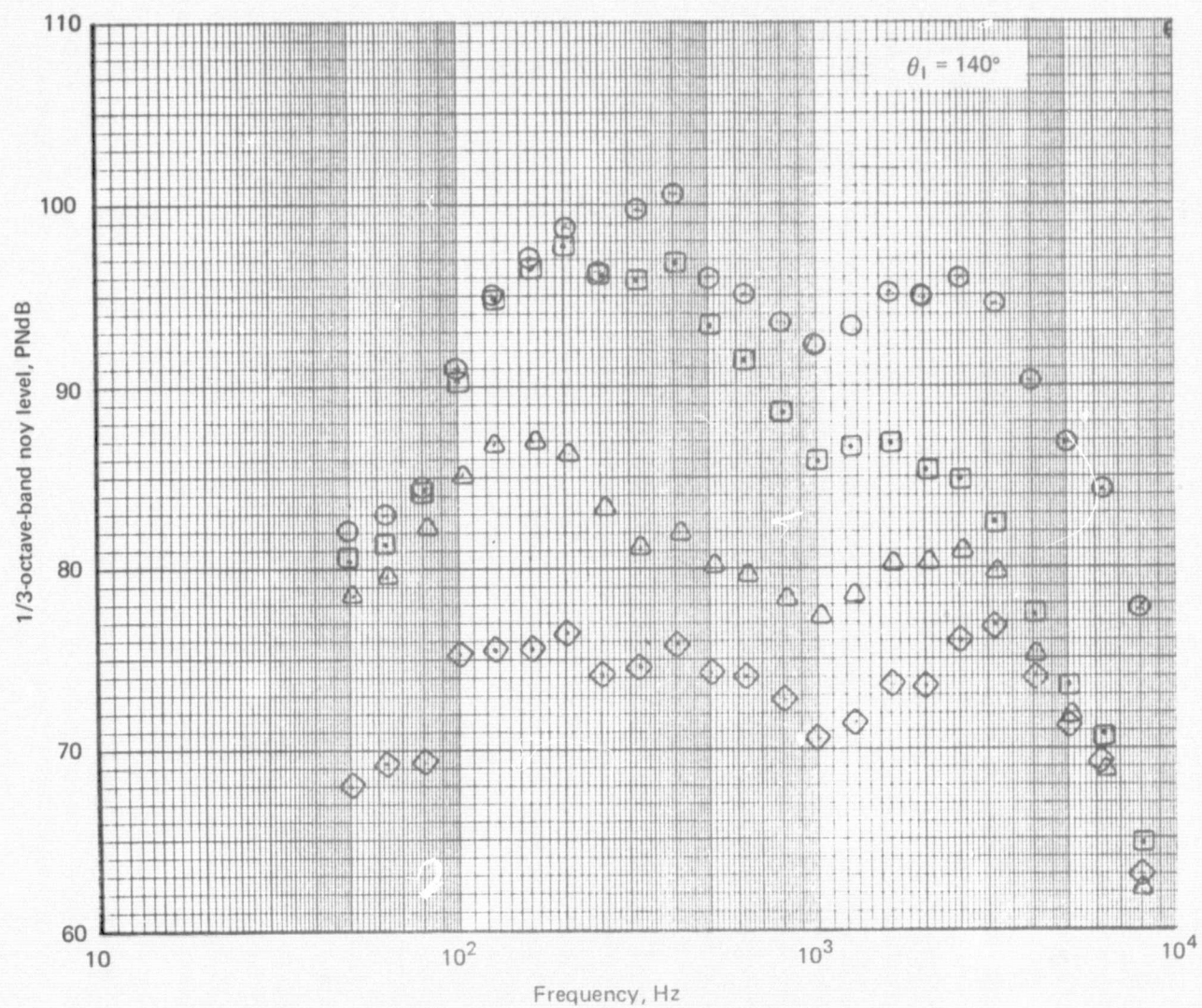


Figure 110.—(Concluded)

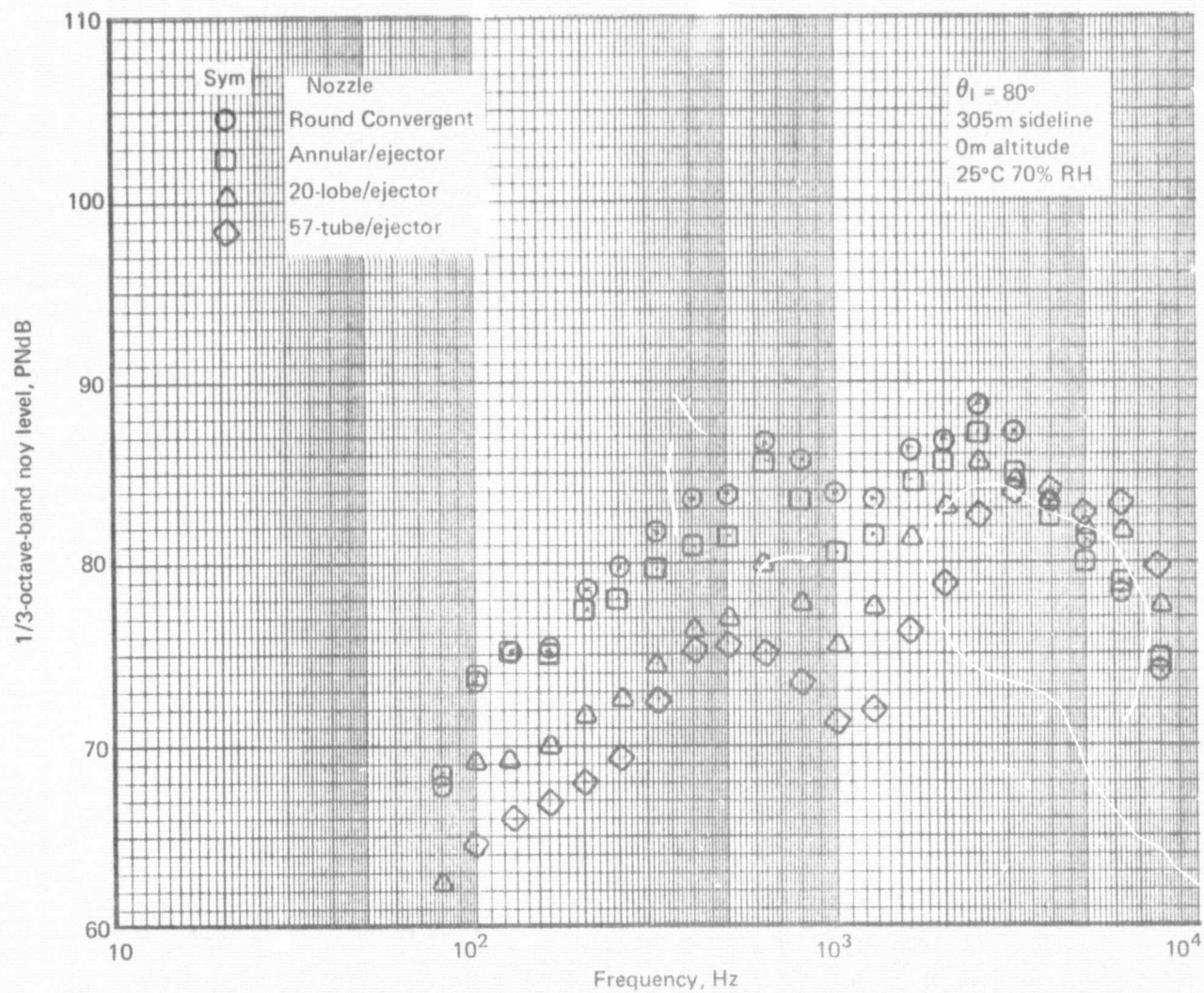


Figure 111.—Comparison of Flight Noy Weighted Jet Noise Spectra for the Baseline and Suppressor Ejector Nozzles $NPR = 2.25$, $V_j = 594$ m/s, $V_A = 68.6$ m/s

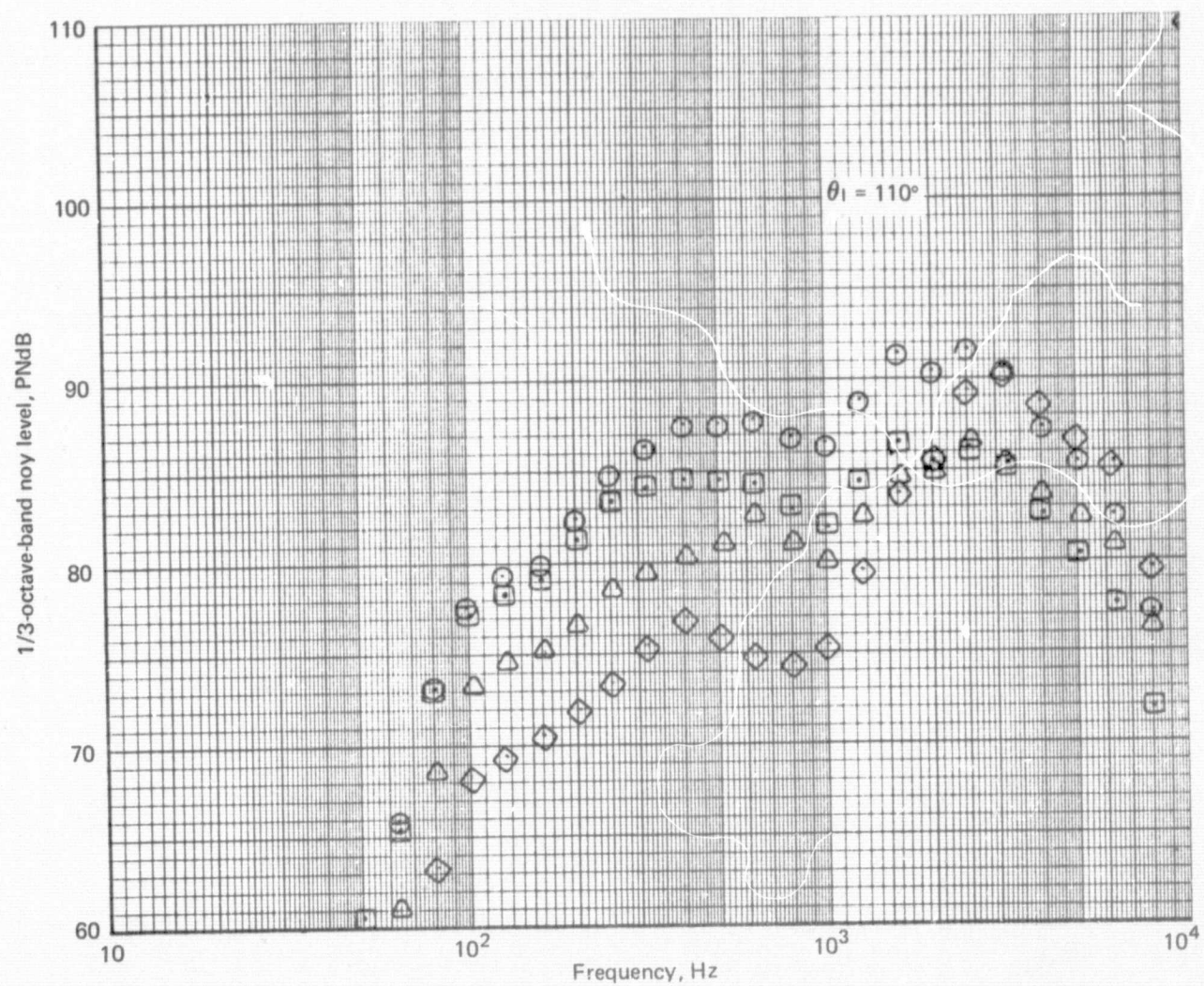


Figure 111 —(Continued)

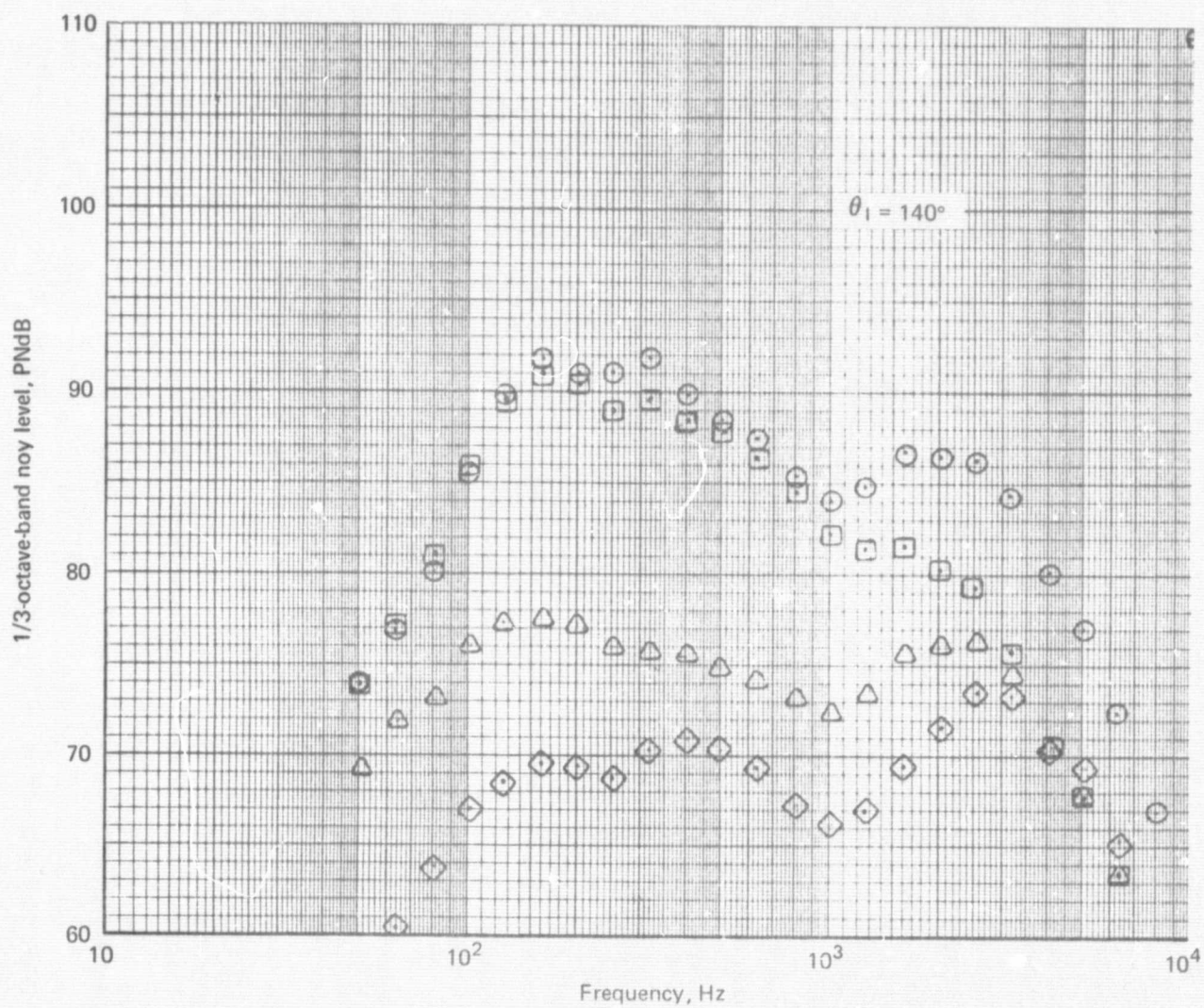


Figure 111.--(Concluded)